Studies in Computational Intelligence 651

Nilanjan Dey
Vikrant Bhateja
Aboul Ella Hassanien *Editors*

Medical Imaging in Clinical Applications

Algorithmic and Computer-Based Approaches

Springer

Studies in Computational Intelligence

Volume 651

Series editor

Janusz Kacprzyk, Polish Academy of Sciences, Warsaw, Poland
e-mail: kacprzyk@ibspan.waw.pl

About this Series

The series "Studies in Computational Intelligence" (SCI) publishes new developments and advances in the various areas of computational intelligence—quickly and with a high quality. The intent is to cover the theory, applications, and design methods of computational intelligence, as embedded in the fields of engineering, computer science, physics and life sciences, as well as the methodologies behind them. The series contains monographs, lecture notes and edited volumes in computational intelligence spanning the areas of neural networks, connectionist systems, genetic algorithms, evolutionary computation, artificial intelligence, cellular automata, self-organizing systems, soft computing, fuzzy systems, and hybrid intelligent systems. Of particular value to both the contributors and the readership are the short publication timeframe and the worldwide distribution, which enable both wide and rapid dissemination of research output.

More information about this series at http://www.springer.com/series/7092

Nilanjan Dey · Vikrant Bhateja
Aboul Ella Hassanien
Editors

Medical Imaging in Clinical Applications

Algorithmic and Computer-Based Approaches

Springer

Editors
Nilanjan Dey
Techno India College of Technology
Kolkata, West Bengal
India

Vikrant Bhateja
Shri Ramswaroop Memorial Group of
Professional Colleges (SRMGPC)
Lucknow, Uttar Pradesh
India

Aboul Ella Hassanien
Faculty of Computers and Information
Cairo University
Giza
Egypt

ISSN 1860-949X ISSN 1860-9503 (electronic)
Studies in Computational Intelligence
ISBN 978-3-319-33791-3 ISBN 978-3-319-33793-7 (eBook)
DOI 10.1007/978-3-319-33793-7

Library of Congress Control Number: 2016939377

Printed on acid-free paper

This Springer imprint is published by Springer Nature
The registered company is Springer International Publishing AG Switzerland

Preface

Recently, developments in the domain of biomedical sensing and imaging along with its associated clinical applications attract the focus of researchers. The main goal is to develop algorithmic and computer-based approaches to design efficient CAD systems using medical images obtained through various imaging modalities. The application of computer-based approaches to medical applications has opened numerous challenging problems for both the medical computing field and the mathematical community. CAD systems are often utilized to achieve accurate diagnosis, which provide early detection of life-threatening diseases.

This volume comprises of 21 chapters, including two overview chapters, abdominal imaging in clinical applications supported computer-aided diagnosis approaches as well as different techniques for solving the pectoral muscle extraction problem in the preprocessing part of the CAD systems for detecting breast cancer in its early stage using digital mammograms. Afterward, some chapters related to swarms-based segmentation in several medical applications are involved. These chapters included segmentation framework that is based on fractional-order Darwinian particle swarm optimization (FODPSO) and mean shift (MS) techniques, 3D brain tumor segmentation based on hybrid clustering techniques using multi-views of MRI, and an automatic segmentation method that performs multilevel image thresholding by using the spatial information encoded in the gray-level co-occurrence matrix (GLCM). Moreover, some chapters proposed several classification techniques including comparison of CAD systems for three class breast tissue density classification using mammographic images, developing novel automated glaucoma diagnosis system which analyze and classify retinal images using based on feature selection and static classifier selection schemes, proposing automated classification of ultrasound liver tumors using support vector machine (SVM) with the aid of fuzzy c-means (FCM) and level set method, and classification of motor imagery BCI based on variable precision multigranulation rough set and game theoretic. Furthermore, other chapters that included an ultrasound-based three-dimensional computer-aided diagnosis (CAD) tool for the diagnosis of anterior Talofibular ligament, introducing an advancements of

electroanatomic mapping systems, providing details about the approaches for development of methods for image quality assessment followed by brief introduction on existing image quality assessment methods, discussing a human–computer interface (HCI)-based novel approach for designing a computer-aided control and communication system using electrooculogram (EOG) and electromyogram (EMG) signals for people with severe hindrance to motor activities and communication and highlighted the theory of parallel MRI and Cartesian SENSE reconstruction. Finally, some chapters are concerned with an elaborate and illustrative discussion about various bioinformatics tools used for gene prediction; sequence/phylogenetic analysis as well as function prediction, realizing a decision support system based on the technique of case-based reasoning and dedicated to the diagnosis of a very dangerous pulmonary pathology, and describing various gene structure prediction programs which based on individual/hybrid soft computing approaches as a bioinformatics approach.

We would like to express gratitude to the authors for their contributions. It would not have been possible to reach this publication quality without the contributions of the many anonymous referees involved in the revision and acceptance process of the submitted manuscripts. Our gratitude is extended to them as well. It is expected very good promote for almost all readers for this book—from undergraduate students to postgraduate levels and also for researchers, professionals, and engineering. As the editors, we wish this book will stimulate further research in medical imaging applications based algorithmic- and computer-based approaches and utilize them in real-world clinical applications. We would like to thank also the reviewers for their diligence in reviewing the chapters. Special thanks go to our publisher, Springer.

We hope that this book will present promising ideas and outstanding research results supporting further development of computer-based approaches in medical imaging for clinical applications.

Nilanjan Dey
Vikrant Bhateja
Aboul Ella Hassanien

Contents

Part I
Clinical Applications of Medical Imaging

Abdominal Imaging in Clinical Applications: Computer Aided Diagnosis Approaches

Amira S. Ashour, Nilanjan Dey and Waleed S. Mohamed

Abstract Computer aided diagnosis (CAD) is considered one of the main research subjects in medical image processing and diagnostic radiology. The development of CAD systems would provide anatomical knowledge coupled with image processing procedures to improve diagnosis/healthcare. For accurate diagnosis and treatment, researchers are interested with clinical image analysis. Since, the abdominal organs are characterized by complexity and high inconsistency. Thus, the identification of distinct algorithms to model the organs and abnormalities it is vital for understanding anatomy and disease. Moreover, a survey on CAD based abdominal image enhancement, segmentation, classification and fusion is included. Finally, challenging topics are addressed to explore new fields for development.

Keywords Computer aided diagnosis · Medical image processing · Abdominal imaging · Magnetic resonance imaging · Computed tomography · X-ray

A.S. Ashour (✉)
Faculty of Engineering, Department of Electronics and Electrical Communications Engineering, Tanta University, Tanta, Egypt
e-mail: amirasashour@yahoo.com

A.S. Ashour
CIT College, Taif University, Taif, Kingdom of Saudi Arabia

N. Dey
Department of Information Technology, Techno India College of Technology, Kolkata, India

W.S. Mohamed
Faculty of Medicine, Internal Medicine, Tanta University, Tanta, Egypt

W.S. Mohamed
Medicine College, Taif University, Taif, Kingdom of Saudi Arabia

N. Dey et al. (eds.), *Medical Imaging in Clinical Applications*,
Studies in Computational Intelligence 651, DOI 10.1007/978-3-319-33793-7_1

1 Introduction

Clinical imaging plays a crucial role in the continuum of abdominal diseases diagnosis, prognosis, and treatment assessment. Imaging studies are concerned with the identification of the location, size, and features of the organ under concern. Over the past decade, image processing in radiological imaging have developed to be currently considered a crucial tool for extracting instructive information from the enormous amount of data. Thus, researchers' intensive focus is attracted to medical image processing and analysis [1, 2]. In the medical domain, it is significant to assess the relation between accurate diagnosis and treatment. Consequently, medical imaging which refers to several diverse technologies is used to view the human body for diagnoses and monitoring medical conditions. Different modalities are invented and developed for the target of collecting data that assist diagnosis as well as holistic process of research that consists of data (in the form of signals and/or images) collection, data evaluation and decision-making. It is used for the visualization of body parts, organs, tissues, for clinical diagnosis, disease monitoring and thus proper treatment. Therefore, medical images are very supportive to diagnose diseases, support the anatomy of the human body, pathological lesion detection, therapeutic management of the patient and to presume diverse problems in the medical field. Consequently, diverse methods of diverse modalities in medical imaging techniques can be employed for the abdomen, such as: Computed Tomography (CT), Magnetic Resonance Imaging (MRI), Positron Emission Tomography (PET), Single-photon emission computed tomography (SPECT), X-ray, Endoscopy, Ultrasound as well as Microscopic imaging [3–5]. These medical imaging techniques encompass various fields that used for imaging the different abdomen parts.

There are diverse abdominal diseases such as the Peptic ulcer, Cholcystitis, Cancer, Liver cirrhosis, Intestinal obstruction, inflammatory bowel diseases and Metastasis that require accurate diagnosis. Generally, each modality provides dissimilar information about certain abdomen area under study or treat, related to possible disease. Moreover, each abdominal modality has its advantage and disadvantage as well as accuracy level for a particular abdomen imaging [6–8]. According to the patient case, the physician determines which type of these instruments to be used. For example, CT is a non-invasive medical examination where algorithms are used to construct an image representing a "slice" through the object. The CT is often the preferable method for diagnosing numerous cancers, such as liver and pancreatic cancers. As well as, CT images for internal organs, soft tissue, and blood vessels provide greater clarity and more details than conventional X-ray images. It can provide detailed information to diagnose, plan treatment, and evaluate many conditions. Therefore, it is used to evaluate a wide range of diagnoses where its benefits are far exceeding its limitations. Effective assessment and evaluation of diagnosis is required in order to capture the current health status of several populations [9]. This procedure involves several steps such as the

systematic monitoring of data, identification of the optimum measures and reasonable evaluation of outcomes.

However, medical images are often deteriorated due to various distortion caused by diverse sources of interference and other equipments' artifact that affect the data acquisition system as well as the measurement processes in imaging. In addition, the desired objects of interest are not well identified from others. Therefore, a challenge of the modern health society is to work towards improving and developing medical image modalities augments to improve the visibility of significant features in a medical image that assist accurate diagnosis process and eliminate/reduce the effect of the artifacts. Thus, medical image analysis includes images de-noising, pattern recognition, features extraction, segmentation, classification are essential for accurate diagnosis [10]. This field takes compensation of computer progress in sake of effective diagnosis. Thus, computer aided systems become a must to construe and combine the acquired images for the purpose of diagnosis and intervention.

Automatic system deployed for analysis and visualization of images involves the recognition of objects and their correlations [11]. Afterward, specialists deal with images for identification of a particular structure. Thus, computer assisted disease prognosis participates an imperative role and has become a foremost research focus for microscopic imaging and diagnostic where different image processing techniques that can be used to analyze these images for disease diagnosis.

Computer-aided diagnosis (CAD) helps physicians to cope with this complexity by providing computer output based on biomedical data quantitative analysis. It has become one of the main research subjects in medical imaging and diagnostic radiology. The essential concept of CAD is to offer a computer output which serves as a "second opinion" to assist biomedical data analysis. Hence, for the progress of a successful CAD scheme, it is necessary to develop computer algorithms and investigate how useful the computer output would be for the diagnosis, how to quantify the benefits of the computer output as well as how to maximize the effect of the computer output on the diagnoses. Thus, large-scale observer performance studies using a reliable methodology, such as receiver operating characteristic (ROC) analysis are as significant as the development of computer algorithms in the CAD field [12, 13].

From the previously mentioned diverse constraints, it is understandable that research and development of CAD has occupied a team effort by investigators with different backgrounds such as physicists, computer scientists, radiologists, engineers, psychologists and statisticians. The concept of CAD is broad; thus it can be applied to both imaging modalities, and bio-signals [14]. Conversely, the majority of CAD schemes developed in the past include the detection of liver, pancreas, kidney lesions as well as the detection of polyps in CT Colonography. However, there is a gap which opens up during systems design. This gap results from the fact that the demand for reliability impacts on the system requirements, because the reliability requirement is more difficult to achieve for complex systems. In this case, the word difficulty expresses the increase in resources or cost in general to meet the requirement. Over time, the increase in system complexity coupled with similar

levels of reliability has caused an exponential rise in the complexity to achieve the system requirements.

This chapter considers the major techniques of medical image analysis and modalities concerning different abdominal diseases. It deals with image analysis techniques with computer-assisted image analysis. The structure of the remaining sections is as follows. Section 2 represented the abdominal medical image modalities. Section 3 included computer aided diagnosis supported abdominal imaging applications which focused on the CT abdominal image processing. The discussion is conducted in Sect. 4, and finally the conclusion in Sect. 5.

2 Abdominal Medical Image Modalities

Advanced imaging techniques have a significant role to improve the quality of medical care of the patients. Non-invasive medical imaging modalities assist the physician to render accurate diagnoses and precise required treatment. A massive amount of medical imaging modalities is accessible and subject to active and promising research. Each modality gives a variety of information about the body's organ under investigation, which related to possible disease. The imaging modality selection for a targeted clinical study requires medical insights specific to organs under study [15–19]. Figure 1 demonstrated different modalities that can be used for abdominal medical imaging based on the body part under investigation.

These several modalities that used in the abdominal diagnosis are discussed as follows.

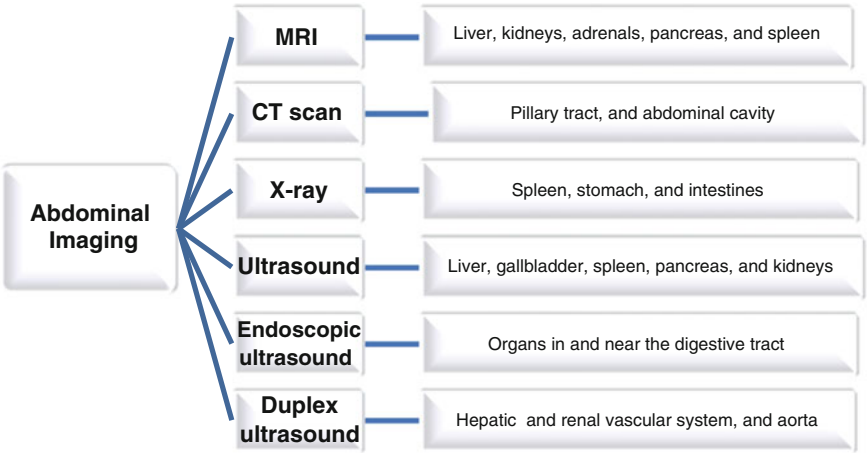

Fig. 1 Medical images classification structure

2.1 Magnetic Resonance Imaging for Abdominal Diagnosis

An abdominal MRI scan is an imaging technique that uses dominant magnets and radio waves in order to create images of the inside of the abdomen region. It is considered a non-invasive and non-ionizing device that provided three dimensional (3D) images, high spatial resolution and excellent soft-tissue contrast.

The foremost uses of MRI including the investigation of: (i) Kidney disease diagnosis, (ii) Blood flow in the abdomen, (iii) Blood vessels in the abdomen, (iv) The abdominal pain or swelling cause, (v) Liver or kidney problems, (vi) Lymph nodes in the abdomen and (vii) Masses in the liver, adrenals, kidneys, pancreas, or spleen. Furthermore, the MRI can be used to distinguish tumors from normal tissues. In addition, it assists the physician to determine the tumor characteristics such as severity, size, and spread.

The MRI has the advantages of avoiding the dangers of angiography and in providing better information about masses in the abdomen than CT in some cases. Differential contrast between soft tissues can be represented with high spatial resolution by varying the data acquisition parameters. Conversely, it has the disadvantages of the malfunction due its metal parts. In addition, the strong magnetic fields produced during the use of MRI can affect the heart pacemakers and other implants which attached to the patient [20, 21].

2.2 X-ray for Abdominal Diagnosis

X-ray imaging is a transmission-based procedure in which X-rays source pass through the patient body. This X-ray is detected either by an ionization chamber or a film on the opposite side of the body. Differential attenuation of X-rays in the body leads to different contrast in the image between different tissues. Planar X-ray radiography generates 2D projection of the tissues lying between the film and the X-ray source. It is used to study the liver, kidney stones and structures in the abdomen including the stomach, spleen, and intestines [22].

X-ray technique produces low radiation exposure. As it is regulated to provide minimum amount of radiation exposure, which required to produce the image. However, it has several disadvantages such as (i) Its 2D nature of the images can result in false positives, (ii) Not good for distinguishing anomalies in the dense tissues, and (iii) Its resolution is low.

2.3 Computed Tomography for Abdominal Diagnosis

Computed tomography is a type of specialized X-ray devices that can display cross-sectional images of a precise area of the body. In the CT process, the X-ray source is compactly collimated to interrogate a thin slice throughout the patient. To

produce a series of one-dimensional projections at different angles, the source and detectors rotate jointly around the patient. Afterword, these data are restructured to provide a two-dimensional (2D) image with reasonable contrast between soft tissues. Mathematically, Radon transform is used to reconstruct the image from a series of projections. Typically, CT scan can be used in the abdominal investigations in cases such as (i) Palpable abdominal mass, (ii) Abdominal pain, (iii) Kidney stones, (iv) Intestinal obstruction, and (v) Inflammation of the intestines, such as Crohn's disease.

An abdominal CT is a relatively safe technique, but there are risks including the exposure to radiation during the test, which is higher than the amount with an X-ray, allergy to contrast dye, and can lead to kidney malfunction from contrast dye [23].

2.4 Ultrasound for Abdominal Diagnosis

Ultrasound imaging (US) produces images through the backscattering of mechanical energy from the interfaces between tissues and small structures within tissue. It operates at frequencies within the range of 1 and 10 MHz. At high frequencies, it has high spatial resolution and involves no ionizing radiation. The main clinical applications of US include intra-abdominal imaging of the liver, kidney, and the compromised blood flow detection in veins and arteries.

Thus, US is considered a non-invasive, portable, and inexpensive diagnostic modality which has extensive use in the clinic [24]. The weakness of the US technique comprise (i) the relatively poor soft-tissue contrast, (ii) the gas and bone impede the path of ultrasound waves, meaning that certain organs cannot easily be imaged, (iii) not useful for imaging deep within the body, and (iv) its resolution is fairly limited.

2.5 Endoscopic Ultrasound for Abdominal Diagnosis

Since, US is a procedure that used to investigate the inside of the body using high-frequency sound waves. Thus, endoscopic US has a thin, flexible tube device that passed either through the mouth or through the rectum till it reach the digestive tract. Sound waves are sent out the end of the endoscopy's tube and bounce off the organs in the body. Afterward, a computer receives these waves and creates an image of the body inside. The endoscopic US can be used to: (i) find the abdominal pain cause, (ii) find the cause weight loss, (iii) diagnose diseases of the pancreas, gallbladder, and bile duct, and (iv) investigate cysts, tumours, and cancers. It is used also to get sample or biopsy by using a thin needle that can be passed through the tube to collect tissue/fluid.

This technique does not produce harmful radiation. However, breathing and bleeding problems may occur during the investigation [25].

2.6 Duplex Ultrasound for Abdominal Diagnosis

Typically, ultrasonic energy can be applied to interrogate vessels at great depth as well as arteries in the abdomen. Duplex US combines the traditional ultrasound with Doppler ultrasound, where the traditional US uses sound waves that bounce off blood vessels to create images, while the Doppler US records sound waves reflecting off blood. It can be used for examination of: (i) the blood vessels and blood flow in the abdominal area, and (ii) the kidney and its blood vessels [26]. There are no risks for using the Duplex US technique.

3 Computer Aided Diagnosis Supported Abdominal Imaging Applications

Recently, advancement of digital imaging technologies supports high-resolution images to be interpreted rapidly. Thus, CAD systems become important for medical image understanding and interpretation for accurate diagnosis. The CAD concept is universal for different modalities/disease types. Physicians use the output of a computerized technique for automated image analysis and processing as a diagnostic aid. The main aim for the CAD is to perform medical image analysis and processing that support diagnosis.

Medical image analysis is concerned with the transformation of an image to produce information representation for the original image to be more reliable for further analysis. It is used to derive consistent visualizations and models. Generally, medical image analysis has several stages, namely (i) image formation: using the suitable modality to capture the medical image, (ii) image visualization: using image enhancement techniques to manipulate the captured image, (iii) image analysis, including features extraction, restoration, segmentation and classification, finally (iv) image management, including techniques that provide efficient storage, communication, transmission, archiving, and retrieval of the image data to facilitate telemedicine. Based on these steps, some clinical applications based CAD system for CT abdominal image processing are presented as follows.

3.1 Abdominal Image Enhancement

Medical image enhancement plays a significant role in CAD systems for correct diagnosis decision based on the image information. It improves the medical image for physicians to diagnose, reduce/remove unwanted information and contrast enhancement. Spatial domain and frequent domain are the traditional medical image enhancement methods. Researchers are interested with developing various medical image enhancement techniques.

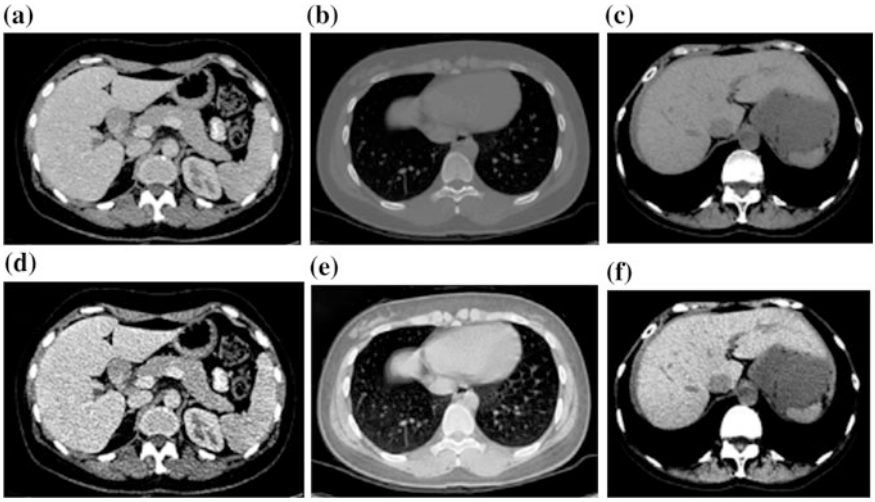

Fig. 2 Abdominal images enhancement: **a**, **b** and **c** original images, and **d**, **e** and **f** the final enhanced images [27]

Jiang et al. suggested an enhancement algorithm by combining the histogram equalization along with image details conservation and bi-dimensional empirical mode decomposition [27]. The overall image contrast has been increased through the histogram equalization with the image details conservation; followed by the bi-dimensional empirical mode decomposition. Thus, the medical image has been decomposed into image information with different frequency that had different levels to perform image enhancement. The dataset has been consisted of 60 sets of CT abdominal images. The experimental results are illustrated in Fig. 2.

Figure 2d depicted that the internal structure of the abdominal organs such as the liver and pancreas as well as the adhesion between the parts of the organ became clearly displayed compared to the original image. In Fig. 2e the lung was clearly appeared. Moreover, Fig. 2f proved that the enhanced liver image was clearly seen with the liver's blood vessels.

Ashour et al. [28] proposed an abdominal image enhancement algorithm using log transform in an optimization framework. The optimization has been achieved using a well know meta-heuristic algorithm, namely the Cuckoo search (CS) algorithm to determine the optimal parameter settings for log transform. The proposed technique performance has been studied on a low contrast CT abdominal image dataset. The experimental results proved that the CS based approach has superior convergence and fitness values compared to Particle swarm optimization (PSO). In addition, the Image Quality Analysis (IQA) justified the robustness of the proposed enhancement technique. Figure 3 illustrated different assessments when using the CS or the PSO compared to the original CT multiple liver lesion images.

Figure 3 established that using CS provided more enhanced images than that obtained using PSO. It is obvious that the enhanced images based CS for the log

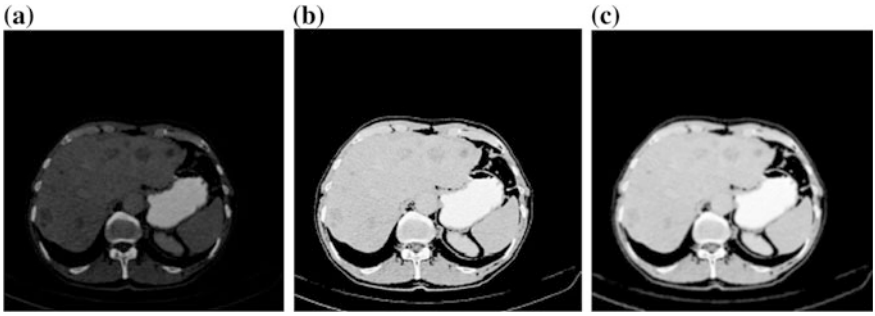

Fig. 3 Output images using PSO and CS compared to the original image: **a** the original image; **b** the enhanced image based on PSO algorithm and **c** the enhanced image based on the Cuckoo Search algorithm [28]

transformation parameters optimization was clearer than the images based PSO. In addition, the enhanced image using CS displayed clearly all portions of the liver with obvious lesion appearance compared to those based on PSO.

3.2 Abdominal Image Segmentation

Segmentation of the different body's organ is often considered the first step in CAD after the image enhancement. Segmentation of abdominal organs, such as the kidneys, liver, and spleen attracts researchers recently, where it faces many challenges. In CT scan, several artifacts can arise due to beam-hardening artifacts, partial-volume artifacts, and streak artifacts [29]. Moreover, the difficulties arise due to lack of organ tissue homogeneity in shape and texture. Liver and tumor segmentation can be performed on the CT images manually or semi automatically.

Karssemeijer [30] presented a stochastic model and gray level distribution model for 3D abdominal geometry. An iterative relaxation segmentation procedure has been used, where obtained information from the model and the measurements were weighted concurrently. The authors used two iterative procedures, namely iterative conditional modes and the simulated annealing. Kumar et al. [31] proposed an automatic segmentation approach of liver tumor in abdominal CT images. Region growing method has been used by pre- and post- processing functions for automatic segmentation of liver and Alternative Fuzzy C-Means (AFCM) algorithm for tumor segmentation. The results included quantitative comparison, which demonstrated a close correlation between the automatic and manual segmentation along with high spatial overlap between the regions-of-interest (ROIs) generated by the two methods. Figure 4 illustrated the segmentation of the original liver and tumor images.

Figure 4 illustrated the simplified image created by analyzing the histogram after removing unwanted structures and tissues. However, the small and unconnected

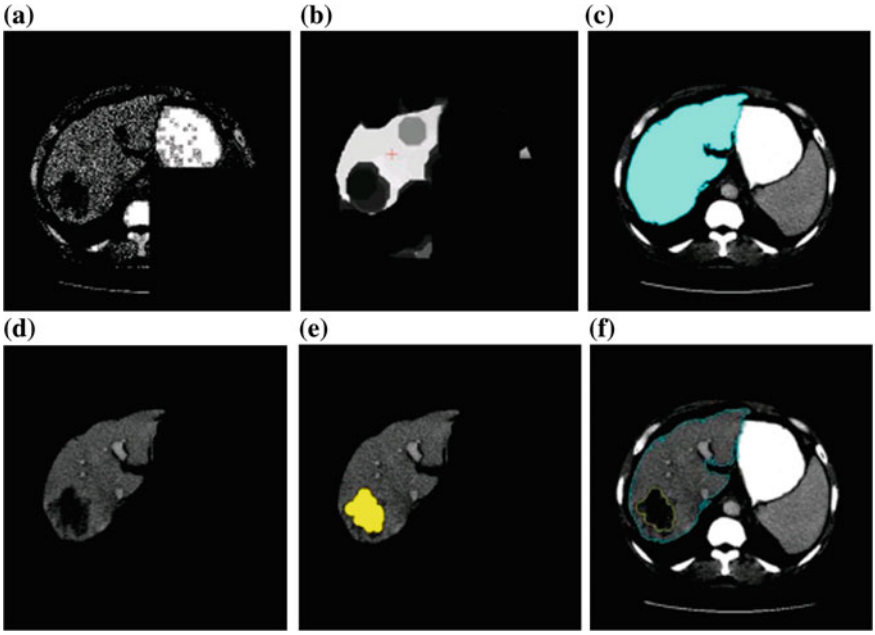

Fig. 4 CT liver image segmentation: **a** Simplified image, **b** Eroded image with centroid, **c** Region grown liver, **d** Segmented liver, **e** Segmented tumor using the AFCM approach, and **f** Segmented liver and tumor [31]

tissues remain. Afterward, morphological erosion was performed to eliminate these remaining objects and retain the liver region. The liver region centroid was found. The centroid's co-ordinates acted as seed point for automatic region growing. The segmented liver using the proposed method is shown in Fig. 4d, while the segmented tumor using the AFCM approach is shown in Fig. 4e. Finally, the segmented liver and tumor on the original CT image is shown in Fig. 4f.

3.3 Abdominal Image Classification

Generally, classification refers to the assignment of a physical object into one of a set of predefined categories. Thus, it requires analysis of the numerical properties of various image features to organize data into categories. Sharma et al. [32] achieved an auto-segmentation and tissue characterization effective system for analysis of medical images based on hybridization of syntactic and statistical approaches using artificial neural network (ANN). This proposed algorithm performed segmentation and classification, which recognized objects, identified different textures, curved surfaces, or a surface inclination by texture information and brightness. The followed steps were: (i) image filtering, (ii) segmentation, (iii) feature extraction, and

(iv) extracted features' classification. The ANN is used to classify the soft tissue using texture-primitive features. The proposed algorithm was first tested on Markov textures, which achieved 100 % classification.

Kumar and Moni [33] proposed a novel feature extraction scheme based on multi-resolution fast discrete curvelet transform (FDCT) for CAD of liver diseases. The liver was segmented from CT images by adaptive threshold detection and morphological processing. The suspected tumor regions were extracted from the segmented liver using fuzzy c-means (FCM) clustering. The FDCT was used to textural information from the extracted tumor. These features were used to train and classify the liver tumor into hemangioma and hepatoma utilizing artificial neural network classifier. Näppi et al. [34] compared the relative performance of the support vector machine (SVM) and the random forests (RF) classifiers for automated detection of colorectal lesions in the computed tomographic colonography (CTC). The experimental results established that the performance of the RF classifier was superior compared to the SVM classifier in CTC.

3.4 Abdominal Image Fusion

Typically, each modality has its artifacts as well advantages. Thus, combining the images captured form two modalities for the same organ will enable the benefit from two imaging modalities in one examination. This can be performed through medical image fusion, which defined as the process of superimposing and aligning images obtained using two different modalities.

Ewertsen et al. [35] evaluated the accuracy of aligning varying parameters such as the respiratory phase, patient position, and distance from the co-registration points/planes measured form the CT or MRI. A total of 80 co-registrations achieved the highest accuracy, when the respiratory phase for the co-registration method was the same. Moreover, the accuracy is improved by choosing co-registration points/planes close to the area of interest. The results depicted that image fusion involving real-time US is an accurate procedure for abdominal examinations. Figure 5 illustrated the liver overlaid/fused images in one single image. After a

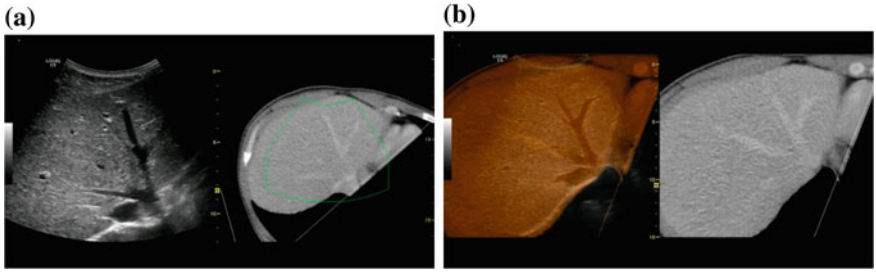

Fig. 5 **a** Co-registered images of the liver shown side by side (ultrasound (US): *left* computed tomography (CT): *right*), and **b** CT and US images of the liver overlaid (*left*) and corresponding CT-image (*right*)

preliminary co-registration, the MRI or CT images were reformatted in a projection to fit the live US images.

4 Discussion

Generally, medical imaging provides information on the causes of the patients' symptoms and diseases. Since, abdomen contains various organs that have subtle and complex appearances. Furthermore, accurate diagnosis relies on the organs' and/or lesions' measurements including their shape and volume. These measurements are considered indicators for any disorder. In the clinical practice, this process is challenging task which requires development of algorithms and CAD systems. In the last two decades, CAD has been developing fast to support radiologists in the interpretation of medical images by using computer systems. The preceding sections depicted that CAD systems are effective in improving diagnostic accuracy of radiologists. In CAD research, is concerned with the detection and diagnosis of abdominal diseases, including Lymphoma, intestinal obstruction, liver cirrhosis, renal failure as well as masses/stones/cysts in liver and kidney. Accordingly, in medical imaging, CAD has been an active research area to support the different modalities. Since, medical image processing includes:

(A) Medical image enhancement: to reduce/remove the noise and any unwanted objects in the medical image,
(B) Pattern recognition: to detect certain shape/texture as well as to identify objects,
(C) Features extraction: to transform the existing features into a lower dimensional space,
(D) Medical image segmentation: to partition the medical image into multiple segments in order to locate objects, structures and boundaries in the image,
(E) Medical image classification: to assign the detected objects into one of a predefined categories, and
(F) Medical image fusion: to combine images of two different modalities.

During these processes for abdominal image processing, different challenges can be addressed as follows:

- The classification process if the CAD for CTC suffers from large numbers of false-positive detections. Thus, the SVM classifiers can be improved as it is considered popular classifier for reducing false-positive detections in CAD systems.
- Texture analysis plays a significant role in the future of medical image interpretation for monitoring disease progression.
- Computer aided detection and diagnosis is a promising field in image classification, which requires new algorithms.

- Automatic diagnosis systems have cover all medical imaging aspects and to replace all manual or semi-automated existing systems.
- Image fusion is a promising process, which gathers the advantages of using several modalities.
- Meta-heuristic optimization algorithms can be used to support the CAD systems.

5 Conclusions

Abdominal diagnosis relies on the inclusive analysis of its complex organs. Thus, different modalities are employed to capture images for the organ under concern. Computer-based systems for the analysis of the obtained images are promising over human interpreters. These systems provided large knowledge base for diagnostic information, high speed, and non-sensitivity to fatigue. Recently, CAD systems are being used routinely in hospitals and for clinical applications. Therefore, image based knowledge detection plays significant roles in several CAD applications. It has great potential to be incorporated into the next-generation picture archiving and communication systems (PACS). Robust medical image analysis/processing are vital for such discovery in various CAD applications. In this chapter, the different modalities uses as well as their advantages/disadvantages are addressed. Various applications for CT based different image processing approaches are included. It is concluded that CAD systems is a wide domain that can support different abdominal and medical clinical applications. It provides accurate, efficient and high speed image analysis for reliable diagnosis.

References

1. Deserno, T.M.: Fundamentals of biomedical image processing. In: Biomedical Image Processing, pp. 1–51. Springer, Berlin (2010)
2. Hassanien, A.E., Moftah, H.M., Azar, A.T., Shoman, M.: MRI breast cancer diagnosis hybrid approach using adaptive ant-based segmentation and multilayer perceptron neural networks classifier. Appl. Soft Comput. **14**, 62–71 (2014)
3. McAuliffe, M.J, Lalonde, F.M., McGarry, D., Gandler, W., Csaky, K., Trus, B.L.: Medical image processing, analysis and visualization in clinical research. In: 14th IEEE Symposium on 2001 Computer-Based Medical Systems, CBMS 2001. Proceedings, pp. 381–386 (2011)
4. Pluim, J.P., Maintz, J.A., Viergever, M.A.: Mutual-information-based registration of medical images: a survey. IEEE Trans. Med. Imaging **22**(8), 986–1004 (2003)
5. Dhawan A.P.: Medical Image Analysis. Wiley (2011)
6. Bae, K.T., Giger, M.L., Chen, C.T., Kahn Jr, C.E.: Automatic segmentation of liver structure in CT images. Med. Phys. **20**(1), 71–78 (1993)
7. Huda, W., Scalzetti, E.M., Levin, G.: Technique factors and image quality as functions of patient weight at abdominal CT 1. Radiology **217**(2), 430–435 (2000)

8. Marin, D., Nelson, R.C., Schindera, S.T., Richard, S., Youngblood, R.S., Yoshizumi, T.T., Samei, E.: Low-tube-voltage, high-tube-current multidetector abdominal ct: improved image quality and decreased radiation dose with adaptive statistical iterative reconstruction algorithm—initial clinical experience 1. Radiology **254**(1), 145–153 (2009)
9. Bushberg, J.T, Boone, J.M.: The Essential Physics of Medical Imaging. Lippincott Williams & Wilkins (2011)
10. Shih, F.Y.: Image Processing and Pattern Recognition: Fundamentals and Techniques. Wiley (2010)
11. Solomon, C, Breckon, T.: Fundamentals of Digital Image Processing: A Practical Approach with Examples in Matlab. Wiley (2011)
12. De Dombal, F.T., Leaper, D.J., Staniland, J.R., McCann, A.P., Horrocks, J.C.: Computer-aided diagnosis of acute abdominal pain. Br. Med. J. **2**(5804), 9–13 (1972)
13. Adams, I.D., Chan, M., Clifford, P.C., Cooke, W.M., Dallos, V., De Dombal, F.T., Edwards, M.H., Hancock, D.M., Hewett, D.J., McIntyre, N.: Computer aided diagnosis of acute abdominal pain: a multicentre study. BMJ **293**(6550), 800–804 (1986)
14. Semmlow, J.L, Griffel, B.: Biosignal and Medical Image Processing. CRC Press (2014)
15. Giedd, J.N., Blumenthal, J., Jeffries, N.O., Castellanos, F.X., Liu, H., Zijdenbos, A., Rapoport, J.L.: Brain development during childhood and adolescence: a longitudinal MRI study. Nat. Neurosci. **2**(10), 861–863 (1999)
16. Gohagan, J.K., Marcus, P.M., Fagerstrom, R.M., Pinsky, P.F., Kramer, B.S., Prorok, P.C.: Lung Screening Study Research Group. Final results of the Lung Screening Study, a randomized feasibility study of spiral CT versus chest X-ray screening for lung cancer. Lung Cancer **47**(1), 9–15 (2005)
17. Dey, N., Roy, A.B., Pal, M., Das, A.: FCM based blood vessel segmentation method for retinal images. Int. J. Comput. Sci. Netw. **1**(3) (2012)
18. Dey, N., Ashour, A.S., Ashour, A.S., Singh, A.: Digital analysis of microscopic images in medicine. J. Adv. Microsc. Res. **10**, 1–13 (2015)
19. Hore, S., Chakroborty, S., Ashour, A.S., Dey, N., Ashour, A.S., sifaki-pistolla, D., Bhattacharya T, Chaudhuri S.R.B.: Finding contours of Hippocampus brain cell using microscopic image analysis. J. Adv. Microsc. Res. **10**(2) (2015)
20. Kim, D.H., Pickhard, P.J.: Diagnostic imaging procedures in gastroenterology. In: Goldman, L., Schafter, A.I. (eds.) Goldman's Cecil Medicine, 24th edn. Elsevier Saunders, Philadelphia (2011)
21. Wilkinson, I.D., Graves, M J.: Magnetic resonance imaging. In: Adam, A., Dixon, A.K., Gillard, J.H., et al. (eds.) Grainger & Allison's Diagnostic Radiology: A Textbook of Medical Imaging, 6th edn. Churchill Livingstone, New York (2014)
22. Morrison, I.D., McLaughlin, P., Maher, M.M.: Current status of imaging of the gastrointestinal tract. In: Adam, A., Dixon, A.K., Gillard, J.H., Schaefer-Prokop, C.M. (eds.) Grainger & Allison's Diagnostic Radiology: A Textbook of Medical Imaging, 6th edn. Elsevier Churchill-Livingstone, New York (2015)
23. Shaw, A.S., Prokop, M.: Computed tomography. In: Adam, A., Dixon, A.K., Gillard, J.H., et al. (eds.) Grainger & Allison's Diagnostic Radiology: A Textbook of Medical Imaging, 6th edn. Churchill Livingstone, New York (2014)
24. Taval, V.S.: Emergency ultrasound. In: Marx, J.A., Hockberger, R.S., Walls, R.M., et al. (eds.) Rosen's Emergency Medicine: Concepts and Clinical Practice, 8th edn. Mosby Elsevier, Philadelphia (2013)
25. McNally, P.R.: Endoscopic ultrasound. In: McNally (ed.) GI/Liver Secrets Plus, 4th edn. Elsevier Mosby, Philadelphia (2010)
26. Taylor, D.C., Kettler, M.D., Moneta, G.L., Kohler, T.R., Kazmers, A., Beach, K.W., Strandness, D.E.: Duplex ultrasound scanning in the diagnosis of renal artery stenosis: a prospective evaluation. J. Vasc. Surg. **7**(2), 363–369 (1988)
27. Jiang, H., Lou, B., Liao, S.: Medical image enhancement method based on mode decomposition. Adv. Multim. Technol. (AMT) **1**, 21–31 (2012)

28. Ashour, A.S., Samanta, S., Dey, N., Kausar, N., Abdessalemkaraa, W.B., Ella, Hassanien Aboul: Computed tomography image enhancement using cuckoo search: a log transform based approach. J. Signal Inf. Process. **6**(03), 244 (2015)
29. Slone, R.M., Fisher, A.J., Pickhardt, P.J., Gutierrez, F.R., Balfe, D.M.: Body CT: A Practical Approach. McGraw-Hill, New York (2000)
30. Karssemeijer, N.: A statistical method for automatic labeling of tissues in medical images. Mach. Vis. Appl. **3**(2), 75–86 (1990)
31. Kumar, S.S., Moni, R.S., Rajeesh, J.: Automatic segmentation of liver and tumor for CAD of liver. J. Adv. Inf. Technol. **2**(1), 63–70 (2011)
32. Sharma, N., Ray, A.K., Sharma, S., Shukla, K.K., Pradhan, S., Aggarwal, L.M.: Segmentation and classification of medical images using texture-primitive features: application of BAM-type artificial neural network. J. Med. Phys. **33**(3), 119 (2008)
33. Kumar, S.S., Moni, R.S.: Diagnosis of liver tumor from CT images using curvelet transform. Int. J. Comput. Sci. Eng. **2**(4), 1173–1178 (2010)
34. Näppi, J.J., Regge, D., Yoshida, H.: Comparative performance of random forest and support vector machine classifiers for detection of colorectal lesions in CT colonography. In: Abdominal Imaging. Computational and Clinical Applications 2011 Sept 18, pp. 27–34. Springer, Berlin (2011)
35. Ewertsen, C., Hansen, K.L., Henriksen, B.M., Nielsen, M.B.: Improving accuracy for image fusion in abdominal ultrasonography. Diagnostics **2**(3), 34–41 (2012)

An Overview of Pectoral Muscle Extraction Algorithms Applied to Digital Mammograms

Suhas Sapate and Sanjay Talbar

Abstract Substantial numbers of patients are reaching to a progressive breast cancer stage due to increase in the false negatives coming out of cumbersome and tedious job of continuously observing the mammograms in fatigue. Hence, the early detection of cancer with more accuracy is highly expected to reduce the death rate. Computer Aided Detection (CADe) can help radiologists in providing a second opinion increasing the overall accuracy of detection. Pectoral muscle is a predominant density area in most mammograms and may bias the results. Its extraction can increase accuracy and efficiency of cancer detection. This work is intended to provide the researchers a systematic and comprehensive overview of different techniques of pectoral muscle extraction which are categorized into groups based on intensity, region, gradient, transform, probability and polynomial, active contour, graph theory, and soft computing approaches. The performance of all these methods is summarized in tabular form for comparison purpose. The accuracy, efficiency and computational complexities of some selected methods are discussed in view of deciding a best approach in each of the categories.

Keywords Breast cancer · Mammography · Computer aided detection · Pectoral muscle extraction · Segmentation

S. Sapate (✉)
Department of Computer Science and Engineering, SGGS IE&T, Nanded, India
e-mail: sapatesuhas@sggs.ac.in

S. Talbar
Department of Electronics and Telecommunications, SGGS IE&T, Nanded, India
e-mail: sntalbar@sggs.ac.in

N. Dey et al. (eds.), *Medical Imaging in Clinical Applications*,
Studies in Computational Intelligence 651, DOI 10.1007/978-3-319-33793-7_2

1 Introduction

1.1 Overview of Mammography

Breast cancer is the most common cancer and is the second most common cause of cancer deaths in women. Breast cancer incidences worldwide are increasing over the years with more than 1 million new cases reported each year. The chances of success are more if further treatment and therapeutic actions are taken in the early stages of the breast cancer. Thus, early detection plays an important role for improving breast cancer prognosis [1–3].

A mammogram is an X-ray image of the human breast. A careful observation of this image can allow us to identify and evaluate indicators of abnormalities at early stage in the human breast. Screening mammograms are useful in finding likelihood of cancer in patients without any external symptom, whereas patients with some abnormal symptoms or lumps in breast undergo diagnostic mammography. Mammographic images are generated by passing low dose X-ray across each breast. This produces a picture which highlights the soft tissues, dense tissues, pectoral muscle, and fibro-glandular region etc. Expert radiologists can read these mammograms to find out the abnormalities, if are there, in the breast. Any change in two or more mammograms taken over a period, say a year or two, may signify cancer in its early stage. A mammogram can depict changes in the breast up to a year or two before any symptoms observed by patient or physician [1, 4]. If the significant changes are confirmed as early stage cancer, further extensive treatments can be avoided and probability of breast conservation can be improved. Modern mammography machines are with low radiation doses, 0.4 mSv, of X-ray and produces high-quality digital images with 2 views of each breast [5]. In mass screening programs, mammography is the most effective, more popular, cheaper and hence commonly used imaging modality for breast than Magnetic Resonance Imaging (MRI), Nuclear Imaging and Ultrasound [6]. The **mediolateral oblique** (MLO-taken at around 30–70° angle) **view** and **craniocaudal** (CC-top to down) **view**, are two standard mammographic projections used for screening mammography. In MLO view, maximum portion of the breast, including pectoral muscle, is exposed. It is always better to expose maximum portion of pectoral muscle in MLO view to guarantee that each and every part of the breast is covered neatly. Hence, it is the most important projection. Thus, the pectoral muscle on the MLO view is a vital component in confirming correct patient positioning which results in a accurate mammogram of adequately good quality. This is very important to minimize the number of false positives (FP), false negatives (FN) and improve the sensitivity of the mammographic images [7].

As shown in the Fig. 1, the mammographic image consists of various parts apart from the region of interest required for automatic detection of abnormalities. These parts include low and high intensity labels, scanning artifacts etc. all in the background. Pectoral muscle located on top left (left MLO view) or top right (right MLO view) occupies major portion of the breast. The labels, scanning artifacts and

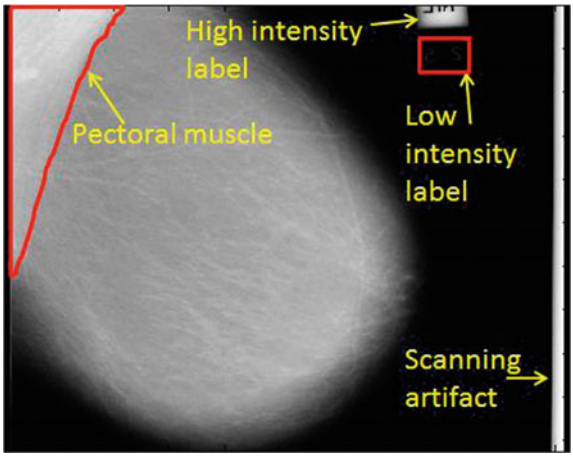

Fig. 1 A typical left MLO view mammographic image

pectoral muscle may increase the computational complexity of the detection process and also cause the reduction in detection accuracy. Hence to remove all these unnecessary parts from the breast region in the mammogram is a vital preprocessing task in CADe system of the breast cancer.

Segmentation of mammographic image into its representative anatomically distinct regions such as background (the non-breast area), pectoral muscle, a nipple, fibro-glandular region (parenchyma), and adipose region etc., is very crucial. It is the first preprocessing step in Computer Aided Diagnosis (CADx) of breast cancer. The different methods available for automatic extraction of pectoral muscle have been categorized as shown in the Fig. 2.

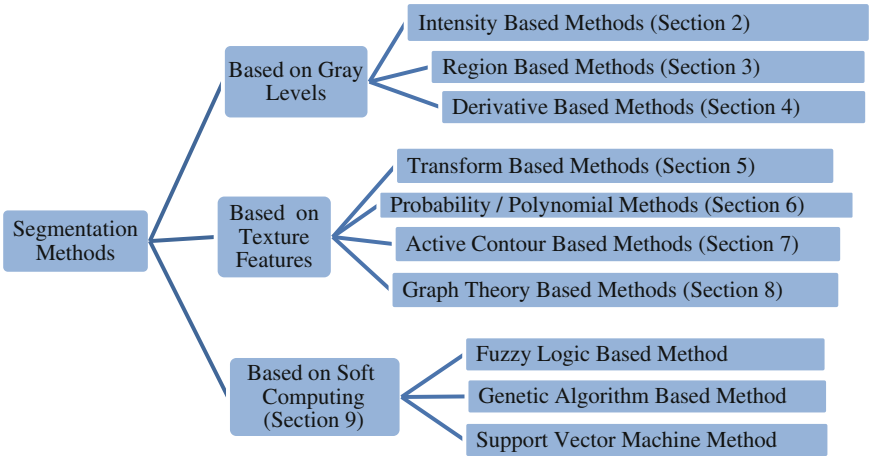

Fig. 2 Mammogram segmentation methods

Table 1 Performance measurement parameters

Performance parameter	Formula to calculate the parameter
Sensitivity	TP cases/total positive cases
Specificity	TN cases/total negatives cases
Precision	TP cases/(TP cases + FP cases)
Accuracy	(TP cases + TN cases)/total samples

The performance, indicating the degree of correctness of the segmentation results and their respective ground truth, is evaluated based on various parameters. It can be assessed subjectively by a expert radiologist by ranking the results or objectively by comparing the results with the ground truth using different metrics. The most widely used interpretation is the confusion matrix consisting of true positives (TP), true negatives (TN), false positive (FP), false negatives (FN). The performance of many methods is measured in terms of: specificity, sensitivity, precision, accuracy rates which are defined Table 1.

Similarly, the metrics used for error evaluation includes average error, Hausdorff distance, Absolute Error Distance etc. are also used in some techniques. Another metric used is 'Receiver Operating Characteristic' curve determined by true positives and false negatives results of a given experiment.

1.2 Significance

The accuracy of the automatic detection of breast cancer using CADe systems may be improved by separating region of interest in mammographic images. The presence of labels, noise, artifacts and majorly the pectoral muscle in the breast region may affect the performance and accuracy of the CADe system. Removing these parts out from the mammogram can increase computational complexity of the CADe systems. The presence of the pectoral muscle occupying a predominant region in the MLO view mammogram of breast, as shown in Fig. 1, may affect the results of cancer detecting process very badly. Pectoral muscle extraction is essential to provide effective results in the preprocessing step in CADe of breast cancer. An automatic pectoral muscle extraction plays a vital role in reducing the computational complexity and the errors of CADe systems. The further image analysis for breast cancer detection may become easier in the cancer detection process. The pectoral muscle extraction can also be useful in

- image registration for analyzing abnormality as like bilateral symmetry;
- automatic breast tissue density quantification;
- 3-D reconstructions from multiple mammographic views;
- mammogram-pair registration and comparison etc.

The following are the common preprocessing tasks [8] performed on the input mammographic image.

- Improving the quality of the input image by enhancing its contrast
- Finding out RoI by delineating the breast border in a simple, effective way
- Pectoral muscle is then extracted using a particular segmentation technique

1.3 Challenges

In most of the mammographic images, pectoral muscle detection still remains a challenging task. The major challenges of Pectoral Muscle Extraction [9] are due to its

- unclear and superimposed boundaries due to overlapping features;
- total absence in some cases;
- varying position, size, shape and texture from image to image;
- textural information similar to that of breast tissue, in most of cases;
- concave or convex border with its appearance varying in every other mammogram;
- border which cannot be modeled with any common geometrical or mathematical representation;

Thus, to devise a solution that extract a pectoral muscle accurately and efficiently over a wide variety of mammographic images, possibly from different databases [10, 11], is really a great challenge.

1.4 Motivation

The very solution to the pectoral muscle extraction problem lies in the domain of image segmentation. A variety of techniques are available to solve the basic segmentation problem. However to apply the technique commonly on a variety of images, one has to modify the fundamental segmentation algorithm or support it with some other supplementary methods. A few soft computing and other supporting techniques are also available to modify the basic segmentation algorithm so that the desired result of pectoral muscle extraction is achieved efficiently with sufficient accuracy over a different set of mammographic images.

1.5 Hypothesis

The different methods available for automatic extraction of pectoral muscle have been summarized under different categories in this chapter. The reason behind this detailed overview of automatic pectoral muscle extraction methods is to understand

the merits, demerits, limitations, problems and challenges encountered in each and every method while applying them over a different set of mammographic images. The performance of all the methods under similar category is enlisted for comparison purpose. This book chapter is intended to provide the researchers a systematic and comprehensive overview of different techniques of pectoral muscle extraction from digital mammograms.

1.6 Contributions

One of the intentions behind the work is to bring all the methods applied for pectoral muscle extraction, in a single chapter, so that the researchers get the consolidated information required and the further directions to devise a new simpler approach with even better accuracy, perhaps by combining some good concept proposed in some or the other algorithms enlisted here.

1.7 Organization of Chapter

The rest of this chapter is organized as follows. The Sect. 2 covers all the Intensity and histogram based methods. Region based approaches are discussed in Sect. 3. Section 4 describes all the gradient based approaches. Wavelet based approaches are presented in Sect. 5. Section 6 consists of the probability and polynomial based approaches. Section 7 includes active contour based approaches. Section 8 outlines graph theory based methods and Sect. 9 incorporates the soft computing methods.

2 Intensity Based Approaches

In the intensity based approaches, it is considered that the pectoral muscle area in the mammogram is dense and with high intensity compared to its surrounding tissues. These approaches try to find out change in the intensity levels of the pectoral muscle area and its adjacent parenchymal region. Rise and fall in the intensity levels all over the pectoral muscle plays a vital role in delineating the pectoral muscle border with better accuracy. Though, finding the exact pectoral muscle border in some cases is highly difficult; especially, with overlapping of surrounding tissues. From the literature surveyed, the different solutions based on either intensity, histogram, morphology or their combination with varying rates of success are discussed as given below.

A pectoral muscle extraction using histogram thresholding is proposed by Thangavel and Karnan [12] in a very efficient manner. The global optimum

threshold value is selected first and then the intensities less than this threshold are assigned with zero, whereas the remaining intensities are assigned with one. Morphological operators such as erosion and dilation are then applied for preserving details nearby the pectoral muscle region. This result is then converted to a binary image from which upper left region of white pixels represent a pectoral muscle region of the mammogram image. This proposed algorithm is very simple, easy to implement and yet with goof performance. The experimental setup, results, image dataset used etc. are not discussed and the accuracy of the method is also not calculated in the paper.

An automatic method based on interesting properties of watershed transformation was explored by Camilus et al. [13]. In this approach, application of Watershed Transform on gradient images leads to a watershed line matching to the pectoral muscle border which in turn allows an efficient extraction of the pectoral edge. The problem of over-segmentation of the pectoral muscle region is resolved by applying merging algorithm which combines the suitable catchment basins to extract pectoral muscle with better accuracy. This method is validated by performing an experiment on 84 mammographic images form MIAS database which reveals a mean FP to be 0.85 % whereas mean FN is 4.88 %. The cases with FP and FN greater than 0.10 are almost zero, which indicates a good accuracy. The overall performance is claimed to be better than other techniques in this domain. The performance of this simple method is very accurate and efficient. The result is not validated with variety of images over multiple datasets.

A fully automatic breast region segmentation algorithm based on multilevel Otsu [14], gradient estimation and linear regression is presented by Kamila and Justyna [15]. After morphological preprocessing, a fast algorithm for multilevel thresholding classifies pixels in the multiple classes based on a number of gray levels. This separates the region of low intensity background from that of the breast skin-air interface in the image. Applying gradient on this image produces a rough pectoral muscle border which is smoothed by using a linear regression. This linear regression leads to finding the exact border of the pectoral muscle. The algorithm when tested on 300 MIAS database images showed an accuracy of 95–97 % which is quiet high in comparison with existing methods. The efficiency of this algorithm measured in terms of total percentage error was found to be 98–99 %. The major success of this method lies in elimination of wrong detection. However, the method is not tested on variety of images from different datasets.

Liu et al. [16] proposed a accurate extraction of pectoral muscle border efficiently. The algorithms works on the basis of position related features of pectoral muscle in the breast area. The method makes repetitive use of the Otsu thresholding along with the morphology based operators to line out a rough edge of the pectoral muscle. This rough approximate edge then passes through a ‘multiple regression analysis’ to give out a refined pectoral muscle edge accurately. When tested on 150 MIAS database images, this algorithm gives almost the same results as that of the expert radiologists over a wide range of mammograms with varying appearances. It is also observed that the algorithm is effective even when the pectoral muscle edge

is obscured by overlapping breast tissue or other artifacts. The performance of this algorithm is validated over the different error metrics such as mean error (1.7188), misclassification error (0.0083), extraction error rate (0.00134), modified Hausdorff distance (0.08702) and average error is quite less. However, the repetitive use of thresholding makes this algorithm computationally intensive.

Duarte et al. [17] presented an automatic method, based on morphological filters, to estimate the pectoral muscle in mammograms. Morphological filters improve the image contrast between breast contour and background, also, between the pectoral muscle and the breast parenchyma. Original image gray level is first reduced from 256 to 9 in a heuristic way. By considering pectoral muscle as one of the densest region of the image, it is segmented by using the seventh and sixth gray-levels as thresholds, which are negated producing images N7 and N6, as shown in [17]. A morphological opening (disc-shaped SE with a 21-pixels diameter) is applied to N7, intending to exclude the smaller bright pixels that are out of the pectoral muscle region. An inferior reconstruction (disc-shaped SE with an 11-pixels diameter) is also applied but to the resulting image (mark), using N6 as its mask. Then, a morphological closing (again, a disc-shaped SE with an 11-pixels diameter) is applied to fill gaps in the reconstructed image contour. The gradient of the image obtained in the previous procedure is determined and a first-order polynomial is adjusted to estimate pectoral muscle. Then, it is tested if this estimated pectoral muscle comes into contact with the upper image edge or any of the lateral edges, as well as, if it does not cross the breast contour. If the above occur, then pectoral muscle is considered the densest region and hence adequately estimated. This method is evaluated by an experienced radiologist. The results of applying such methodology on 154 images (300 dpi, 8 bits) from the DDSM database show acceptable results with 93.6 % accuracy. This morphological operations based method is simple yet effective. However, the method is robust over different sets of images with varying appearances of pectoral muscle.

Burcin et al. [18] presented a novel segmentation algorithm for a pectoral muscle extraction based on Otsu's method in mammograms. The proposed system includes a pectoral muscle extraction on the basis of automatically selected threshold in an unsupervised manner. The process starts with preprocessing operations to remove the artifacts out of the breast border and to enhance the region of interest. A nonparametric, unsupervised extended version of Otsu's segmentation method with N = 2 is applied for segmenting the pectoral muscle. Connected component labeling algorithm is used for labeling the segmented regions. A upper of the two largest regions is selected as pectoral muscle. A limit area control mechanism proposed in this method with area value 21000 pixels for 512 × 512 mammographic images, allows to prevent false segmentation; especially for images with no pectoral muscle. The experimental results on 96 MIAS database images show 93 % accuracy. This method is simple, effective but its experimental results are not validated on different sets of images.

Performance evaluation of intensity based methods for pectoral muscle extraction is tabulated in Table 2.

Table 2 Performance evaluation of intensity based methods

Year authors	Main theme	# Images success%	Advantage/disadvantage
2005 Thangavel and Karnan [12]	Histogram-based thresholding	– –	• Easy, efficient • Accuracy not calculated
2011 Camilus et al. [13]	Watershed transformation	84 MIAS FP 0.85	• Accurate, efficient • Not robust
2012 Kamila and Justyna [15]	*Multilevel Otsu, gradient estimation, linear regression*	*300 MIAS* *95-97*	• *No wrong detection* • *Not robust*
2012 Liu [16]	Iterative Otsu Thresholding and morphological processing	150 MIAS HD-0.087	• Accurate, robust, efficient • Computationally intensive
2012 Duarte et al. [17]	Morphological filters, gradient and first order polynomial	154 93.6	• Simple, accurate • Not robust
2014 Burcin et al. [18]	Nonparametric, unsupervised extended version of Otsu's method	96 MIAS 93	• ccurate, effective, no false segmentation • Not robust

As mentioned in Table 2, a multilevel Otsu's algorithm based method with gradient estimation and linear regression suggested by Kamila and Justyna [15] gives the best performance in this category. This is because of a fast multilevel Otsu's segmentation method that delineates the highlighted pectoral muscle in the preprocessing part and this is accurately marked by the linear regression. There are very rare cases in which computational complexity of the algorithms in terms of speed and time is considered. Further it is revealed that, in a few cases, the density of the pectoral muscle is high and is approximately same as that of the fibro glandular disc or small doubtful masses. Hence, most of the intensity based techniques are not able to discriminate the pectoral muscle from above mentioned dense parts of the breast. Consequently, the performance of all such techniques in these cases is very poor.

3 Region Based Methods

Region is a group of connected pixels with similar properties. Region based segmentation is a technique that allows to determine the regions directly in the given image. Mammographic images can be segmented using initial seed points until some condition or criterion based on distance etc. is satisfied. Region based methods are better than the edge based techniques (Sect. 4) in noisy images where edges are difficult to detect. These methods are simple, fast, leak through weak boundaries. From the literature surveyed, the different solutions provided on the pectoral muscle extraction with the help of region based segmentation techniques with varying rates of success are summarized below.

Raba et al. [19], illustrated an automatic pectoral muscle suppression method using a novel selective region growing algorithm. Initially selected seed point gives a rough approximation of the pectoral muscle region. This rough region is then refined with the help of morphological operations such as opening and closing. With this refinement, pectoral muscle border is highlighted clearly and hence extracted easily. This algorithm when tested on 320 images from MIAS database, showed around 98 % results as "near accurate" out of which 86 % are the good extractions of the pectoral muscle. Moreover, this technique is robust enough to give consistently good results over a wide variety of pectoral muscle appearances among all the mammograms. However, the method is weak in producing correct results when a tissue appears near the pectoral border [9]. The accuracy of the technique can further be improved by taking into account few more shape based and other related features.

Saltanat et al. [20], proposed a different method comprising pixel intensity levels values mapping in an exponential scale followed by a modified thresholding algorithm to line out the pectoral muscle area accurately in an efficient way. A region growing algorithm finds out an approximation of the pectoral muscle area and then verifies the same for exact match with that in the ground truth marked image. If it is not matching exactly, the rough region is adjusted to match with the desired pectoral muscle. This results into a mapped image with brighter regions which is enhanced further to divide it into regions with enhanced contrast. This is followed by specialized thresholding and region growing algorithm with lesser overflow of regions. The method is claimed to be robust over a large number of images with varying size, shape and positions of pectoral muscles appearances. When applied on 322 images of Mammogram Image Analysis Society (MIAS) database, the proposed algorithm gives 84 and 94 % accurate results when evaluated by two radiologists respectively.

A very good effect with simplicity is explored by Nagi et al. [21] through an automated technique for breast segmentation using a seeded region growing algorithm with morphological preprocessing. The process starts with removal of noise in the image using 2-D median filtering. Artifacts are suppressed and background is separated using thresholding and contrast enhancement. A seeded region growing algorithm is then applied to extract the pectoral muscle from the mammogram. A fully automated segmentation leading to accurate breast contour and the better computational performance over a wide range of mammograms with fatty, fatty-glandular and dense-glandular breasts are the two major contributions of the proposed algorithm claimed by the authors. The experimental setup includes two ground truth marked datasets, one is MIAS and the other is UMMC. The proposed method works well on a wide range of mammographic images with varying appearances pectoral muscles and shows good accuracy in pectoral muscle extraction. However, how the initial seed points are selected is not explained at all. The metric of accuracy and the quantified accuracy is not specified.

Nanayakkara et al. [22] proposed a method based on modified Fuzzy C-Means (mFCM) clustering algorithm. The process starts with preprocessing separating out

the region of interest and filtering out unwanted artifacts. A standard FCM is modified to avoid random initialization of cluster seeds and to show better pixel clustering in a speedy way using a block density approach. mFCM makes use of local information to estimate region modes robustly and to classify noisy pixels near the pectoral muscle border. The approximate pectoral muscle boundary obtained is then fitted by using a local maximum average gradient search. The contour obtained thus is smoothed using locally weighted least square fitting mechanism. Performance of the proposed method is tested by using 277 MIAS images with all types of breast tissues and pectoral muscle appearances. The experimental results indicate that the mean FP is 3.35, mean FN is 11.12 and mean Hausdorff distance is 14.83. The performance is also evaluated on some other error metrics and is quite acceptable. The performance of the proposed method is also compared with standard algorithms and it outperforms in terms of parameters such as percent overlap area (POA) and Hausdorff Distance (HD). The method works effectively even in case of pectoral muscle overlapping with breast parenchyma. The experiment is not validated on different sets of images; hence not robust.

The performance evaluation of the above mentioned region based methods for pectoral muscle extraction is presented in Table 3. The solution based on modified Fuzzy C-Means algorithm in [22] is the best among all the methods proposed so far in the region based methods group. This is because this proposed method works accurately well for all images having pectoral muscle overlapping with parenchymal region of breast. However, the computational complexity of the same method is not discussed. It is desired that the researchers should explore region based segmentation further and present a modified version which is simple yet effective on a wide variety of images.

Table 3 Performance evaluation of region based methods

Year authors	Main theme	# Images success %	Advantage/disadvantage
2005 Raba et al. [19]	Region growing and morphological operations	320 86	• Robust method, consistent results • Fails when muscle border is near breast tissue
2010 Saltanat et al. [20]	Specialized thresholding algorithm	322 84 and 94	Efficient, robust
2010 Nagi et al. [21]	Seeded region growing and morphological processing	MIAS UMMC	• Fully automatic, simple, works on images with varying breast densities • Initial seed points selection is not explained
2013 Klein [22]	*Modified fuzzy C-means*	*277 MIAS FP 3.35 FN 11.12*	• *Accurate, efficient, tested on different metrics* • *Fails where dense tissue and pectoral muscle overlaps*

4 Gradient Based Approaches

Pectoral muscle can be separated from the breast region by a straight or curved line between them. Hence, gradient based line detection methods are becoming a de facto standard for this purpose. A few researchers have proposed gradient based techniques using a straight line estimation to identify the pectoral muscle edge with quiet good accuracy. However, the actual pectoral muscle edge is not always straight; instead it is concave at some places and convex at other places. In the literature, few techniques refine the estimated straight line to fit the actual curved pectoral edge in the mammogram. Based on the available research literature, the different gradient based solutions for pectoral muscle extraction with varying rates of success are explained as given below.

Bezdek et al. [23] described a novel method for pectoral muscle edge and breast border detection effectively in four different stages. First, conditioning which is an important determinant of image quality is either by means of histogram equalization, spatial filtering or contrast enhancement to normalize the image intensities required for linear cumulative histogram. The second stage of feature extraction deals with visualizing more apparent edges, digital butte and canyon. This is achieved by means of Sobel and Prewitt masks followed by the geometric characteristics like range and standard deviation. These parameters lead to an exact separation of flat areas and the edge walls with flat top and steep sides as well as steep-walled valleys. These chosen features are then used in a blending function such as Minkowski norms, generalized logistic function or computational learning model to aggregate the information about the edges and to produce a wide range of edge images. The original "byte images" becomes "float images" after feature extraction and the same are reconverted to "byte images" using 'dynamic scaling' functions in the last stage. Once the extracted features match with the proposed blending function, it gives rise to an optimal edge image with full details. A pectoral muscle edge can be easily extracted from this detailed edge image. The overall performance of the algorithm seems to be acceptable for most of the images; however the result analysis with regard to sensitivity, specificity or any other parameter is not carried out in the work undertaken.

Chandrasekhar and Attikiouzel [24] addressed the segmentation of pectoral muscle by modifying the conventional edge detection paradigms to tunable parametric edge detection. The method makes use of four neighborhood based edge features, two directed digital gradients and two statistical descriptors. The pixels in a 3×3 window around a current pixel are "strung out" as a vector $\boldsymbol{\omega}$ of dimensions 9, from top to bottom, left to right, in the original neighborhood. The authors have relaxed the constraint that the edge vector component should only be directed digital gradient. Instead, they allowed any combination of edge sensitive features defined as given below.

$$\varphi_1(\omega) = |(\omega_9 + 2\omega_8 + \omega_7) - (\omega_1 + 2\omega_2 + \omega_3)| \tag{1}$$

$$\varphi_v(\omega) = |(\omega_3 + 2\omega_6 + \omega_9) - (\omega_1 + 2\omega_4 + \omega_7)| \tag{2}$$

$$\varphi_r(\omega) = \max_{1 \le i \le 9}[\omega_i] - \min_{1 \le i \le 9}[\omega_i] \tag{3}$$

$$\varphi_s(\omega) = \sqrt{\left[\frac{1}{9}\sum_{i=1}^{9}\omega_i^2\right] - \left[\frac{1}{9}\sum_{i=1}^{9}\omega_i\right]^2} \tag{4}$$

Here φ_h is horizontal Sobel digital gradient, φ_v is vertical Sobel digital gradient φ_r is range and φ_s is the standard deviation. In order to ensure compatibility between the ranges of the different features, each is normalized so that the range of all four is [0, 4]. The algorithm also relaxed the constraint that the function that combines vector components to yield a real scalar magnitude must satisfy the properties of a norm, and instead allowed a generalized logistic function, $b_L(x)$ as a sigmoid blending function to yield a real scalar and defined as given below.

$$\mathrm{b_L(x)} = \frac{1}{1 + \exp(-\lambda(\mathrm{x} - \beta))} \tag{5}$$

where, λ and β are real positive constants. Thus a modification of the conventional edge detection paradigm gives rise to families of tunable parametric edge detectors, one of which has been used to extract the pectoral edge simply, controllably and reliably from mammograms. When tested on 12 MIAS images with λ = 100 and β = 0.5, it gives simple, controllable and reliable segmentation of the edge of the pectoral muscle for 10 images. However, the algorithm fails to yield a binary pectoral edge image alone.

Ferrari et al. [25] discussed a automatic technique of segmenting pectoral muscle edge by means of Hough Transform. The algorithm starts with binarization procedure that automatically identifies the pectoral muscle edge from the selected region of interest (ROI). The limited and bounded ROI minimizes the possibility of other linear structures biasing pectoral muscle edge representation. High frequency noise is then suppressed using Gaussian Filter. Hough transform of the Sobel gradient of ROI is then computed using

$$p = (x - x_o)\,cos(\Theta) + (y - y_o)\,sin(\Theta) \tag{6}$$

where (x_o, y_o) is the origin of the coordinate system of the image, p indicates the distance and Θ is the angle made by the pixel coordinates under analysis. This method is simple and efficient. However the detailed discussion on the experimental results is not covered.

A fully automatic method for segmenting the pectoral muscle consisting of the muscle edge estimation by straight line and cliff detection is presented by Kwok et al. [26]. The algorithm starts with an iterative thresholding that separates the

pectoral muscle from the parenchymal region. This is followed by a median filtering to remove unwanted noise. A gradient test then eliminates the problematic portions of separating straight line which is then fitted to minimize the least square error. In order to avoid the worst results, the straight line estimation is followed by validation test in an iterative manner till the line is fitted. To refine the muscle edge along this estimated straight line, cliff detection is used. This cliff detection consists of surface smoothing for removal of noise, rough texture etc. and edge detection to find a real shape of the muscle edge. Detecting the cliff is a dynamic process which is carried out until the best curved approximation is determined. Essentially, the intensity drops are identified and the intensity rises are ignored for the better results. This algorithm was tested on MIAS database images and approximately 94 % of images were acceptably segmented. However, this method is weak in detecting exact texture and the vertical pectoral borders especially.

Kwok et al. [27] presented a new adaptive automatic pectoral muscle extraction algorithm in which pectoral muscle edge is roughly identified by a straight line followed by its validation for its location and orientation. The algorithm uses the prior information about position and shape of the muscle edge to approximate the straight line estimation by means of iterative threshold selection to optimize the binarization. Enough care is taken to preserve the average luminance in the binary image. The result which is not always accurate and hence is corrected using cliff detection in a iterative manner to precisely find out the pectoral muscle edge. The algorithm is slightly modified from that of [26] and is designed to identify the intensity cliff nearby the pectoral border. The identified cliff locations are used to remove unwanted locations and to add intermediate values wherever necessary by using two point linear interpolations. This yields an image which is smoothed using average filter to produce a detected curve with some reduction in the sharpness. An iterative refinement then sharpens the edge that separates the pectoral muscle from the parenchymal region to a higher degree of accuracy. The algorithm when applied to MIAS database of 322 images, was found to be robust over a wide range of appearances of the pectoral muscles from all the images. Two expert mammographic radiologists evaluated that the proposed method gives an accuracy of 83.9 %.

Another interesting approach for pectoral muscle extraction is presented by Kwok et al. [28]. The algorithm starts with finding an approximation of the rough straight line along the pectoral muscle edge. Normal's to all the pixels along this rough line directed inwards are calculated to find out the curved portions of the pectoral border. The angles of these normal's vary between 180 to −180. The value of difference between two consecutive normal's can be negative or zero indicating convex and otherwise concave. Thus overall extraction of the pectoral muscle is acceptably accurate. This method is simple and novel. The experiment performed on 322 MIAS images shows an accuracy of 79.5 %. The method is computationally intensive due to iterative nature.

A novel pectoral muscle edge detection method that overcomes a few drawbacks of the conventional techniques to give high precision results is proposed by Weidong et al. [29]. Firstly, a rough portion of the pectoral border consisting of

various texture features is separated by computing optimal threshold curve and local mean square deviation (MSD) curve. These curves help to find an appropriate threshold with respect to the distributed intensities over the mammographic image. A zonal Hough Transform, which is different than the conventional one, is applied to roughly fit the line along pectoral muscle border. This rough boundary is then refined by using a proposed elastic thread method to fit the actual muscle border which is slightly curved. When tested on 60 MLO view mammograms, the proposed method showed an accuracy of 96 % with a high acceptable precision.

Zhou et al. [30] designed and developed an automated algorithm to identify a pectoral muscle edge based on texture field orientation that utilizes a combination of prior information, local and global image features. The a priori knowledge on this muscle is its approximate direction and high intensities compared to its adjacent region. The local information at a pixel is represented by the high gradient in a direction approximately normal to the pectoral boundary, while the global information is represented by the relationship between the potential pectoral muscle boundary points. This is used in this proposed texture-field orientation (TFO) method that utilized two gradient-based directional kernel (GDK) filters: one enhances the linear texture parts followed by extracting a texture orientation of the image on the basis of calculated gradient. This represents the dominant texture orientation at each pixel in the image which is then improved by a second GDK filter for extracting the ridge point. After validation of the extracted ridge points, a shortest-path finding method is applied to prepare the estimation of the probability of each ridge point lying on the actual pectoral border. Thus the ridge points with higher probability are connected to form the pectoral muscle edge. A data set of 130 MLO-view digitized film mammograms (DFMs) from 65 patients, data set of 637 MLO-view DFMs from 562 patients, and data set of 92 MLO view full field digital mammograms (FFDMs) from 92 patients etc. were tested to find out how much adaptive is TFO algorithm. The evaluation showed that 91.3 % of the tested images give out a correct pectoral muscle edge in a acceptable form. Also the technique works well proving its robustness over a wide range of variety of images.

A very simple yet accurate novel method for the detecting the pectoral muscle edge by making use of gradient and shape dependent characteristic traits is highlighted by Chakraborty et al. [31]. The algorithm starts with the pectoral muscle border estimation as a rough line by means of some characteristic traits of the pectoral muscle. This straight line passes through a refinement process to produce a pectoral muscle border more accurately. The method is applied on 200 mammograms (80-MIAS, 80 DR, and 40-CR images) and assessed based upon the false positive (FP), false negative (FN) pixel percentage which was 4.22, 3.93, 18.81 %, and 6.71, 6.28, 5.12 % for selected three databases, respectively. Whereas, mean distance closest point (MDCP) values for the same set of images are 3.34, 3.33, and 10.41 respectively. When compared with two similar techniques for identifying pectoral muscle developed by Ferrari et al. [26] and Kwok et al. [28], proposed technique results are found more accurate. The accuracy of the proposed algorithm still can be improved.

For the detection of pectoral muscle, Molinara et al. [32] presented a new approach based on a preprocessing step useful to normalize the image and highlight

the border separating the pectoral muscle from parenchymal region. This method is based on a preprocessing step that highlights the boundary separating the pectoral muscle from parenchymal region and on the evaluation of the gradient of the image along the x-axis direction. A subsequent step including edge detection and regression via RANSAC algorithm gives rise to a straight line separating pectoral muscle from the parenchymal region. The experiments performed on 55 images from DDSM database, showed that 89.1 % results are acceptable while 10.9 % un-accurate. One of the drawbacks is that this method includes repetitive processes and hence is computationally expensive and slow.

4.1 Proposed Method Using Morphological Operations and RANSAC

A slight modification, in the method suggested in [32], which is based on **RANdom SAmpling Concensus** (RANSAC) algorithm, in terms of the preprocessing for a good quality image followed by a computationally efficient RANSAC algorithm has reflected in acceptable results. In the proposed method, the unwanted noise and artifacts are removed using morphological operations. The upper and lower end points along the pectoral muscle in the top row and left column based on intensity variations is determined. The contrast of the image is them stretched following a binarization using Otsu's graythresh. A sobel operator then used to find out the estimation of edges near pectoral muscle border of the smoothed image. This estimation of the pectoral muscle edge is verified two to three times. The points in between upper and lower end points along approximate pectoral muscle edge are then recorded for RANSAC algorithm.

4.1.1 RANSAC Algorithm

The RANSAC algorithm divides given data into inliers and outliers and yields estimate computed from minimal set of inliers with maximum number of support points. The algorithm used is as given below.

1. Select minimal subset of data points in a random way required to fit a sample model
2. Points within some distance threshold t of model are a consensus set. Size of consensus set is model's support
3. Repeat for N such samples; model with maximum number of points is most robust fit
   - Points within distance t of best model are inliers
   - Fit final model to all inliers.

4.1.2 Experimental Results and Discussion

In order to test the performance of the RANSAC algorithm implemented, 40 images have been selected from mini MIAS database [10] consisting of 322 mammograms. Each of these MLO view mammographic images is having a size of 1024 × 1024 pixels with 8 bits per pixel. The spatial resolution of each pixel is 200 mm per pixel. Though the images are old and outdated, they are chosen for experimental purpose because they are publicly available. The snapshots of the output images are in Fig. 3. The results of pectoral edge segmentation are evaluated visually by the authors and show promising effects as enlisted in the Table 4.

From the experimental analysis, it is revealed that the algorithm works well in case of strong pectoral muscle borders which are nearly straight. In case of curved edges, the performance of the algorithm is poor and below average. The segmentation is even worse in a few cases. The segmentation in some cases fails due to overlapping of the pectoral muscle in the lower part of the breast tissue as the edge is not at all detectable. The time complexity of RANSAC algorithm is given on the basis of Eq. 7.

$$t = \frac{k}{1-a}(\mathrm{Tm} + \mathrm{Ms} * \mathrm{N}) \tag{7}$$

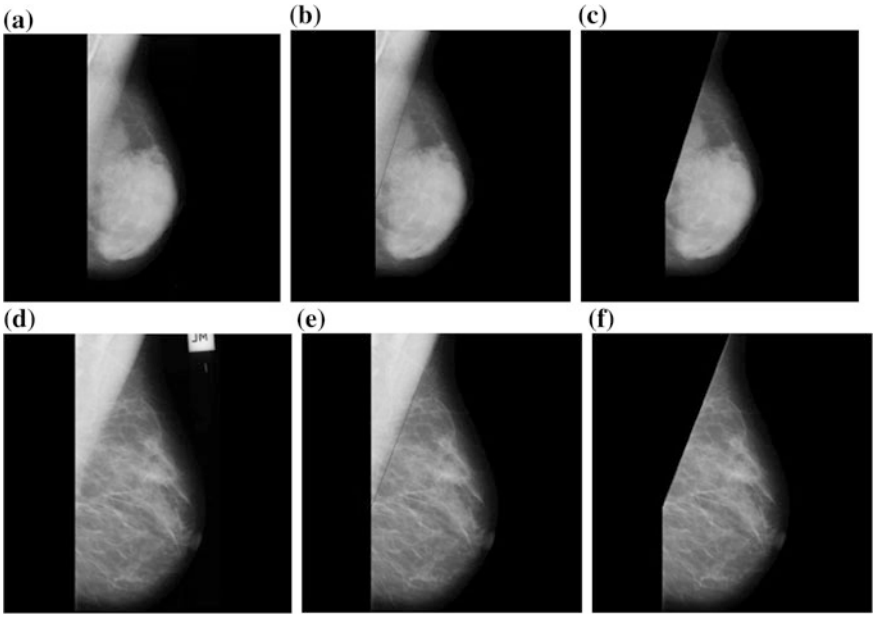

Fig. 3 Experimental results of RANSAC Algorithm. **a** Original image mdb038. **b** Line by RANSAC. **c** Extracted ROI of mdb-038. **d** Original image mdb046. **e** Line by RANSAC. **f** Extracted ROI of mdb-046

Table 4 Experimental results of RANSAC algorithm

Accurate	Acceptable	Unacceptable	Overall accuracy
22	10	8	82 %

Table 5 Computations required for RANSAC algorithm

	Time to compute single model—Tm	Number of samples	Number of models	Total computations
Addition	L	M − 1	k	L(M − 1) (k)
Subtractions	L(L − 1)/2			L(L − 1)/2
Multiplications	L			L
Divisions	0			0
Combinations	L + L/2	M − 1	k	

where, α is probability that a good model is rejected, k is number of samples drawn, N is number of data points, Tm is time to compute a single model, Ms average number of models per sample. k is a function of I, N and h, where I is the number of inliers and h is confidence in the solution. The computations required for implementation of RANSAC algorithm are shown in Table 5.

For N data points, there are L = N(N − 1)/2 possible estimated lines altogether as all the points are treated equally. The computational complexity of all the lines is O(L) which is approximately $O(N^2)$, and the time required to select the suitable line fitting the pectoral muscle border is approximately $O(kMN^2)$. Thus, The contribution here lies in the RANSAC algorithm with limited number of iterations (k) and less number of samples (M) to select the best fit. However RANSAC algorithm fails sometimes at producing the correct model with the user-defined probability leading to an inaccurate model output.

Performance evaluation of gradient based methods for pectoral muscle extraction is tabulated in Table 6.

With the aid of Table 6 in Chap. “Electroanatomical Mapping Systems.An Epochal Change in CardiacElectrophysiology”, the method based on Straight Line Estimation and Cliff Detection presented Kwok et al. [26] gives the best results in terms of 322 number of images. The reason behind the better accuracy of this robust method lies in a special cliff detection mechanism designed to refine the straight line estimate of the pectoral muscle border. This technique succeeds majorly due to its two components, surface smoothing and edge detection. The method presented by Weidong et al. [29] gives 96 % successful results but only on 60 images. No particular method based on gradient that works accurately for identifying the pectoral muscle on a wide range of images with varying positions of pectoral muscle. In majority of the techniques, the solution developed is tested over a specific set of images or a specific problem in given context. There are very rare cases in which computational complexity of the algorithms in terms of speed and time is considered.

Table 6 Performance evaluation of gradient based methods

Year authors	Main theme	# Images success%	Advantages/disadvantages
1998 Bezdek et al. [23]		– –	• Simple, effective • No result analysis
2000, Chandrasekhar and Attikiouzel [24]	Tunable parametric edge detection	12 MIAS 93	• Easy, efficient • Fails on curved muscles
2000 Ferrari et al. [25]	Hough transform	– –	• Simple, effective • Fails on curved muscles
2001 Kwok et al. [26]	*Straight line estimation and Cliff detection*	*322 MIAS* *94*	• *Efficient, accurate* • *Difficult, complex*
2004 Kwok et al. [27]	Modified Cliff detection	322 MIAS 83.9	• Effective accurate • Computation intensive
2004 Kwok et al. [28]	Straight line, iterative curve method	322 MIAS 79.5	• Simple effective • Iterations adds into computational complexity
2007 Weidong et al. [29]	Polyline fitting and elastic thread approach	60 MIAS 96	• High precision, effective • Not robust
2010 Zhou et al. [30]	Texture-field orientation method	– 91.3	• Robust • Computation intensive
2012 Jayasree [31]	Average gradient and shape based feature	MIAS 4.22FP 6.7FN	• Efficient, simple, robust • Fails only on few very complicated images
2013 Molinara et al. [32]	Edge detection, regression via RANSAC	DDSM-55 89.1	• Efficient, avg. accuracy • Fails on images with curved pectoral muscles
2015 Proposed method	Morphological operations and RANSAC algorithm	MIAS 40 82	• Simple, efficient • Not robust

Hence, there is a tremendous scope to develop several new theories to solve this problem. What is required is a simple method that gives a perfect detection with maximum possible accuracy in terms of sensitivity and specificity in a robust way over a wide range of variety of images from different datasets available.

5 Transform Based Approaches

Texture features are useful and successful in the analyzing and interpreting mild textured mammograms. Texture features and intensity variations can be observed closely by decomposing the complex image to elementary form through wavelet analysis by means of Gabor wavelets, dyadic wavelets, Radon transform, Hough transform etc. These elementary components at different positions and scale helps radiologists to analyze the strong intensity level variations precisely. Wavelet transform analyzes various frequency components at various resolution scales and reveals the spatial as well as frequency components simultaneously from the image.

The original image can be perfectly constructed from these decomposed components. However, only a few researchers have exploited the power of wavelet based analysis to extract the pectoral muscle from the mammographic images. From the literature reviewed, the different ideas presented on transform based segmentation techniques with varying rates of success are described as given below.

Ferrari et al. [33] discussed a 'Gabor wavelet' based technique for automatic pectoral muscle edge identification. The algorithm starts with defining a region of interest (ROI) consisting of pectoral muscle in its entirety. This ROI image is then convolved with a specially designed bank of tunable 'Gabor filters' which encapsulate maximum information. This convolution enhances the appearances of all the ROI components in terms of their directional gradients, orientation and scale. The 'Gabor filter' designed in this method with scale parameter S = 4 and K = 12 orientations. This set of 48 parameters leads to 48 filters spanning the entire frequency spectrum. Angular bandwidth of each filter is 15°. Assuming the MLO view of optimally positioned breast, the Gabor filters are applied with 12 orientations and 4 scales. Vectored summation of K filtered images separates out phase Ø(x, y) and magnitude A(x, y) images at each pixel location (x, y), which represent the edge flow vector. Series of nonzero vectors from the opposite directions become candidates for pectoral muscle edge. As optimally positioned MLO view expects the pectoral muscle located within 30°–80°, the corresponding Gabor filter frequency responses can be oriented at 45°, 60° and 75° in the image domain. Disjoint boundary parts are connected by using iterative linear interpolation method. The longest line with maximum pixels is declared as a pectoral muscle border. This method delineates the pectoral muscle edge accurately with FP rate of 0.58 % and FN rate of 5.77 % from 84 mammographic images of mini MIAS database. Though this method gives accurate results, it is computationally more intensive.

Hough Transform and Radon transform are related to each other. Hough transform can make use of radon function for straight line detection. Hough transform is a special form of a radon transform. Linear features from images with high noise can be extracted using radon transform. Kinoshita et al. [34] presented a novel method for pectoral muscle extraction using radon transform. The preprocessing step includes application of Wiener filter to remove minor artifacts with high contrast and preserves the edge information at the same time. The algorithm proposed starts with finding and edge image using 'Canny filter'. Radon transform is then applied on this edge image in an appropriate angular interval of 5° to 50° and −5° to −50° for right and left breast respectively. This leads to a number of straight line candidates representing pectoral muscle edge. The longest high gradient straight line candidate is then selected to delineate pectoral muscle edge separating the breast tissue. Localized radon transform used in this algorithm reduces the computational complexity and increases the speed. However, when tested on 540 mammograms, experimental results for 156 images are 'accurate' with FP < 5 %, acceptable for 220 images with FN < 15 % whereas 164 images are not accepted. Analysis of the experimented results shows that the algorithm works well for straight line edges while its performance with curved edges is not so good.

Mustra et al. [35] presented a hybrid method for extracting pectoral muscle edge. The algorithm starts with determining a reduced region of interest to understand the breast region orientation with its height multiple of 2^n, usually half of the height of image, and width based on skin-air interface of the breast on top line. Height and width chosen at power of 2 allows proper wavelet decomposition. In order to make edge detection an easy task, it reduces the original image to a 3-bit image. Dyadic wavelet of fourth level decomposes this image into approximate edge images. This approximate edge image undergoes interpolation on the basis of wavelets to prepare the image with same size and brightness as that of the original one. A blurring filters of size 40×40 is then applied for smoother edges. The image is thresholded for spreading the gray intensities evenly over the image. A Sobel filter then finds out the pectoral edge which is approximated then to a straight line separating pectoral muscle and breast tissue. When tested on 40 digital mammograms, the experimental results show 'good and acceptable' segmentation on 85 % images. Further analysis reveals that the algorithm works well when there is a high contrast between pectoral muscle and breast tissue. It fails when either the pectoral muscle is small or its contrast is low.

Mencattini et al. [36] presented a method for optimal pectoral muscle extraction using local active contour scheme and Gabor filters in a special combination. As described in [33], original image is initially decomposed using 'Gabor filters' and then the magnitude and phase of the image are then calculated. Vectored summation of 48 'Gabor filters' detect the candidate lines for the pectoral muscle profile, as per the process narrated in [33]. However the candidates selected may mislead increasing the False Negative rate of accuracy. Hence, this method eliminates the false pectoral edge candidates by using different logical conditions as described in [36]. These logical conditions allows to remove false candidate lines and the absent muscle problem is also addressed as well. The experimental results exhibit a very good accuracy up to 90 % on mini MIAS database images.

All the methods discussed above assume that the pectoral muscle can be fitted with a straight line. However, many a times, it is either concave, convex or both. Li et al. [37] presented a homogeneous texture and intensity deviation based method for pectoral muscle segmentation. This method diminishes the limitations of pectoral muscle extraction with a straight line. The process starts with a non-sub-sampled pyramid (NSP) which decomposes the original image into low-frequency and high-frequency sub-bands. The pectoral muscle is represented by means of likelihood maps in texture field calculated through clustering based segmentation and in intensity field calculated using neighbor Mean Square Deviation (MSD) matrix. By combining likelihood maps in a row, initial point on the border of the pectoral muscle is found out first and later other points are obtained by the same process in an iterative manner. The ragged edge obtained this way is further refined with the help of Kalman filter efficiently. The experimental results show an accuracy of 90.06 % on 322 MIAS database images and 92 % on images from DDSM database.

Performance evaluation of transform based methods for pectoral muscle extraction is enlisted in the Table 7. As mentioned in the Table 7, a method

Table 7 Performance evaluation of transform based methods

Year authors	Main theme	#Images success%	Advantages/disadvantages
2004 Ferrari et al. [33]	Tunable Gabor wavelet filters	84 MIAS FP 0.58, FN 5.77	• Accurate, efficient • Sensitivity not analyzed
2008 Kinoshita et al. [34]	Weiner filter, radon filters	540 69.62	• Fast, less complex • Fails at curved borders
2009 Mustra et al. [35]	Dyadic wavelet decomposition of 4th level	40 85 %	• Simple, efficient • Fails if pectoral muscle is small
2011 Mencattini et al. [36]	Gabor filters with logical conditions	90 MIAS 90	• Efficient, easy • Not so accurate
2013 Li et al. [37]	*Texture and intensity deviation, Kalman filter*	*322 MIAS, DDSM 90.06, 92*	• *Robust, efficient* • *Complex*

presented by Li [37] is the best with 92 % accuracy on 322 MIAS database images. The best results are possible because of the efficient Kalman filter applied on approximately correct rough estimation of pectoral muscle edge. There are very few methods that identify the pectoral muscle border accurately and efficiently, over different sets of mammograms. Assumption that the pectoral muscle edge can be fitted with straight line is not always true and limits the accuracy of the results. It is revealed that the research published in the domain of pectoral muscle separation based on transform is really low. Hence there is tremendous scope to develop several new theories to solve this problem. What is required is a simple method that gives a perfect detection with maximum possible accuracy in terms of sensitivity and specificity in a robust way over a wide range of variety of images from different datasets available.

6 Probability and Polynomial Based Approaches

The texture, appearance and density of the breast structures can be used to deduce the different statistical parameters for classifying the pixel intensities of digital mammograms. This approach is successfully used by a few researchers to statistically identify the 'pectoral muscle edge' in a effective way. From the literature surveyed, the different techniques presented on probability and polynomial based 'pectoral muscle segmentation' with varying rates of success are discussed as given below.

Sultana et al. [38] presented a new method with excellent tolerance to noise, for detecting a 'pectoral muscle' in 'mammograms' by making use of 'Mean Shift Approach'. Assumption that a straight line can be fitted to a 'pectoral muscle edge' fails increasing 'False positive rate' which in turn decreases the segmentation

accuracy. This new method smashes out the drawbacks of straight line assumptions and obtains more accurate segmentation results. The process starts with removal of high frequency components in the image that may degrade the segmentation results. 'Region of Interest' consisting of 'pectoral muscle' is selected by using 'Histogram Equalization' followed by thresholding with low value. In the 'mean shift approach', firstly, 'probability density functions' (PDF) is used to estimate the initial points on the edge. To estimate this PDF, the proposed method uses a 'Gaussian kernel' which helps to find out the convergence in a few steps only and forms the cluster of pixels. Approximation of all possible paths in the direction of each point's gradient far from valleys and closer to PDF peak is performed. The process stops after assigning all the pixels a peak value. Thus a labeled map is obtained for each region. The mean value of each region in the map is calculated and the region with mean value bigger than T = 150 are registered as selected candidates for the 'pectoral muscle edge'. The selected region fulfilling the local contrast feature is then declared as a 'pectoral muscle edge'. The experimental results show an 84 % TP rate per image and 13 % FP rate per image. The very advantage of this new method is that it is a parameter-less clustering method which doesn't need any priori information about number of clusters and size of each cluster.

A statistical approach using the idea of 'Goodness of Fit' is discussed by Liu et al. [39] for detecting the 'pectoral muscle edge'. This method works on the basis of joint normal distribution applied to determine the probability of a pixel lying along a either high or low intensity region in the image. Based on this decision, a contour is finalized to remove pectoral muscle from breast tissue. The algorithms assumes the mammogram as a set of independent random intensity variables modeled as a normal distribution $N(\mu, \sigma^2)$ where μ is the mean and, σ^2 is the variance. This is kxk distribution of pixels sharing the same statistical features in the flat regions with strong features. An Anderson Darling (AD) test is applied on this set of pixels to perform a 'Goodness of Fit' test. This AD value is calculated as per the equation given in [39]. A smaller AD value indicates that the pixel belongs to a flat or slow changing (low frequency) component. A larger AD value represents a pixel from the high frequency component or related brighter region in the image. Thus AD value acts as image and edge enhancement measure which is insensitive to the amplitude of intensity variations in the image. Thus when this AD measure is applied on the mammograms, the pectoral muscle with brighter pixels along with its border full of stronger intensity variations is identified very easily. The experimental results on the randomly selected 100 images from MIAS database show that the proposed method gives 'accurate and acceptable' segmentation on 81 images while 'unacceptable' on 19 images. Thus the proposed method works more effectively on 'pectoral muscle extraction'.

Mustra and Grgic [40] discussed a pectoral muscle extraction method that combines conventional pectoral muscle edge identification with the polynomial approximation of curved muscle in six steps. First part includes finding the location where pectoral muscle is situated. This portion is usually 2/3 of the breast height and thus forms a region of interest. Second step is to enhance the contrast using

Contrast Limited Adaptive Histogram Equalization ('CLAHE') algorithm. Third, this is followed by a morphological opening with 3 × 3 structuring element which eliminates small objects and background noise while preserving the larger objects. Fourth step, a preliminary binary mask is created using previously calculated threshold. The rough pectoral muscle border achieved is then smoothed with the help of cubic polynomial fitting in an iterative manner. In fifth step, from the binary mask, 10 points are selected randomly for polynomial fitting of the muscle boundary. A cubic fitting function is chosen with 4 coefficients as shown in the equation:

$$y = p_1 x_3 + p_2 x_2 + p_3 x + p_4 \tag{8}$$

where y is the horizontal coordinate and x is the vertical coordinate and pi are the coefficients. In sixth step, a cubic polynomial function has been chosen because of the curved shape of pectoral muscle. An iterative linear fit function which finds correct slope is chosen to avoid wrong choice of points and is defined as

$$y = p_5 x + p_6 \tag{9}$$

where y is the horizontal coordinate and x is the vertical coordinates. This proposed method when applied on MIAS database of 322 images showed 91.61 % successful results, 7.45 % acceptable results and 0.93 % unacceptable results.

Oliver et al. [41] presented a different pectoral muscle extraction technique using a supervised single strategy. The process starts by computing the probability density function, A_R for each pixel location (x) which is belonging to either background, pectoral muscle or breast. The method takes the advantage of the fact that usually background is dark, pectoral muscle is bright and breast region is in between bright and dark. There are exceptions as well. The intensity range, $I_{R,}$ of these regions is determined based on histogram of each of these regions through a training over a set of images. Local binary patterns (LBP) is then used to characterize each pixel based on its texture probability, T_R. The likelihood of the pixel belonging to a particular region is then calculated by multiplying all three probabilities A_R, I_R and T_R. Finally all the pixels are assigned to the region with higher probability. This allows us to extract pectoral muscle easily. The experimental results on 149 MIAS images show a high degree of accuracy. The exact metric of the accuracy and its analysis is not discussed. The method is easy to implement and efficient. Performance evaluation of statistics and probability based methods for pectoral muscle extraction is tabulated in Table 8.

As observed in the Table 8, the method based on edge detection and polynomial estimation, presented by Mustra and Grgic [40] is the best among all methods in this class. The reason behind the success of this method lies in very good rough estimation and the best results with polynomial refinement over estimated pectoral border. It is very clear that the domain of 'Probability and statistics' is not fully explored but there is enough potential as like other application domains.

Table 8 Performance evaluation of statistics and probability based methods

Year authors	Main theme	# Images success%	Advantages/disadvantages
2010 Sultana et al. [38]	Mean-shift segmentation approach	TP 84, FP-13	• Accurate, efficient • Computation intensive
2011 Liu et al. [39]	Goodness of fit measure	100 MIAS 81	• Simple, effective • Not robust
2013 Mustra and Grgic [40]	*Edge detection, polynomial estimation*	*322 MIAS 92–97*	• *Highly accurate* • *Little-bit complex*
2014 Oliver et al. [41]	Position, intensity, and texture information	149 MIAS High	• Fast, reliable • No result analysis

7 Active Contour Based Approaches

'Active contours' which are also known as snakes are widely applied in medical image processing for detecting edge or curves, segmenting the image, shape modeling etc. Given the set of contours in the image, the snake tries to minimize the internal and external potential energies of all the possible surrounding neighbors of points along the contours. The internal deformation energy controls the capability of snake for stretching or blending of the contour. The external energy though the local minima attract the snake, The Gaussian smoothing filter defines the local minima which give gradient intensity edge that attracts the snake. Thus the classical snake has capability of extracting smooth edge accurately. However, it cannot deal with images with topological variations. Hence, number of improvements in the classical snake methods is suggested by the researchers in the literature. From the literature reviewed, the different studies presented on 'active contour' based segmentation techniques with varying rates of success are discussed as given below.

Wirth and Stapinski [42] suggested a slight modification to the classical 'active contour method' to segment the breast region and identify the 'pectoral muscle edge'. All the initial contour points are identified by applying a dual threshold which is obtained using 'Uni-modal Thresholding Algorithm'. The edges obtained this way are then enhanced using directed edge enhancing method. The enhanced edges are enlarged by removing noise after applying morphological erosion. A modified snake using a greedy algorithm calculated the energy for all the neighbors of all the pixels along continuity, curvature or gradient in the image. Thus lowest energy pixel is selected and again the energy levels in its neighborhood are calculated. At last the snake stops after defining a contour that represents the pectoral muscle edge. The algorithm when applied on 25 images from MIAS database shows acceptable results.

Ferrari et al. [43] discussed a novel method using adaptive contour model for extracting the breast and pectoral muscle boundary. The algorithm starts with contrast enhancement of the image by applying a logarithmic operation. This results in a significant improvement in the low density regions with fewer details near the

pectoral muscle border and breast border. This is followed by a low distortion binarization using Lloyd-Max algorithm. A morphological opening is then applied to reduce the minute unwanted objects and the noise. This demarks the pectoral muscle border approximately. An adaptive active deformable contour model is then applied on the image by adjusting the internal and external energy controlling parameters at each point. The proposed contour model minimizes the energy by means of a greedy algorithm developed by Williams and Shah (1992). The pectoral muscle segmentation results are evaluated based on the FP rate is 0.41 % and FN rate is 0.58 % for 84 mammographic images from MIAS database.

Though the 'active contour models' are useful in accurate extraction of pectoral muscle and other breast regions, the evolution of snake poses several limitations such as (i) sensitivity to initial contour position, quantity of internal parameters, weak edges, noise etc. (ii) an appropriate local minimum may be missed creating problem for convergence of points. (iii) Placing an initial contour closer to expected border (iv) lack of hard constraint regarding specific distance between two pixels.

The approaches discussed below try to eliminate the above mentioned limitations and suggest the modifications in the 'active contour model' to optimize the results.

Chaabani et al. [44] illustrated a method for identifying a pectoral muscle using Hough Transform and active contour. The algorithm starts with application of Canny edge detection followed by a Hough Transform in the angle interval between 135^{o} to 165^{o}. A line with the maximum number of pixels belonging to the contour is selected as pectoral muscle edge. This estimated line is further refined using the active contour model by virtue of energy minimizing spline. The algorithm when applied on DDSM database of mammograms showed that the success rate of pectoral muscle extraction was 92.5 % whereas there are 7.5 % images are unaccepted.

Wang et al. [45] presented a novel method for detecting pectoral muscle edge automatically with the help of 'discrete time Markov Chain' (DTMC) along with a 'active contour' method. Markov chain represents a portion of the object in a random discrete set of current pixel locations over time. The next pixel location is determined by using n-step transition probabilities. This is combined with two properties such as continuity and uncertainty belonging to pectoral muscle region for detecting the approximate border of the pectoral muscle. In the given algorithm, the rows and columns of the image are represented by time and state of the DTMC respectively. Thus DTMC algorithm obtains a rough edge of the pectoral muscle in an iterative manner. The detailed procedure for finding a rough pectoral border is explained in [45]. This rough border is further validated by replacing the false part with a straight line. This coarse pectoral muscle edge is refined by a snake algorithm with a slight modification. The internal energy parameter in the modified snake obtains a smooth pectoral muscle border whereas the external energy stretches the pectoral border as long as possible. The experiment performed on 200 images from DDSM database shows a 'good' segmentation on 75 % images and 'acceptable' segmentation on 91 % images. Accuracy of the detection can further be improved by developing a method searching the pectoral muscle border on the initial row itself.

The multiphase segmentation model proposed by Vese and Chan combines each phase using 'level set functions' for representing 2^n regions. At every stage of contour evolution, the 'level set function' is deviated aside from 'signed distance function' (SDF). Hence it requires costly re-initialization in each curve evolution.

In a topological analysis of medical images, isocontour mapping is very useful in retrieving meaningful information. Kim et al. [46] developed an algorithm focusing on intensity analysis of mammographic images and generates a adaptive contour map using a modified 'active contour model'. In this approach, the complex mammographic images are analyzed to extract topographic features from rough to fine scale and are represented in an isocontour map. This isocontour map image causes the reduction in analysis complexity. The algorithm presented here starts with applying a denoising method for reducing interference noise from the image. This image then undergoes two-phase segmentation and two sub-regions are created. This partitioning is achieved by using the Mumford Shah energy functional recursively. A multipass 'active contour' that is based on 'active contour without edges' (AWCE) proposed by Chan and Vese is used to extract local regional information. In an image with weak edges and intense noise, AWCE model partitions the regions based on energies. The algorithm again partitions one sub-region iteratively by using level set evolution without re-initialization (LSEWR) by minimizing a new energy model. This LSEWR introduces an internal energy term which doesn't allow the 'level set function' to deviate from a 'signed distance function' (SDF) in every contour evolution. This segmentation of sub-regions results into a tree-like structure of all the sub partitions forming a map of adaptive contours. This map is then finalized after skipping the isocontours with same energy. Thus the algorithm works very well on mammographic images with weak and blurred edge effectively and also reduces the isocontour maps quantity from 206 to 11.

Looking into the several limitations posed by snakes based methods, Akram et al. [47] proposed a preprocessing algorithm to remove a pectoral muscle edge along with the other unwanted artifacts from the mammograms. This algorithm makes use of a modified 'active contour method' proposed by Chan and Vese which is based on the Mumford Shah model. The algorithm in its first part, converts a given image into a binary image using a threshold T = 15, and then removes the low and high intensity labels along with scanning artifacts by computing a row and column wise pixel summation method. In its second stage, the pectoral muscle border is traced by using multiphase 'active contour method' which is based on Mumford Shah model. The algorithm introduces a new term M^k which allows moving the contour inwards and also computes its stopping point based on the difference between consecutive contours. Thus the contour of the pectoral muscle and other breast regions is derived. In the third part, the pectoral muscle is extracted out using M^k value. The algorithm when tested on few images from mini MIAS database, shows an accuracy of 77.10 % on images with bad preprocessing results while it is 97.84 % on images with accurate preprocessing results. Thus, the accuracy of the technique discussed herein is highly dependent on the preprocessing results and the value of stopping point in the contour model.

Table 9 Performance evaluation of active contour based methods

Year authors	Main theme	# Images success%	Advantages/disadvantages
2003 Wirth and Stapinski [42]	'Unimodal Thresholding Algorithm' and modified contour model	25 MIAS • Good	• Simple, efficient • No result analysis
2004 Ferrari et al. [43]	Adaptive contour model	84 MIAS FP 0.41, FN-0.58	• Efficient, accurate • Not robust
2010 Chaabani et al. [44]	*Hough transform and active contour*	*DDSM 92.5*	• *Accurate, effective* • *Not robust*
2010 Wang et al. [45]	Time Markov chain and active contour model	200 DDSM 75, 91	• Simple, efficient • Not robust
2013 Kim et al. [46]	Active contour without edges, level set evolution without re-initialization	– –	• Simple • Not robust
2013 Akram et al. [47]	Multiphase active contour method	MIAS 77.10, 97.84	• Accurate with good preprocessing • Not robust

Performance evaluation of active contour based methods for pectoral muscle extraction is tabulated in Table 9. As mentioned in Table 9, the method based on Hough Transform and active contour by Ali Cherif [44], gives the best results among all. The best results in this method are possible due to effective refinement work by the active contour model suggested. As such, there is no particular method that works satisfactorily with better accuracy for the problem of identifying the pectoral muscle, uniformly over a wide variety of mammograms. In majority of the methods, the solution developed is tested over a set of limited images or a specific database images only. There are very rare cases in which computational complexity of the algorithms is considered. Though the researchers are trying their level best to find out an accurate solution, it is revealed from the literature reviewed that the research published in the domain of pectoral muscle separation based on active contour methods is really low. And hence there is tremendous scope to develop several new theories to solve this problem.

8 Graph Based Methods

Image segmentation based on graph theory based methods though computationally intensive can be applied for pectoral muscle edge detection to obtain the expected results. Recently, the appropriate selection of local and global information features along with simplified efficient techniques such as Minimum Spanning Trees and Shortest path have come up with promising results. Based on the research work

studied from the available literature, the different solutions presented on the basis of graph theory for pectoral muscle border identification with varying rates of success are discussed as given below.

Ma et al. [48] presented two methods, one on the basis of adaptive pyramids (AP) and other on minimum spanning tree (MST), for pectoral muscle identification in digital mammograms. The first method implemented in this paper is based on the algorithms suggested by Jolion and Montanvert for building a pyramid graph of vertices (pixels) in the given image. The 'interest operator' and 'two state variables' allow choosing the surviving vertices while exploiting different characteristics of the image. The two state processes for selecting these two state variables is explained in [48]. Thus a graph pyramid consisting of significant components of the image with non surviving vertex as a root is constructed. The reduction in the level of pyramid is dependent on the changing image information and hence the pyramid is adaptive. The second method based on MST constructs a graph of edges (connecting pixels as vertices) with weights defined by a function based on intensity differences. The algorithm proceeds forming a segment of pixels with minimum internal variation and merging two segments with less internal variations. The implementation of MST based algorithm is computationally intensive. None of these methods give accurate pectoral muscle segmentation; any one can be chosen for further smoothing of the results. An active contour is used to bring the rugged pectoral muscle edge closer to the real one. The internal and external energies represented in [48] produce smoothing and highlighting effects on the pectoral muscle border. The implementation of the methods with the selected 84 mammographic images from mini MIAS database shows moderately acceptable results. The performance of the methods based on the error measure of average distance between actual and computed border is less than 2 mm for 80 % and it is less than 5 mm for 97 % of the selected 84 images. Being a first attempt to identify the pectoral muscle using graph theory based methods; the results are encouraging and open a wide scope for further experiments with different local and global characteristics features of the image.

Camilus et al. [49] proposed a graph cut based method to automatically identify the pectoral muscle edge in digital mammograms in an efficient way. The algorithm starts with careful observation of anatomical features and cropping of the mammogram to a region of interest which completely includes pectoral muscle and thus eliminates the unwanted components while reducing the time complexity. The proposed method achieves the segmentation in three major steps. The first step formulates the weighted graph of edges formed by joining the image pixels as vertices. The dissimilarity in the pixels (usually intensities or Euclidean distance) determines the weight on the edges which are then sorted in non decreasing order of weights. The second step of the algorithm sorts the edges based on their weights and homogeneity of edges. Here the ROI gets divided into different segments based on intra region and inter region dissimilarity factors. The mean of all the edges known as intra-region edge average (IRA) calculated with formula specified in

Eq. (1) in [49] represents the homogeneity of the probable image segment. Similarly, inter region edge mean (IRM), as defined in Eq. (6) of [49], allows merging two closely resembling regions. Selection of proper values of parameters δ1 and δ2 for dynamic threshold ultimately leads to a coarse region identified at the top left corner of the ROI. The third step includes the application of Bezier curves to rough pectoral muscle edge. The experiment performed on randomly selected 84 images from MIAS database with ground truth marked by the expert radiologists gives consistent accuracy in terms of FP as 0.64 % and FN as 5.58 %. In most of the tested images, the error rate is very less; especially FP and FN either of which may be less than 0.05 but not both at a time. Thus the results are quite superior to earlier method [48]. The proposed method even works well in case of pectoral muscle border near to the dense tissues and also in case of very small pectoral muscle. However, the results of the method can be improved further by incorporating a few more low level features along with high level features and some more anatomical constraints.

Cardoso et al. [50] presented an algorithm based on a shortest path on a graph to detect the pectoral muscle border automatically. The algorithm assumes that the pectoral muscle, if present, is the change in the intensity levels of the image pixels which ranges from top margin of the image to the left margin. Assuming the origin at the top left corner, the left columns are mapped to the bottom rows due to which the pixels along the pectoral muscle border remains in vertical direction along top to bottom rows with one and only one pixel along each row. A weighted graph of the image is then constructed to find out the optimal vertical path using the cumulative minimum cost C for each pixel using the formula given in [50]. The weight on each edge in the graph is computed with a formula given in [50]. Once the shortest path is constructed, the pectoral muscle edge is finalized. The rows are then transformed back to the Cartesian coordinate system. The contour validation rule is applied to verify if there is no pectoral muscle present in the image. The experiment performed on a set of 50 DDSM images and 100 images from HSJ Portugal, with ground truth marked by expert radiologists, shows the Hausdorff distance of 0.1387 and 0.1426 whereas Mean distance of 0.0545 and 0.0387 respectively. These results are quite good among all the graph based methods for the same task. However, this method may give wrong results in case of multiple strong pectoral muscle borders present in the image.

Performance Evaluation of graph theory based methods for pectoral muscle extraction is enlisted in the Table 10. As seen in the Table 10, the method based on shortest path and support vector machine approach, by Cordoso et al. [50], is the best among all. The better result is possible because of the accurately constructed weighted graph using cumulative minimum cost measure. Further, it is revealed that the crucial tasks in all the graph based methods include constructing the graph, sorting the edges and determining the edge weights in the given image. The different parameters selected to provide either local or global image information plays a vital role in the overall algorithm. The results of some of the recent methods have proved to be really promising but still there is a lot expectation from the accuracy point of view. Hopefully, the researchers will be able to exploit the real power of

Table 10 Performance evaluation of graph theory based methods

Year authors	Main theme	# Images success%	Advantages/disadvantages
2007 Ma et al. [48]	Adaptive pyramids (AP), minimum spanning tree (MST), active contours	84 MIAS 2 mm, Error 80 5 mm, Error 97	• Accurate, effective • Computation intensive
2010 Camilus et al. [49]	Graph cut based method, Bezier curve	84 MIAS FP 0.64 FN5.58	• Efficient • Complex
2011 *Cardoso et al.* [50]	*Shortest path method*	*50 DDSM,* *100 FSJ* *HD 0.1387,* *0.1426* *MD 0.0545* *0.0387*	• *Accurate, effective* • *Computation intensive*

graph theory with some other concepts leading to a accurate solution for the pectoral muscle identification efficiently.

9 Soft Computing Methods

Soft computing is a new emerging trend of obtaining precise solution for complicated cases of the problems. The elements of soft computing includes fuzzy logic, genetic algorithm, neural computing and evolutionary computation. Soft computing techniques can be used for wide range of applications including image segmentation. A few important soft computing based methods for pectoral muscle extraction are explored briefly below.

Karnan and Thangavel [51] presented a two step approach to detect a breast border separating a pectoral muscle indirectly using Genetic Algorithm. The breast border identification process in the proposed work starts with binarization of the given mammographic image using local minima of the histogram as the threshold value. The connected components in the binary image are then smashed out using morphological operations. This results into a binary image showing a breast border. Pixels on this border with a neighborhood window of size 3×3 form a binary kernel which represents the population string in the proposed genetic algorithm. Population strings along fitness values which are sum of intensities along border, generates new population using the genetic 'reproduction' for crossover. The crossover operator then allows exchanging of bits in the 2×2 window of reproduced kernels. This is followed by a 2 dimensional mutation operation in which a transformation is performed if the kernel matches any one of the 14 windows shown in [52]. The kernels in final population represent the enhanced border points on the breast border which indirectly separates a pectoral muscle in the left top corner of

mammogram. The performance of the algorithm analyzed on 114 images with malignancy from MIAS database shows the accuracy of 90.60 % for detection. Further analysis plotting True Positives versus False Positives shows True Positive Fraction as 0.71 and 0.938 whereas False Positive Fraction 0.2890 and 0.0614 with threshold 50 and 150 respectively.

Domingues et al. [53], proposed a fully automatic yet simpler method to detect the pectoral muscle border using a shortest path and support vector machine approach. The method first finds out the region of interest by removing unwanted labels and artifacts in the background by using an adaptive thresholding approach. The image is then cropped to reduce the area of the breast and the computational complexity subsequently. The two endpoints on the pectoral muscle are detected based on two support vector regression (SVR) models. The end point on the pectoral muscle on the top row is detected using a SVR model which is based on the input features obtained from a 32 × 32 thumbnail from the upper half of the cropped image. The other end point on the pectoral muscle on the left column is detected using a SVR model which is based on the input features obtained from a 32 × 32 thumbnail from the lower half of the cropped image. The pectoral muscle border is along the shortest path through edges represented in a graph, in between these two end points. A weighted graph with pixels as nodes and edges connecting neighboring pixels with its magnitude as weight, is searched for a shortest path which demarks the pectoral muscle. When tested, this algorithm shows the Haus-dorff distance of 0.0860 and 0.1232 whereas Mean distance of 0.1232 and 0.0340 on 50 images from DDSM database and HSJ database respectively. Though the accuracy of the proposed algorithm is low, its simplicity is really very acceptable by different manufacturers for devising a solution.

Aroquiaraj et al. [54], proposed a novel pectoral muscle extraction method which is merely a combination of straight line techniques, Connected Component Labeling algorithm (CCL) and, Fuzzy Logic. The method is validated on 322 images from the Mammographic Image Analysis Society (MIAS) database. The evaluation was done using various parameters such as Mean Absolute Error (MAE), Hausdroff Distance (HD), Probabilistic Rand Index (PRI), Local Consistency Error (LCE) and Tanimoto Coefficient (TC). The combination of fuzzy with straight line algorithm gives more than 95.5 % accuracy which is quite high and acceptable.

Sapate and Talbar [55] discussed a modified ‘K-means clustering’ [56] for eliminating a pectoral muscle from the breast tissue leading to a substantial accuracy. The algorithm starts with applying a combination of image filters and morphological operations for removing noise, scanning artifacts, low and high intensity labels from the mammographic images along with accentuating some specific features. A modified K-means algorithm presented in this method attempts to improve the original algorithm in both of its major phases i.e. computing cluster centers and assigning pixels to appropriate clusters with K = 4. The automatic selection of initial cluster centers improves the accuracy of segmentation in the proposed method. The experimental results show that the accuracy and the computational complexity, both, are improved over the original algorithm.

Table 11 Performance evaluation of soft computing based methods

Year authors	Main theme	# Images success%	Advantages/disadvantages
2007 Karnan [51]	Genetic algorithm	114 MIAS 90.60	• Accurate, efficient • Not robust
2010 Domingues et al. [53]	Shortest path and support vector machine approach	50 DDSM HD.0860	• Simpler, efficient • Less accurate, not robust
2014 *Laurence* [54]	*Connected component labeling, fuzzy logic, straight line estimation*	*MIAS322* *95.5*	• *Accurate, efficient* • *Complex, computation intensive*
2015 Sapate [55]	Modified K means clustering method	150 MIAS 86	• Simple, efficient • Not robust

Experimental results on 130 images from MIAS database show the accuracy of pectoral muscle extraction is 86 %. The method is not robust as its results are not validated with different datasets of mammograms.

Performance evaluation of soft computing methods for pectoral muscle extraction is tabulated in Table 11. With aid of the Table 11, the method by Aroquiaraj et al. [54] combining connected component labeling, fuzzy logic and straight line estimation approaches is the best among all. The reason behind these best results is that the fuzziness of the gray scale mammograms is correctly modeled by this fuzzy based approach. The soft computing based approaches give better performance over the existing traditional techniques for the pectoral muscle extraction. However, very few of the soft computing approaches are explored for extracting the pectoral muscle. Therefore, there is tremendous scope for exploring further the potential of soft computing based other approaches to improve the accuracy of the pectoral muscle extraction problem.

10 Conclusions

The overview of the different techniques covered in this chapter focuses on the efforts made in the direction of solving the pectoral muscle extraction problem in the preprocessing part of the CADe systems for detecting breast cancer in its early stage using digital mammograms. The discussion about all the different methods proposed by researchers in literature reveals that there exists very few methods which give more accurate results on a wide range of images with varying position, shape and size of the pectoral muscle in the mammographic image of the breast. On the other hand, there are very rare cases where the computational complexity of the proposed algorithm has been calculated with a due importance. The performance and accuracy of techniques enlisted may be useful for comparison purpose. Hopefully, this study will be useful for the researchers to find out a better scope to devise a robust yet simple pectoral muscle extraction algorithm with better accuracy

over a wide range of mammograms with varying positions, shapes and intensities of the pectoral muscle regions.

Acknowledgments The authors are thankful to Dr. L.M. Waghmare, Director, SGGS IE&T, Nanded and Dr. M.B. Kokare, Coordinator, Center of Excellence in Signal and Image Processing, for their constant encouragement, great support and 24 × 7 open access to state of the art laboratory facilities. Authors are thankful to Dr. Ravindra C. Thool for his constant encouragement. Authors are really very grateful to the referees for their valuable suggestions and comments.

References

1. The American College of Radiology.: http://www.mammographysaveslives.org/Facts
2. Amin, I.I., Hassanien, A.E., Kassim, S.K., Hefny, H.A.: Big DNA Methylation data analysis and visualizing in a common form of breast cancer. In: Hassanien, A.E. et al. (eds.) Big Data in Complex Systems, Studies in Big Data, vol. 9. Springer International Publishing Switzerland (2015). doi:10.1007/978-3-319-11056-1_13
3. Hassanien, A.E., Moftah, H.M., Azar, A.T., Shoman, M.: MRI breast cancer diagnosis hybrid approach using adaptive ant-based segmentation and multilayer perceptron neural networks classifier. Appl. Soft Comput. **14**, 62–71 (2014)
4. Moftah, H.M., Azar, A.T., Al-Shammari, E.T., Ghali, N.I., Hassanien, A.E., Shoman, M.: Adaptive K-means clustering algorithm for MR breast image segmentation. Neural Comput. Appl. **24**(7–8), 1917–1928 (2014)
5. American Cancer Society.: http://www.cancer.org/treatment/understandingyourdiagnosis
6. BreastCancer.Org.: http://www.breastcancer.org/symptoms/testing/types/mammograms
7. Radiopaedia.org.: http://radiopaedia.org/articles/mediolateral-oblique-view
8. Bhateja, V., Misra, M., Urooj, S., Lay-Ekuakille, A.: A robust polynomial filtering framework for mammographic image enhancement from biomedical sensors. IEEE Sens. J. **13**(11), 4147–4156 (2013)
9. Karthikeyan, G., Rajendra, A., Kuang, C.C., Lim, C.M., K Thomas, A.: Pectoral muscle segmentation: a review. Elsevier J. Comput. Methods Progr. Biomed. 48–57 (2013)
10. Suckling, J.: The Mammographic image analysis society digital mammogram database. In: Exerpta Medica. International Congress Series, vol. 1069, pp. 375–378 (1994)
11. Heath, M., Bowyer, K., Kopans, D., Moore, R., Kegelmeyer, W.P.: the digital database for screening mammography. In: Proceedings of the 5th International Workshop on Digital Mammography, pp. 212–218. Med. Physics Publishing (2001)
12. Thangavel, K., Karnan, M.: Computer aided diagnosis in digital mammograms: detection of micro-calcifications by meta heuristic algorithms. GVIP J. **5**(7) (2005)
13. Camilus, K., Govindan, V., Sathidevi, P.: Pectoral muscle identification in mammograms. J. Appl. Clin. Med. Phys. North America **12**(3), 215–230 (2011)
14. Otsu, N.: A threshold selection method from gray-level histogram. IEEE Trans. Syst. Man Cybern. **9**(1), 62–66 (1979)
15. Kamila, C., Justyna, W.: Automatic breast-line and pectoral muscle segmentation. Schedae Inf. **20**, 195–209 (2012)
16. Liu, C.C., Tsai, C.Y., Liu, J., Yub, C.Y., Yub, S.S.: A pectoral muscle segmentation algorithm for digital mammograms using Otsu thresholding and multiple regression analysis. Elsevier J. Comput. Math. Appl., 1100–1107 (2012)
17. Duarte, M.A., Alvarenga, A.V., Azevedo, C.M., Infantosi, A.F.C., Pereira, W.C.A.: Estimating the pectoral muscle and the nipple positions in mammographies using morphological filters. In: XXIII Congresso Brasileiro em Engenharia Biomédica (2012)

18. Burcin, K., Nabiyevb, V.V., Turhanc, K.: A novel automatic suspicious mass regions identification using Havrda & Charvat entropy and Otsu's N thresholding. Comput. Methods Progr. Biomed., 349–360 (2014)
19. Raba, D., Oliver, A., Joan, M., Marta, P., Joan, E.: Breast segmentation with pectoral muscle suppression on digital mammograms. Lecture Notes in Computer Science, pp. 153–158 (2005)
20. Saltanat, N., Hossain, M.A., Alam, M.S.: An efficient pixel value based mapping scheme to delineate pectoral muscle from mammograms. In: IEEE Fifth International Conference on Bio-Inspired Computing: Theories and Applications (BIC-TA), pp. 1510–1517 (2010)
21. Nagi, J., Kareem, S.A., Nagi, F., Ahmed, S.K.: Automated breast profile segmentation for ROI detection using digital mammograms. In: IEEE EMBS Conference on Biomedical Engineering and Sciences (IECBES), pp. 87–92 (2010)
22. Nanayakkara, R.R., Yapa, Y.P.R.D., Hevawithana, P.B., Wijekoon, P.: Automatic breast boundary segmentation of mammograms. Int J. Soft Comput. Eng. (IJSCE). **5**(1) (2015)
23. Bezdek, J.C., Chandrasekhar, R., Attikiouzel, Y.: A Geometric approach to edge detection. IEEE Trans. Fuzzy Syst. **6**(1), 52–75 (1998)
24. Chandrasekhar, R., Attikiouzel, Y.: Segmentation of the pectoral muscle edge on mammograms by tunable parametric edge detection. In: Australian Research Centre for Medical Engineering (ARCME) (2000)
25. Ferrari, R.J., Rangayyan, R.M., Desautels, J.E.L., Frère, A.F.: Segmentation of mammograms: identification of the skin–air boundary, pectoral muscle, and fibro-glandular disc. In: Proceedings of 5th International Workshop on Digital Mammography, Toronto, ON, Canada. pp. 573–579 (2000)
26. Kwok, S.M., Chandrashekar, R. and Attikkiouzel, Y.: Automatic pectoral muscle segmentation on mammograms by straight line estimation and Cliff detection. In: Seventh Australian and New Zealand Intelligent Information Systems Conference, Perth, Western Australia, pp. 67–72 (2001)
27. Kwok, S.M., Chandrasekhar, R., Attikiouzel, Y., Rickard, M.T.: Automatic pectoral muscle segmentation on mediolateral oblique view mammograms. IEEE Trans. Med. Imaging **23**(9), 1129–1139 (2004)
28. Kwok, S.M., Chandrasekhar, R.A., Attikiouzel, Y.: Automatic assessment of mammographic positioning on the mediolateral oblique view. In: International Conference on Image Processing ICIP '04, vol. 1, pp. 151–154 (2004)
29. Weidong, X., Lihua, L., Wei, L.A.: Novel pectoral muscle segmentation algorithm based on polyline fitting and elastic thread approaching. In: The 1st International Conference on Bioinformatics and Biomedical Engineering, pp. 837–840 (2007)
30. Zhou, C., Wei, J., Chan, H.P., Paramagul, C., Hadjiiski, L.M., Sahiner, B.: Computerized image analysis: texture-field orientation method for pectoral muscle identification on MLO-view mammograms. Am. Assoc. Med. Phys., 2289–2299 (2010)
31. Chakraborty, J., Mukhopadhyay, S., Singla, V., Khandelwal, N., Bhattacharyya, P.: Automatic detection of pectoral muscle using average gradient and shape based feature. J. Digit. Imaging **25**(3), 387–399 (2012)
32. Molinara, M., Marrocco, C., Tortorella, F.: Automatic Segmentation of the pectoral muscle in mediolateral oblique mammograms. In: IEEE Conference on Computer-Based Medical Systems, pp. 506–509 (2013)
33. Ferrari, R.J., Rangayyan, R.M., Desautels, J.E.L., Borges, R.A., Frere, A.F.: Automatic identification of the pectoral muscle in mammograms. IEEE Trans. Med. Imaging **23**(2), 232–245 (2004)
34. Kinoshita, S.K., Azevedo-Marques, P.M., Pereira Jr, R.R., Rodrigues, J.A.H., Rangayyan, R. M.: Radon-domain detection of the nipple and the pectoral muscle in mammograms. J. Digit. Imaging **21**(1), 37–49 (2008)
35. Mustra, M., Bozek, J., Grgic, M.: Breast border extraction and pectoral muscle detection using wavelet decomposition. In: Proceedings of IEEE Conference EUROCON'09, pp. 1426–1433 (2009)

36. Mencattini, A., Salmeri, M., Casti, P., Pepe, M.L.: Local active contour models and Gabor wavelets for an optimal breast region segmentation. Int. J. Comput. Assist. Radiol. Surg. (2012)
37. Li, Y., Chen, H., Yang, Y., Yang, N.: Pectoral muscle segmentation in mammograms based on homogenous texture and intensity deviation. Elsevier J. Pattern Recogn. **46**(3), 681–691 (2013)
38. Sultana, A., Ciuc, M., Strungaru, R.: Detection of pectoral muscle in mammograms using a mean-shift segmentation approach. In: IEEE 8th International Conference on Communications, pp. 165–168 (2010)
39. Liu, L., Wang, J., Wang, T.: Breast and pectoral muscle contours detection based on goodness of fit measure. In: IEEE 5th International Conference on Bioinformatics and Biomedical Engineering, pp. 1–4 (2011)
40. Mustra, M., Grgic, M.: Robust automatic breast and pectoral muscle segmentation from scanned mammograms. Elsevier J. Signal Process. **93**(10), 2817–2827 (2013)
41. Oliver, A., Llado, X., Torrent, A., Marti, J.: One-shot segmentation of breast, pectoral muscle, and background in digitized mammograms. In: IEEE International Conference on Image Processing (ICIP), pp. 912–916 (2014)
42. Wirth, M.A., Stapinski, A.: Segmentation of the breast region in mammograms using active contours. In: Visual Communications and Image Processing, International Society for Optics and Photonics, pp. 1995–2006 (2003)
43. Ferrari, R.J., Frere, A.F., Rangayyan, R.M., Desautels, J.E.L., Borges, R.A.: Identification of the breast boundary in mammograms using active contour models. J. Med. Biol. Eng. Comput. **42**(2), 201–208 (2004)
44. Chaabani, A.C., Boujelben, A., Mahfoudhi, A., Abid, M.: An automatic-pre-processing method for mammographic images. Int. J. Digit. Content Technol. Appl. **4**(3) (2010)
45. Wang, L., Zhu, M., Deng, L., Yuan, X.: Automatic pectoral muscle boundary detection in mammograms based on Markov chain and active contour model. J. Zhejiang Univ.-Sci. C (Computers & Electronics) **11**(2), 111–118 (2010). ISSN 1869-1951
46. Kim, J.H., Park, B.Y., Akram, F., Hong, B.W., Choi, K.N.: Multipass active contours for an adaptive contour map. Sensors **13**(3), 3724–3738 (2013). ISSN 1424-8220
47. Akram, F., Kim, J.H., Whoang, I., Choi, K.N.: A preprocessing algorithm for the CAD system of mammograms using the active contour method. Appl. Med. Inf. **32**(2), 1–13 (2013)
48. Ma, F., Bajgera, M., John, P., Slavotinekb, Bottemaa, M.J.: Two graph theory based methods for identifying the pectoral muscle in mammograms. J. Pattern Recogn. **40**, 2592–2602 (2007)
49. Camilus, K.S., Govindan, V.K., Sathidevi, P.S.: Computer-aided identification of the pectoral muscle in digitized mammograms. J. Digit. Imaging **23**(5), 562–580 (2010)
50. Cardoso, J.S., Domingues, I., Amaral, I., Moreira, I., Passarinho, P., Comba, J.S., Correia, R., and Cardoso, M.J.: Pectoral muscle detection in mammograms based on polar coordinates and the shortest path. In: Engineering in Medicine and Biology Society, Annual International Conference of the IEEE., pp. 4781–4784 (2010)
51. Karnan, M., Thangavel, K.: Automatic detection of the breast border and nipple position on digital mammograms using genetic algorithm for asymmetry approach to detection of micro-calcifications. Comput. Methods Programs Biomed. **87**(1), 12–20 (2007)
52. Shi, J., Malik, J.: Normalized cuts and image segmentation. IEEE Trans. Pattern Anal. Mach. Intell. **22**(8), 888–905 (2000)
53. Domingues, I., Cardoso, J.S., Amaral, I., Moreira, I., Passarinho, P., Comba, J.S., Correia, R., Cardoso, M.J.: Pectoral muscle detection in mammograms based on the shortest path with endpoints learnt by SVMs. In: 32nd Annual Internatioanal Conference of the IEEE Engineering in Medicine and Biology Society, pp. 3158–3161 (2010)
54. Aroquiaraj, I.L., Thangavel, K.: Pectoral Muscles Suppression in Digital Mammograms using Hybridization of Soft Computing Methods (2014). arXiv:1401.0870
55. Sapate, S.G., Talbar, S.N.: Pectoral muscle extraction using modified K-means algorithm for digital mammograms. J. Med. Phys. (2016)
56. Hartigan, J.A., Wong, M.A.: A K-means clustering algorithm. J. R. Stat. Soc. Blackwell Publishing **28**(1), 100–108 (1979)

Magnetic Resonance Brain Imaging Segmentation Based on Cascaded Fractional-Order Darwinian Particle Swarm Optimization and Mean Shift Clustering

Hala Ali, Mohammed Elmogy, Eman El-Daydamony, Ahmed Atwan and Hassan Soliman

Abstract A digital image can be partitioned into multiple segments, which is known as image segmentation. There are many challenging problems for making image segmentation. Therefore, medical image segmentation technique is required to develop an efficient, fast diagnosis system. In this paper, we proposed a segmentation framework that is based on Fractional-order Darwinian Particle Swarm Optimization (FODPSO) and Mean Shift (MS) techniques. In pre-processing phase, MRI image is filtered, and the skull stripping is removed. In segmentation phase, the output of FODPSO is used as input to MS. Finally, we make a validation to the segmented image. The proposed system is compared with some segmentation techniques by using three standard datasets of MRI brain. For the first dataset, proposed system was achieved 99.45 % accuracy, whereas the DPSO was achieved 97.08 % accuracy. For the second dataset, the accuracy of the proposed system is 99.67 %, whereas the accuracy of DPSO is 97.08 %. Proposed system improves the accuracy of image segmentation of brain MRI as shown in the experimental results.

H. Ali (✉) · M. Elmogy (✉) · E. El-Daydamony · A. Atwan (✉)
Faculty of Computers and Information, Department of Information Technology, Mansoura University, Mansoura, Egypt
e-mail: Hala_ahmed703@yahoo.com

M. Elmogy
e-mail: melmogy@mans.edu.eg; elmogy@gmail.com

A. Atwan
e-mail: Atwan_2@yahoo.com

E. El-Daydamony
e-mail: Eman.8.2000@gmail.com

H. Soliman
Faculty of Engineering, Department of Electronics and Communication Engineering, Mansoura University, Mansoura, Egypt
e-mail: hhsoliman@yahoo.com

N. Dey et al. (eds.), *Medical Imaging in Clinical Applications*,
Studies in Computational Intelligence 651, DOI 10.1007/978-3-319-33793-7_3

Keywords Medical image segmentation · MRI brain images · Multi-level segmentation, Fractional-order darwinian particle swarm optimization (FODPSO) · Mean shift (MS) clustering

1 Introduction

Today medical imaging technologies provide the physician with some complementary diagnostic tools, such as X-ray, computer tomography (CT), magnetic resonance imaging (MRI), and ultrasound (US). Human anatomy can be visualized by using two widely used methodologies, which are MRI and X-ray. The human soft tissue anatomy can be visualized by using MRI that provides information in 3D, whereas X-ray imaging is used to visualize bones [1]. The most complex organ is the brain of the human body. So, the differentiation between various components and deeply analyze them is a difficult task. The most common images are MRI images for brain image analysis. The magnetic field and radio waves are utilizing by MRI for providing a detailed image of the brain. Moreover, conventional imaging techniques have not many advantages as MRI. Few of them are [2]: high spatial resolution, excellent discrimination of soft tissues, and rich information about the anatomical structure. Brain tumors are classified by neuroradiologists into two groups, namely: glial tumors (gliomas) and non-glial tumors. There are different types of brain tumors that more than 120 types, which leads to the complexity of the effective treatment [3].

For MRI images, segmentation into different intensity classes is required by many clinical and research applications. The best available representation is doing by these classes for biological tissues [4, 5]. Therefore, image segmentation is a crucial process for deciding the spatial location, shape and size of the focus, establishing and amending the therapeutic project, selecting operation path, and evaluating the therapeutic effect. In general, the interest tissues in the brain MRI images are White Matter (WM), Gray Matter (GM), and Cerebrospinal Fluid (CSF). Multimodal medical image fusion is carried out to minimize the redundancy. Also, it enhances the necessary information from the input images that is acquired using different medical imaging sensors. The essential aim is to yield a single fused image that could be more informative for an efficient clinical analysis [6]. The retrieval of complementary information is facilitated by using image fusion for medical images and has been diversely employed for computer-aided diagnosis (CAD) of life-threatening diseases. Fusion has been performed using various approaches, such as pyramids, multi-resolution, and multi-scale. Each and every approach of fusion depicts only a particular feature (i.e. the information content or the structural properties of an image) [7].

On the other hand, Images can be divided into constituent sub-regions this process known as image segmentation. The group of segments or sub-regions is the result of image segmentation that collectively covers the whole image or a set of contours derived from the image. Color, intensity, or textures are some

considerations or computed properties for classifying the pixels in some regions. Adjacent regions are significantly different with respect to the tested characteristic (s) [8]. The manual segmentation takes much time, but it is possible. Therefore, automated detection and segmentation of brain abnormalities are a challenging problem of research since decades [9].

The complexity of the segmentation arises from the different characteristics of the images. Therefore, medical image segmentation is considered as a challenging task [10]. Image segmentation divides digital images into non-overlapping regions. It extracts significant and meaningful information from the processed images. In addition, the numerous analysis can be performed to extract critical areas from the images [11]. MRI is the most commonly used technique for evaluating the anatomical of human brain structures. It provides a comprehensive vision of what happen in patient's brain. It consists of the typical structures of brains, such as GM, WM, CSF, and damage regions. They are presented in single common structures or overlapped areas [12]. WM, GM, and CSF need the accurate measurement for the quantitative pathological analyzes. Segmentation of the MRI brain image data is a goal that is required to process these regions [13].

Segmentation divides an image into regions that are meaningful for a particular task. Region-based and boundary-based methods are two major segmentation approaches. The first approach is based on detecting the similarities. The second approach is based on the continuous boundaries around regions that are formed by detecting discontinuities (edges) and linking them.

Region-based methods find connected regions based on some similarities between the pixels [14]. The most fundamental feature of defining the regions is image gray level or brightness, but other features, such as color or texture, can also be used. However, if we require that the pixels in a region be very similar, we may over segment the image. If we allow too much dissimilarity, we may merge what should be separate objects. The goal is to find regions that correspond to objects as humans see them, which is not an easy goal [15]. Region-based methods include thresholding (either using a global or a locally adaptive threshold; optimal thresholding (e.g., Otsu, isodata, or maximum entropy thresholding)). If this results in overlapping objects, thresholding of the distance transform of the image or using the watershed algorithm can help to separate them. Other region-based methods include region growing (a bottom-up approach using "seed" pixels) and split-and-merge (a top-down quad tree-based approach).

Boundary-based methods tend to use either an edge detector (e.g., the canny detector) and edge linking to link any breaks in the edges, or boundary tracking to form continuous boundaries. Alternatively, an active contour (or snake) can be used. It is a controlled continuity contour that elastically snaps around and encloses a target object by locking on to its edges [14, 16].

There are many image segmentation techniques for medical applications. The specific applications and different imaging modalities control the selection between the various methods of segmentation. The performance of segmentation algorithms is still challenging because there are several imaging problems, such as noise, partial volume effects, and motion. Some of these methods, such as thresholding

methods, region-growing methods, and clustering methods, were studied by many researchers [17–19].

The most frequently used techniques for medical image segmentation is the thresholding. Different classes can be obtained according to the thresholding, which is separating pixels to their gray levels. Partitioning the scalar image intensities to a binary is made by using thresholding approaches. In the segmentation of thresholding techniques, the threshold value is compared with all pixels. If the threshold value is less than the pixels' intensity value, the pixels are grouped into one class. Otherwise, another class grouped other pixels.

Multi-thresholding can be determined by processing the threshold with many values instead of only one value. In digital image processing, the most popular and simple method is a multi-thresholding technique. It can be divided into three different types: global, local, and optimal thresholding methods. In the former, global thresholding methods are used to determinate a threshold for the entire image. It only concerns the binarization of image after segmentation. The second is the local thresholding methods, which are fast methods. In the case of multilevel thresholding, the local methods are suitable. However, the number of the threshold determination is a major drawback. The usage of the objective function is the main advantage of the optimal thresholding methods [20]. Indeed, the determining of the best threshold values amounts to optimize the objective function. There are different types of optimization approaches, such as the Genetic Algorithms (GAs), Firefly Algorithm, and Particle Swarm Optimization (PSO). GAs has a problem for finding an exact solution but is good at reaching a near optimal solution. In contrast, an optimal solution is enhanced by using PSO. The FODPSO is especially used in this paper because it presents a statistically significant improvement in terms of both fitness value and CPU time. In other words, the optimal set of thresholds and less computational time is achieved by using the FODPSO approach with a larger between-class variance than the other approaches [21].

In image segmentation, the most common used techniques are clustering algorithms. It is an unsupervised learning technique, in addition to the number of clusters should be determined by the user in advance to classify pixels [22, 23]. As a result, the grouping of similar pixels or dissimilar pixels in one group is called clustering process [24]. Partitioning and grouping pixels are the two ways of clustering [25]. In partitioning type, dividing the whole image can be done by clustering algorithm into smaller clusters in a successive way. In contrast the grouping type, larger clusters are obtained by starting each element as a separate cluster after then are gathered. The decision of grouping pixels together is based on some assumptions. Mean Shift is an example of an unsupervised clustering technique that does not require prior knowledge, such as the number of the data cluster. It is an iterative method that starts with an initial estimation [26]. MS segmentation is used for making concatenation for both the spatial and range domains of an image. In addition, it is used for identifying modes in this multidimensional joint spatial-range feature space. The bandwidth parameter (the value of kernel size) is free and is not restricted to a constant value. Several methods are used for estimating a single fixed bandwidth. Over-clustering and under-clustering arise from

the chosen value of the bandwidth. The too small value of the bandwidth produces over-clustering, and also the too large value of bandwidth provide critical modes that can be merged under-clustering. When the feature space has significantly different local characteristics across space, under- or over-clustering arise from the use of a single fixed bandwidth that is considered as a drawback [27].

In this chapter, we concentrate on both clustering and multilevel thresholding methods for medical brain MRI image segmentation. Our experiments were conducted by using the most used multilevel thresholding and clustering techniques. This paper is organized into six sections. Section 2 introduces the basic concepts of some different medical image segmentation systems. Section 3 presents some different medical image segmentation systems for the current related work. In Sect. 4, the proposed medical image segmentation system is discussed. It is based on Cascaded FODPSO and Mean Shift Clustering. The experimental results are conducted on three different standard datasets in Sect. 5. The conclusion and the future work are presented in Sect. 6.

2 Related Work

Image segmentation plays a significant role in the field of medical image analysis. The most frequently used techniques for medical image segmentation is the thresholding. Therefore, many researchers have proposed many segmentation techniques for obtaining optimal threshold values based on a multi-thresholding method for image segmentation. In the rest of this section, we will speak about some current research effort in medical image segmentation.

Parvathi et al. [28] proposed for high-resolution remote sensing images a new segmentation algorithm. It can also be applied to medical and nonmedical images. Frist, the remote sensing image is decomposed in multiple resolutions by using a biorthogonal wavelet. A suitable resolution level is determined. The simple grayscale morphology is used for computing the gradient image. The selective minima (regional minima of the image) had imposed to avoid over-segmentation on the gradient image. Second, they applied the watershed transform, and the segmentation result is projected to a higher resolution, using the inverse wavelet transform until the full resolution of the segmented image is obtained. The main drawback in preprocessing step they did not make skull removing this leads to increasing the amount of used memory and processing time.

Clustering techniques are the most common used for medical image segmentation. For example, Khalifa et al. [29] proposed a system for MRI brain image segmentation that is based on wavelet and FCM (WFCM) algorithm. Their algorithm is a robust and efficient approach to segmenting noisy medical images. Feature extraction and clustering are the two main stages of the proposed system. The multi-level 2D wavelet decomposition is used to make extraction of Features. The FCM clustering is provided with the feature of the wavelet decomposition. Finally, the image is segmented into (WM, GM, and CSF) these three classes are

the brain tissue. The limitation of their work is that they did not apply skull removal. Without removing the skull, scalp, eyes, and all structures, which are not of interest, increases the amount of used memory and increase the processing time.

Bandhyopadhyay and Paul [30] proposed a way for brain tumor diagnosis that it is an efficient and fast way. Multiple phases are included in their system. The first phase consists of more than MR images registration taken on adjacent layers of the brain. In the second phase, to obtain a high-quality image, a fusion between registered images is performed. Finally, improved K-means algorithm is performed with the dual localization methodology for segmentation. The main disadvantage is the large grid dimension. The fine anatomic details also were ignored, such as an overlapping region of gray and white matters in the brain or twists and turns in the boundary of the tumor.

Arakeri and Reddy [31] proposed an approach for MRI brain tumor by using wavelet and modified FCM clustering that provides efficient segmentation of brain tumor. In the first phase, the wavelet transform is used for making decomposition of the image and in the next phase modified FCM algorithm is used to segment the approximate image in the highest wavelet level. The low-resolution image is restraining noise and reducing the computational complexity. Then, the low-resolution segmented image is projected on to the full resolution image by taking inverse wavelet transform. The main limitation of this work is the use of highest wavelet level decomposition this may lead to neighboring features overlapped of the lower band signals.

On the other hand, many researchers do this best to improve the FCM algorithm performance for image segmentation. For example, Mostfa and Tolba [32] proposed a wavelet multi-resolution with EM algorithm for segmenting the medical image known as (WMEM). In the first stage, a spatial correlation between pixels is detected by Haar transform with length 2. In the second stage, EM algorithm receives the original image. The two scaled images are generated from 2D Haar wavelet transform to make segmentation separately. Then, these three segmented images are produced with their weighted or thresholding value. Each pixel in the image is classified depending on these three segmented images. They did not demonstrate what about the time of each algorithm or in the integration method.

Javed et al. [11] proposed a system for noise removal and image segmentation. Their system comprised of two major phases that involved a multi-resolution based technique and k-means technique. False segmentation is arisen from noise corrupted images, which this is primary issues of Uncertainty and ambiguity. Therefore, on the input image multi-resolution based noise removal is applied as a preprocessing step. The image free noise is segmented by k-means based technique to identify different objects present in image data automatically. The main disadvantage is they did not make skull removing in preprocessing step that increases the amount of used memory and increases the processing time.

Jin et al. [13] proposed a multispectral MRI brain image segmentation algorithm. This algorithm based on kernel clustering analysis. The algorithm is called as multi-spectral kernel based fuzzy c-means clustering (MS-KFCM). In their proposed system, MRI T1-weighted and T2-weighted brain image are filtered and then

make a selection to the features as the input data. The separation improvement of the input data is doing by mapping the input data to a high-dimensional feature space. The output of FCM clustering is used as the initial clustering center of MS-KFCM. The performance of MS-KFCM is better than FCM and KFCM, but FCM and KFCM are similar in the performance. The advantage of using the multi-spectral image segmentation is to achieve higher accuracy than to use single-channel image segmentation. The limitation of their work is that they did not make skull removal. Without removing the skull, scalp, eyes, and all structures, which are not of interest, the memory usage and the processing time are increased.

Mangala and Suma [33] presented brain MRI image segmentation algorithm that is called Fuzzy Local Gaussian Mixture Model (FLGMM). They removed noise by applying Gaussian filter. They handled the bias field estimation by using BCFCM. Second, all techniques initialized by using K-means. Then, they used FLGMM to make segmentation to the processed image. The Jaccard similarity (JS) is used for measuring the segmentation accuracy. The JS value is [0, 1], and the higher value of JS means that the segmentation is more accurate than the lower values. They did not deal with reducing the computational complexity and improving the robustness.

The most frequently used techniques for medical image segmentation is the thresholding. Therefore, many researchers have proposed many segmentation techniques for obtaining optimal threshold values based on a multi-thresholding method for image segmentation. For example, Ghamisi et al. [34] presented two methods for images segmentation to identifying the n − 1 optimal for the n-level threshold. The FODPSO and (DPSO) are proposed for image segmentation. Delineating multilevel threshold, the disadvantages of preceding methods in terms of limitation of the local optimum, and high CPU process time are solved by using these two methods [34]. The efficiency of other well-known thresholding segmentation methods is compared with their proposed methods. When taking into consideration some different measures, such as the fitness value, STD, and CPU, their experimental results showed that their proposed methods superior to other compared methods. On the other hand, they did not handle real-time image segmentation.

Ghamisi et al. [35] introduced two main segmentation approaches for classification of hyperspectral images. They used FODPSO and MS segmentation techniques. The support vector machine (SVM) is used for classifying the output of these two methods. In their proposed system, in the beginning, the input image with (B bands) enters to the FODPSO to perform segmentation. Second, the output of FODPSO is supplied to MS as input to make segmentation to the (B bands) image. Finally, the classification process of (B bands) to produce (1 band) image is done by using SVM. The main disadvantage of MS is the tuning size of the kernel, and the obtained result may be affected considerably by the kernel size.

Hamdoui et al. [36] proposed an approach that known as Multithresholding based on Modified Particle Swarm Optimization (MMPSO). They implemented their proposed method for segmenting images based on PSO to identify a multilevel threshold. They mentioned that their proposed method was suitable for complex gray-level images. Their results indicated that the MMPSO is more efficient than

PSO and GA. The main drawbacks of this method are that their approach is better only when the level of segmentation increase and the image is with more details.

AbdelMaksoud et al. [37, 38] proposed a system based on hybrid clustering techniques for medical image segmentation to provide the detection of brain tumor with an accurate way and minimal execution time. The integration clustering techniques are doing between K-means and FCM or K-means and PSO. In each stage, the accuracy and minimum execution time are putting into account. In the preprocessing phase, the median filter is used to enhance the quality of the image and making skull removal, this leads to reducing the time and the used amount of memory. In segmentation stage, all advantages are preserved for K-means, FCM, and PSO; while the proposed techniques solved their main problems. The thresholding is applied for clear brain tumor clustering. Finally, the contoured tumor area is obtained by the level set stage on the original image.

Samanta et al. [39] proposed a multilevel thresholding technique that has been used for image segmentation. An optimal threshold value is selected by using a new approach of Cuckoo Search (CS). CS is used to achieve the best solution for the initial random threshold values or solutions. It evaluates the quality of a solution correlation function. Finally, MSE and PSNR are measured to understand the segmentation quality. For CS, the first phase is to initial generations of the population for the cuckoo nest. Second, the original image is segmented by the candidate solution and rank the solution as per the correlation value. Third, the current best solution is found. Fourth, randomly few nests are distorted by pa probability. Finally, the final segmented image is doing by the best candidate solution.

Dey et al. [40] presented a system that extracted blood vessels from retinal images. It provides early diagnosis of diseases like diabetic retinopathy, glaucoma, and macular degeneration. The most frequent disease that can occur glaucoma. It has serious ocular consequences, which can even lead to blindness if it is not detected early. First, they made a conversion from the green channel of the Color Retinal Fundus to grayscale image. Second, the gray image is used to apply an adaptive histogram equalization [6]. Third, the median filter is used to make subtracting the background from the foreground. Fourth, they used FCM followed by binarization and filtering. Fifth, the corresponding disease is compared with the ground truth image. Finally, the calculation of the sensitivity, specificity, PPV, PLR, and accuracy are applied.

3 Basic Concepts

3.1 Thresholding Techniques

Several techniques for image segmentation are proposed for medical applications. The specific applications and different imaging modalities control the selection of the various methods. Imaging problems, such as noise, partial volume effects, and motion can also have significant consequences on the performance of the

segmentation algorithms. In the thresholding, different classes can be obtained according to separating pixels to their gray levels. The approaches that perform a binary partitioning of the image intensities to scalar segment images is called Thresholding approaches. In the thresholding segmentation, the threshold value is compared with all pixels. The threshold value that is less than pixel's intensity value is grouped into one class. Otherwise, another class grouped other pixels. The multi-thresholding determined more than one threshold values [11, 41]. The main restriction of thresholding the spatial characteristics of an image does not typically take into consideration. Therefore, noise and intensity inhomogeneities were susceptible to it, which can occur in MRI images. Thresholding is defined mathematically by Eq. (1) [42]:

$$g(\mathrm{x,y}) = \begin{cases} 1, & \text{if f(x, y } > T) \\ 0, & \text{if f(x, y)} \leq \mathrm{T} \end{cases} \tag{1}$$

where f(x, y) represent the input image and T the value of the threshold. g(x, y) is the segmented image that is given by Eq. (1). Using the above Eq. (1), we can be segmented the image into two groups. The multi-threshold point is used when we want to segment the given image into multiple groups. This equation Eq. (2) segments the image into three groups If we have two threshold values.

$$g(\mathrm{x,y}) = \begin{cases} \mathrm{a}, & \text{if f(x, y)} > \mathrm{T}_2 \\ \mathrm{b}, & \text{if } \mathrm{T}_1 < f(\mathrm{x,y}) \leq T_2 \\ \mathrm{c}, & \text{if f(x, y)} \leq \mathrm{T}_1 \end{cases} \tag{2}$$

The algorithm for the thresholding is given by Gonzalez et al. [43] as follows:

Step 1 An initial estimation is selected for the global threshold, T.
Step 2 The image is segmented by using the value of threshold (T), as shown in Eq. (4), to get 2 groups of pixels. If pixels with intensity values > T are contained in G1, else the pixels with values $\leq$ T are contained in G2.
Step 3 m1 and m2 are the average mean intensity values that are computed for the pixels in G1 and G2 respectively.
Step 4 The new threshold value is computed.
Step 5 If the difference between a predefined parameter. Δ T is smaller than values of T in successive iterations. This process is repeated for steps 2 through 4. Otherwise, it is stopped.

3.1.1 Global Thresholding

In the Global thresholding method, for the entire image, only one threshold value is selected. Bimodal images are used to Global thresholding where the image foreground and background has the homogeneous intensity and high contrast between them, the Global thresholding method is simple and faster in computation time.

3.1.2 Local Thresholding

An image is divided into sub-images and the threshold value computed for each part. Global thresholding takes less computation time than a local threshold. When there is a variation in the background in an image, Its result is satisfactory. It can extract only small regions [44].

Histogram Thresholding

It is based on thresholding of histogram features and gray level thresholding. The threshold is mathematically defined by Eq. (1). The algorithms as follows [45–49]:

Step 1 The histogram is drawn for each part of the MRI brain image that is divided around its central axis into two halves.
Step 2 Threshold point of the histogram is calculated based on the comparison technique made between two histograms.
Step 3 The segmentation process for both the halves is doing by the threshold point.
Step 4 For finding out the physical dimension of the tumor, the detected image is cropped along its contour.
Step 5 The segmented image pixel value is checked for creating an image of the original size. If the threshold value is less than the pixel value, then assign a value equal to 255 else 0.
Step 6 Segment the tumor area.
Step 7 The tumor region is calculated.

3.2 An Overview of PSO Algorithm

One of the evolutionary optimization methods is the PSO algorithm. Typically, the evolutionary methods are successful as shown in the experiments for segmentation purposes [50, 51]. Evolutionary algorithms ideally do not make any assumption about the underlying problem. Therefore, all types of problems are performed well approximating solutions. In the traditional PSO, the particles are called candidate solutions. To find an optimal solution, these particles travel through the search space, by interacting and sharing information with neighbor particles, namely their individual best solution (local best) and computing the neighborhood best. Also, in each step of the procedure, the global best solution obtained in the entire swarm is updated. Using all of this information, particles realize the locations of the search space where success was obtained and are guided by these successes.

3.3 Multilevel Thresholding Method Based on FODPSO

An efficient way to perform image analysis is to use multi-level segmentation techniques. However, the selection of a robust optimum n-level threshold is required to be automatic. In the following discussion, a more accurate formulation of the problem is introduced.

Image analysis can be performed in an efficient way by using multi-level thresholding segmentation techniques. The essential challenge in the image segmentation is the selection of the optimum n-level threshold. However, the selection of the optimum n-level threshold is required to be automated. The rest of this section presents a more precise formulation of the problem, introducing some basic notation.

In the proposed system, a gray image is used as the color image takes more computation time. For each image, there are L intensity levels, which are in the range $of\{0, 1, 2, \ldots, L-1\}$. Then, we can define the probability distribution as [52]:

$$\mathrm{p_i} = \frac{\mathrm{h_i}}{\mathrm{N}}, \sum_{\mathrm{i}=1}^{\mathrm{N}} \mathrm{p_i} = 1 \tag{3}$$

where i represents a particular intensity level, i.e.,$1 \leq i \leq L-1$. The total number of the pixels in the image is N. The number of pixels can be represented by h_i for the corresponding intensity level i. In other words, image histogram is represented by h_i, which can be normalized and considered as the probability distribution p_i for component of the image. The total mean (i.e., combined mean) can be simply computed as:

$$\mu_{\mathrm{T}} = ip_i \tag{4}$$

The generic n-level thresholding can be derived from the 2-level thresholding in which $\mathrm{n}-1$ threshold levels $\mathrm{t_j}$, $\mathrm{j}-1, \ldots, \mathrm{n}-1$, are necessary and where the operation is performed as expressed below in Eq. (5):

$$F(x,y) = \begin{cases} 0 & f(x,y) \leq t_1 \\ \frac{1}{2}(t_1 + t_2), & t_1 < f(x,y) \leq t_2 \\ \vdots & \\ \frac{1}{2}(t_{n-2} + t_{n-1}), & t_{n-2} < f(x,y) \leq t_{n-1} \\ L, & f(x,y) > t_{n-1} \end{cases} \tag{5}$$

The image is represented by x, which is the width (W) of the image, and y, which is the height (H) of the image. Then, the size can be represented by $\mathrm{H} \times \mathrm{W}$ denoted by $\mathrm{f(x, y)}$ with L intensity gray levels. In this situation, the pixels of a given image will be divided into n classes $(\mathrm{D_1}, \ldots, \mathrm{D_n})$ It may represent multiple objects or even specific features on such objects (e.g., topological features).

The method that maximizes the between-class variance is used for obtaining the optimal threshold. It is the most efficient computational method that can be generally defined by:

$$\sigma_B^2 = \sum_{j=1}^{n} W_J(\mu_j - \mu_T)^2, \tag{6}$$

where j represents a particular class in such a way that W_J and μ_j are the probability of occurrence and the mean of the class j, respectively. The probabilities of occurrence W_J of classes $(D_1, \ldots, D_n)$ are given by:

$$W_J = \begin{cases} \sum_{i=1}^{t_j} p_i, j = 1 \\ \sum_{i=t_{j-1}+1}^{t_j} p_i, 1 < j < n, \\ \sum_{i=t_{j-1}+1}^{L} p_i, j = n, \end{cases} \tag{7}$$

W_J is the mean of each class that is computed as:

$$\mu_j = \begin{cases} \sum_{i=1}^{t_j} \frac{ip_i}{W_j}, j = 1 \\ \sum_{i=t_{j-1}+1}^{t_j} \frac{ip_i}{W_j}, 1 < j < n, \\ \sum_{i=t_{j-1}+1}^{L} \frac{ip_i}{W_j}, j = n, \end{cases} \tag{8}$$

In other words, the n-level thresholding problem is limited to an optimization problem. It searches for the thresholds t_j that make maximization for the objective function (i.e., a fitness function) defined as:

$$\varphi = \max_{1 < t_1 \cdots < t_{n-1} < L} \sigma_B^2(t_j) \tag{9}$$

As the number of threshold levels increases, this optimization problem involves a much larger computational effort. It makes us think of the question: Which type of methods that the researcher can use for solving this optimization problem for real-time applications? [52]. FODPSO is an example of such methods that recently presented. FODPSO is a new version that derived from the DPSO. To control the convergence rate of FODPSO, the fractional calculus is used to solve this kind of problems [35].

When the threshold levels and image components increase the optimization problem, it needs much computational effort. Recently, biologically inspired

methods, such as PSO, are alternatives to analytical methods to solve efficiently optimization problems [13]. An example of such methods that is presented recently is the FODPSO. This method is a natural extension of the DPSO. It is presented using fractional calculus to control the convergence rate. It was extended for the classification of remote sensing images in [18, 35, 52].

As in the classical PSO, to find an optimal solution particles travel through the search space in FODPSO by interacting and sharing information with other particles. In each step of the algorithm t, the success for a particle is evaluated by a fitness function. Each particle n, moves in a multidimensional space to model the swarms according to a position $x_n^s[t], 0 \leq x_n^s[t] \leq L-1$, and velocity v_n^s [t]. the individually best $\tilde{x}_n^s$ [t] and the globally best $\tilde{g}_n^s$ [t] information are highly control the position and velocity values.

$$\begin{aligned} v_n^s[t+1] = {} & \alpha\, v_n^s[t] + \frac{1}{2}\alpha\, v_n^s[t-1] + \frac{1}{6}\alpha(1-\alpha)v_n^s[t-2] \\ & + \frac{1}{24}\alpha(1-\alpha)(2-\alpha)v_n^s[t-3] + \rho_1 r_1\left(\tilde{g}_n - x_n^s[t]\right) \\ & + \rho_2 r_2\left(\tilde{x}_n^s - x_n^s[t]\right) \end{aligned} \tag{10}$$

$$x_n^s[t+1] = x_n^s[t] + v_n^s[t\ +\ 1] \tag{11}$$

The global and individual performance are controlled by weights coefficients ρ_1 and ρ_2. Within the FODPSO algorithm, the fractional coefficient controls the inertial influence of particles. The random vectors r_1 and r_2, which is a uniform randomly number between 0 and 1 with each component. The fractional coefficient is parameter α, will weigh the influence of past events in determining a new velocity,$0 < \alpha < 1$. The velocities of particles' are initially set to zero when applying multilevel thresholding FODPSO of images and their position is randomly set within the boundaries of the search space, i.e., $v_n^s[0] = 0$ and $0 < x_n^s[0] < L-1$. In other words, the number of intensity levels L determine the search space, i.e., if an 8-bit image segmentation, and then particles will be deployed between 0 and 255. Hence, each particle in the same swarm will be found and compared to all particles, a possible solution φ^c. The higher between-class variance φ^c the particle will be the best performing particle (i.e., $\tilde{g}_n^s$), thus luring other particles toward it. It is also noteworthy that when a particle improves, i.e., when a particle is able to find a higher between-class variance from one step to another, the fractional extension of the algorithm outputs a higher exploitation behavior. This allows achieving an improved collective convergence of the algorithm, thus allowing a good short-term performance. FODPSO is a method with a higher between-class variance to specify a predefined number of clusters. In [35], the authors demonstrated that the FODPSO-based segmentation method performs considerably better in terms of accuracies than genetic algorithm, bacterial algorithm, PSO, and DPSO, thus finding different number of clusters with a higher between-class variance and more stability in less computational processing time.

4 The Proposed MRI Image Segmentation System

There are many medical image segmentation systems that are used for detecting brain structure and tumor. All of these systems are not equal in accuracy and in execution time. Therefore, our goal is to build a robust segmentation system to deal with the brain images. As all thresholding-based methods, FODPSO segmentation suffers from two main disadvantages. First, inhomogeneity cannot be handled. Second, when the object intensity does not appear as a peak in the histogram. In the MS method, the size of the kernel needs to be tuned by the user [35]. The tuning may be a difficult task, and the final results may be dramatically affected. The proposed medical image segmentation system consists of three main phases: pre-processing, segmentation, and validation, as shown in Fig. 1. We take into

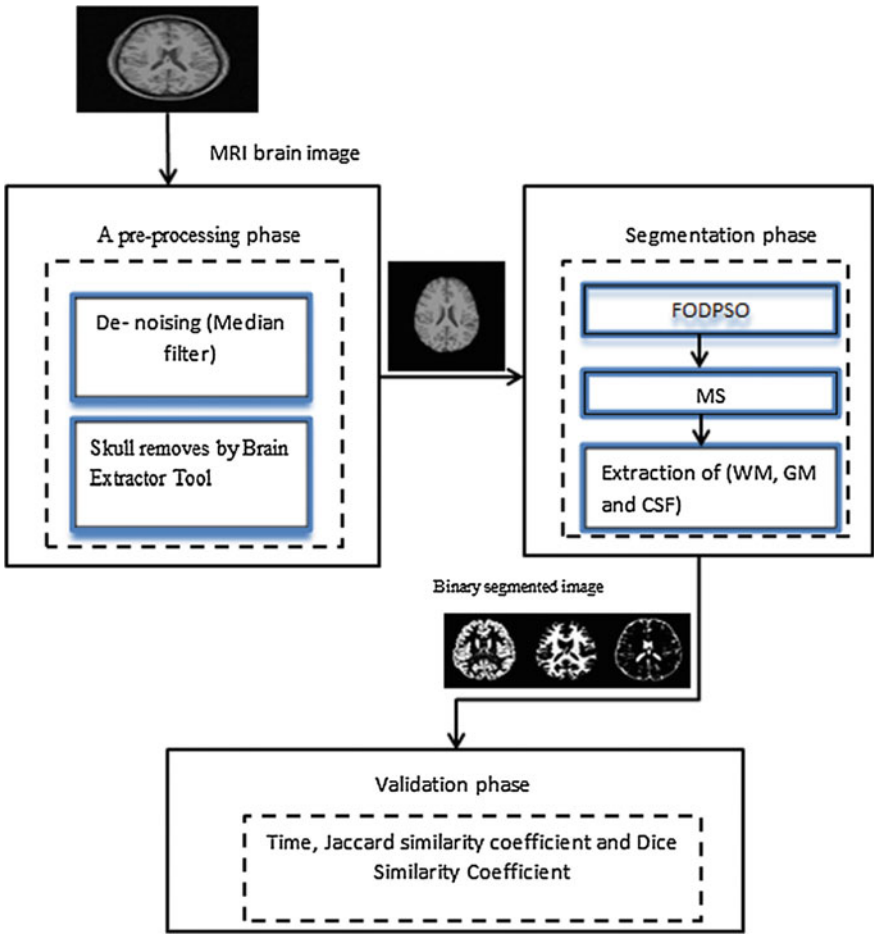

Fig. 1 The block diagram of the proposed framework

account the accuracy and the time. In the preprocessing stage, we used the median filter and brain extractor tool for skull stripping from the processed image. In the segmentation phase, we make integration between MS and FODPSO that takes all advantages of them. Finally, validation is performed on the proposed system and the ground truth.

The CT is used for image segmentation method, but it is not used alone. In addition, it is not good as MRI. It is used with MRI in the fusion process to improve the data. The image resolution of lesion or target is high in MRI rather than CT scans in stereotactic surgery. The stereotactic frame makes artifacts in images but less in MRI because it is used contrast enhancement or different pulse sequences. Especially, the benefits of using MRI rather than CT that is high contrast ventriculography, when performing stereotactic surgery in patients with brain lesions or normal anatomical targets [53].

Ghamisi et al. [35] proposed an approach that is based on two segmentation methods: FODPSO and mean shift segmentation. The proposed framework is used for dealing with Hyperspectral image analysis. In contrast, we applied the same proposed approach with a different data type of image for brain MRI. We applied proposed approach in MRI brain medical image. As compared the hyperspectral image with MRI brain medical image, there are many disadvantages of hyperspectral image. The cost and complexity are the primary disadvantages. Large data storage capacities, fast computers, and sensitive detectors are needed for hyperspectral data analysis. Large hyperspectral cubes require significant data storage capacity, multidimensional datasets, and potentially exceeding hundreds of megabytes. The processing hyperspectral data, cost, and time are greatly increased. Therefore, our proposed system is applied on MRI brain medical image that gives better accuracy and small time consuming of the segmented image as compared to Hyperspectral image.

4.1 The Preprocessing Phase

The improvement of image quality and noise removal are the main target of this stage. The de-noising and skull stripping are sub-stages of the pre-processing stage. In medical images, de-noising is necessary for sharping, clearing, and eliminating noise and artifacts. Gaussian and Poisson's noise are usually affected by MRI images [54]. By using a median filter, the numerically sorted order is obtained from all pixel values in the window, and then the processed pixel is replaced by the median of the pixel values. Linear filtering is not better as median filtering for removing noise in the existence of edges [55]. The MR images also corrupted by Rician distributed noise. It is assumed to be white, and these images are suffered from reducing a contrast of signal-dependent bias. However, a widely used acquisition technique to decrease the acquisition time gives rise to correlated noise [56, 57]. On the other hand, the skull and the background of the image are removed while they do not contain any useful information. Decreasing the amount of the

memory usage and increase the processing speed are done by removing unhelpful information, such as background, skull, scalp, eyes, and all other structures. Skull removal is done by using BET (Brain Extractor Tool) algorithm [58].

4.2 The Segmentation Phase

In this stage, we make integration between MS and FODPSO to take the advantages of these segmentation techniques. First, FODPSO will segment the input MRI brain image as shown in Table 1. Then, MS will segment the output of this step again. In other words, the result of FODPSO is used as an input to MS. The number of the clusters can be predefined by FODPSO, and a higher between-class variance to find the optimal set of thresholds in less computational time can be obtained by it. So, it

Table 1 FODPSO segmentation algorithm [18]

Initialize α, ρ_1, ρ_2 // fractional coefficient , global and local weight
Initialize N,N_{min}, N_{max} //initial, minimum and maximum number particles with each swarm
Initialize N^s,N^s_{min}, N^s_{max} // initial, minimum and maximum number swarm
Initialize Δv // maximum number of levels a practical can travel between iterations
I_T, N_{kill} // total number of iteration and maximum stagnation of swarms

$$p_i = \frac{h_i}{N}, \sum_{i=1}^{N} p_i = 1$$

$\mu_T = ip_i$
Initialize $0 \le x_n^s[t] \le L-1$// initial position of all particles from all swarm
Initialize$\tilde{x}_n^s$, $\tilde{g}_n^s$ based on $x_n^s[0]$ //initial local best of all particles and global best of all swarm
For each iteration t until I_T // main loop
  For each particles n of swarm s

$$v_n^s[t+1] = \alpha\, v_n^s[t] + \frac{1}{2}\alpha v_n^s[t-1] + \frac{1}{6}\alpha(1-\alpha)v_n^s[t-2] + \frac{1}{24}\alpha(1-\alpha)(2-\alpha)v_n^s[t-3] + \rho_1 r_1(\tilde{g}_n - x_n^s[t]) + \rho_2 r_2(\tilde{x}_n^s - x_n^s[t])$$

    $x_n^s[t+1] = x_n^s[t] + v_n^s[t+1]$ $0 \le x_n^s[t+1] \le L-1$
    Compute (4) and (5) based on the threshold defined on $x_n^s[t+1]$
    $\sigma_n^2 = \sum_{j=1}^{n} w_j \left(\mu_j - \mu_t\right)$ //compute the solution of each particle n of swarm s
    If $\sigma_{n\_B}^2 > \sigma_{n\ best\_B}^2$ //particles n has improved
      $\sigma_{n\ best\_B}^2 = \sigma_{n\_B}^2$
      $\tilde{x}_n^s = x_n^s[t+1]$
  For each swarm s
    If $max\ \sigma_{s\_B}^2 > \varphi$ // swarm s has improved
      $\varphi = max\ \sigma_{s\_B}^2$
      $\tilde{g}_n = x_n^s[t+1]$
      $I_k = 0$ //reset stagnancy counter
        If $N_s < N_{max}$ // the current number of particles of swarm s is inferior to the maximum allowed number of particles
          $N_s = N_s + 1$
          Randomly swamp anew particles in the swarm
          If $N^s < N^s_{max}$ and rand() $\frac{N_s}{N_{max}} >$ rand()
            // small probability of creating a new swarm
            $N^s = N^s + 1$
            Randomly swamp a new swarm within a number of N particles
    Else // swarm s has not improved
      $I_k = I_k + 1$
      If $I_k = I_{Kill}$ // swarm s has improved for too long
        If $N_s > N_{min}$ // swarm s has currently more than the minimum number of allowed particles from a swarm
          Delete worse particles form swarm s,i.e., lower local solution
        Else // swarm s does not have currently the minimum number of allowed number of particles to from swarm
          Delete whole the swarm s, i.e., all particles from
End

is a favorable method. Therefore, we extract brain structure (WM, GM, and CSF) from the segmented image to the binary image then the proposed system is validated in the next phase.

4.3 The Validation Phase

In this stage, the result of the image segmentation with the proposed clustering techniques was compared to the ground truth as illustrated in the experimental results. The calculated measures are time, Jaccard similarity coefficient, and Dice similarity coefficient. The performance of the segmented images is shown in the experimental results in details and how to compute each of the performance measures. The accuracy of segmented image (SA) can define as:

$$\mathrm{SA} = \frac{\text{Number of correctly classified}}{\text{Total number of pixels}} \times 100\,\% \tag{12}$$

5 The Experimental Results and Discussion

The proposed system is implemented by using MATLAB R2011a on a Core(TM) 2 Due, 2 GHz processor, and 4 GB RAM system. We used three standard datasets. The first dataset is BRATS [59] database from Multimodal Brain Tumor Segmentation. It consists of 30 glioma patients with multi-contrast MRI scans (both low-grade and high-grade, and both with and without resection) along with expert observation for "active tumor" and "edema". For each patient, there are many available types of images, such as T1, T2, FLAIR, and post-Gadolinium T1 MRI images. This database contains 81 images and has ground truth images to compare the results of our method with them. These images are got from Brain Web Database at the McConnell Brain Imaging Centre of the Montreal Neurological Institute, McGill University.

The second dataset is the Brain Web [60] database. It contains phantom and simulated brain MRI data based on two anatomical models: normal and multiple sclerosis. For both of these models, the data volumes of the full 3-dimensional data are emulating by using the three sequences (T1-, T2-, and proton density- (PD-) weighted). On the other hand, there is a variety of slice thicknesses, noise levels, and non-uniformity levels of intensity. It is a T1 modality, 1 mm slice thickness. This dataset consists of 152 images.

The third dataset is the Digital Imaging and Communications in Medicine (DICOM) [61]. DICOM consists of 22 images that contain brain tumors. All DICOM image files are encoded in JPEG2000 transfer syntax with ".DCM" extension. It has no ground truth images for the contained images.

5.1 Measuring the Segmentation Performance

To provide a proper comparison between the tested methods, we use different performance measures, such as:

1. **Jaccard similarity coefficient** [62, 63]: It is a widely used overlap measure, which is public and used usually as similarity indices for binary data. The area of overlap *JSC* is computed between the segmented image S_1 and the gold standard image S_2 as shown in Eq. (13).

$$JSC = (S_1 \cap S_2)/(S_1 \cup S_2) \tag{13}$$

2. **Dice similarity coefficient** [62, 63]: It measures the number of the extent of spatial overlap between two binary images. It is the most widely used for measuring the performance of segmentation. Its values range between 0 and 1 if the value is zero there is no overlap. If the value is one, this means a good agreement.The Dice coefficient is defined as:

$$D = 2(S_1 \cap S_2)/vol(S_1 \cup S_2) = 2JSC/(1 + JSC) \tag{14}$$

3. **Accuracy**

$$True\ Positive(TP) = \frac{No\ of\ resulted\ images\ having\ brain\ tissue}{total\ No\ of\ images} \tag{15}$$

$$True\ Negative(TN) = \frac{No\ of\ images\ that\ haven't\ brain\ tissue}{total\ No\ of\ images} \tag{16}$$

$$False\ Positive(FP) = \frac{No\ of\ images\ that\ non\ brain\ and\ detected\ positive}{total\ No\ of\ images} \tag{17}$$

$$False\ Negative(FN) = \frac{No\ of\ images\ have\ brain\ tissue\ and\ not\ detected}{total\ No\ of\ images} \tag{18}$$

$$Accuracy = \left[\frac{(TP + TN)}{(TP + TN + FP + FN)}\right] \tag{19}$$

TP is true positive, and FP is false positive. They are correctly and incorrectly classified a number of voxels as brain tissue by the automated algorithm. TN is true negative, and FN is false negative. They are correctly and incorrectly classified a number of voxels as non-brain tissue by the automated algorithm.

In Table 2, we listed the main parameter of FODPSO. The maximum number of iterations is I_T. N is initial number particles with each swarm. The coefficients $\rho_{1\,\text{and}}\rho_2$ are weights, which control the global and individual performance. The fractional coefficient is commonly known as $\propto$. It will weigh the influence of past

Table 2 The parameters of FODPSO

Parameters method	I_T	N	ρ_1, ρ_2	Δv	N_{max}	N_{min}	N^s	N^s_{max}	N^s_{min}	N_{kill}	$\propto$
FODPSO	150	30	0.8	3	50	10	4	6	2	10	0.6

Table 3 The main steps of the proposed framework

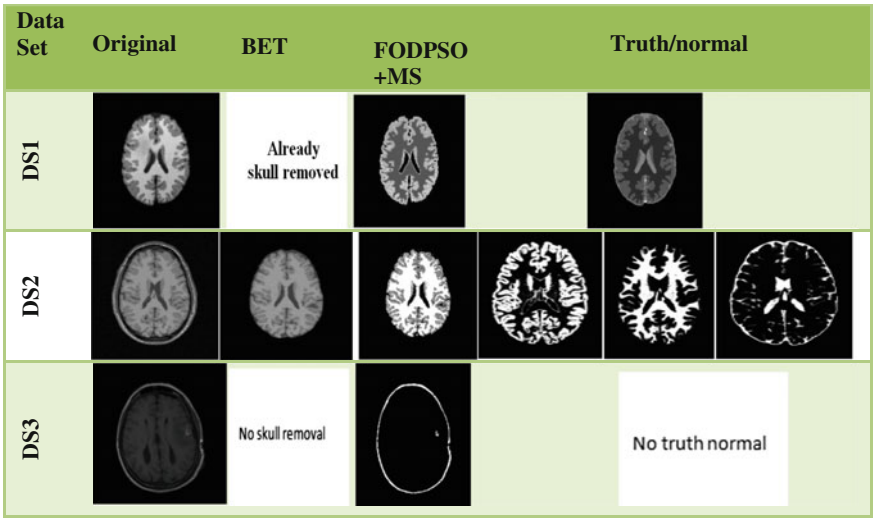

events in determining a new velocity, $0 < \propto < 1$. The number of swarms is N^s where N^s_{max} represents the maximum number of allowed swarms. N^s_{min} represents the minimum number of allowed swarms. The number of particles is described by N_{kill}, no enhancement in fitness means that the number of particles was deleted by the swarm over a period. Initialize Δ v maximum number of levels a practical can travel between iterations.

Table 3 shows the main stages of the proposed method. The first stage is the skull removal that performed by using BET algorithm [58]. The second stage uses the FODPSO algorithm combined with the MS algorithm. The output of FODPSO is supplied as an input to MS. By doing the experiments on all images of the three datasets using the MS; we found that the best results in image clusters can be got if bandwidth = 0.2 that proved by try and error. By decreasing the bandwidth for the same threshold, it processes the images in less time. Over-clustering and under-clustering arise from the chosen value of the bandwidth. The too small value of the bandwidth produces over-clustering, and also, the too large value of bandwidth provide critical modes that can be merged under-clustering. Also, in the third dataset, we make detection of the tumor by FODPSO algorithm combined with the MS algorithm (Tables 4, 5, and 6).

Table 4 The comparison between five different segmentation techniques on the two tested datasets

Data Sets	Original	BET	FCM	MS	PSO	DPSO	FODPSO +MS
Ds1	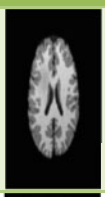	Already skull removed	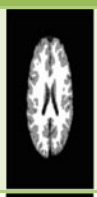	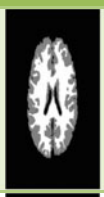	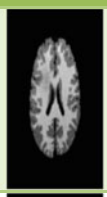	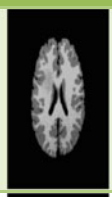	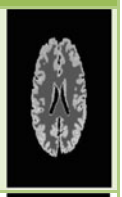
Ds2	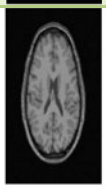	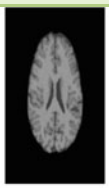				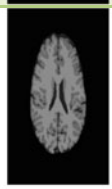	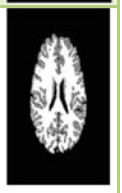
Ds3	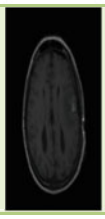	No skull removed				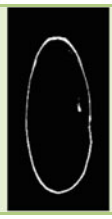	

Table 5 The comparison between FCM, Mean Shift, PSO segmentation algorithms

Data Sets	Original	FCM	Time	MS	Time	PSO	Time
Ds1	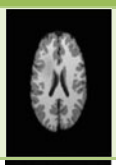	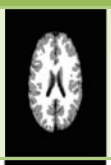	**11.47670 s**	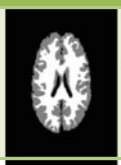	0.748976 s	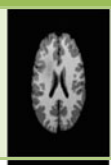	9.8863 s
Ds2	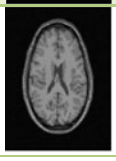	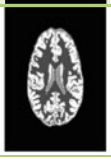	**10.65768 0s**	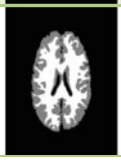	0.685284 s	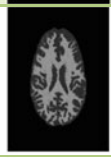	9.4908 s

Table 6 The comparison between DPSO and FODPSO + MS segmentation algorithms

Data Sets	Original	DPSO	Time	FODPSO+MS	Time
Ds1	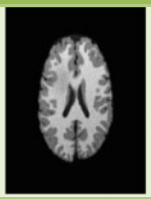	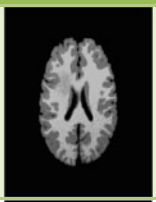	7.7962s	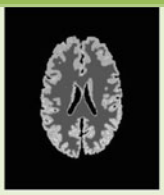	7.9069s
Ds2	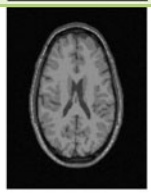	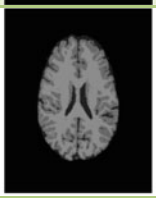	4.4876s	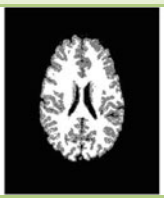	4.5191s

Table 7 The mean errors for the Jaccard and the Dice similarity coefficients for DS1

Segmentation techniques for DS1					
	FCM	MS	PSO	DPSO	FODPSO + MS
JSC	0.9136	0.9178	0.9312	0.9433	0.9821
Dice	0.9548	0.9571	0.9644	0.9708	0.9910
Time (s)	11.47670	0.785911	31.3395	30.9704	12.8960

Table 8 The mean errors for the Jaccard and the Dice similarity coefficients for DS2

Segmentation techniques for Ds2					
	FCM	MS	PSO	DPSO	FODPSO + MS
JSC	0.9223	0.9223	0.9389	0.9478	0.9825
Dice	0.9596	0.9596	0.9685	0.9732	0.9912
Time (s)	10.228735	0.654596	28.1894	24.8010	12.2559

In Tables 7 and 8, the mean of errors is measured in the two tested datasets by using the JSC and Dice. It is established that the proposed technique (FODPSO + MS) gives the best result than any other tested techniques.

In Table 9, we can observe that the accuracy of FCM same as MS for the two datasets. In Table 10, the accuracy of DPSO is better than PSO. In Table 11, the FODPSO + MS is superior to the previous techniques with accuracy 99.67 % (Figs. 2 and 3).

Table 9 The performance metrics of FCM and Mean Shift

Clustering techniques										
FCM						Mean shift				
Datasets	TP	TN	FP	FN	Accuracy	TP	TN	FP	FN	Accuracy
DS1	95.67	0	0	4.33	95.67	95.67	0	0	4.33	95.67
DS2	96.03	0	0	3.97	96.03	96.03	0	0	3.97	96.03
DS3	86	0	0	14	86	86	0	0	14	86

Table 10 The performance metrics of PSO and DPSO

Clustering techniques										
PSO						DPSO				
Datasets	TP	TN	FP	FN	Accuracy	TP	TN	FP	FN	Accuracy
DS1	96.03	0	0	3.97	96.03	97.08	0	0	2.92	97.08
DS2	96.90	0	0	3.10	96.90	97.67	0	0	2.33	97.67
DS3	86.23	0	0	13.77	86.23	86.96	0	0	13.04	86.96

Table 11 The performance metrics of FODPSO + MS

Clustering techniques					
FODPSO + MS					
Datasets	TP	TN	FP	FN	Accuracy
DS1	99.45	0	0	0.55	99.45
DS2	99.67	0	0	0.33	99.67
DS3	94.67	0	0	5.33	94.67

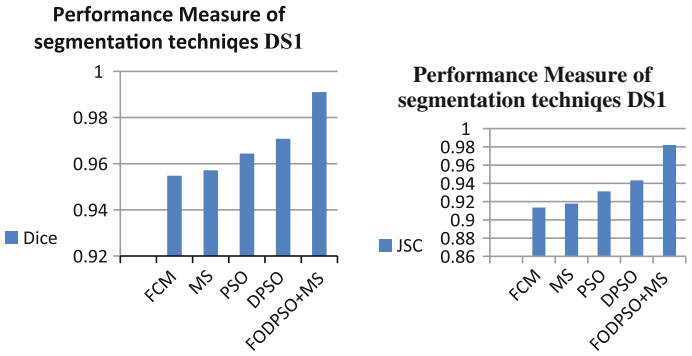

Fig. 2 The performance measure of the segmentation techniques in seconds for DS1

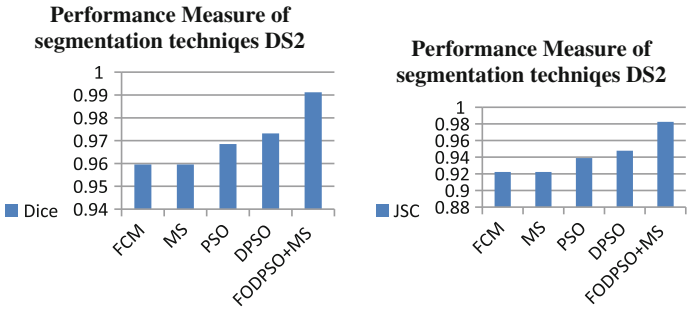

Fig. 3 The performance measure of the segmentation techniques in seconds for DS2

6 Conclusion

Achieving acceptable performance is a hard target in the segmentation process because unknown noise is contained in the medical images. The proposed approach is based on the combination of FODPSO and MS techniques. A number of clusters can be predefined by FODPSO, and a higher between-class variance for finding the optimal set of thresholds in less computational time can be obtained by it. In the proposed approach, the result of FODPSO is used as the input to MS to develop a pre-processing method for the classification. The main difficulty of MS is tuning the size of the kernel, and the obtained result may be affected by the kernel size. Results indicate that the use of both segmentation methods can overcome the shortcomings of each of them. The combination can significantly improve the outcome of the classification process. In the future, a hybrid technique based on clustering algorithms and multilevel thresholding like FODPSO can be combined to work on input dataset for better results.

In the future, the chaos-based concept will be integrated with PSO. Also, a hybrid technique based on clustering algorithms like FCM and multilevel thresholding like FODPSO can be combined to work on input dataset for better results. In the future, We can also use a multi-modal image like MRI and CT for improving results. To overcome the issue of trapping the solution in local optima is solved by Clustering based a biologically inspired Genetic algorithm was developed that we can apply in the future work.

References

1. Bodkhe, S.T., Raut, S.A.: A unique method for 3D MRI segmentation. IEEE Trans. Comput. Sci. Inf. Technol. **8**,118–122 (2008)
2. Manohar, V., Gu, Y.: MRI Segmentation Using Fuzzy C-Means and Finite Gaussian Mixture Model, Digital Image Processing—CAP 5400

3. Srivastava1, A., Alankrita, Raj, A., Bhateja, V.: Combination of wavelet transform and morphological filtering for enhancement of magnetic resonance images. In: Proceedings of International Conference on Digital Information Processing and Communications (ICDIPC 2011), Part-I, Ostrava, Czech Republic, CCIS-188, pp. 460–474 July (2011)
4. He, R., Datta, S., Sajja, B.R., Narayana, P.A.: Generalized fuzzy clustering for segmentation of multi-spectral magnetic resonance images. Comput. Med. Imaging Graphics. **32**, 353–366 (2008)
5. Ruan, S., Moretti, Fadili, B.J., Bloyet, D.: Fuzzy Markove segmentation in application of magnetic resonance images. Comput. Vis. Image Understand. **85**, 54–69 (2002)
6. Bhateja, V., Patel, H., Krishn, A., Sahu, A., Lay-Ekuakille, A.: Multimodal medical image sensor fusion framework using cascade of wavelet and contourlet transform domains. IEEE Sens. J. (2015)
7. Bhateja, V., Krishna, A., Patel, H., Sahu, A.: Medical image fusion in wavelet and ridgelet domains: a comparative evaluation. Int. J. Rough Sets Data Anal. (IJRSDA). **2**(2), 78–91 (2015)
8. Begum, S.A., Devi, O.M.: Fuzzy algorithms for pattern recognition in medical diagnosis. Assam Univ. J. Sci. Technol. **7**(2), 1–12 (2011)
9. Raj, A., Alankrita, Srivastava, A., Bhateja,V.: Computer aided detection of brain tumor in MR images. Int. J. Eng. Technol. (IACSIT-IJET). **3**, 523–532 (2011)
10. Bindu, C.H., Qiscet, O.: An improved medical image segmentation algorithm using OTSU method. Int. J. Recent Trends Eng. **2**, 88–90 (2009)
11. Javed, A., Chai, W.Y., Thuramaiyer, N.K., Javed, M.S., Alenezi, A.R.: Automated segmentation of Brain MR images by combining contourlet transform and K-means clustering techniques. Int. J. Theoret. Appl. Inf. Technol. **54**, 82–91 (2013)
12. Gang, Z., Dan, Z., Ying, H., Xiaobo, H., Yong, Z., Weishi, L., Yang, Z., Dongxiang, Q., Jun, L., Jiaming, H.: An unsupervised method for brain MRI segmentation. Int. J. Emerg. Technol. Adv. Eng. **3**, 704–709 (2013)
13. Jin, X.: Multi-Spectral MRI brain image segmentation based on kernel clustering analysis. In: International Conference on System Engineering and Modeling. vol. 34, pp. 141–146 (2012)
14. Dougherty, G.: Pattern Recognition and Classification, Chapter 2. Springer
15. Siddharth, Bhateja, V.: A modified unsharp masking algorithm based on region segmentation for digital mammography. In: 4th International Conference on Electronics & Computer Technology (ICECT-2012). vol. 1, pp. 63–67, IEEE (2012)
16. Bhateja, V., Swapna, S Urooj, H.: An evaluation of edge detection algorithms for mammographic calcifications. In: 4th International Conference on Signal and Image Processing (ICSIP 2012). vol. 2, pp. 487–498. Springer (2012)
17. Ajala, A.F., Oke, A.O., Alade, M.O., Adewusi, A.E.: Fuzzy k-c-means clustering algorithm for medical image segmentation. J. Inf. Eng. Appl. **2**, 21–32 (2012)
18. Ghamis, P.I., Couceiro, M.S., Benediktsson, J.A., Ferreira, N.M.F.: Multilevel image segmentation based on fractional-order Darwinian particle swarm optimization. IEEE Trans. Geosci. Remote Sens., 1–13 (2013)
19. Araki, T., Molinari, N., et al.: Effect of geometric-based coronary calcium volume as a feature along with its shape-based attributes for cardiological risk prediction from low contrast intravascular ultrasound. J. Med. Imaging Health Inf. **4**(2) (2014)
20. Hamdaoui, F., Sakly, A., Mtibaa, A.: An efficient multithresholding method for image segmentation based on PSO. In: International Conference on Control, Engineering and Information Technology (CEIT'14) Proceedings—Copyright IPCO-2014, vol. 2014, pp. 203–213 (2014)
21. Liu, J., Li, M., Wang, J., F. Wu, Liu, T., Pan, Y.: A survey of MRI-based brain tumor segmentation methods. Tsinghua Sci. Technol. **19**(6) (2014)
22. Begum, S.A., Devi, O.M.: Fuzzy algorithms for pattern recognition in medical diagnosis. Assam Univ. J. Sci. Technol. **7**(2), 1–12 (2011)

23. Moftah, M., Azar, H., Al-Shammari, A.T., Ghali, E.T., Hassanien, Aboul Ella, Shoman, M.: Adaptive K-means clustering algorithm for MR breast image segmentation. Neural Comput. Appl. **24**(7–8), 1917–1928 (2014)
24. Lawrie, S.M., Abukmeil, S.S.: Brain abnormality in schizophrenia—A systematic and quantitative review of volumetric magnetic resonance imaging studies. Br. J. Psychiatry **172**, 110–120 (1998)
25. Tanabe, J.L., Amend, D., Schuff, N.: Tissue segmentation of the brain in Alzheimer disease. AJNR Am. J. Neuroradiol. **18**, 115–123 (1997)
26. Padole, V.B., Chaudhari, D.S.: Detection of brain tumor in MRI images using mean shift algorithm and normalized cut method. Int. J. Eng. Adv. Technol (IJEAT). **1**, 53–56 (2012)
27. Mahmood, Q., Chodorowski, A., Mehnert, A.: A novel Bayesian approach to adaptive mean shift segmentation of brain images. In: IEEE Symposium on Computer-Based Medical Systems, pp. 1–6 (2012)
28. Parvathi, K., Rao, B.S.P., Das, M.M., Rao, T.V.: Pyramidal watershed segmentation algorithm for high-resolution remote sensing images using discrete wavelet transforms. In: Discrete Dynamics in Nature and Society, pp. 1–11 (2009)
29. Khalifa, I., Youssif, A., Youssry, H.: MRI brain image segmentation based on wavelet and FCM algorithm. Int. J. Comp. Appl. **47**(16), 32–39 (2012)
30. Bandhyopadhyay, S., Paul, T.: Automatic segmentation of brain tumour from multiple images of brain MRI. Int. J. Appl. Innov. Eng. Manag. **2**(1), 240–248 (2013)
31. Arakeri, M.P., Reddy, G.R.M.: Efficient fuzzy clustering based approach to brain tumor segmentation on MR images. Commun. Comput. Inf. Sci. **250**, 790–795 (2011)
32. Mostfa, M.G., Tolba, M.F.: Medical image segmentation using a wavelet based multiresolution EM algorithm. In: International Conference on Industrial Electronics, Technology &Automation. IEEE (2001)
33. Mangala, N., Suma, B.: FLGMM algorithm for brain MR image segmentation. Int. J. Latest Res. Sci. Technol. **2**, 2147–2152 (2013)
34. Ghamisi, P., Couceiro, M.S., Benediktsson, J.A., Ferreira, N.M.F.: An efficient method for segmentation of images based on fractional calculus and natural selection. Expert Syst. Appl. **39**, 12407–12417 (2012)
35. Ghamisi, P., Couceiro, M.S., Benediktsson, J.A., Ferreira, N.M.F.: Integration of segmentation techniques for classification of hyperspectral images. IEEE Geosci. Remote Sens. Lett. **11**, 342–346 (2014)
36. Hamdaoui, F., Sakly, A., Mtibaa, A.: An efficient multithresholding method for image segmentation based on PSO. In: International Conference on Control, Engineering & Information Technology (CEIT'14), pp. 203–213 (2014)
37. Abdel-Maksoud, E., Elmogy, M., Al-Awadi, R.: Brain tumor segmentation based on a hybrid clustering technique. Egyptian Inf. J. **10**, 1 (2015)
38. Abdel-Maksoud, E., Elmogy, M., Al-Awadi, R.: MRI brain tumor segmentation system based on hybrid clustering techniques. Commun. Comput. Inf. Sci. **488**, 401–412 (2014)
39. Samanta, S., Dey, N., Das, Acharjee, P.S., Chaudhuric, S.S.: Multilevel threshold based gray scale image segmentation using cuckoo search. In: Proceedings of ICECIT, pp. 27–34. Elsevier (2012)
40. Dey, N., Roy, Pal, M., Das, A.: FCM based blood vessel segmentation method For retinal images. Int. J. Comput. Sci. Netw. (IJCSN) **1**, 1–5 (2012)
41. Ajala, A.F., Oke, A.O., Alade, M.O., Adewusi, A.E.: Fuzzy K-C-means clustering algorithm for medical image segmentation. J. Inf. Eng. Appl. **2**(6), 21–32 (2012)
42. Selvaraj, D., Dhanasekaran, R.: MRI brain image segmentation techniques-A. Indian J. Comput. Sci. Eng. (IJCSE) **4**(5), 364–381 (2013)
43. Gonzalez, R.C., Richard, E. W.: Digital Image Processing Pearson Education, 3rd edn (2007)
44. Wirjadi, O.: Survey of 3D image segmentation methods. Technical report (2007)
45. Srimani, P., Mahesh, K. S.: A Comparative study of different segmentation techniques for brain tumour detection. In: IJETCAS, pp. 192–197 (2013)

46. Selvaraj, D., Dhanasekaran, R.: Automatic detection of brain tumour from MRI brain image by histogram thresholding and segmenting it using region growing. Karpagam J. Comput. Sci. **2**, 1–7 (2013)
47. Selvaraj, D., Dhanasekaran, R.: MRI brain tumour detection by histogram and segmentation by modified GVF model. IJECET **4**(1), 55–68 (2013)
48. Selvaraj, D., Dhanasekaran, R.: MRI brain tumour segmentation using IFCM and comparison with FCM and k-means. In: Proceedings of NC-Event 2013, pp. 47–52 (2013)
49. Selvaraj, D., Dhanasekaran, R.: Segmentation of cerebrospinal fluid and internal brain nuclei in brain magnetic resonance images. IRECOS **8**(5), 1063–1071 (2013)
50. Moallem, P., Razmjooy, N.: Optimal threshold computing in automatic image thresholding using adaptive particle swarm optimization. J. Appl. Res. Technol. **10**, 703:712 (2012)
51. Kriti, K., Virmani, J., Dey, N., Kumar, V.: PCA-PNN and PCA-SVM based CAD Systems for Breast Density Classification. Springer (2015)
52. Ghamis, P.I., Couceiro, M.S., Benediktsson, J.A., Ferreira, N.M.F.: An efficient method for segmentation of images based on fractional calculus and natural selection. Expert Syst. Appl. **39**, 12407–12417 (2012)
53. KestIe, J.R.W., Tasker, R.R.: A comparison between magnetic resonance imaging and computed tomography for stereotactic coordinate determination. In: The Congress of NeuroJogical Surgeons, vol. 30, issue no. 3 (1992)
54. Rodrigues, I., Sanches, J., Dias, J.: Denoising of medical Images corrupted by Poisson Noise. In: 15th IEEE International Conference on Image Processing ICIP. IEEE Press, San Diego, pp. 1756–1759 (2008)
55. Kumar, S.S., Jeyakumar, A.E., Vijeyakumar, K.N., Joel, N.K.: An adaptive threshold intensity range filter for removal of random value impulse noise in digital images. J. Theoret. Appl. Inf. Technol. **59**, 103–112 (2014)
56. Nicolas, W.D., Sylvain, P., Pierrick, C., Patrick, M.S., Christian, B.: Rician noise removal by non-local means filtering for low signal-to-noise ratio MRI: applications to DT-MRI. In: International Conference on Medical Image Computing and Computer Assisted Intervention, vol. 11, pp. 171–179 (2008)
57. Shri Ramswaroop, V., Harshit, S., Ramswaroop, Srivastava, A., Ramswaroop, S.: A non-local means filtering algorithm for restoration of Rician distributed MRI. emerging ICT for bridging the future. In: 49th Annual Convention of the Computer Society of India (CSI-2014), vol. 2, pp. 1–8 (2014)
58. Medical image processing analysis and visualization.: http://mipav.cit.nih.gov/pubwiki/index.php/Extract_Brain:_Extract_Brain_Surface_ (BET). Accessed 27 March 2015
59. MICCA nice 2012: http://www2.imm.dtu.dk/projects/BRATS2012/data.html. Accessed 9 Aug 2014
60. Simulated Brain Database.: McConnell Brain Imaging Centre, Montreal Neurological Institute, McGill University: http://www.bic.mni.mcgill.ca/brainweb. Accessed 27 June 2014
61. DICOM samples image sets.: http://www.osirix-viewer.com/datasets/. Accessed 9 Sept 2014
62. Zou, K.H., Warfield, S.K., Bharatha, A., Tempany, C.M., Kaus, M.R., Haker, S.J., Wells, W. M., Kikinis, R.: Statistical validation of image segmentation quality based on a spatial overlap index. Acad. Radiol. **11**, 178–189 (2004)
63. Agrawal, R., Sharma, M.: Review of segmentation methods for brain tissue with magnetic resonance images. Comput. Netw. Inf. Secur. **4**, 55–62 (2014)

3D Brain Tumor Segmentation Based on Hybrid Clustering Techniques Using Multi-views of MRI

Eman A. Abdel Maksoud and Mohammed Elmogy

Abstract 3D medical images segmentation is a very difficult task. It may not be accurate and takes extreme time. In this chapter, we accurately detect the brain tumor from 3D MRI image with less time. The 3D image consists of multiple 2D slices. Segmenting each 2D slice by using the 2D techniques gives more accuracy rather than segmenting the whole 3D image. The integration between K-Means and Particle Swarm Optimization was proposed to segment the 2D MRI slices of the 3D MRI image. We solved the time problem of segmenting all 2D slices of the 3D image. The experiments emphasized the effectiveness of our proposed system in segmenting the 2D and 3D medical images. It achieved 100 % accuracy for the tested 3D dataset and 98.75 % average accuracy for all tested 2D and 3D datasets. The proposed integration reduced time by a mean of 10 min for the tested 2D and 3D datasets.

Keywords 3D medical image segmentation · 2D MRI slices · K-means · Particle swarm optimization

1 Introduction

Image processing is a fundamental task in computer vision that is used in many different fields, especially the medical field. It is critical to analyze images. The medical image processing transforms the raw images into numerically symbolic form for better representation and evaluation. This transformation or extraction is

E.A. Abdel Maksoud (✉)
Faculty of Computers and Information, Information System Department,
Mansoura University, Mansoura, Egypt
e-mail: eng.eman.te@gmail.com

M. Elmogy (✉)
Faculty of Computers and Information Technology Department,
Mansoura University, Mansoura, Egypt
e-mail: melmogy@mans.edu.eg; elmogy@gmail.com

N. Dey et al. (eds.), *Medical Imaging in Clinical Applications*,
Studies in Computational Intelligence 651, DOI 10.1007/978-3-319-33793-7_4

integrated with the information that is generated from multiple imaging modalities to aid diagnosis and surgeries [1]. It is noteworthy that, medical images have poor contrasts, noises, and missing or widespread boundaries. On the other hand, medical images exhibit intensity inhomogeneity. A single tissue class varies over the extent of the image gradually due to the intensity level. Moreover, the intensity of a pixel may not be consistent with any class [2].

Image segmentation techniques have been developed in order to locate objects, boundaries, and shapes in medical images. However, the selection of an appropriate technique for a particular type of image or application is a difficult problem. Thus, there is no universally accepted method for image segmentation. Therefore, it is still a challenging problem in image processing [3], besides, the over-segmentation and under-segmentation problems. On the other hand, image segmentation techniques may be supervised or unsupervised. They also can be categorized as thresholding, texture analysis, clustering, region, and edge-based methods [4].

The images need to be geometrically aligned for better observation. This alignment procedure maps points from one image to their corresponding points in another one [5]. This process is called image registration that aligns two or more images of the same scene. These images may be taken from different views or at different times or from different sensors [6].

These sensors in medical imaging provide different imaging modalities, such as Computed Tomography (CT), Magnetic Resonance Imaging (MRI), and Positron Emission Tomography (PET). Response(s) to these imaging modalities generate an enormous amount of useful information that is extracted and analyzed by the radiologists for the purpose of analysis, detection and the diagnosis of diseases. The obtained sensor responses of the various medical imaging modalities are often complementary in nature, i.e. a particular sensor modality is deprived of the features acquired by another sensor (imaging modality). For example, CT images deal with the demonstration of the extent of disease and provides information about denser tissues with less distortion; while MRI contains the information regarding soft tissues. Hence, a radiologist always purposes to analyze the sensor responses to the different modalities simultaneously [7].

Although some of the imaging modalities help the physicians to diagnose the lesions, they have some limitations. Some of them provide only functional information and the other provide anatomical information. The ones that give best results are very expensive and cannot be used in all laboratories, such as PET. The others are not comfortable and negatively affect the patient like CT. Ultrasound (US) suffers from poor contrast like X-rays. The scanners or imaging modalities take multiple images at different times and different views.

In many cases, MRI provides information that cannot be obtained from other scans [8]. MRI displays the anatomy in the axial, sagittal, and coronal planes. The slice thickness of the images varies between 1 and 10 mm. MRI is good for coronal and sagittal imaging. In each of these modalities, a relative set of 2D slices provides a 3D array of image intensity values. A 3D image can be obtained from many consecutive or sequent 2D slices. The segmentation of 3D medical images is very difficult, but it is paramount in image processing. There is no doubt that, the major

advantage of 3D imaging is improving the small image component visualization. It visualizes the hidden details of the organs that cannot be observed by the 2D images.

The realization of 3D visualization of the medical images is to carry on correct and reasonable segmentation of the image at first [9]. In this respect, although segmenting the 2D slices needs extra time compared to the time required for 3D volume, the 2D techniques provide higher reliability for image quality [10]. On the other hand, the brain tumor disease is critical and serious. It affects the human body and cause death if it is not detected quickly and accurately. Therefore, developing a new medical system depending on the clustering techniques is needed to detect the brain tumor accurately and with less time especially when we use the 3D MRI images.

In this chapter, the framework is started with the pre-processing phase. Then, the tumor area is extracted by using our proposed KPSO technique [11, 12]. After that, the post-processing and segmentation phases are applied. We use all 2D slices of the 3D image to get the actual volume of the tumor in the brain. Finally, the performance and accuracy are evaluated in the validation phase. There are multiple methods that are used to segment directly the 3D images, such as Atlas-based segmentation. However, it is limited by the fact that the segmentation results highly depend on the quality of affine registration and consumed time in Atlas construction. A slight misalignment of the issues usually leads to a dramatic decrease in segmentation accuracy [13]. On the other hand, segmenting each slice provides more precision.

The current chapter is organized as follows, in Sect. 2; we introduce some of the current scientific work in medical image segmentation. Section 3 presented the materials and methods used in this work. It describes the image dataset used in this work. It shows the proposed medical image segmentation system based on our proposed hybrid clustering technique to detect the brain tumor based on 3D MRI images. Section 4 depicts the experimental results obtained from the evaluation of our framework using the before mentioned dataset and discusses the main questions derived from it. Finally, conclusion and future work are drawn in Sect. 5.

2 Related Work

Many researchers presented methods for 3D brain tumor segmentation. They used several image segmentation techniques based on different imaging modalities. For example, Jiang et al. [14] performed a method based on multimodal brain MR images, like T1, T2, post-Gadolinium T1, and FLAIR sequences. It depends on two classifiers. The first is a global classifier and the second is a custom classifier. The global was trained by using samples from the population feature set, and the custom classifier was trained by using samples from seed points in the testing image. The procedure of their proposed method consisted of four steps started with feature extraction by Gabor filter, and the feature volumes were generated by stacking the 2D image slices features. Then they did a distance metric learning and classifiers training. After that, they did the optimization by graph cut. The main limitations of

this method are that it was a semi-automatic method. Besides that, the high dimension of the features slowed down the convergence of the algorithm. It was time-consuming especially in training the global classifier. It takes about 2 h to train the global classifier containing 57 cases with four modalities.

Ali et al. [15] determined volume of Brain Tumor from multiple MRI slices in the 3D image. The authors enhanced the slices of MRI brain images by filtering the image using a bilateral filter and make the erosion and dilation by the morphological process then they made edge detection by Sobel operator. After that, they made skull removal by morphological operations. In the end, they contoured the tumor area, constructed the 3D image for the tumor and determining the location of the tumor within the brain. The limitation of this method, they made morphological operations many times to extract the tumor only in each slice, of course, that is time-consuming especially with a large number of slices. They put into account only the accuracy and ignored time. In addition, it is not an entirely automatic method.

Alomoush et al. [16] produced another method combined with a firefly algorithm FA and Fuzzy C-Means FCM to detect the brain tumor in the brain MRI image. They used FA in generating near-optimal initial cluster centers for FCM in the initialization step of FCM algorithm. At first, the FA examined the search space of the given data set to determine the near-optimal cluster centers. The cluster centers were assessed by using FCM objective function. Second, the generated cluster centers that had been identified were employed as the preliminary cluster centers for the FCM algorithm. They tested their algorithm on 3D MRI images of multiple 2D slices. The authors compared their method, with FCM algorithm that used the random initialization and proved that FCM with FA was faster than FCM with random initialization. Although the authors did stripping skulls and other unwanted contents in the image, they ignored removing noises by modern filters. FCM is very sensitive to noises. It will not work well in the presence of these noises.

Thiagarajan and Bremananth [17] detected the brain tumor by using conditional random field and artificial bee colony optimization. First, they extracted the MINC dataset file or 3D MRI image to multiple 2D slices with a jpeg format. Then the authors removed film artifacts like patient name and age by using tracking algorithm. After that, they made image enhancement by using histogram equalization and the median filter. Then they used the conditional random field to accelerate the performance of the artificial bee colony optimization algorithm. By using the binarization, they detected and calculated the shape of the tumor. The main disadvantage of their method is that they did not use any algorithm to remove skulls as they used tracking algorithm to eliminate film artifacts and used filters to remove noises from the image. When they used the binarization to calculate the tumor area by calculated the white pixels of total pixels some mistakes will do by calculating some skull pixels also in addition to the tumor pixels. Moreover, although they dealt with the 3D MRI image, they did not make the 3D reconstruction and visualization.

Wu et al. [18] proposed a new image segmentation method to extracts the pelvic on the structure. They used a combination of anatomical knowledge and computational techniques. They tested the performance of the training models by using cross validation process has been designed to identify how segmentation can be

affected variations in training sets. They also used "mean distance" and "mis-segmented area." to evaluate accuracy and results of segmentation. They used multiple slices of CT. Their framework consisted of preprocessing as the first part. The First part consisted of sub-steps including filtering, morphological operations, and image enhancement. The second part is the edge detection by the canny edge detector. The third part of their method is a shape matching template detection. In this part, they used about 100 bone templates to be compared to each CT slice. The fourth part is using the registered active shape model to extract pelvic bone tissues. Finally, the 3D pelvic model reconstruction from the multiple 2D segmenting CT slices using the iso surface method. They made the comparisons between using their method and the deformable snake model. The disadvantages of this method, it is time-consuming. Using the training models and segmenting all the 2D CT slices take much time to produce the segmenting 3D image. They used only five training models because more training models cause more and more time-consuming and not adding much to the accuracy of segmentation! Besides that, the authors used the poor contrast CT image with less resolution.

Narkbuakaew et al. [19] made a 3D model of ribs cage. Their work depended on the KM clustering technique and organized the clustered regions in subsequent indexes of the background, soft-tissue, and hard tissue regions. The framework started with the feature extraction of the entire image. Then they made clustering by KM, which results in two regions. The authors after that identify the object region. The clustering indexes were done. The authors made the 3D rib cage surface modeling by Marching Cubes algorithm. The authors made the comparisons between their method, 2D k-means, and 2D FCM. The advantage of this method is that its running time is less than 2D KM, and 2D FCM. On the other hand, it is not fully automatic because it requires manual adjustment of several parameters. Moreover, the clustering relied on the basic feature components, gray and median gray. The thing that cannot completely remove some undesirable regions appears in the clustering results such as large kidney regions.

Piao et al. [20] segmented the kidneys cysts from the CT slices by making two stages of segmentation. They segmented the kidney regions by graph cut method at first and then segmented the cysts regions by combining FCM with the level set method. After that, they made the 3D visualization and calculated the volume of the cysts in the kidney. They calculated the volume of the organ or the cysts by multiplying the cyst area and thickness of each CT slice image. The sum of all cyst volumes in all CT slices represents the total cyst volume. The disadvantages of this method, the authors did not make image preprocessing to remove noises as the used techniques such as FCM is so sensitive to noise. They used poor contrast CT images and didn't make resolution enhancement that was affect the 3D visualization negatively.

Ananth et al. [21] segmented the liver and hepatic tumors from the 3D CT images. They made segmentation for the liver then for the tumors in the livers. Their method depended on the geodesic graph cut based methods. In the processing phase, authors used mean shift filter and thresholding method to reduce the processing region and identify the edges by contouring. Then they made the segmentation by the graph-based method for the liver. The authors segmented the liver

from the background. Then they made the same steps to segment the tumors from the liver in the CT images.

The disadvantages of this method are that they cannot be able to make an estimation of the execution time. It was always different in terms of computational power. Large hepatic tumors of the outer liver rim cannot be detected by the both used (graph cut and geodesic graph cut) methods as they were excluded from the surface liver volume. Moreover, the accuracy of tumor segmentation is not as high as for liver surface. Finally, the authors used a mean shift filter that represented more than 70 % of the total processing time, so, they can use an alternative filtering to reduce time.

Bandhyopadhyay and Paul [22] segmented the brain tumor based on KM. They made segmentation of images due to normal brain cell of (gray matter GM, white matter WM, and CSF) and the tumor cells of the brain. Their workflow concludes images enhancement. They made the enhancement by a 3–by–3 'unsharp' contrast enhancement filters. The authors made the registration by feature detection, the feature matching, transform model estimation, and image resembling and transformation. Fusing registered images is the determination of how to combine the sensor images. They stripped the skull by using a mask generated from the original image. They made the segmentation by KM in order to extract WM, GM, and Tumor by calculating the histogram of the segmented image. The last step of their workflow is an analysis of tumor dimension by applying a scan line method. The method consists of three steps; the first is KM algorithm, the second is local standard deviation guided grid based coarse grain localization, and final step is local standard deviation guided grid based fine grain localization. In their experiments, they used three types of MRI images. One is Sagittal view images (Side view), the other is Coronal view images (Back view), and the last type is Axial view images (Top view). The disadvantages of their work are, the image fusion technique gives good result infusing multiple images. However, in some cases, it results in loss of intensity and ignores anatomic details in the boundary of the tumor or overlapping region of GM and WM in the brain. In addition, although KM clustering technique is very simple and fast, it fails in some cases to detect the brain tumor specifically if it is malignant tumor type. Another limitation is that the authors used slices of sagittal, coronal and axial but segmented each view slices alone and did not perform the 3D visualization of all slices to preview the 3D volume of the tumor.

We detected the brain tumor accurately with minimal time in 2D images by our hybrid clustering technique in our proposed medical system [11, 12]. We kept in mind to achieve the same objective in detecting the brain tumor on 3D images. The same framework with 2D images is used, but we add some phases such as post-processing and 3D modeling.

We used the KPSO clustering technique on the 2D slices of the 3D image to guarantee the accuracy and reducing time as possible. By the proposed technique and medical system, as far as we know, the time of segmenting 2D slices of the 3D image is reduced. On the same time, the accuracy of segmenting the 3D image that contains multiple 2D slices is increased by using 2D segmentation techniques. The brain was modeled, and we visualized the real tumor area accurately. The results

were compared with the ground truth. The total time of segmenting the 2D slices was calculated. The total time was compared with the segmentation time of the automatic method in ground truth; the result was very near. Besides that, we provide three main images: clustering, thresholding, and contouring that is a very helper to the user. Moreover, the 3D reconstruction that displays all clustering slices of the 3D image to the user. The user in this phase can move the clustering slices through x, y and z to observe all details containing small parts. Finally, display the volumetric brain and the tumor area from the 2D slices after aligning them. The preprocessing and post-processing phases are critical and help in accurate detection, reducing the time and saving memory. We cannot deny that using accurate and contrast imaging modality helps in the processing process as we used the MRI scanner.

3 The Proposed Segmentation Framework

The 3D image segmentation framework consists of six phases applied on the 2D and 3D MRI images to detect the brain tumor, as shown in Fig. 1. The six phases are the preprocessing, the clustering, the segmentation, the post processing, the 3D

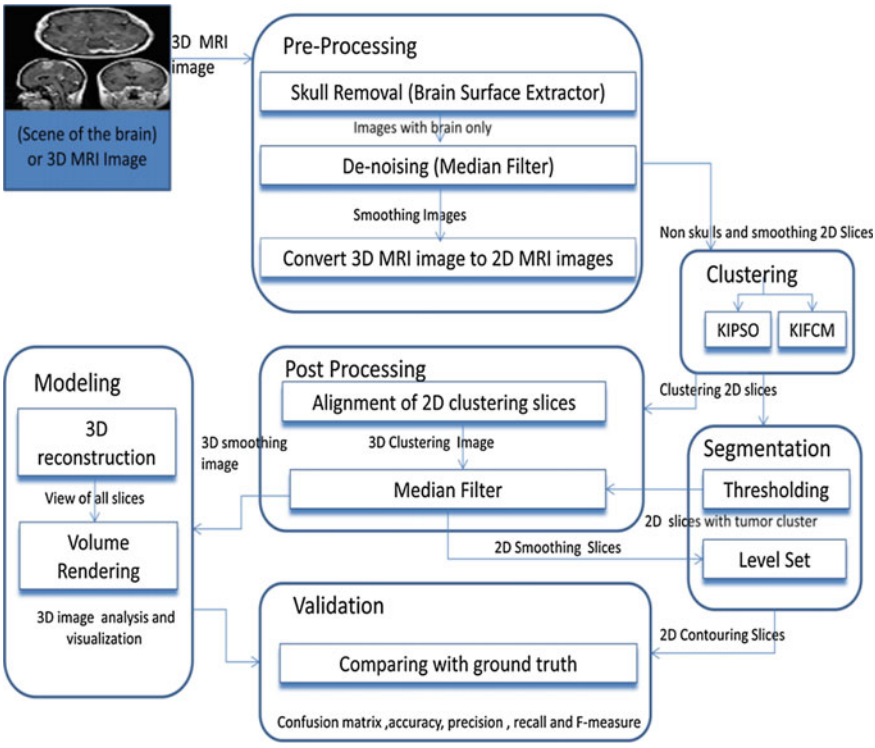

Fig. 1 The proposed 2D/3D medical image segmentation system

modeling, and the evaluation stages. It is starting from the preprocessing which consists of three steps skull removal, filtering and conversion of MRI from 3D to 2D slices. The next phase is the clustering by our proposed KPSO. Then the post-processing that consists of alignment and filtering. The alignment means concatenating all the 124 2D clustering slices again to produce the 3D clustering image.

After that, segmentation is done by a combination of the two segmentation methods thresholding and level set. The former extracts the tumor from the brain by making the binarization process that increases the brightness of the brain tumor cells and darkens the background. The thresholding or binarization process clarifies the tumor area to the physician. The thresholded image is used as an output to display the tumor area and is matched with the smoothed image in the level set process. This matching allows the level set to determine the tumor area from the thresholded image to contour accurately. The second method or level set is used to mark the brain tumor area in the smoothed image. It seems as an expert or physician marks the tumor area in the MRI scan by a green color marker.

By using binarization and level set processes, our system provides the physician with a good observation for the tumor area. We get benefits of using these image segmentation methods thresholding and level set after clustering, and we avoided the problems of them if they were used alone.

In parallel to the phase of segmentation, the modeling phase is used to view all slices that were clustered by the 3D reconstruction and viewed the volume of tumor in the brain from all clustering slices. The phases of the framework will be declared in the subsequent.

3.1 Pre-processing Stage

In this phase, a series of processes is applied on the entered 3D MRI image before clustering and segmentation. This 3D image consists of multiple 2D slices. We make the processing for each slice because we will detect the tumor cells in each one. So, the 3D image must be extracted to the 2D slices. The 3D image is in the NRRD extension that has to be converted to JPG extension. However, before the extraction and to save time we have to make skull removal and filtering.

- Skull removal: The contents of the brain image, such as the skull, scalp, spinal and other unwanted structure are not necessary and take a long time in processing besides they waste memory. Therefore, our objective in this phase is to isolate only the brain that has the tumor cells to be detected from the entire image. We used the brain surface extractor algorithm BSE to filter the image and removed irregularities. It detects edges in the image. Then, it performs morphological erosions and isolates the brain. It also performs surface cleanup and image masking. The output of this sub-step is the isolated brain from the image in NRRD image. The skull removal was done on the 3D image and, of course, applied to all slices.

- De-noising: Medical images suffer from poor contrasts, noises, artifacts, missing or diffusive boundaries. They are very sensitive to noises especially the brain images. MRI images are usually corrupted by disturbances, such as Gaussian and Poisson noise. Gaussian noise prevails, which degrades the integrity of the relevant image information. Gaussian noise is statistical noise that has the probability density function equivalent to a normal distribution and tends to make the image data Gaussian distributed. This noise has a property of being additive in nature [23]. The vast majority of the de-noising algorithms assume additive white Gaussian noise. There are some algorithms that designed for Gaussian noise elimination, such as edge-preserving bilateral filter, total variation, and non-local means [11]. In this chapter, the median filter is used. We provide free noised images into our proposed method to avoid over-segmentation, under-segmentation, reduce processing time and raise the accuracy.

The noises and artifacts in images were eliminated by using strong filtering algorithm that is the median filter. The before mentioned algorithm is a nonlinear filter. It is used as an effective method of removing noise without effect edges. It preserves edges. Image processing researchers commonly assert that median filtering is better than linear filtering for removing noise in the presence of edges [14]. On the other hand, the noise is removed by using a linear filter (bilateral filter) in the experiments before using a median filter. We found that median filter removed noise and gave the image more contrast and sharpness than a bilateral filter. It moves pixel by pixel through the image and then it replaces each value with the median value of neighboring pixels. The pattern of neighbors is called the window, which slides, pixel by pixel over the image. The median is calculated by sorting all values of the pixels of the window into numerical order and replacing the pixel being considered with the middle or median pixel value.

The median filter is an effective method for eliminating certain kinds of noise, specifically impulsive noise, such as salt and pepper. Although the median filter is well suited for suppressing noise, under the median operation, fine details may be erased, and the result may be similar to capillarity when the objects in the image are close enough. Moreover, rounding the corners and mapping texture region to a uniform shade are the other deficiencies of the median filter. To mitigate these disadvantages, various approaches of the median filter have been developed such as stack filters, multistage median, weighted median, rank conditioned rank selection, and relaxed median [24].

The output of this step is the free noised brain image with no skulls. All slices in the 3D image also have no noises and without skulls or unwanted structures.

- 3D Images to 2D Images Conversion: MRI displays the anatomy in the axial, sagittal and coronal planes. The slice thicknesses of the images vary between 1 to 10 mm. MRI is especially useful for coronal and sagittal imaging. A contiguous set of 2D slices provides a 3D array of image intensity values in the imaging modality. A 3D image can be obtained from many consecutive or

relative 2D slices. By using the MIPAV program, we can extract the 3D image into multiple 2D slices that can be segmented accurately with our system and in minimal time. The input is the NRRD 3D MRI images. The output of this sub-step is 2D MRI slices with a dimension of 256 × 256 with the extension of JPG, which we can deal with in our MATLAB platform.

3.2 Clustering Stage

In this phase, the integration was done between K-means (KM) and particle swarm optimization (PSO) to produce KPSO. KM and PSO are from different categories.

- K-Means Clustering Technique (KM): It is an exclusive clustering technique. Data points are belonging to only one cluster and cannot be included in another cluster. It is the most popular, simple and fast clustering technique. It depends on initializing a number of clusters at the start of the algorithm [25]. The algorithm then determines the cluster centers. It depends on the number of clusters that the user will initialize. The user may initialize a false number of clusters that will lead to false or inaccurate results. It is not suitable for real-world datasets in which there are no boundaries between the clusters. Moreover, it is sensitive to outliers and skewed distributions. It may miss small clusters if it converges to a local minimum, the thing that may lead to the poor or false representation of data [26, 27].
- Particle Swarm Optimization (PSO): It is an optimizing clustering technique. This technique works similar to fishes or birds flocking in search of food [28]. There is a good chance that the flock will find a place with the highest concentration of food if each bird follows the track that combines three common rules. First, keep flying in the same direction. Second, return to the location where it found the highest concentration of insects so far. Finally, move toward the neighboring bird that cries the loudest. The merits of the PSO encouraged us to make the integration between it and KM. The advantages of PSO are that it has no overlapping and depends on the particle speed in the search. Moreover, calculations are very simple. It has significant optimization ability. On the other hand, the disadvantage of the PSO and other optimization techniques is that of becoming trapped in a local optimum. Thus, it may work in some problems but may fail on others. The behavior of the swarm can be divided into two types: exploitation and exploration. The former allows a good short term performance. However, if the exploitation level is too high, then the algorithm may be stuck in local solutions. The second allows exploring new solutions. Thus, it improves the long-term performance. However, if the exploration level is too high, then the algorithm may take too much time to find the global solution.

KPSO approach is applied on the resulting 2D slices as, in the same way that we explained in our paper [11, 12]. The KPSO approach is the integration of KM and

the optimization clustering technique PSO. KPSO provides global optimization with less processing time. It helps KM to escape from local optima by using PSO and helps PSO to reduce computation time by using KM.

Figure 2 shows the flowchart of our hybrid clustering technique KPSO. The idea of the PSO is alike with the bird's flock or fish school. A swarm is a set of particles or birds moving around dimensional search space to reach the target or food. Particles are the pixels, and the search space is the image. Each particle in the swarm makes use of its memory and knowledge gained by the swarm as a whole to find the best solution. Also, every particle has a personal position and velocity that affect its movement in space. The k, No of particles, an inertial weight that controls the velocities are initialized. It has maximum weight (0.9) and minimum weight (0.4). It decreases from 0.9 to 0.4., randsor (r1, r2) that balancing the exploitation or local search and the exploring or global search. The value is from [0, 1], constants c1 = c2 = 2, that control how far a particle will move in once a generation and No of iterations.

The algorithm starts with calculating the centers depending on the number of clusters that was initialized. After that, grouping the points or pixels to the nearest centroids depending on the Euclidian distance. The loop is continuous till there are no points to be grouped to the centroids. The new centroids values are used for particles in the resulting image to redistribute the scattered points and get the optimal solution. Of course, there are two best values update each particle. The first is the personal best (p***best***) which is the best solution or fitness that has achieved so far by that particle. The second value is global best (g***best***) which is the best value obtained so far by any particle in the neighborhood of that particle.

At first, we evaluate the fitness value after that calculate the current particle position and current velocity by formulas 1 and 2 respectively. If the fitness value of the particle is greater than pbest then modifying p***best*** and asking if that fitness value of a particle is greater than gbest. If not and the fitness value is not greater than modified pbest then updating velocity and position but if the fitness value of a particle is greater than gbest then modifying gbest. Each particle modifies its position using the current positions, velocities, the distance between the current position and ***pbest***, and the distance between the current position and the ***gbest***. Each particle updates its velocity and position until reach the max number of iteration. The output of the algorithm is clustered image, optimal clusters centers, and computation time.

$$v_i^{new} = w \times v_i^{old} + cl \times rl \times \left(pbest_i - X_i^{old}\right) + c2 \times r2 \times \left(gbest_{is} - X_i^{old}\right) \quad (1)$$

where v_i^{new} the new velocity of the particle i, w is the inertia weight, v_i^{old} is the old velocity of the particle i, X_i^{old} is the old position of the particle, c1 = c2 = 2, r1, r2 between [0, 1].

$$X_i^{new} = X_i^{old} + X_i^{new} \quad (2)$$

where X_i^{new} is the new position of the particle i.

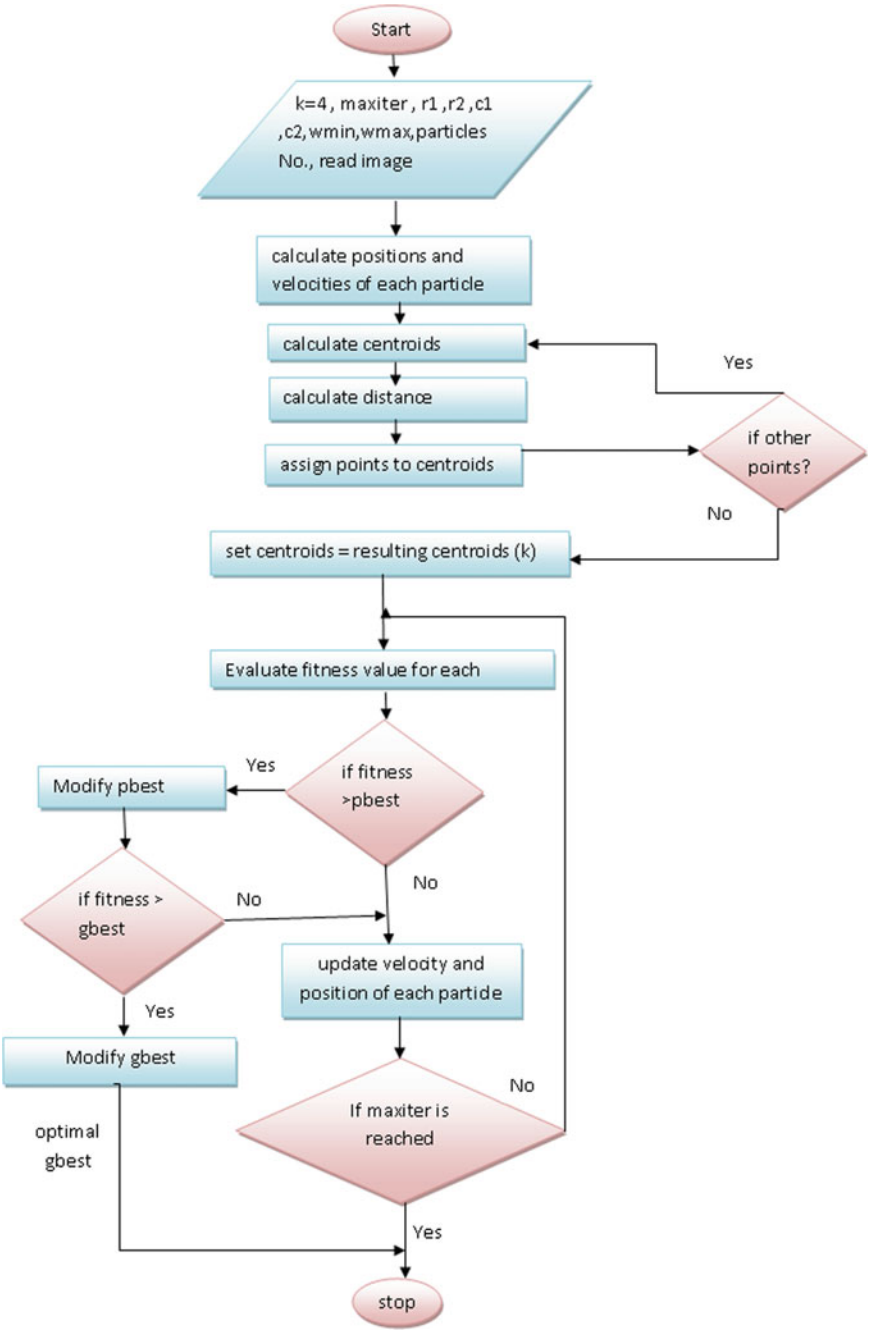

Fig. 2 The flowchart of the KPSO clustering technique

3.3 Segmentation Stage

In this phase, the output of the best results from KPSO hybrid technique will be entered to the segmentation technique. Two segmentation techniques we used: thresholding and active contour level set (for more details see [11, 12]). We got only the tumor cells from the brain as the lighting areas in a dark background on the other hand; we got the contouring areas of tumor in the original smoothing image. They are represented as an expert marked the tumor areas with a green marker pen. After thresholding, the 2D slices may be entered into the post-processing phases to be denoised again to remove scattered points that are not belonging to any cluster.

3.4 Post-processing Stage

The post processing phase consists of two sub-steps. The first is an alignment of 2D clustering slices or registration of the 2D clustering slices. The second is the filtering by the median filter used for the clustering slices before be inserted during the phase of modeling. The filtering can also be done after the thresholding and before level set through the segmentation phase as we demonstrated before. The output clustering images come from the clustering step will be entered in this phase in the alignment of 2D clustering slices. In this sub-step, the slices are concatenated again to be one 3D image as it was. They are converted from JPG slices to one NRRD image (3D image again). Then, in parallel with the segmentation step, the 3D image will be entered to the median filter to be enhanced after clustering and then will be ready to be fed to the next phase.

3.5 Modeling Stage

In the modeling phase, the multiple clustering slices of the 3D image are visualized from several views to be very obvious to the user. The goal of multi-viewing by 3D reconstruction is to infer the geometrical structure of a scene captured by a collection of images. After that, volume rendering was made to visualize the surface of the brain.

- **3D Reconstruction**: The output of the post-processing phase that is the 3D MRI image with the extension of NRRD will be fed the 3D reconstruction. The view of the 3D image is from the three orthogonal views (X, Y, Z) at their different levels. The user can view the slides by clicking and holding on one slice, then move it to see the effect. Of course, we make an MAT-file in Matlab that reads all the slices of the 3D image and uses this MAT-file in the 3D reconstruction procedure. We load the file after that containing the matrix of all 2D slices then getting the coordinates x, y and z from using mesh grid. Plot slices by default in

Table 1 The confusion matrix

Predicted			
		Positive	Negative
Actual	Positive	TP	FN
	Negative	FP	TN

middle position and put labels. The volumetric slices were plotted by slice function in MATLAB.

- **Volume Rendering**: The same 2D clustering slices that are converted to one 3D image will be entered into the volume rendering sub-step that visualizing the volume of the tumor in the brain. The tumor was clustered in the 2D slices images. The surface rendering is done on the NRRD 3D image. The output of this sub-step is the volumetric brain with segmenting volumetric tumor.

3.6 Validation Stage

In the validation phase, the segmenting images by KPSO were compared with the ground truth. The results were evaluated by confusion matrix as shown in Table 1. True positive (TP) means that the case contains the tumor, and the tumor is detected by the system. True negative (TN) means that the case does not contain tumor, and the system does not detect the tumor. False positive (FP) means that the case has not the tumor and system detects the tumor. False negative (FN) means that the case has a tumor, and the system does not detect the tumor.

Precision is the correct segmentation that refers to the percentage of true positive. In other words, it is the number of pixels that belong to a cluster and is segmented into that cluster. Recall, or sensitivity is defined as the number of the true positives divided by the total number of elements that belong to the positive cluster [29]. The performance matrix will be illustrated in details in experimental results.

4 Experimental Results

4.1 Dataset

The dataset we used in brain tumor segmentation is called tumor base. It was created as a joint effort between the Department of Neurosurgery, the Surgical Planning Laboratory, Department of Radiology of the Harvard Medical School at the Brigham, and Women's Hospital in Boston MA [30]. The data set consists of

MRI images of several brain tumor patients and segmentation images of the brain tumor from these MRI images.

Manual segmentations obtained by neurosurgeons and automated segmentations obtained by the method of [31, 32]. The dataset format with no header, unsigned short 16 bit (byte order: MSB-LSB), the Acquisition information is SPGR T1 POST GAD, the resolution: 256 × 256 × 124, Pixel size: 0.9375 × 0.9375 mm, slice thickness: 1.5 mm, slice gap: 0.0 mm and acquisition order: LR. The data set consists of ten cases each case with different tumor type, location and number of slices. The used dataset in case 1 has 124 slices.

4.2 Results

Figure 3 illustrates the steps of our framework on the tumor base dataset on the slice # 50. Image (a) shows the original 3D MRI. Image (b) displays the noisy slice number 50 with the skull. Image (c) shows the processed image after applying the median filter on the 3D MRI image with its 124 -2D slices. Image (d) displays the output of the brain surface extractor procedure on the 3D MRI. Image (e) illustrates the clustering of each 2D slice of the 3D image by using our proposed method KPSO. Of course, the 3D image was extracted to its 2D slices before clustering process. Image (f) shows the form of the concatenated clustered 2D slices to be aligned again into 3D clustered image that contains slice # 50. On the other hand, image (g) shows the binarization process on the clustering 2D slices. Also, it shows that the image after thresholding has pepper and salt noise. Therefore, we use median filter again in the post-processing to remove noise. Image (h) shows the output of median filter on the resulting thresholding image. Image (i) introduces the contouring of the tumor area that was determined by clustering and thresholding. The contouring is done on the smoothed image by the level set method. The tumor area is determined by the green line. Image (j) shows the ground truth of that image to be compared with the output image.

Figure 4 illustrates the steps of our framework on the tumor base data set on the slice # 60 as examples of the 2D slices. As in Fig. 3, the steps are the same, but we can observe that slice # 60 differs from slice # 50. In addition, the tumor area differs from the tumor area in slice # 50.

After we had made the validation of the 2D slices by comparing the clustering results with the ground truth, we constructed the 3D modeling phase. In the 3D modeling phase, the 3D reconstruction of all 122 2D slices of the 3D image. After that, the volume rendering was made. We made the volume rendering for our concatenated clustering 2D slices and also the automated ground truth result to compare the brain and the tumor volume with the automated ground truth.

Figure 5 shows the 3D reconstruction of the 2D clustering slices of the 3D MRI image in the MATLAB platform. The user in this phase can use the mouse to move

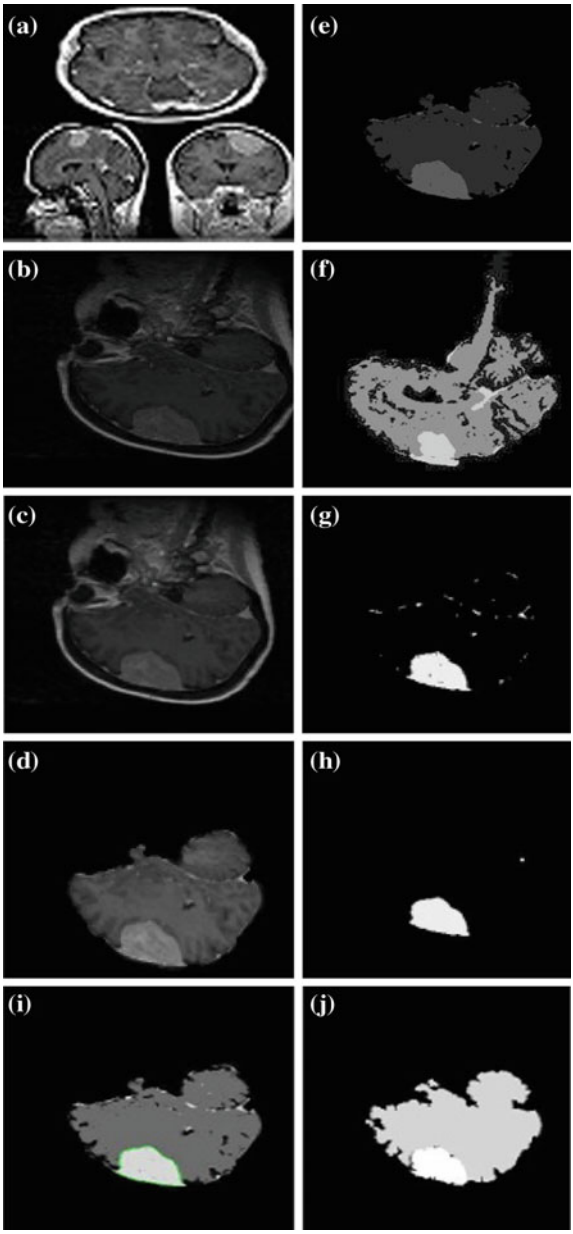

Fig. 3 Applying the proposed 3D framework on 3D MRI data set slice # 50. **a** Original 3DMRI image. **b** Slice # 50. **c** Median filter in preprocess. **d** BSE. **e** Clustering. **f** Concatenate all 124 2D slice. **g** Thresholding. **h** Median filter in post process. **i** Level set. **j** Ground truth

the slices through x, y and z-axis. The user can see all the clustering 2D slices and detect the tumor by the vision before the segmentation by thresholding and level set.

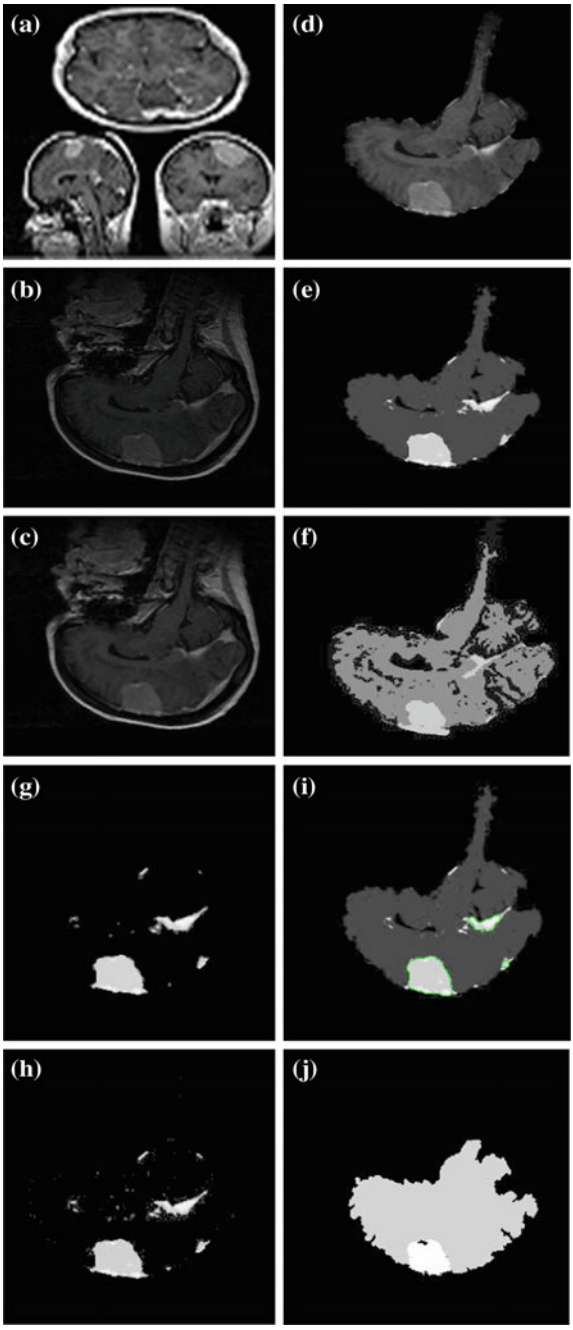

Fig. 4 Applying proposed 3D framework on 3D MRI data set slice # 60. **a** Original 3DMRI image. **b** Slice # 60. **c** Median filter in pre-process. **d** BSE. **e** Clustering. **f** Concatenate all 2D slices. **g** Thresholding. **h** Median filter in post-processing. **i** Level set. **j** Ground truth

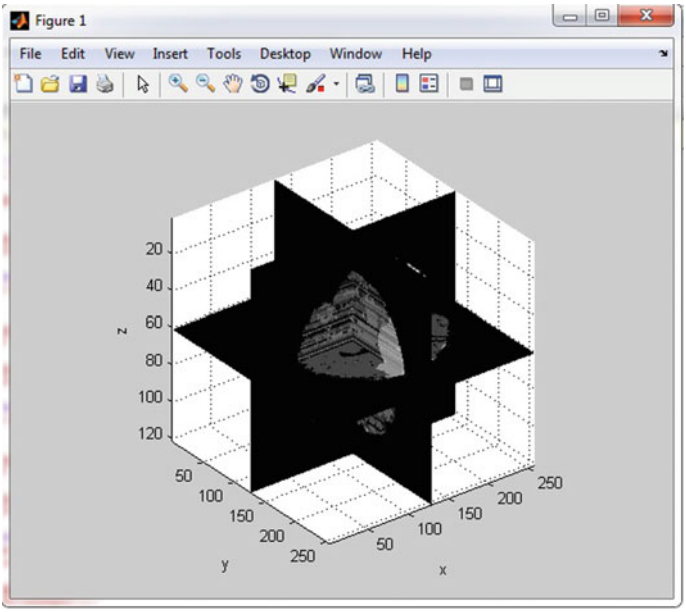

Fig. 5 The snapshot of the 3D reconstruction of 2D clustering slices

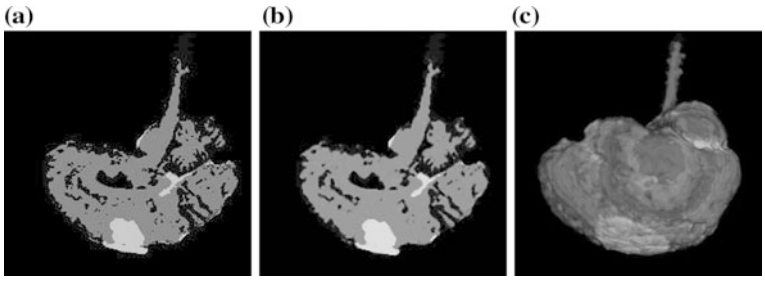

Fig. 6 The volume rendering of a concatenating image of 124 clustering 2D slices. **a** A concatenating image of the clustering 2D slices before filter. **b** A concatenating image of the clustering 2D slices after filter. **c** Our proposed system result

Figure 6 illustrates the difference between using and not using the median filter on the concatenated 122-2D clustering slices before volume rendering. Of course, by using a median filter, it increases the smoothness of the image but still the gabs between the 2D slices make less smoothness in edges.

The next step is the volume rendering. Figure 7 shows the snapshot of the volume rendering phase. The brain and the tumor cells were represented in three images due to holding and dragging the image with a mouse. We put the snapshot of three images to clarify that the user can move the resulting brain with the tumor in any direction as he wants for most accurate observation. The importance of this

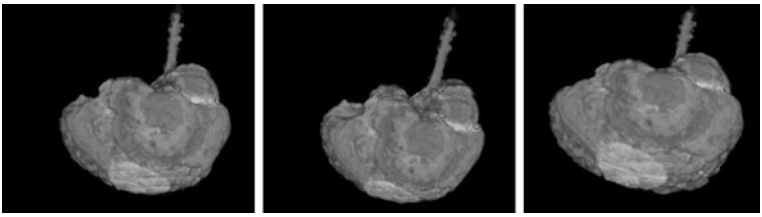

Fig. 7 The volume rendering of the 3D image

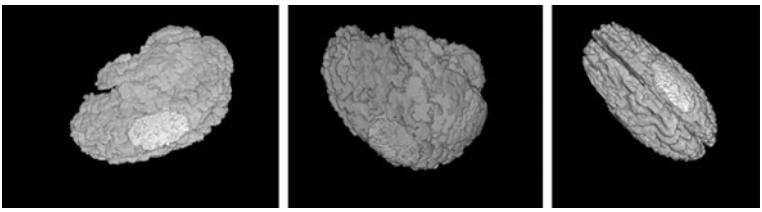

Fig. 8 The volume rendering of automated 3D image ground truth

phase is hidden in clarifying all the infected parts containing the small cells that cannot be seen in the 2D slices. By this movement, the user can see all parts of the brain clearly. We can observe that the surface is not smoothed enough because of the gaps between the slices when were extracted and aligned or concatenated. If the 3D image is clustered a whole once, the gaps will be avoided.

Figure 8 shows the volume rendering of the ground truth 3D image. The figure consists of three snapshots of the image after holding and dragging. We made the comparison between the clustering slices that were resulted from our method KPSO in our framework and the ground truth slices. Also, we made the volume rendering for the ground truth slices by MIPAV program (Medical Image Processing and Analysis Visualization) to evaluate our volume rendering results with the ground truth.

On the other hand, we evaluated the performance of the 3D medical image segmentation according to the confusion matrix as shown in Table 1.

The following formulas identify each element in the confusion matrix [33]:

$$\text{True Positive (TP)} = \frac{\text{No. of resulted n images having brain tumor}}{\text{total No. of images}} \tag{3}$$

$$\text{True Negative (TN)} = \frac{\text{No. of images that haven't tumor}}{\text{total No. of images}} \tag{4}$$

$$\text{False Positive (FP)} = \frac{\text{No. of images that haven't tumor and detected positive}}{\text{total No. of images}} \tag{5}$$

$$\text{False Negative (FN)} = \frac{\text{No. of images have tumor and not detected}}{\text{total No. of images}} \tag{6}$$

$$\text{Precision} = \left[\frac{\text{TP}}{(\text{TP}+\text{FP})}\right] \tag{7}$$

$$\text{Recall} = \left[\frac{\text{TP}}{(\text{TP}+\text{FN})}\right] \tag{8}$$

$$\text{Accuracy} = \left[\frac{(\text{TP}+\text{TN})}{(\text{TP}+\text{TN}+\text{FP}+\text{FN})}\right] \tag{9}$$

By applying these formulas and comparing the results of the clustering slices with the ground truth, we found that TP = 1, TP rate = 100 %, FN = 0, TN = 0, FP = 0. On the other hand, Precision, recall and accuracy rates are 100 % for the tested dataset.

F-measure considers precision and recalls measuring the accuracy of the clustering. F-measure ranging from 0 to 1 is a weighted average of the precision and recall, whereas 0 shows worst score and 1 shows the best score. The F-measure can be calculated using the following formula:

$$\text{F} - \text{score} = 2 \times \frac{precision \times recall}{precision + recall} \tag{10}$$

From formula (10) we found that F-score = 1 which means the best score.

Table 2 shows the difference between the clustering time in minutes (m) by using PSO and using the integration between KM and PSO. The table clarifies the time of the four 2D and 3D datasets [11, 12].

Table 3 shows the mean of accuracies of the tested 2D and 3D images [11, 12]. The mean accuracy that the proposed system achieved based on the proposed hybrid clustering technique KPSO is 98.75 % where it reduces the clustering time by a mean of 10 min.

Table 2 The clustering time of PSO and KPSO

Datasets [11, 12]	PSO (m)	KPSO (m)	Reduced time (m)
DS1	12.61	4.36	8.25
DS2	65.3	42.50	22.8
DS3	23.61	18.52	5.41
The tested dataset (DS4)	17	13	4

Table 3 The means of accuracy and reduced time

The mean of the reduced time is	10 min
The mean of accuracy is	98.75 %

Table 4 The proposed system execution time

System phases	Time (seconds (s) or minutes (m))
BSE	30 s
Median filter	10 s
Slices extraction	91 s
Clustering by KPSO	13 m
Concatenation	1 m
Thresholding	2 s
Median filter	1.5 s
Level set	17 m
3D reconstruction	1.5 s
Volume rendering	57 s
Total execution time is	34 m

Table 5 The comparison between proposed system and the other systems in tumor base

System	Accuracy (%)	Execution time (m)	Operator time of interaction for initialization
Warfield et al. [31]	99.68	76	4
Manual [31]	98.60	180	1–3 for each slice
The proposed system	100	34 for case 1	

Table 6 The comparison between the proposed system and other systems in BRATS

System	Sensitivity (%)	Specificity (%)	Total time
Jiang et al. [33]	87.45	83.12	Not estimated
Wang et al. [35]	91.9	91.9	120 m for 198 images
The proposed system	100	100	43 m for 81 images

Table 4 clarifies the details of the total execution time (s) of the proposed system.Table 5 shows the comparisons between our system and the other systems based on the atlas to segment 3D images due to fourth dataset tumor base (DS4) [29]. Table 6 shows the comparison between our system and other systems due to sensitivity, specificity and total execution time in the third dataset BRATS (DS3) [34].

The systems [31, 33, 35] based on Atlas approaches that consume time in Atlas construction and training dataset. For example, Wang et al. [35] takes 30 min to drive Atlas. The previous tables clarify the comparison between segmenting the 3D image by 2D segmentation techniques that segment each 2D slice and the others that segment the whole 3D image once. Segmenting 2D slices of the 3D image takes more time than segmenting the whole 3D image once, but the former is more accurate than the second.

For 3D MRI images, the real total execution time of clustering 124-2D slices in case one by our KPSO technique is 13 min. On the other hand, the operator time of the automated system [31] is between 5 and 10 min for the ten cases. It takes 76 m in segmentation. The accuracy is 99.68 %. The manual segmentation operator time is from 3 to 5 h of the 10 cases in the ground truth images. From this result, we can prove that our approach solved the problem of the segmenting the 2D slices of the 3D image. It needs extremely time as reduced the execution time as shown in Table 2 and also segmented the tumor accurately.

4.3 Discussion

We can make a constant number of clusters and calculating the means of these clusters. When k clusters equal 4, it gives best results with our techniques. When applying cluster no. = 3 on the dataset, we found that TP = 98.4 %, FN = 1.6 %.

The skull removal is critical because it reduces the time of execution and this item indeed affect the time of overall segmentation system, especially if in dealing with 3D images. Skull removal affects the calculation of the tumor area. Therefore, the calculation will be false if not removing skulls. In addition, the skull removal saves memory. On the other hand, BSE cannot be used on the MRI DICOM images with dcm extension.

The 3D images with the extension of NRRD should be transformed into another extension such as JPEG or JPG to be read in MATLAB.

The Median filter is critical after clustering the slices of the 3D MRI image. The resulting concatenating 3D image will be affected by the smoothing accuracy. From Fig. 7, we can see that the smoothing degree of the resulting image is low because of the differences or gabs between slices.

The 2D clustering images that were saved in MAT file in MATLAB must be smoothed by the median filter before saving to be used in the 3D reconstruction.

5 Conclusion and Future Work

Image segmentation plays a significant role in the medical image to help physicians to diagnose the lesion and put the true treatment plane. A brain tumor is very dangerous if not detected early. On the other hand, the brain images are very sensitive. In the same time, it is very important to segment the 3D brain image. The 3D image segmentation visualizes the small hidden parts that may not be detected by the physician. Therefore, segmenting the 3D medical images is very difficult. We developed new medical image segmentation system to detect the brain tumor from the 3D MRI, which consists of multiple 2D slices. By this system, we detected the brain tumor accurately with minimum execution time from the 3D MRI images. Although we extracted the 3D image to the 2D slices and segmented each slice to

determine the tumor accurately in each one, we reduced the time by using our approach KPSO. Besides that, we put into account reducing time in each phase of the proposed system. Therefore, as far as we know, we broke down the base that "Although segmenting the slices of the 3D image is accurate but it takes a long time rather than segmenting the 3D image by the 3D techniques."

The prospered system helps the physicians to see clearly the tumor areas and cells in the brain image by resulting three images from each 2D slice in the 3D MRI image. These images are the clustering, the thresholding, and the level set image. After that, the system visualizes all of these 2D slices in 3D reconstruction. In the last step, the system makes the volumetric vision of the 3D image to visualize the brain and the tumor from the 2D clustering slices. The experiments proved the effectiveness of our proposed system and integration method in detecting 2D and 3D images accurately with minimal execution time.

In the future, we will solve the problem of less brain surface smoothness in volume rendering step and will also reduce the time without affecting the accuracy. We will use different datasets not only in MRI brain images but also in other imaging modalities on different lesions in other parts of the human body.

References

1. El-Baz, A.S., Acharya, U.R., Laine, A.F., Suri, J. (eds.): Multi-Modality State-of-the-Art Medical Image Segmentation and Registration Methodologies. Springer Science & Business Media, vol. 1, pp. 33–65. Springer, New York (2011)
2. Cui, W., Wang, Y., Fan, Y., Feng, Y., Lei, T.: Localized FCM clustering with spatial information for medical image segmentation and bias field estimation. Int. J. Biomed. Imaging **13** (2013)
3. Dass, R., Priyanka Devi, S.: Image segmentation techniques. Int. J. Electron. Commun. Technol. **3**(1), 66–70 (2012)
4. Ghamisi, P., Couceiro, M.S., Martins, F.M., Atli Benediktsson, J.: Multilevel image segmentation based on fractional order Darwinian particle swarm optimization. IEEE Trans. IEEE Geosci. Remote Sens. **52**(5), 2382–2394 (2014)
5. Wyawahare, M.V., Patil, P.M., Abhyankar, H.K.: Image registration techniques: An overview. Int. J. Signal. Proc. Image Proc. Pattern Recognit. **2**(3), 11–28 (2009)
6. Saxena, S., Singh, R.K.: A survey of recent and classical image registration methods. Int. J. Signal Proc. Image Proc. Pattern Recognit. **7**(4), 167–176 (2014)
7. Bhateja, V., Patel, H., Krishn, A., Sahu, A., Lay-Ekuakille, A.: Multimodal medical image sensor fusion framework using cascade of wavelet and contourlet transform domains. IEEE Sens. J. **15**(12), 6783–6790 (2015)
8. Eden Medical Center.: http://www.edenmedicalcenter.org
9. Xinwu, L.: A new segmentation algorithm for medical volume image based on K-means clustering. J. Chem. Pharm. Res. **5**(12), 113–117 (2013)
10. The National Center for Biotechnology Information.: http://www.ncbi.nlm.nih.gov/pmc/articles/PMC2830087/
11. Abdel Maksoud, E.A., Elmogy, M., Al-Awadi, R.M.: Brain tumor segmentation based on a hybrid clustering technique. Egypt. Inf. J. **16**(1), 71–81 (2015)

12. Abdel Maksoud, E.A., Elmogy, M., Al-Awadi, R.M.: MRI Brain Tumor Segmentation System Based on Hybrid Clustering Techniques. vol. 488, pp. 401–412. AMLTA Springer International Publishing (2014)
13. Jiang, J., Wu, Y., Huang, M., Yang, W., Chen, W., Feng, Q.: 3D Brain tumor segmentation in multimodal MR images based on learning population- and patient-specific feature sets. J. Comput. Med. Imaging Graph. **37**(7), 512–521 (2013)
14. Castro, A., Donoho, D.L.: Does median filter truly preserve edges better than linear filtering? Ann. Stat. **37**(3), 1172–1206 (2009)
15. Ali, S.M., Abood, L.K., Abdoon, R.S.: Automatic technique to produce 3D image for brain tumor of MRI images. J. Univ. Babylon. Pure Appl. Sci. **22**(7), 1896–1907 (2014)
16. Alomoush, W., Abdullah, S.N.H.S., Sahran, S., Hussain, R.I.: MRI brain segmentation via hybrid firefly search algorithm. J. Theor. Appl. Inf. Technol. **61**(1), 73–90 (2014)
17. Thiagarajan, B., Bremananth, R.: Brain image segmentation using conditional random field based on modified artificial bee colony optimization algorithm. WASET Int. J. Med. Heal. Pharm. Biomed. Eng. Brain. **344** (2014)
18. Wu, J., Belle, A., Hargraves, R.H., Cockrell, C., Tang, Y., Najarian, K.: Bone segmentation and 3D visualization of CT images for traumatic pelvic injuries. Int. J. Imaging Syst. Technol. **24**(1), 29–38 (2014)
19. Narkbuakaew, W., Nagahashi, H., Aoki, K., Kubota, Y.: Bone segmentation in CT-liver images using K-means clustering for 3D rib cage surface-modeling. WSEAS Trans. Biol. Biomed. **11**, 183–193 (2014)
20. Piao, N., Kim, J.G., Park, R.H.: Segmentation of cysts in kidney and 3-D volume calculation from CT images. Int. J. Comput. Graph Animat. **5**(1), 1–16 (2015)
21. Ananth, C., Bai, D.R., Renuka, K., Vidhya, A., Savithra, C.: Liver and hepatic tumors segmentation in 3D CT images. Int. J. Adv. Res. Comput. Eng. Technol. **3**(2), 496–503 (2014)
22. Bandhyopadhyay, S.K., Paul, T.U.: Automatic segmentation of brain tumour from multiple images of brain MRI. Int. J. Appl. Innov. Eng. Manag. **2**(1), 240–248(2013)
23. Srivastava, A., Bhateja, V., Tiwari, H., Satapathy, S.C.: Restoration algorithm for gaussian corrupted MRI using non-local averaging. Inf. Syst. Des. Intell. Appl., 831–840. Springer, India (2015)
24. Arastehfar, S., Pouyan, A.A., Jalalian, A.: An enhanced median filter for removing noise from MR images. J. AI. Data. Min. **1**(1), 13–17 (2013)
25. Rai, P., Singh, S.: A survey of clustering techniques. Int. J. Comput. Appl. **7**(12), 1–5 (2010)
26. Sulaiman, S.N., Isa, N.A.M.: Adaptive fuzzy-K-means clustering algorithm for image segmentation. IEEE Trans. Consumer. Electron. **56**(4), 2661–2668 (2010)
27. Eberhart, R.C., Kennedy, J.: A new optimizer using particle swarm theory. In: Proceedings 6th International Symposium on Micro Machine and Human Science, vol. 1, pp. 39–43 (1995)
28. Dakua, S.P.: Use of chaos concept in medical image segmentation. Comput. Methods Biomech. Biomed. Eng. Imaging Vis. **1**, 28–36 (2013)
29. Surgical Planning Laboratory.: http://www.spl.harvard.edu/publications/item/view/1180
30. Kaus, M.R., Warfield, S.K., Nabavi, A., Black, P.M., Jolesz, F.A., Kikinis, R.: Automated segmentation of MRI of brain tumors. Radiology **218**(2), 586–591 (2001)
31. Warfield, S.K., Kaus, M., Jolesz, F.A., Kikinis, R.: Adaptive, template moderated, spatially varying statistical classification. Med. Image Anal. **4**(1), 43–55 (2000)
32. Dey, N., Roy, A.B., Pal, M., Das, A.: FCM based blood vessel segmentation method for retinal images. Int. J. Comput. Sci. Netw. **1**(3) (2012)
33. Jiang, J., Wu, Y., Huang, M., Yang, W., Chen, W., Feng, Q.: 3D brain tumor segmentation in multimodal MR images based on learning population- and patient-specific feature sets. Comput. Med. Imaging Graph. **37**(7), 512–521 (2013)
34. MICCA nice 2012.: http://www2.imm.dtu.dk/projects/BRATS2012/data.html
35. Wang, L., Shi, F., Li, G., Gao, Y., Lin, W., Gilmore, J.H., Shen, D.: Segmentation of neonatal brain MR images using patch-driven level sets. NeuroImage **84**, 141–158 (2014)

Part II
Classification and Clustering

Comparison of CAD Systems for Three Class Breast Tissue Density Classification Using Mammographic Images

Kriti and Jitendra Virmani

Abstract It is well known that the changes in the breast tissue density are strongly correlated with the risk of breast cancer development and therefore classifying the breast tissue density as fatty, fatty–glandular and dense–glandular has become clinically significant. It is believed that the changes in the tissue density can be captured by computing the texture descriptors. Accordingly, the present work has been carried out with an aim to explore the potential of Laws' mask texture descriptors for description of variations in breast tissue density using mammographic images. The work has been carried out on the 322 mammograms taken from the MIAS dataset. The dataset consists of 106 fatty, 104 fatty–glandular and 112 dense–glandular images. The ROIs of size 200 × 200 pixels are extracted from the center of the breast tissue, ignoring the pectoral muscle. For the design of a computer aided diagnostic system for three class breast tissue density classification, Laws' texture descriptors have been computed using Laws' masks of different resolutions. Five statistical features i.e. mean, skewness, standard deviation, entropy and kurtosis have been computed from all the Laws' texture energy images generated from each ROI. The feature space dimensionality reduction has been carried out by using principal component analysis. For the classification task *k*NN, PNN and SVM classifiers have been used. After carrying out exhaustive experimentation, it has been observed that PCA–SVM based CAD system design yields the highest overall classification accuracy of 87.5 %, with individual class accuracy values of 84.9, 84.6 and 92.8 % for fatty, fatty–glandular and dense–glandular image classes respectively. These results indicate the usefulness of the proposed CAD system for breast tissue density classification.

Keywords Breast density · Mammograms · Laws' mask texture descriptors · Principal component analysis · *K*NN classifier · PNN classifier · SVM classifier

Kriti (✉) · J. Virmani (✉)
Thapar University, Patiala, Punjab, India
e-mail: kriti.23gm@gmail.com

J. Virmani
e-mail: jitendra.virmani@gmail.com

N. Dey et al. (eds.), *Medical Imaging in Clinical Applications*,
Studies in Computational Intelligence 651, DOI 10.1007/978-3-319-33793-7_5

1 Introduction

The most commonly diagnosed disease among women that has become a major health concern for the past few decades is breast cancer [1–3]. For the women in United Kingdom, the lifetime risk of being diagnosed with breast cancer is 1 in 8 [4]. The study in [5] reported 1.67 million new cases of breast cancer worldwide in the year 2012. It has been strongly advocated by many researchers in their study that increased breast density is strongly correlated to the risk of developing breast cancer [5–15]. The association between increased breast density and breast cancer risk can be explained on the basis of effects that are caused by the hormones mitogens and mutagens. The mitogens are known to affect the size of the cell population in the breast and cell proliferation while mutagens increase the likelihood of damage to these cells. Due to increased cell population, there is an increase in reactive oxygen species (ROS) production and lipid peroxidation. The products of lipid peroxidation; malondialdehyde (MDA) and isoprostanes catalyze the proliferation of cells [14].

Breast cancer has a very high mortality rate but the chances of survival are significantly improved if it is detected at an early stage. Different imaging modalities like MRI, computerized tomography, ultrasound, etc. are used in the diagnosis of breast abnormalities but mammography is considered to be the best choice for detection due to its higher sensitivity [14, 16–24]. Mammography is an X–ray imaging technique used to detect any abnormalities in the breast. There are two types of mammography examination:

(a) *Screening Mammography*: Screening mammography is used to check for breast abnormalities in asymptomatic women. This examination is used to detect breast cancer at an early stage when there are no symptoms present.
(b) *Diagnostic Mammography*: Diagnostic mammography is performed when either a patient has complaint of some lumps in the breast, pain or any abnormality is detected during the screening process. It helps in determining whether the symptoms indicate the presence of a malignancy and is also used to find the exact location of the abnormalities.

On the basis of density, breast tissue can be classified into the following classes:

(a) *Two–class classification*: Fatty tissue (F)/Dense tissue (D).
(b) *Three–class classification*: Fatty tissue (F)/Fatty–glandular tissue (FG)/Dense–glandular tissue (DG).
(c) *Four–class BI–RADS classification*: Almost entirely fatty tissue (B–I)/some fibro–glandular tissue (B–II)/heterogeneously dense breast tissue (B–III)/extremely dense breast tissue (B–IV).

The typical fatty tissue being translucent to X–rays appears dark on a mammogram whereas the dense tissues appear bright on the mammograms. The fatty–glandular breast tissue is an intermediate stage between fatty and dense tissues therefore a typical fatty–glandular breast tissue appears dark with some bright

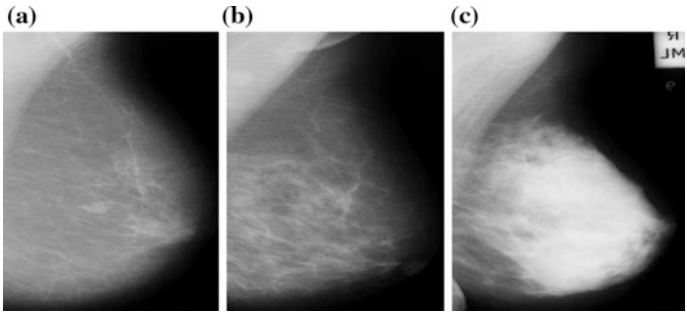

Fig. 1 Sample mammograms showing typical cases. **a** Fatty class 'mdb078'. **b** Fatty–glandular class 'mdb094'. **c** Dense–glandular class 'mdb172'

streaks on the mammogram. The mammograms are visually analyzed by the radiologists to identify and differentiate between different density patterns of the breast tissue. The typical breast tissue density patterns are easy to identify and analyze. This analysis is however subjective and depends on the experience of the radiologist. The appearances of atypical cases of the breast tissue density patterns are highly overlapping and differentiating between these atypical cases through visual analysis is considered to be a highly daunting task for the radiologists. The sample images depicting the typical and atypical cases of breast tissue density patterns are shown in Figs. 1 and 2, respectively.

In order to provide the radiologists with a second opinion tool for validating their diagnosis and identify the atypical mammographic images correctly, various computer aided diagnostic (CAD) systems have been developed in the past for breast tissue density classification. A brief description of the related studies is tabulated in Table 1.

From the extensive literature survey presented in Table 1, it can be observed that most of the related studies are based on the pre–processing of mammograms to

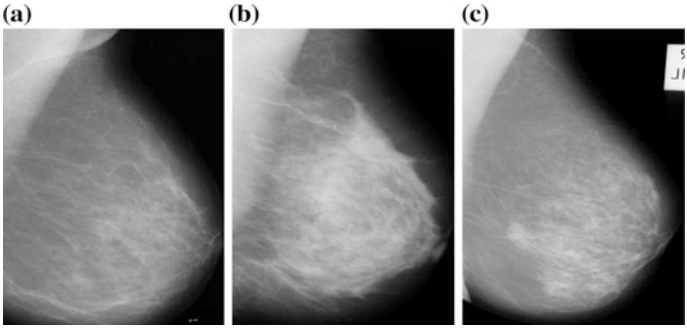

Fig. 2 Sample mammograms showing atypical cases. **a** Fatty class 'mdb156'. **b** Fatty–glandular class 'mdb228'. **c** Dense–glandular class 'mdb058'

Table 1 A description of studies carried out for breast tissue density classification

Investigators	Dataset description				
	Database	Classes	ROI size	No. of images	Accuracy (%)
Miller et al. [25]	Collected by investigator	2	SBT	40	80.0
Karssemeijer [26]	Nijmegen (SBMD)	4	SBT	615	65.0
Blot et al. [27]	MIAS (SBMD)	3	SBT	265	63.0
Bovis et al. [28]	DDSM (SBMD)	2	SBT	377	96.7
Wang et al. [29]	Collected by investigator	4	SBT	195	71.0
Petroudi et al. [30]	Oxford database (SBMD)	4	SBT	132	76.0
Oliver et al. [31]	DDSM (SBMD)	4	SBT	300	47.0
Bosch et al. [32]	MIAS (SBMD)	3	SBT	322	91.3
		4			95.4
	DDSM (SBMD)	4		500	84.7
Muhimmah et al. [33]	MIAS (SBMD)	3	SBT	321	77.5
Castella et al. [34]	Collected by investigator	4	256 × 256	352	83.0
Oliver et al. [35]	MIAS (SBMD)	4	SBT	322	86.0
	DDSM (SBMD)			831	77.0
Subashini et al. [36]	MIAS (SBMD)	3	SBT	43	95.4
Tzikopoulos et al. [37]	MIAS (SBMD)	3	SBT	322	84.4
Li [38]	MIAS (SBMD)	3	SBT	42	94.4
Mustra et al. [39]	MIAS (SBMD)	3	512 × 384	322	82.0
	KBD–FER (collected by investigator)	2		144	97.2
Silva et al. [40]	MIAS (SBMD)	3	300 × 300	320	77.1
Sharma et al. [41]	MIAS (SBMD)	2	200 × 200	322	96.4
Sharma et al. [42]	MIAS (SBMD)	2	200 × 200	212	97.2
Kriti et al. [43]	MIAS (SBMD)	2	200 × 200	322	94.4
Virmani et al. [44]	MIAS (SBMD)	2	200 × 200	322	96.2
Kriti et al. [45]	MIAS (SBMD)	2	200 × 200	322	95.6
Kumar et al. [46]	DDSM (SBMD)	4	128 × 128	480	73.7

Note SBMD Standard benchmark database, *ROI* Region of interest, *SBT* Segmented breast tissue

extract the segmented breast tissue (SBT) after removing the pectoral muscle and the background while very few studies have been carried out that report CAD system designs based on ROIs extracted from the breast. It has also been shown in [47] that the ROIs extracted from the center of the breast result in highest performance as this region of the breast is densest. The ROI extraction method results in

the elimination of an extra step of pre–processing to obtain the SBT after removing the background and pectoral muscle.

K.I. Laws developed a method for texture analysis where an image was filtered with various two–dimensional masks to find its texture properties which proved to be useful for texture analysis. In this method five kernels namely Level (L), Edge (E), Spot (S), Wave (W) and Ripple (R) are used to form different masks used for filtering purposes [48]. Laws' mask analysis is considered to be one of the best methods for texture analysis in image processing applications like breast cancer detection [49, 50], classification of liver diseases [51], bone texture analysis [52] etc.

Thus in the present work, considering the effect of ROI size and location on performance of the algorithms, a CAD system design is proposed for three–class classification of different breast tissue density patterns based on their underlying texture characteristics computed using Laws' mask texture analysis.

The rest of the paper is organised into 3 sections. Section 2 explains the methodology adopted in the present work for three–class breast tissue density classification, giving a brief description of the dataset and proposed CAD system design. The various experiments carried out for classifying the mammographic images are explained in Sect. 3 and the conclusions drawn from the present work are reported in Sect. 4.

2 Methodology

2.1 Description of the Dataset

For the present work mammographic images have been taken from a publicly available database, mini–MIAS (Mammographic Image Analysis Society). The database contains 322 Medio Lateral Oblique (MLO) view mammographic images. The size of each image is 1024 × 1024 pixels with 256 gray scale tones and a 96 dpi horizontal and vertical resolution. The images in the database are divided into three categories on the basis of density, fatty (106 images), fatty–glandular (104 images) and dense–glandular (112 images). The database includes the name of each image in form of a mnemonic with prefix 'mdb' and a three digit number. The database also includes nature of the breast tissue, location of abnormality, the radius of the circle enclosing the abnormality and its severity [53].

2.2 Region of Interest (ROI) Selection

The ROI size is selected carefully, considering the fact that with the selected ROI size, there should be a good population of pixels available for calculating the texture properties. For evaluation, the present work considers an ROI of size

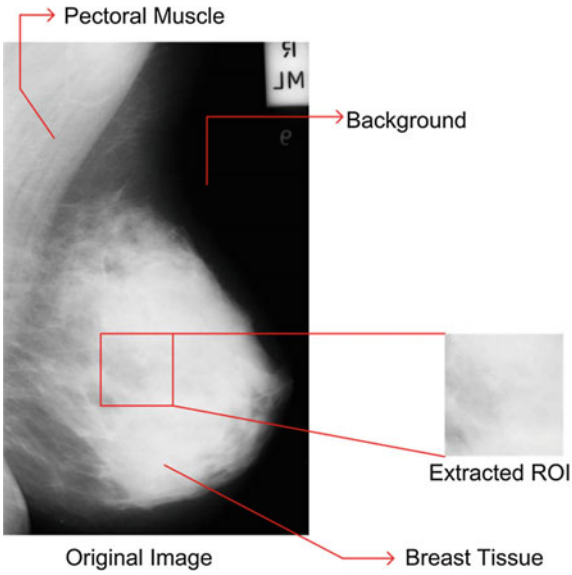

Fig. 3 Process of ROI extraction

200 × 200 pixels extracted manually from the center of the breast tissue for each mammographic image. The ROI size of 200 × 200 has been taken based on the reference in the previous studies [41, 42]. The process of extraction of ROI from the mammographic image is shown in Fig. 3.

2.3 Proposed CAD System Design

The computer aided diagnostic (CAD) systems are nowadays widely used to identify the hidden abnormalities that might be missed by the radiologists during visual analysis hence improving the overall diagnostic accuracy [54–67]. The experimental workflow to design a CAD system for three–class breast tissue density classification is shown in Fig. 4.

The proposed CAD system consists of three modules: feature extraction module, feature space dimensionality reduction module and classification module. From the extracted ROIs, Laws' texture descriptors are calculated using Laws' masks of different lengths to form the feature vectors (FVs). In the feature space dimensionality reduction module, to remove the redundant features from the FVs, the principal component analysis (PCA) algorithm has been applied and reduced feature vectors (RFVs) consisting of principal components (PCs) have been computed. In the classification module, the computed FVs and RFVs have been fed to different classifiers namely k–nearest neighbour (*k*NN), probabilistic neural network (PNN) and support vector machine (SVM) to classify the mammographic images

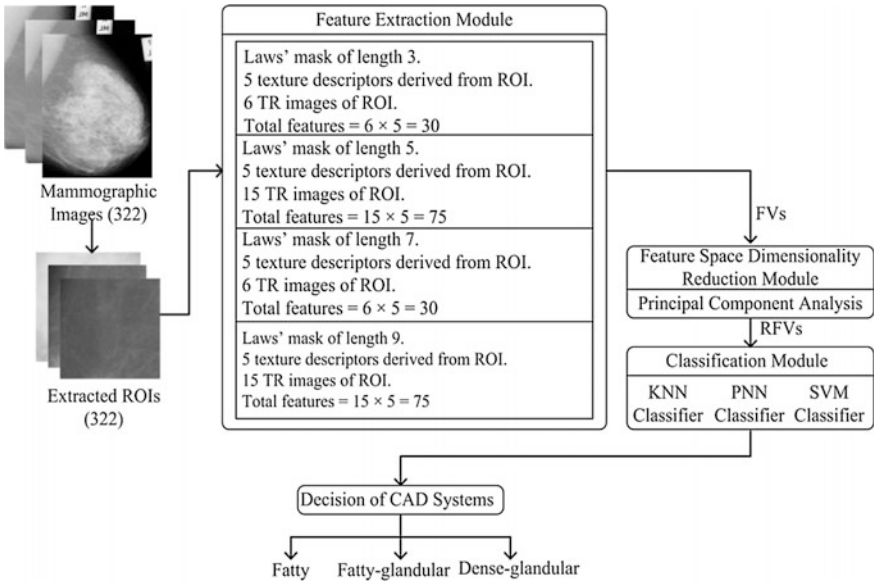

Fig. 4 Experimental workflow for the design of CAD system

into one of the three classes: fatty, fatty–glandular and dense–glandular according to the density information.

Feature Extraction Module. In the field of medical imaging, the process of feature extraction is used to convert the texture features of an image into mathematical descriptors to quantify the textural properties exhibited by the image. The textural features from images can be extracted using different methods–statistical methods, signal processing based methods and transform domain methods. These methods have been depicted in Fig. 5.

In the present work, a signal processing based technique called Laws' mask analysis is used. In this technique the images are filtered with specific masks to extract different textural properties from the images. The masks are formed by combinations of different one–dimensional kernels. Five kernels namely Level (L), Edge (E), Spot (S), Wave (W) and Ripple (R) are used to form different masks used in feature extraction process. Further, the length of these kernels can be 3, 5, 7 and 9 [48, 51, 52, 68, 69]. A description of these one–dimensional kernels is given in Table 2.

The one–dimensional kernels shown in Table 2 are convolved with each other to form the two–dimensional masks used for filtering the images to calculate texture features. The resultant two–dimensional masks for each kernel length are shown in Fig. 6. The process of feature extraction using Laws' mask analysis is depicted in Fig. 7.

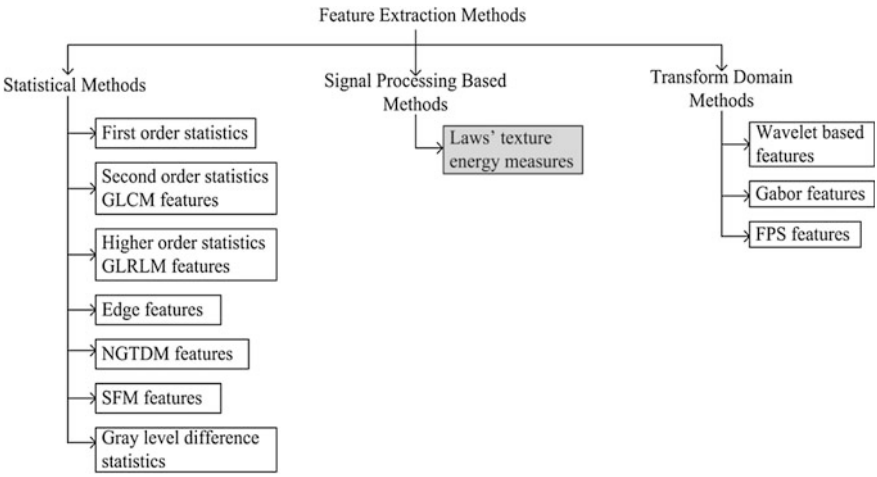

Fig. 5 Different methods used for feature extraction

Table 2 Laws' kernels of different lengths

l	1D Filter coefficients	No. of 2D laws' masks	No. of TR images
3	Level 3 = [1, 2, 1], Edge 3 = [–1, 0, 1], Spot 3 = [–1, 2, –1]	9	6
5	Level 5 = [1, 4, 6, 4, 1], Edge 5 = [–1, –2, 0, 2, 1], Spot 5 = [–1, 0, 2, 0, –1], Wave 5 = [–1, 2, 0, –2 1], Ripple 5 = [1, –4, 6, –4, 1]	25	15
7	Level 7 = [1, 6, 15, 20, 15, 6, 1], Edge 7 = [–1, –4, –5, 0, 5, 4, 1], Spot 7 = [–1, –2, 1, 4, 1, –2, –1]	9	6
9	Level 9 = [1, 8, 28, 56, 70, 56, 28, 8, 1], Edge 9 = [1, 4, 4, –4, –10, –4, 4, 4, 1], Spot 9 = [1, 0, –4, 0, 6, 0, –4, 0, 1], Wave 9 = [1, –4, 4, –4, –10, 4, 4, –4, 1], Ripple 9 = [1, –8, 28, –56, 70, –56, 28, –8, 1]	25	15

Note *l* Length of kernel, *TR* Rotation invariant texture images

The above steps are demonstrated with an example below:

Step 1 Consider Laws' mask of length 3. Convolve the extracted ROIs with each of the above nine 2D filters. Suppose the ROI of size 200 × 200 is convolved with the 2D filter S3S3 to form a texture image (TI_{S3S3}).

$$TI_{S3S3} = ROI \otimes S3S3 \tag{1}$$

Step 2 The mask L3L3 having zero mean is used to form contrast invariant texture images.

(a)

L3L3	E3L3	S3L3
L3E3	E3E3	S3E3
L3S3	E3S3	S3S3

(c)

L7L7	E7L7	S7L7
L7E7	E7E7	S7E7
L7S7	E7S7	S7S7

(b)

L5L5	E5L5	S5L5	W5L5	R5L5
L5E5	E5E5	S5E5	W5E5	R5E5
L5S5	E5S5	S5S5	W5S5	R5S5
L5W5	E5W5	S5W5	W5W5	R5W5
L5R5	E5R5	S5R5	W5R5	R5R5

(d)

L9L9	E9L9	S9L9	W9L9	R9L9
L9E9	E9E9	S9E9	W9E9	R9E9
L9S9	E9S9	S9S9	W9S9	R9S9
L9W9	E9W9	S9W9	W9W9	R9W9
L9R9	E9R9	S9R9	W9R9	R9R9

Fig. 6 2D Laws' masks: **a** Law's masks derived from kernel length 3. **b** Laws' masks derived from kernel length 5. **c** Law's masks derived from kernel length 7. **d** Laws' masks derived from kernel length 9

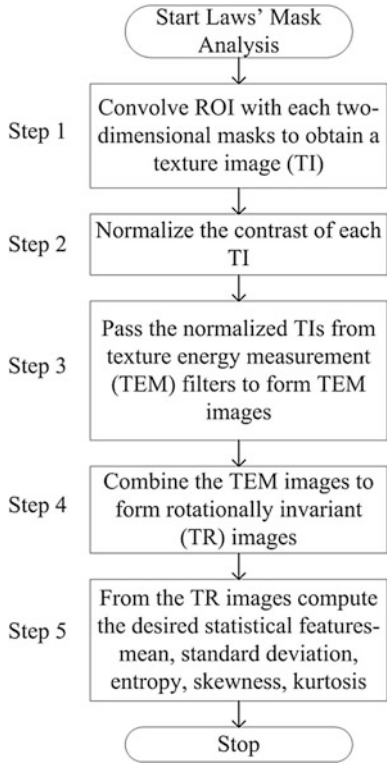

Fig. 7 Steps followed in process of feature extraction Laws' mask analysis

$$\text{Normalise}\ (\text{TI}_{\text{mask}}) = \frac{\text{TI}_{\text{mask}}}{\text{TI}_{\text{L3L3}}} \tag{2}$$

Step 3 The resultant normalized TIs are passed through a 15 × 15 window to derive 9 texture energy images (TEMs).

$$\text{TEM}_{\text{i,j}} = \sum_{\text{u}=-7}^{7} \sum_{\text{v}=-7}^{7} \left|\text{Normalize}\left(\text{TI}_{\text{i}+\text{u,j}+\text{v}}\right)\right| \tag{3}$$

Step 4 Out of 9 TEMs, 6 rotationally invariant texture energy images (TRs) are obtained by averaging.

$$\text{TR}_{\text{S3L3}} = \frac{\text{TEM}_{\text{S3L3}} + \text{TEM}_{\text{L3S3}}}{2} \tag{4}$$

Step 5 From the derived TRs five statistical parameters–mean, standard deviation, skewness, kurtosis and entropy [51, 68] are computed, thus a total of 30 Laws' texture features (6 TRs × 5 statistical parameters) are calculated for each ROI. These statistical parameters are defined as:

$$\text{Mean} = \frac{\sum_{\text{i}=0}^{\text{M}} \sum_{\text{j}=0}^{\text{N}} \left(\text{TR}_{\text{i,j}}\right)}{\text{M} \times \text{N}}. \tag{5}$$

$$\text{SD} = \sqrt{\frac{\sum_{\text{i}=0}^{\text{M}} \sum_{\text{j}=0}^{\text{N}} \left(\text{TR}_{\text{i,j}} - \text{Mean}\right)^2}{\text{M} \times \text{N}}} \tag{6}$$

$$\text{Skewness} = \frac{\sum_{\text{i}=0}^{\text{M}} \sum_{\text{j}=0}^{\text{N}} \left(\text{TR}_{\text{i,j}} - \text{Mean}\right)^3}{\text{M} \times \text{N} \times \text{SD}^3} \tag{7}$$

$$\text{Kurtosis} = \frac{\sum_{\text{i}=0}^{\text{M}} \sum_{\text{j}=0}^{\text{N}} \left(\text{TR}_{\text{i,j}} - \text{Mean}\right)^4}{\text{M} \times \text{N} \times \text{SD}^4} - 3 \tag{8}$$

$$\text{Entropy} = \frac{\sum_{\text{i}=0}^{\text{M}} \sum_{\text{j}=0}^{\text{N}} \left(\text{TR}_{\text{i,j}}\right)^2}{\text{M} \times \text{N}} \tag{9}$$

Proceeding in the similar manner as above, Laws' texture features can also be computed for the masks of length 5, 7 and 9 as shown in Table 2.

The brief description of FVs computed using Laws' mask analysis as used in the present work are described in Table 3.

Feature Space Dimensionality Reduction Module. Some of the computed feature vectors (FVs) may contain redundant or correlated features which must be eliminated. In the present work, the principal component analysis (PCA) algorithm

Table 3 FVs description

FV	Description	*l*
FV1	FV formed by Laws' mask of length 3	30 (5 features calculated from 6 TR images)
FV2	FV formed by Laws' mask of length 5	75 (5 features calculated from 15 TR images)
FV3	FV formed by Laws' mask of length 7	30 (5 features calculated from 6 TR images)
FV4	FV formed by Laws' mask of length 9	75 (5 features calculated from 15 TR images)

Note *FV* Feature vector, *l* Length of FV, *TR* Rotation invariant image

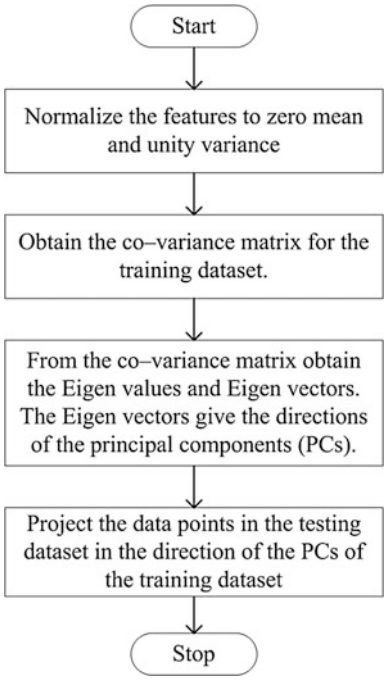

Fig. 8 Steps followed in Principal component analysis algorithm

has been used to obtain optimal attributes for the classification task [70–74]. The main steps followed in the PCA algorithm are shown in Fig. 8.

The optimal number of PCs resulting in highest classification accuracy for training dataset is used for obtaining reduced feature vectors (RFVs) as described in Table 4.

Classification Module. Classification is a technique used in machine learning to predict the class of an unknown data instance based on the training data set,

Table 4 RFVs description

RFV	Description
RFV1	Obtained by applying PCA to FV1
RFV2	Obtained by applying PCA to FV2
RFV3	Obtained by applying PCA to FV3
RFV4	Obtained by applying PCA to FV4

Note *RFV* Reduced feature vector, *FV* Feature vector

containing instances whose class membership is known. In the present work, classifiers like *k*NN, PNN and SVM are used to classify the instances of the testing dataset. Before feeding the extracted FVs and RFVs to the classifiers, the features are normalised in the range [0, 1] by using min–max procedure to avoid any bias caused by unbalanced feature values.

(1) *k–nearest neighbour* (*kNN*) *classifier*: The *k*NN classifier is used to estimate the class of an unknown instance from its neighbouring instances. It tries to assemble together the instances of the training feature vector into separate classes based on distance metric. The class of an unknown instance is decided by a majority vote of its neighbouring instances in the training dataset [71, 75–77]. There are many distance metrics that can be used in *k*NN classification such as Manhattan distance, Minkowski distance, Hamming distance, Mahalanobis distance etc., but Euclidean distance is the most commonly used distance metric. In order to design an efficient *k*NN classifier the optimal value of *k* is required. In the present work, the optimal values of (*a*) the parameter *k* and (*b*) the number of PCs to be retained are determined by exhaustive experimentation with $k \in \{1, 2, \ldots, 9, 10\}$ and number of PCs $\in \{1, 2, \ldots, 14, 15\}$. In case the accuracy values are same for more than one value of the parameter *k*, smallest value of *k* is selected for the classification task.

(2) *Probabilistic neural network* (*PNN*) *classifier*: The PNN classifier belongs to a class of supervised (feed–forward) neural network classifiers used for determining the probability of class membership of an instance [78–80]. The PNN architecture has four layers: input layer, pattern layer, summation layer and output layer. The input layer consists of *'n'* neurons which accept the primitive values. The results obtained in the input unit are transmitted to the hidden units of the pattern layer where the response of each unit is calculated. In the pattern layer, there are *'p'* neurons, one for each class. The *pdf* (probability density function) of each class is defined in the pattern layer on the basis of training data and the optimized kernel width parameter S_p also called the spread parameter. The summation layer sums the values of each hidden unit to get response in each category. To obtain the class of the unknown instance, decision layer selects the maximum response from all categories. The optimal choice of S_p is crucial for the classification task. In order to design an efficient PNN classifier the optimal value of S_p is required. In the present work, the optimal values of (*a*) the spread parameter S_p, and (*b*) the number of PCs to be retained are determined by exhaustive experimentation with $S_p \in \{1, 2, \ldots, 9, 10\}$ and number of PCs $\in \{1, 2, \ldots, 14, 15\}$.

(3) *Support vector machine* (*SVM*) *classifier*: In the present work, SVM classifier has been implemented using one-against-one (OAO) approach for multiclass SVM provided by LibSVM library [81]. The Gaussian radial basis function kernel has been used for non-linear mapping of training data into higher dimensional feature space. In order to design an efficient SVM classifier, the optimal value of C and γ are obtained by grid-search procedure i.e., for each

combination of (C, γ) such that, $C \in \{2^{-4}, 2^{-3}, \ldots, 2^{15}\}$ and $\gamma \in \{2^{-12}, 2^{-11}, \ldots, 2^{4}\}$ the 10-foldcross validation accuracy is obtained for training data. The combination of C and γ yielding the maximum training accuracy are selected for generating the training model. Further, the optimal number of PCs to be retained is determined by repeating the experiments with different number of PCs $\in \{1, 2, \ldots, 14, 15\}$ [73, 82–85].

Classification Performance Evaluation. The performance of the CAD system for breast tissue density classification can be measured using overall classification accuracy (OCA) and individual class accuracy (ICA). These values can be calculated using the confusion matrix (CM).

$$\text{OCA} = \frac{\sum \text{No. of correctly classified ROIs of each class in testing datset}}{\text{Total ROIs in testing dataset}} \tag{10}$$

$$\text{ICA}_{\text{Class}} = \frac{\text{No. of correctly classified ROIs of a particular class in testing dataset}}{\text{Total no. of ROIs of a particular class in the testing dataset}} \tag{11}$$

3 Results

The performance of the proposed CAD system to classify the mammographic images based on their density has been evaluated by conducting various experiments. A description of these experiments is given in Table 5.

Table 5 Description of experiments

Experiment I	Classification performance evaluation of different FVs using *k*NN classifier
Experiment II	Classification performance evaluation of different FVs using PNN classifier
Experiment III	Classification performance evaluation of different FVs using SVM classifier
Experiment IV	Classification performance evaluation of different RFVs using PCA–*k*NN classifier
Experiment V	Classification performance evaluation of different RFVs using PCA–PNN classifier
Experiment VI	Classification performance evaluation of different RFVs using PCA–SVM classifier

Note *FV* Feature vector. *RFV* Reduced feature vector

Table 6 Classification performance of different FVs using *k*NN classifier

FV (*l*)	CM				OCA (%)	ICA_F (%)	ICA_{FG} (%)	ICA_{DG} (%)
		F	FG	DG				
FV1 (*30*)	F	44	6	3	83.2	83.0	82.6	83.9
	FG	4	43	5				
	DG	0	9	47				
FV2 (*75*)	F	43	9	1	83.8	81.1	84.6	85.7
	FG	4	44	4				
	DG	0	8	48				
FV3 (*30*)	F	46	5	2	86.9	86.7	84.6	89.2
	FG	3	44	5				
	DG	0	6	50				
FV4 (*75*)	F	39	11	3	78.8	73.5	82.6	80.3
	FG	3	43	6				
	DG	2	9	45				

Note *FV* Feature vector, *l* Length of FV, *CM* Confusion Matrix, *F* Fatty class, *FG* Fatty–glandular class *DG* Dense–glandular class, *OCA* Overall classification accuracy, ICA_F Individual class accuracy for fatty class, ICA_{FG} Individual class accuracy for fatty–glandular class, ICA_{DG} Individual class accuracy for dense–glandular class

3.1 kNN Classifier Results: Experiment I

This experiment evaluates the classification performance of different FVs using the *k*NN classifier. The results are reported in Table 6.

From Table 6, it is observed that for FV1, FV2, FV3 and FV4, the OCA values are 83.2, 83.8, 86.9 and 78.8 %, respectively. For fatty class the ICA values are 83.0, 81.1, 86.7 and 73.5 % for FV1, FV2, FV3 and FV4, respectively. For fatty–glandular class, the ICA values are 82.6, 84.6, 84.6 and 82.6 % for FV1, FV2, FV3 and FV4, respectively. For the dense–glandular class the ICA values are 83.9, 85.7, 89.2 and 80.3 % for FV1, FV2, FV3 and FV4, respectively. For testing dataset with 161 instances, in case of FV1, the total misclassified instances are 27 (27/161), for FV2, the total misclassified instances are 26 (26/161), for FV3, the total misclassified instances are 21 (21/161) and for FV4, the total misclassified instances are 34 (34/161).

3.2 PNN Classifier Results: Experiment II

This experiment evaluates the classification performance of different FVs using the PNN classifier. The results are reported in Table 7.

From Table 7, it can be observed that for FV1, FV2, FV3 and FV4, the OCA values are 85.0, 81.9, 83.8 and 78.2 %, respectively. For fatty class, the ICA values

Table 7 Classification performance of different FVs using PNN classifier

FV (*l*)	CM				OCA (%)	ICA_F (%)	ICA_{FG} (%)	ICA_{DG} (%)
		F	FG	DG				
FV1 (*30*)	F	45	6	2	85.0	84.9	90.3	80.3
	FG	3	47	2				
	DG	2	9	45				
FV2 (*75*)	F	44	9	0	81.9	83.0	84.6	78.5
	FG	7	44	1				
	DG	3	9	44				
FV3 (*30*)	F	45	7	1	83.8	84.9	88.4	78.5
	FG	4	46	2				
	DG	2	10	44				
FV4 (*75*)	F	40	13	0	78.2	75.4	88.4	71.4
	FG	5	46	1				
	DG	6	10	40				

Note *FV* Feature vector, *l* Length of FV, *CM* Confusion Matrix, *F* Fatty class, *FG* Fatty–glandular class *DG* Dense–glandular class, *OCA* Overall classification accuracy, ICA_F Individual class accuracy for fatty class, ICA_{FG} Individual class accuracy for fatty–glandular class, ICA_{DG} Individual class accuracy for dense–glandular class

are 84.9, 83.0, 84.9 and 75.4 % for FV1, FV2, FV3 and FV4, respectively. For fatty–glandular class, the ICA values are 90.3, 84.6, 88.4 and 88.4 % for FV1, FV2, FV3 and FV4, respectively. For the dense–glandular class the ICA values are 80.3, 78.5, 78.5 and 71.4 % for FV1, FV2, FV3 and FV4, respectively. For testing dataset with 161 instances, in case of FV1, the total misclassified instances are 24 (24/161), for FV2 the total misclassified instances are 29 (29/161), for FV3, the total misclassified instances are 26 (26/161) and for FV4, total misclassified instances are 35 (35/161).

3.3 SVM Classifier Results: Experiment III

This experiment evaluates the classification performance of different FVs using the SVM classifier. The results are reported in Table 8.

From Table 8, it can be observed that for FV1, FV2, FV3 and FV4, the OCA values are 86.3, 86.9, 83.2 and 84.4 %, respectively. For fatty class, the ICA values are 86.7, 88.6, 90.5 and 81.1 % for FV1, FV2, FV3 and FV4, respectively. For fatty–glandular class, the ICA values are 78.8, 78.8, 65.3 and 82.6 % for FV1, FV2, FV3 and FV4, respectively. For the dense–glandular class the ICA values are 92.8, 92.8, 92.8 and 89.2 % for FV1, FV2, FV3 and FV4, respectively. For testing dataset with 161 instances, in case of FV1, the total misclassified instances are 22 (22/161), for FV2 the total misclassified instances are 21 (21/161), for FV3, the total misclassified instances are 27 (27/161) and for FV4, total misclassified instances are 25 (25/161).

Table 8 Classification performance of different FVs using SVM classifier

FV (*l*)	CM				OCA (%)	ICA_F (%)	ICA_{FG} (%)	ICA_{DG} (%)
		F	FG	DG				
FV1 (*30*)	F	46	5	2	86.3	86.7	78.8	92.8
	FG	8	41	3				
	DG	0	4	52				
FV2 (*75*)	F	47	5	1	86.9	88.6	78.8	92.8
	FG	7	41	4				
	DG	0	4	52				
FV3 (*30*)	F	48	5	0	83.2	90.5	65.3	92.8
	FG	12	34	6				
	DG	0	4	52				
FV4 (*75*)	F	43	9	1	84.4	81.1	82.6	89.2
	FG	3	43	6				
	DG	0	6	50				

Note *FV* Feature vector, *l* Length of FV, *CM* Confusion Matrix, *F* Fatty class, *FG* Fatty–glandular class *DG* Dense–glandular class, *OCA* Overall classification accuracy, ICA_F Individual class accuracy for fatty class, ICA_{FG} Individual class accuracy for fatty–glandular class, ICA_{DG} Individual class accuracy for dense–glandular class

3.4 PCA–kNN Classifier Results: Experiment IV

This experiment evaluates the classification performance of different RFVs using the PCA–*k*NN classifier. The results are reported in Table 9.

From Table 9, it can be observed that for RFV1, RFV2, RFV3 and RFV4, the OCA values are 85.0, 81.9, 86.9 and 79.5 %, respectively. For fatty class, the ICA values are 77.3, 77.3, 83.0 and 69.8 % for RFV1, RFV2, RFV3 and RFV4, respectively. For fatty–glandular class, the ICA values are 90.3, 88.4, 86.5 and 88.4 % for RFV1, RFV2, RFV3 and RFV4, respectively. For the dense–glandular class the ICA values are 87.5, 80.3, 91.0 and 80.3 % for RFV1, RFV2, RFV3 and RFV4, respectively. For testing dataset with 161 instances, in case of RFV1, the total misclassified instances are 24 (24/161), for RFV2 the total misclassified instances are 29 (29/161), for RFV3, the total misclassified instances are 21 (21/161) and for RFV4, total misclassified instances are 33 (33/161).

3.5 PCA–PNN Classifier Results: Experiment V

This experiment evaluates the classification performance of different RFVs using the PCA–PNN classifier. The results are reported in Table 10.

From Table 10, it can be observed that for RFV1, RFV2, RFV3 and RFV4, the OCA values are 83.8, 77.6, 85.0 and 74.5 %, respectively. For fatty class, the ICA

Table 9 Classification performance of different RFVs using PCA–*k*NN classifier

RFV (*l*)	CM				OCA (%)	ICA_F (%)	ICA_{FG} (%)	ICA_{DG} (%)
		F	FG	DG				
RFV1 (*7*)	F	41	10	2	85.0	77.3	90.3	87.5
	FG	2	47	3				
	DG	0	7	49				
RFV2 (*7*)	F	41	11	1	81.9	77.3	88.4	80.3
	FG	1	46	5				
	DG	1	10	45				
RFV3 (*6*)	F	44	5	4	86.9	83.0	86.5	91.0
	FG	1	45	6				
	DG	0	5	51				
RFV4 (*10*)	F	37	15	1	79.5	69.8	88.4	80.3
	FG	2	46	4				
	DG	2	9	45				

Note *RFV* Reduced feature vector, *l* Optimum number of PCs, *CM* Confusion Matrix, *F* Fatty class, *FG* Fatty–glandular class *DG* Dense–glandular class, *OCA* Overall classification accuracy, ICA_F Individual class accuracy for fatty class, ICA_{FG} Individual class accuracy for fatty–glandular class, ICA_{DG} Individual class accuracy for dense–glandular class

Table 10 Classification performance of different RFVs using PCA–PNN classifier

RFV (*l*)	CM				OCA (%)	ICA_F (%)	ICA_{FG} (%)	ICA_{DG} (%)
		F	FG	DG				
RFV1 (*6*)	F	45	8	0	83.8	84.9	90.3	76.7
	FG	4	47	1				
	DG	2	11	43				
RFV2 (*9*)	F	40	13	0	77.6	75.4	88.4	69.6
	FG	2	46	4				
	DG	7	10	39				
RFV3 (*6*)	F	46	7	0	85.0	86.7	90.3	78.5
	FG	3	47	2				
	DG	2	10	44				
RFV4 (*10*)	F	40	13	0	74.5	75.4	86.5	62.5
	FG	7	45	0				
	DG	11	10	35				

Note *RFV* Reduced feature vector, *l* Optimum number of PCs, *CM* Confusion Matrix, *F* Fatty class, *FG* Fatty–glandular class *DG* Dense–glandular class, *OCA* Overall classification accuracy, ICA_F Individual class accuracy for fatty class, ICA_{FG} Individual class accuracy for fatty–glandular class, ICA_{DG} Individual class accuracy for dense–glandular class

values are 84.9, 75.4, 86.7 and 75.4 % for RFV1, RFV2, RFV3 and RFV4, respectively. For fatty–glandular class, the ICA values are 90.3, 88.4, 90.3 and 86.5 % for RFV1, RFV2, RFV3 and RFV4, respectively. For the dense–glandular

class the ICA values are 76.7, 69.6, 78.5 and 62.5 % for RFV1, RFV2, RFV3 and RFV4, respectively. For testing dataset with 161 instances, in case of RFV1, the total misclassified instances are 26 (26/161), for RFV2 the total misclassified instances are 36 (36/161), for RFV3, the total misclassified instances are 24 (24/161) and for RFV4, total misclassified instances are 41 (41/161).

3.6 PCA–SVM Classifier Results: Experiment VI

This experiment evaluates the classification performance of different RFVs using the PCA–SVM classifier. The results are reported in Table 11.

From Table 11, it can be observed that for RFV1, RFV2, RFV3 and RFV4, the OCA values are 87.5, 85.7, 86.3 and 85.7 %, respectively. For fatty class the ICA values are 84.9, 81.1, 86.7 and 83.0 % for RFV1, RFV2, RFV3 and RFV4, respectively. For fatty–glandular class, the ICA values are 84.6, 86.5, 78.8 and 82.6 % for RFV1, RFV2, RFV3 and RFV4, respectively. For the dense–glandular class the ICA values are 92.8, 89.2, 92.8 and 91.0 % for RFV1, RFV2, RFV3 and RFV4, respectively. For testing dataset with 161 instances, in case of RFV1, the total misclassified instances are 20 (20/161), for RFV2 the total misclassified instances are 23 (23/161), for RFV3, the total misclassified instances are 22 (22/161) and for RFV4, total misclassified instances are 23 (23/161).

Table 11 Classification performance of different RFVs using PCA–SVM classifier

RFV (*l*)	CM				OCA (%)	ICA_F (%)	ICA_{FG} (%)	ICA_{DG} (%)
		F	FG	DG				
RFV1 (*7*)	F	45	8	0	87.5	84.9	84.6	92.8
	FG	5	44	3				
	DG	0	4	52				
RFV2 (*8*)	F	43	9	1	85.7	81.1	86.5	89.2
	FG	5	45	2				
	DG	1	5	50				
RFV3 (*8*)	F	46	7	0	86.3	86.7	78.8	92.8
	FG	6	41	5				
	DG	0	4	52				
RFV4 (*8*)	F	44	9	0	85.7	83.0	82.6	91.0
	FG	5	43	4				
	DG	0	5	51				

Note *RFV* Reduced feature vector, *l* Optimum number of PCs, *CM* Confusion Matrix, *F* Fatty class, *FG* Fatty–glandular class *DG* Dense–glandular class, *OCA* Overall classification accuracy, ICA_F Individual class accuracy for fatty class, ICA_{FG} Individual class accuracy for fatty–glandular class, ICA_{DG} Individual class accuracy for dense–glandular class

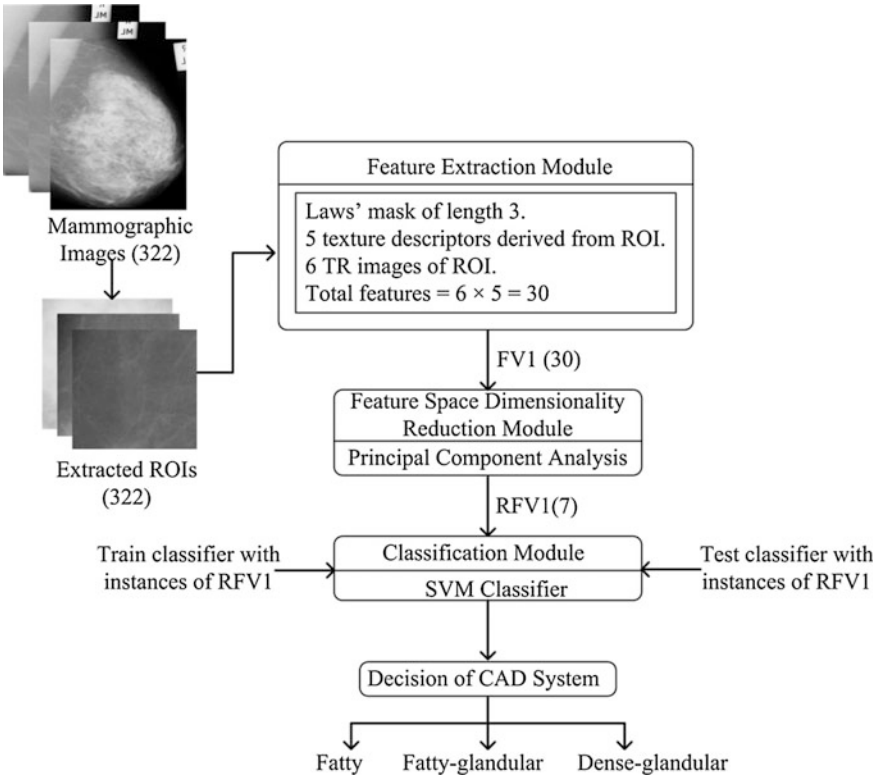

Fig. 9 Proposed CAD system design for three-class breast tissue density classification

4 Conclusion

In the present work the efficacy of Laws' texture features derived using Laws' masks of different resolutions have been tested for three-class breast tissue density classification. From the results obtained, it can be observed that the RFV1 consisting of first 7 PCs computed by applying PCA algorithm to FV1computed using Laws' mask of length 3 with SVM classifier is significant to discriminate between the breast tissues exhibiting different density patterns achieving the highest overall classification accuracy of 87.5 %. The proposed CAD system design for the present work is shown in Fig. 9.

The proposed CAD system is different from earlier studies as most of the related studies have pre–processed the mammograms for segmenting the breast tissue by removal of pectoral muscle for their analysis while in the proposed CAD system design a fixed size ROI (200 × 200 pixels) is manually extracted from the center of the breast tissue thus eliminating the pre–processing step.

The high density of the breast tissue tends to mask the lesions present in the breast which may be malignant or benign therefore, it is recommended that if the proposed CAD system design classifies a testing instance to be of high density i.e. belonging to either fatty-glandular class or dense-glandular class, then the radiologists should re-examine that particular mammogram for any the presence of any lesion behind the high density tissue.

References

1. Breast cancer awareness month in October, World Health Organisation (2012).: http://www.who.int/cancer/events/breast_cancer_month/en/
2. Jain, A., Singh, S., Bhateja, V.: A robust approach for denoising and enhancement of mammographic breast masses. Int. J. Converg. Comput. **1**(1), 38–49 (2013)
3. Bhateja, V., Misra, M., Urooj, S., Lay-Ekuakille, A.: A robust polynomial filtering framework for mammographic image enhancement from biomedical sensors. IEEE Sens. J. **13**(11), 4147–4156 (2013)
4. Cancer stats: key stats, Cancer Research UK.: http://www.cancerresearchuk.org/cancer–info/cancerstats/keyfacts/
5. Hassanien, A.E., Moftah, H.M., Azar, A.T., Shoman, M.: MRI breast cancer diagnosis hybrid approach using adaptive ant-based segmentation and multilayer perceptron neural networks classifier. Appl. Softw. Comput. **14,** 62–71 (2014)
6. Hassanien, A.E.: Classification and feature selection of breast cancer data based on decision tree algorithm. Stud Inf. Control **12**(1), 33–40 (2003)
7. Wolfe, J.N.: Risk for breast cancer development determined by mammographic parenchymal pattern. Cancer **37**(5), 2486–2492 (1976)
8. Boyd, N.F., Martin, L.J., Yaffe, M.J., Minkin, S.: Mammographic density and breast cancer risk: current understanding and future prospects. Breast Cancer Res. **13**(6), 223–235 (2011)
9. Boyd, N.F., Martin, L.J., Chavez, S., Gunasekara, A., Salleh, A., Melnichouk, O., Yaffe, M., Friedenreich, C., Minkin, S., Bronskill, M.: Breast tissue composition and other risk factors for breast cancer in young women: a cross sectional study. Lancet Oncol. **10**(6), 569–580 (2009)
10. Boyd, N.F., Rommens, J.M., Vogt, K., Lee, V., Hopper, J.L., Yaffe, M.J., Pater–son, A.D.: Mammographic breast density as an intermediate phenotype for breast cancer. Lancet Oncol. **6** (10), 798–808 (2005)
11. Vachon, C.M., Gils, C.H., Sellers, T.A., Ghosh, K., Pruthi, S., Brandt, K.R., Pankratz, V.S.: Mammographic density, breast cancer risk and risk prediction. Breast Cancer Res. **9**(6), 217–225 (2007)
12. Boyd, N.F., Guo, H., Martin, L.J., Sun, L., Stone, J., Fishell, E., Jong, R.A., Hislop, G., Chiarelli, A., Minkin, S., Yaffe, M.J.: Mammographic density and the risk and detection of breast cancer. New Engl. J. Med. **356**(3), 227–236 (2007)
13. Warren, R.: Hormones and mammographic breast density. Maturitas **49**(1), 67–78 (2004)
14. Boyd, N.F., Lockwood, G.A., Byng, J.W., Tritchler, D.L., Yaffe, M.J.: Mammographic densities and breast cancer risk. Cancer Epidemiology Biomarkers Prev. **7**(12), 1133–1144 (1998)
15. Al Mousa, D.S., Brennan, P.C., Ryan, E.A., Lee, W.B., Tan, J., Mello-Thomas, C.: How mammographic breast density affects radiologists visual search patterns. Acad. Radiol. **21**(11), 1386–1393 (2014)
16. Papaevangelou, A., Chatzistergos, S., Nikita, K.S., Zografos, G.: Breast density: computerized analysis on digitized mammograms. Hellenic J. Surg. **83**(3), 133–138 (2011)

17. Colin, C., Prince, V., Valette, P.J.: Can mammographic assessments lead to consider density as a risk factor for breast cancer? Eur. J. Radiol. **82**(3), 404–411 (2013)
18. Heine, J.J., Carton, M.J., Scott, C.G.: An automated approach for estimation of breast density. Cancer Epidemiol. Biomarkers Prev. **17**(11), 3090–3097 (2008)
19. Zhou, C., Chan, H.P., Petrick, N., Helvie, M.A., Goodsitt, M.M., Sahiner, B., Hadjiiski, L.M.: Computerized image analysis: estimation of breast density on mammograms. Med. Phys. **28**, 1056–1069 (2001)
20. Jagannath, H.S., Virmani, J., Kumar, V.: Morphological enhancement of microcalcifications in digital mammograms. J. Inst. Eng. Ser. B (India), **93**(3), 163–172 (2012)
21. Huo, Z., Giger, M.L., Vyborny, C.J.: Computerized analysis of multiple-mammographic views: potential usefulness of special view mammograms in computer-aided diagnosis. IEEE Trans. Med. Imaging **20**(12), 1285–1292 (2001)
22. Yaghjyan, L., Pinney, S.M., Mahoney, M.C., Morton, A.R., Buckholz, J.: Mammographic breast density assessment: a methods study. Atlas J. Med. Biological Sci. **1**(1), 8–14 (2011)
23. Bhateja, V., Urooj, S., Misra, M.: technical advancements to mobile mammography using non-linear polynomial filters and IEEE 21451–1 NCAP information model. IEEE Sens. J. **15** (5), 2559–2566 (2015)
24. Virmani, J., Kumar, V.: Quantitative evaluation of image enhancement techniques. In: Proceedings of International Conference on Biomedical Engineering and Assistive Technology (BEATS), pp. 1–8. IEEE Press, New York (2010)
25. Miller, P., Astley, A.: Classification of breast tissue by texture analysis. Image Vis. Comput. **10**(5), 277–282 (1992)
26. Karssemeijer, N.: Automated classification of parenchymal patterns in mammograms. Phys. Med. Biol. **43**(2), 365–378 (1998)
27. Blot, L., Zwiggelaar, R.: Background texture extraction for the classification of mammographic parenchymal patterns. In: Proceedings of Conference on Medical Image Understanding and Analysis, pp. 145–148 (2001)
28. Bovis, K., Singh, S.: Classification of mammographic breast density using a combined classifier paradigm. In: 4th International Workshop on Digital Mammography, 1–4 (2002)
29. Wang, X.H., Good, W.F., Chapman, B.E., Chang, Y.H., Poller, W.R., Chang, T.S., Hardesty, L.A.: Automated assessment of the composition of breast tissue revealed on tissue–thickness–corrected mammography. Am. J. Roentgenol. **180**(1), 257–262 (2003)
30. Petroudi, S., Kadir T., Brady, M.: Automatic classification of mammographic parenchymal patterns: a statistical approach. In: Proceedings of 25th Annual International Conference of IEEE on Engineering in Medicine and Biology Society, pp. 798–801. IEEE Press, New York (2003)
31. Oliver, A., Freixenet, J., Bosch, A., Raba, D., Zwiggelaar, R.: Automatic classification of breast tissue. In: Maeques, J.S., et al. (eds.) Pattern Recognition and Image Analysis. LNCS, vol. 3523, pp. 431–438. Springer, Heidelberg (2005)
32. Bosch, A., Munoz, X., Oliver, A., Marti, J.: Modelling and classifying breast tissue density in mammograms. in: computer vision and pattern recognition. In: IEEE Computer Society Conference, vol. 2, pp. 1552–1558. IEEE Press, New York (2006)
33. Muhimmah, I., Zwiggelaar, R.: Mammographic density classification using multiresolution histogram information. In: Proceedings of 5th International IEEE Special Topic Conference on Information Technology in Biomedicine (ITAB), pp. 1–6. IEEE Press, New York (2006)
34. Castella, C., Kinkel, K., Eckstein, M.P., Sottas, P.E., Verdun, F.R., Bochud, F.: Semiautomatic mammographic parenchymal patterns classification using multiple statistical features. Acad. Radiol. **14**(12), 1486–1499 (2007)
35. Oliver, A., Freixenet, J., Marti, R., Pont, J., Perez, E., Denton, E.R.E., Zwiggelaar, R.: A Novel breast tissue density classification methodology. IEEE Trans. Inf. Technol. Biomed. **12**, 55–65 (2008)
36. Subashini, T.S., Ramalingam, V., Palanivel, S.: Automated assessment of breast tissue density in digital mammograms. Comput. Vis. Image Underst. **114**(1), 33–43 (2010)

37. Tzikopoulos, S.D., Mavroforakis, M.E., Georgiou, H.V., Dimitropoulos, N., Theodoridis, S.: A fully automated scheme for mammographic segmentation and classification based on breast density and asymmetry. Comput. Methods Programs Biomed. **102**(1), 47–63 (2011)
38. Li, J.B.: Mammographic image based breast tissue classification with kernel self-optimized fisher discriminant for breast cancer diagnosis. J. Med. Syst. **36**(4), 2235–2244 (2012)
39. Mustra, M., Grgic, M., Delac, K.: Breast density classification using multiple feature selection. Auotomatika **53**(4), 362–372 (2012)
40. Silva, W.R., Menotti, D.: Classification of mammograms by the breast composition. In: Proceedings of the 2012 International Conference on Image Processing, Computer Vision, and Pattern Recognition, pp. 1–6 (2012)
41. Sharma, V., Singh, S.: CFS–SMO based classification of breast density using multiple texture models. Med. Biol. Eng. Comput. **52**(6), 521–529 (2014)
42. Sharma, V., Singh, S.: Automated classification of fatty and dense mammograms. J. Med. Imaging Health Inform. **5**(3, 7), 520–526 (2015)
43. Kriti., Virmani, J., Dey, N., Kumar, V.: PCA–PNN and PCA–SVM based cad systems for breast density classification. In: Hassanien, A.E., et al. (eds.) Applications of Intelligent Optimization in Biology and Medicine. vol. 96, pp. 159–180. Springer (2015)
44. Virmani, J., Kriti.: Breast tissue density classification using wavelet–based texture descriptors. In: Proceedings of the Second International Conference on Computer and Communication Technologies (IC3T–2015), vol. 3, pp. 539–546 (2015)
45. Kriti., Virmani, J.: Breast density classification using laws' mask texture features. Int. J. Biomed. Eng. Technol. **19**(3), 279–302 (2015)
46. Kumar, I., Bhadauria, H.S., Virmani, J.: Wavelet packet texture descriptors based four-class BI-RADS breast tissue density classification. Procedia Comput. Sci. **70**, 76–84 (2015)
47. Li, H., Giger, M.L., Huo, Z., Olopade, O.I., Lan, L., Weber, B.L., Bonta, I.: Computerized analysis of mammographic parenchymal patterns for assessing breast cancer risk: effect of ROI size and location. Med. Phys. **31**(3), 549–555 (2004)
48. Laws, K.I.: Rapid texture identification. Proc. SPIE Image Process. Missile Guidance **238**, 376–380 (1980)
49. Mougiakakou, S.G., Golimati, S., Gousias, I., Nicolaides, A.N., Nikita, K.S.: Computer-Aided diagnosis of carotid atherosclerosis based on ultrasound image statistics, laws' texture and neural networks. Ultrasound Med. Biol. **33**, 26–36 (2007)
50. Polakowski, W.E., Cournoyer, D.A., Rogers, S.K., DeSimio, M.P., Ruck, D.W., Hoffmeister, J.W., Raines, R.A.: Computer-Aided breast cancer detection and diagnosis of masses using difference of gaussians and derivative-based feature saliency. IEEE Trans. Med. Imaging **16** (6), 811–819 (1997)
51. Virmani, J., Kumar, V., Kalra, N., Khandelwal, N.: Prediction of cirrhosis from liver ultrasound b–mode images based on laws' mask analysis. In: Proceedings of the IEEE International Conference on Image Information Processing, (ICIIP–2011), pp. 1–5. IEEE Press, New York (2011)
52. Rachidi, M., Marchadier, A., Gadois, C., Lespessailles, E., Chappard, C., Benhamou, C.L.: laws' masks descriptors applied to bone texture analysis: an innovative and discriminant tool in osteoporosis. Skeletal Radiol. **37**(6), 541–548 (2008)
53. Suckling, J., Parker, J., Dance, D.R., Astley, S., Hutt, I., Boggis, C.R.M., Ricketts, I., Stamatakis, E., Cerneaz, N., Kok, S.L., Taylor, P., Betal, D., Savage, J.: The mammographic image analysis society digital mammogram database. In: Gale, A.G., et al. (eds.) Digital Mammography. LNCS, vol. 1069, pp. 375–378. Springer, Heidelberg (1994)
54. Doi, K.: Computer-Aided diagnosis in medical imaging: historical review, current status, and future potential. Comput. Med. Imaging Graph. **31**(4–5), 198–211 (2007)
55. Doi, K., MacMahon, H., Katsuragawa, S., Nishikawa, R.M., Jiang, Y.: Computer-Aided diagnosis in radiology: potential and pitfalls. Eur. J. Radiol. **31**(2), 97–109 (1997)
56. Tang, J., Rangayyan, R.M., Xu, J., El Naqa, I., Yang, Y.: Computer-Aided detection and diagnosis of breast cancer with mammography: recent advances. IEEE Trans. Inf Technol. Biomed. **13**(2), 236–251 (2009)

57. Tagliafico, A., Tagliafico, G., Tosto, S., Chiesa, F., Martinoli, C., Derechi, L.E., Calabrese, M.: Mammographic density estimation: comparison among bi–rads categories, semi-automated software and a fully automated one. Breast **18**(1), 35–40 (2009)
58. Giger, M.L., Doi, K., MacMahon, H., Nishikawa, R.M., Hoffmann, K.R., Vyborny, C.J., Schmidt, R.A., Jia, H., Abe, K., Chen, X., Kano, A., Katsuragawa, S., Yin, F.F., Alperin, N., Metz, C.E., Behlen, F.M., Sluis, D.: An intelligent workstation for computer-aided diagnosis. Radiographics **13**(3), 647–656 (1993)
59. Li, H., Giger, M.L., Olopade, O.I., Margolis, A., Lan, L., Bonta, I.: Computerized texture analysis of mammographic parenchymal patterns of digitized mammograms. Int. Congr. Ser. **1268**, 878–881 (2004)
60. Tourassi, G.D.: Journey toward computer aided diagnosis: role of image texture analysis. Radiology **213**(2), 317–320 (1999)
61. Kumar, I., Virmani, J., Bhadauria, H.S.: A review of breast density classification methods. In: Proceedings of 2nd IEEE International Conference on Computing for Sustainable Global Development, (IndiaCom–2015), pp. 1960–1967. IEEE Press, New York (2015)
62. Virmani, J., Kumar, V., Kalra, N., Khandelwal, N.: Neural network ensemble based CAD system for focal liver lesions from B-Mode ultrasound. J. Digit. Imaging **27**(4), 520–537 (2014)
63. Zhang, G., Wang, W., Moon, J., Pack, J.K., Jean, S.: A review of breast tissue classification in mammograms. In: Proceedings of ACM Symposium on Research in Applied Computation, pp. 232–237 (2011)
64. Chan, H.P., Doi, K., Vybrony, C.J., Schmidt, R.A., Metz, C., Lam, K.L., Ogura, T., Wu, Y., MacMahon, H.: Improvement in radiologists' detection of clustered micro-calcifications on mammograms: the potential of computer-aided diagnosis. Instigat. Radiol. **25**(10), 1102–1110 (1990)
65. Virmani, J., Kumar, V., Kalra, N., Khandelwal, N.: Prediction of liver cirrhosis based on multiresolution texture descriptors from B-Mode ultrasound. Int. J. Converg. Comput. **1**(1), 19–37 (2013)
66. Virmani, J., Kumar, V., Kalra, N., Khandelwal, N.: A rapid approach for prediction of liver cirrhosis based on first order statistics. In: Proceedings of the IEEE International Conference on Multimedia, Signal Processing and Communication Technologies, pp. 212–215. IEEE Press, New York (2011)
67. Virmani, J., Kumar, V., Kalra, N., Khandelwal, N.: Prediction of cirrhosis based on singular value decomposition of gray level co–occurrence matrix and a neural network classifier. In: Proceedings of Development in e–systems Engineering (DESE–2011), pp. 146–151 (2011)
68. Vince, D.G., Dixon, K.J., Cothren, R.M., Cornhill, J.F.: Comparison of texture analysis methods for the characterization of coronary plaques in intravascular ultrasound images. Comput. Med. Imaging Graph. **24**(4), 221–229 (2000)
69. Seng, G.H., Chai, Y., Swee, T.T.: Research on laws' mask texture analysis system reliability. Reasearch J. Appl. Sci. Eng. Technol. **7**(19), 4002–4007 (2014)
70. Virmani, J., Kumar, V., Kalra, N., Khandelwal, N.: Characterization of primary and secondary malignant liver lesions from B-Mode ultrasound. J. Digit. Imaging **26**(6), 1058–1070 (2013)
71. Virmani, J., Kumar, V., Kalra, N., Khandelwal, N.: A comparative study of computer–aided classification systems for focal hepatic lesions from B–mode ultrasound. J. Med. Eng. Technol. **37**(44), 292–306 (2013)
72. Romano, R., Acernese, F., Canonico, R., Giordano, G., Barone, F.: A principal components algorithm for spectra normalisation. Int. J. Biomed. Eng. Technol. **13**(4), 357–369 (2013)
73. Virmani, J., Kumar, V., Kalra, N., Khandelwal, N.: PCA–SVM based CAD system for focal liver lesions using B–mode ultrasound images. Def. Sci. J. **63**(5), 478–486 (2013)
74. Kumar, I., Bhadauria, H.S., Virmani, J., Rawat, J.: Reduction of speckle noise from medical images using principal component analysis image fusion. In: Proceedings of 9th International Conference on Industrial and Information Systems, pp. 1–6. IEEE Press, New York (2014)

75. Yazdani, A., Ebrahimi, T., Hoffmann, U.: Classification of EEG signals using dempster shafer theory and a k–nearest neighbor classifier. In: Proceedings of 4th International IEEE EMBS Conference on Neural Engineering, pp. 327–330 (2009)
76. Amendolia, S.R., Cossu, G., Ganadu, M.L., Galois, B., Masala, G.L., Mura, G.M.: A comparative study of k–Nearest neighbor, support vector machine and multi-layer perceptron for thalassemia screening. Chemom. Intell. Lab. Syst. **69**(1–2), 13–20 (2003)
77. Wu, Y., Ianakiev, K., Govindaraju, V.: Improved *k*NN classification. Pattern Recogn. **35**(10), 2311–2318 (2002)
78. Specht, D.F.: Probabilistic neural networks. Neural Netw. **1**, 109–118 (1990)
79. Specht, D.F., Romsdahl, H.: Experience with adaptive probabilistic neural network and adaptive general regression neural network. In: Proceedings of the IEEE International Conference on Neural Networks, pp. 1203–1208. IEEE Press, New York (1994)
80. Georgiou, V.L., Pavlidis, N.G., Parsopoulos, K.E., Vrahatis, M.N.: Optimizing the performance of probabilistic neural networks in a bioinformatics task. In: Proceedings of the EUNITE 2004 Conference, pp. 34–40 (2004)
81. Chang, C.C., Lin, C.J.: LIBSVM, a library of support vector machines. ACM Trans. Intell. Syst. Technol. **2**(3), 27–65 (2011)
82. Virmani, J., Kumar, V., Kalra, N., Khandelwal, N.: SVM–based characterization of liver cirrhosis by singular value decomposition of GLCM matrix. Inter. J. Artif. Intell. Soft Comput. **3**(3), 276–296 (2013)
83. Hassanien, A.E., Bendary, N.E., Kudelka, M., Snasel, V.: Breast cancer detection and classification using support vector machines and pulse coupled neural network. In: Proceedings of 3rd International Conference on Intelligent Human Computer Interaction (IHCI 2011), pp. 269–279 (2011)
84. Virmani, J., Kumar, V., Kalra, N., Khandelwal, N.: SVM–Based characterization of liver ultrasound images using wavelet packet texture descriptors. J. Digit. Imaging **26**(3), 530–543 (2013)
85. Azar, A.T., El–Said, S.A.: Performance analysis of support vector machine classifiers in breast cancer mammography recognition. Neural Comput. Appl. **24**, 1163–1177 (2014)

Ensemble Classifiers Construction Using Diversity Measures and Random Subspace Algorithm Combination: Application to Glaucoma Diagnosis

Soraya Cheriguene, Nabiha Azizi and Nilanjan Dey

Abstract Glaucoma is a group of eye diseases caused due to excessively high intraocular pressure within the eye. Ensemble classifier construction has attracted increasing interest in the field of pattern recognition and machine learning. Diversity among the classifiers is important factor for each ensemble to be successful. The most widely generation techniques are focused on incorporating the concept of diversity by using different features or training subsets. a classifier selection process becomes an important issue of multiple classifier system by choosing the optimal subset of members that maximizes the performance. The main goal of this study is to develop novel automated glaucoma diagnosis system which analyze and classify retinal images using a novel classification approach based on feature selection and static classifier selection schemes. Experimental results based on RIM-ONE dataset are very encouraging.

Keywords Machine learning · Ensemble classifier construction · Diversity measure · Retinal images · Random subspace · Static classifier selection

S. Cheriguene (✉) · N. Azizi (✉)
Labged Laboratory, Badji Mokhtar Annaba University, Annaba, Algeria
e-mail: Soraya_cheriguene@yahoo.fr

N. Azizi
e-mail: azizi@labged.net

S. Cheriguene · N. Azizi
Computer Science Department, Badji Mokhtar University, PO BOX 12,
23000 Annaba, Algeria

N. Dey
Department of Computer Science, Bengal College of Engineering & Technology,
Durgapur, India

N. Dey et al. (eds.), *Medical Imaging in Clinical Applications*,
Studies in Computational Intelligence 651, DOI 10.1007/978-3-319-33793-7_6

1 Introduction

Glaucoma is a group of eye diseases caused due to excessively high intraocular pressure (IOP) within the eye. This increased pressure within the eye is usually caused nerve damage resulting in progressive, permanent vision loss, starting with unnoticeable blind spots at the edges of the field of vision, getting to tunnel vision, so to blindness [1]. It has been reported that almost 30 million people worldwide have glaucoma; the overall number of glaucomatous subjects is anticipated to increase within the course of the current decade. By 2020, it is estimated that approximately 80 million people worldwide will be diagnosed with glaucoma [2]. The yank Academy of ophthalmology recommends a routine screening once in each 2–4 years, for people between the age bracket of 40–64 years and in each 1–2 years, after 65 years of age which might help in detecting the disease in its early stage.[1] Glaucoma leads to (i) structural changes of the nerve fiber layer and the optic nerve head (ONH) and (ii) synchronous functional failure of the field of vision. Glaucoma is generally diagnosed based on the patient's medical record, IOP, visual field loss tests and also the manual assessment of the ONH via ophthalmoscopy or stereo fundus imaging [3].

Since, the feature is an attribute that may capture a precise property of the visual image, either locally for objects or globally for the whole image. Thus, extracted feature is an important widely used for analyzing medical images. An assortment of approaches can be derived from features extraction such as: signal processing (hilbert transform and Wavelet transformation) [4, 5], co-occurrence matrices [6]. Fourier power spectrum and neural networks [7] etc.

A number of classifiers are tested to improve the diagnosis of glaucoma disease and minimizing possible errors that may be done because of inexperienced specialists. The latest researches have been proposing the combination of multiple classifiers models as an attempt to improve the accuracy and efficiency of a classification system [8–10]. During learning, the base classifiers are created separately on the training data set, then the next step is to choose an effective combination rule such as majority voting for combining the outputs and produce the final ensemble decision on a test pattern [11, 12].

The diversity between the classifiers forming the ensemble is recognized to be one of the required characteristics to achieve high degree of accuracy [10, 13]. In other words, there is no gain in combining identical components. Many methods have been developed to enforce diversity among the base learners [14].

The largest set of methods generates ensemble classifiers by using different training sets. Bagging and Boosting [15, 16] are two of the most popular ensemble approaches based on the latest method. Bagging (after Bootstrap aggregating) produces diversity by generating different bootstrap samples from the original training set for each base classifier. Bootstrapping is less effective when the training sample size is large compared with the data dimensionality. Hence, in bagging,

[1] http://www.glaucoma.org/glaucoma/diagnostic-tests.php.

when the number of training objects decreases, classifiers in the ensemble become less diverse. Boosting is a deterministic procedure, in which the training sets are sampled sequentially based on the results of the previous iteration. In contrast, bagging obtained the training sets and the classifiers in parallel and randomly. The most widely used boosting method is Adaboost (Adaptive Boosting) and its numerous variants.

In another group of ensemble classifiers, the diversity among the base members is achieved by dividing the input feature space where the base classifiers are trained on different feature subsets, i.e. Random Sub [17]. The Random Subspaces method based on selecting different subsets of attribute to train each of the component classifiers.

Given a large number of classifiers, a classifier selection process becomes an important issue of multiple classifier system (MCS) design. The selection of a classifier can be either static or dynamic. In Static Selection, the classifiers that will form the ensemble are chosen at the optimization phase, once and for all and used to classify the test instances. In Dynamic Selection, the classifiers are chosen at the classification phase. That is, different testing samples can be classified by different classifiers. Currently, most of the existing classifier selection schemes for MCSs use as choice criterion either the accuracy or the diversity.

A system for the classification of different entities of glaucoma is proposed. Proposed approach begins with features extraction phase; indeed, we used three heterogeneous families of characteristics and integrate them into a single vector with the aim of assuring diversity of information that can be offer by each feature family. These families are based on texture and shape features and which are: the matrix of co-occurrence (which aims to extract texture characteristics), the moments of Hu and central moments (these two families aims to describe image shape). A new multiple classifier system is then exploited to classify and analyze automatically the normal and the abnormal eye images using a combination of Random subspace method and Static selection strategy based on diversity and accuracy. The subset of classifiers selected in the static selection procedure is combined using majority voting.

The rest of this paper is organized as follows. Multiple classifier systems are briefly described in Sect. 2. In Sect. 3, details about the proposed method are presented. Then, the experiments and the results are presented in Sect. 4. Section 5 provides information of related work. Section 6 closes the paper with some final remarks.

2 Multiple Classifier System

As previous mentioned, MCS consists of an ensemble of different classification algorithms and a fusion function for combining classifier outputs. The goal of using MCS is to improve the accuracy and efficiency of a pattern recognition system and reliability of individual classifiers [18, 19]. There are three main issues in the design of a MCS: the ensemble components, the selection of the components and the

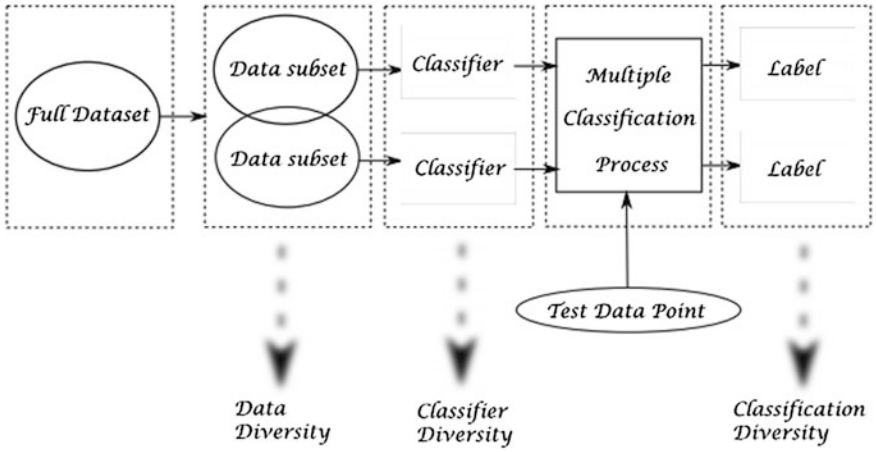

Fig. 1 Traditional multiple classifier system: diverse data splitting is implemented to generate diverse data subsets, which are then used to train classifiers. Consequently, classifier outputs are likely to be diverse classifications

combination methods that will be used. Figure 1 shows the general architecture of a classifier ensemble [20].

The concept of Diversity [21] plays a crucial role in the ensemble generation. The base members should be diverse among themselves with uncorrelated errors. Traditionally, there have been several methods for generating diversity: Variations of the parameters of the base classifiers (e.g., initial parameters, such as the weights and topology, of a neural network model [22, 23], Use of different training datasets of the classifiers (e.g., the use of learning strategies such as Bagging, Boosting and Random Subspace [15–17], Variations of the type or topologies of classifiers, using the same topology, but with different parameters.

In addition, in some real world applications the number of members required to form an ensemble with a reasonable accuracy could be enormously large [24, 25]. Therefore, it is important to apply a classifier selection process that maximizes the performance, in order to reduce the number of ensemble members and at the same time, keeping the diversity within the selected members [26]. In other words, diversity must be generated to improve accuracy, but this is far from sufficient. In order to do this, it is important to define a process to choose appropriate subset of classifiers from the pool of employed to make the decision, which is typically based on the input pattern to be classified [27]. Currently, most of the existing classifier selection methods for MCSs use accuracy and diversity of the classifiers as choice criterions [24, 28–31].

Once a set of classifiers has been created and selected the next step is to choose an effective aggregation method to derive the ultimate class label of an object from the individual classifier outputs. There are a vast number of effective combination methods reported in the literature. They could be assorted according to their characteristics as Linear or Non-linear [26].

- Linear combination methods. Currently, the simplest ways to combine multiple classifier system are the sum and average of the classifiers outputs [29].
- Non-linear methods. This group includes rank-based combiners, such as majority voting strategies [11, 32], the Dempster-Shafer technique [33], Borda Count [27], fuzzy integral [18], neural networks [18] and genetic algorithms [29].

3 Proposed Approach

In order to classify the retinal images into glaucoma or normal, the proposed system represented in Fig. 2.

3.1 Image Acquisition

This study uses the fundus images acquired from RIM-ONE database. RIM-ONE [34] is exclusively focused on ONH segmentation (Fig. 3); it has 169 high-resolution pictures and five manual reference segmentations and a gold criterion of each one. The high number of professional segmentations allows the creation of reliable gold standards and the development of high accurate

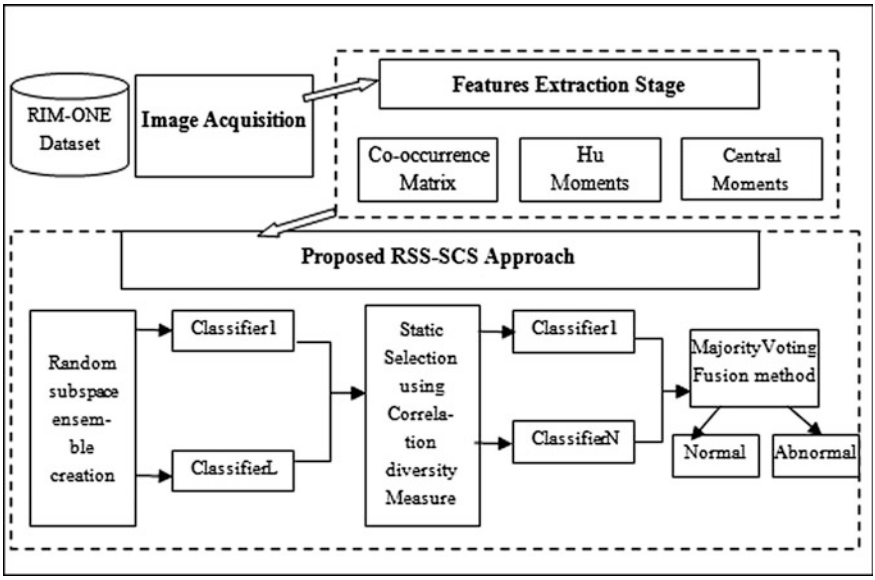

Fig. 2 The proposed ensemble classifier construction technique for glaucoma eye diseases

segmentation algorithms. The designed database consists of 169 ONH images obtained from 169 full fundus images of different subjects. RIM-ONE is composed by joint collaboration of three Spanish organizations, i.e. Hospital Miguel Servet, Universidad Nacional de Educación a Distancia and Universidad Complutense. This public database contains 169 images. Out of these 51 images are for glaucoma affected and 118 images are normal.

3.2 Feature Extraction

Feature extraction is a crucial step within the classification process and depends on the purpose (general description, Local description) and the type of image to be analyzed (binary image, image grayscale, and color image). In our proposed approach, we have represented the image by three families which are characteristic: the co-occurrence matrix, Hu moments and central moments.

Hu Moments. Hu moments are used as basic feature descriptors for images, for the reasons that they are invariant with respect to translation, scaling, as well as rotation. They have been widely used in image analysis [35–37]. Hu moments have two advantages: (1) the first absolute orthogonal invariant of Hu moments can evaluate the degree how the energy is concentrated to the center of energy gravity for two dimensional data; (2) Hu moments are invariant with respect to translation, scaling, as well as rotation [38].

Based on normalized central moments, Hu introduced seven moment invariants which can be summarized as follow:

$$
\begin{aligned}
\phi_1 &= \eta_{20} + \eta_{02} \\
\phi_2 &= (\eta_{20} + \eta_{02})^2 + 4\eta_{11}^2 \\
\phi_3 &= (\eta_{30} + \eta_{12})^2 + (3\eta_{21} - \mu_{03})^2 \\
\phi_4 &= (\eta_{30} + \eta_{12})^2 + (\eta_{21} + \eta_{03})^2 \\
\phi_5 &= (\eta_{30} + 3\eta_{12})(\eta_{30} + \eta_{12})\left[(\eta_{30} + \eta_{12})^2 - 3(\eta_{21} + \eta_{03})^2\right] \\
&\quad + (3\eta_{21} - \eta_{03})(\eta_{21} + \eta_{03})\left[3(\eta_{30} + \eta_{12})^2 - 3(\eta_{21} + \eta_{03})^2\right] \\
\phi_6 &= (\eta_{20} - \eta_{02})\left[(\eta_{30} + \eta_{12})^2 - (\eta_{21} + \eta_{03})^2\right] + 4\eta_{11}(\eta_{30} + \eta_{12})(\eta_{21} + \eta_{03}) \\
\phi_7 &= (3\eta_{21} - \eta_{03})(\eta_{30} + \eta_{12})[(\eta_{30} + \eta_{12})^2 - 3(\eta_{21} + \eta_{03})^2] \\
&\quad - (\eta_{30} - 3\eta_{21})(\eta_{21} + \eta_{03})[3(\eta_{30} + \eta_{12})^2 - (\eta_{21} + \eta_{03})^2
\end{aligned}
\tag{1}
$$

Gray Level Co-occurrence Matrix. Grey Level Co-occurrence Matrices (GLCM) is earliest strategies for texture feature extraction suggested by Haralick et al. [39] back in 1973. Since then it is been widely employed in several texture analysis applications and remained to be a very important feature extraction

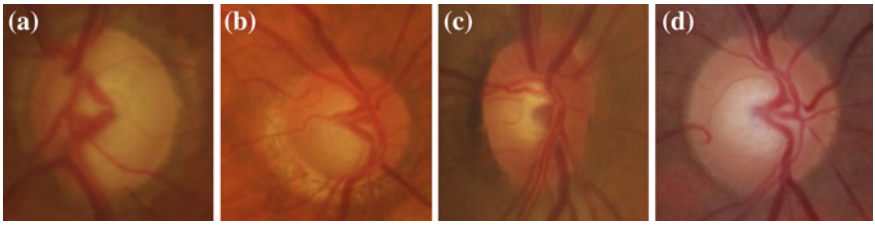

Fig. 3 Typical fundus images taken from RIM-One database: **a** and **b** glaucoma, **c** and **d** normal

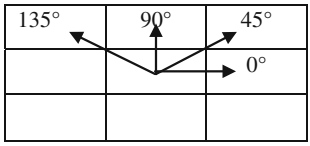

Fig. 4 The four directions of adjacency for calculating the Haralick texture features

technique within the domain of texture analysis. Fourteen features were extracted by Haralick from the GLCMs to characterize texture [6].

The Grey Level Co-occurrence Matrix is calculated by finding a square matrix G of order N, where g is the number of gray levels in the image. The (i, j)th entry of G represents the sum of the number of times that the gray level pixel with intensity i is adjacent in a specific spatial relationship to a pixel with intensity j and then each element of G by the total number of such comparisons made. The adjacency can be defined to take place in each of the four directions (horizontal, vertical, left and right diagonal) as shown in Fig. 4. The Haralick texture features are calculated for each of these directions of adjacency [39].

The texture features are calculated by averaging over the four directional co-occurrence matrices. To extend these concepts to n-dimensional Euclidean space, we tend to exactly define grey scale images in n-dimensional space and the above mentioned directions of adjacency in n-dimensional images (Table 1).

Let, H is a spatial dependence matrix. $H(i, j)$ is an element at (i, j) location in the spatial matrix (i, j) be the (i, j)th entry in a normalized gray tone spatial matrix dependence matrix = $H(i, j)$/R, where, R is a normalizing constant. Further, let $h_x(i)$ be the ith entry in the marginal probability matrix obtained by summation of rows of $h(i, j)$. It is represented mathematically as $\sum_{j=1}^{N_g} H(i, j)$, where

$$h_{x+y} = \sum_{\substack{i=1 \\ i+j=k}}^{N_g} \sum_{j=1}^{N_g} h(i,j), \quad \text{where}, k = 2, 3, \ldots, N_g \tag{2}$$

$$h_{x-y} = \sum_{\substack{i=1 \\ |i-j|=k}}^{N_g} \sum_{j=1}^{N_g} h(i,j), \quad \text{where}, k = 0, 1, \ldots, N_{g-1} \tag{3}$$

Table 1 Haralick features

Feature	Equation
Angular second moment	$P_1 = \sum_i \sum_j h(i,j)^2$
Contrast	$P_2 = \sum_{n=0}^{N_2-1} n^2 \{\sum_{i=1}^{N_2}\sum_{j=1}^{N_2} h(i,j)\}, \lvert i-j\rvert = n$ where n is an integer
Correlation	$P_3 = \frac{\sum_i \sum_j (ij)h(i,j)^2 - \mu_x\mu_y}{\sigma_x\sigma_y}$
Sum of squares: variance	$P_4 = \sum_i \sum_j (i-\mu)^2 h(i,j)$
Inverse difference moment	$P_5 = \sum_i \sum_j \frac{1}{1+(i-j)^2} h(i,j)$
Sum average	$P_6 = \sum_{i=2}^{2N_2} i h_{x+y}(i)$ where x and y are the coordinates (row and column) of an entry in the co occurrence matrix
Sum variance	$P_7 = \sum_{i=2}^{2N_2} (i-f_8)^2 h_{x+y}(i)$
Sum entropy	$P_8 = -\sum_{i=2}^{2N_2} p_{x+y}(i) \log\{h_{x+y}(i)\} = P_g$
Entropy	$P_9 = -\sum_i \sum_j h(i,j) \log(h(i,j))$
Difference variance	$P_{10} =$ variance of h_{x-y}
Difference entropy	$P_{11} = -\sum_{i=0}^{N_2-1} h_{x-y}(i) \log\{h_{x-y}(i)\}$

In the previous equations, N_g is the number of distinct gray levels in the quantized image. $h_{x+y}(k)$ is the probability of occurrence matrix coordinates summing to $x + y$ and k is the index. $h_{x-y}(k)$ is the probability of occurrence matrix coordinates summing to x-y and k is the index. Let h_x, h_y are the partial probability density function. μ_x, μ_y are the mean of hx, hy and σx, σy are the standard deviations of h_x and h_y [40]. The used Haralick features in our approach are described below:

Central Moments. In image processing, an image moment is a certain specific weighted average (moment) of the image pixel intensities, or a function of such moments, typically chosen to have some enticing property or interpretation [41]. As the name suggests, the central moments are calculated from the center of the shape. They are defined as:

$$\mu_{pq} = \int_{-\infty}^{\infty} \int_{-\infty}^{\infty} (x-\bar{x})^p (y-\bar{y})^q f(x,y) dxdy \tag{4}$$

where $\bar{x} = \frac{M_{10}}{M_{00}}$ *and* $\bar{y} = \frac{M_{01}}{M_{00}}$ are the components of the centroid.

3.3 Learning and Classification

The classification method proposed (RSS-SCS) in this paper is based first on the Random Subspace method (RSS) which creates the initial pool of diverse classifiers by using different subsets of features to train classifiers and based secondly on Static Classifier Selection (SCS) using the diversity measure, in which the testing patterns are classified by the same ensemble configuration. Once a selection method is used to choose the ensemble members, the resulting set of classifiers are then combined by combination rule. Many methods can be used to combine the outputs of classifiers among which the majority voting is a most widely used method [11, 32]. It is in fact the simplest ensemble scheme: given a test pattern x, each classifier vote for a target class. The class that gets the highest number of votes is selected. With this approach, we can reduce the time needed for classifier training for ensemble creation and also reduce the ensemble selection search space.

Random Subspace Method. The Random Subspace is an ensemble construction method proposed by Ho [17]. This method has taken the lead in many application domains characterized by high-dimensional data. Examples include, but are not limited to, phenotype recognition [42], cancer diagnosis [43] and face recognition [44].

Random subspace methods use the subspace rate (the quantitative relation of selected attributes over total attributes stock) to randomly choose features to construct data subsets. After construction of data subsets, base classifiers are trained on the different sub datasets. The main idea is to enhance the diversity among the member's classifiers while keeping their accuracies at the same time. By using random feature subsets, RSS achieves some advantages for constructing and aggregating classifiers, especially when the number of available training objects is much smaller than the feature dimensionality.

Static Classifier Selection. The classifier selection mechanism is assigned to select best classifiers from a pool of different classifiers, so that the selected subset of classifiers can achieve the optimum recognition rates. In static selection the best performing classifier ensemble is chosen during a training phase and used for the classification of unseen patterns [29]. In general, the chosen classifiers are alleged to be diverse and accurate to results in highly accurate ensembles, however precisely how this is enforced within the selection process is not obvious. In our approach we create all possible subsets of classifier ensemble contain the most accurate classifier then we select the most diverse subset using diversity measures [13].

The diversity measures can be divided into pairwise and non-pairwise measures. The pairwise measures define the average of a specific agreement/disagreement diversity measures between all potential pairings of classifiers in ensemble classifiers. The non-pairwise measures either use the concept of entropy or calculate a correlation of every ensemble member with the (weighted) mean of the individual outputs.

In this study, based on the pairwise measures, we select four measures. The diversity among the whole set of classifiers over the test set is then defined as an average over all the pairs of diversity below:

$$div = \frac{2}{M(M-1)} \sum_{i=1}^{M} \sum_{j=i+1}^{M} div_{i,j} \tag{5}$$

where M is the size of classifiers set and $div_{i,j}$ is the diversity between the classifiers i and j. The diversity measures applied in this work are:

Correlation between the errors
As it is reasonable to expect that the independence of occurring errors ought to be helpful for classifier combining, the correlation of the errors is a natural choice to compare the classifiers subsets of classifiers [24]. Here the correlation coefficient a, b for the vectors of correctness of classification for classifiers a and b is calculated as

$$\rho_{a,b} = \frac{\mathrm{Cov}(\mathrm{v}^{\mathrm{a}}, \mathrm{v}^{\mathrm{b}})}{\sqrt{\mathrm{Var(a)Var(b)}}} \tag{6}$$

where Var(•) refers to variance and Cov(•) covariance. The most effective subset of classifiers is chosen by selecting that with the minimal mean pairwise correlation. Where ρ is within the range from −1 to 1. If ρ = −1 then it implies that the agreement of classifiers equals that expected by chance, while ρ = 1, indicating that classifiers agree on all the test instances.

Q statistic. statistic Q statistic is defined for two classifiers a, b [45] as

$$\mathrm{Q}_{a,b} = \frac{N^{11}N^{00} - N^{01}N^{10}}{N^{11}N^{00} + N^{01}N^{10}} \tag{7}$$

where N^{00} is the number of patterns that both classifiers wrongly classified; in contrast, N^{11} stands for the number of patterns that both classifiers correctly classified; N^{10} is the number of patterns classified correctly by classifier $\mathrm{D_i}$ but not by $\mathrm{D_j}$; likewise, N^{01} is the total of patterns classified correctly by classifier $\mathrm{D_j}$, but not by $\mathrm{D_i}$.

Q varies in the range from −1 to 1. A positive Q means that a classifier ensemble tends correctly to classify the same instance; otherwise it incorrectly classifies the instance.

Disagreement measure. This measure represents the number of times that one in every of the classifiers was incorrect and other was correct [46]. It will so be defined for two classifiers a and b as

$$\mathrm{D}_{a,b} = \frac{N^{01} + N^{10}}{\mathrm{N}} \tag{8}$$

The diversity decreases with decreasing values of the disagreement measure in the range from 0 to 1.

Weighted Count of Errors and Correct Results. This is a measure takes into account at the same time the correct and the incorrect results of classifiers and gives suitable weight on them

$$\mathrm{WCEC}_{a,b} = N^{11} + \frac{1}{2}\left(N^{01} + N^{10}\right) - \mathrm{N}^{00}_{\text{different}} - 5\mathrm{N}^{00}_{\text{same}} \tag{9}$$

$\mathrm{N}^{00}_{\text{different}}$ is the number of times where two classifiers a and b offer different errors at the same time. $\mathrm{N}^{00}_{\text{same}}$ is the number of times where the classifiers a and b offer the same mistakes. An elevated value of WCEC measure means that classifiers

Majority Voting. Majority Voting Schemes are very important for combining decisions by multiple experts. In this combining schema, each classifier has similar weight classification for test instance which is performed according to the class that obtains the highest number of votes. This rule is computed as in Eq. 9, given a subset of p classifiers, $\mathrm{y_i}$ as the class label output of the ith classifier, and a classification problem with the following set of class labels $\Omega = \{\omega_1, \omega_2, \ldots, \omega_c\}$

$$mv(x) = max^{c}_{k=1} \sum_{i=1}^{p} y_{i,k} \tag{10}$$

Particularly for forward search, the algorithm first selects the most accurate classifier c_i^* in C. Thus, the pair of classifiers, including c_i^*, with lowest majority voting error is identified. Then, at each iteration, a new individual is added to the ensemble. The optimization process is ended when there is no more amelioration on decreasing the majority voting error.

The main code of RSS-SCS can be outlined as follow:

Input: a p-dimensional labeled training data set
1. For each $k = 1, \ldots, L$
(a) Select a p^* dimensional random subspace, from the p-dimensional feature space
(b) Project the data from the original p-dimensional feature space into the selected p^*-dimensional subspace
(c) Construct a classifier C_k, on the acquired p^*-dimensional feature
2. Create all possible subsets of classifiers ensemble with N components contain the most accurate classifier
3. Select the most diverse subset of Classifiers
4. Aggregate generated using majority voting combination techniques

4 Experiments

4.1 Experimental Protocol

Proposed approach for glaucoma detection and classification using a sample of 207 images from the RIM-ONE dataset. Out of these 66 images are glaucoma affected and 141 images are normal. Feature extraction step consists in representing the image by three families of features which are: the co-occurrence matrix, Hu moments and central moments. Our image eventually will be represented by a large feature vector including the values from the three families of characteristics, this feature vector contains over than 24 characteristics.

In order to evaluate our method we use the k-fold cross-validation protocol. According to this protocol, given a dataset comprising several examples, we randomly divide it into k subsets, with no repetition. k–1 subsets is chosen as training set, and the remaining subset are used as test set. The cross-validation process is repeated k rounds and each subset is used only once as test set. The final accuracy result from this process is the arithmetic mean of all rounds. In our experiments, we employed a 10-fold cross-validation procedure in which, in each round, any nine of the ten subsets are selected to implement classifier training. The remaining part will be executed for testing the classifier. Thus, all accuracy results conferred in paper refer to the mean over 10 different test sets.

For classifier design, since neural networks and decision trees are two most widely used classification techniques [47]; they are created as the single baseline classifiers. In addition, for the decision tree classifier, we used two types of decision tree J48 and random tree (J48 is a Java implementation of C4.5). The homogeneous initial ensemble of classifiers contains 100 classifiers and the parameter settings for Multilayer Perceptron (MLP), J48 and Random Tree (RT) in this empirical study were set at the default settings. Each classifier was trained using randomly selected 50 % of features from the training dataset. The proposed percentage has been determined by Ho [17]. The author has shown that the best results are obtained when we using half of the feature components set. Note that the WEKA (Waikato Environment for Knowledge Analysis) version 3.6.11 was used to conduct our experiment.

4.2 Experimental Results

The RSS-SCS classifier measure is assigned to the three feature vectors. During this phase, we tried to make several empirical tests to keep the ones that generate the highest rate of classification. First, each family was tested independently with the classifier RSS-SCS then all features are grouped together in a single vector that will be the entrance of our RSS-SCS classifier. Four diversity measures were calculated during training. Experimental results after execution of our progressive algorithm are resumed in Tables 2, 3, 4 and 5 and Fig. 5.

Table 2 Obtained results of Classifiers ensembles using correlation measure with the three families of characteristics

	RSS-SCS with co-occurrence matrix (%)	RSS-SCS with Hu moments (%)	RSS-SCS with central moments (%)	RSS-SCS with all features (%)
J48 ensemble	77.78	77.35	75.35	*90.88*
MLP ensemble	74.85	75.35	76.33	*86.04*
RT ensemble	94.66	91.30	89.90	*96.16*

Table 3 Obtained results of Classifiers ensembles using WCEC measure with the three families of characteristics

	RSS-SCS with co-occurrence matrix (%)	RSS-SCS with Hu moments (%)	RSS-SCS with central moments (%)	RSS-SCS with all features (%)
J48 ensemble	78.78	79.21	76.80	*93.78*
MLP ensemble	76.85	75.35	76.83	*86.04*
RT ensemble	96.11	93.71	90.38	*98.07*

Table 4 Obtained results of classifiers ensembles using Qstatistics measure with the three families of characteristics

	RSS-SCS with co-occurrence matrix (%)	RSS-SCS with Hu moments (%)	RSS-SCS with central moments (%)	RSS-SCS with all features (%)
J48 ensemble	78.28	77.30	76.30	*92.83*
MLP ensemble	75.80	76.35	76.35	*85.57*
RT ensemble	96.11	92.28	89.90	*96.04*

Table 5 Obtained results of classifiers ensembles using disagreement measure with the three families of characteristics

	RSS-SCS with co-occurrence matrix (%)	RSS-SCS with Hu moments (%)	RSS-SCS with central moments (%)	RSS-SCS with all features (%)
J48 ensemble	78.80	78.76	77.78	*84.54*
MLP ensemble	76.78	78.28	80.71	*85.02*
RT ensemble	87.02	85.50	85.52	*90.85*

These results indicate that RT ensembles by RSS-SCS can be regarded as the optimal classifier ensemble technique for detecting the glaucoma disease. Specifically, they can provide the highest rate of accuracy using all features of dataset and WCEC measure for classifiers selection.

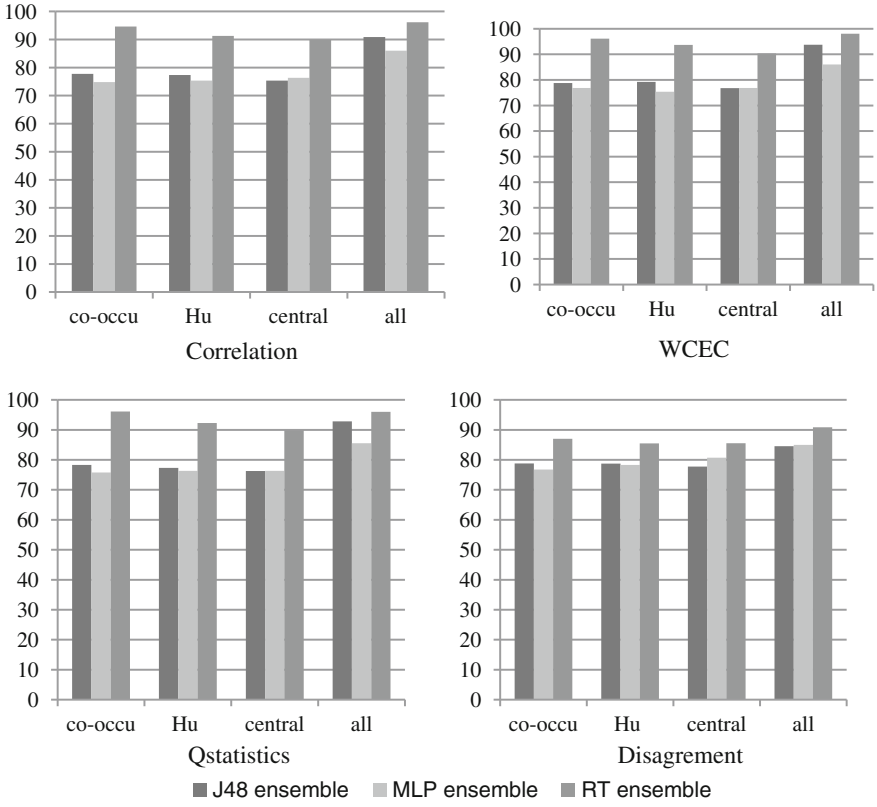

Fig. 5 Obtained results on different RSS-SCS ensembles with the three features families

Amongst the three features extraction methods that have been used during the validation, we observed that the co-occurrence matrix almost gives the higher rate compared to the other two methods using RT classifiers and J48 classifiers. For the MLP ensemble, central moment's method almost gives the higher rate.

From this tables, we can also say that RSS-SCS has again proved its effectiveness in the field of medical diagnosis and especially in the case of retinal images with a high recognition rate (98.07 %).

We also tested three best-known ensemble methods (Bagging (BG), AdaBoost (AD) and Random Subspace (RSS)) in order to compare the results of the classifier RSS-SCS using WCEC diversity measure. Each ensemble contained 100 random trees. Table 6 summarizes the accuracy percentage of each classifier ensemble with the tree families of features. From the obtained results in Table 6 we observed that each classifier ensemble method has given different accuracy rate compared to others, such as the RSS-SCS given the higher rate compared to the other methods amongst the three features extraction methods that have been used during the validation. The experimental results are presented in Fig. 6.

Table 6 Obtained results of classifiers ensembles with the three families of characteristics

	BG (%)	AD (%)	RSS (%)	RSS-SCS (%)
Co-occurrence matrix	76.50	75.40	81.40	*96.11*
Hu moments	79.30	79.30	80.20	*93.71*
Central moments	81.20	77.40	80.20	*90.38*
All features	80.90	76.00	81.80	*98.07*

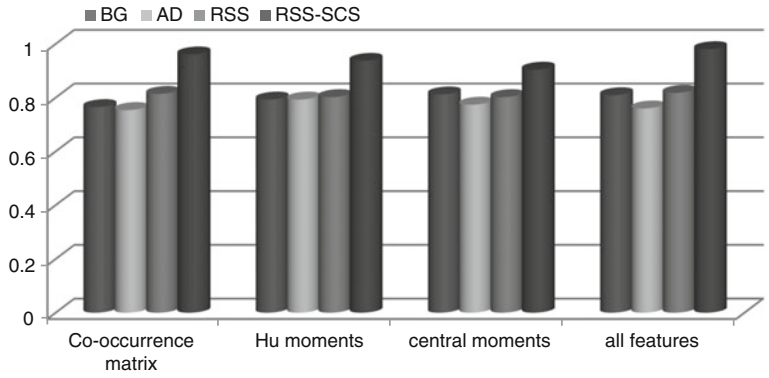

Fig. 6 Obtained results on different classifier ensembles with the three features families

The RSS-SCS method was also evaluated based on Receiver Operating Characteristic (ROC) curves [48] and the results are shown in Fig. 7. The ROC curves are usually constructed by plotting the true positive rate (sensitivity) against the false positive rate (specificity) at various threshold values. We observe that all RSS-SCS ensembles have good ROC curves because all the points of its curves are on the top half part of the ROC space.

Fig. 7 ROC curve

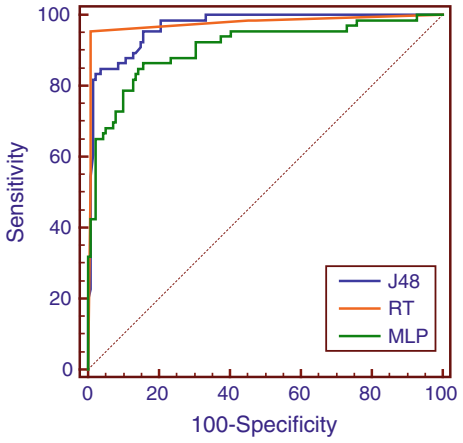

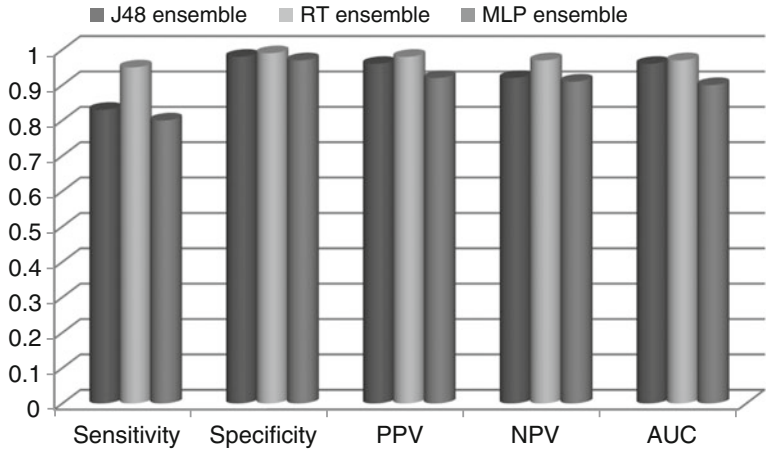

Fig. 8 Obtained results of the different metrics of the proposed system

Table 7 Obtained results of the different metrics of the proposed system using WCEC measure

	Sensitivity	Specificity	PPV	NPV	AUC
J48 ensemble	0.83	0.98	0.96	0.92	0.96
RT ensemble	*0.95*	*0.99*	*0.98*	*0.97*	0.97
MLP ensemble	0.80	0.97	0.92	0.91	0.90

Figure 8 and Table 7 summarizes the specificity, sensitivity, PPV, NPV and the AUC for the different RSS-SCS ensembles. According to the above definitions we can define five metrics [49].

Sensitivity (true positive rate) measures the probability of a positive test when the disease is present.
Specificity (true negative rate) measures the of a negative test probability when the disease is not present.
Positive Predictive Value (PPV) measures the proportion of truly positive cases among the positive cases detected by the test.
Negative Predictive Value (NPV) measures the Proportion of truly negative cases among the negative cases detected by the test.
Area Under Curve (AUC) can be interpreted as the probability of ranking a true positive example ahead of a false positive when ordering examples according to decreasing likelihood of being positive.

$$\textbf{Sensitivity} = \frac{\mathrm{TP}}{\mathrm{TP} + \mathrm{FN}} \tag{11}$$

$$\textbf{Specificity} = \frac{\text{TN}}{\text{TN} + \text{FP}} \tag{12}$$

$$\textbf{PPV} = \frac{\text{TP}}{\text{TP} + \text{FP}} \tag{13}$$

$$\textbf{NPV} = \frac{\text{TN}}{\text{TN} + \text{FN}} \tag{14}$$

5 Discussion

Glaucoma detection is a field of research that has received a lot of attention in the recent decades. Various kinds of techniques have been conducted for improving classification accuracy. In this section we presented the related work done in the area of glaucoma diagnosis by other researchers. Table 8 presents the summary of the automated glaucoma detection studies.

A new automated glaucoma diagnosis system was proposed using a combination of Higher Order Spectra (HOS) and Discrete Wavelet Transform (DWT) features extracted from the digital fundus images [50]. The proposed approach using SVM classifier (with Polynomial kernel order 2) was able to detect the normal and abnormal glaucoma classes with an accuracy of 95 %. Noronha et al. [51] proposed a novel non linear method using 3rd order HOS cumulants extracted from Radon transform (RT) applied on digital fundus images. The 3rd order HOS cumulant features are submitted to linear discriminant analysis (LDA) to minimize the number of characteristic. The proposed technique can detect the mild disease stage with an average accuracy of 92.65 % using Naive Bayes classifier.

Nyul [52] proposed automated glaucoma detection using fundus image features. Firstly, variations, such as non-uniform illumination, size differences, and blood vessels were removed from the images. Then, PCA was applied on the combined characteristics (B-Spline coefficients, Pixel intensities and FFT coefficients). PCA is applied on the decomposed coefficients to improve the spatial resolution and reduce the redundancy [53, 54]. These PCA coefficients combined with classifier were achieve an accuracy of 80 % for detecting glaucomatous retinal fundus images.

A random forest classifier was used to diagnose the fundus images using HOS and texture features which reported an accuracy of 91 % [55]. The wavelet extracted from different groups of wavelet filters were displayed to various feature ranking and feature selection schemes. Haralick features have been used to differentiate between normal and abnormal glaucoma affected retina. Extracted features have been used to train the back propagation neural network [40]. Classification of glaucoma eye disease is successfully achieved an accuracy of 96 %.

Divers morphological features of ONH of fundus image were used to design the artificial neural network which was able to classify the normal and glaucoma images with a sensitivity 100 % and specificity 80 % [56]. Classification of normal,

Table 8 Summary of studies that present various approaches to glaucoma detection

Authors	Features	No. of classes	No. of images	Classifier used	Sn (%)	Sp (%)	Acc (%)
Mookiah et al. [50]	HOS and wavelet	Two (normal/glaucoma)	60	SVM	93.33	96.67	95
Noronha et al. [51]	HOS cumulants	Three (normal/mild/severe)	272	NB	100	92	92.65
Nyul [52]	PCA on pixel intensities, FFT and spline	Two (normal/glaucoma)	200	SVM	NA	NA	80
Acharya et al. [55]	HOS and texture	Two (normal/glaucoma)	60	Random-forest	NA	NA	91
Samanta et al. [40]	texture	Two (normal/glaucoma)	321	BPN	99.51	90.43	96
Nayak et al. [56]	Cup to disk ratio, distance between OD center and ONH, and ISNT ratio	Two (normal/glaucoma)	61	ANN	100	80	NA
Nagarajan et al. [57]	MVEP	Two (normal/glaucoma)	399	ANN	95	94	94
Kolář and Jan [58]	Fractal and power spectral features	Two (normal/glaucoma)	30	SVM	NA	NA	74
Our method		Two (normal/glaucoma)	207	MCS	95	99	98.07

mild glaucoma and moderate/severe glaucoma fundus images is the novelty of this paper [57] using higher order cumulant features with a sensitivity of 100 %. Using artificial neural network (ANN) model glaucoma and M-VEP (multifocal-visual evoked potential) data was detected with 95 % sensitivity and 94 % specificity.

Kolar and Jan used texture analysis and SVM classifier to distinguish normal images from fundus images [58]. Power spectral and fractal features are used to extract the texture and reported a classification accuracy of 74 %.

In the present work, we have reported a classification average accuracy 98.07 % sensitivity of 95 % and specificity of 99 % using 207 fundus images. This current study shows that our integrated index (Table 8) is a highly effective and accurate tool to classify images taken from patients with glaucoma and normal participants.

6 Conclusion

Prolonged glaucoma may cause irretrievable damage to the retina resulting in permanent blindness. The early detection of glaucoma eye disease may prevent the vision loss. Regular screenings of eye will facilitate to diagnose and treat glaucoma. In this work, we developed an automatic glaucoma diagnosis system based on the features extracted from retinal images using three families of characteristics. Our proposed system using new multiple classifier systems is able to detect the glaucoma and normal classes with an accuracy of 98.07 %, sensitivity of 95 % and specificity of 99 % with ten-fold cross validation. This learning paradigm is becoming an effective concept to get a great performance and it is suitable for applications requiring high accuracy classification.

References

1. Lim, T., Chattopadhyay, S., Acharya, U.R.: A survey and comparative study on the instruments for glaucoma detection. Med. Eng. Phys. **34**, 129–139 (2012)
2. Quigley, H.A., Broman, A.T.: The number of people with glaucoma worldwide in 2010 and 2020. Br. J. Ophthalmol. **90**(3), 262–267 (2006)
3. Lin, S.C., Singh, K., Jampel, H.D., Hodapp, E.A., Smith, S.D., Francis, B.A., Minckler, D.S.: Optic nerve head and retinal nerve fiber layer analysis: a report by the American Academy of Ophthalmology. Ophthalmology **114**(10), 1937–1949 (2007)
4. Srivastava, A., Raj, A., Bhateja, V.: Combination of wavelet transform and morphological filtering for enhancement of magnetic resonance images. In: Digital Information Processing and Communications, pp. 460–474. Springer, Heidelberg (2011)
5. Gupta, A., Ganguly, A., Bhateja, V.: A noise robust edge detector for color images using hilbert transform. In: 2013 IEEE 3rd International Advance Computing Conference (IACC), pp. 1207–1212. IEEE (2013)
6. Haralick, R.M.: Statistical and structural approaches to texture. Proc. IEEE **67**(5), 786–804 (1979)

7. Sharma, N., Ray, A.K., Sharma, S., Shukla, K.K., Pradhan, S., Aggarwal, L.M.: Segmentation and classification of medical images using texture-primitive features: Application of BAM-type artificial neural network. J. Med. Phys./Assoc. Med. Physicists India **33**(3), 119 (2008)
8. Oza, N.C., Tumer, K.: Classifier ensembles: Select real-world applications. Inf. Fusion **9**(1), 4–20 (2008)
9. Rokach, L.: Taxonomy for characterizing ensemble methods in classification tasks: a review and annotated bibliography. Comput. Stat. Data Anal. **53**(12), 4046–4072 (2009)
10. Kuncheva, L.: Combining pattern classifiers. Wiley, New York (2005)
11. Kittler, J., Hatef, M., Duin, R.P., Matas, J.: On combining classifiers. IEEE Trans. Pattern Anal. Mach. Intell. **20**(3), 226–239 (1998)
12. Ruta, D., Gabrys, B.: Classifier selection for majority voting. Inf. Fusion **6**(1), 63–81 (2005)
13. Hassanien, A.E., Moftah, H.M., Azar, A.T., Shoman, M.: MRI breast cancer diagnosis hybrid approach using adaptive ant-based segmentation and multilayer perceptron neural networks classifier. Appl. Soft Comput. **14**, 62–71 (2014)
14. Hassanien, A.E.: Classification and feature selection of breast cancer data based on decision tree algorithm. Int. J. Stud. Inform. Control J. SI **12**(1), 33–39 (2003)
15. Breiman, L.: Bagging predictors. Mach. Learn. **26**(2), 123–140 (1996)
16. Freund, Y., Schapire, R.: Experiments with a new boosting algorithm. In: Machine Learning: Proceedings of the Thirteenth International Conference, pp. 148–156 (1996)
17. Ho, T.K.: The random subspace method for constructing decision forests. IEEE Trans. Pattern Anal. Mach. Intell. **20**(8), 832–844 (1998)
18. De Paula Canuto, A.M.: Combining neural networks and fuzzy logic for applications in character recognition. Doctoral dissertation, University of Kent at Canterbury (2001)
19. Modi, P.J., Kim, P.W.T.: Classification of examples by multiple agents with private features. In: IEEE/WIC/ACM International Conference on Intelligent Agent Technology, pp. 223–229. IEEE (2005)
20. Ko, A.H.R., Sabourin, R.: Single Classifier-based Multiple Classification Scheme for weak classifiers: an experimental comparison. Expert Syst. Appl. **40**(9), 3606–3622 (2013)
21. Zouari, H., Heutte, L., Lecourtier, Y.: Controlling the diversity in classifier ensembles through a measure of agreement. Pattern Recogn. **38**(11), 2195–2199 (2005)
22. Maclin, R., Shavlik, J.W.: Combining the predictions of multiple classifiers: using competitive learning to initialize neural networks. IJCAI 524–531 (1995)
23. Yamaguchi, T., Mackin, K.J., Nunohiro, E., Park, J.G., Hara, K., Matsushita, K., Yamasaki, K.: Artificial neural network ensemble-based land-cover classifiers using MODIS data. Artif. Life Robot. **13**(2), 570–574 (2009)
24. Aksela, M.: Comparison of classifier selection methods for improving committee performance. In: Multiple Classifier Systems, pp. 84–93. Springer, Heidelberg (2003)
25. Valentini, G.: An experimental bias-variance analysis of SVM ensembles based on resampling techniques. IEEE Trans. Syst. Man Cybern. Part B: Cybern. **35**(6), 1252–1271 (2005)
26. Santana, A., Soares, R.G., Canuto, A.M., de Souto, M.C.: A dynamic classifier selection method to build ensembles using accuracy and diversity. In: Ninth Brazilian Symposium on Neural Networks, 2006. SBRN'06, pp. 36–41. IEEE (2006)
27. Sharkey, A., Sharkey, N.: Diversity, selection, and ensembles of artificial neural nets. Neural Netw. Appl. (NEURAP'97) 205–212 (1997)
28. Banfield, R.E., Hall, L.O., Bowyer, K.W., Kegelmeyer, W.P.: A new ensemble diversity measure applied to thinning ensembles. In: Multiple Classifier Systems, pp. 306–316. Springer, Heidelberg (2003)
29. Giacinto, G., Roli, F.: An approach to the automatic design of multiple classifier systems. Pattern Recogn. Lett. **22**(1), 25–33 (2001)
30. Lazarevic, A., Obradovic, Z.: Effective pruning of neural network classifier ensembles. In: International Joint Conference on Neural Networks, 2001. Proceedings. IJCNN'01, vol. 2, pp. 796–801. IEEE (2001)

31. Marginenatu, D., Dietterich, T.: Prununig adaptive boosting. In: Proceedings of the 14th International Conference on Machine Learning, pp. 378–387 (1997)
32. Azween, A., Kausar, N., Dey, N.: Ensemble clustering algorithm with supervised classification of clinical data for early diagnosis of coronary artery disease. J. Med. Imaging Health Inform. (2014)
33. Mitchell, T.: Machine Learning. McGraw-hill (1997)
34. Fumero, F., Alayón, S., Sanchez, J.L., Sigut, J., Gonzalez-Hernandez, M.: RIM-ONE: an open retinal image database for optic nerve evaluation. In: 2011 24th International Symposium on Computer-Based Medical Systems (CBMS), pp. 1–6. IEEE (2011)
35. Žunić, D., Žunić, J.: Shape ellipticity from Hu moment invariants. Appl. Math. Comput. **226**, 406–414 (2014)
36. Zhang, L., Xiang, F., Pu, J., Zhang, Z.: Application of improved HU moments in object recognition. In: 2012 IEEE International Conference on Automation and Logistics (ICAL), pp. 554–558. IEEE (2012)
37. Huang, Z., Leng, J.: Analysis of Hu's moment invariants on image scaling and rotation. In: 2010 2nd International Conference on Computer Engineering and Technology (ICCET), vol. 7, pp. V7–476. IEEE (2010)
38. Hu, M.K.: Visual pattern recognition by moment invariants. IRE Trans. Inf. Theory **8**(2), 179–187 (1962)
39. Haralick, R.M., Shanmugam, K., Dinstein, I.H.: Textural features for image classification. IEEE Trans. Syst. Man Cybern. **6**, 610–621 (1973)
40. Samanta, S., Ahmed, S.S., Salem, M.A.M.M., Nath, S.S., Dey, N., Chowdhury, S.S.: Haralick features based automated glaucoma classification using back propagation neural network. In: Proceedings of the 3rd International Conference on Frontiers of Intelligent Computing: Theory and Applications (FICTA) 2014, pp. 351–358 (2015)
41. Yuan, F.: A double mapping framework for extraction of shape-invariant features based on multi-scale partitions with AdaBoost for video smoke detection. Pattern Recogn. **45**(12), 4326–4336 (2012)
42. Zhang, B., Pham, T.D.: Phenotype recognition with combined features and random subspace classifier ensemble. BMC Bioinform. **12**(1), 128 (2011)
43. Armano, G., Chira, C., Hatami, N.: A new gene selection method based on random subspace ensemble for microarray cancer classification. In: Pattern Recognition in Bioinformatics, pp. 191–201. Springer, Heidelberg (2011)
44. Chawla, N.V., Bowyer, K.W.: Random subspaces and subsampling for 2-d face recognition. In: IEEE Computer Society Conference on Computer Vision and Pattern Recognition, 2005. CVPR 2005, vol. 2, pp. 582–589. IEEE (2005
45. Kapp, M.N., Sabourin, R., Maupin, P.: An empirical study on diversity measures and margin theory for ensembles of classifiers. In: 2007 10th International Conference on Information Fusion, pp. 1–8. IEEE (2007)
46. Partridge, D., Krzanowski, W.: Distinct failure diversity in multiversion software. Res. Rep. **348**, 24 (1997)
47. Lin, W.Y., Hu, Y.H., Tsai, C.F.: Machine learning in financial crisis prediction: a survey. IEEE Trans. Syst. Man Cybern. Part C: Appl. Rev. **42**(4), 421–436 (2012)
48. Bradley, A.P.: The use of the area under the roc curve in the evaluation of machine learning algorithms. Pattern Recogn. **30**(7), 1145–1159 (1997)
49. Dey, N., Roy, A.B., Pal, M., Das, A.: FCM based blood vessel segmentation method for retinal images (2012). arXiv:1209.1181
50. Mookiah, M.R.K., Acharya, U.R., Lim, C.M., Petznick, A., Suri, J.S.: Data mining technique for automated diagnosis of glaucoma using higher order spectra and wavelet energy features. Knowl.-Based Syst. **33**, 73–82 (2012)
51. Noronha, K.P., Acharya, U.R., Nayak, K.P., Martis, R.J., Bhandary, S.V.: Automated classification of glaucoma stages using higher order cumulant features. Biomed. Signal Process. Control **10**, 174–183 (2014)

52. Nyúl, L.G.: Retinal image analysis for automated glaucoma risk evaluation. In: Sixth International Symposium on Multispectral Image Processing and Pattern Recognition, pp. 74971C–74971C. International Society for Optics and Photonics (2009)
53. Krishn, A., et al.: Medical image fusion using combination of PCA and wavelet analysis. In: Proceedings of 3rd (IEEE) International Conference on Advances in Computing, Communications and Informatics, pp. 986–991 (2014)
54. Himanshi, et al.: An improved medical image fusion approach using PCA and complex wavelets. In: Proceedings of (IEEE) International Conference on Medical Imaging, m-Health and Emerging Communication Systems, pp. 442–447 (2014)
55. Acharya, U.R., Dua, S., Du, X., Vinitha Sree, S., Chua, C.K.: Automated diagnosis of glaucoma using texture and higher order spectra features. IEEE Trans. Inf. Technol. Biomed. **15**(3), 449–455 (2011)
56. Nayak, J., Acharya, R., Bhat, P.S., Shetty, N., Lim, T.C.: Automated diagnosis of glaucoma using digital fundus images. J. Med. Syst. **33**(5), 337–346 (2009)
57. Nagarajan, R., Balachandran, C., Gunaratnam, D., Klistorner, A., Graham, S.: Neural network model for early detection of glaucoma using multi-focal visual evoked potential (M-Vep). Invest. Ophthalmol. Vis. Sci. **43**(13), 3902–3902 (2002)
58. Kolář, R., Jan, J.: Detection of glaucomatous eye via color fundus images using fractal dimensions. Radioengineering **17**(3), 109–114 (2008)

Motor Imagery Classification Based on Variable Precision Multigranulation Rough Set and Game Theoretic Rough Set

K. Renuga Devi and H. Hannah Inbarani

Abstract In this work classification of motor imagery BCI based on Variable Precision Multigranulation Rough Set and Game theoretic Rough Set is proposed. The efficient classification of motor imagery movements of patients can lead to accurate design of Brain Computer Interface (BCI). Data set are collected from BCI Competition III dataset 3a and BCI competition IV data set I. During acquisition there are several noises that affect classification of Electroencephalogram (EEG) Signal, so pre-processing is carried out with Chebyshev type1 filter between 4–40 Hz in order to remove the noises that may exist in signal. The Daubechies wavelet is used for extraction of features from EEG Signal. Variable Precision Multigranulation Rough Set is applied for classification of EEG Signal. Game theoretic Rough set is applied to determine best combination of α and β are based on accuracy of Variable Precision Multigranulation Rough Set. An experimental result depicts higher accuracy with Variable Precision Multigranulation Rough Set and Game Theoretic rough set compared to existing technique.

Keywords Chebyshev type 1 filter · Daubechies wavelet · Variable precision multigranulation rough set · Game theoretic rough set

1 Introduction

A Brain-Computer Interface (BCI) provides a functional interaction between the human brain and the external device [1]. A Brain-Computer Interface (BCI) helps to move artificial hand, leg, wheel chair based on motor imagery brain signals of subject [2–4]. The subject sends the signal through BCI can be considered as being the only way of communication for people affected by motor disabilities [5–7].

K.R. Devi (✉) · H.H. Inbarani (✉)
Department of Computer Science, Periyar University, Salem, India
e-mail: renuga.star@yahoo.co.in

H.H. Inbarani
e-mail: hhinba@gmail.com

N. Dey et al. (eds.), *Medical Imaging in Clinical Applications*,
Studies in Computational Intelligence 651, DOI 10.1007/978-3-319-33793-7_7

Motor imagery involves imagination of various body parts which modulates sensorimotor oscillation resulting in sensorimotor cortex activation in Electroencephalogram (EEG) [8]. The frequency of the sensorimotor rhythm is in the range of 13–15 Hz. Event Related Desynchronization (ERD) is a temporary decrease in power of the mu (8–13 Hz) and beta (13–50 Hz) brain waves [1, 6, 7]. When a subject performs or imagines movement, ERD can be recorded using Electroencephalography. Event Related Synchronization (ERS) which is an increase in power in the mu and beta bands that occurs when the subject stops imagining a movement [1, 9–12]. Contralateral hemisphere is the hemisphere on the side of the body opposite to the limb for which the motor imagery task is executed, whereas ipsilateral hemisphere on the same side of the body [1, 13, 14]. If the subject imagines a movement with his or her right hand, event-related desynchronization and synchronization occurs mostly in the left hemisphere. Similarly, if the subject imagines a movement with his or her left hand, the ERD/ERS occurs mostly in the right hemisphere. Larger areas of motor cortex are affected during Feet and arms movements so it is difficult to separate them [1, 15, 16]. The application of BCI are helping paralyzed [4], video games and virtual reality [8], creative expression [9, 17], neural prosthetics [18], wheelchairs [18], access to the internet [18] etc.

An efficient algorithm for classifying different user commands is an important part of a brain-computer interface. The goal of this paper is to classify different motor imagery tasks, left hand, right hand, both feet, or tongue. Recently, rough set theory is a technique was used for the data reduction data reduction, discovery of data dependencies, rule induction from databases and approximate set classification [19–21]. Rough-set data analysis avoids prior model assumptions such as probabilistic distribution, membership function used in fuzzy sets theory, and basic probability assignment in Dempster–Shafer theory of evidence and uses only internal knowledge, and does not depend on external parameters [19]. Rough Set can result in information loss, extensions of Rough set such as Variable Precision Rough set, Multigranulation Rough set, Game Theoretic Rough Set can handle real-valued domains [20]. Variable precision multigranulation rough set (VPMGRS) is an extension to Rough set with flexible classification of uncertain objects needs only slight modifications of the original Variable Precision Rough Set (VPRS) model [22]. Variable precision multigranulation rough set (VPMGRS) is applied to Motor imagery dataset collected from BCI Competition website. In VPMGRS thresholds values α, β are determined with game theoretic rough set. Classification accuracy is evaluated and compared with existing techniques. Section 2 discusses related work, Sect. 3 discusses the preliminaries, Sect. 4 depicts proposed algorithm, Sect. 5 depicts results and discussion and Sect. 6 concludes the proposed work.

2 Related Work

Duan et al. [16] presents an approach to classify BCI Competition 2003 dataset Ia. To eliminate redundancy and extract high-dimensional EEG signals Principle Component Analysis (PCA) and Linear Discriminant Analysis (LDA) are used. LDA after PDA shows an accuracy of 88.89.

Velásquez-Martínez et al. [15] applied Common Spatial Pattern for preprocessing and eigen decomposition method to identify main features to discriminate EEG Signals in Motor Imagery dataset. The proposed method obtained average accuracy of about 95.21 ± 4.21.

Nicolas-Alonso et al. [7] proposed adaptive classification framework for BCI Competition IV dataset 2a to address non-stationary in EEG classification. It is based on Filter Bank Common Spatial Pattern and comprises following stages. Multiple bandpass filtering using Finite Impulse response filters, spatial filtering using common spatial pattern algorithm. The results yields a significantly higher mean kappa of 0.62 compared to 0.58 from the baseline probabilistic generative model without adaptive processing.

Ang et al. [23] proposed three approaches of multi-class extension to the FBCSP algorithm on Dataset 2a, namely, Divide-and-Conquer (DC), Pair-Wise (PW), and One Versus-Rest (OVR).Feature selection algorithms the Mutual Information-based Best Individual Feature (MIBIF) and Mutual Information-based Rough Set Reduction (MIRSR) are used to select discriminative CSP features. Filter Bank Common Spatial Pattern (FBCSP) algorithm is used to optimize the subject-specific frequency band for CSP on Datasets 2a and 2b of the Brain-Computer Interface (BCI) Competition IV. The FBCSP algorithm yielded a 10×10-fold cross-validation classification accuracy of 90.3.

Rodríguez-Bermúdez et al. [17] proposed fast adaptive BCI system for feature extraction and classification of EEG Signal. Power spectral density, Hjorth parameters and autoregressive modeling are used for feature extraction. The most relevant features for linear discrimination are selected using a fast and robust wrapper methodology. The proposed method is evaluated using EEG signals from nine subjects during motor imagery tasks and experimental results show its advantages over the state-of-the-art methods, especially in terms of classification accuracy and computational cost.

Zhou et al. [24] applied improved support vector machine for classifying Graz BCI Competition 2003 dataset. EEG signals with Daubechies order 4 (db4) wavelets in 10 and 21 Hz at C3 channel, and in 10 and 20 Hz at C4 channel, for these frequencies are prominent in discrimination of left and right motor imagery tasks according to EEG frequency spectral. Classification error rate of the presented approach was as low as 9.29 %.

3 Preliminaries

The Proposed Methodology involves acquisition of EEG Signal from BCI Competition III website http://www.bbci.de/competition/iii/ and BCI Competition IV website http://www.bbci.de/competition/iv/. The acquired EEG Signal has noises with in it and needs to be preprocessed before proceeding to feature extraction and classification. Features are extracted with Daubechies wavelet, since it contains both time and frequency information in it. Extracted features are classified with variable precision multigranulation rough set and compared with existing approaches. Figure 1 depicts proposed methodology of motor imagery classification.

3.1 Daubechies Wavelet

Discrete Wavelet Transform (DWT) invented by Mallat in 1998 shows that it can be viewed as a multi-resolution decomposition of signal [25]. DWT provides sufficient information both for analysis and synthesis of signal with significant reduction in computation time. While Continuous Wavelet Transform (CWT) wavelet series is a sampled version of CWT provides highly redundant information DWT decomposes the signal into its components in different frequency bands [26]. A wavelet transform is multi-resolution analysis as it gives localization in both space and frequency domains [27]. DWT using filter bank decomposes input signal into high and low frequency component. It decomposes signal into several frequency band. Wavelet transformation involves convolution of ψ (t) with signal x (t) mother wavelet function [28].

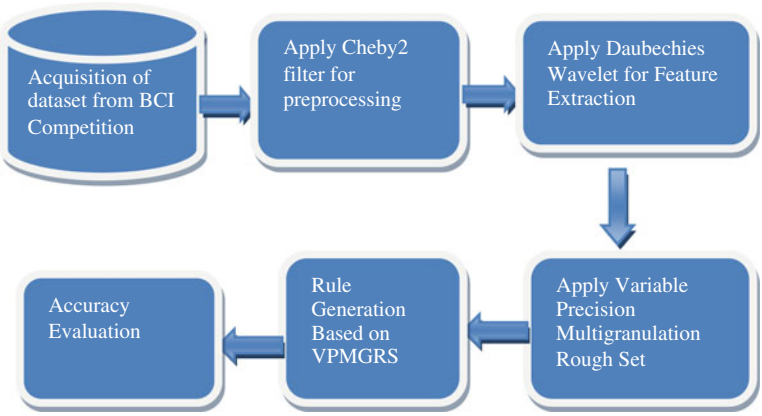

Fig. 1 Proposed methodology of motor imagery classification

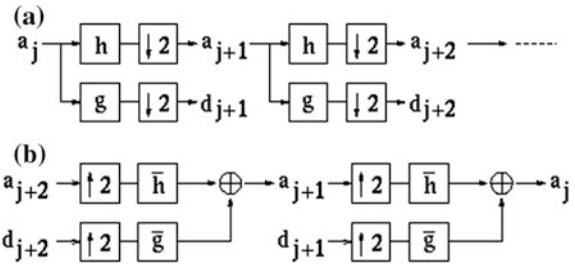

Fig. 2 **a** Decomposition. **b** Reconstruction

$$\gamma(s,\tau) = \int f(t)\Psi^{*}_{s,t}(t)dt \tag{1}$$

$$f(t) = \iint \gamma(s,\tau)\Psi_{s,t}(t)d\tau ds \tag{2}$$

$$\Psi_{s,t}(t) = \frac{1}{\sqrt{s}}\Psi\left(\frac{t-\tau}{s}\right) \tag{3}$$

where, $\Psi_{s,t}(t)$-wavelet with scale s and time t [29], τ-Shift in time, s-change in scale, $\frac{1}{\sqrt{s}}$ is used for normalization. The original signal approximation at scale index is the combination of approximation and detail signal at the next lower scale [29, 30]. Figure 2 shows decomposition and reconstruction of signal

$$a_{j+1}(p) = \sum_{n} h(n-2p)a_j(n) \tag{4}$$

$$d_{j+1}(p) = \sum_{n} g(n-2p)a_j(n) \tag{5}$$

where the set of numbers represents $a_j(n)$ the approximation of the signal at the resolution 2^{-j} and the set of numbers d_j (n) represents the details in approximating the signal at resolution 2^{-j-1}. This is referred to as multi-resolution analysis of a signal using wavelet transform

$$\phi(x/2) = 2^{1/2}\sum_{n} h(n)\phi(x-n) \tag{6}$$

$$\Psi(x/2) = 2^{1/2}\sum_{n} g(n)\phi(x-n) \tag{7}$$

Discrete Wavelet Transform is used in this work, to decompose the signal through low-pass and high-pass filtering into low and high frequency proportion of the signal [17, 24, 31]. In real life problem, DWT is more suitable in area of biomedical applications. DWT determination examines the signal with different resolutions at

different frequency bands by decomposing the signal into detailed coefficients (cD) and Approximation coefficients (cA) [32]. In short, wavelet transform analysis of time domain at high frequency and frequency domain at low frequency [30]. Wavelet algorithm provides a way of representing a time frequency information [31]. It also transforms the Electroencephalograph (EEG) signal to allow further extraction and classification because EEG signals are non-stationary [17].

An Electroencephalograph signal can be classified into orthogonal, symmetry, compact support, and non-stationary signals, but these signals can be further classified according to their characteristics and properties. The wavelet must be suitable for analyzing EEG signal to give a better reconstruction with fewer decomposition levels.

An orthogonal signal is important because it conserves the energy of the signal throughout the wavelet transform so that no information will be lost [25, 33]. It allows wavelet transformation that can extract high and low frequency details. because its wavelets are smoother and can enhance the illustration of transients in the signal. Besides that, EEG signals that contain the features information such compact support also allows the wavelet transform to efficiently characterize [23, 25, 33]. Wavelet families such as Haar, Daubechies, Symlets, and Coiflets have sufficient properties to analyze signal. The Haar wavelet is comprised of a Daubechies order of 1 (db1). Reconstruction coefficient number that had to be more than two, So Haar wavelet was not selected. The Morlet and Mexican Hat wavelet are not selected because they are not suitable for biomedical signal processing [25].

Morlet (mor1) wavelet has no scaling function but is explicit. Mexican Hat (mexh) wavelet has no scaling function and is derived from a function that is proportional to the second derivative function of Gaussian. Meyer (meyr) Scaling function is defined in the frequency domain. Haar (haar) Discontinuous and resembles a step function. Haar represent as Daubechies db1. Symlets (symN) wavelet is modification to the db family. Coiflets (coifN) built by Ingrid Daubechies that has 2N moments. Splines biorthogonal wavelets (biorNr.Nd) wavelet needed two wavelets for signal and image reconstruction. So Daubechies wavelet is chosen because of the smoothing features, without losing any information, the down-sampling of a time domain signal can be divided into low and high filtering [25]. Down-sampling occurs when the original signal x(n), passes through a high-pass filter, g(n), (detail coefficient) and then a low-pass filter, h(n) (approximation coefficient) [25].

3.2 Variable Precision Rough Set

Rough Set model proposed by pawlak can be extended to characterize a set in terms of uncertain information under some levels of certainty [19]. Variable Precision Rough Set (VPRS) is useful for addressing problems where data sets have lots of boundary objects. Variable Precision Rough Set (VPRS) has the additional desirable property of allowing for partial classification instead of complete classification

required by Rough Set (RST) [20]. When an object is classified using Rough set it involves complete certainty that is it goes for a correct classification [21, 34–36]. VPRS has a degree of confidence for detailed analysis of the data in classification, which is achieved through the use of a majority inclusion relation. The measure c (X, Y) of the *relative degree of misclassification* (8) of the set X with respect to set Y defined as

$$\begin{aligned} c(X,Y) &= 1 - |X \cap Y|/|X| \; if \; |X| > 0 \\ or\, c(X,Y) &= 0 \; if \; |X| = 0 \end{aligned} \tag{8}$$

The *majority inclusion relation* (9) under an admissible classification error β (which must be within the range $0 \leq \beta \leq 0.5$ is defined as

$$X \subseteq \beta \quad Y \Leftrightarrow C(X,Y) \leq \beta \tag{9}$$

Let I = (U, A) be an information system, where U is a non-empty, finite set of objects and A is a non-empty, finite set of attributes such that $a : U \rightarrow Va$ for every $a \in A$ [22]. Va is the set of values that attribute a might hold [37]. The information system assigns a value a(x) from Va to each attribute a and object x in the universe U. With any $R \subseteq A$ there is an associated equivalence relation [22, 37]

$$\mathrm{IND(R)} = \{(x, y) \in U2 | \forall a \in R, a(x) = a(y)\} \tag{10}$$

The relation IND(R) is called a *R-indiscernibility relation* (10). The partition of U is a family of all equivalence classes of IND(R) and is denoted by U/IND(R) [37–39].

Let $X \subseteq U$ using equivalence classes induced with attribute subset R By replacing the inclusion relation with majority inclusion relation in the original definition of lower approximation and upper approximation, the generalized notion of *β-lower approximation* (11) and *β-upper approximation* (12)

$$\underline{R}_\beta X = \cup \left\{ [x]_R \in \cup / R : [x]_R \subseteq_\beta X \right\} \tag{11}$$

$$\overline{R}_\beta X = \cup \left\{ [x]_R \in \cup / R : [x]_R \subseteq_{1-\beta} X \right\} \tag{12}$$

The *β-positive region* (13), *β-negative region* (14) and *β-Boundary region* (15) are defined based on upper and lower approximation [40].

$$POS_{R,\beta}(X) = \underline{R}_\beta X \tag{13}$$

$$NEG_{R,\beta}(X) = U - \underline{R}_\beta X \tag{14}$$

$$BN_{R,\beta}(X) = \overline{R}_\beta X - \underline{R}_\beta X \tag{15}$$

The quality of the classification is defined as the proportion of cardinality of positive regions of all the equivalence classes of decision based on the equivalence

classes for a subset P of the condition attributes C [37]. The quality of classification is dependent on the β min value associated with all the condition attributes [37–39].

3.3 Multigranulation Rough Set

The Multigranulation Rough Set (MGRS) is formulated on the basis of a family of binary relations instead of a single indiscernibility relation, where the set approximations are defined by using multi equivalence relations on the universe [41]. A concept of approximation reduct is introduced to describe the smallest attribute subset that preserves the upper approximation and lower approximation of all decision classes in MGRS [41, 42]. The form of decision rules in MGRS is "OR" unlike the "AND" rules from classical rough set model.

In classical Rough set, upper and lower approximations are defined under a single granulation, i.e., the concept is induced from a single relation (such as equivalence relation, reflexive relation and tolerance relation) on the universe. Let us assume P and Q are two sets from predictor features and $X \subseteq U$ is a desired target approach, then the rough set of X is derived from the quotient set U/(PUQ) [41]. The *quotient set* (16) is equivalent to the formula

$$P \cup Q = \{P_i \cap Q_j : P_i \in \cup/P,\ Q_j \in \cup/Q,\ P_i \cap P_j \neq 0\} \tag{16}$$

The above assumption cannot always be satisfied in following cases. In some data analysis issues, for the same object, there is a inconsistent relationship between its values under one attribute set P and those under another attribute set Q [21, 22, 41]. In other words, we cannot perform the intersection operations between their quotient sets and the target concept and cannot be approximated by using U/(PUQ). The decision makers may have independent view for the same project in the universe [21, 22, 41]. In this situation, the intersection operations of one quotient set will be redundant with another quotient set for decision making. The time complexity of rule extractions can be reduced, by not performing the intersection operations in all the sites of distributive information systems. In this approach two models are defined they are optimistic multigranulation rough set and pessimistic multigranulation rough set [22].

Let S = {U, A, V, f} is an information system where U represents universe contains non-empty and finite set of objects and A represents non-empty and finite set of attributes, Va is the domain of the attribute a, V = S a ∈ A Va and f: U × A → V is a function f(x, a) ∈ Va for each a ∈ A. $X \subseteq U$ and $P = \{P_i \subseteq A | P_i \cap P_j = \phi(i \neq j),\ i,j \leq l\}$ [22, 41].

The optimistic lower and upper approximation sets of X with respect to P can be defined as follows [41]

$$\underline{OM}(X) = \left\{ x\varepsilon \cup |\vee([x]_{pi} \subseteq X),\ i \leq l \right\} \tag{17}$$

$$\overline{OM}(X) = \left\{ x\varepsilon \cup |\wedge([x]_{pi} \cap X \neq \phi),\ i \leq l \right\} \tag{18}$$

The pessimistic lower and upper approximation sets of X with respect to P can be defined as follows [41]

$$\underline{PM}(X) = \left\{ x\varepsilon \cup |\wedge([x]_{pi} \subseteq X), i \leq l \right\} \tag{19}$$

$$\overline{PM}(X) = \left\{ x\varepsilon \cup |\vee([x]_{pi} \cap X \neq \phi),\ i \leq l \right\} \tag{20}$$

3.4 Variable Precision Multigranulation Rough Set

Variable Precision Multigranulation Rough Set is general notions of multi-granulation rough sets model to process data with noise and it allows for a controlled degree of misclassification (8) with majority inclusion relation (9) [43]. In the variable precision multi-granulation rough set model, the requirement of accuracy on each granulation is determined by means of parameter α, β and supporting characteristic function wi^{α}, $\mu^{x}_{pi}(x)$ [13]. Let $S = (U; A)$ be an information system, U represents universe contains non-empty and finite set of objects and A is a non-empty and finite set of attributes, $X \subseteq U$ and $P = \{P_i \subseteq A | P_i \cap P_j = \phi(i \neq j),\ i,j \leq l\}$ [43]. l is the number of partitions. Then lower and upper approximation sets of X with respect to P can be defined as follows

$$\underline{VP}(x)^{\alpha}_{\beta} = \{ x\varepsilon \cup | \sum_{i=1}^{l} w^{\alpha}_{i} \mu^{x}_{pi}(x) \geq \beta \} \tag{21}$$

$$\overline{VP}(x)^{\alpha}_{\beta} = \sim \underline{P}(\sim X)^{\alpha}_{\beta} \tag{22}$$

$$wi^{\alpha} = \begin{cases} \frac{1}{7} & \alpha \leq \mu^{X}_{pi}(x) \leq l \\ 0 & \mu^{X}_{pi}(x) < \alpha \end{cases} \tag{23}$$

The parameter α determines the precision of every granulation which are used to approximate the target concept. $\sim$ denotes complementary operation of the set [43]. Let S = (U, A) be an information system, X $\subseteq$ U and $P = \{P_i \subseteq A | P_i \cap P_j = \phi(i \neq j),\ i,j \leq l\}$. If α = 1, then

$$\begin{aligned}\underline{VP}(x)_{\beta}^{1} &= \{x\,\varepsilon\,\cup\,|\sum_{i=1}^{l} w_i^1 \mu_{pi}^x(x) \geq \beta\} \\ &= \{x\,\varepsilon\,\cup\,|\sum_{i=1}^{l} \mu_{pi}^x(x) = 1^{1/l} \geq \beta\} \\ &= \underline{P}(X)_{\beta}^{1}\end{aligned} \tag{24}$$

$$\begin{aligned}\overline{VP}(x)_{\beta}^{1} &= \sim\underline{P}(\sim X)_{\beta}^{1} \\ &= \sim\{x\,\varepsilon\,\cup\,|\sum_{i=1}^{l} \mu_{pi}^x(x) = 1^{1/l} \geq \beta\} \\ &= \sim\{x\,\varepsilon\,\cup\,|\sum_{i=1}^{l} \mu_{pi}^x(x) = 1^{1/l} \geq \beta\} \\ &= \sim\{x\,\varepsilon\,\cup\,|\sum_{i=1}^{l} \mu_{pi}^x(x) = 0^{1/l} \geq \beta\} \\ &= \sim\{x\,\varepsilon\,\cup\,|\sum_{i=1}^{l} \mu_{pi}^x(x) \neq 0^{1/l} \geq \beta\} \\ &= \overline{P}(X)_{\beta}^{1}\end{aligned} \tag{25}$$

These proposed models generalize the multigranulation rough set approach, and are helpful to enhance its capability of dealing with noisy data [43].

3.5 *Game Theoretic Rough Set*

The conventional Pawlak rough set theory does not allow any errors in the positive and negative regions [44]. Researchers argued that the intolerance to errors (or) qualitative absoluteness can lead to limitations in practical applications [45]. Extensions of rough sets were introduced through some measures and thresholds to introduce error tolerance [40]. The probabilistic rough set models is an extension of rough set and include the decision-theoretic rough set model, the Bayesian rough set model, the variable precision rough set model, the information-theoretic rough set model and the game-theoretic rough set model [40, 45]. In these models, a pair of thresholds α, β is used to define the rough set approximations and the resulting three regions [44]. The determination of thresholds value is an important issues in the Variable Precision Multigranulation rough sets [40]. So Game Theoretic Rough Set is applied for determination of α, β pair.

Game theory is a mathematical structure to govern competition in games between two or more parties [44]. It can be used to analyze the classification ability based on different threshold values [44]. It is used to observe the trade-off between accuracy and

precision and the relationships between this trade-off and threshold values [44]. Each player has a strategies (set of actions) with expected payoffs (benefits) as a result of taking that action [40]. A payoff function returns a payoff value by determining the utility of a chosen action [40]. An Assumption is made that all players are rational. Rational players choose strategies (set of actions) that improve their position in the game. Rational players choose strategies (set of actions) that maximize their wining ability while minimizing the other players' ability to do the same. Games are formulated into payoff tables, indicating players involved, possible strategies, and expected payoffs. A single game is defined as G = {O, S, F} O represents a set of players, S represents set of strategies, F represents Action payoffs [40].

Algorithm Input: Dataset in the form of an Information table, Initial values of α^{-}, α^{--}, β^{+}, β^{++}

Output: Thresholds (α, β)

1. Initialize $\alpha = 1.0$, $\beta = 0$
2. Repeat
3. Calculate utilities of player based on Eqs. (26) and (27)
4. Populate the pay off table with calculated values
5. Calculate Equilibrium in a payoff table using Eqs. (28) and (29)
6. Determine Selected Strategies and corresponding Thresholds (α', β')
7. Calculate α^{-}, α^{--}, β^{+}, β^{++} based on Eqs. (30)–(33)
8. (α, β) = (α', β') Until P(BND(α, β)(C)) = 0 or P(POS(α, β)(C)) > P(C) (or) $\alpha \prec 0.5$ *or* $\beta \geq 0.5$

The goal of our work is to improve classification, therefore, each player will represent a measure to achieve a maximum value. Two players are chosen as Accuracy and Dependency. Accuracy is determined by number of objects that are correctly classified as $Pos_{(\alpha,\beta)}$ and $Neg_{(\alpha,\beta)}$. Dependency is determined by number of objects that are in Positive Region divided by total objects in universe.

$$Accuracy(\alpha, \beta) = \frac{\left|(Pos_{(\alpha,\beta)}(C) \cap C) \cup Neg_{(\alpha,\beta)}(C) \cap C^{c}\right|}{\left|Pos_{(\alpha,\beta)}(C) \cup Neg_{(\alpha,\beta)}(C)\right|} \tag{26}$$

$$Dependency(\alpha, \beta) = \frac{\left|(Pos_{(\alpha,\beta)}(C)\right|}{|U|} \tag{27}$$

C^{C} is the set complement of C, containing all objects in U that are not in C. A particular player would prefer a strategy (set of action) over another strategy (set of action) if it provides higher payoff during the game. A strategy profile (s_m, s_n) would be the game solution (or) Nash equilibrium if the following conditions holds.

$$\text{For player A} : \forall s'_m \in S_1, u_A(s_m, s_n) \geq u_A(s'_m \neq s_m) \; with \; (s'_m \neq s_m) \tag{28}$$

$$\text{For player D} : \forall s'_m \in S_1, u_D(s_m, s_n) \geq u_D(s'_m \neq s_m) \; with \; (s'_n \neq s_n) \tag{29}$$

α^- occurs when Single Player Suggest to decrease α, α^- occurs when both players suggest to decrease α, β^+ occurs when single player suggest to increase β, β^{++} occurs when both players suggest to increase β [44].

$$\alpha^{--} = \alpha - (\alpha \times \text{Accuracy}(\alpha', \beta') - \text{Accuracy}(\alpha, \beta)) \tag{30}$$

$$\alpha^{--} = \alpha - \text{C}(\alpha \times \text{Accuracy}(\alpha', \beta') - \text{Accuracy}(\alpha, \beta)) \tag{31}$$

$$\beta^{+} = \beta - (\beta \times \text{Accuracy}(\alpha', \beta') - \text{Accuracy}(\alpha, \beta)) \tag{32}$$

$$\beta^{++} = \beta - \text{c}(\beta \times \text{Accuracy}(\alpha', \beta') - \text{Accuracy}(\alpha, \beta)) \tag{33}$$

4 Proposed Methodology

4.1 Acquisition of Dataset

Motor Imagery data are collected from BCI Competition IV dataset 1. The recording was made using 59 Channel BrainAmp MR plus amplifiers and a Ag/AgCl electrode cap of 10-20 System. These data sets were recorded from healthy subjects. The dataset epoch size is about 190594 × 59 of which 200 positions are marked in training data. For each subject two classes (Hand, Foot) of motor imagery were selected where the class Hand may be either Left Hand (or) Right Hand. Signals from 59 EEG positions were measured that were most densely distributed over sensorimotor areas as shown in Fig. 2. Seven calibration data has been used for training and eight evaluation data has been used for testing. Band-pass filtered are applied for signal between 0.05 and 200 Hz and then digitized at 1000 Hz with 16 bit (0.1 μV) accuracy. Another Motor imagery data is collected from BCI Competition III dataset 3a which is Multiclass motor imagery data set. EEG amplifier 64-channel was used for recording from Neuroscan cap of 10-20 System. Sixty EEG channels were recorded. The dataset epoch size is about 986780 × 60 of which 300 positions are marked in k3b dataset and 240 position are marked in k6b and l1b dataset. Data was collected from three subjects (ranging from quite good to Fair Performance).

4.1.1 BCI Competition IV Dataset 1

Calibration data

In the first two trial runs (or) test, arrows pointing left, right, or down were presented as visual cues on a screen. Cued motor imagery task involves displaying

cues for a period of 4 s. After these periods 2 s of blank screen are displayed and then displays fixation cross in the center of the screen for period of 2 s. The fixation cross was superimposed with cues, i.e. it was displayed for 6 s. These data sets are provided to user with complete marker information.

4.1.2 BCI Competition III Dataset 3a

In BCI Competition III dataset 3a training data and test data were recorded with the same task and from the same subject, but on two different days with about 1 week in between. EEG was sampled with 250 Hz, it was filtered between 1 and 50 Hz. The task was to perform imagery left hand, right hand, foot or tongue movements according to a cue. The random cues was displayed to subject. The recording of BCI data consists of several runs (at least 6) with 40 trials each after trial begin, the first 2 s were displayed nothing, at t = 2 s an cross "+" is displayed indicating the beginning of the trial, then from t = 3 s an arrow to the left, right, up or down was shown for 1 s; at the same time the subject was asked to imagine a, tongue or foot movement, left hand, right hand, until the cross disappeared at t = 7 s.

4.2 Chebyshev Type 2 Filter for Pre-processing

EEG signals has very small amplitudes and they can be easily contaminated by noise [26, 27, 31]. The electrode noise can be generated from the body itself. Artifacts are noises in the EEG signals and need to be removed from the original signal for the analysis of the EEG signals [17, 28]. The various noises that can occur in the signals during recordings are the power line Interference, baseline movement, electrode noise, EMG disturbance and so on [24].

Chebyshev filters is Infinite Impulse Response (IIR) Filter that have steeper roll off and more pass band ripple than other filters [23]. Chebyshev filters have the property that they minimize the error between the actual and the idealized filter characteristic over the range of the filter with ripples in the pass band. Because of the passband ripple inherent in Chebyshev filters, they have a smoother response in the passband. [23, 30, 32]. They are used to separate one band of frequencies from another. It performs faster than butter worth and elliptic filter since they are carried out by recursion rather than convolution. Sensorimotor rhythm occurs in the range of mu (6.25–12.5) and beta (12.5–25) rhythm. In the BCI competition data set, since our goal is to classify sensorimotor rhythm (12.5–15.5). Passband cutoff frequency is a scalar vector with values between 0 and 1, with 1 corresponding to the normalized Nyquist frequency, π radians per sample. Hence the frequency band range is set between 4–40 Hz with cutoff frequency 0.7 Hz [30, 32].

Table 1 Decomposition level with BCI competition dataset

Decomposition levels	Frequency range
D_1 (Theta, Alpha)	4–13
D_2 (Alpha, Beta)	13–22
D_3 (Beta)	22–31
D_4 (Gamma)	31–40

4.3 Daubechies Wavelet for Feature Extraction

The Discrete Wavelet Transform is used to decompose EEG signal at resolution levels of the components of the EEG signal (Delta (δ)—0.5–3 Hz, Theta (θ)—4–7 Hz, Alpha (α)—8–13 Hz, Beta (β)—13–31 Hz and Gamma (γ)—above 31 Hz) with the Multi-Resolution Analysis (MRA) [29]. The object of wavelet analysis is to decompose signals into several frequency bands [25, 33]. Selection of appropriate wavelet and the number of decomposition levels are very important for the analysis of signals using DWT [29]. The number of decomposition levels is chosen based on the dominant frequency components of the signal.

In the wavelet coefficient, the levels are chosen such that parts of signal that correlate well with the frequencies for classification of the signal. In this work, Daubechies 4 (db4) is selected because its smoothing feature can detect changes of the EEG signal. The frequency band [fm/2 : fm] of each detail scale of the Discrete Wavelet Transform is related to the original signal sampling rate, which is given by fm = fs/2 l + 1, where fs is the sampling frequency, and l is the level of decomposition [25]. In this study, the sampling frequency is 100 Hz of the EEG signal. Nyquist theorem suggest that the highest frequency of signal would be fs/2. Among this decomposition levels D1 and D2 contains sensorimotor rhythm (12.5–15.5) which is passed as input. Frequency bands corresponding to five decomposition levels for wavelet db4 were listed in Table 1. The signals were decomposed into details D1–D4.

4.4 Classification Based on VPMGRS

Algorithm for Variable Precision multigranulation Rough set is as follows. Input are decomposed frequency bands D_1, D_2 (alpha, Beta) of EEG Signal.

Algorithm 1: Variable Precision Multigranulation Roughset An information system is a 4-tuple S = {U, A, V, f} where U is a non-empty and finite set of objects, called a universe, and A is a non-empty and finite set of attributes, Va is the domain of the attribute a, and f: $U \times A \rightarrow V$ is a function $f(x, a) \in Va$ for each $a \in A$. An

indiscernibility relation RB = {(x, y) ∈ U × U | a(x) = a(y), ∀a ∈ B} was determined by a non-empty subset B ⊆ A. Assign P_i to P. Let m represents number of elements [10, 43].

(1) $P = \{P_i \subseteq A | P_i \cap P_j = \phi(i \neq j), i, j \leq l\}$. Partition Generated with OR rules (Multigranulation Rough Set) instead of AND rules (Pawlak Rough Set) l is the number of partitions [10].

(2) Find the Supporting Characteristic Function wi^{α} and $\mu_{pi}^{X}(x)$

For i = 1:l
For j = 1:m

$\mu_{pi}^{X}(x_j)$ = Number of elements that match Decision and Subpartition/Total number of elements in subpartition

$$wt_j^{\alpha} = \begin{cases} \frac{1}{l} & \alpha \leq \mu_{pi}^{X}(x_j) \leq l \\ 0 & \mu_{pi}^{X}(x_j) < \alpha \end{cases}$$

End For

End For

(3) Then lower and upper approximation sets of X with respect to P can be defined as follows and explained in detail in Sect. 3.4

$$\underline{VP}(x)_{\beta}^{\alpha} = \{x \varepsilon \cup | \sum_{i=1}^{l} w_i^{\alpha} \mu_{pi}^{x}(x) \geq \beta\}$$
$$\overline{VP}(x)_{\beta}^{\alpha} = \sim \underline{P}(\sim X)_{\beta}^{\alpha}$$

Let us consider the Sample data

U = {x_1, x_2, x_3, x_4, x_5, x_6, x_7, x_8, x_9, x_{10}} and X denotes one of the decision variable X = {x_1, x_2, x_6, x_8, x_9} [10]

Let p1, p2 be the two partitions under consideration computed with Multigranulation Rough Set [10]

$$U/p_1 = \{\{x_1, x_7\}\{x_2, x_3, x_4, x_6, x_8, x_9\}\{x_5\}\{x_{10}\}\}$$
$$U/P_2 = \{\{x_1\}\{x_2, x_3, x_6, x_8, x_9\}\{x_4, x_5\}\{x_7\}\{x_{10}\}\}$$

Step 2

$X = \{x_1, x_2, x_6, x_8, x_9\}\, U/p_1 = \{\{x_1, x_7\}\{x_2, x_3, x_4, x_6, x_8, x_9\}\{x_5\}\{x_{10}\}\}$
$\mu_{P1}^{X}(x_1) = 0.5\, P1 = \{x1, x7\}$

Here Total Number of elements are 2
Only x1 are in X so Supporting Characteristic Function is ½ = 0.5.

$\mu^X_{P1}(x_2) = 0.6$ In P1 = {x2, x3, x4, x6, x8, x9}

Here Total Number of elements are 6

x_2, x_6, x_8, x_9 are in X so Supporting Characteristic Function is

4/6 = 0.6. Likewise all the elements supporting characteristic function for each partitions are found.

$$\begin{aligned}
\mu^X_{P1}(x_1) &= 0.5 \quad \mu^X_{P2}(x_1) = 1 \\
\mu^X_{P1}(x_2) &= 0.6 \quad \mu^X_{P2}(x_2) = 0.6 \\
\mu^X_{P1}(x_3) &= 0.6 \quad \mu^X_{P2}(x_3) = 0.6 \\
\mu^X_{P1}(x_4) &= 0.6 \quad \mu^X_{P2}(x_4) = 0 \\
\mu^X_{P1}(x_5) &= 0 \quad \mu^X_{P2}(x_5) = 0 \\
\mu^X_{P1}(x_6) &= 0.6 \quad \mu^X_{P2}(x_6) = 0.6 \\
\mu^X_{P1}(x_7) &= 0.5 \quad \mu^X_{P2}(x_7) = 0 \\
\mu^X_{P1}(x_8) &= 0.6 \quad \mu^X_{P2}(x_8) = 0.6 \\
\mu^X_{P1}(x_9) &= 0.6 \quad \mu^X_{P2}(x_9) = 0.6 \\
\mu^X_{P1}(x_{10}) &= 0 \quad \mu^X_{P2}(x_{10}) = 0
\end{aligned}$$

wi^{α} varies according to the $\mu^X_P(x_i)$ [10]. If $\mu^X_P(x_i)$ is greater than α then wi^{α} is 1/l, where l is the number of partitions. If $\mu^X_P(x_i)$ is less than α then wi^{α} is 0 [10]. When the product of wi^{α} and $\mu^X_P(x_i)$ is greater than or equal to β then it is added to lower approximation [10].

$$\begin{aligned}
\underline{VP}(x)^{0.3}_{0.3} &= \{x_1, x_2, x_3, x_4, x_6, x_8, x_9\} \\
\underline{VP}(x)^{0.6}_{0.6} &= \{x_2, x_3, x_6, x_8, x_9\} \\
\underline{VP}(x)^{0.7}_{0.3} &= \{x_1\}
\end{aligned}$$

5 Experimental Results and Discussion

In Variable precision multigranulation rough set Classification accuracy is evaluated using accuracy measures. Confusion matrix visualizes performance of the algorithm. Each column of the matrix represents the instances in a predicted class, while each row of the matrix represents the instances in an actual class. The accuracy (AC) gives total number of correct predictions. The recall or true positive rate (TP) is the proportion of correctly identified positive cases. The false positive rate (FP) is the proportion of incorrectly classified negatives cases. The true negative rate (TN) is defined as the proportion of correctly classified negatives cases that were classified correctly The false negative rate (FN) is the proportion of incorrectly classified positives cases. A confusion matrix is a visualization tool used

in supervised machine learning for classification. Instances of the predicted class and actual class are represented in each column and each row. The confusion matrix calculates the number per class of well classified and mislabeled instances and evaluate the performance of a classifier.

Cohen's kappa measures the similarity between two raters who each classify N items into C mutually exclusive categories [46, 47]. The motivation of this measure is to extract from the correctly classified percentage the actual percentage expected by chance [46, 47]. The equation is as follows

$$\kappa = \frac{P(D) - P(E)}{1 - P(E)} \tag{34}$$

where *P(D)* is the percentage of classified instances that are correct and *P(E)* is the Expected Proportion by chance [46, 47]. A κ Coefficient equals to one means perfect agreement and zero means poor agreement. In BCI Competition III Dataset IIIa contains three data with 60 channels and 4 class labels where 1 indicates Left Hand, 2 indicates Right Hand, 3 indicates Foot and 4 indicates Tongue. In BCI Competition IV Dataset I Seven Calibration data with 59 channels has been used. It contains two classes where 1 indicates Right Hand (or) Left Hand and 2 indicates Foot. The proposed methodology follows k-fold cross validation. In *k*-fold cross-validation, the original sample is randomly partitioned into k equal sized subsamples. Of the k subsamples, a single subsample is retained as the validation data for testing the model, and the remaining $k - 1$ subsamples are used as training data. The cross-validation process is then repeated k times (the *folds*), with each of the k subsamples used exactly once as the validation data. The k results from the folds can then be averaged (or otherwise combined) to produce a single estimation. The advantage of this method over repeated random sub-sampling is that all observations are used for both training and validation, and each observation is used for validation exactly once.

Thresholds α and β are determined with game theoretic rough set and assigned the constant $\alpha = 0.5$, $\beta = 0.25$. The proposed methodology has been compared with existing techniques Naïve Bayes, Multi layer Perceptron, IBk, Decision Table, Random Tree, J48. IBk is K-Nearest Neighbour Classifier where k is chosen as 2 for BCI Competition IV and k is chosen as 4 for BCI Competition III dataset. Distance weighting method Linear NN Search (Euclidean distance) method is used in IBk.

Naive Bayes Classifier is based on estimator classes. Numeric estimator precision values are chosen based on analysis of the training data. Multilayer perceptron classifier that uses backpropagation to classify instances. The network can also be monitored and modified during training time. The nodes in this network are all sigmoid (except for when the class is numeric in which case the output nodes become unthresholded linear units), Rate is assigned with value 0.3, Momentum (weight updation) is assigned with value 0.2, number of hidden layers is assigned based on formula number of attributes including class attribute divided by 2 and Validation threshold is assigned with value 20. J48 generates a pruned C4.5 decision tree where confidence factor (For Pruning) is assigned with value 0.25, MinNumObj

(Minimum number of Instances per leaf) is assigned with value 2. numFolds is assigned with value 3 and it determines the amount of data used for reduced-error pruning. One fold is used for pruning, the rest for growing the tree. seed is assigned with value 1 for randomizing the data when reduced-error pruning is used.

Table 2 Classifiication of BCI competition IV dataset 1

Method used	Calib ds1a	Calib ds1b	Calib ds1c	Calib ds1d	Calib ds1e	Calib ds1f	Calib ds1 g
	Kappa value						
Naïve bayes	0.56	0.50	0.55	0.55	0.59	0.51	0.52
Multi layer perceptron	0.57	0.54	0.62	0.61	0.65	0.67	0.68
IBk	0.58	0.58	0.69	0.69	0.79	0.62	0.63
Random tree	0.58	0.53	0.59	0.59	0.62	0.56	0.56
J48	0.58	0.52	0.58	0.59	0.58	0.57	0.57
VPMG RS	1	0.68	0.63	0.63	1	0.84	0.77

Table 3 Classification of BCI competition III data set 3a

Technique used	K3b	K6b	L1b
Naïve bayes	0.43	0.55	0.53
Multilayer perceptron	0.44	0.53	0.50
IBK	0.49	0.57	0.57
Random tree	0.46	0.46	0.50
J48	0.45	0.47	0.52
VPMGRS	1	0.74	0.74

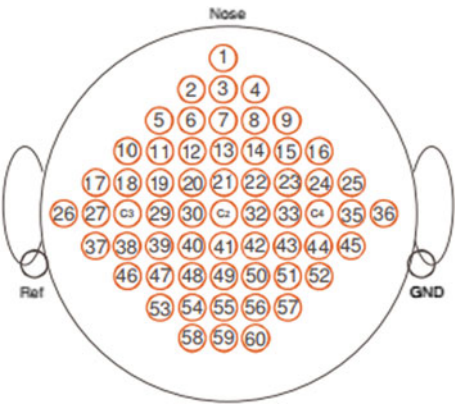

Fig. 3 EEG electrode placement for BCI competition III dataset 3a

In Random Tree Method a tree is constructed by considering K randomly chosen attributes at each node. It performs no pruning. Also has an option to allow estimation of class probabilities based on a hold-out set (backfitting). Max Depth is assigned the value 0. It determines the maximum depth of the tree, 0 for unlimited. minNum is assigned with value 1.0 It determines the minimum total weight of the instances in a leaf. numFolds is assigned with value 0. It determines the amount of data used for backfitting. One fold is used for backfitting, the rest for growing the

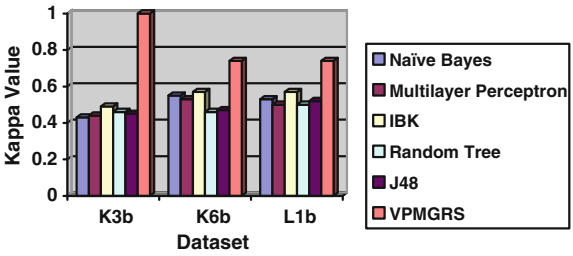

Fig. 4 Classification of BCI competition III data set 3a

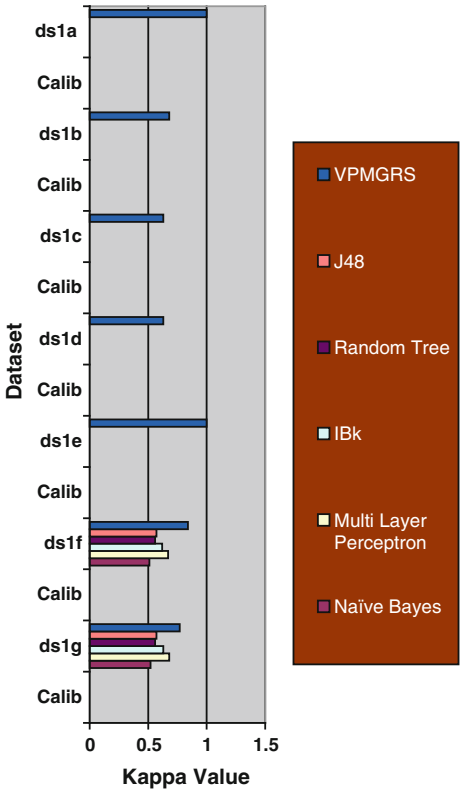

Fig. 5 Classification of BCI competition IV data set 1

tree. (Default Value: 0 denotes no backfitting). seed is assigned with value 1. The random number seed used for selecting attributes.

It is clear from Tables 2, 3 and Figs. 3, 4, 5 that the proposed methodology (VPMGRS) gives higher kappa value compared to existing methods. In Calib_ds1a, Calib_ds1e highest accuracy obtained using existing technique is about 0.58, 0.79 but proposed technique gives about 100 % accuracy. In Calib_ds1b, highest accuracy obtained using existing technique is about 0.58 but proposed technique gives 0.68. In Calib_ds1f, highest accuracy obtained using existing technique is about 0.67 but proposed technique gives 0.84. In Calib_ds1g, highest accuracy obtained using existing technique is about 0.68 but proposed technique gives 0.77. In Calib_ds1c and Calib_ds1d highest accuracy obtained using existing technique is about 0.69 but proposed technique gives 0.63 which is almost nearer to highest accuracy. In k3b dataset existing techniques gives accuracy of less than 50 % accuracy but proposed methodology gives 100 % accuracy. In k6b and L1b dataset highest Kappa obtained from existing techniques is about 0.57 but proposed methodology gives 0.74 kappa value.

6 Conclusion

Thus the BCI Competition IV dataset 1, BCI Competition III data set 3a shows higher accuracy when compared with existing techniques. BCI Competition IV dataset 1 is a two class problem (Right Hand, Foot). BCI Competition III data set 3a is a four class problem left hand, right hand, both feet, and tongue. Variable precision multigranulation rough set involves partition by multigranulation rough set and then based on partition μ values are computed and supporting characteristic function are computed based on partition. Both Supporting Characteristic Function w_i^{α}, μ, α, β values determine classification accuracy. The variation of α, β values in both BCI Competition Data set depicts higher accuracy. The flexibility to handle uncertain information in EEG data is the main advantage over state of art methods.

References

1. Frolov, A.A., Husek, D., Snasel, V., Bobrov, P., Mokienko, O., Tintera, J., Rydlo, J.: Brain-computer interface based on motor imagery: the most relevant sources of electrical brain activity. In: Proceedings of Soft Computing in Industrial Applications, pp. 1–10 (2012)
2. Lécuyer, A., Lotte, F., Reilly, R.B., Leeb, R., Hirose, M., Slater, M.: Brain-computer interfaces, virtual reality, and videogames. Computer **10**(41), 66–72 (2008)
3. Rebsamen, Brice, Burdet, Etienne, Guan, Cuntai, Zhang, Haihong, Teo, Chee Leong, Zeng, Qiang, Laugier, Christian, Jr Ang, Marcelo H.: Controlling a wheelchair indoors using thought. Intell. Syst. IEEE **22**(2), 18–24 (2007)

4. Mugler, E.M., Ruf, C.A., Halder, S., Bensch, M., Kubler, A.: Design and implementation of a P300-based brain-computer interface for controlling an internet browser. In: Neural Syst. Rehabil. Eng., IEEE Trans. **18**(6), 599–609 (2010)
5. Lotzea, Martin, Halsband, Ulrike: Motor imagery. J. Physiol. **99**, 386–395 (2006)
6. Grosse-Wentrup, Moritz: Understanding brain connectivity patterns during motor imagery for brain-computer interfacing. Adv. Neural Inf. Process. Syst. (NIPS) **21**, 561–568 (2008)
7. Nicolas-Alonso, L.F., Corralejo, R., Álvarez, D., Hornero, R.: Adaptive classification framework for multiclass motor imagery-based BCI, Chapter XIII. In: Mediterranean Conference on Medical and Biological Engineering and Computing, vol. 41, pp. 762–765 (2013)
8. Miranda, Eduardo Reck, Brouse, Andrew: Interfacing the brain directly with musical systems: on developing systems for making music with brain signals. Leonardo **38**(4), 331–336 (2005)
9. Cabredo, Rafael, Legaspi, Roberto, Inventado, Paul Salvador, Numao, Masayuki: Discovering emotion-inducing music features using EEG signals. J. Adv. Comput. Intell. Intell. Inform. **17** (3), 362–370 (2013)
10. Renuga Devi, K., Hannah Inbarani, H.: Motor imagery classification based on variable precision multigranulation rough set. Adv. Intell. Syst. Comput. **412**, 145–154 (2016)
11. Sitaram, Ranganatha, Zhang, Haihong, Guan, Cuntai, Thulasidas, Manoj, Hoshi, Yoko, Ishikawa, Akihiro, Shimizu, Koji, Birbaumer, Niels: Temporal classification of multichannel near-infrared spectroscopy signals of motor imagery for developing a brain–computer interface. NeuroImage **34**, 1416–1427 (2007)
12. Corralejo, Rebeca, Nicolás, Luis F., Alonso, Álvarez, Daniel, Hornero, Roberto: A P300 based brain–computer interface aimed at operating electronic devices at home for severely disabled people. Med. Biol. Eng. Comput. **52**, 861–872 (2014)
13. Kaiser, Vera, Bauernfeind, Günther, Kaufmann, Tobias, Kreilinger, Alex, Kübler, Andrea, Neuper, Christa: Cortical effects of user learning in a motor-imagery BCI training. Int. J. Bioelectromag. **13**(2), 60–61 (2011)
14. Wolpaw, J.R., Birbaumer, N., McFarland, D.J., Pfurtscheller, G., Vaughan, T.M.: Braincomputer interfaces for communication and control. Clin. Neurophysiol. **113**(6), 767–791 (2002)
15. Velásquez-Martínez, L.F., Álvarez-Meza, A.M., Castellanos-Domínguez, C.G.: Motor imagery classification for BCI using common spatial patterns and feature relevance analysis. Nat. Artif. Comput. Eng. Med. Appl. **7931**, 365–374 (2013)
16. Duan, L., Zhong, H., Miao, J., Yang, Z., Ma, W., Zhang, X.: A voting optimized strategy based on ELM for improving classification of motor imagery BCI data. Cogn. Comput. **6**, 477–483 (2014)
17. Rodrıguez-Bermudez, G., García-Laencina, P.J.: Analysis of EEG signals using nonlinear dynamics and chaos: a review. Appl. Math. Inf. Sci. **9**(5), 2309–2321 (2015)
18. Kubler, A., Kotchoubey, B., Kaiser, J., Wolpaw, R.J., Birbaumer, N.: Brain-computer communication: unlocking the locked in. Psychol. Bull. **127**(3), 358–375 (2001)
19. Calvo-Dmgz, D., Galvez, J.F., Glez-Pena, D., Gomez-Meire, S., Fdez-Riverola, F.: Using variable precision rough set for selection and classification of biological knowledge integrated in DNA gene expression. J. Integr. Bioinf. **9**(3), 1–17 (2012)
20. Wei, Jin-Mao, Wang, Ming-Yang, You, Jun-Ping: VPRSM based decision tree classifier. Comput. Inform. **26**, 663–677 (2007)
21. Beynon, Malcolm J., Peel, Michael J.: Variable precision rough set theory and data discretisation: an application to corporate failure prediction. Omega **29**, 561–576 (2001)
22. ziarko, Wojciech: Variable precision rough set model. J. Comput. Syst. Sci. **46**, 39–59 (1993)
23. Ang, K.K., Chin, Z.Y., Wang, C., Guan, C., Zhang, H.: Filter bank common spatial pattern algorithm on BCI competition IV datasets 2a and 2b. Front. Neurosci. 6–39 (2012)
24. Zhou, H., Wang, Y., Xu, Q., Huang, J., Wu, J.: An improved support vector machine classifier for EEG-based motor imagery classification. Adv. Neural Netw. **5552**, 267–275 (2009)
25. Mohd Tumari, S.Z., Sudirman, R., Ahmad, A.H.: Selection of a suitable wavelet for cognitive memory using electroencephalograph. Signal Eng. **5**, 15–19 (2013)

26. Procházka, A., Mudrová, M., Vyšata, O., Gráfová, L., Araujo, S.P.S.: Computational intelligence in multi-channel EEG signal analysis. Recent Adv. Intell. Eng. Syst. **378**, 361–381 (2012)
27. Deepa, V.B., Thangaraj, P.: A study on classification of EEG data using Filters, (IJACSA) Int. J. Adv. Comput. Sci. Appl. **2**(4) (2011)
28. Kang, D., Zhizeng, L.: A method of denoising multi-channel EEG signals fast based on PCA and DEBSS algorithm. In: International Conference on Computer Science and Electronics Engineering (ICCSEE), vol. 3, pp. 322–326 (2012)
29. Omerhodzic, I., Avdakovic, S., Nuhanovic, A., Dizdarevic, K.: Energy distribution of EEG signals: EEG signal wavelet-neural network classifier. World Acad. Sci. Eng. Technol. **4**, 1–24 (2010)
30. Sviderskaya, N.E., Bykov, P.V.: EEG spatial organization during intense hyperventilation (Cyclic breathing) EEG correlates of psychovisceral phenomena. Hum. Physiol. **32**(3), 270–277 (2006)
31. Chen, Chih-Wei, Ming-Shaung, Ju, Sun, Yun-Nien, Lin, Chou-Ching K.: Model analyses of visual biofeedback training for EEG-based brain-computer interface. J. Comput. Neurosci. **27**, 357–368 (2009)
32. Li, Xiaowei, Zhao, Qinglin, Liu, Li, Peng, Hong, Qi, Yanbing, Mao, Chengsheng, Fang, Zheng, Liu, Quanying: Improve affective learning with EEG approach. Comput. Inform. **29**, 557–570 (2010)
33. Yu, L.: EEG de-noising based on wavelet transformation. In: International Conference Bioinformatics and Biomedical Engineering, pp. 1–4 (2009)
34. Inuiguchi, Masahiro: Attribute reduction in variable precision rough set model. Int. J. Uncertainty Fuzziness Knowl. Based Syst. **14**(4), 61–479 (2006)
35. Inuiguchi, Masahiro: Structure-based attribute reduction in variable precision rough set models. J. Adv. Comput. Intell. Intell. Inform. **10**(5), 657–665 (2006)
36. Ningler, Michael, Stockmanns, Gudrun, Schneider, Gerhard, Kochs, Hans-Dieter, Kochs, Eberhard: Adapted variable precision rough set approach for EEG analysis. Artif. Intell. Med. **47**, 239–261 (2009)
37. Kusunoki, Yoshifumi, Inuiguchi, Masahiro: Variable precision rough set model in information tables with missing values. J. Adv. Comput. Intell. Intell. Inform. **15**(1), 110–116 (2011)
38. Gong, Zengtai, Shi, Zhanhong, Yao, Hongxia: Variable precision rough set model for incomplete information systems and its -reducts. Comput. Inform. **31**, 1385–1399 (2012)
39. Ziarko, W.: A variable precision rough set model. J. Comput. Syst. Sci. **46**, 39–59 (1993)
40. Yao, J.T., Herbert, J.P.: A game-theoretic perspective on rough set analysis. J. Posts Telecommun. **20**(3), 291–298 (2008)
41. Xu, W., Zhang, X., Wang, Q.: A generalized multigranulation rough set approach. ICIC 681–689 (2012)
42. Yao, Y., Qian, Y., Liang, J., Dang, C.: MGRS: a multigranulation rough set. Inf. Sc. 1–22 (2009)
43. Wei, W., Liang, J., Qian, Y., Wang, F.: Variable precision multi-granulation rough set. In: IEEE International Conference on Granular Computing, pp. 639–643 (2012)
44. Azam, Yao, J.T.: Analyzing uncertainties of probabilistic rough set regions with game-theoretic rough sets. Int. J. Approx. Reason. **55**(1), 142–155 (2014)
45. Azam, Nouman, Yao, JingTao: Game-theoretic rough sets for recommender systems. Knowl. Based Syst. **72**, 96–107 (2014)
46. de Vries, Sjoerd, Mulder, Theo: Motor imagery and stroke rehabilitation. A Crit. Discuss. J. Rehabil. Med. **39**, 5–13 (2007)
47. Vaughan, T.M., Heetderks, W.J., Trejo, Lj, Rymer, W.Z., Weinrich, M., Moore, M.M., Kubler, A.: Brain-computer interface technology: a review of the second international meeting. IEEE Trans. Neural Syst. Rehabil. Eng. **11**(2), 94–109 (2003)

Computer Aided Diagnosis System for Mammogram Abnormality

Ahmed M. Anter and Aboul Ella Hassenian

Abstract In this chapter, computer aided detection and diagnosis for Breast tumor detection and classification in Mammography is proposed. The proposed system based on four phases. In the first phase, mammogram image is segmented to sub images with size 64 × 64 pixel then high intensity value of pixel is defined in this sub image and specifies this intensity as a seed point to region growing (RG) algorithm which used to specify the ROI. In the second phase, texture features were extracted using gray-level co-occurrence matrix (GLCM) and combined with shape features to characterize region of interest (ROI) to normal, benign or malignant. In the third phase, malignant ROIs are diagnosed and specified to aided doctor for decision taking. Finally, different methods for evaluating classifier are used using confusion matrix, kappa coefficient and response receiver operating characteristic curve (ROC). The effectiveness of the proposed system was measured using 322 mammogram images from the mammographic image analysis society (MIAS) database. From experimental results show that, the accuracy obtained from ROC curve analysis is AUC 94 % with standard error 0.11. The experimental results shows that the proposed system can accurately segment the breast region in a large range of digitized mammograms.

Keywords Segmentation · Region growing · GLCM · ROC · Mammogram · k-NN · Classification

A.M. Anter (✉)
Faculty of Computers and Information, Beni-Suef University, Beni Suef, Egypt
e-mail: sw_anter@yahoo.com
URL: http://www.egyptscience.net

A.E. Hassenian
Faculty of Computers and Information, Cairo University, Giza, Egypt

A.M. Anter · A.E. Hassenian
Scientific Research Group in Egypt (SRGE), Giza, Egypt

N. Dey et al. (eds.), *Medical Imaging in Clinical Applications*,
Studies in Computational Intelligence 651, DOI 10.1007/978-3-319-33793-7_8

1 Introduction

Breast cancer is the most common form of cancer among women and is the second leading cause of cancer death in the world wide after lung cancer [1]. Thus, a variety of Computer Aided Diagnosis (CAD) systems have been proposed to increase the efficiency and effectiveness of screening procedures by using a computer system, as a second opinion, to aid the radiologist by indicating locations of suspicious abnormalities in mammograms, and diagnosis this abnormality. Radiologists carefully search each image for any visual sign of abnormality. However, at times it may be difficult for radiologists to detect some lesions on mammograms because abnormalities are often embedded in and camouflaged by varying densities of breast tissue structures [2]. Indeed, estimates indicate that between 15 and 30 % of breast cancers are missed by radiologists during routine screening. Missed detections may be due to the subtle nature of the radiographic findings, poor image quality, eye fatigue or oversight by the radiologists [2].

The field of computer aided interpretation in mammography deals with the development of computer tools for automated diagnostic of mammograms. CAD techniques typically follow a two stage approach, Computer Aided Detection (CADe) and Diagnosis (CADx). Initially, region of interest will be specified, subsequently, textural features are automatically extracted from these regions. The features are merged with linear classifiers or artificial intelligence techniques to diagnosis abnormalities regions. A mass is defined as lesion seen in at least two different projections [3]. Masses are described by their shape (Round, Oval, Lobulated, Irregular, architecture distortion) and margin characteristics (Circumscribed, Micro-lobulated, Obscured, Spiculated, Ill-Defined). On mammograms, mass areas usually appear brighter than healthy tissues. However, the patterns of mass lesion are hard to be defined by simple features such as intensities or gradients because of huge variations among individuals. For example, masses are quite difficult to be recognized from dense breasts [4].

These phenomenons increase the difficulty in the detection of masses, but still this cannot be visually observed from the image. In such a case, the masses may not be found by simply using the thresholding segmentation method. Our system uses shape and texture for the discrimination of malignant and benign and diagnosis these malignant type. The texture features are adopted using second order statistics co-occurrence matrix and shape features are adopted using Circularity, Brightness, Radial Angle and Compactness. According to the medical view, shape feature is one of the most important features used for differentiating malignant from benign masses, four kinds of shape features including circularity, contrast, radial angle and compactness were adopted as features for mass malignancy and benignancy classification [5].

The output of texture and shape features is a matrix of size $M \times 52$, where M is the number of region of interest and 52 is the number of features extracted from co-occurrence matrix at distance 1 pixel and 4 directions with 12 descriptor and 4 features extracted from shape. The resulting matrix is stored in a database of

features. The classifier used in this chapter is k-Nearest Neighbor (k-NN) classifier which is a supervised nonparametric technique. The k-NN method computes the k-nearest training samples in terms of a distance metric using Euclidean distance and then assigns the sample to the class that occurs most frequently among the k-nearest training samples.

There is growing interest in using CAD systems that aid in detection of breast abnormalities at earlier stages, and there are various image processing methods proposed for the detection of masses in mammograms. Yin et al. [6] investigated mammographic asymmetries for the identification of mass lesions. Kegelmeyer et al. [7] utilized the analysis of local oriented edges and a subset of Laws texture features to detect spiculated masses. In [8] Zouras investigated the potential of incorporating a temporal subtraction scheme to the bilateral subtraction technique. Matsubara et al. [9] used different grey level threshold values depending on the type of tissue of the breast based on histogram analysis.

In [10] Petrick et al. reported a two-stage adaptive density weighted contrast enhancement (DWCE) algorithm for mass detection. In [11] the authors first detect spicules using second order Gaussian derivatives operators. In [12], the authors used statistical approaches to detect mass in mammogram. Li et al. [13] extract lesion site selection by morphological enhancement and contextual segmentation. Campanini et al. [14] work on mass detection in digital mammograms based on support vector machines (SVM) to classify mass into benign or malignant. Zheng [15], detect breast cancer depend on Gabor Features.

Wei et al. [16], also used texture features and linear discrimination to classify between masses and normal texture. Tourassi [17] was based on directly comparing a new ROI image with all the ROI images in the database. In the first one, the gray level and the shape were used as a likelihood measure, while on the second one the similarity was based on mutual information. Chan et al. [18], consisted in extracting a huge set of features, selecting the most discriminative ones using genetic algorithms, and then classifying by using linear classifiers or neural networks.

The proposed system starts by obtaining features that passed into the k-NN as the input vectors for classifying the masses as benignancy or malignancy and diagnosis this mass. However, it should be noted that the accuracy of segmentation significantly affects the extraction of shape features. Thus Region Growing method was used in the mass segmentation module to obtain fine segmented masses from the image. The main idea is to indicate locations of suspicious abnormalities in mammograms and diagnose these suspicious abnormalities to type of mass (calcification, Architectural distortion, obscured, circumscribed, speculated, and ill-defined) to aided radiologist take decision for biopsy or chemotherapy protocol.

The remainder of this chapter is structured as follows: Sect. 2 discuss the mammogram abnormalities. The proposed mammogram CAD System in Sect. 3. Experimental Results and discussion presented in Sect. 4. Finally, conclusion in Sect. 5.

2 Preliminaries: Mammogram Abnormalities

This section describe a variety of masses which appear in mammogram images. Masses are a space occupying lesion. Masses come in a wide range of shapes, sizes, and contrast. They can be extremely subtle, often obscured by normal tissue. Studies have shown that breast masses comprise the overwhelming majority of missed cancers [19]. Clinicians try to assess the likelihood of malignancy depending on the morphological characteristics of the mass (size, shape, margin, density). There are several types of masses found in mammogram images. Masses are categorized by their shape, density, and margins. The shapes include: round, oval, lobular, and irregular. The margins include: circumscribed, microbulated, obscured, ill defined and Speculated [20]. Figure 1 shows samples of such masses.

The densities include: high density, low density, equal density, and fat containing. These categories help radiologists to precisely describe masses found in mammograms and to classify masses as benign or malignant. The focus of this research is the location of masses in mammogram images and therefore masses will be discussed at length and pictorial examples presented. Figure 1 illustrates some mass shapes found in mammogram images. Round masses are generally circular and oval masses are elliptical in shape. Lobular masses display contours and undulations. Masses with shapes that cannot be characterized are termed irregular as shown in Fig. 1. As shown in Fig. 1 malignant increases from top to down, Round masses and oval masses are benign mass but masses with shape architectural, lobulated or with speculated margin are malignant.

Figure 2 shows the varying types of real masses margins or boundaries observed in mammogram images. Circumscribed masses display distinct well-defined boundaries. Micro-lobulated masses have margins, which undulate in small cycles. Obscured masses are those that are hidden by superimposed or adjacent normal tissues.

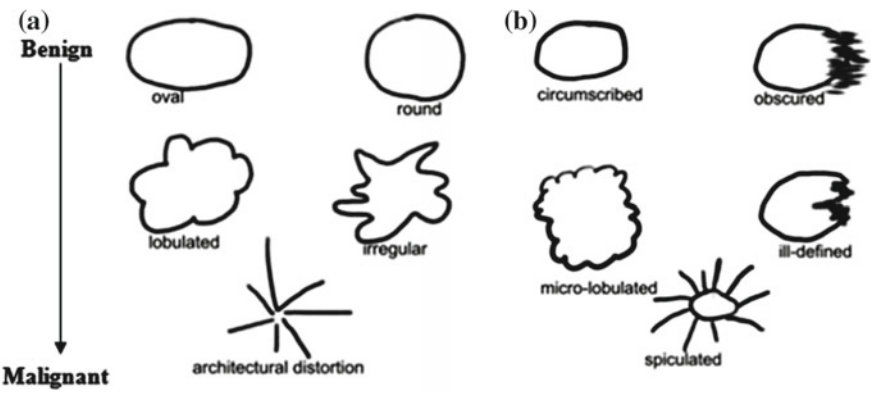

Fig. 1 The shape and margin of a mass are strong signs of their malignancy/benignancy degree. Image extracted from the web of GE Healthcare [20]. **a** Mass shapes. **b** Mass margin

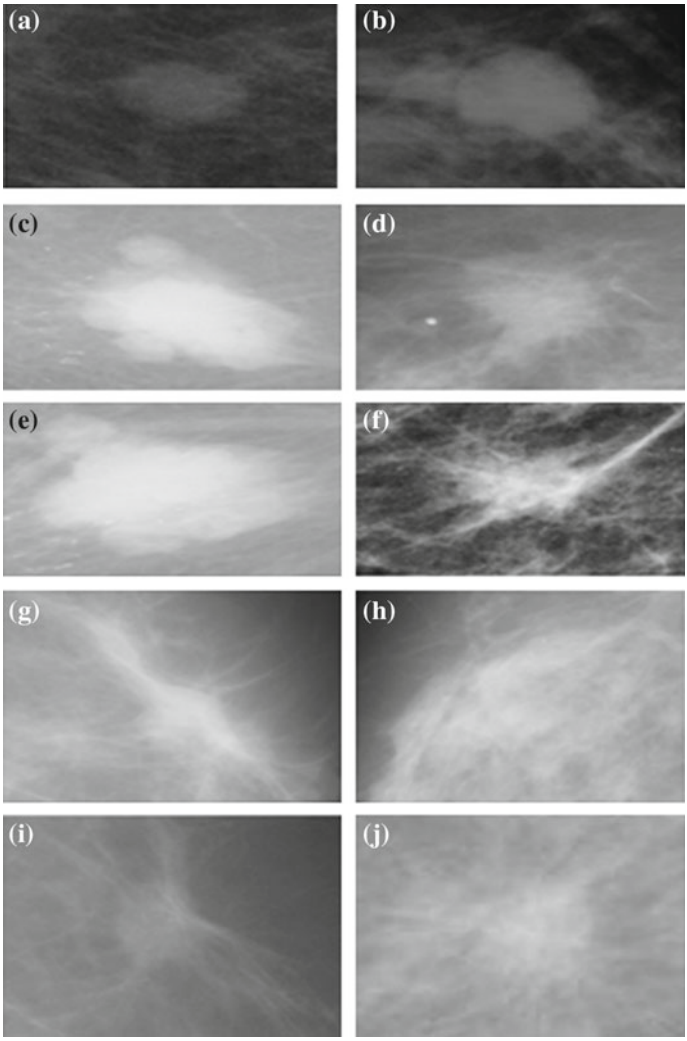

Fig. 2 Masses examples. **a** Round mass, **b** lobular mass, **c** oval mass, **d** irregular mass, **e** circumscribed mass, **f** microlobulated mass, **g** obscured mass, **h** ill-defined mass, **i** speculated mass, **j** architectural distortion mass

Indistinct masses have poorly defined boundaries that taper into the background. Speculated masses have spoke-like lines radiating out from the mass. The margins refers to the border of a mass, and it should be examined carefully because it is one of the most important criteria in determining whether the mass is the result of a benign or malign process [21]. Radiologists classify the margin among these five classes of margins (refer to Table 1).

Table 1 The classification of mammogram masses (shape, margin, and density)

Shape	Margin	Density
Round: Spherical, ball-shaped, circular or globular	Circumscribed (Well-Defined or Sharply-Defined) Margins: Sharply demarcated with an abrupt transition between the lesion and the surrounding tissue	High Density: Clearly higher than surrounding, suspicious
Oval: Elliptical or egg-shaped	Microlobulated Margins: Undulate with short cycles producing small undulations	Equal (isodense) Density: Density not appreciably different, neutral significance
Lobular: Contours with undulations	Obscured Margins: Hidden by superimposed or adjacent normal tissue and cannot be assessed any further	Low Density: Density lower, but not fat containing, neutral significance
Irregular: Cannot be characterized by any of the above	Indistinct (Ill-Defined) Margins: There may be infiltration by the lesion and this is not likely due to superimposed normal breast tissue	
Architectural distortions: This includes speculated areas and/or retraction from a focal point. Characterized by lines radiating	Speculated Margins: Characterized by lines radiating from the margins of a mass	

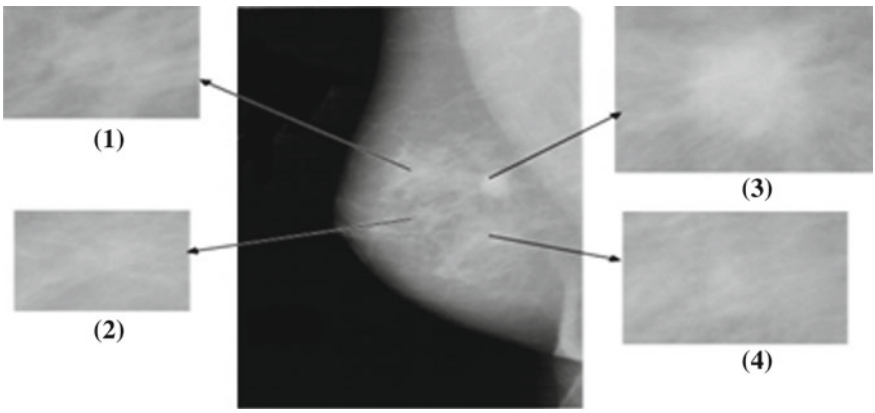

Fig. 3 Possible masses from mammogram image manually selected

The probability to find a malignancy mass is normally ordered according to this classification. The more ill-defined and speculated the margin, the higher the probability to be associated with a malignant process. It should be clear that these

morphological aspects can be very subtle and difficult to diagnose, even for an expert radiologist [22].

In order to find the optimal solution to these classes classification problem, as shown in Fig. 3. The dataset that represent the mass class are 100 masses. Mass classes are benign and malignant, benign represent 55 and malignant represent 45, whereas the crops representing the non mass class are 207. All the crops are extracted and then resized to 64 × 64 from the mammographic images belonging to the MIAS.

3 The Proposed Computer Aided Diagnosis System for Mammogram Abnormality

The proposed CAD system for mammogram abnormality classification is comprised from four phases as shown in Fig. 4. In the first phase, mammogram image is segmented to sub images with size 64 × 64 pixel then define high intensity value of pixel in this sub image and specify this intensity as a seed point in the region growing (RG) algorithm was used to specify the ROI. In the second phase, texture features are extracted using GLCM and combined with shape features to categorize

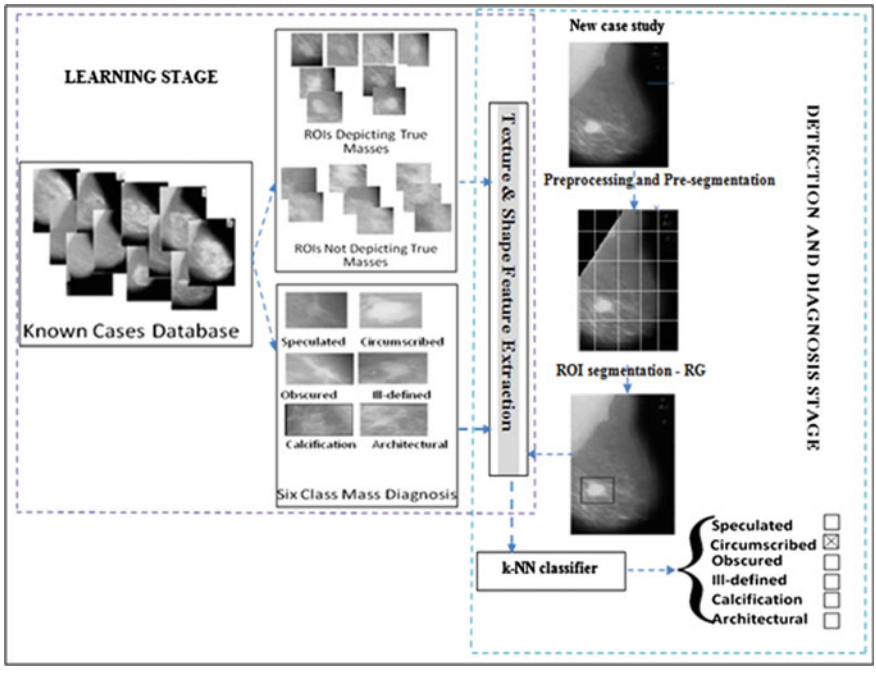

Fig. 4 Proposed CAD system for mammogram abnormality classification

ROI to normal or abnormal masses. In the third step, diagnosis the ROI and specify which type of malignant. Finally, different methods used to evaluate non parametric k-NN classifier.

4 Experimental Results and Discussion

4.1 Mammogram Dataset

Mammograms were obtained from the database of the Mammographic Images Analysis Society (MIAS) [23] is composed by a set of 322 Medio-Lateral Oblique (MLO) view digitized mammograms corresponding to the left and right breasts of 161 women. The films were extracted from the UK National Breast Screening Program, and digitized to 50 micron pixel. The size of each image was 1024 $\times$ 1024 pixels.

Abnormalities are classified into calcifications architectural distortions, asymmetries, circumscribed masses, speculated masses, and ill-defined masses. Sub-images were cropped as ROIs from each mammogram by experienced. 329 ROIs were used to analyze shape and texture features. 122 ROIs (including 29 images in calcification class, 19 in architectural distortion class, 15 in asymmetry class, 25 in circumscribed masses class, 19 in speculated masses class, and 15 in other or ill-defined masses class) were selected from abnormal tissues. Another 207 ROIs were obtained from normal tissues.

4.2 Experimental Results and Discussion

In this chapter, CAD system for mammogram abnormality detection and diagnosis was presented. The proposed system based on four phases. The first phase is ROI specification by segment mammogram image to sub images with size 64 $\times$ 64 pixel then define high intensity value of pixel in this sub image and specify this intensity as a seed point in the region growing (RG) algorithm. The second phase, the rule based classification of the ROI is specified from GLCM texture feature and combined with shape features to classify ROI to benign, malignant or normal by using, In the Third phase, ROIs are diagnosed to identify malignant type to aided doctor for decision taking. Finally, different methods for evaluating classifier are used using confusion matrix, kappa coefficient and Response Receiver Operating Characteristic Curve (ROC). The effectiveness of the proposed system was measured using 322 mammogram images from the MIAS database.

1. **Pre-processing and Pre-segmentation**

Detection is important in selecting the candidate regions that highly resemble masses in terms of their intensity and statistical texture value. Firstly, Pre-processing median filter is applied to remove high frequencies component, smooth

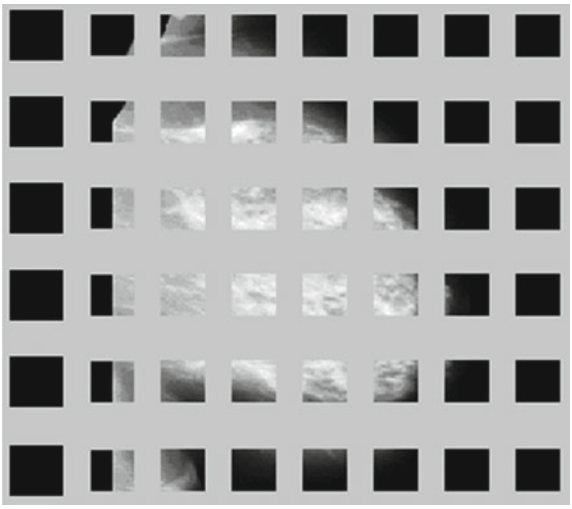

Fig. 5 Mammogram image divided into sub-images

mammogram image and increase the efficiency of the proposed CAD system. Then background and annotation in mammogram removed using adaptive threshold and connected component and Pectoral muscle is suppressed using Region Growing for more details see our work in [24].

After that, the process of mammogram segmentation is done based on block processing windows or tiles. Therefore, this entire mammogram is divided into tiles area before extraction of features is done to each tile. Figure 5 shows the mammogram image divided into sub-images.

In this work, the whole attention is devoted to the crops classification, rather than to the scanning of the entire mammographic image. The dataset is composed of 329 crops with pixel size 64 × 64 representing the three classes, normal, benign, and malignant.

In order to find the optimal solution to this three classes classification problem. The dataset that represent the abnormality class are 100 classes. Abnormality classes are benign and malignant, benign represent 55 and malignant represent 45, whereas the crops representing the normal class are 207. All the crops are extracted and then resized to 64 × 64 from the mammographic images belonging to the MIAS.

2. **ROIs Segmentation**

It is well known that tumor segmentation is one of the most important aspects of computer aided diagnosis (CAD) because one of the main characteristics of malignant tumors is (micro-calcification, architectural distortion, obscured, circumscribed, speculated, and ill-defined). Conversely, benign tumors typically have well-defined, rounded borders. Segmentation is therefore extremely important because the diagnosis of a tumor can strongly depend upon image features.

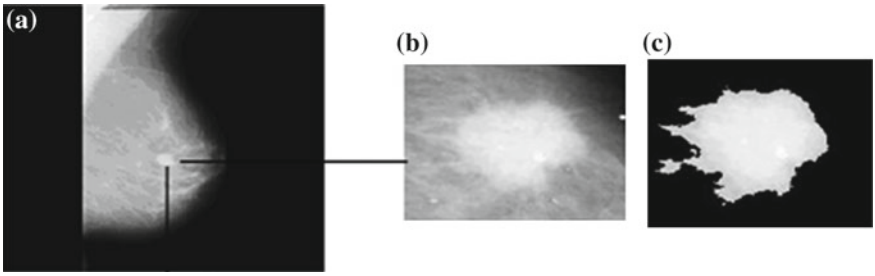

Fig. 6 Mammogram image. **a** Segmented to sub images. **b** The results for a malignant tumor produced by the RG technique

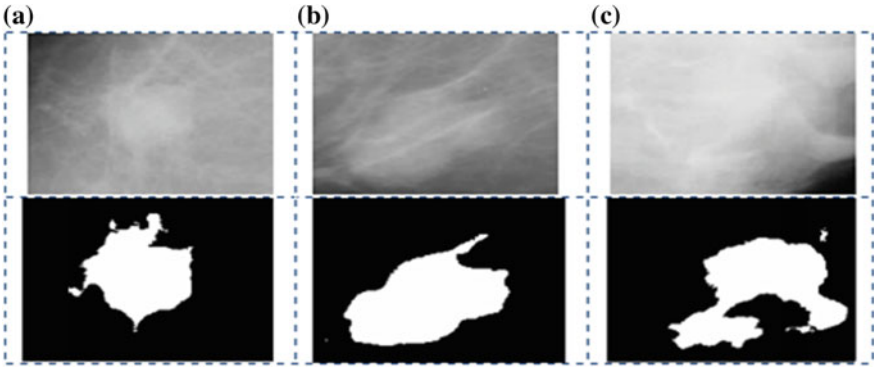

Fig. 7 *Upper row* mammographic sub images show masses, and *bottom row* show segmentation by region growing (RG)

Region growing (RG) is an automated segmentation method in which the region of interest begins as a single pixel and grows based on surrounding pixels with similar properties. It is a commonly used method [25] due to its simplicity and accuracy. The algorithm will use the maximum intensity as the seed point. Figure 6 show a pixel that is similar to the suspected lesion and located somewhere inside the suspected lesion. The next 4-neighboring pixel is checked for similarity so that the region can grow. If pixels in the 4-neighboring region are similar, they are added to the region. The region continues to grow until there are no remaining similar pixels that are 4-neighbors of those in the grown region. Figure 7 show different tumor regions and efficiency of segmentation by region growing algorithm.

3. Texture Feature Extraction

The texture feature and shape feature are two kinds of major features for the discrimination between the benign and malignant masses. Once the ROI segmented, the next step is to extract mass features from the ROI, GLCM used to extract features from texture. The co-occurrence of gray-levels can be specified as a matrix

of relative frequencies, in which two pixels separated by a distance d and angle. A set of features derived from co-occurrence matrices [24] were used to represent ROIs. Here we use four different directions: 0, 45, 90, and 135, and one distance equal to 1 pixel. Note that these values were empirically determined and are related to the scale of textural features found in mammographic images. A large number of textural features derived from matrices have been proposed. For each co-occurrence matrix the following statistics were used: angular second moment (ASM), energy, entropy, contrast, correlation, Dissimilarity, sum average, sum entropy, Sum Variance, difference variance, difference entropy, and homogeneity features, thus the resulting in a total of 48 texture features for each ROI.

4. **Shape Feature Extraction**

It is important to classify tumor whether it is malignant or benign. Several primary features such as shape, size, appearance, edges, volume and location of masses can be used as criteria for this purpose. Four shape features are used as descriptors including circularity, brightness, radial angle and compactness. These descriptors will be applied on the segmented mass for the shape feature extraction.

Circularity The main purpose of circularity is to show the circular degree of masses. The roundness is one of the criteria of benign masses, the probability of masses as being benign is higher when circularity is higher. The circularity value would be between 0 and 1. If the ratio is 1, this means that the mass matches exactly, implying the mass is circular. On the other hand, if the circularity is much smaller than 1, this implies the mass is far from a circle [26].

$$\text{Circularity} = \frac{4\pi A}{p2} \tag{1}$$

where A is the area of the mass and P is the mass perimeter.

Brightness Generally speaking, the intensities of malignant masses are higher than those of benign masses. Therefore, the Brightness of masses with respect to the background in malignancy is higher than in benignancy [26].

$$\text{Brightness} = \text{mean}\,(\text{O}) \tag{2}$$

where O is a set of pixel that belong to the abnormality segmented region.

Radial angle

The speculation is usually an important indicator of the malignant masses. The Radial Angle is used to differentiate the shape of edges of the masses as speculated or as round and smooth. The Radial Angle is the smaller included angle θ between the direction of the gradient and the radial direction of the edge, as shown in Fig. 8. As we know, when the mass tend to be more rounds, its Radial Angles tend to be near 180 and the average of the Radial Angles tends to be larger. Conversely, a mass with speculated edge will have a smaller averaged Radial Angle. Therefore, the value of the averaged Radial Angles provides one indicator to the differentiation between benign and malignant masses [26].

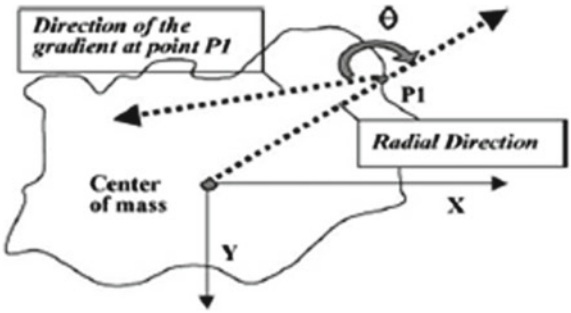

Fig. 8 Example of radial angle [26]

Compactness

$$\text{Area} = |\text{O}| \tag{3}$$

$$\text{Perimeter} = \text{length}\,(\text{E}) \tag{4}$$

$$\text{Compactness} = \frac{\text{Perimeter}^2}{\text{Area}} \tag{5}$$

where *O* is a set of pixel that belong to the abnormality segmented and E edge pixels (subset of O).

5. Rule-Based classification (ROIs)

The objective of the classification module is to categorize the specified ROIs as normal or abnormal (true mass or non-masses). The classification stage consists of two phases, training phase and testing phase. In the training phase, we let the system get trained by giving the features and decisions that are previously known. In the testing phase, unknown data are given and the classification is performed using the classifier after learning. The classifier used for the classifying this process is the k-Nearest Neighbor (k-NN) [24, 27].

The k-Nearest Neighbor classifier is a supervised nonparametric technique. Briefly, given a set of training samples and a test sample, the k-NN method computes the k-nearest training samples in terms of a distance metric (Euclidean distance) and then assigns the sample to the class that occurs most frequently among the k-nearest training samples. To learn and classify new cases we used in training phase 120 normal cases and 75 abnormal cases (benign and malignant). In testing phase we used 87 normal cases and 25 abnormal cases to decided the rate of classifier accuracy.

6. Classifier Performance Evaluation

Different methods for evaluating classifiers were used. These methods are; confusion matrix, kappa (k) coefficient and Response Receiver Operating Characteristic Curve (ROC) for more details in [27–29]. The results of proposed k-NN classifier at k = 1 for classifying tissue to malignant and benign obtained

Table 2 Parameters extracted from confusion matrix

Parameters	%
Accuracy	97
Sensitivity (TP)	98
Specificity (TN)	96
False positive rate (FP)	3.6
Area under curve (AUC)	100

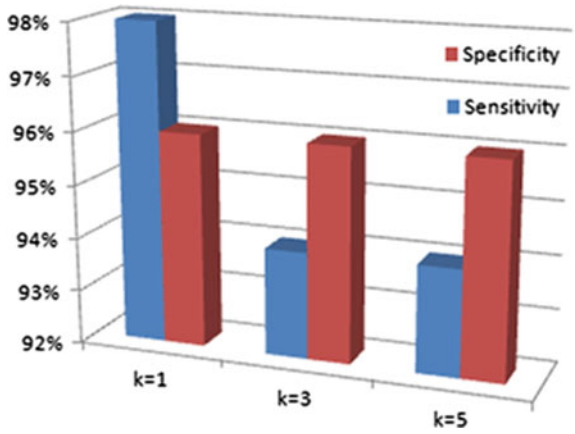

Fig. 9 Results of k-NN classifier at k = 1, 3, 5

sensitivity is 98 % and specificity is 96 % as shown in Table 2. The result of another measure sensitivity and specificity obtained from k-NN with k = 3 is sensitivity 94 % and specificity 96 %, and results obtained with k = 5 is sensitivity 94 % and specificity 96 %.

In Fig. 9, show comparing between the results obtained from the k-NN classifier, sensitivity and specificity results with k = 1 is much better than results with k = 3 and 5.

As mentioned before, we had initially attempted to classify masses into six classes. The classification accuracy of correct masses classification for obscured is around 73 %, whilst for the other cases, the percentages are 72 % for circumscribed, 95 % for speculated, 66 % for calcification, 84 % for architectural, and 87 % for ill defined and for over all mass accuracy is 80 % as shown in Fig. 10.

Table 3 shows the accuracy of kappa coefficient and ROC analysis. Kappa coefficient values in the range 0.61–0.8 suggest that the agreement is substantial, whereas, Kappa values in the range 0.41–0.6 suggest that the agreement is moderate. The kappa κ value is equal to 0.73 and error rate 0.05, this value represent substantial agreement for classifier . The result of ROC curve analysis is the AUC 94 % with standard error 0.11, this result is excellent test.

Table 4 gives comparison between proposed mass detection algorithm and other related work. Most detection algorithms consist of two stages. In the first stage the

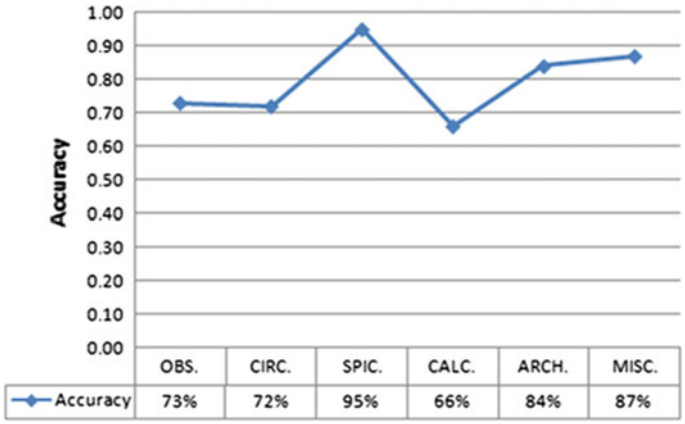

Fig. 10 The accuracy obtained from confusion matrix for six classes, (*OBS*. obscured, *CIRC*. circumscribed, *SPIC*. speculated, *CALC*. calcification, *ARCH*. architectural, and *MISC*. ill defined)

Table 3 Precision and accuracy for tumor classification

Parameters	ROC analysis		Overall accuracy	Kappa accuracy	
	AUC.	S.E.	–	κ	κ err.
Accuracy	94 %	0.11	80 %	0.73	0.045

Table 4 A comparison between proposed mass detection algorithm and other related work on mammograms

Author	Year	No. of Images	Sensitivity (TP) (%)	Specificity (FP/image)
Yin	1991	46	95	3.2
Zouras	1996	79	85	4
Matsubara		85	82	0.65
Petrick		168	90	4.4
Karssemeijer		50	90	1
Zwiggelaar	1999	54	70	0.01
Liu	2001	38	84.2	1
Campanini	2004	512	88	1.7
Zheng	2009	512	90	1.21
Proposed system	2010	322	97	3.6

goal is to achieve high sensitivity True Positive (TP). The second stage aims to reduce the number of False Positive (FP) without drastically reducing the sensitivity.

Table 5, show the summary of a representative selection of mass detection algorithms applied on ROIs compared with the proposed CAD system. The inputs to these algorithms are ROIs.

Table 5 A summary of a representative selection of mass diagnosis algorithms applied on ROIs compared with the proposed CAD system

Author	No. of ROI	AUC (Area under ROC curve)
Wei	168	0.92
Edwards	495	0.93
Tourassi	1465	0.87
Sahiner	678	0.87
Proposed system	329	0.94

5 Conclusions and Future Work

It is well known that mammogram interpretation is a very difficult task even for experienced radiologists. The key concept of our proposed mass detection and diagnosis is to use all the information available on raw images to perform the detection step. Indeed, instead of using a set of characteristics prefixed by experts, the system is able to extract automatically a set of discriminate features from scratch by means of statistical analysis through a dataset of images which contain diagnosed lesions. To locate suspicious lesion, region growing segmentation technique was used, features are extracted from GLCM and shape features together to fully represent the ROIs. Once the descriptors are extracted, k- nearest neighbor (k-NN) was used for classifying the detected masses. It was found that the best results appeared from k-NN classifier when k = 1 for both the sensitivity and the specificity. Each region depict mass define category type that belong to it. Experiments show that GLCM features are effective and efficient for false positive reduction even at different mass sizes. The results show that the GLCM at 0, 45, 90 and 135 with a block size of 64×64 give significant texture information to identify between masses and non-masses tissues with Sensitivity 98 % for of detecting cancer while there is really cancer in the image and Specificity 96 % for detecting normal breast while the true state of the breast is normal. This simplicity leads to less computational time. Thus, this approach is suitable for automated real time breast cancer diagnosis system. The result of ROC curve analysis is the AUC 94 % with standard error 0.11, this result is excellent test.

In future work, the efforts are directed to increase the performance of the algorithms. In this sense, a set of different directions are possible: to improve the false positive reduction approach, to reduce the computational time, to change the initial breast profile segmentation algorithm, or also to use more than one mammographic view in order to increase the performance of the full algorithm. Also we will focus to enrich the feature vector with new features and to improve the networks models that allow better abnormalities classification.

References

1. International Agency for Research on Cancer: Latest world cancer statistics global cancer burden rises to 14.1 million new cases in 2012: marked increase in breast cancers must be addressed. WHO, December (2013)
2. Baines, C.J., McFarlane, D.V., Miller, A.B.: The role of the reference radiologist: estimates of interobserver agreement and potential delay in cancer detection in the national screening study. Investiga Radiol. **25**(9), 971–976 (1990)
3. Oliver, A., Mart, J., Mart, R., Bosch, A., Freixenet, J.: A new approach to the classification of mammographic masses and normal breast tissue. In: International Conference on Pattern Recognition, pp. 707710, Hong Kong, August (2006)
4. Freer, T.W., Ulissey, M.J.: Screening mammography with computer aided detection: Prospective study of 12860 patients in a community breast center. Radiology **220**(3), 781–786 (2001)
5. Hall, F.M., Storella, J.M., Siverstond, D.Z., Wyshak, G.: Nonpalpable breast lesions: recommendations for biopsy based on suspicion of carcinoma at mammography. Radiology **167**(2), 353–358 (1988)
6. Yin, M., Giger, L., Doi, K.: Computerized detection of masses in digital mammograms: analysis of bilateral subtraction images. Med. Phys. **18**(5), 955–963 (1991)
7. Kegelmeyer, J.M., Pruneda, P., Bourland, D., Hillis, A.: Computer aided mammographic screening for spiculated lesions. Radiology **191**(2), 331–337 (1994)
8. Zouras, M., Giger, L., Lu, P., Wolverton, D.E., Vyborny, C.J., Doi, K.: Investigation of a temporal subtraction scheme for computerized detection of breast masses in mammograms. In: Digital Mammography (1996)
9. Matsubara, T., Fujita, H., Kasai, S., Goto, M., Tani, Y., Hara, T., Endo, T.: Development of new schemes for detection and analysis of mammographic masses. In: International Conference on Information and Intelligent Systems, pp. 63–66 (1997)
10. Petrick, N., Chan, H.P., Sahiner, B., Wei, D.: An adaptive density-weighted contrast enhancement filter for mammographic breast mass detection. IEEE Trans. Med. Imaging **15** (1), 59–67 (1996)
11. Karssemeijer, N., te-Brake, G.M.: Combining single view features and asymmetry for detection of mass lesions. In: International Workshop on Digital Mammography, vol. 13, pp. pp 95–102 (1998)
12. Zwiggelaar, R., Blot, L., Raba, D., Denton, E.: Set-permutation occurrence matrix based texture segmentation. Comput. Sci. **2652** (2003)
13. Li, Y., Wang, K., Liu, S., Lo, C., Freedman, M.: Computerized radiographic mass detection—Part I: Lesion site selection by morphological enhancement and contextual segmentation. IEEE Trans. Med. Imaging **20**(4), 289–301 (2001)
14. Campanini, R., Dongiovanni, D., Iampieri, E., Lanconelli, N., Masotti, M., Palermo, G., Riccardi, A., Roffilli, M.: A novel featureless approach to mass detection in digital mammograms based on support vector machines. Phys. Med. Biol. **49**(6), 961–975 (2004)
15. Zheng, Y.: Breast Cancer Detection with Gabor Features from Digital Mammograms. Alcorn State University (2009)
16. Wei, D., Chan, H.P., Helvie, M.A.: Classification of mass and normal breast tissue on digital mammograms: multiresolution texture analysis. Med. Phys. **22**(9), 1501–1513 (1995)
17. Tourassi, G.D.: Journey toward computer-aided diagnosis: role of image texture analysis. Radiology **213**(2) (1999)
18. Chan, H.P., Sahiner, B., Helvie, M.A., Petrick, N., Roubidoux, M.A.: Improvement of radiologists characterization of mammographic masses by using computer-aided diagnosis: an ROC study. Radiology **212**(3), 817–827 (1999)
19. Bellotti, R., Carlo, F., Tangaro, S., Gargano, G., Maggipinto, G., Castellano, M., Massafra, R., Cascio, D., Faucio, F., Magro, R., Raso, G.: A completely automated CAD system for mass detection in large mammographic database. Med. Phys. **33**(8) (2006)

20. GE health care (2010). http://www.gehealthcare.com/euen/patient/mammography/mammography-info.htm
21. Heywang, S.H., Dershaw, D.D., Schreer, I.: diagnostic breast imaging. Mammography, sonography, magnetic resonance imaging, and Interventional Procedures. Thieme, Stuttgart, Germany (2001)
22. El-Naqa, I., Yang, Y., Galatsanos, N.P., Nishikawa, R.M., Wernick, M.N.: A similarity learning approach to content-based image retrieval: Application to digital mammography. IEEE Trans. Med. Imaging **23**(10), 1233–1244 (2004)
23. Suckling, J., Parker, J., Dance, D.R., Astley, S.M., Hutt, I., Boggis, C.R.M., Ricketts, I. Taylor, P., Betal, D., Savage, J.: The mammographic image analysis society digital mammogram database. In: International Workshop on Digital Mammography (1994)
24. Anter, A., ElSoud, M., Hassanien, A.: Automatic mammographic parenchyma classification according to BIRADS dictionary. Comput. Vis. Image Process. Intell. Syst. Multimedia Technol. **22**, 22–37 (2014)
25. Anter, A., Azar, A., Hassanien, A., El-Bendary, N., ElSoud, M.: Automatic computer aided segmentation for liver and hepatic lesions using hybrid segmentations techniques. In: IEEE Proceedings of Federated Conference on Computer Science and Information Systems, 8–11 Sept. 2013, Krakow, Poland, pp. 193–198 (2013)
26. Ehab, M., Abd-Elfatah, H., Amr, B.: Automatic mass detection and classification in mammograms. Egypt. Comput. Sci. J. **30** (2008)
27. Duda, R.O., Hart, P.E., Stork, D.G.: Pattern Classification, 2nd edn. Wiley, New York (2001)
28. Landis, R., Koch, G.G.: The measurement of observer agreement for categorical data. Biometrics **33**(1), 159–174 (1977)
29. Metz, C.E.: Evaluation of digital mammography by ROC analysis. In: International Workshop on Digital Mammography (1996)

Automated Segmentation and Classification of Hepatocellular Carcinoma Using Fuzzy C-Means and SVM

Mai R. Ibraheem and Mohammed Elmogy

Abstract For successful classification of Hepatocellular Carcinoma (HCC) in ultrasound (US) images, effective preprocessing steps are highly desirable. Most of Computer Aided Diagnostic (CAD) systems miss the most important steps of image preprocessing and image segmentation. In such a framework, only some texture features, which are obtained directly from the images or ROIs, are used as inputs of classifiers. Image preprocessing and segmentation of US images are useful for better judgment of normal and cancerous cases. Although, there are many studies on the classification of medical images, the fully automatic classification is still a difficult task. In this work, we propose an automated classification of US liver tumors using SVM with the aid of Fuzzy c-means (FCM) and level set method. A large number of features were extracted by using statistical, textual, and histogram-based features to discriminate the HCC maximally by developing an SVM classification system. SVMs work on maximizing the margin between the separating hyperplane and the data to minimize upper bound of the generalization error. The proposed Fuzzy C-SVM based system is compared with the K-Nearest Neighbor (KNN) based approach. Experimental results demonstrated that the Fuzzy C-SVM based system greatly outperforms KNN-based approach.

Keywords Hepatocellular carcinoma (HCC) · Computer aided diagnostic (CAD) systems · Ultrasound liver images · Fuzzy c-means (FCM) clustering · Support vector machine (SVM) · K-nearest neighbor (KNN) classification

M.R. Ibraheem (✉)
Faculty of Science, Statistical and Computer Science Department, Mansoura University, Mansoura, Egypt
e-mail: dr_mai_ramadan@yahoo.com

M. Elmogy (✉)
Faculty of Computers and Information, Information Technology Department, Mansoura University, Mansoura, Egypt
e-mail: melmogy@mans.edu.eg; elmogy@gmail.com

N. Dey et al. (eds.), *Medical Imaging in Clinical Applications*,
Studies in Computational Intelligence 651, DOI 10.1007/978-3-319-33793-7_9

1 Introduction

Disease diagnosis based on medical imaging is an invaluable tool for medical experts to plan a patients' rehabilitation process. Imaging modalities, including US imaging, MRI, CT, and digital mammography, help physicians diagnosing the disease accurately in a non-invasive way. However, as the volume of medical images has exponentially grown, manual analysis and interpretation of these images is no more feasible. A CAD system is highly desirable to provide additional support to the radiologists. Particularly, efficient computer algorithms are required to illustrate automatically the structures and region of interest (ROI) [12, 13]. Although, there are many studies on the classification of medical images, the fully automatic classification is still a difficult task. Most of the CAD systems require user intervention [1, 7, 8, 15, 25, 31]. Sometimes intervention from an inexperienced user may lead to false results.

For successful classification of HCC in liver US images, effective preprocessing steps are highly desirable. HCC is the most common liver malignancy [3]. It can be single or multiple, and it has a variable, imprecise delineation. It may have a very pronounced circulatory signal and has a heterogeneous structure. However, US images are contaminated with an inherent noise called 'speckle.' It tends to have a granular effect on the image, thereby degrading its visual quality [30]. The US images should have a minimum amount of noise for simplifying the therapeutic decision-making and diagnosis. It calls for the development of speckle filtering techniques over past decades.

To extract the subtle sonographic features, the contrast of the US image is enhanced by using a bilateral filter. It is a non-linearly filter that considers both similarities of gray level and geometric closeness of the neighboring pixels [16]. In some present work, a large number of features are extracted by using statistical, textual, and histogram-based techniques to discriminate the HCC maximally by developing an SVM classification system [19, 21–24]. SVMs work on maximizing the margin between the separating hyperplane and the data to minimize upper bound of the generalization error. To help radiologists to decide the normal and cancerous cases, a new approach to the two-phase FCM clustering is developed to classify the liver tumor with high performance. The proposed Fuzzy C-SVM based system is compared with the KNN based approach. Experimental results have demonstrated that the Fuzzy C-SVM based system outperforms KNN-based approach.

This paper is organized into six sections. Section 2 reviews the current literature on the interpretation of US images. Section 3 describes the used material and the proposed methodology. Section 4 reviews the proposed diagnostic system. Section 5 refers to the obtained experimental and the classification results. The conclusion and future work are discussed in Sect. 6.

2 Related Work

Many researchers proposed and implemented CAD systems for analyzing liver images. For example, Mittal et al. [18] proposed a CAD system to assist in identifying focal liver lesions in B-mode US images. The proposed system discriminated focal liver diseases, such as Cyst, Hemangioma, HCC, and Metastases, against the normal liver. The images were enhanced using a new methodology that simultaneously operates both an enhancement and speckle reduction process. Subsequently, 208-texture based features are extracted using spectral, statistical, and TEM methods. A two-step neural network classifier is designed for the classification of five liver image categories. Classification using two-step neural network showed correct decisions of 432 out of 500 images with a classification accuracy of 86.4 %.

Sohail et al. [25] presented a combined method of content-based retrieval and classification. The used medical US images include three different types of ovarian cysts: Simple Cyst, Endometrioma, and Teratoma. The features were a combination of histogram moments and Gray Level Co-Occurrence Matrix (GLCM) that based on statistical texture descriptors. The classification performed by using Fuzzy KNN classification technique. Features were extracted from 200 images of the databases. They used to train the classifier by applying "k-Fold Cross-Validation" technique with k = 5. The performance of the proposed method is compared with other popular classification techniques namely, SVM (with RBF, Sigmoid, and Polynomial kernels), ordinary KNN, and ANN.

Ribeiro et al. [24] proposed a semi-automatically liver segmentation system. It helped in identification and diagnosis of diffuse liver diseases. The extracted features from the liver contour were used with clinical and laboratory data. Using the despeckle image, the liver surface contour was obtained using a snake technique. The classification results were compared with the SVM, a Bayesian, and a KNN classifier. Using Leave-one-out cross-validation strategy, the best results are obtained using the KNN classifier, with an accuracy of 80.68 %.

Ribeiro et al. [21] addressed identification and diagnosis of the chronic liver diseases. They used commonest features described in the literature including first order statistics, co-occurrence matrices, wavelet transform, attenuation, and backscattering parameters and coefficients. The classification results of an SVM, a decision tree, and a KNN classifier are compared. The best results were obtained using the SVM with a radial basis kernel, with 73.20 % of overall accuracy.

Ribeiro et al. [23] proposed a semi-automatic procedure for the stage based on US liver images, clinical, and laboratory data. The proposed algorithm was based on a set of laboratory and clinical features from The US. The classification was tested using two classifiers: a KNN and an SVM, with different kernels. The SVM, polynomial kernel, outperformed the others classifiers in every class studied, achieving a sensitivity of 91.67 %. From the attained results, the SVM with polynomial kernel outperformed the KNN and the SVM with the radial basis kernel classifier.

The previously mentioned studies show that the SVM and other methods are used as classifiers for the tissue in US images. However, these systems miss the image preprocessing and image segmentation components. Thus, the features extracted from ROIs directly may not provide accurate performance. The proposed method outperforms these studies and the study of James and Skowron [14] which reported with 77.31 % accuracy, and Garla et al. [10] which reported sensitivity 94.3 %.

3 Materials and Methods

3.1 Data Acquisition

The research in the area of liver diseases using US images had been carried out using some collected individual databases due to non-availability of benchmark image database.

From 150 different liver diseases pictures, we have chosen 94 of the best quality and applicability in pattern recognition area. The age of the patients in the dataset ranges from 38 to 78 years. Further, patient's privacy has been protected by labeling the data with numeric dummy values and keeping patients' credential undisclosed. We have obtained data from the Egyptian Liver Research Institute and Hospital in Sherbin, Dakahlia Governorate, Egypt. Figure 1 shows some pictures for the chosen diseases with the different appearance of hepatocellular carcinoma.

It is critical to processing the liver tumor US images by image preprocessing and image segmentation stages for better judgment of normal and cancerous cases. These two stages will facilitate and increase the performance of the classification stage in liver tumor applications.

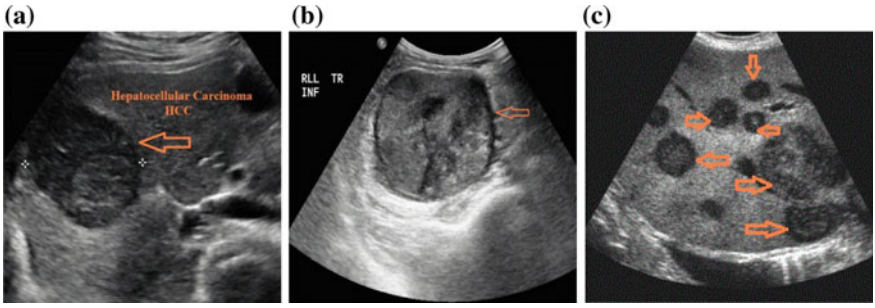

Fig. 1 Ultrasound liver images with different appearance of Hepatocellular carcinoma, **a** small HCC, **b** large HCC, and **c** multiple masses

3.2 Pre-processing Stage

3.2.1 Image Enhancement and Noise Removal

To improve the visualization of US images, the process of image enhancement is done in such a way that the visual details of the texture should remain preserved. Since image noise and artifacts often impair the performance of the classification, it would be attractive to incorporate spatial information into the classifier. Spatial filters have been widely used for noise elimination in the presence of additive noise. The Gaussian filter is a local and linear filter. It smoothes the whole image irrespective of its details or edges. Whereas the bilateral filter is also local but non-linearly that considers the gray level similarity and geometric closeness without smoothing edges [16].

Bilateral filtering is a non-linear filtering technique introduced by Tomasi et al. [29]. It extends the technique of Gaussian smoothing by weighting the coefficients of the filter with their corresponding relative pixel intensities. Bilateral Filter considers intensity and spatial information between each point and its neighboring points. It is unlike the conventional linear filtering where only spatial information is considered. It preserves the sharp boundaries well and averages the noise out as it average pixels belonging to the same region as the reference pixel. Mathematically, the bilateral filter output at a pixel location p is calculated as follows [16]:

$$I_F(p) = \frac{1}{W}\sum_{q\epsilon S} G_{\sigma_s}(\|p-q\|)G_{\sigma_r}(|I(p)-I(q)|)I(q) \tag{1}$$

$$G_{\sigma_s}(\|p-q\|) = e^{-\frac{p-q^2}{2\sigma_s^2}} \tag{2}$$

$$G_{\sigma_r}(|I(p)-I(q)|) = e^{-\frac{|I(p)-I(q)|^2}{2\sigma_r^2}} \tag{3}$$

$$W = \sum_{q\,\epsilon\, S} G_{\sigma_s}(\|p-q\|)G_{\sigma_r}(|I(p)-I(q)|) \tag{4}$$

Equation (2) represents a geometric closeness function, whereas Eq. (3) is a gray level similarity function. Equation (4) is a normalization constant, whereas $\|p-q\|$ is the Euclidean distance between p and q. The two parameters σ_s and σ_r control the behavior of the bilateral filter. Also the optimal σ_s value is relatively insensitive to noise variance compared to the optimal σ_r value and is chosen based on the desired amount of low-pass filtering. A large σ_s blurs more, i.e., it combines values from more distant image locations [28].

3.2.2 Segmentation of Region-of-Interest

FCM is an unsupervised fuzzy segmentation technique. The clusters are obtained iteratively by minimizing a cost function that depends on the distance of pixels to the cluster centers. Each data point may belong to more than one cluster with certain degrees of membership [9]. Therefore, it is especially useful for medical image segmentation where objects in the images do not have well-separated boundaries [9, 32]. FCM assigns pixels to clusters based on their fuzzy membership values. It strives to minimize the following cost function [9]:

$$J = \sum_{j=1}^{N} \sum_{i=1}^{c} u_{ij}^{m} \left\| x_j - c_i \right\|^2, \ 1 \le m \le \infty \tag{5}$$

where u_{ij} shows the membership of pixel x_j to *i*th cluster $\forall\ x_j \in \Omega$, where Ω represents the set of points that an image is composed. C and N represent a total number of clusters and data points in Ω, and vi is the centroid of the *i*th cluster. The constant m is also known as the degree of fuzziness and is usually set to 2 for most applications. The following mathematical expressions [4] are used to update the fuzzy membership functions and cluster centers, respectively:

$$u_{ij} = \frac{1}{\sum_{k=1}^{c} \left(\frac{\left\| x_j - c_i \right\|}{\left\| x_j - c_k \right\|} \right)^{\frac{2}{m-1}}} \tag{6}$$

$$c_i = \frac{\sum_{j=1}^{N} u_{ij} x_j}{\sum_{j=1}^{N} u_{ij}^{m}} \tag{7}$$

In this work, FCM image segmentation was employed to extract the contours of liver tumors automatically from US images. It integrates FCM with 'level set' technique to extract contours of liver tumors from US images with high reliability.

3.3 *Feature Extraction and Selection*

Feature extraction and selection are the most critical steps in CAD systems [2, 7, 17, 23–25, 31]. For the liver, the most commonly used features are textural measures by constructing spatial gray level dependence matrices, also termed as co-occurrence matrices that were introduced by Haralick et al. [11]. These features are normalized [0, 1] and then used as input to the SVM classifier.

In the proposed CAD system, five kinds of features (statistical, textural, run length, difference method, and histogram based features) were analyzed and extracted from the suspicious areas and ROIs. Usually, many features are extracted,

and we need to select the significant ones. In this paper, we apply the rough set theory [27] to select an optimal subset of features. These five sets of texture features were calculated for each ROI and combined into one set of features for image characterization. The five sets of texture features are listed as follows.

(1) **First order statistics (FOS)**: First order texture measures are statistically calculated from the original image values, such as variance. They do not consider pixel neighborhood relationships. Based on the image histogram, six features are used [26, 31]. Average gray level, standard deviation, entropy, the coefficient of variance, skewness, and kurtosis are obtained from each ROI [19].

(2) **Textural**: It based on co-occurrence matrices of the texture information also it is called the spatial gray-level dependence (SGLD) matrices. The gray level co-occurrence matrix (Second-order statistical model) gives relevant information about the inter-pixel relationship, periodicity, and spatial gray level dependencies. The analysis consists of the construction of sixteen different GLCM considering angles between pixels of 0°, 45°, 90° and 135°, for an inter-pixel distance equal to 1, 2, 3, and 4. Twenty-two descriptors have been extracted from each ROI, producing 325 features (22 GLCM features × 16 different GLCM). According to [24], it is using only the "near" and "far" displacements, which are enough to capture the spatial properties of the texture for the liver. It produces 88 features (22 GLCM features × 2 different GLCM).

(3) **Gray-Level Run Length Matrix Features**: Another measure of texture is based on run length. The image is scanned line by line and the length in pixels of each line is noted. Then, the relationship between each run length is identified. This relationship of all these statistical parameters run length makes a pattern. This pattern is a measure of the image texture. The average of all the line lengths (in pixels) in a region gives a measure of coarseness of the texture. GLRLM expresses the number of the consecutive image elements that have the same gray level (gray level run) [2]. Seven features are computed from GLRLM, as long run emphasis, short run emphasis, low gray level run emphasis, high gray level run emphasis, run length non-uniformity, gray level non-uniformity, and run percentage [7]. Feature values are averaged over four basic angular directions, 0°, 45°, 90°, 135°.

(4) **Gray-Level Difference Method (GLDM)**: The GLDM is based on the probability of occurrence that two pixels separated by a particular displacement vector have a given difference [26]. Four kinds of displacement vectors are considered, such as (0, d), (−d, d), (d, 0), (−d, −d), where d is the inter-sampling spacing distance. The five textural features used in the experiments are contrasted, angular second moment, entropy, mean, and inverse difference moment. In this study, the probability density functions are computed according to four kinds of vector displacements and textural features for each probability density function.

(5) **Histogram-Based Features**: It provides many clues to describe the characteristics of the image. Six statistical features are extracted from the histogram. They are mean, variance, skewness, kurtosis, energy, and entropy. The mean is the average intensity level, whereas the variance implies the variation of intensities around the mean. The skewness shows whether the histogram is symmetric about the mean. The kurtosis is a measure of whether the data are peaked or flat about a normal distribution. Entropy is a measure of the system disorder.

Many features are extracted with a strong correlation with each other. To select the significant ones from them. Feature selection is a very effective preprocessing step to the data mining in reducing dimensionality, increasing learning accuracy, and improving comprehensibility. To find the optimal subsets of the feature, the Rough set theory provides a mathematical approach to finding optimal feature subset. The Rough Set Theory (RST) was applied to reduce these features successfully and decide the most efficient ones.

Most classification problems involve a large set of potential features that must identify feature selection. Principal component analysis (PCA) is the most widely adopted traditional statistical method. However, the features selected using PCA are variable-independent but may not be the most benefit for a particular problem [32]. RST deals with the approximation of sets assembled from empirical data. RST is helpful in discovering the decision rules and minimizing the conditional attributes [27].

After extracting and selecting of the histogram features, FOS, GLDM, GLRM, and GLCM based texture features are calculated for the processed image. They are organized into a single feature vector. Each feature vector x_k consists of 112 features. Then, it is normalized and used as an input to the SVM classifier.

3.4 SVM Classification

SVMs are a new type of pattern classifier based on a novel statistical learning technique that recently proposed by Asa and Jason [2] and Ng [20]. Unlike (e.g. Neural Networks), which works on minimizing the empirical training error [20]. The criterion used by SVMs is based on maximizing the margin between the separating hyperplane and the data. The maximum margin classifier is the discriminant function. It maximizes the geometric margin $1/\|w\|$, which is equivalent to minimizing $\|w\|^2$. It leads to the following constrained optimization problem:

$$\begin{aligned} &\text{Minimize} \quad \tfrac{1}{2}\|w\|^2 \\ &\quad w; b \\ &\textit{subject to}: \; y_i(w^T xi + b) \geq 1 \;\; i = 1, \ldots, n \end{aligned} \tag{8}$$

Maximizing the margin, means searching for the classification function that can most safely separate the two data classes. The threshold separating two data classes is the line in the middle between the two margin boundaries, which are represented as $x^T w + b = 1$ and $x^T w + b = -1$. Thus, margin is $2/||w||$, where $||w||$ is the norm of the vector w. To determine the separating hyperplane, the margin between positive class and a negative class has to be maximized to produce good generalization ability [5]. In general, the RBF kernel maps samples into a higher dimensional space nonlinearly. Unlike the linear kernel, which handles the nonlinear case between class labels and attributes [6].

$$K(x_i, x_j) = \exp(-\gamma ||x_i - x_j||^2), \ \gamma > 0 \tag{9}$$

Gauss radial basis function SVM classification system was developed to discriminate the HCC. Five objective measurements (accuracy, sensitivity, specificity, positive predictive value, and negative predictive value) are used to evaluate the classification results. The higher the five measurements are, the more reliable and valid the CAD system is.

4 The Proposed Diagnostic System

The developed CAD system architecture is composed of four modules: preprocessing steps, feature extraction, feature selection and Multi-SVM classifier (Fig. 2).

The performance of the proposed CAD system was evaluated using the overall accuracy that expresses the correct percentage of classifier predictions. We have used the k-fold method to perform the cross-validation testing. The 10-fold cross-validation method randomly divides the dataset into ten groups. Nine groups of them are used for training and rest group for classifiers testing. This procedure is repeated until all groups have been used in the testing. The final result corresponds to the average accSX1uracy estimated for each iteration [17].

The classification performance is in terms of the four objective measurements Classification accuracy (ACC), sensitivity, specificity, and Negative Predictive value (NPV) were used to test the performance of classifiers models. ACC, sensitivity, specificity, and NPV are defined as follows according to the confusion matrix that is shown in Table 1 as follows [32]:

$$\text{Accuracy} = \frac{\text{TP} + \text{TN}}{(\text{TP} + \text{FP} + \text{TN} + \text{FN})} \times 100 \tag{10}$$

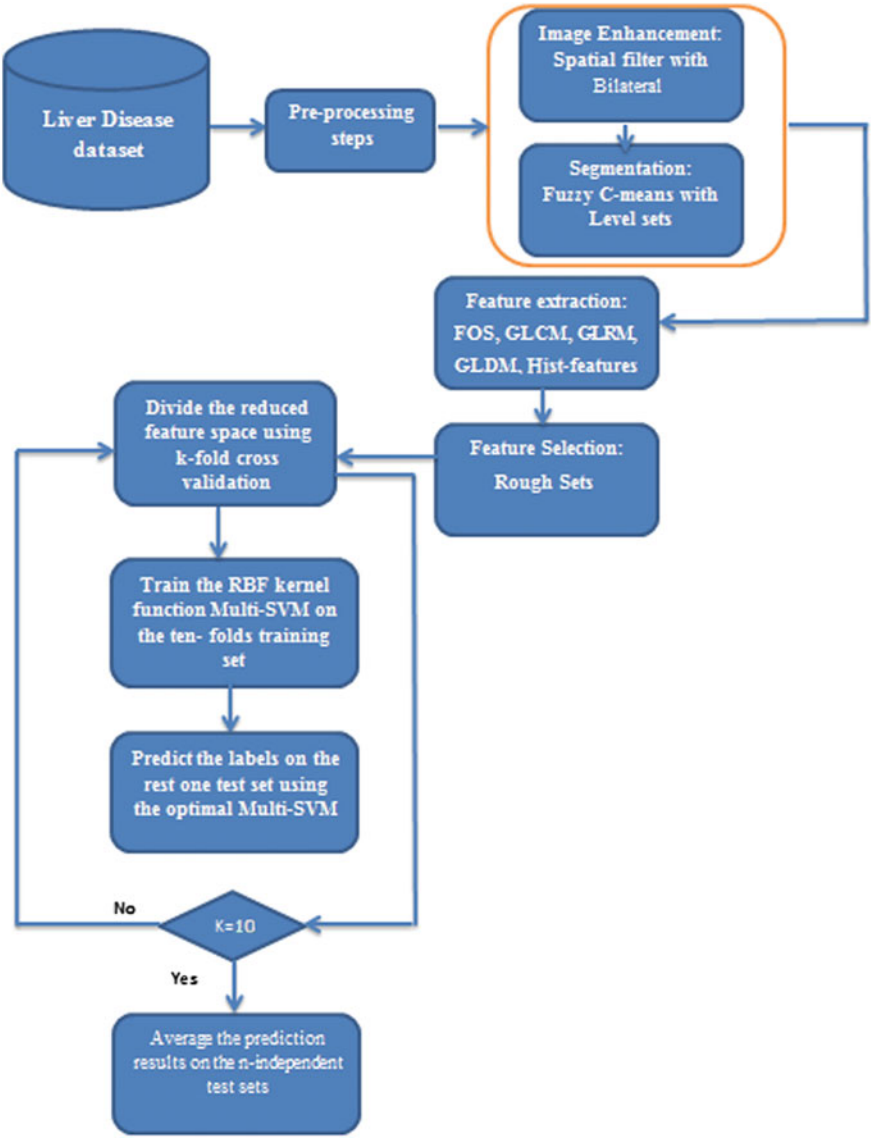

Fig. 2 Overall procedure of the proposed HCC multi-SVM-based diagnostic system

$$\text{Sensitivity} = \frac{\text{TP}}{\text{TP} + \text{TN}} \tag{11}$$

$$\text{Specificity} = \frac{\text{TN}}{\text{TN} + \text{FP}} \tag{12}$$

Table 1 Confusion matrix

		Predicted label	
		Positive	Negative
Known label	Positive	True positive (TP)	False negative (FN)
	Negative	False positive (FP)	True negative (TN)

$$\text{NPV} = \frac{\text{TN}}{(\text{TN} + \text{FN})} \times 100 \tag{13}$$

In the confusion matrix, TP is the number of true positives, which means that some cases with 'HCC' class are correctly classified as HCC. FN is the number of false negatives, which means that some cases with the 'HCC' class are classified as healthy persons. TN is the number of true negatives, which means that some cases with the 'Healthy' class are correctly classified as healthy persons. FP is the number of false positives, which means that some cases with the 'Healthy' class are classified as HCC [32].

5 Results and Discussion

The liver tumor US images are segmented and classified by our proposed technique. Figure 3a shows one of the original HCC ultrasound images. To reduce the speckle noise and improve the visualization of US images, bilateral filter, and non-linear noise reduction is applied to the original image, as shown in Fig. 3b.

As previously described, contours for tumor initialization has been determined automatically using the Level set, as shown in Fig. 3c. These contours are used for initializing FCM to obtain an accurate segmentation of HCC US images, as shown in Fig. 3d. The proposed approach of classifying the liver tumor US images is automatic, and hence no user intervention is required.

Higher classification accuracy has been obtained corresponding to images segmented by the mentioned technique that verify the positive influence of the proposed FCM-SVM algorithm for the classification process. For the liver case, the most commonly used features are related to textural measures by constructing spatial gray level dependence matrices also termed as co-occurrence matrices that were introduced by Haralick. These features are normalized in the range of [0, 1] and then used as input to the SVM classifier.

In this work, a total of 112 features has been extracted from each ROI of liver ultrasound images, namely six histogram features, 6 FOS, 5 GLDM, 7 GLRM and

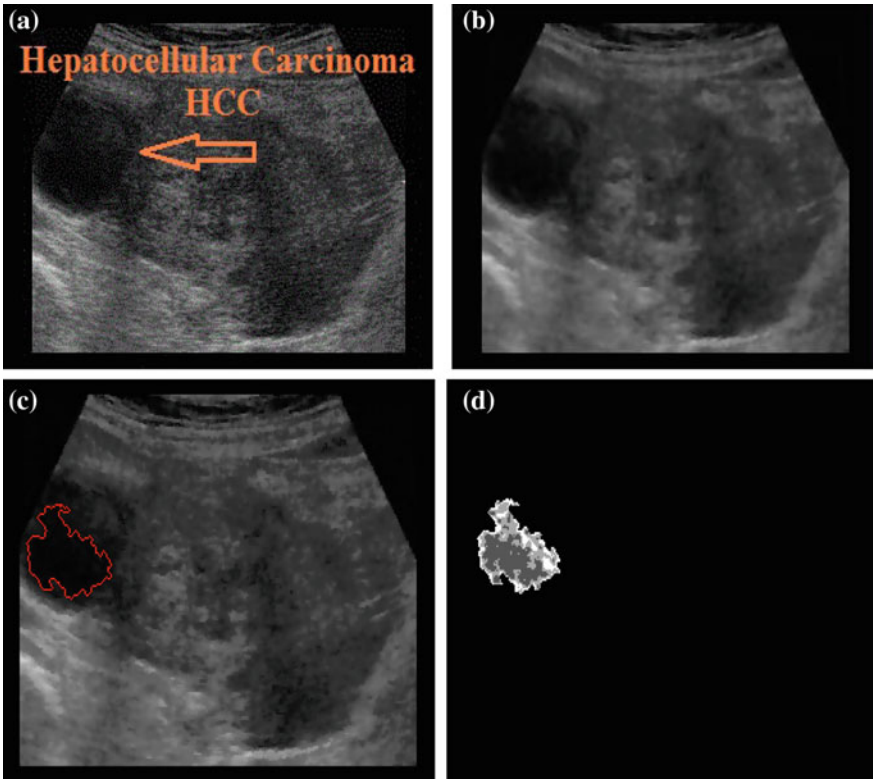

Fig. 3 The results using our proposed approach to automatic segmentation and classification system. **a** The original HCC image, **b** image enhanced by the bilateral filter, **c** initial contour of the level set, **d** segmented image by FCM

88 GLCM based texture features. These features have been measured from ROI for every normal and abnormal image. After dimensionality reduction using rough sets, 38 features were obtained. These features are used to train and test SVM classifier using k-fold cross validation (Table 2).

Table 3 shows the classification results based on 38 features obtained. It can be observed from Table 3 that classifying HCC using these features shows significant performance in terms of the four objective measurements accuracy, sensitivity, specificity, and Negative Predictive value (NPV). Furthermore, to check the performance of our proposed approach, KNN have been applied on the given dataset.

Table 3 shows a comparison between the proposed approach and KNN at different quality measures. From Table 2, it is clear that SVM gives superior performance compared to other techniques. Figure 4 shows the graphical performance comparison of KNN and Fuzzy C-SVM at various validity measures. Classification

Table 2 A comparison with some approaches to clustering and classification of Liver tissue

Authors	Liver image classes	Features	Pre-processing steps		Classifier	Dataset description	Evaluation method	Accuracy (%)
			Enhancement	Segmentation				
This study	Ultrasound focal liver lesions: Cyst, HEM, and HCC	FOS, GLCM, GLDM, GLRLM, histogram features	Spatial bilateral non-linear filter	FCM and level set	Multi-SVMRBF	Individual collected database, included 24Cyst, 33 HEM, 28 HCC and 11 normal	10-fold cross-validation	96.11
Virmani et al. [31]	Cyst, HEM, HCC, and MET	FOS, SGLDM, GLRLM, and Gabor wavelet methods	No pre-		PCA-SVM	Individual collected database, included 21 NOR images, 12 Cyst, 15 HEM, 28 HCC and 32 MET images with 35 MET	10-fold cross-validation	87.2
Andreia et al. [1]	Ultrasound steatosis liver	GLCM features × 9 different displacements 0°, 45° and 90°, for an inter-pixel distance equal to 1, 2 and 3	No pre-		SVM	Individual collected database, included 36 patients as normal and steatosis liver	10-fold cross-validation	76.92
Kumar and Shreyamsha [16]	Ultrasound focal liver lesions: Cyst, HCC, HEM, and MET	FOS, SGLDM, GLRLM, texture energy measures and Gabor wavelet methods	Using diamond shape template	Marked by an expert radiologist	A two-step neural network classifier	Individual collected database, included 16 normal, 17 Cyst, 15 HCC, 18 HEM and 45 MET	Manual	86.4

(continued)

Table 2 (continued)

Authors	Liver image classes	Features	Pre-processing steps		Classifier	Dataset description	Evaluation method	Accuracy (%)
			Enhancement	Segmentation				
Ribeiro et al. [19]	Chronic Hepatitis without cirrhosis, Cirrhosis, and HCC	Liver contour features with laboratory and clinical parameters	De-speckled	A snake technique	k-nearest neighbor	Individual collected database, included 88 image	Leave-one-out cross-validation	80.68
Ribeiro et al. [20]	Chronic Hepatitis without cirrhosis, Cirrhosis, and HCC	First order statistics, co-occurrence matrices, wavelet transform, with clinical and laboratory data	De-speckled	A snake technique	Kernel SVM	Individual collected database, included 97 patients	Leave-one-out cross-validation	73.20
Ribeiro et al. [21]	Chronic Hepatitis without cirrhosis, Cirrhosis, and HCC	First order statistics, co-occurrence matrices, wavelet transform, with clinical and laboratory data	De-speckled	Snake technique	Kernel SVM	Individual collected database, included 115 images	Leave-one-out cross-validation	81.25

Table 3 The performance of the proposed approach compared with KNN approach

		Accuracy (%)	Sensitivity (%)	1-Specificity (%)	NPV (%)
Classifier	Fuzzy C-SVM	84.44	97.3	75.00	66.66
	K-nearest neighbor	71.11	75.68	50.00	30.76

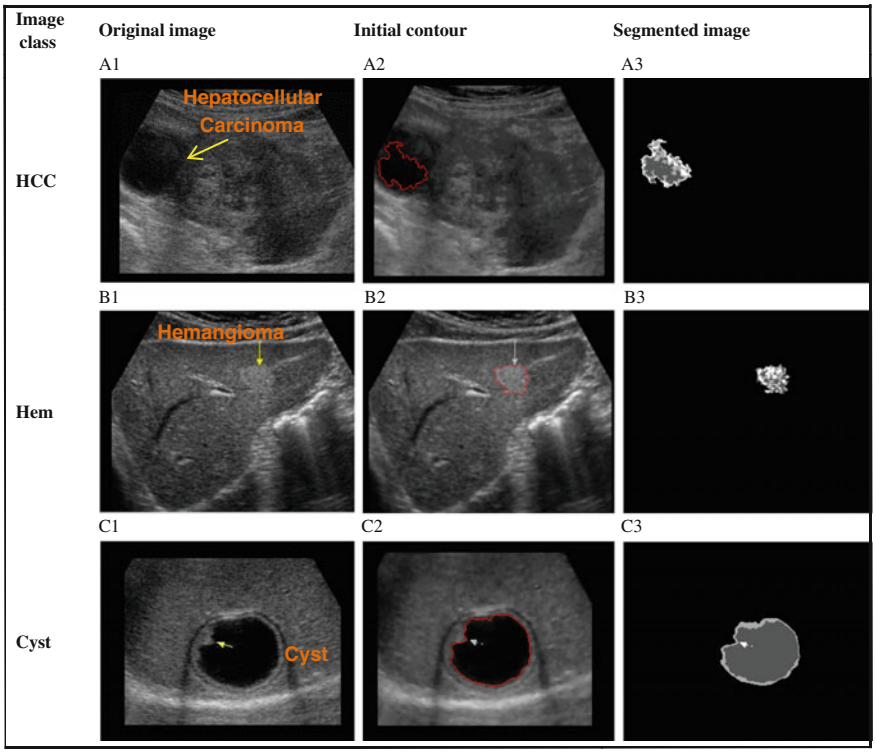

Fig. 4 Original, initialized, and segmented ultrasound images of three liver image categories

using SVM outperforms KNN technique at all validity measures. Image classification is one of the most important steps to know about the presence of HCC in liver images. In the proposed approach, SVM has been used for the classification of normal and abnormal images (Fig. 5).

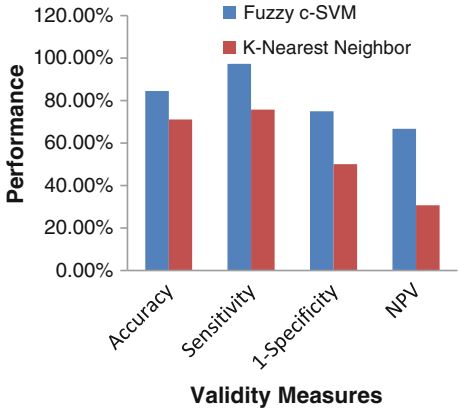

Fig. 5 Performance comparison of SVM and KNN classification techniques at different classification validity measures

6 Conclusion

This paper proposes using the image processing and image segmentation components prior to classification to improve decision accuracy. Another contribution of this work is developing an automatic classification system for HCC ultrasound images. Therefore, it is useful to discriminate normal and cancerous cases. The proposed approach of automatic contour initialization by level set shows the effectiveness of the method. The estimated features extracted from statistical, histogram, difference method, run length and textural approaches have led to encouraging results as inputs of the used classifiers. In our proposed approach, we have used SVM for the classification of normal and abnormal images. Different types of validity measures are calculated to show the effectiveness of the proposed approach. Using k-fold cross-validation to train and test Fuzzy C-SVM classifier, we have obtained 84.44 % classification accuracy and sensitivity 97.3 % using a 10-fold cross-validation method. A numerical comparison is made with K-nearest neighbor at different validity measures. In the future, we intend to extend the automatic classification system for various types of medical images to show the seriousness of other diseases. Further, exploring various types of features, which may be used to improve the accuracy of the classifier.

References

1. Andreia, A., Jose, S., Santos, J., et al.: Classifier approaches for liver steatosis using ultrasound images. Proc. Technol. **5**, 763–770 (2012)
2. Asa, B., Jason, W.A.: User's guide to support vector machines. Springer, data mining techn for the life sciences. Methods Mol. Biol. **609,** 223–239 (2010)
3. Badea, R., Ioanitescu, S.: Ultrasound imaging of liver tumors - current clinic apps. Liver Tumors (2012)

4. Balafar, M., Ramli, A., Saripan, M., Mahmud, R., et al.: Medical image segmentation using fuzzy c-mean (FCM). In: Learning Vector Quantization (LVQ) and User Interaction, vol. 15, pp. 177–184. Springer, Heidelberg (2008)
5. Bhat, H., Wani, M.: Modified one-against-all algorithm based on support vector machine. Int. J. Adv. Res. Comput. Sci. Softw. Eng. **3**(12) (2013)
6. Chih, W., Chih, C., Chih, J.: A Practical Guide to Support Vector Classification. Citeseerx (2010)
7. Dimitris, G., Ioannis, K., Theocharakis, P., et al.: A multi-classifier system for the characterization of normal, infectious, and cancerous prostate tissues employing transrectal ultrasound images. Comput. Methods Programs Biomed. **97**, 53–56 (2010)
8. Dimitris, K., Eystratios, G., Dimitris, M.: Fusion of fuzzy statistical distributions for classification of thyroid. Artif. Intell. Med. **50**, 33–41 (2010)
9. Dzung, L., Chenyang, X., Jerry, L.: A survey of current methods in medical image segmentation. Ann. Rev. Biomed. Eng. **2**, 315–338 (2000)
10. Garla, V., Taylor, C., Brandit, C.: Semi-supervised clinical text classification with Laplacian SVMs: an application to cancer case management. J. Biomed. Inform. **46**(5), 869–875 (2013)
11. Haralick, R., Shanmugam, K., Dinstein, H.: Textural features for image classification. IEEE Trans. Syst. Man Cybern. SMC8211 **3**(6), 610–621 (1973)
12. Hassanien, A.E.: Classification and feature selection of breast cancer data based on decision tree algorithm. Int. J. Stud. Inform. Control J. SI **12**(1), 33–39 (2003)
13. Hassanien, A.E., Moftah, H.M., Azar, A.T., Shoman, Mahmoud: MRI breast cancer diagnosis hybrid approach using adaptive ant-based segmentation and multilayer perceptron neural networks classifier. Appl. Soft Comput. **14**, 62–71 (2014)
14. James, P., Skowron, A.: Transactions on Rough Sets. Springer, Heidelberg (2008)
15. Jeon, J., Choi, J., Sihyoung, L., et al.: Multiple ROI selection based focal liver lesion classification in ultrasound images. Expert Syst. Appl. **40**, 450–457 (2013)
16. Kumar, B., Shreyamsha, K.: Image denoising based on gaussian/bilateral filter and its method noise thresholding. SIViP **7**, 1159–1172 (2013). Springer, London
17. Liu, B., Cheng, H., Jianhua, H.: Fully automatic and segmentation-robust classification of breast tumors based on local texture analysis of ultrasound images. Pattern Recogn. **43**, 280–298 (2010)
18. Mittal, D., Kumar, V., Suresh, C., et al.: Neural network based focal liver lesion diagnosis using ultrasound images. Comput. Med. Imaging Graph. **35**, 315–323 (2011)
19. Namita, A., Agrawal, R.: First and second order statistics features for classification of magnetic resonance brain images. J. Signal Inf. Process. **3**, 146–153 (2012)
20. Ng, A.: Support Vector Machines, Lecture notes. CS 229 Machine Learning, Course Materials, CS229 Lecture Notes (2008)
21. Ribeiro, R., Marinho, R., Velosa, J., et al.: The usefulness of ultrasound in the classification of chronic liver disease. In: IEEE Annual International Conference, Engineering in Medicine and Biology Society, EMBC, pp. 5132–5135 (2011)
22. Ribeiro, R., Marinho, R., Velosa, J., et al.: Diffuse Liver Disease Classification from Ultrasound Surface Characterization, Clinical, and Laboratorial Data, pp. 167–175. Springer, Heidelberg (2011)
23. Ribeiro, R., Rui, M., Velosa, J., Ramalho, F., et al.: Chronic liver disease staging classification based on ultrasound clinical and laboratorial data. In: IEEE International Symposium, Biomedical Imaging: From Nano to Macro, pp. 707–710 (2011)
24. Ruchaneewan, S., Daniela, R., Jacob, F., et al.: A co-occurrence texture semi-invariance to direction, distance, and patient size. In: Proceedings of SPIE, Medical Imaging: Image Proceedings, vol. 6914, p. 69141Y (2008)
25. Sohail, A., Bhattacharya, P., Sudhir, P., et al.: Content-based retrieval and classification of ultrasound medical images of ovarian cysts. Artif. Neural Netw. Pattern Recogn. **5998**, 173–184. Springer, Heidelberg
26. Srinivasan, G.: Statistical texture analysis proceedings of world academy of science engineering, and technology. **36**, 1264–1269 (2010)

27. Stoean, R., Stoean, C., Lupsorb, M., et al.: Evolutionary-driven support vector machines for determining the degree of liver fibrosis in chronic hepatitis c. Artif. Intell. Med. **51**, 53–65 (2011)
28. Sylvain, P., Pierre, K., Jack, T., Fredo, D.: Gentle introduction to bilateral filtering and its applications. In: Proceeding ACM SIGGRAPH '8, Article No. 1, New York, USA (2008)
29. Tomasi, C., Manduchi, R.: Bilateral filtering for gray and color images. In: Proceedings of the IEEE International Conference on Computer Vision, pp. 839–46, New Delhi, India (1998)
30. Vikrant, B., Gopal, S., Atul, S.A.: Novel weighted diffusion filtering approach for speckle suppression in ultrasound images. In: Proceedings of (Springer) International Conference on Frontiers in Intelligent Computing Theory and Applications (FICTA 2013), AISC, vol. 247, pp. 459–466 (2013)
31. Virmani, J., Kumar, V., Kalra, N., Khandelwal, N.: PCA-SVM based CAD System for Focal Liver Lesions using B-Mode Ultrasound Images. Defence Sci. J. **63**(5), 478–486 (2013)
32. Wen, J., Shih, W., Lin, W., et al.: Combining support vector machine with genetic algorithm to classify ultrasound breast tumor images. Comput. Med. Imaging Graph. **36**, 627–633 (2012)

Part III
Computer Aided Diagnosis (CAD) Tools and Case Studies

Ultrasound Based Three Dimensional Computer Aided Diagnosis (CAD) Tool for the Diagnosis of Anterior Talofibular Ligament

Vedpal Singh, Irraivan Elamvazuthi, Varun Jeoti, John George, Norashikin Yahya and Dileep Kumar

Abstract Ultrasound imaging is an investigative tool to imagine the internal organisms of human beings. Ultrasound imaging has benefits such as low cost, portability, non-ionization and real time nature. However, ultrasound imaging has limitations also like homogenous intensity regions, homogeneous textures and low contrast regions. To overcome these investigated problems, this research is developed a Computer Aided Diagnosis (CAD) system that helped in the achievement of efficient segmentation and three dimensional reconstruction of anterior talofibular ligament to enhance the diagnosis. The developed CAD system would provide the information about the input dataset, segmented results and statistical analysis of injured anterior talofibular ligament. The analysis based on the obtained results indicates the improved performance of the developed CAD system with more than 94 % accurate results. In addition, this research opens new research dimensions for efficient musculoskeletal ultrasound modelling that makes it useful in clinical settings with accurate and cost effective diagnosis of anterior talofibular ligament injuries.

1 Introduction

1.1 General Introduction

Human beings are increasingly surrounded by injuries and abnormalities in various anatomical parts specifically ankle ligaments. Ankle ligament is a short band of tough fibrous connective tissues made by long, strongly collagen fibers. Generally,

V. Singh · I. Elamvazuthi (✉) · V. Jeoti · N. Yahya · D. Kumar
Department of Electrical and Electronic Engineering, Centre for Intelligent Signal and Imaging Research (CISIR), Universiti Teknologi Petronas, 32610 Bandar Seri Iskandar, Perak Darul Ridzuan, Malaysia
e-mail: irraivan_elamvazuthi@petronas.com.my

J. George
Research Imaging Centre, University of Malaya, 50603 Kuala Lumpur, Malaysia

N. Dey et al. (eds.), *Medical Imaging in Clinical Applications*,
Studies in Computational Intelligence 651, DOI 10.1007/978-3-319-33793-7_10

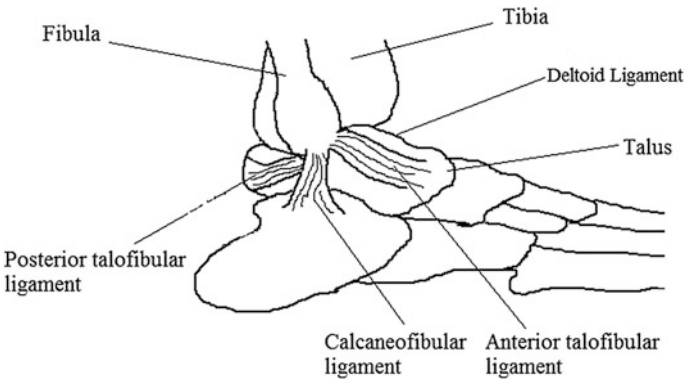

Fig. 1 Ankle ligaments

ligaments connect bones to the other bones for making a joint [1]. Although ligaments by nature are very strong and rigid, but sometimes strains and sudden forces may be the main causes of injuries such as tear, bruise, rupture etc. [2]. Ligament injuries were frequently seen in association with joint debris and diffuse bone marrow edema. Indeed, there was often coexistence of these features, so it was difficult to determine which may have occurred first in the patients [3].

Basically, ankle comprises of four (4) kinds of ligaments such as Anterior Talofibular Ligament (ATFL), Posterior Talofibular Ligament (PTFL), Calcaneofibular Ligament (CFL) and Deltoid Ligament (DL) [3] that are illustrated in Fig. 1.

Figure 1 is indicating the location of all four ligaments as well as fibula, tibia and talus bones of ankle. Generally, ankle ligaments prone to injuries due to sports, accidents, high ankle sprains and inflammation [4]. The most common cause of injuries in ankle ligaments is due to the inversion of foot [3, 5] that mostly damaged the ATFL ligament [6]. However, a total rupture involves the injuries in CFL and PTFL as well [7]. Another kind of injury is eversion that leads to damage in DL ligament [8], which is rare. Generally, ankle can be visualized into lateral and medial views. In lateral view, only ATFL, PTFL and CFL ligaments are visualized, but DL ligament can be seen in medial view [9, 10]. The causes of injuries in lateral and medial views of ankle [11] is presented in Fig. 2.

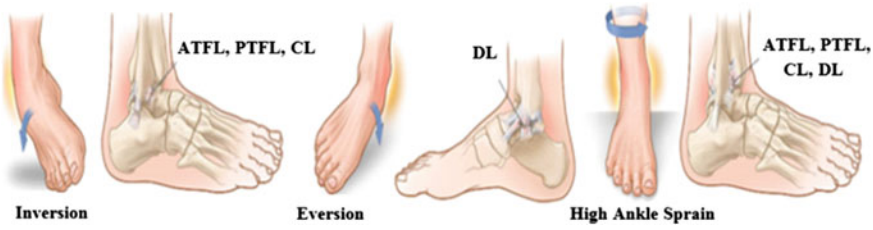

Fig. 2 Causes of ligament injury [11]

1.2 Prevalence of ATFL Injuries

ATFL is a most injury prevalent ligament of ankle during sports, accidents and active life style. However, sport is an important recreational and professional activity, which is growing worldwide, which are the main causes of injuries. In earlier studies, it was estimated that 20 % sports persons sustain injuries every year [12]. Moreover, it was reported in earlier studies that 15–20 % of the sports injuries are belong to ankle and out of these 80 % injuries related to ligaments. Therefore, the ATFL is found to be the most injury prevalent ligament of ankle [3, 13, 14]. Ankle distortions and ligament injuries are among the most frequent of all injuries. The incidence in general population was estimated that 1 ankle injury per 10,000 people per day [5]. It means, approximately 23,000 patients in the USA and approximately 5,000 patients in Great Britain have to receive medical treatment for ankle injuries every day [13]. Moreover, in Netherlands, the number of ankle injuries at an annual incidence rate of 12.8 persons per 1000 is estimated at approximately 200,000 per year [14]. Applying these figures to Malaysia means approximately 3000 ankle injuries can be expected per day, which equals more than 1 million patients per year [5, 6]. Acute ankle injuries are the most frequent in all kinds of injuries due to the rapid changes in foot direction, high jumps and contact with opposing objects are especially risky for the ankle ligaments. In all kinds of sports, high incidence of acute ankle injuries in football (20–25 %), basketball and volleyball (25–30 %) [15]. Surprisingly enough, there does not appear to be a significant difference in the injury rates among recreational and professional athletes [16].

The earlier studies are estimated that the ankle injury rates duration the training of rugby (4.2 injuries per 1000 h of training), football (2.52 injuries per 1000 h of training), volleyball (1.99 injuries per 1000 h of training), and basketball (1.00 injuries per 1000 h of training) [15]. The frequency of injuries rises significantly during competitions up to 11.68 injuries per 1000 h of play in football [16]. However, occurrences of injuries are also depends on anatomical regions as shown in Fig. 3 [17, 18].

Figure 3 illustrated the injury frequency in specific anatomical portions such as abdomen, arm, head, knee, ankle, hands, shoulder, foot, leg, wrist, dorsal region and lumber region of spinal cord [19–21]. In recent studies, many researchers [22–25] investigated some current problems such as ligament laxity, damage, inflammation and calcification related to ankle using 2D ultrasound imaging.

1.3 Current Imaging Methods for Diagnosis

Currently, Magnetic Resonance Imaging (MRI), X-Ray and Computed Tomography (CT) are capable to visualize the injuries in ATFL ligament, but they have some limitations such as limited availability, high cost, long examination time and patient

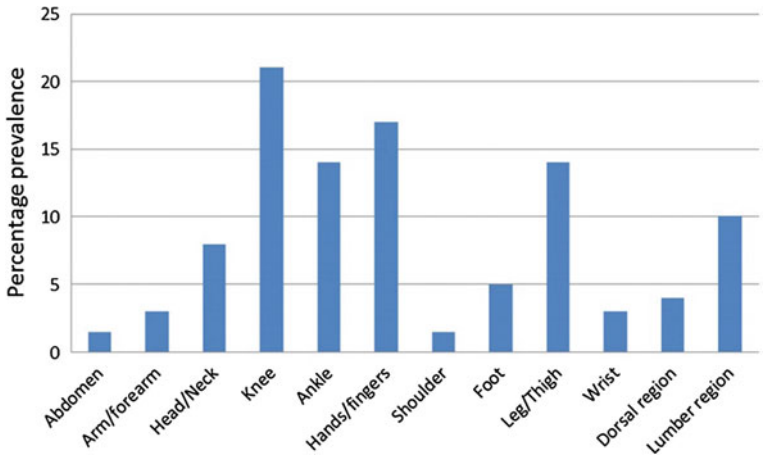

Fig. 3 Injury frequency according to specific anatomical regions (in percentage) [17]

agitation [26]. Alternatively, ultrasound imaging is emerged as a popular imaging modality in a number of medical imaging applications due to its lower cost, wide reach, flexibility, lack of radiation, and intra-operability nature [14, 27, 28]. In addition, earlier studies [29–33] have been stated that inflammation in joints and ligaments can easily detected by ultrasound method with good specificity and sensitivity. In general, the ATFL ligament is indicated by green boundary in 2D ultrasound image with labelling of ligament, bones and cartilages as shown in Fig. 4.

As shown in Fig. 4, ultrasound image introduces the difficulties for less-experienced clinicians to estimate the location of injuries in ATFL during diagnosis. Therefore, clinicians are demanding more advancement in 2D ultrasound imaging. The investigated problems can be resolved by image processing like segmentation and 3D reconstruction of desired region.

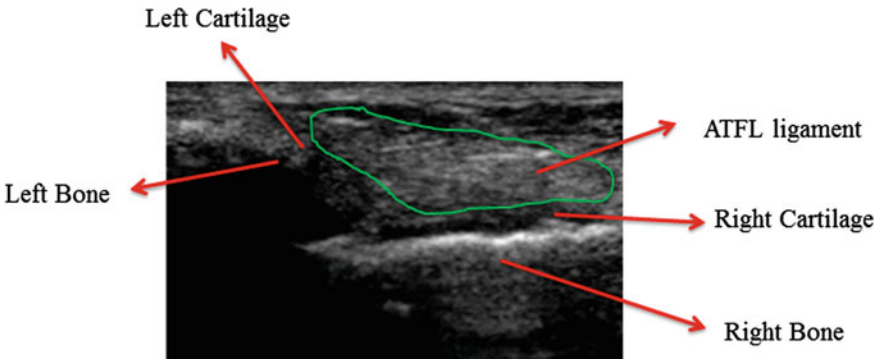

Fig. 4 Ultrasound image of ATFL ligament: irregular shape and structure of ATFL represented by *green boundaries*

2 Problem Formulation

As seen earlier in Fig. 4, ATFL ligament is indicated in ultrasound image by the green color boundary with diverse thickness at different locations that turn to wrong interpretation. The some other main causes of wrong interpretation in ultrasound images of ATFL exhibit homogeneous texture and homogeneous signal intensities compared to surrounded organs as shown in Fig. 5a, b, respectively. Moreover, low contrast in some regions of ATFL makes it difficult to interpret the defects in ATFL as shown in Fig. 5c. Due to the issues existing with ultrasound images of ATFL, direct interpretation and visualisation of defects associated with injured ATFL is not recommended that requires involvement of computation methods to delineate the ATFL from ultrasound images, which leads to produce enhanced results prior to start the treatment.

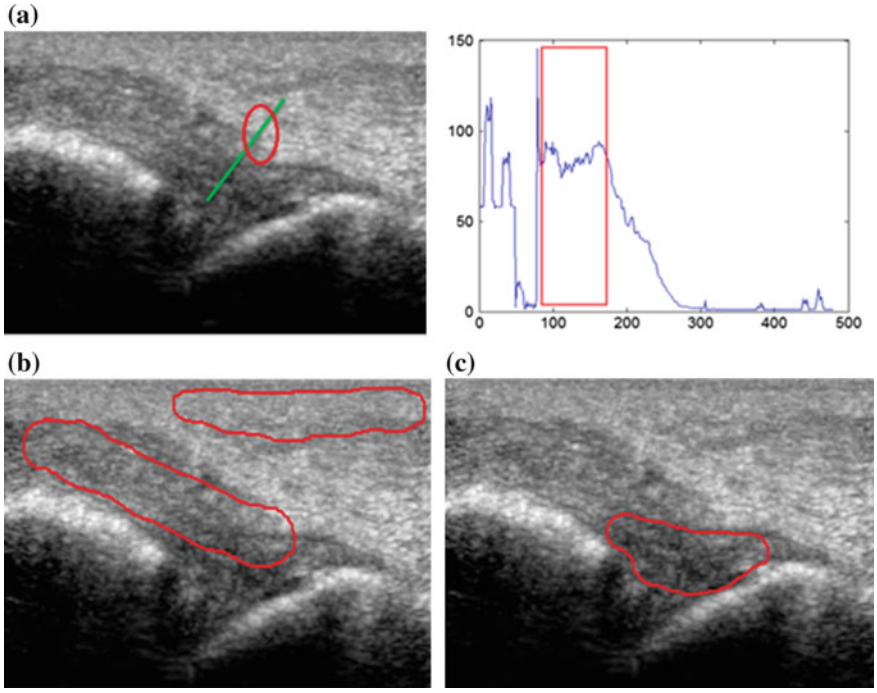

Fig. 5 Ultrasound image of Ankle ATFL ligament. **a** Ultrasound image of ATFL and corresponding intensity graph showing homogeneous nature between ATFL and surrounding tissues, **b** homogeneous texture in ATFL and surrounding tissues is represented region of interest highly by *red circles* and **c** low contrast within ATFL region represented by region of interest in *red color*

Due to the challenges mentioned above, segmentation of ATFL from ultrasound images remains a challenging task that has not been studied at wide, but it can lead to disease diagnosis in therapy and image guided interventions. Research has shown that there are numerous methods such as region based, edge based, thresholding based, wavelet based, pattern or texture classification based and deformable based, which are available for the segmentation [26, 34]. However, each method have own limitations such as dependency based on edge, region and thresholding. In addition, a specific association of segmentation methods such as non-parametric probabilistic model with shape driven based methods are researched earlier [18, 35]. Likewise, this research used the association of region of interest initialization, adaptive histogram equalization, Darwinian Particle Swarm Optimization (DPSO), Chan-Vese method and morphological operations to achieve the better results. This unique association would leads to enhanced diagnosis of ATFL by producing the 2D segmented results. However, segmented ultrasound images introducing some problems such as limited view visualization, inaccurate qualitative and quantitative estimation during diagnosis [14]. In order to resolve these problems, this research developed a CAD system that uses the integration of data acquisition, segmentation and 3D reconstruction approaches. Computer Aided Diagnosis (CAD).

3 The Developed Computer Aided Diagnosis (CAD) System

This section demonstrates the process flow of the developed CAD system that comprises of data acquisition, segmentation and 3D reconstruction as shown in Fig. 6. The functionalities of the segmentation include data acquisition using readily available device, pre-processing, optimization and ROI (Region of Interest) extraction, morphological operations that would produce the accurate segmented results. Furthermore, the 3D reconstruction involved four steps such as image registration, enhanced Marching Cube method to reconstruct a 3D mesh, which is followed by patching and rendering to reconstruct a 3D model. The reconstructed 3D model is used in volume calculation.

Table 1 demonstrated the pseudocode of the developed CAD system, which provides the process information about each step. Furthermore, the CAD system is tested on acquired datasets using Matlab version 2012b [36–39]. The total images that represent the ATFL ligament at different locations, contrast and patterns are processed using the developed CAD system. In addition, performance evaluation of this CAD system is carried out on the basis of obtained results to validate this research.

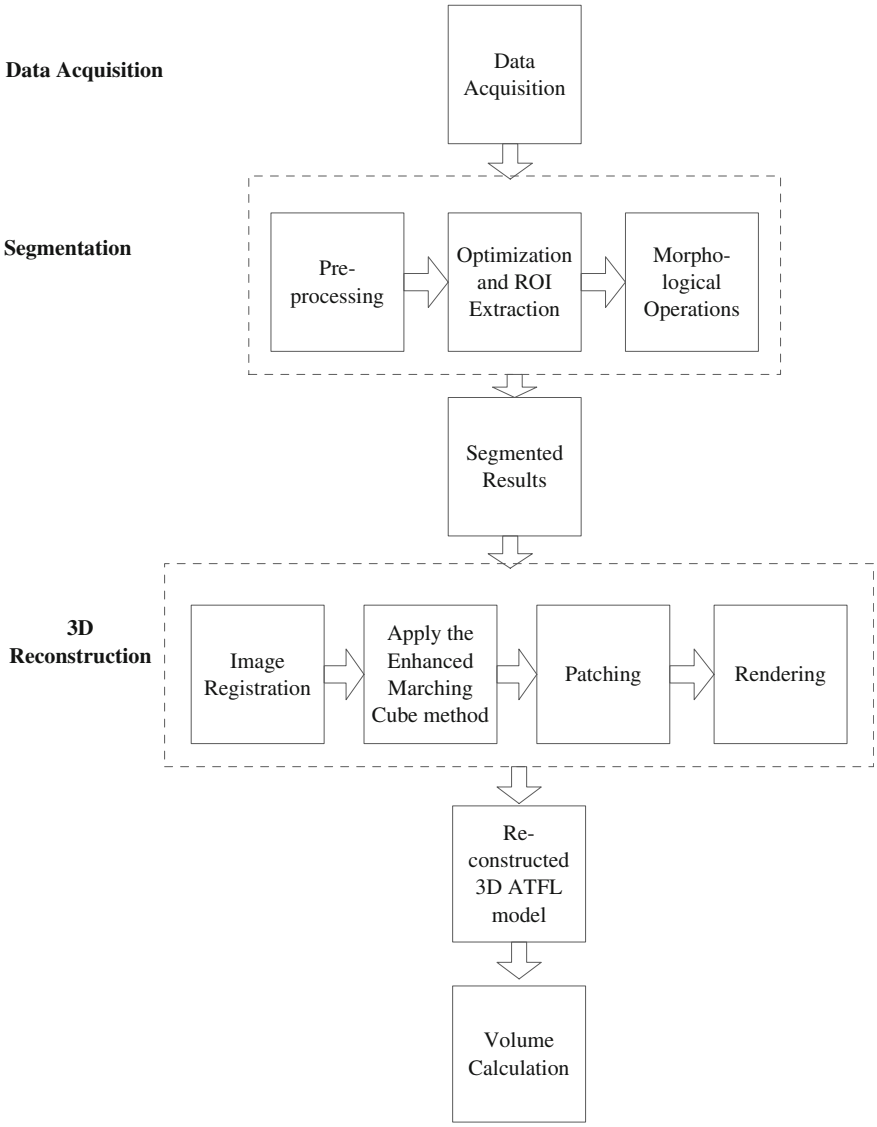

Fig. 6 Flow chart of the developed CAD system

Table 1 Pseudocode of the developed CAD system

if acquired data is *accurate*
    Go for *image _segmentation*
else
    Collect data again
end

if *image _segmentation* is successful
    Adjust the images through *image _ registration*
else
    Apply *image _segmentation*
end
if *image _ registration* is *accurate*
    Apply $3D$ smoothing
else
    Apply *image _segmentation*
end
if $3D$ smoothing *is successful*
    Apply $3D$ median filtering
else
    Try to smooth again
end
if $3D$ median filtering *is successful*
    Apply *s* tan*dard _marching _cube* method
else
    Filter using $3D$ median filtering
end
Patching is performed on the obtained $3D$ mesh
Patched $3D$ mesh is smoothed by the *Rendering method* for better visualization

4 Validation Metrics

4.1 Performance Evaluation Metrics for Segmentation

4.1.1 Peak Signal to Noise Ratio (PSNR)

PSNR is the ratio between the maximum possible power of signal and power of corrupted noise that presents the accuracy of the image as presented in Eq. 1 as follows:

$$\begin{aligned} PSNR &= 10 \cdot \log_{10}\left(\frac{MAX_I^2}{MSE}\right) \\ &= 20 \cdot \log_{10}\left(\frac{MAX_I}{\sqrt{MSE}}\right) \\ &= 20 \cdot \log_{10}(MAX_I) - 10 \cdot \log_{10}(MSE) \end{aligned} \tag{1}$$

where, MAX_I represents the maximum possible pixel value in image and MSE is the Mean Square Error [40, 41].

4.1.2 Standard Deviation (SD)

Standard deviation determines the variation of a set of data values. Low value represents the closeness to the mean and standard deviation indicates the extreme gap to the mean, which is described in Eq. 2.

$$S_N = \sqrt{\frac{1}{N}\sum_{i=1}^{N}(x_i - \bar{x})^2} \tag{2}$$

where $\{x1, x2, \ldots, xN\}$ are the observed values of the sample items and $\bar{x}$ is the mean value of these observations, while the denominator N stands for the size of the sample: this is the square root of the sample variance, which is the average of the squared deviations about the sample mean [42].

4.1.3 Root Mean Square Error (RMSE)

RMSE helps in the calculation of the root of power two (2) for Standard Deviation that measures the difference between predicted and actual values as demonstrated in Eq. 3:

$$RMSE = \sqrt{\frac{\sum_{i=1}^{n}(\bar{y}_i - y_i)^2}{n}} \tag{3}$$

where, $\bar{y}_i$ depicts the predicted value and y_i presents the actual value. n indicates the total number of predictions [40].

4.1.4 Universal Image Quality Index (UIQI)

UIQI is an integration of three elements such as loss of correlation, luminance distortion and contrast distortion as presented in Eq. 4:

$$Q = \left(\frac{\sigma_{xy}}{\sigma_x \sigma_y}\right) * \left(\frac{2\bar{x}\,\bar{y}}{(\bar{x})^2 + (\bar{y})^2}\right) * \left(\frac{2\sigma_x \sigma_y}{\sigma_x^2 \sigma_y^2}\right) \tag{4}$$

where, $x = \{x_i | i = 1, 2, \ldots, N\}$ and $y = \{y_i | i = 1, 2, \ldots, N\}$. The σ_x and σ_y are the estimate of the contrast of x and y [40].

4.1.5 Mean Absolute Error (MAE)

MAE used to measure how close forecasts or our predictions are to the eventual outcomes, which is defined in Eq. 5 [40]:

$$MAE = \frac{1}{n}\sum_{i=1}^{n} |f_i - y_i| = \frac{1}{n}\sum_{i=1}^{n} |e_i| \tag{5}$$

where f_i is the predicted value and y_i is the actual value. The e_i depicts the absolute error and n is the total number of predictions [40].

4.1.6 Normalized Absolute Error (NAE)

NAE measures the closeness between the two digital images by exploiting the difference in the statistical distribution of the pixel values as presented in Eq. 6.

$$NAE = \frac{\sum_{i=1}^{M}\sum_{j=1}^{N} [\bar{I}(i,j) - I(i,j)]}{\sum_{i=1}^{M}\sum_{j=1}^{N} |I(i,j)|} \tag{6}$$

where $\bar{I}(i,j)$ represents the pixel values of original image and $I(i,j)$ depicts the pixel values of enhanced image [40].

4.1.7 Normalized Cross Correlation (NCC)

In image processing, normalization is required in variable circumstances of brightness, lighting and exposure situations. It can be done by the NCC method, which is represented in Eq. 7:

$$\frac{1}{n}\sum_{x,y}\frac{(f(x,y)-\bar{f})(t(x,y)-\bar{t})}{\sigma_f\sigma_t}=\frac{\frac{1}{n}\sum_{x,y}f(x,y)t(x,y)-\bar{f}.\bar{t}}{\sigma_f\sigma_t} \tag{7}$$

where $t(x,y)$ represents the cross-correlation of template and $f(x,y)$ is the sub image. The number of pixels is n in $t(x,y)$ and $f(x,y)$, $\bar{f}$ is the average of f and σ_f is standard deviation of f. In functional analysis terms, this can be thought of as the dot product of two normalized vectors [40].

4.1.8 Sensitivity

Sensitivity is the proportion of true positives that are correctly identified by a diagnostic test. It shows how good the test is at detecting a disease, which is illustrated in Eq. 8 [43].

$$Sensitivity=\frac{TP}{TP+FN} \tag{8}$$

where, True Positive (TP) is the number of pixels correctly labelled as ATFL region, False Negative (FN) is the number of pixels incorrectly labelled as non-ATFL region.

4.1.9 Specificity

Specificity is the proportion of the true negatives correctly identified by a diagnostic test. It suggests how good the test is at identifying normal condition (see Eq. 9) [43].

$$Specificity=\frac{TN}{TN+FP} \tag{9}$$

where, True Negative (TN) is the number of pixels correctly labelled as non-ATFL region, False Positive (FP) is the number of pixels incorrectly labelled as ATFL region.

4.1.10 Accuracy

Accuracy is the proportion of true results, either true positive or true negative, in a population. It measures the degree of accuracy of a diagnostic test on a condition (see Eq. 10) [43].

$$Accuracy = \frac{TP + TN}{TP + FP + FN + TN} \tag{10}$$

4.2 Performance Evaluation Metrics for 3D Reconstruction

This research used the MINKOWSKI measures [44] to validate the performance of the proposed method. The utilized parameters are explained in Eqs. 11–15 as follow.

4.2.1 Volume Calculation

The ordinary way for volume estimation is to determine the total number of voxels in reconstructed 3D model and multiply with the size of a voxel. Likewise, MINKOWSKI measures also used the similar method to calculate the volume as defined in Eq. 11:

$$V_d(B) = \Delta_1\Delta_2\Delta_3 \#\{X_d \cap B\} \quad B \subset L^d \tag{11}$$

where V represents the volume, d depicts the dimensions (for 3D model $d = 3$), B indicates the used 3D model to calculate the volume. $\Delta_1\Delta_2\Delta_3$ and $\#\{X_d \cap B\}$ are presents voxel size and number of voxels in the 3D model, respectively. X indicates the digitized structure of a 3D model and L^d represents the rectangular grid, where $d = 3$ [44].

4.2.2 Thickness Calculation

MINKOWSKI measurement is also used in the calculation of thickness of the reconstructed 3D model as presented in Eqs. 12 and 13:

$$AT = \frac{S_v}{\pi L_v} \tag{12}$$

$$S_v = \frac{S}{W} \tag{13}$$

where, AT represents the Average Thickness of the 3D model. S depicts the surface and W is the sampling window of volume. L_v indicates the edge density and S_v is the surface density of 3D model [45].

4.2.3 Roughness Calculation

Surface roughness (R'_{zi}) is a component of surface texture, which can be calculated as presented in Eqs. 14 and 15:

$$R'_z = \frac{\sum_{i=0}^{N-M} R'_{zi}}{N - M + 1} \tag{14}$$

$$R'_{zi} = \max\{p_{i+1}, \ldots, p_{i+M}\} - \min\{p_{i+1}, \ldots, p_{i+M}\} \tag{15}$$

where, R'_{zi} represents the surface roughness. M is the measured amplitudes from the total of N amplitudes $p_1, \ldots, p_N$ [46].

5 Results and Analysis

5.1 Segmentation of ATFL Ligament Through Developed CAD System

The performance of the developed CAD system is determined by the implementation on 25 patients' datasets. However, only one sample image is used to demonstrate the complete process flow of segmentation with the corresponding results as depicted in Fig. 7.

Initially, the input image is pre-processed using the ROI initialization as shown in Fig. 7a. Thereafter, the obtained image is enhanced by the contrast enhancement method (e.g. adaptive histogram equalization method) as shown in Fig. 7b, in which the ATFL region is visualized more clearly than the original image. The pre-processed results are further used in optimization and ROI extraction as illustrated in Fig. 7c, d, respectively that aim to extract the desired ATFL region more accurately through the energy minimization and curve evolution process. The extracted ATFL region is illustrated Fig. 7e, whose boundaries are not smooth enough. To overcome this issue, morphological operation is applied that produced the more accurate results (see Fig. 7f). Furthermore, the smoothed image is overlaid on the input image to get the better and actual visualization, which is presented in Fig. 7g.

5.2 3D Reconstruction of ATFL Ligament Through Developed CAD System

The obtained segmented results further used in 3D reconstruction of ATFL ligament for better diagnosis. In this study, only 50 images per patient were used in the

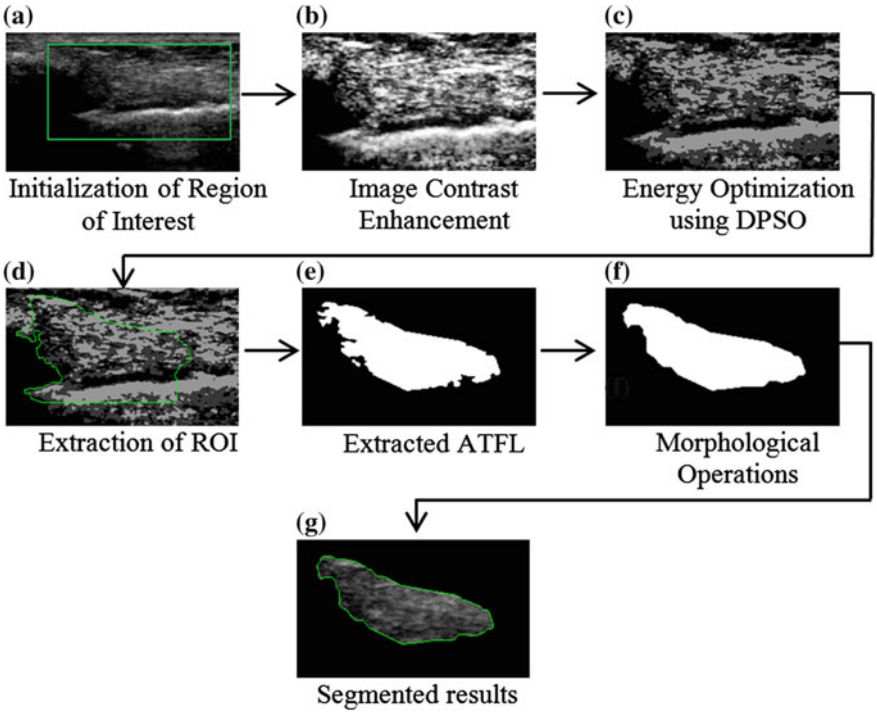

Fig. 7 The developed CAD segmentation processing

experiments. For 3D reconstruction, this research initially used the image registration algorithm to adjust the orientation of segmented images with respect to one reference image as shown in Fig. 8a.

As illustrated in Fig. 8a, the accurately oriented images are further processed by the enhanced marching cube algorithm to design the 3D mesh model. The obtained 3D mesh is efficiently converted into the 3D model by the patching operation (see Fig. 8c), which is not smooth enough. To produce the smooth 3D models need to use rendering as described in Fig. 8c. For better understanding, the reconstructed 3D model is depicted in Fig. 9.

Figure 9 illustrated the reconstructed 3D model of the ATFL ligament that comprises of ligament, both side cartilage and bones, which are labelled by the different colors for better understanding. Ligament is indicated by light brown color and cartilage is presented by red color. Likewise, green color is used for the presentation of bones.

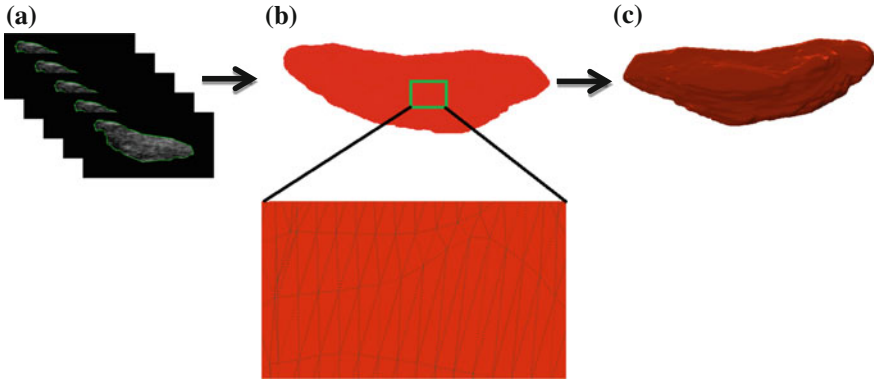

Fig. 8 3D reconstruction of ATFL. **a** Segmented and accurately oriented images, **b** 3D mesh image and data patching by the marching cube algorithm, **c** rendering

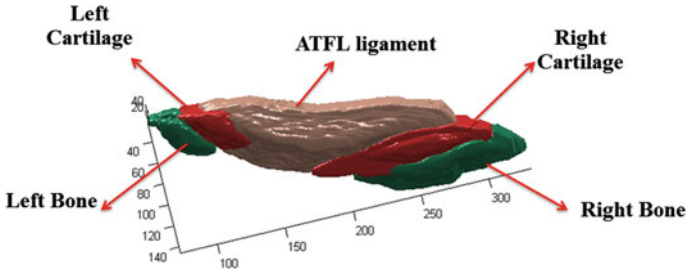

Fig. 9 Reconstructed 3D model by the developed CAD system

5.3 *Graphical User Interface (GUI) of the Developed CAD System*

Figure 10 shows the main GUI of the developed CAD system that comprises of main information, segmentation, 3D reconstruction, volume calculation, statistical analysis, input dataset, repository of segmented results, 3D models, and contact us facility.

Figure 10 presents the key buttons of the GUI for the developed CAD system that consists of more functions insides to perform the corresponding action. Moreover, Fig. 11 presents the CAD system with specific operations such as segmentation, 3D reconstruction and volume calculation.

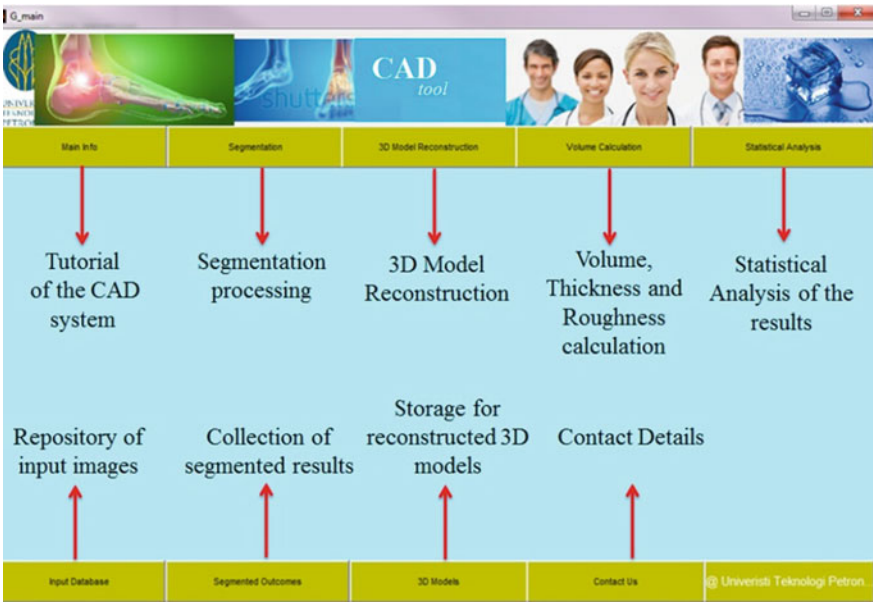

Fig. 10 GUI of the developed CAD system

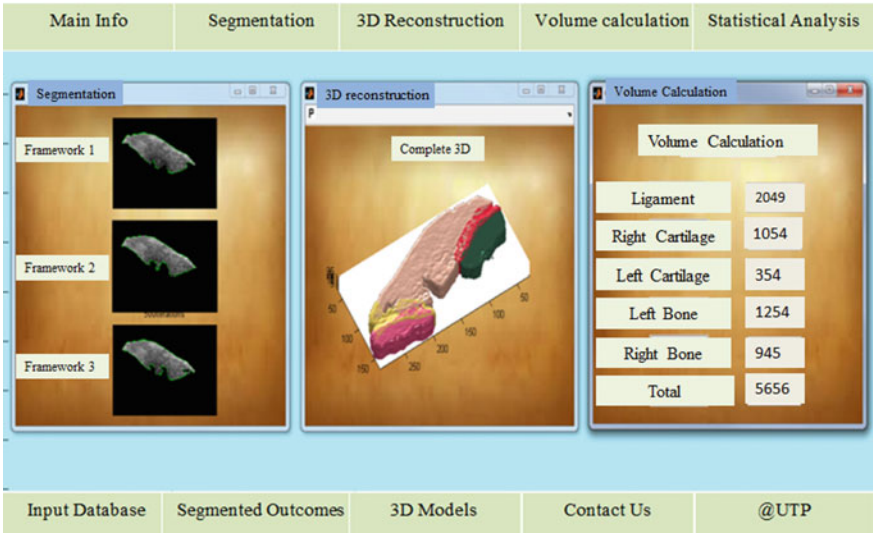

Fig. 11 2D segmentation, 3D reconstruction and volume calculation

5.4 Performance Evaluation of the Developed CAD System Based on Image Features

In order to evaluate the performance of the developed CAD system, this research used some parameters such as Peak Signal to Noise Ratio (PSNR), Standard Deviation (SD), Root Mean Square Error (RMSE), Universal Image Quality Index (UIQI), Mean Absolute Error (MAE), Normalized Absolute Error (NAE) and Normalized Cross Correlation (NCC) that are demonstrated in Table 2.

The Table 2 presents the quantitative analysis of the developed CAD system that provides information regarding the noise ratio, image energy, error rate and correlation between the original and resultant images. The PSNR and RMSE value varies from minimum 30.20 to maximum 30.29 and minimum 7.79 to minimum 7.85, respectively, which are indicating the better signal strength and lowest error ratio of the obtained results produced by the developed CAD system. Likewise, SD range from 42 to 43 that show variance. In addition, other parameter such as MAE

Table 2 Statistical analysis of the developed CAD system for ankle ATFL ligament

Image ID	PSNR	SD	RMSE	UIQI	MAE	NAE	NCC
1	30.22	42.62	7.85	0.5835	17.16	1.06	0.2026
2	30.21	42.71	7.86	0.5805	17.16	1.06	0.2110
3	30.21	42.76	7.86	0.5778	17.14	1.06	0.2167
4	30.21	42.76	7.86	0.5828	17.13	1.06	0.2157
5	30.20	42.75	7.87	0.5771	17.16	1.06	0.2135
6	30.20	42.76	7.87	0.5899	17.12	1.06	0.2151
7	30.24	42.81	7.83	0.8039	17.03	1.06	0.2204
8	30.25	42.81	7.83	0.5880	17.04	1.06	0.2205
9	30.26	42.84	7.82	0.5867	17.00	1.05	0.2227
10	30.25	42.83	7.83	0.5840	17.05	1.06	0.2205
11	30.26	42.82	7.81	0.5863	16.98	1.05	0.2220
12	30.28	42.85	7.80	0.5848	16.96	1.05	0.2228
13	30.27	42.85	7.81	0.5848	16.93	1.05	0.2272
14	30.27	42.85	7.81	0.5842	16.97	1.05	0.2273
15	30.29	42.92	7.79	0.5877	16.90	1.05	0.2344
16	30.29	42.95	7.79	0.5873	17.04	1.05	0.2282
17	30.29	43.00	7.79	0.5877	17.05	1.05	0.2297
18	30.29	43.02	7.79	0.5909	17.06	1.05	0.2300
19	30.29	43.00	7.79	0.5911	17.07	1.05	0.2299
20	30.29	43.00	7.79	0.5852	17.01	1.04	0.2355
21	30.25	43.06	7.83	0.5888	17.07	1.04	0.2421
22	30.27	43.38	7.81	0.5902	16.97	1.02	0.2571
23	30.29	43.76	7.79	0.5928	17.04	1.02	0.2699
24	30.28	43.91	7.80	0.5896	17.05	1.01	0.2761

is varied from 16 to 17, which depicted the absolute error rate of the obtained results. To identify the similarity correlation of segmented image with respect to input image, this research used the NCC that ranges from 0.2110 to 0.2761. The parameter NAE has shown the values 1.01–1.06. These are provided the information about the error and anatomical similarity index. Therefore, obtained results are indicating the better performance of the developed CAD system.

5.5 *Performance Evaluation Against the Existing Methods*

Quantitative performance evaluation of the proposed method is accomplished by the calculation of sensitivity, specificity and accuracy metrics results as compared to the existing methods such as Chan-Vese method [47], Kass's method [48], Yuan's method [49] and Achuthan's method [50] that are demonstrated in Table 2.

As illustrated in Table 2, the estimated sensitivity (by Eq. 2) of the proposed method (84.68 ± 2.92 %) is highest as compared to the Chan-Vese method (82.67 ± 3.67 %), Kass's method (76.43 ± 4.09 %), Yuan's method (80.23 ± 3.72 %) and Achuthan's method (72.34 ± 3.19 %), which indicated the better performance of the proposed method as compared to existing methods. Similarly, specificity is calculated by Eq. 3 to evaluate the performance of the proposed method as compared to existing methods. As depicted in Table 2, the specificity of the existing methods (Chan-Vese method (89.78 ± 3.04 %), Kass's method (71.12 ± 4.87 %), Yuan's method (74.09 ± 3.23 %) and Achuthan's method (67.54 ± 4.07 %)) is not better than the proposed method (94.83 ± 1.47 %). Furthermore, estimated accuracy (by Eq. 4) of the proposed method is 91.67 ± 2.23 %, which is higher than the accuracy of the existing Chan-Vese method (85.56 ± 3.82 %), Kass's method (78.45 ± 4.12 %), Yuan's method (81.05 ± 4.10 %) and Achuthan's method (74.23 ± 3.81 %). Therefore, on the basis of obtained results, the proposed method is found as a more optimal method with more than 91 % accuracy and less than 3 % standard deviation, which indicates its applicability in clinical settings.

After the segmentation performed by the developed CAD system, three experts are requested to do the manual segmentation based on their experience. The results obtained from the developed CAD system are compared with manual segmented results by the use of sensitivity, specificity and accuracy metrics as demonstrated in Table 3.

Table 3 Performance evaluation of the proposed method as compared to existing methods

	Proposed method	Chan-Vese method [47]	Kass's method [48]	Yuan's method [49]	Achuthan's method [50]
Sensitivity	84.68 ± 2.92	82.67 ± 3.67	76.43 ± 4.09	80.23 ± 3.72	72.34 ± 3.19
Specificity	94.83 ± 1.47	89.78 ± 3.04	71.12 ± 4.87	74.09 ± 3.23	67.54 ± 4.07
Accuracy	91.67 ± 2.23	85.56 ± 3.82	78.45 ± 4.12	81.05 ± 4.10	74.23 ± 3.81

Table 4 Performance evaluation: sensitivity, specificity and accuracy measurements

Image ID	Sensitivity	Specificity	Accuracy
1	81.28	96.04	93.79
2	80.49	96.13	93.74
3	79.51	96.14	93.60
4	84.23	96.24	94.51
5	82.03	96.04	94.00
6	85.94	95.78	94.43
7	81.83	96.34	94.15
8	82.75	96.27	94.28
9	81.09	96.73	94.29
10	83.59	96.51	94.62
11	83.64	96.62	94.70
12	84.71	96.62	94.85
13	83.15	97.00	94.84
14	80.93	96.66	94.23
15	82.25	96.65	94.47
16	75.28	97.01	93.39
17	74.34	96.83	93.07
18	73.69	96.87	92.98
19	76.89	96.74	93.62
20	76.39	97.30	93.81
21	79.23	96.39	93.87
22	82.29	97.10	94.85
23	78.53	97.40	94.36
24	83.51	96.29	94.52
Average	80.73	96.29	94.12

As presented in Table 3, sensitivity ranges from 73.69 to 85.94 %. Similarly, specificity varies from minimum 95.78 % to maximum 97.40 %. The obtained accuracy is lies between 92.98 and 94.85 %. Thus, on the basis of all obtained outcomes, the average sensitivity, specificity and accuracy of the proposed method are 80.73 %, 96.29 % and 94.12 %, respectively. Therefore, obtained outcomes are indicating the better performance of the developed CAD system that produced the more accurate results (more than 94 %).

Furthermore, in order to determine the performance of the developed CAD system based on the reconstructed 3D models, this research estimated the volume, thickness and roughness of the reconstructed 3D models for 5 patients for illustration, which are presented in Table 4.

As demonstrated in Table 5, the estimated volume ranges from minimum 1023.38 mm^3 to maximum 1095.54 mm^3. Similarly, thickness varies from minimum 2.07 mm to maximum 2.20 mm. Furthermore, surface roughness of the reconstructed 3D model is minimum 0.101 mm and maximum is 0.178 mm, which indicated the smoothness of the obtained results. Therefore, obtained results are

Table 5 Volume, thickness and roughness calculation

Dataset	Volume (mm^3)	Thickness (mm)	Roughness (mm)
1	1095.54	2.09	0.110
2	1023.38	2.16	0.101
3	986.67	2.07	0.103
4	1129.12	2.20	0.150
5	1089.78	2.12	0.178

indicated the promising performance of the developed CAD system that would lead to accurate and enhanced diagnosis of ATFL (Table 5).

5.6 Clinical Significance of the Developed CAD

The estimated optimal values of the measurements metrics (such as PSNR, SD, RMSE, UIQI, MAE, NAE, NCC, sensitivity, specificity, accuracy, volume, thickness and roughness) used in this study are indicating the strong clinical significance of this research. The obtained segmentation and 3D reconstruction results would greatly help in accurate assessment and better visualisation of ATFL injuries and abnormalities that can further be adopted for the diagnosis of ATFL at orthopedic clinics and hospitals. Moreover, this research opened new dimensions for ATFL diagnosis that may assist clinicians to locate the damaged region as well as the feasibility to measure the degree of damages associated with the estimation of volume, thickness and surface roughness, which would be helpful is the estimation of healing rate of the incurred injury.

6 Conclusions and Future Directions

This research developed a novel CAD system for accurate diagnosis of ATFL injuries by segmentation and 3D reconstruction from 2D ultrasound images. This research uses the integration of data acquisition, segmentation and 3D reconstruction approaches for enhanced results. The obtained results are indicated the promising performance of the developed CAD system. Since, ATFL segmentation and 3D reconstruction from 2D ultrasound images have not been investigated earlier. Therefore, the developed CAD system has opened new entrances for clinicians, radiologists, orthopedist, rheumatologists and sports physician to diagnosis the injuries of ATFL ligament more accurately. In future, the developed CAD system would be extended to other musculoskeletal anatomical parts such as knee, shoulder and wrist with some amendments.

Acknowledgements The authors would like to thank UTP, Malaysia for their assistance and Ministry of Education (MOE) for sponsoring the project under grant entitled 'Formulation of Mathematical Model for 3-D Reconstruction of Ultrasound Images of MSK Disorders' (Grant no. 0153AB-I55).

References

1. Ligaments, L.A.: Current methods for the evaluation of ankle ligament injuries (1994)
2. Bland-Sutton, J.: Ligaments; Their Nature and Morphology. Lewis (1897)
3. Tegner, Y., Lysholm, J.: Rating systems in the evaluation of knee ligament injuries. Clin. Orthop. Relat. Res. **198**, 42–49 (1985)
4. Flegel, M.: Sport first aid, 5E. Hum. Kinet. (2013)
5. Muschol, M., Müller, I., Petersen, W., Hassenpflug, J.: Symptomatic calcification of the medial collateral ligament of the knee joint: a report about five cases. Knee Surg. Sports Traumatol. Arthrosc. **13**(7), 598–602 (2005)
6. Smith, R.W., Reischl, S.F.: Treatment of ankle sprains in young athletes. Am. J. Sports Med. **14**(6), 465–471 (1986)
7. van Dijk, C.N.: On Diagnostic Strategies in Patients with Severe Ankle Sprain. Rodopi (1994)
8. Broström, L.: Sprained ankles. V. Treatment and prognosis in recent ligament ruptures. Acta Chirurgica Scandinavica **132**(5), 537–550 (1966)
9. Anderson, K.J., Lecocq, J.F.: Operative treatment of injury to the fibular collateral ligament of the ankle. J. Bone Joint Surg. **36**(4), 825–832 (1954)
10. Boss, A.P., Hintermann, B.: Anatomical study of the medial ankle ligament complex. Foot Ankle Int. **23**(6), 547–553 (2002)
11. Perrich, K.D., Goodwin, D.W., Hecht, P.J., Cheung, Y.: Ankle ligaments on MRI: appearance of normal and injured ligaments. Am. J. Roentgenol. **193**(3), 687–695 (2009)
12. Singh, V., Elamvazuthi, I., Jeoti, V., George, J., Swain, A., Kumar, D.: Impacting clinical evaluation of anterior talofibular ligament injuries through analysis of ultrasound images. BioMed. Eng. Online **15**(1), 1 (2016)
13. Eisenhart, A.W., Gaeta, T.J., Yens, D.P.: Osteopathic manipulative treatment in the emergency department for patients with acute ankle injuries. JAOA: J. Am. Osteopath. Assoc. **103**(9), 417–421 (2003)
14. Singh, V., Elamvazuthi, I., Jeoti, V., George, J.: 3D reconstruction of ATFL ligament using ultrasound images. In: 2014 5th International Conference on Intelligent and Advanced Systems (ICIAS), pp. 1–5. IEEE (2014)
15. Singh, V., Elamvazuthi, I., Jeoti, V., George, J., Swain, A.K., Kumar, D.: 3D reconstruction of CFL ligament based on ultrasonographic images. In: Advances in Visual Informatics, pp 503–513. Springer (2015)
16. Van Rijn, R.M., Van Os, A.G., Bernsen, R., Luijsterburg, P.A., Koes, B.W., Bierma-Zeinstra, S.: What is the clinical course of acute ankle sprains? A systematic literature review. Am. J. Med. **121**(4),324–331 (2008)
17. Yeung, M., Chan, K.-M., So, C., Yuan, W.: An epidemiological survey on ankle sprain. Br. J. Sports Med. **28**(2), 112–116 (1994)
18. Singh, V., Elamvazuthi, I., Jeoti, V., George, J.: Automatic ultrasound image segmentation framework based on darwinian particle swarm optimization. In: Proceedings of the 18th Asia Pacific Symposium on Intelligent and Evolutionary Systems, Vol. 1, pp. 225–236. Springer (2015)
19. Silva, ASd, Abdalla, R.J., Fisberg, M.: Incidence of musculoskeletal injuries in elite female basketball athletes. Acta Ortopédica Brasileira **15**(1), 43–46 (2007)
20. Wexler, R.K.: The injured ankle. Am. Fam. Physician **57**(3), 474–480 (1998)

21. Singh, V., Elamvazuthi, I., Jeoti, V., George, J., Kumar, D.: Computer aided diagnosis (CAD) tool for the analysis of calcaneofibular ligament using ultrasonographic images. In: Malaysian Technical Universities Conference on Engineering and Technology (2015)
22. Bahk, M.S., Cosgarea, A.J.: Physical examination and imaging of the lateral collateral ligament and posterolateral corner of the knee. Sports Med. Arthrosc. Rev. **14**(1), 12–19 (2006)
23. Duffy, P.S., Miyamoto, R.G.: Management of medial collateral ligament injuries in the knee: an update and review. Phys. Sports Med. **38**(2), 48–54 (2010)
24. Kennedy, J., Hawkins, R., Willis, R., Danylchuk, K.: Tension studies of human knee ligaments. J. Bone Joint Surg. A **58**(3), 350–355 (1976)
25. Mulligan, S.A., Schwartz, M.L., Broussard, M.F., Andrews, J.R.: Heterotopic calcification and tears of the ulnar collateral ligament: radiographic and MR imaging findings. Am. J. Roentgenol. **175**(4), 1099–1102 (2000)
26. Boukerroui, D., Baskurt, A., Noble, J.A., Basset, O.: Segmentation of ultrasound images—multiresolution 2D and 3D algorithm based on global and local statistics. Pattern Recogn. Lett. **24**(4), 779–790 (2003)
27. Schneck, C.D., Mesgarzadeh, M., Bonakdarpour, A.: MR imaging of the most commonly injured ankle ligaments. Part II. Ligament Injuries. Radiol. **184**(2), 507–512 (1992)
28. Singh, V., Elamvazuthi, I., Jeoti, V., George, J., Swain, A., Kumar, D.: Modeling of interpolation methods for robot assisted and freehand ultrasound imaging system. Procedia Comput. Sci. **76**, 15–20 (2015)
29. Bhateja, V., Singh, G., Srivastava, A.: A novel weighted diffusion filtering approach for speckle suppression in ultrasound images. In: Proceedings of the International Conference on Frontiers of Intelligent Computing: Theory and Applications (FICTA) 2013, pp. 459–466. Springer (2014)
30. Bhateja, V., Srivastava, A., Singh, G., Singh, J.: A modified speckle suppression algorithm for breast ultrasound images using directional filters. In: ICT and Critical Infrastructure: Proceedings of the 48th Annual Convention of Computer Society of India, vol. II, pp 219–226. Springer (2014)
31. Singh, B.K., Verma, K., Thoke, A.: Objective and optical evaluation of despeckle filters in breast ultrasound images. IETE Tech. Rev. (ahead-of-print) 1–15 (2015)
32. Khan, M.A.H.: 3D Reconstruction of Ultrasound Images. MSc in Vision and Robotics University of Burgundy, University of Girona and University of Heriot Watt (2008)
33. Khan, M.H.: 3D Reconstruction of Ultrasound Images. University of Burgundy, University of Girona and University of Heriot Watt, MSc in Vision and Robotics (2008)
34. Kaewkamnerdpong, B., Bentley, P.J.: Perceptive particle swarm optimisation: An investigation. In: Swarm Intelligence Symposium, 2005. SIS 2005. Proceedings 2005 IEEE, pp. 169–176. IEEE (2005)
35. Destrempes, F., Roy Cardinal, M.-H., Allard, L., Tardif, J.-C., Cloutier, G.: Segmentation method of intravascular ultrasound images of human coronary arteries. Comput. Med. Imaging Graph. **38**(2), 91–103 (2014)
36. Guide MUs: The MathWorks Inc, vol. 4, p. 382. Natick, MA (1998)
37. MathWorks I: MATLAB: the language of technical computing. Desktop Tools and Development Environment, version 7, vol. 9. MathWorks (2005)
38. Guide MUs: The Mathworks, Inc, vol. 5, p. 333. Natick, MA (1998)
39. Gonzalez, R.C., Woods, R.E., Eddins, S.L.: Digital Image Processing Using MATLAB. Pearson Education India (2004)
40. Nimkar, S., Varghese, S., Shrivastava, S.: Contrast enhancement and brightness preservation using multi-decomposition histogram equalization (2013). arXiv:13073054
41. Singh, S., Jain, A., Bhateja, V.: A comparative evaluation of various de-speckling algorithms for medical images. In: Proceedings of the CUBE International Information Technology Conference, pp. 32–37. ACM (2012)
42. Bland, J.M., Altman, D.G.: Stat. Notes: Meas. Error. BMJ **313**(7059), 744 (1996)

43. Zhu, W., Zeng, N., Wang, N.: Sensitivity, specificity, accuracy, associated confidence interval and ROC analysis with practical SAS® implementations. In: NESUG Proceedings: Health Care and Life Sciences, Baltimore, Maryland (2010)
44. Legland, D., Kiêu, K., Devaux, M.-F.: Computation of Minkowski measures on 2D and 3D binary images. Image Anal. Stereol. **26**(2), 83–92 (2011)
45. Charemza, M., Thönnes, E., Bhalerao, A., Parr, D.: Integral geometry descriptors for characterizing emphysema and lung fibrosis in HRCT images. In: First International Workshop on Pulmonary Image Processing (MICCAI 2008), pp. 155–164 (2008)
46. Schmähling, J.: Statistical characterization of technical surface microstructure (2006)
47. Chan, T.F., Vese, L.A.: Active contours without edges. IEEE Trans. Image Process. **10**(2), 266–277 (2001)
48. Kass, M., Witkin, A., Terzopoulos, D.: Snakes: active contour models. Int. J. Comput. Vis. **1** (4), 321–331 (1988)
49. Yuan, Y., He, C.: Adaptive active contours without edges. Math. Comput. Model. **55**(5), 1705–1721 (2012)
50. Achuthan, A., Rajeswari, M., Ramachandram, D., Aziz, M.E., Shuaib, I.L.: Wavelet energy-guided level set-based active contour: A segmentation method to segment highly similar regions. Comput. Biol. Med. **40**(7), 608–620 (2010)

Electroanatomical Mapping Systems. An Epochal Change in Cardiac Electrophysiology

Carlo Pappone, Carmine Garzillo, Simonetta Crisà and Vincenzo Santinelli

Abstract In the last two decades new mathematical and computational models and systems have been applied to the clinical cardiology, which continue to be developed particularly to quantify and simplify anatomy, physio-pathological mechanisms and treatment of many patients with cardiac arrhythmias. The Authors report our large experience on electroanatomical mapping systems and techniques that are currently used to quantify and analyze both anatomy and electrophysiology of the heart. In the last 15 years the Authors have performed more than 15,000 invasive catheter ablation procedures using different non-fluoroscopic three-dimensional (3D) electroanatomical mapping and ablation systems (CARTO, Ensite) to safely and accurately treat many patients with different cardiac arrhythmias particularly those with atrial fibrillation with a median age of 60 years (IQR, 55-64). The Authors have also developed and proposed for the first time a new robotic magnetic system to map and ablate cardiac arrhythmias without use of fluoroscopy (Stereotaxis) in >500 patients. Very recently, epicardial mapping and ablation by electroanatomical systems have been successfully performed to treat Brugada syndrome at risk of sudden death in a series of patients with a median age of 39 years (IQR, 30-42). Our experience indicates that electroanatomic mapping systems integrate several important functionalities. (1) Non-fluoroscopic localization of electrophysiological catheters in three-dimensional space; (2) Analysis and 3D display of cardiac activation sequences computed from local or calculated electrograms, and 3D display of electrogram voltage; (3) Integration of 'electroanatomic' data with non-invasive images of the heart, such as computed tomography or magnetic resonance images. The widespread use of such 3D systems is associated with higher success rates, shorter fluoroscopy and procedure times, and accurate visualization of complex cardiac and extra-cardiac anatomical structures needing to be protected during the procedure.

C. Pappone (✉) · S. Crisà · V. Santinelli
Department of Arrhythmology, Policlinico San Donato,
University of Milan, Milan, Italy
e-mail: carlo.pappone@af-ablation.org

C. Garzillo
Department of Public Health, University of Naples, Federico II, Napoli, Italy

N. Dey et al. (eds.), *Medical Imaging in Clinical Applications*,
Studies in Computational Intelligence 651, DOI 10.1007/978-3-319-33793-7_11

Keywords Cardiac arrhythmias · Atrial fibrillation · Electroanatomical mapping and ablation systems · Robotic magnetic system

1 Introduction

Recent progress in biomedical engineering and imaging technology [1–6] is providing an ever-increasing body of knowledge on the mechanism and onset of cardiac disease, with new options for accurate detection and effective treatment. In the last years, considerable progress has been made in mathematical and computational models/systems, which provide further insights into clinical electrophysiology imaging processing in order to better quantify/simplify from the acquired image data both anatomy and mechanisms of complex cardiac arrhythmias, including but not limited to atrial fibrillation. The development of relatively inexpensive computer systems that have the capacity to process signals rapidly has allowed the development of mapping systems that reliably localize intracardiac catheter positions [7–10]. One such system is the CARTO system (Biosense Webster, Diamond Bar, CA). The system uses a magnet mounted under the catheterization table coupled with a proprietary catheter placed in the intracardiac chamber of interest. The magnet under the table locates the catheter tip in three-dimensional space when an endocardial signal is measured and the system stores the spatial and electrical information. The computer then constructs a virtual three-dimensional electroanatomic map of the chamber. The catheter tip location within the mapped space is displayed on the computer screen allowing catheter manipulation without fluoroscopy. In current versions of CARTO, real-time structural data from intracardiac ultrasound (CartoSound) or changes in impedance (CARTO 3) can be integrated to refine the displayed image. The LocaLisa (Medtronic Inc, St. Paul, MN) system was used in early studies of non-fluoroscopic procedures. The technology was acquired by Endocardial Solutions, which subsequently was acquired by the St. Jude Medical Corporation. The technology was incorporated into the EnSite NavX system (St. Jude Medical, St Paul, MN). Patches are placed on the skin and used to generate an electrical signal sensed by the catheters inside the body. A catheter in a stable position is used as a reference for creating the geometry. The ablation catheter is manipulated within the chamber of interest and when contact with the wall is demonstrated by the measured electrical signal, the catheter position is recorded. Electrical impedance changes are sensed by the system and indicate a change in catheter position, and the system then displays the new catheter position. The system then can simultaneously track 64 separate electrodes on up to 12 different catheters. Their positions are displayed relative to each other within a virtual representation of the cardiac chamber(s) of interest. Although both the CARTO and EnSite systems produce a virtual image of the cardiac chambers and catheter(s), there are differences in them. However, with both systems, there are increased equipment costs associated with both the CARTO and NavX systems. Because the CARTO system is based on changes within a magnetic

field, the ablation catheter has to be magnetically active. This proprietary catheter is more expensive to purchase than commonly used ablation catheters. The NavX system is compatible with most commonly used catheters, but the patches applied to the skin are one-time use only and must be purchased for every case. It is difficult to make a global statement about the absolute cost increase as there may be differences based on volume and specific center preferences. Initially, their use has been in arrhythmias in which the ablation target was difficult to identify, such as ventricular tachycardias in structural heart disease, atypical atrial flutters, or arrhythmias in patients with complex congenital heart defects. In the recent years, electroanatomic mapping systems have also been used to guide catheter-based isolation of the pulmonary veins, an important component of the modern management of atrial fibrillation. Electroanatomic mapping systems integrate three important functionalities, namely (i) non-fluoroscopic localization of electrophysiological catheters in three-dimensional (3D) space; (ii) analysis and 3D display of activation sequences computed from local or calculated electrograms, and 3D display of electrogram voltage ('scar tissue'); and (iii) integration of this 'electroanatomic' information with non-invasive images of the heart (mainly computed tomography or magnetic resonance images). Although better understanding and ablation of complex arrhythmias mostly relies on the 3D integration of catheter localization and electrogram-based information to illustrate re-entrant circuits or areas of focal initiation of arrhythmias, the use of electroanatomic mapping systems in atrial fibrillation is currently based on integration of anatomic images of the left atrium and non-fluoroscopic visualization of the ablation catheter. Currently available registration techniques rely on preprocedural 3D computed tomography or magnetic resonance imaging (MRI) data sets which are aligned with or superimposed to intraprocedural electroanatomical information. Although a reasonable accuracy and usability can be achieved with these techniques, preprocedural anatomic images carry inherent disadvantages: atrial volumes are variable and may change between the imaging session and atrial fibrillation ablation session. Especially in larger atria, the integration error is considerable. Three-dimensional transesophageal ultrasound systems have already been used to guide catheter-based septal defect closures. Although image integration is a fascinating and easily adopted addition to electroanatomical mapping, especially in atrial fibrillation, it has to be appreciated that left atrial anatomy is variable and depends, among other factors, on cardiac rhythm, volume status, respiration, and deformation of the left atrium by electrophysiological catheters during the procedure. Image fusion and non-fluoroscopic catheter visualization can therefore probably not fully replace fluoroscopy or other forms of direct catheter visualization during catheter ablation procedures. About two decades ago, Haissaguerre et al. and Pappone et al. [11–17] firstly reported a potential role of radiofrequency catheter ablation in the treatment of patients with atrial fibrillation, which required an accurate reconstruction of complex anatomic structures. Therefore, continuous technology progresses have been made to realize and perform safer and more effective catheter ablation procedures. The wide area circumferential ablation, as initially proposed by Pappone et al. [12–16], firstly used electro-anatomic systems and this approach was

associated with lower rates of atrial fibrillation recurrence than the initially proposed approach by ostial pulmonary vein isolation [17]. In the last ten years, thanks to further technology advancements many multicenter randomized studies worldwide reported higher success rates in maintaining a stable sinus rhythm in patients with refractory paroxysmal recurrent atrial fibrillation [17–31]. Unfortunately, despite technology progresses, currently less consensus exists as to the most appropriate approach strategy in persistent long-standing atrial fibrillation [22, 23], in which there are multiple substrates for re-entry outside pulmonary veins (PVs) or multiple rotors, both of which are difficult to identify and eliminate. As a result, multiple complex lesions are required in a step-wise fashion, which require their accurate anatomic localization with longer procedure times. As a result, further technical advancements are required in persistent atrial fibrillation to overcome these important limitations while refining the best ablation approach in terms of both safety and efficacy. Despite these limitations, if performed in a modern electrophysiology laboratory, catheter ablation of atrial fibrillation may be considered as an effective and safe procedure and this is at least in part due to the use of new tools.

2 An Epochal Change of Cardiac Electrophysiology. Evolution of Electro-anatomic Three-Dimensional Mapping Systems from 2000 to 2015

Currently, the traditional X-ray imaging and catheter diagnostic mapping methods are increasingly being complemented by recent 3D mapping imaging modalities, each with specific strengths and options for improving diagnostic accuracy and effectiveness. High-quality data points offer electrical and anatomical detail in simple and complex cases by traditional and advanced diagnostic catheters. Advanced 3-D mapping modules can integrate multiple data sets and images into one resource for highly detailed, real-time information by image integration tools, as well as several tachyarrhythmias—specific software. With the broadest portfolio of catheters available it is possible deliver optimal treatment, whether it's to ablate or wait by irrigated ablation technology. As a result, currently, chronic antiarrhythmic drug therapy has been replaced in patients with complex arrhythmias by catheter-based interventions. This development is supported by continuous developments in 3D imaging and navigation techniques with newer devices, which enable more complex percutaneous procedures with improved outcomes. In the last 15 years the rapid expansion of indications for catheter ablation from supraventricular tachycardia to very complex tachyarrhythmias, such as atrial fibrillation and ventricular tachycardia led electrophysiologists to face prolonged procedure times with excessive fluoroscopy exposure and the need for stable and reproducible catheter movement, all of which require significant and continuous improvements in the existing traditional 2D mapping technology, and new developments.

3 Current Electroanatomical Mapping Systems

The most commonly used systems are CARTO® System (Biosense Webster, Inc., Diamond Bar, CA, USA) (Figs. 1, 2, 3, 4 and 5) and EnSite NavX™ (St. Jude Medical, Inc., St. Paul, MN, USA) (Figs. 6, 7, 8, 9 and 10, 11). These mapping systems have helped to decrease procedural complexity, procedure time, and improve safety. The CARTO and EnSite NavX system use magnetic or impedance measurements between the individual catheter electrodes and the patches usually placed on the patient's chest and abdomen. Bipolar mapping is the gold standard technique to characterize substrate, and a bipolar voltage amplitude of ≥ 1.5 mV identifies healthy tissue and areas with voltage of 0.5–1.5 mV are considered border zones. Electroanatomical mapping systems accurately depict in different colors (color-coded maps) such areas. During the activation sequence mapping, data points are acquired as the catheter moves across the chamber of interest and the timing of these electrograms are compared with a predetermined reference. As this process continues, a color scheme begins to emerge. Currently, areas of red color usually indicate sites of "early activation" and activation becomes progressive later proceeding through the colors of the rainbow to yellow-green, and finally the blue and purple one that define the sites of late activation relative to the reference electrogram. These colors are displayed as an isochronal time bar adjacent to the 3D map.

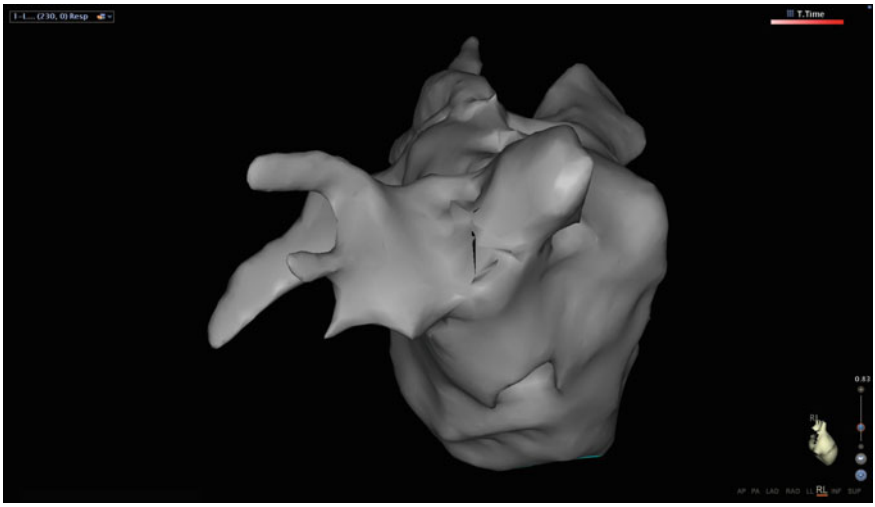

Fig. 1 Pre-ablation endocardial anatomical map of the left atrium in right lateral view obtained by the CARTO system in a patient undergoing atrial fibrillation ablation. The map was created during coronary sinus pacing, as a stable reference point

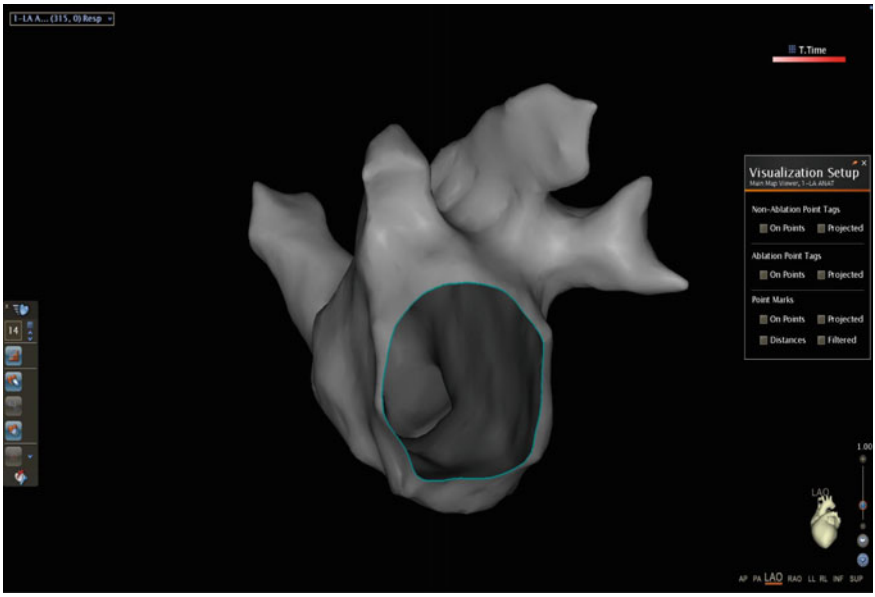

Fig. 2 Pre-ablation endocardial anatomical map of the left atrium in left anterior oblique projection by the CARTO system. Note the mitral valve annulus

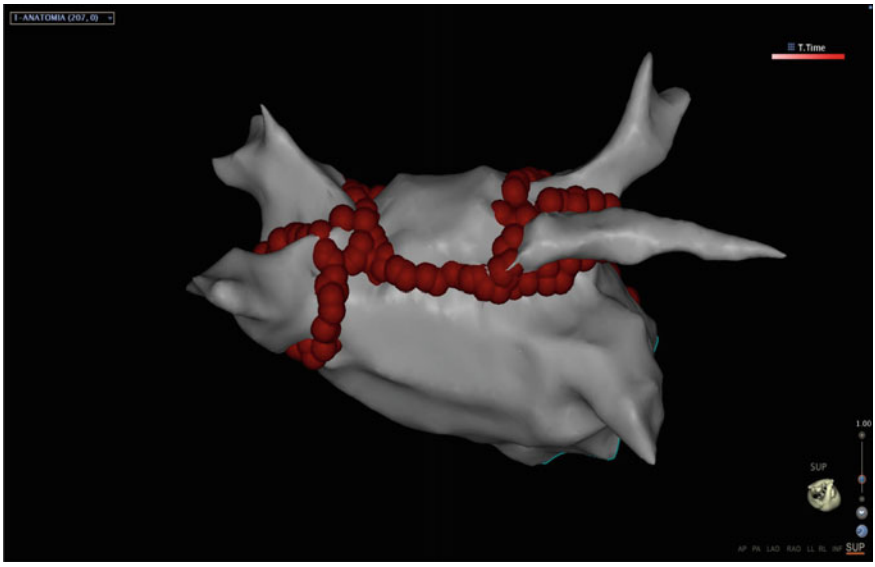

Fig. 3 Pre-ablation endocardial anatomical map in the superior view to validate continuity of the lesion set around the superior pulmonary veins. The map was reconstructed by the CARTO system

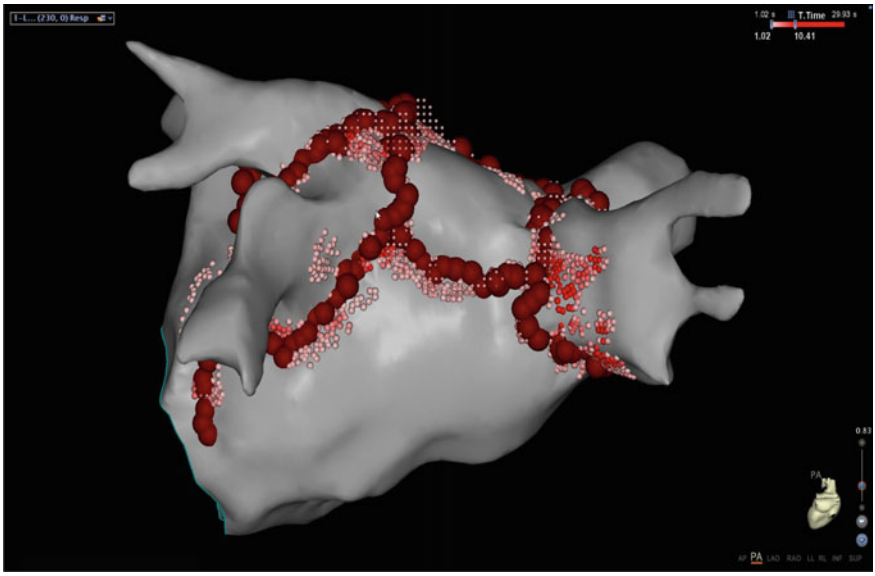

Fig. 4 The figure shows an endocardial anatomical map of the left atrium in the antero-posterior view and the typical lesion set encircling the four pulmonary veins (*red dots*) with superimposed grid points due to every single catheter contact count. The map was reconstructed by the last version of CARTO system

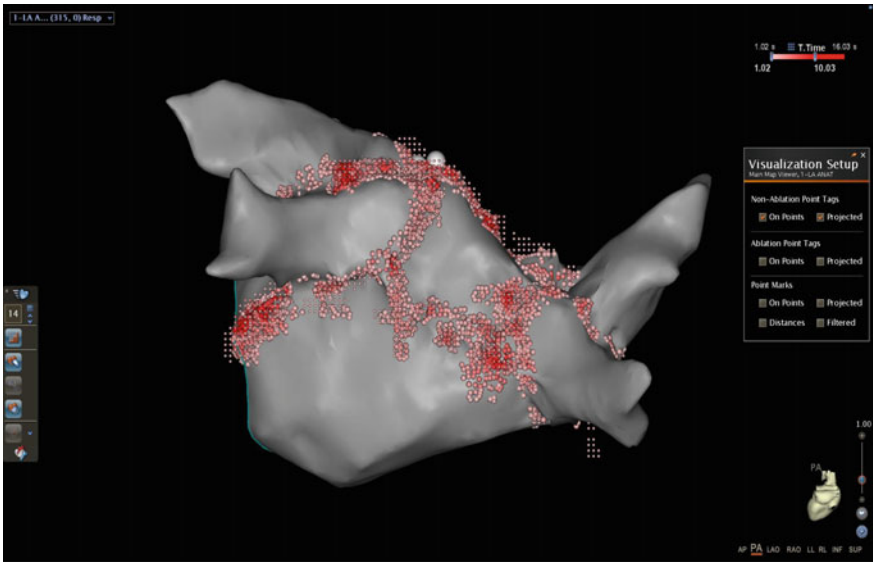

Fig. 5 Same map in the same patient without red ablation points. The endocardial map was reconstructed by CARTO system

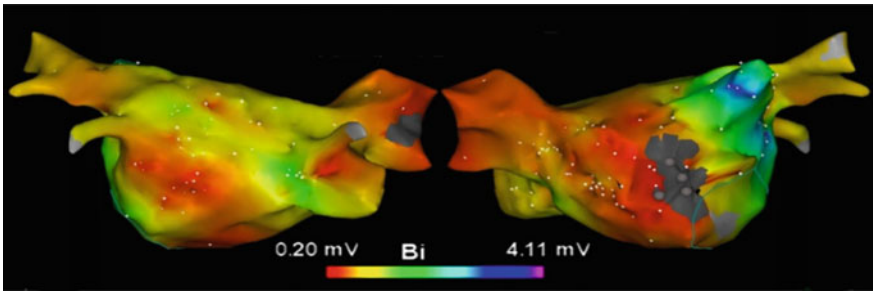

Fig. 6 Electroanatomic color-coded voltage map of the left atrium in postero-anterior (*left panel*) and antero-posterior view (*right panel*) by CARTO system. Red color represents low-voltage areas due to radiofrequency applications while green and blue colors depict higher voltage areas. Post-ablation areas within and around the ablation lines, involving to some extent the left atrial posterior wall, show lo-amplitude electrograms. This purely anatomic approach yields a profound atrial electroanatomic remodeling, as expressed by the voltage abatement inside the encircled areas

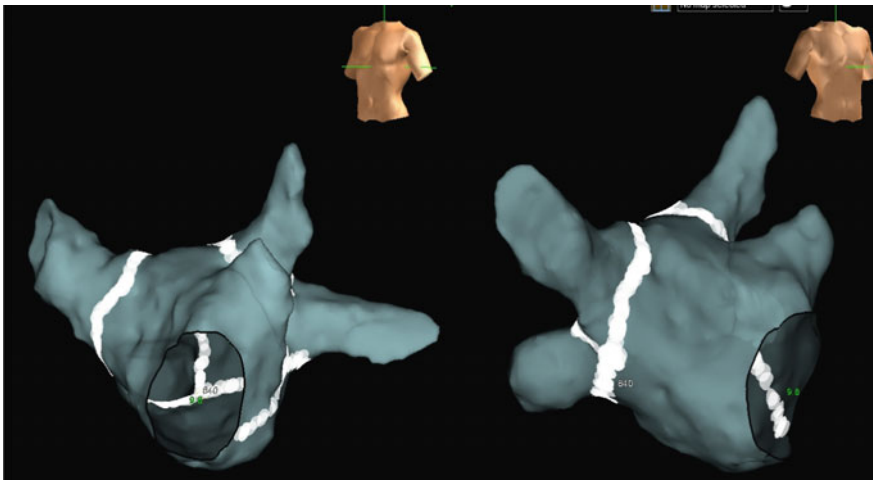

Fig. 7 Anatomical maps of the left atrium geometry in LAO (*left*) and RAO (*right*) view obtained by the NavX EnSite mapping system. The white line markers correspond to the lesions indicating the path of RF ablation for the modified pulmonary vein isolation

4 Electroanatomic Mapping Systems. Newer Advanced Versions

Recent technical advances resulted in the development of new versions of both systems. Carto Express version allows quicker mapping and reconstruction of heart cavities and great vessels geometry as compared to previous versions of Carto XP. EnSite Velocity system incorporates more precise catheter visualization,

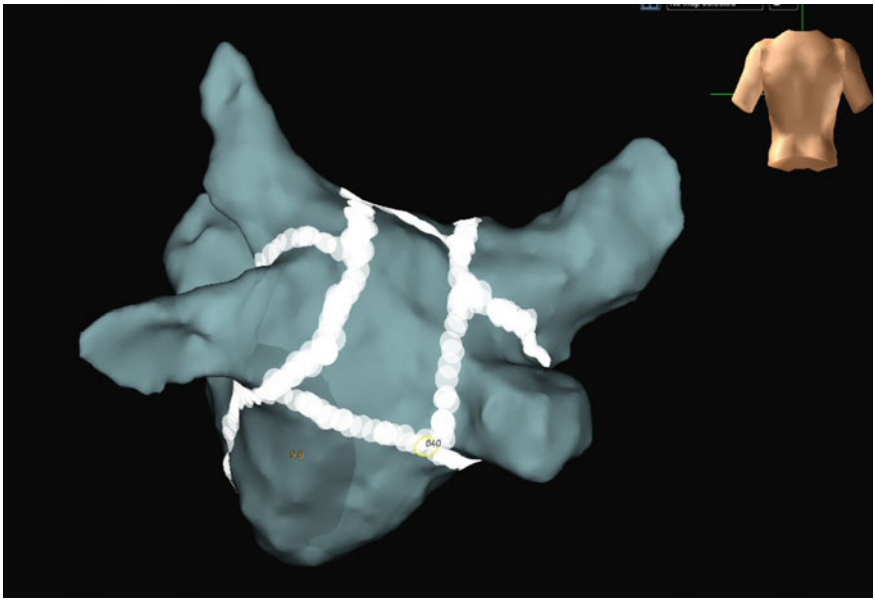

Fig. 8 Postero-anterior view of the left atria geometry created by the EnSite mapping system. The complete set of lesions created during RF ablation are evidenced by the white lesions markers around the pulmonary veins and posterior wall line

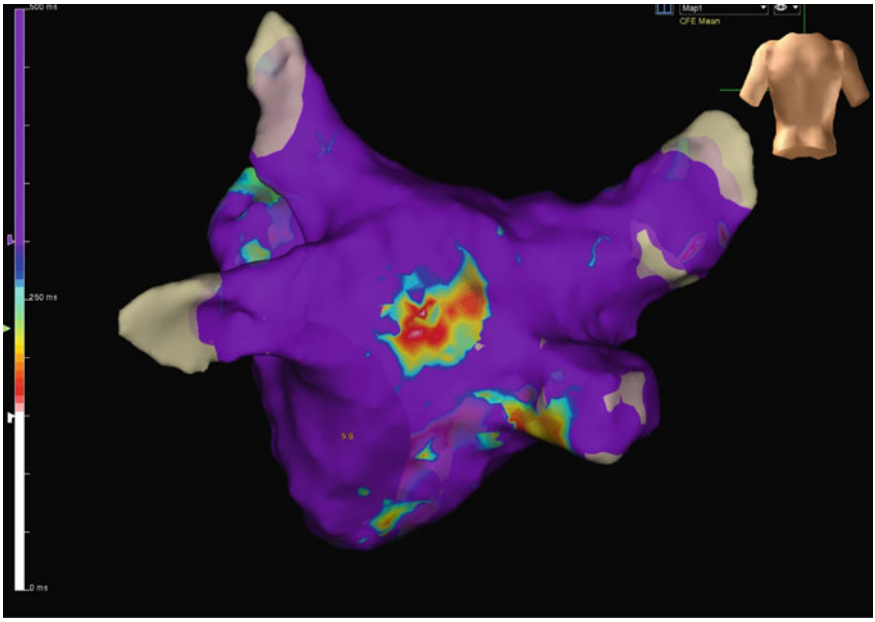

Fig. 9 Postero-anterior view of a color-coded activation map of the left atrium created by the EnSite mapping system in a patient with incessant atrial tachycardia. The color scale is expressed in msec, corresponding to the earliest area of activation (*red color*) located on the posterior left atrium

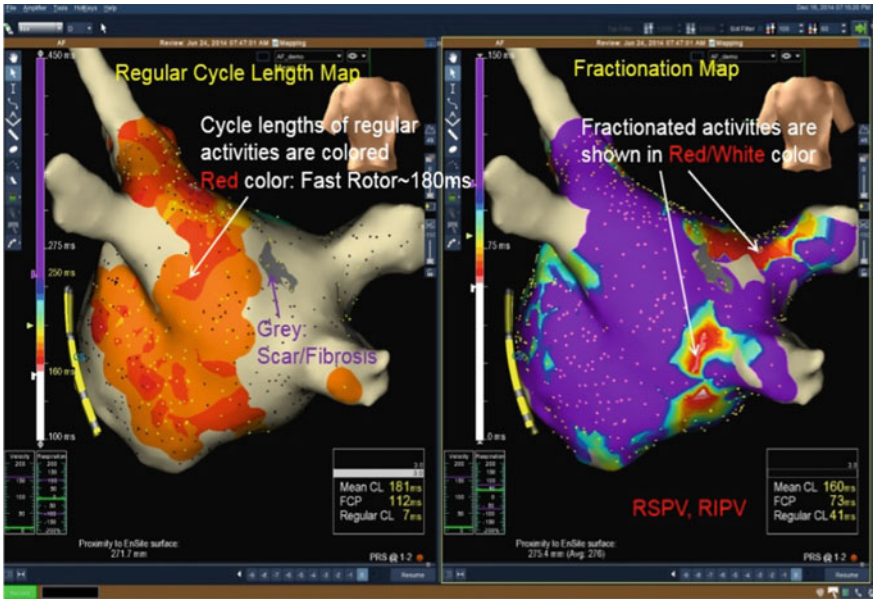

Fig. 10 Postero-anterior views of electroanatomical color-coded maps of the left atrium created by the Ensite mapping system in a patient with atrial fibrillation. The map on the left shows the regions that have the most regular cycle length with the fast "rotor" activity (*red/orange color* scale corresponding to 180 ms) representing the ablation targets. Note that the regular rotor activity is characterized by short cycle length or fractionated potentials (*right panel*)

and allows Fig. 3. One kernel at *xs* (*dotted kernel*) or two kernels at *xi* and *xj* (*left and right*) lead to the same summed estimate at *xs*. This shows a figure consisting of different types of lines. Elements of the figure described in the caption should be set in italics, in parentheses, as shown in this sample caption.

Quicker mapping as compared to previous version of EnSite. The CARTO system utilizes magnetic location technology to provide accurate visualization of the magnet sensor-equipped catheter tip. The original electroanatomic 3D Carto® system is essentially based on three active weak magnetic fields (5x10-6 to 5x10-5 T), generated by a 3-coil location pad placed underneath the patient's thorax. Magnetic field strengths are measured with mini-sensors embedded in the catheter tip on a continuous basis providing data about the real time and exact position and orientation of the sensor in space. One sensor attached to the patient's skin within the working space of interest serves as a location reference. Patient movement or dislocation of the location pad may lead to uncorrectable map shifts. Recent versions of Carto System (Carto3®) integrate a hybrid of magnetic and current-based catheter localization technology enabling visualization of multiple catheters simultaneously without fluoroscopy use. For this, six electrode patches positioned at the patient's back and chest continuously screen the current emitted at a unique frequency from different catheter electrodes. Localization of the

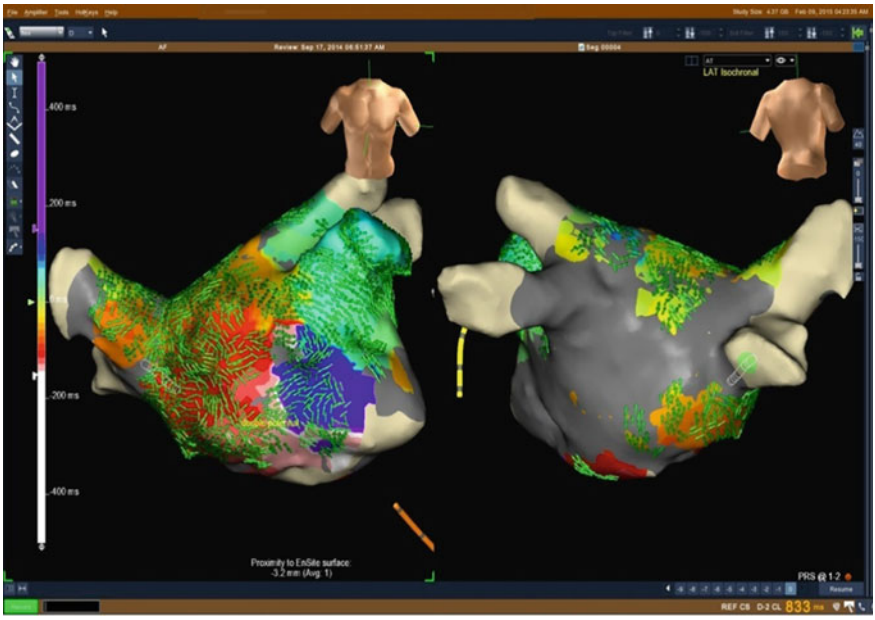

Fig. 11 The map shows color-coded left atrial activation time in a patient with atrial fibrillation obtained by the EnSite mapping system. The activation time is calculated from a reference marker (in this example the coronary sinus catheter distal to second electrode signal), allowing identifying the propagation path of the arrhythmia. Note post-ablation dense scar low voltage areas in grey (*right panel*) in the posterior wall and residual very fast rotor activity in the anterior septum (*left panel*)

non-magnetic electrodes can be calibrated by the detection of the magnetic sensor within the coordinate system in order to overcome distortions from non-uniform intrathoracic resistances. Other newer development of the Carto3® system is the fast anatomical mapping (FAM) which allows real time accurate reconstruction of detailed shells by a multipolar mapping catheter simply moving the catheter all around in the chamber of interest, thus providing a better reconstruction than the point-by-point maps in the earlier Carto® versions. Another development targeting the accuracy of surface reconstructions is accomplished by a unique type of respiratory gating in which varying thoracic impedances are measured throughout the respiratory cycle. The new developments in the current Carto3® version have already been shown beneficial in terms of fluoroscopy requirements, when compared to the older CartoXP® version. The other electroanatomical mapping systems currently used is the EnsiteNavX® system, which is essentially based on the LocaLisa® technology using six skin electrode patches to create high frequency electric fields (approximately 8 kHz in the current version) in three orthogonal planes. The 3D-localization of conventional electrophysiology catheters is calculated based on an impedance gradient in relation to a reference electrode. The body's non-linear impedance may be partially corrected by a process called field

scaling. To improve compensation for cardiac and respiratory motion artifacts, a stable reference catheter in the proximal coronary sinus is placed to avoid uncorrectable map shifts. The advantage of the EnSiteNavX® system over the Carto® system is that it allows for visualization of multiple catheters from different manufacturers and that all electrodes of any catheter can be used simultaneously for a relatively quick reconstruction of cardiac chambers providing not only anatomical information but also electrophysiological mapping data. In the last 15 years the Authors have performed more than 15,000 invasive catheter ablation procedures using both CARTO and Ensite systems (Figs. 1, 2, 3, 4, 5, 6, 7, 8, 9, 10 and 11), particularly in patients with atrial fibrillation with a median age of 60 years (IQR, 55-64). Our experience indicates that multi-electrode mapping represents a significant advancement in mapping technology, allowing physicians to acquire multiple mapping points simultaneously with a high level of detail and accuracy. Combined with the new Pentarray Navigation Catheter, it is possible to reduce the number of required catheter maneuvers to quickly diagnose any arrhythmia. (Unpublished observations). This would further support the safety, effectiveness and efficiency of cardiac ablation procedures.

5 Electroanatomic Mapping Systems. Image Integration

Image integration is a new tool which can be used to further increase the understanding of the patient's complex atrial anatomy, such as the pulmonary vein-atrial junction and the ridge between the left pulmonary veins and the left atrial appendage. CT or MRI data, which are acquired prior to the procedure, are integrated in the EAMS. After image processing (segmentation), 3D images are either merged or fused with the 3D reconstructions with fusion usually requiring a more extensive registration process. Utilization of intracardiac echocardiography (ICE) is less frequently used for guidance of transseptal puncture, and early detection of complications such as pericardial effusion, thrombus formation, or tissue overheating (microbubble formation). The most widely used ICE technology runs integrated in the Carto® system (CartoSound®, Biosense Webster). It uses a phased-array ultrasound tipped catheter consisting of a 64-element transducer (Sound29Star® Catheter, Biosense Webster). The high-resolution, multiple-frequency transducer (5–10 MHz) is incorporated into a 10F steerable catheter and provides 90° sector images with depth control [31]. The CartoSound® module is capable of creating 3D models by combining multiple 2D ultrasound cross sections generated by the transducer. The latter can be merged with segmented CT/MRI left atrial models. The technology allows improvement in success and complication rates as well as shortening of LA catheter dwell and fluoroscopy times when compared with the fluoroscopy-only approach [31]. Use of intracardiac ultrasound requires an additional 11F sheath for transducer introduction, potentially raising the risk of femoral access complications as well as adds a non-negligible cost to the procedure all of which strongly limit its widespread use.

6 Electroanatomic Mapping Systems. Remote Navigation/Ablation

Remote-controlled navigation technology provides for precise navigation with the hope that this translates to improved lesion contiguity. Recently, remote-controlled robotic catheter ablation has emerged as a new ablation approach to achieve these goals [20, 21]. Two remote-controlled systems, which have the added benefit of reducing the physician's radiation exposure, have been developed to facilitate catheter navigation and ablation by increasing catheter stability. The first one available for clinical use is a magnetic navigation system (Niobe II system, Stereotaxis, St. Louis, Missouri) and the second one is a robotic navigation system (Sensei system, Hansen Medical, Mountain View, California). Although both systems have shown the feasibility and safety of remote-controlled ablation, further technological innovations are required to expand applicability and research is needed to establish non-inferiority to manual approaches. Therefore, technical innovations are clearly warranted which could: *a)* minimize the physician's fluoroscopy exposure; *b)* reduce physical demands on the operator by allowing for a more relaxed ablation procedure from within the control room; *c)* improve catheter stability and reproducibility of the procedure; and *d)* increase patients' safety by avoiding serious complications. The Stereotaxis navigation system includes two large external magnets positioned on either side of the fluoroscopy table to generate a uniform magnetic field (0.08 T) of approximately 15-cm diameter within the patient's chest [20, 21]. The ablation catheters are extremely floppy along their distal end with small magnets embedded at the tip of the catheter. The catheter tip aligns with the orientation of the generated magnetic field. Using a software interface, the operator can manipulate the magnetic field and, by extension, the tip of the ablation catheter, providing the first level of freedom of movement with this new system. The other level of freedom of movement is the ability remotely to advance or retract the catheter tip by a computer-controlled catheter advancer system (CardioDrive), which consists of a disposable plastic unit positioned at the femoral catheter insertion site. The catheter shaft is affixed to a CardioDrive unit where it enters the sheath, and can transduce the remote operator instructions to advance or retract the catheter appropriately. This combination of remote catheter advancement-retraction and magnetic field manipulation allows the operator a great deal of flexibility for navigation, mapping and ablation. The magnetic navigation system is integrated with one of the electroanatomic mapping systems (CARTO RMT, Biosense Webster, Diamond Bar, CA), which also allows integration of 3-dimensional computed tomography or MRI models. Once integrated, the magnetic field can be directly controlled with the computer mouse. The mapping system can precisely localize the catheter tip in space to a submillimeter resolution. By precisely tracking the catheter location, the combination of mapping and navigation systems allows automated chamber mapping. The operator can remotely manipulate the magnetic catheter within the left atrium to a predefined anatomic location, such as PV ostia or mitral valve annulus. Based on these parameters, the system

automatically manipulates the catheter throughout the chamber to facilitate generation of an electroanatomic map. New software allows the system to manipulate the catheter tip automatically to create linear ablation lesions with in the chamber as per the operator's wishes. The efficiency and accuracy of these automatic software solutions, however, remain to be demonstrated. The other significant advance is the ability to incorporate pre-acquired 3-dimensional MRIs or computed tomography scans into the system to allow mapping on a realistic model of the heart. With the current generation software, clinical data are available on its efficacy for atrial fibrillation ablation. In more than 500 patients with atrial fibrillation, the Authors have demonstrated that electroanatomic maps are accurate and have recently reported that the standard set of lesions with remote PV isolation can be reproducibly achieved using an irrigated ablation catheter [24, 25].

7 Clinical Benefit of Electroanatomic Mapping Systems

In patients with complex tachyarrhythmias such as atrial fibrillation and/or atrial tachycardia electroanatomical mapping systems are useful for substrate identification and successful ablation. The accurate identification and modification of complex arrhythmogenic substrates is considered as primary ablation strategy in contemporary ablation procedures. Comparative studies have shown that by means of the 3D electroanatomic mapping systems both, radiation exposure and procedure duration can be significantly shortened versus conventional fluoroscopy-guided atrial fibrillation ablation procedures. Small single-center studies comparing the two systems in atrial fibrillation ablation directly demonstrated similar clinical results, but advantages of Carto® over EnsiteNavX® in terms of fluoroscopy use and procedure durations. There are many limitations of integration of virtual models: (1) different volume status during CT/MRI and during the procedure may result in mismatches of image integration; (2) additional radiation exposure due to CT scans, potential kidney damage or allergic reactions induced by contrast agents; (3) additional logistic and economic burden.

8 Discussion

It has become clear that the introduction and advances of the electroanatomical mapping system technology have facilitate many ablation strategies including but not limited to PV isolation serving as a prerequisite for more complex substrate modification followed by successful treatment of several and different tachyarrhythmias including incessant refractory primary or post-interventional atrial tachycardias. The two most widely used contact-based electroanatomic mapping systems worldwide in the context of atrial fibrillation ablation are the Carto® and EnsiteNavX® systems, which have evolved as the standard electroanatomic

mapping systems today leading to EAMS-based strategies [14–21]. In the last few years, although the electroanatomical mapping technology has been enhanced by integrating data from other imaging modalities, such as computed tomography and cardiac magnetic resonance, the contact-based electroanatomic mapping systems remains the standard of care in most patients, while non-contact and/or multipolar catheters enable high-density mapping of arrhythmias in as few as a single beat. More recently, the remote technology applied to electroanatomic mapping systems has made the ablation procedures shorter in duration, easier, less dependent on fluoroscopy, safer, and last but not least more effective but have reasonable additive costs for hardware installations [25]. Image integration and precise autoregistration of 3D models may result in (1) less fluoroscopy use due to improved awareness of the individual anatomy, and (2) in prevention of complications like pulmonary vein stenosis or esophageal thermal damage [32–39]. Although these potential advantages have not yet been proven in clinical trials, further clinical benefits of image integration remain controversial. Indeed, there are significant limitations of integration of virtual models, which require to be considered and discussed. First, contemporary 3D models represent static representations of a moving organ and not all motion artifacts from the beating heart or respiration can currently be entirely compensated. Second, the different volume status during CT/MRI and during the procedure may result in mismatches of image integration. Further disadvantages relate to the additional radiation exposure due to CT scans, to potential kidney damage or allergic reactions induced by contrast agents, or to an additional logistic and economic burden. In our experience activation mapping using multielectrode catheters should be considered as a standard tool in a modern electrophysiology laboratory particularly in treating complex arrhythmic substrates in patients with cardiomyopathies, who are increasingly referred for catheter ablation. In such patient population enhanced efficacy should be associated with lower risks of the procedure remaining one of the most important goals of future advances in ablation tools.

9 Conclusion and Future Work

The introduction and advancements of electroanatomic mapping systems have facilitated many complex catheter ablation procedures, such as atrial fibrillation ablation or incessant atrial tachycardia. The newer versions of Carto® and EnsiteNavX® systems are very effective and safe and currently are considered worldwide as the standard electroanatomic mapping systems making mapping and ablation procedures shorter, easier, less dependent on fluoroscopy, safer, and more effective with reasonable costs. Due to improved awareness of the individual anatomy, prevention of major complications of complex procedures, such as atrial fibrillation ablation, may be expected, as demonstrated in large multicenter studies. In conclusion, electroanatomical mapping systems have three major clinically relevant advantages. They visualize catheter positions in 3D space during the

procedure without ionizing radiation. They allow the detailed analysis of arrhythmia mechanisms and to guide ablation procedures in patients with complex arrhythmia substrates such as atrial fibrillation. Finally, they allow movement of electrophysiological catheters in a 'virtual anatomy' showing the catheter position visualized onto preprocedural and, in the near future, in accurate intraprocedural anatomic images ('image fusion'). Although the first advantage has been demonstrated in controlled trials, the latter two did so far not undergo rigorous clinical testing. Real-time feedback on tissue-catheter contact and multi-electrode high-resolution mapping with automatic point annotation further increase current mapping tools. Our primary future goal should be to improve effectiveness of mapping with the help of electroanatomic mapping systems through advancement of technologies available, along with implementing state-of-the-art technology in as many electrophysiology labs worldwide with rational cost. In the future, substrate modification in atrial fibrillation ablation should move toward individualized patient-tailored ablation procedures. Magnetic resonance imaging could play a major role for noninvasively describing the localization and extent of fibrotic areas. Specific new strategies that could be used include precise localization and ablation of rotors that maintain the arrhythmia using multielectrode mapping during atrial fibrillation and box isolation of fibrotic areas guided by electroanatomic voltage mapping during sinus rhythm. Predicting the future is hard, but that doesn't stop us from trying. Advances are getting bigger and bigger and happening more and more quickly.

References

1. Dey, N., Bardhan Roy, A., Pal, M., Das, A.: FCM based blood vessel segmentation method for retinal images. Int. J. Comput. Sci. Netw. (IJCSN) **1**(3), 148-15 (2012)
2. Payel Roy, P., Goswami, S., Chakraborty, S., Taher Azar, A., Dey, N.: Image segmentation using rough set theory: a review. Int. J. Rough Sets Data Anal. (IJRSDA) **1**(2), 62–74 (2014). doi:10.4018/ijrsda.2014070105
3. Samanta, S., Dey, N., Das, P., Acharjee, S., Sinha Chaudhuri, S.: Multilevel threshold based gray scale image segmentation using cuckoo search. In: International Conference on Emerging Trends in Electrical, Communication and Information Technologies. Elsevier—S&T Books, vol. 1, pp. 27–34 (2012)
4. Chakraborty, S., Mukherjee, A., Chatterjee, D., Maji, P., Acharjee, S., Dey, N.: A semi-automated system for optic nerve head segmentation. In: Digital Retinal Images ICIT '14 Proceedings of the 2014 International Conference on Information Technology, IEEE Computer Society Washington, DC, USA, pp. 112–117 (2014). doi:10.1109/ICIT.2014.51
5. Ikeda, N., Gupta, A., Dey, N., Bose, S., Shafique, S., Arak, T., Godia, E.C., Saba, L., Laird, J.R., Nicolaides, A., Suri, J.S.: Improved correlation between carotid and coronary atherosclerosis SYNTAX score using automated ultrasound carotid bulb plaque IMT measurement. Ultrasound Med. Biol. **41**(5), 1247–1262 (2015). doi:10.1016/j.ultrasmedbio.2014.12.024
6. Dey, N., Samanta, S., Yang, X.-S., Das, A., Sinha Chaudhuri, S.: Optimisation of scaling factors in electrocardiogram signal watermarking using cuckoo search. Int. J. Bio-Inspired Comput **5**(5), 315–326 (2013). doi:10.1504/IJBIC.2013.057193

7. Klemm, H.U., Ventura, R., Steven, D.: Catheter ablation of multiple ventricular tachycardias after myocardial infarction guided by combined contact and noncontact mapping. Circulation **115**, 2697–2704 (2007)
8. Marchlinski, F.E., Callans, D.J., Gottlieb, C.D., Zado, E.: Linear ablation lesions for control of unmappable ventricular tachycardia in patients with ischemic and nonischemic cardiomyopathy. Circulation **101**, 1288–1296 (2000)
9. Brunckhorst, CB., Etienne Delacretaz, E., Soejima, K., Maisel, W.H., Friedman, P.L., Stevenson, WG.: Identification of the ventricular tachycardia isthmus after infarction by pace mapping. Circulation **110**, 652–659 (1992)
10. Kimura, M., Sasaki, S., Owada, S., Horiuchi, D., Sasaki, K., Itoh, T., Ishida, Y., Kinjo, T., Okumura, K.: Validation of accuracy of three-dimensional left atrial CartoSound™ and CT image integration: influence of respiratory phase and cardiac cycle. J. Cardiovasc. Electrophysiol. **24**(9), 1002–1008 (2013)
11. Haissaguerre, M., Jais, P., Shah, D.C., Takahashi, A., Hocini, M., Quiniou, G., et al.: Spontaneous initiation of atrial fibrillation by ectopic beats originating in the pulmonary veins. N. Engl. J. Med. **339**, 659–666 (1988)
12. Pappone, C., Rosanio, S., Oreto, G., Tocchi, M., Salvati, A., Dicandia, C., et al.: Circumferential radiofrequency ablation of pulmonary vein ostia: a new anatomic approach for curing atrial fibrillation. Circulation **102**, 2619–2628 (2000)
13. Pappone, C., Oreto, G., Rosanio, S., Vicedomini, G., Tocchi, M., Gugliotta, F., et al.: Atrial electroanatomic remodeling after circumferential radiofrequency pulmonary vein ablation. Circulation **104**, 2539–2544 (2001)
14. Pappone, C., Manguso, F., Vicedomini, G., Gugliotta, F., Santinelli, V., Ferro, A., et al.: Prevention of iatrogenic atrial tachycardia following ablation of atrial fibrillation. a prospective randomized study comparing circumferential pulmonary vein ablation with a modified approach. Circulation **110**, 3036–3042 (2004)
15. Pappone, C., Santinelli, V., Manguso, F., Vicedomini, G., Gugliotta, F., Augello, G., et al.: Pulmonary vein denervation enhances long-term benefit after circumferential ablation for paroxysmal atrial fibrillation. Circulation **109**, 327–334 (2004)
16. Pappone, C., Rosanio, S., Augello, G., Gallus, G., Vicedomini, G., Mazzone, P., et al.: Mortality, morbidity and quality of life after circumferential pulmonary vein ablation for atrial fibrillation. outcomes from a controlled not randomized long-term study. J. Am. Coll. Cardiol. **42**, 185–197 (2003)
17. Oral, H., Scharf, C., Chugh, A., Hall, B., Cheung, P., Good, E., et al.: Catheter ablation for paroxysmal atrial fibrillation: segmental pulmonary vein ostial ablation versus left atrial ablation. Circulation **108**, 2355–2360 (2003)
18. Wazni, O.M., Marrouche, N.F., Martin, D.O., Verma, A., Bhargava, M., Saliba, W., Themistoclakis, S., Rossillo, A., Bonso, A., Natale, A.: Radiofrequency ablation vs antiarrhythmic drugs as first-line treatment of symptomatic atrial fibrillation: a randomized trial. JAMA **293**, 2634–2640 (2005)
19. Stabile, G., Bertaglia, E., Senatore, G., de Simone, A., Zoppo, F., Donnici, G., et al.: Catheter ablation treatment in patients with drug refractory atrial fibrillation: a prospective, multi-centre, randomized, controlled study (catheter ablation for the cure of atrial fibrillation study). Eur. Heart J. **27**, 216–221 (2006)
20. Oral, H., Pappone, C., Chugh, A., Good, E., Bogun, F., Pelosi, F., et al.: Circumferential pulmonary vein ablation for chronic atrial fibrillation: a randomized, controlled study. N. Engl. J. Med. **354**, 934–941 (2006)
21. Pappone, C., Augello, G., Sala, S., Gugliotta, F., Vicedomini, G., Gulletta, S., et al.: A Randomized trial of circumferential pulmonary vein ablation versus antiarrhythmic drug therapy in paroxysmal atrial fibrillation. The ablation for paroxysmal atrial fibrillation (APAF) study. J. Am. Coll. Cardiol. **48**, 2340–2347 (2006)

22. Haissaguerre, M., Sanders, P., Hocini, M., Takahashi, Y., Rotter, M., Sacher, F., et al.: Catheter ablation of long-lasting persistent atrial fibrillation: critical structures for termination. J. Cardiovasc. Electrophysiol. **11**, 1125–1137 (2005)
23. Nademanee, K., McKenzie, J., Kosar, E., Schwab, M., Sunsaneewitayakul, B., Vasavakul, T., et al.: A new approach for catheter ablation of atrial fibrillation: mapping of the electrophysiologic substrate. J. Am. Coll. Cardiol. **43**, 2044–2053 (2004)
24. Pappone, C., Vicedomini, G., Manguso, F., Mazzone, P., Gugliotta, F., Sala, S., et al.: Robotic magnetic navigation for atrial fibrillation ablation. J. Am. Coll. Cardiol. **47**, 1390–1400 (2006)
25. Pappone, C., Santinelli, V.: Remote navigation and ablation of atrial fibrillation. J. Cardiovasc. Electrophysiol. Suppl. **1**, S18–S20 (2007)
26. Pappone, C., Santinelli, V.: Multielectrode basket catheter: a new tool for curing atrial fibrillation? Heart Rhythm **3**, 385–386 (2006)
27. Pappone, C., Radinovic, A., Manguso, F., Vicedomini, G., Ciconte, G., Sacchi, S., et al.: Atrial fibrillation progression and management: a 5-year prospective follow-up study. Heart Rhythm **5**, 1501–1507 (2008)
28. Themistoclakis, S., Raviele, A., China, P., Pappone, C., De Ponti, R., Revishvili, A., Aliot, E., Kuck, K.H., Hoff, P.I., Shah, D., Almendral, J., Manolis, A.S., Chierchia, G.B., Oto, A., Vatasescu, R.G., Sinkovec, M., Cappato, R.: Prospective European survey on atrial fibrillation ablation: clinical characteristics of patients and ablation strategies used in different countries. atrial fibrillation survey investigators. J. Cardiovasc. Electrophysiol. **25**, 1074–1081 (2014)
29. Pappone, C., Santinelli, V.: Atrial fibrillation ablation. Rev. Esp. Cardiol. **65**, 560–569 (2012)
30. Pappone, C., Vicedomini, G., Augello, G., Manguso, F., Saviano, M., Baldi, M., Petretta, A., Giannelli, L., Calovic, Z., Guluta, V., Tavazzi, L., Santinelli, V.: Radiofrequency catheter ablation and antiarrhythmic drug therapy: a prospective, randomized, 4-year follow-up trial: the APAF study. Circ. Arrhythm. Electrophysiol. **4**, 808–814 (2011)
31. Wilber, D.J., Pappone, C., Neuzil, P., De Paola, A., Marchlinski, F., Natale, A., Macle, L., Daoud, E.G., Calkins, H., Hall, B., Reddy, V., Augello, G., Reynolds, M.R., Vinekar, C., Liu, C.Y., Berry, S.M., Berry, D.A.: ThermoCool AF trial investigators. JAMA **303**, 333–340 (2010)
32. Estner, H.L., Deisenhofer, I., Luik, A., Ndrepepa, G., von Bary, C., Zrenner, B., Schmitt, C.: Electrical isolation of pulmonary veins in patients with atrial fibrillation: reduction of fluoroscopy exposure and procedure duration by the use of a non-fluoroscopic navigation system (NavX). Europace **8**, 583–587 (2006)
33. Rotter, M., Takahashi, Y., Sanders, P., Haissaguerre, M., Jais, P., Hsu, L.F., Sacher, F., Pasquie, J.L., Clementy, J., Hocini, M.: Reduction of fluoroscopy exposure and procedure duration during ablation of atrial fibrillation using a novel anatomical navigation system. Eur. Heart J. **26**, 1415–1421 (2005)
34. Liu, X., Wang, X.H., Gu, J.N., Zhou, L., Qiu, J.H.: Electroanatomical systems to guided circumferential pulmonary veins ablation for atrial fibrillation: Initial experience from comparison between the EnSite/NavX and carto system. Chin. Med. J. (Engl.) **118**, 1156–1160 (2005)
35. Khaykin, Y., Oosthuizen, R., Zarnett, L., Wulffhart, Z.A., Whaley, B., Hill, C., Giewercer, D., Verma, A.: Carto-guided vs. NavX-guided pulmonary vein antrum isolation and pulmonary vein antrum isolation performed without 3-D mapping: effect of the 3-D mapping system on procedure duration and fluoroscopy time. J. Interv. Card. Electrophysiol. **30**, 233–240 (2011)
36. Kistler, P.M., Rajappan, K., Jahngir, M., Earley, M.J., Harris, S., Abrams, D., Gupta, D., Liew, R., Ellis, S., Sporton, S.C., Schilling, R.J.: The impact of ct image integration into an electroanatomic mapping system on clinical outcomes of catheter ablation of atrial fibrillation. J. Cardiovasc. Electrophysiol. **17**, 1093–1101 (2006)
37. Martinek, M., Nesser, H.J., Aichinger, J., Boehm, G., Purerfellner, H.: Impact of integration of multislice computed tomography imaging into three-dimensional electroanatomic mapping on clinical outcomes, safety, and efficacy using radiofrequency ablation for atrial fibrillation. Pacing Clin. Electrophysiol. **30**, 1215–1223 (2007)

38. Kistler, P.M., Rajappan, K., Harris, S., Earley, M.J., Richmond, L., Sporton, S.C., Schilling, R.J.: The impact of image integration on catheter ablation of atrial fibrillation using electroanatomic mapping: a prospective randomized study. Eur. Heart J. **29**, 3029–3036 (2008)
39. Marrouche, N.F., Martin, D.O., Wazni, O., Gillinov, A.M., Klein, A., Bhargava, M., Saad, E., Bash, D., Yamada, H., Jaber, W., Schweikert, R., Tchou, P., Abdul-Karim, A., Saliba, W., Natale, A.: Phased-array intracardiac echocardiography monitoring during pulmonary vein isolation in patients with atrial fibrillation: impact on outcome and complications. Circulation **107**, 2710–2716 (2003)

Image Quality Assessment: A Case Study on Ultrasound Images of Supraspinatus Tendon

Rishu Gupta, I. Elamvazuthi and J. George

Abstract With the advancement of technologies on visual contents and the rate at which data is being captured, viewed, stored, and shared, the importance of assessment of quality of the contents has major importance. Image quality assessment has remained a topic of research over the last several decades for optical as well as medical images. User oriented image quality assessment is playing a key role in the assessment of visual contents. Studies are conducted to imitate the accuracy of human visual system for assessment of images. This chapter details about the approaches for development of methods for image quality assessment followed by brief introduction on existing image quality assessment methods. Later in the chapter, challenges for validation and development of image quality assessment metric for medical images are briefly discussed followed by the case study for assessment of ultrasound images of supraspinatus tendon.

1 Introduction

Digital imaging and image processing technologies have constructively changed the way in which the visual contents is captured, stored, viewed, received and transferred over decades. With the advent of the technology sharing of images, videos or online streaming of the high definition videos have become a reality which was unthinkable two decades back. Despite the emerging technologies and advancements, the consumer or the human visual system has remain unchanged, although with time persons perception towards the visual contents may change due to underlying neural circuitry and its biological processing strategies. Digital imaging

R. Gupta · I. Elamvazuthi (✉)
Department of Electrical and Electronic Engineering, Universiti Teknologi Petronas, Bandar Seri Iskandar, Perak, Malaysia
e-mail: irraivan_elamvazuthi@petronas.com.my

J. George
University of Malaya Research Imaging Centre, Kuala Lumpur, Selangor, Malaysia

N. Dey et al. (eds.), *Medical Imaging in Clinical Applications*,
Studies in Computational Intelligence 651, DOI 10.1007/978-3-319-33793-7_12

can alter images in ways which can be perceived as detrimental or beneficial for impact on visual quality of images.

Because of occurrence of alterations in the visual contents due to various reasons such as the system properties of capturing device, noise or disturbance introduced by medium of transfer, or by disturbance introduced by system on consumer end, it is utmost important to keep track of the image quality. To meet this requirement, several algorithms and methods for image quality assessment has been developed over decades. The preliminary efforts to explain the quality evaluation of optical imaging systems and display systems can be found in [1]. Although no image quality assessment metric was proposed in [1], but many recent IQA metric do apply the factors such as definition, contrast range, gradation, brilliance, flicker, geometric distortion, size, color and noise introduced in this work. In [2], Fellgett and Linfoot introduced two key factors for assessment of image quality: "assessment by similarity and assessment by information". Indeed, many IQA algorithms have used these ideas or their variation for development of image assessment algorithms. It is interesting to note that idea of incorporating human visual system properties such as luminance, contrast, and visual making for the assessment of quality of images was put forward by researchers [3–5] in early 1970s but yet no metric was proposed. Although it was established that full evaluation of the quality of images is impossible yet but in the foreseeable future these metric are very likely to develop. Looking at the development after 45 years remarkable progress has been made for quality evaluation but still technology is far from being accurate.

At first instance, the development of IQA algorithm does not seem to be an intimidating problem because image is basically a collection of pixels and any alteration in the image can be traced by numerical mapping of the pixels. However to develop algorithm that incorporates characteristics of human visual system perfectly is difficult task as humans do not perceive images in the form of collection of pixels but the perception depends on image and type of processing and on the psychological interaction between these two factors and many more numerous features. It is mentioned by Schade [6] that image quality is a subjective judgment made by mental comparison of an external image with image impressions off external image with impression stored and remembered more or less distinctly by observer. Moreover, the rating given to an image may be greatly influenced by the availability of reference image, if much better or worse image for comparison purposes is provided.

The IQA algorithms can be categorized into three types based on the quality assessment with respect to the reference images [7]:

1. Full reference
2. Reduced reference
3. No reference

In full reference category the original image is provided for comparison with the processed image whereas in reduced reference for the evaluation of image quality original image is not provided rather some of the features from original image are

provided [7–9]. In the case of no reference IQA neither any information regarding the original image nor the original image is provided to evaluate the quality of the processed images.

Most of the IQA algorithms developed takes into consideration full-reference category which evaluates the processed image in comparison with that of the original image. All the three categories of IQA algorithm can produce good results for predicting the quality of the image but some of full reference IQA algorithm has matured compared to that of reduced or no reference IQA algorithms. However, with the recent advancements in the technology, reduced or no reference IQA methods have shown to produce results which are very close to human visualization ratings. Further in the chapter attributes of human visual system is briefly explained followed by detail discussion regarding the three categories of IQA techniques. Thereafter, challenges faced by research community in development of image quality assessment technique are also discussed briefly. In the end of the chapter, assessment method for medical images is also discussed in short with focus on ultrasound imaging.

2 Approaches for Development of IQA

The development of IQA algorithm can generally be categorized into two approaches. In first approach IQA metric is a result of considering physical attributes of images that human visual system finds intriguing or distinct. With the understanding of how the physical changes in the images are perceived by human visual system, an algorithm can be developed to assess the quality of image based on the changes occurring in images. Several studies have been conducted to understand and quantify the visual response of humans based on psychophysical and neural impact with changes in the images. As a result of these studies, detailed insights about the human visual system and its response is provided and further used for the development of IQA metrics.

Second approach for incorporating the human visual system response for creating the quality ratings is by allowing the evaluation of several images and their variations by group of human subjects or experts and save their ratings. Many of the quality rating studies have been conducted to build a database of images based on human perception and evaluation which could be further used to assess the quality of images. These generated databases contain reference images and their various versions of transformed images with their ratings included. This type of approach is very common for medical images such as ultrasound images or MRI images where lack of ground truth image is an impediment and also the images are used for the examination of human subjects, therefore, the quality of the images should be with the standards of the medical practitioners. Brief discussion regarding the human visual system attribute followed by validation method or development of IQA for assessment of medical images is provided in subsequent sections.

2.1 Attributes of Human Visual System for IQA

The purpose of study on the visual psychophysics is to understand the physical attributes of human visual system that can be monitored to better understand how the changes in the visual scenario can be mapped to the perception and cognition of humans. The study involves carefully designed protocols for human subjects in controlled environment with exact understanding of visual stimuli and viewing condition. Most of the visual perception parameters that are used for development of IQA are designed with the help of these studies. The primary goal for study on visual psychophysics is to understand the knowledge and functionality of human visual system with less emphasis on its image quality. As a result, it is a responsibility of the developer of IQA to utilize the findings of these studies [10–15] and incorporate them to develop an algorithm to monitor image quality. The psychophysical attributes that are incorporated in the development of IQA algorithms are briefly discussed below with referred articles for detailed understanding:

(1) Contrast sensitivity function: The study conducted on human visual system revealed that minimum contrast needed for detection of target is depended on the spatial frequency of target [16]. The minimum needed contrast is termed as contrast detection threshold (CST) and inverse of CST is contrast sensitivity. A thorough investigation of using contrast sensitivity function for development of IQA is provided in [17].

(2) Visual Masking: The understanding of fact, using studies on the human visual system, that some parts of images can conceal the information or distortions better than others [18] are used in the development of IQA algorithms. The visual masking is phenomenon where the presence of mask deters the perception of object in the image by observer. The visual masking can be categorized into three types: (1) noise masking (2) Contrast masking (3) Entropy masking [19]. Due to the simplicity of computation of contrast sensitivity, contrast masking is exploited in many IQA algorithms [20, 21]. The quantification of noise and entropy masking is difficult and henceforth less common in IQA algorithms [22].

(3) Model of human visual system: Based on the studies conducted on human visual system [23, 24] it was concluded that HVS decomposes the image's local spatial frequency which are further independently detected by multiple spatial frequency channels known as multichannel model of human visual system [25], this information is further processed in the form of multiscale decomposition methods for assessment of images.

(4) Computational neural models: The multichannel model of HVS has inspired researchers to develop neural model for human visual cortex. The developed neural models (V1 model) have been used for development of IQA algorithms [20, 26, 27]. The method first develops the reference image, then model neural responses for distortions and then assigns the detectable distortion if different sets of neural responses have sufficient difference.

Second approach for the development of image quality database for the assessment of images is qualitative assessment by humans which is discussed subsequently.

2.2 *Qualitative Assessment by Human*

To determine the quality of images another approach is development of image quality database based on the human interpretation of images and its several variations. The ratings for individual images should be provided by group of peoples or subjects and should be recorded to evaluate the image quality and also to refine the existing IQA algorithms. Image quality database contains ground truth information regarding the reference images and altered images with the average rating from several users. The information for the existing database of images can be found in [28].

The human observer plays a vital role in the validation of medical images as it involves the examination and diagnosis for human pathologies. Not only the validation from single observer but multiple observers and cross validation of the responses should be recorded for inter and intra-observer variability which is variability between two different observers and variability within the same observer respectively when observation is performed at different time intervals. Validation of research in medical imaging is of utmost importance. For validation purposes, phantoms, animal model, clinical studies based on the manual delineation performed by radiologists are generally preferred. In some of the cases of medical imaging it is very difficult to obtain the phantoms or animal models for validation, therefore assessment by medical practitioners plays vital role. In ultrasound imaging, very little work is performed using phantoms or simulated images which clearly explain the difficulty faced to procure realistic phantoms and simulations for tissues. Another impediment for validation of research on ultrasound images is non-availability of standard database for images for comparison of results. Field II ultrasound simulation package is used in limited cases in some of the applications [29, 30] for validation purposes. Details about validation method for developed algorithms for enhanced, focused assessment of ultrasound images of supraspinatus tendon is discussed later. Challenges faced by researchers for development of image quality assessment metric is briefly described in subsequent section.

3 Challenges for Image Quality Assessment Metric

The challenges in the development of image quality assessment metric are directly related to development in the understanding of the human visual system. The current understanding of the visual cortex is based on the primary visual cortex, the computation model developed for imitating primary visual cortex (V1) are very complex

due to the fact that response of visual neurons for different images is different in controlled environment and open environment. Due to the non-linear nature of neural response it is very difficult to estimate the response of human visual system towards natural or medical images. Apart from understanding of the human visual system the absence of ground truth data for natural images and medical images is also crucial for development of IQA, there is no available database for contrast detection threshold for natural images (related work can be found in [31, 32]). The database for images such as low contrast images, high contrast images, blurry images, natural scene images, medical images and other variations are necessary to develop database that can assist for the development of improved IQA metric.

For medical images the development of IQA metric is a relatively more challenging task due to unavailability of database for ground truth images and also variation in the anatomy with patients and its response towards different imaging modality. Medical imaging modalities such as magnetic resonance imaging (MRI), computed tomography (CT), positron emission tomography (PET), single photon emission computed tomography (SPECT), ultrasound (US) show different response towards different anatomical part. The interpretation of the images is highly dependent on the expertise of the medical practitioner and final assessment relies on radiologist delineation of the images. The IQA for ultrasound images can be done using several metrics such signal to noise ratio, similarity index, structural index, image quality index. Not one index can incorporate the details of medical images, [33] introduced a method for quantitative assessment of calcium lesion in intravascular ultrasound images. Further discussion on image assessment for ultrasound images are detailed in Sect. 5.

Some of the medical imaging modalities show better contrast compared to other, however others have different added advantages such as the images taken from MRI have good contrast but imaging is difficult for claustrophobic patients or patients with metal transplants and is also expensive compared to ultrasound which has relatively lower contrast and resolution but patient acceptability is high and is cost effective. For medical images inter-variability and intra-variability exist in the assessment of images by different medical practitioners at varied time intervals. The subsequent sections briefly provides the limitations of IQA techniques.

4 Limitations of Image Quality Assessment

The image quality assessment metric are the result of imitating HVS for assessment of quality of images. HVS is capable to perceives different kinds of image in a different and efficient manner and evaluate them on quality, developing an IQA which incorporates variations in images is not yet available due to our lack of understanding of HVS. Some of the limitations of IQA techniques are as follows:

1. Assessment of image quality in absence of ground truth or reference image.
2. Limited understanding of human visual system

3. Computational cost of the metric incorporating the details of HVS
4. Lack of ground truth database for individual form of images such as for optical images and medical images. In case of medical images, diagnostics are mostly dependent on observers experience and knowledge.

For ultrasound images, evaluation of quality of speckle is assessed using ultrasound despeckling assessment index (USDSAI) [34], however different application of ultrasound images cannot be assessed using single metric. Therefore for medical applications use of multiple relevant metrics is introduced. In the subsequent section of this chapter a case study on enhancement and segmentation of supraspinatus tendon ultrasound images is provided along with its impact on assessment of supraspinatus tendon using statistical analysis and metric values.

5 Proposed Method Adopted for Assessment of SSP Tendon Ultrasound Images

Lack of standardized measures for quantitative assessment of ultrasound images and also absence of ground truth database makes it difficult to compare results obtained using different methods. Therefore by far, most extensively used technique for validation of results in ultrasound imaging is manual delineation of clinical data with the help of radiologist [35]. In most of the recent literature [35–40], for validation of segmentation in ultrasound images, models manually delineated by radiologist are used as ground truth. Numerous literature, suggests use of manual delineation being used as a reference for research validation in applications on different anatomical part such as cardiac, prostate, IVUS, kidney and many others [30, 36, 40, 41]. Inter- and intra- variability is a concern because manual segmentation is not the task radiologist intends to do often. Therefore, the comparisons for the results are performed by statistical methods generally using the clinical assessment of images with delineation performed by different radiologists. Inter and intra variability for diagnosis is calculated based on radiologist's assessment of several images at different time intervals. After the procurement of assessment results statistical methods are used to validate the results of the algorithm. The total of 116 images of supraspinatus tendon were included in the study with following details shown in Table 1.

Table 1 Summary of dataset

Pathological condition	Number of patients	Number of images
Normal	11	31
Tendinosis	13	29
Tear	15	29
Tear within Tendinosis	12	27
Total	51	116

5.1 Enhancement

For medical ultrasound images, to be able to design the reliable and accurate algorithm for assessment of ultrasound images, it is necessary that images are relevant as per radiologist satisfaction. When observing an image, the quality depends on many factors such as sharpness, contrast, viewing angle, resolution and other factors [42]. For ultrasound images, unfortunately subjective quality of an image cannot be explained figuratively, and hence final opinion depends on expert's evaluation of the image. The evaluation of image by radiologist also depends on expertise. Although, ultrasound imaging modality contains artifacts and is subjected to the radiologist assessment; on several occasions it has been verified that ultrasound tend to provide comparable accuracy with that of MRI or arthroscopy [43, 44]. The validation methods espoused in the literature [45–47] have been used in this research work. This observation regarding the nature of ultrasound images motivates use of different image quality assessment and expert's assessment for outcome of different algorithms to quantify the quality of algorithm.

5.1.1 Method

Assessment for enhancement of SSP tendon ultrasound image is performed using qualitative and quantitative methods.

Qualitative Assessment

The performance of the proposed techniques was evaluated based on the radiologist's assessment of the enhanced images. The algorithms were tested for ensuring: (1) consistence performance of method; (2) reliability of the method; (3) overall estimate to check the significance of enhancement. Three rounds of assessments were performed by two radiologists on enhanced images using different methods [48, 49]. The blind evaluation was conducted for each image; the assessment was performed using three enhanced and one original image. The resultant images were provided to radiologist with no prior information given regarding clinical history of patient. All four images were shown to radiologist at the same time for evaluation with no mention about the technique used for enhancement. For intra-observer variability, readings from the same radiologist were taken again after the period of three weeks. The total of three evaluations for each image was performed and images were shown in random manner to radiologist at every evaluation. The assessment sheet for evaluation of the established techniques is shown in Table 2. The sheets were provided for every enhanced technique and image. Therefore, for each image four assessment sheets were given to radiologists one for each technique. The assessment sheets obtained with the help of radiologist was then further evaluated using statistical method to report the accuracy of the method.

Table 2 Assessment sheets for radiologists

Tissue classification	TP	FP	TN	FN
Tendinosis				
Tear in normal SSP				
Rank				

The sheet contains information regarding three different pathological conditions i.e. tear and tendinosis and the pathological conditions were classified as

True Positives (TP)—Pathological condition present and diagnosed correctly
True Negatives (TN)—Pathological condition not present and not diagnosed
False Positives (FP)—Pathological condition not present but diagnosed
False Negatives (FN)—Pathological condition present but cannot be diagnosed

The final row for rank assessment is over-all assessment of the enhancement of image on the scale of 1–4 where 1 was given to worst performer and 4 was given to best performer.

Inter-observer and intra-observer variability was calculated to estimate the enhancement in the images and its relevance to the diagnosis. The analysis was performed based on the overall assessment of the images. The Cohen (κ) value is calculated to determine the inter-observer agreement [45]. Cohen (κ) values [50] greater than 0.80 shows almost complete agreement and less than 0.20 shows no agreement, whereas 0.21–0.40 gives fair, 0.41–0.60 indicates moderate and 0.61–0.80 specifies considerable level of agreement among radiologists The formula for computing κ value is given below,

$$\kappa = \frac{p_0 - p_e}{1 - p_e} \tag{1}$$

where, p_0 overall agreement between two observer, p_e is agreement expected to occur by chance, p_0, p_e can be calculated as follows,

$$p_0 = \frac{P_{pos} + P_{neg}}{T} \tag{2}$$

where, P_{pos} is the positives in agreement, P_{neg} is the negatives in agreement, T is the total number of images and p_e is calculated as the joint positive and joint negative responses from both radiologists, the calculation for p_e is done using formula

$$p_e = \frac{P_{pos1}}{T} * \frac{P_{pos2}}{T} + \frac{P_{neg1}}{T} * \frac{P_{neg2}}{T} \tag{3}$$

where, P_{pos1} and P_{pos2} is the total number of positives for radiologist 1 and radiologist 2 respectively, P_{neg1} and P_{neg2} are the total number of negatives for radiologist 1 and radiologist 2 respectively. For intra-observer variability, separate assessment for tear and tendinosis was performed. Percentage agreement between the readings taken from radiologist was computed, the computation was performed

by taking the average of percentage agreement found in first round-second round (FR-SR), second round-third round (SR-TR) and third round-first round (TR-FR) agreement for both the radiologists.

Quantitative Assessment

The quantitative assessment was further performed using various image metrics to correlate the results obtained qualitatively. For synthetic or optical image, where original image $X_{i,j}$ are available, various quantitative parameters are used to validate the outcome of the resultant image $Y'_{i,j}$ which we have introduced to quantify the performance of enhancement. In the below equations from (4)–(8), μ and σ are respectively the mean and variance within the images. The different quantitative measurement indices investigated are:

(1) Universal quality index (UQI): This performance measure models distortion in image as factor of three components [51], contrast distortion, luminance distortion, and loss of correlation. The numerical formula for the metric is given by

$$\mathrm{UQI} = \frac{\sigma_{XY}}{\sigma_X \sigma_Y} * \frac{2\mu_X \mu_Y}{(\mu_X)^2 + (\mu_Y)^2} * \frac{2\sigma_X \sigma_Y}{\sigma_X^2 + \sigma_Y^2} \tag{4}$$

Metric provides information about extent of structure preservation, luminance variance and contrast dependence of two images.

(2) Mean square error (MSE): estimates the overall change in the quality of the image in original and enhanced image. The computation is performed using

$$\mathrm{MSE} = \frac{1}{\mathrm{NM}} \sum_{i,j=1}^{N,M} \left(X_{i,j} - Y_{i,j}\right)^2 \tag{5}$$

Although mean square error is often used to judge image quality, it does not sufficiently correlate to the perceptual quality of image. Therefore, it is advised to use it in combination with other parameter metrics.

(3) Signal to noise ratio(SNR): although sensitivity to signal and noise are important for algorithms by themselves, what really matters is the ratio of signal to noise which is calculated as

$$\mathrm{SNR} = 10 \log \left(\frac{\sum_{i,j=1}^{N,M} X_{i,j}^2}{\sum_{i,j=1}^{N,M} \left(X_{i,j} - Y'_{i,j}\right)^2} \right) \tag{6}$$

(4) Structural similarity index (SSI): measures any distortion in the image into three factors: luminance, contrast distortion and loss of correlation. The formula for computation of SSI is given by

$$\mathrm{SSI} = \frac{(2\mu_X\mu_Y + c_1)(2\sigma_X\sigma_Y + c_2)}{(\mu_X^2 + \mu_Y^2 + c_1)(\sigma_X^2 + \sigma_Y^2 + c_2)} \tag{7}$$

where, $c_1 = 0.01(\mathrm{DR})$ and $c_2 = 0.03(\mathrm{DR})$ are that depends on the dynamic range (DR = 255) of the image and used to stabilize the division with weak denominator. The range of output values from SSI is from −1 to 1 where −1 stands for poor similarity and 1 stands for good similarity between the original image and enhanced image.

(5) Structural content (SC): explains the similarity between enhanced and the original image; higher value suggests that algorithm employing image enhancement have lenient effect on structures.

$$SC = \frac{\sum_{i=1}^{N}\sum_{j=1}^{M} X_{i,j}^2}{\sum_{i=1}^{N}\sum_{j=1}^{M} Y_{i,j}^2} \tag{8}$$

5.1.2 Enhancement Results

The results obtained after enhancement performed using three different techniques are presented in Fig. 1 for visualization. In the first set of images shown in Fig. 1a–d, the tendon is shown to be suffering from a tear in the interim section of tendon. In all the three enhanced images, the pathological condition has become more prominent after enhancement. In Rayleigh enhanced image, the tear is enhanced at the same time contrast for nearby structures follow the same pattern and does not lead for poor diagnosis or false diagnosis. Whereas in Weibull and normal enhanced image the enhancement for pathological condition is comparatively higher but leads to enhancement of neighborhood region which accounts for false diagnosis.

In second set of images shown in Fig. 1e–h, the SSP tendon of patient is in healthy condition and has no existing pathologies. The Rayleigh enhancement confirms the diagnosis with no false interpretation, whereas for Weibull and normal enhancement of image leads to false interpretation of patients pathological conditions. The diagnosis performed using Weibull and normal enhanced method details the patient to be suffering from calcification which is deposit of calcium in a tendon.

In third set of images shown in Fig. 1i–l, as per the initial diagnosis of the radiologist, the patient is suffering from tear within tendinosis. The Rayleigh enhanced image makes the diagnosis more accurate and definitive. As per radiologist, loss of the tendons and inflammation in the tissue structure is clearly evident

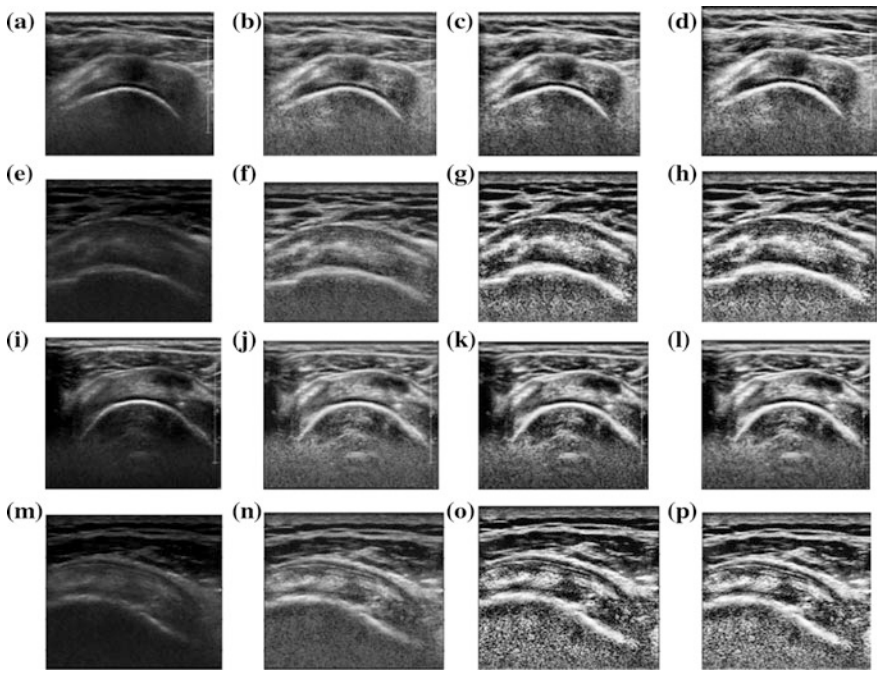

Fig. 1 Column wise enhanced Images for visual analysis (**a**, **e**, **i**, **m**) Original image; (**b**, **f**, **j**, **n**) Rayleigh enhanced image (**c**, **g**, **k**, **o**) Weibull enhanced image (**d**, **h**, **l**, **p**) Normal enhanced image

in enhancement performed using Rayleigh method. Whereas the enhancement performed using Weibull and normal method in some cases leads to false diagnosis of patient suffering from tear.

Last set of images shown in Fig. 1m–p, the patient is suffering from tendinosis; the region can be seen just above humeral cortex. In Rayleigh enhanced image, the region of tendinosis is clearly dominant but at the same time the contrast in neighboring structure is maintained thereby not giving any false indications for non-existent pathologies. On the other hand, the enhancement performed by Weibull and normal method provides good interpretation for tear in tendon but at the same time, it also provides hints for calcification in the region of tendon which is false and misleading for radiologists. With the enhanced images, the diagnosis is more evident for junior medical officers thereby decreasing the variability in the operator's assessment of ultrasound images. The qualitative and quantitative assessment of 116 set of images with different pathological conditions was carried out. The assessment method and results for qualitative and quantitative assessment are presented in following sections.

Qualitative Assessment

The resultant images from the three algorithms along with original image were produced in front of radiologist for blind evaluation. Three assessments of all images were performed at three different time intervals. The result for first assessment of images by radiologist is shown in Table 3. Table 3a–d shows the assessment results of diagnosis based on enhancement performed using Rayleigh distribution method, Weibull distribution method, Normal distribution method and original image respectively. The table is created based on the information filled by radiologist in the assessment sheet provided to them for image visualization. Similarly, Tables 5 and 7, shows the result from the second and third assessment of images by radiologist. The values for overall agreement p_0 between two observers, p_e agreement expected to occur by chance and cohen κ, the chance corrected agreement between the radiologists are calculated to understand the interobserver agreement between the radiologists for three assessments.

The statistical analysis of the results of first assessment obtained from radiologist is summarized in the Table 4.

Table 3 Joint results for first assessment of images

First radiologist	Second radiologist		Tot.
	Positive for disease	Negative for disease	
(a) Rayleigh enhancement technique			
Positive for disease	72	8	80
Negative for disease	9	27	37
Total	81	35	116
(b) Weibull enhancement technique			
Positive for disease	63	9	72
Negative for disease	10	34	44
Total	73	43	116
(c) Normal enhancement technique			
Positive for disease	60	11	71
Negative for disease	9	36	45
Total	69	47	116
(d) Original image			
Positive for disease	54	8	62
Negative for disease	13	41	54
Total	64	52	116

Table 4 Indices of agreement between radiologists for first assessment

Agreement index	Type of agreement	Rayleigh	Weibull	Normal	Original
p_0	Overall	0.853	0.836	0.8276	0.819
p_e	Chance	0.577	0.531	0.521	0.504
κ	Chance corrected	0.7139	0.7058	0.6033	0.6855

Table 5 Joint results for second assessment of images

First radiologist	Second radiologist		Tot.
	Positive for disease	Negative for disease	
(a) Rayleigh enhancement technique			
Positive for disease	72	7	79
Negative for disease	7	30	37
Total	79	37	116
(b) Weibull enhancement technique			
Positive for disease	66	9	75
Negative for disease	7	34	41
Total	73	43	116
(c) Normal enhancement technique			
Positive for disease	59	11	70
Negative for disease	11	35	46
Total	70	46	116
(d) Original image			
Positive for disease	55	7	62
Negative for disease	11	43	54
Total	66	50	116

Table 4 suggests the performance of Rayleigh distribution to be higher with the κ value of 0.7139 compared to Weibull-0.7058, normal-0.6033 and original image-0.6855. The values obtained using Rayleigh, Weibull and original image falls under the category of considerable agreement among radiologist whereas the agreement obtained from normal enhanced image gives moderate agreement. The overall agreement between the radiologist and agreement to occur by chance follow the same trend as observed by cohen (κ) value. Table 5 shows the assessment result of the radiologist for second assessment of images. The tabulated assessment is further used to statistically determine the quality of enhancement technique.

Similar analysis for images from second and third assessment is performed and results are provided as follows. Table 6, summarizes the findings of radiologist assessment in the second round of assessment.

Table 6 indicates, second round of assessment to confirm higher agreement among radiologist for the use of Rayleigh distribution enhanced image for diagnosis of SSP tendon. The chance corrected agreement or cohen (κ) value for Rayleigh distribution is 0.7212, followed by Weibull-0.7013, original-0.6855, and normal enhanced image-0.6033 at the last position. The three images Rayleigh, Weibull and

Table 6 Indices of agreement between Radiologists for second assessment

Agreement index	Type of agreement	Rayleigh	Weibull	Normal	Original
p_0	Overall	0.879	0.862	0.81	0.844
p_e	Chance	0.566	0.538	0.521	0.504
κ	Chance corrected	0.7212	0.7013	0.6033	0.6855

Table 7 Joint results for third assessment of images

First radiologist	Second radiologist		Tot.
	Positive for disease	Negative for disease	
(a) Rayleigh enhancement technique			
Positive for disease	73	6	79
Negative for disease	5	32	37
Total	78	38	116
(b) Weibull enhancement technique			
Positive for disease	68	8	76
Negative for disease	4	36	40
Total	72	44	116
(c) Normal enhancement technique			
Positive for disease	61	8	69
Negative for disease	14	33	47
Total	75	41	116
(d) Original image			
Positive for disease	62	7	69
Negative for disease	9	38	47
Total	64	52	116

original provides considerable agreement among radiologist whereas normal enhanced image gives moderate agreement for the diagnosis of SSP tendon. Table 7, shows the assessment result of radiologist for enhanced method in third assessment.

From the observed results in Table 8, it can be concluded that Rayleigh distribution gives highest chance corrected value or cohen (κ) value of 0.7831 followed by Weibull-0.7624, original-0.6947 and normal enhanced image-0.5983. The results obtained using Rayleigh, Weibull and original image shows considerable agreement between the experts whereas the agreement between the radiologists for normal enhanced image is moderate. All the three assessment performed by radiologist suggests Rayleigh enhanced ultrasound image to provide better diagnostic value compared to other two methods and original image.

Further intra-observer agreement within the radiologists is computed based on the percentage agreement of radiologist among themselves in first round-second round, second round-third round and third round-first round of assessment. Table 9 summarizes the results of assessment agreement within the radiologist in different rounds for the assessment of pathological condition tear.

Table 8 Indices of agreement between radiologists for third assessment

Agreement index	Type of agreement	Rayleigh	Weibull	Normal	Original
p_0	Overall	0.905	0.89	0.81	0.862
p_e	Chance	0.562	0.537	0.527	0.503
κ	Chance corrected	0.7831	0.7624	0.5983	0.6947

Table 9 Intra-observer variability in radiologists assessment for tear

IA round	Percentage agreement (%)	
	Expert 1	Expert 2
(a) Original image		
FR-SR	79	72
SR-TR	74	77
TR-FR	65	80
Average (%)	72.66	76.33
(b) Rayleigh adaptive enhanced		
FR-SR	81	76
SR-TR	77	81
TR-FR	72	84
Average (%)	76.33	80.33
(c) Weibull adaptive enhanced		
FR-SR	77	72
SR-TR	76	77
TR-FR	75	82
Average (%)	76	77
(d) Normal adaptive enhanced		
FR-SR	71	70
SR-TR	76	72
TR-FR	61	64
Average (%)	69.33	68.66

*FR—First round, SR—Second Round, TR—Third Round, IA—Image Assessment

The average value of the agreement was calculated for Rayleigh enhanced image, Weibull enhanced image, normal enhanced image and original image. Observing the results obtained in Table 9, it was found that the percentage agreement with in the radiologist for Rayleigh is comparatively higher compared to other method. The average value of agreement within the radiologist for enhancement performed by Rayleigh is 76.33 % for expert 1 and 80.33 % for expert 2, which was followed by Weibull with percentage agreement of 76 % by expert 1 and 77 % by expert 2, original image shows the agreement of 72.66 % by expert 1 and 76.33 percent by expert 2. The enhancement performed by normal enhanced image gives within agreement for expert 1 to be 69.33 % and for expert 2 to be 68.66 % which is lower than that for original image. The graphical representation of the results for intra-observer agreement for the pathological condition tear is shown in Fig. 2.

Figure 2, shows the average value for both the radiologist for the diagnosis of pathological condition tear is maximum for Rayleigh enhanced method, followed by Weibull, original image and normal enhanced image.

Table 10, summarizes the result of agreement within radiologist for three assessments for pathological condition, tendinosis, using first-second round, second-third round, and third-first round agreement.

The observation of results obtained in Table 10, suggests Rayleigh to be having higher percentage agreement within radiologist with 80 % for expert 1 and 83 %

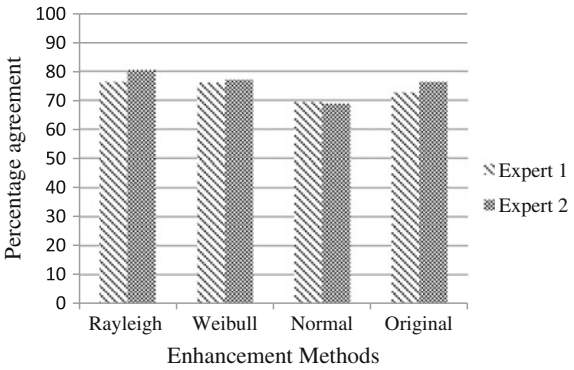

Fig. 2 Average value for intra-observer agreement for tear using different methods

Table 10 Intra-observer variability in radiologists assessment for tendinosis

IA round	Percentage agreement (%)	
	Expert 1	Expert 2
(a) Original image		
FR-SR	73	79
SR-TR	76	78
TR-FR	71	82
Average (%)	73.33	79.66
(b) Rayleigh adaptive enhanced		
FR-SR	75	81
SR-TR	84	86
TR-FR	81	82
Average (%)	80	83
(c) Weibull adaptive enhanced		
FR-SR	72	77
SR-TR	74	73
TR-FR	71	79
Average (%)	72.33	76.33
(d) Normal adaptive enhanced		
FR-SR	69	65
SR-TR	72	69
TR-FR	70	71
Average (%)	70.33	68.33

*FR—First round, SR—Second Round, TR—Third Round, IA—Image Assessment

for expert 2 followed by original with agreement of 73.33 % by expert 1 and 79.33 % from expert 2, Weibull with agreement of 72.33 % and 76.33 % for expert 1 and expert 2 respectively. Normal enhanced image gives the lowest percentage for within agreement between three rounds. The graphical representation of average value of percentage agreement between expert 1 and expert 2 for pathological condition tear can be seen in Fig. 3.

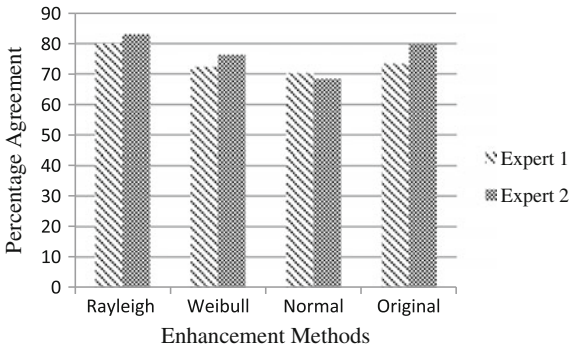

Fig. 3 Average value for intra-observer agreement for tendinosis using different methods

Figure 3 again confirms the diagnosis of pathological condition tendinosis can be better performed using Rayleigh enhanced method, followed by Weibull, original image and normal enhanced image.

Quantitative Assessment

The summary of the quantitative evaluation of enhancement techniques based on universal quality index, signal to noise ratio, structure similarity index, structural content and mean square error parameter metrics is tabulated in Table 11.

The evaluation metrics are calculated for the resultant images from different techniques. The results are consistent with the findings of radiologist with Rayleigh distribution performing best and, conflicts exist in Weibull and original image for number two and number three positions. Weibull is ranked number two by universal quality index, structural similarity index and structural content whereas signal to noise ratio and mean square error is at number two for original image, followed by normal enhanced image which is at number four. The plot for evaluation metrics are shown in Figs. 4, 5, 6, 7, and 8 for universal quality index, signal to noise ratio, structure similarity index, structural content and mean square error respectively.

Figure 4, shows the results for the evaluation of images based on universal quality index. The maximum value of universal quality index is obtained for Rayleigh enhanced ultrasound image which depicts the methods capabilities to

Table 11 Rank of techniques quantitatively

Measurement index	Rayleigh rank	Weibull rank	Normal rank	Original rank
Quality index	1	2	4	3
SNR	1	3	4	2
SSI	1	2	4	3
SC	1	2	4	3
MSE	1	3	4	2

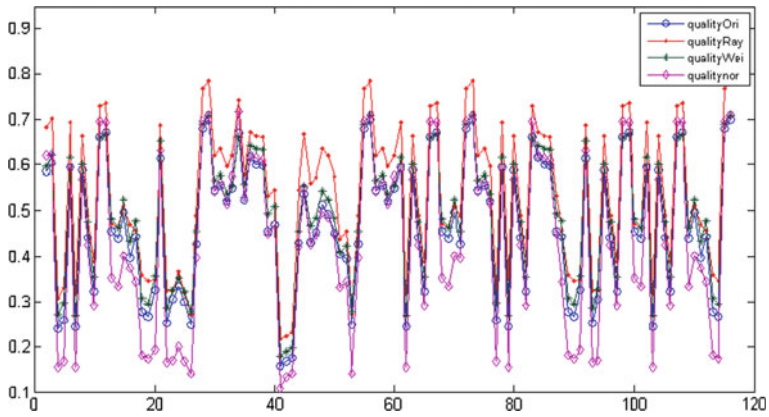

Fig. 4 Universal quality index

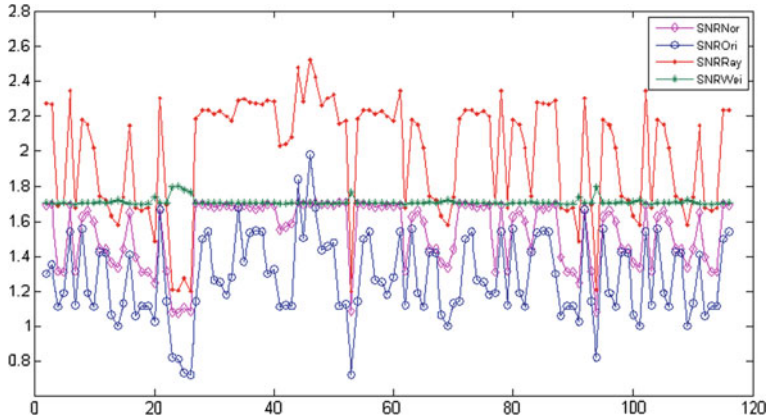

Fig. 5 Signal to noise ratio

preserve the tissue structures in ultrasound image better than the other methods. The Rayleigh enhancement is followed by Weibull which was qualitatively also suggested by experts as the second best enhancement method after the Rayleigh method. Original ultrasound image results to be at number 3 which again justifies the qualitative analysis followed by the normal enhancement at the last. The average value of universal quality index for Rayleigh enhancement is 0.54 followed by 0.49 for Weibull enhanced image and 0.47 for original and 0.43 for normal enhanced image.

Figure 5, shows the result obtained by signal to noise ratio measurement index with maximum average SNR value of 1.98 for Rayleigh enhancement SSP tendon image followed by original image at number 2 with the average SNR value of 1.71 and Weibull enhanced image with very slight difference of 0.03 in the values of SNR with original image at number 3 and finally the performance of normal

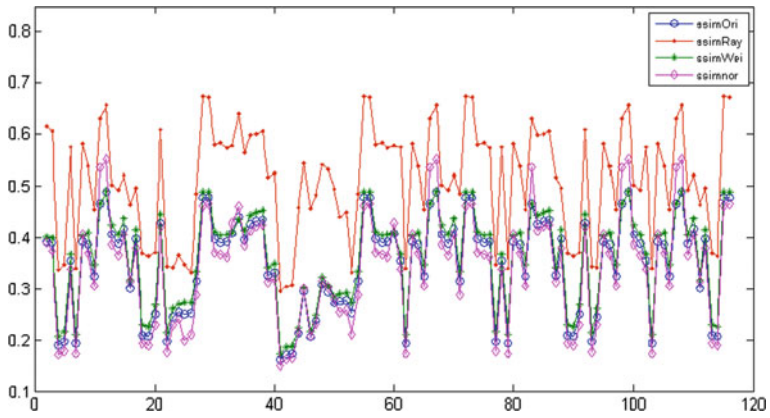

Fig. 6 Structural similarity index

enhanced image is last with the average SNR value of 1.27. The results from SNR values rates Rayleigh enhanced ultrasound image to contain more signal to noise ratio compared to other methods for enhancement.

Figure 6, shows the result of four considered algorithms with respect to the structure similarity index parameter metric. The average value of Rayleigh enhanced image is 0.512 followed by 0.49 for Weibull, 0.43 for normal enhanced image and 0.35 for original image. The results obtained from the SSIM index shows the best preservation of the structure details in Rayleigh enhanced image which is similar to the results obtained from qualitative analysis performed with the help of experienced radiologists.

Figure 7 gives the quantitative result of the algorithm based on the structural content parameter with average value of 13.76 for Rayleigh enhancement followed

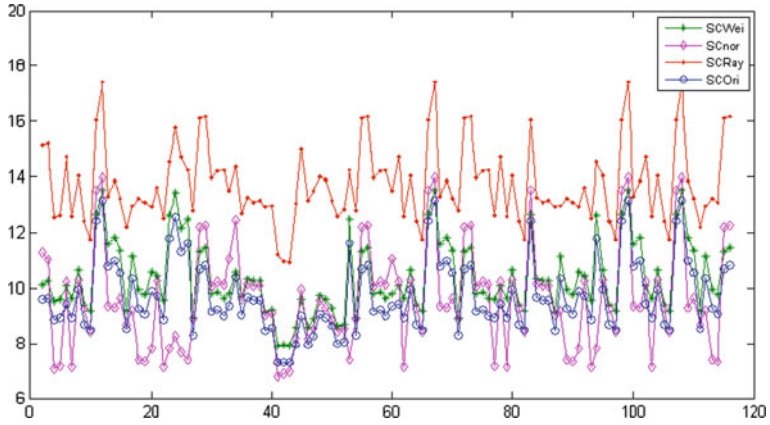

Fig. 7 Structural Content

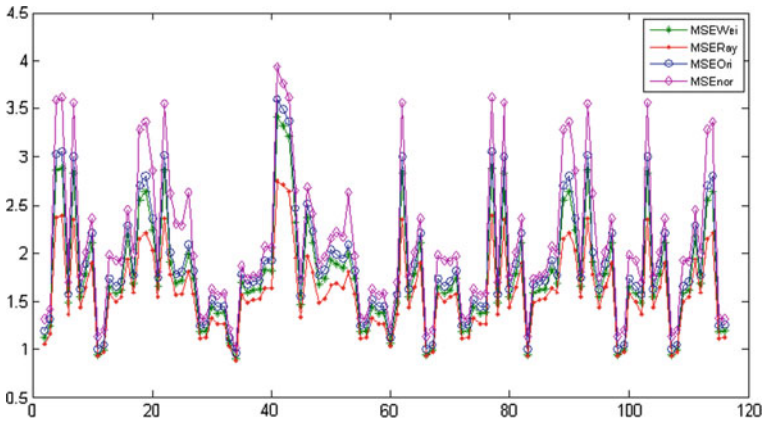

Fig. 8 Mean square error

by 10.4 for Weibull enhancement, 9.74 for original image and 9.61 for normal enhanced ultrasound image. The results are consistent for Rayleigh enhanced ultrasound image showing maximum diagnostic capabilities for detection of pathological region in SSP tendon. The results are also consistent with the radiologist assessment of the ultrasound images.

Figure 8 shows the results from last quantitative parameter introduced based on the error introduced in the images after the enhancement. Mean square error for all the enhanced images was calculated and average value of MSE for Rayleigh is 1.601 followed by 1.78 by Weibull enhanced image, 1.87 from original image and 2.10 from norm enhanced ultrasound image. The MSE for Rayleigh enhancement is lowest suggesting the maximum enhancement and minimum introduction of the unnecessary details to ultrasound images after enhancement.

The qualitative and quantitative analysis performed on the ultrasound images based on the four different distributions suggests Rayleigh enhanced ultrasound image to perform best for assistive diagnosis of the pathological condition in SSP tendon by radiologist. The detailed results obtained at every step in mask extraction for SSP tendon and pathological advantage of using focused SSP tendon image for assessment has been provided subsequently.

5.2 Assessment of Segmentation

For the assessment of region of interest segmentation, qualitative measures were adopted both for performance of the algorithm and improvement in diagnostic capabilities.

5.2.1 Performance of Segmentation Algorithm: Qualitative Assessment

The quantitative method uses three parameter metrics: (1) False positive rate (FPR); (2) True positive rate (TPR) [52]; (3) Accuracy (ACC). The measurement metrics were calculated based on the area of segmentation. The regions were classified as true positives, false positives, and false negatives. Pictorial representation for corresponding area is shown in Fig. 9.

The performance metrics can be calculated using the formula below,

$$\mathrm{TPR} = \frac{\mathrm{TP}}{\mathrm{TP} + \mathrm{FN}}, \tag{9}$$

$$\mathrm{FPR} = \frac{\mathrm{FP}}{\mathrm{FP} + \mathrm{TN}}, \tag{10}$$

$$\mathrm{ACC} = \frac{\mathrm{TP} + \mathrm{TN}}{\mathrm{TP} + \mathrm{FP} + \mathrm{TN} + \mathrm{FN}} \tag{11}$$

where, TP is region of SSP tendon accurately segmented by algorithm, FP is the region segmented by proposed method but does not exist in radiologist delineation, FN is the region delineated by radiologist and not existent in region segmented by proposed method, TN do not exist for assessment of segmentation. The images for visualization were also provided.

5.2.2 Performance on Diagnostics: Qualitative Assessment

The SSP tendon segmentation from ultrasound image results in the focused assessment of the tendon for pathological condition. The results were validated by providing the segmented image to radiologist and performing the assessment based on the radiologist interpretation of pathologies from focused images. The pathological conditions considered for evaluation in this case were tears, which could be

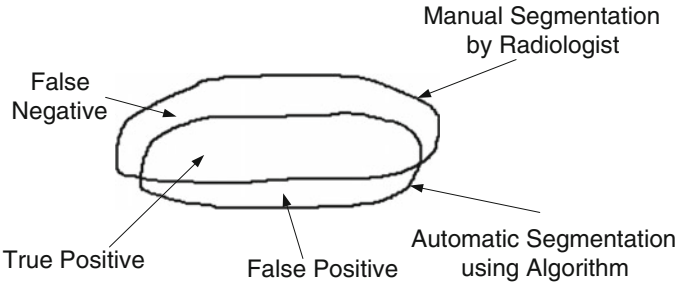

Fig. 9 Corresponding areas for false positive, false negative and true positives

partial thickness tears (PTTs) or full thickness tears (FTTs). The specificity and sensitivity values were calculated from radiologist assessment of the segmented image using the formula,

$$\text{Sensitivity} = \frac{\text{TP}}{\text{TP} + \text{FN}}, \quad \text{Specificity} = \frac{\text{TN}}{\text{FP} + \text{TN}} \tag{12}$$

Also, the results of evaluation performed by radiologist were compared to that of existing results for the evaluation of PTTs and FTTS using ultrasound image.

5.2.3 Results of Segmentation

Out of the total 116 images, 109 images were correctly classified. In 3 images algorithm failed to extract SSP tendon and outliers were more prominent. In 4 images, the complete tendon was segmented but with outliers accompanied with it.

Figure 10, shows visualization of the results using manual segmentation by radiologist and result obtained using proposed algorithm. Figure 10a shows the true positive results wherein accurate segmentation as per radiologist requirement was attained followed by Fig. 10b it can be seen that the region segmented by radiologist is present in the result with an outlier region shown. The false positives arise because of the inaccurate detection of muscle fat outlier which plays important role in segmentation. In Fig. 10c, result shows inaccuracy of the algorithm in the form of detection of false negatives, wherein the reason for inaccuracy is poor visibility of bursae. No cases of true negatives were found (true negatives are cases when the segmentation area completely lies outside the region manually segmented by radiologists).

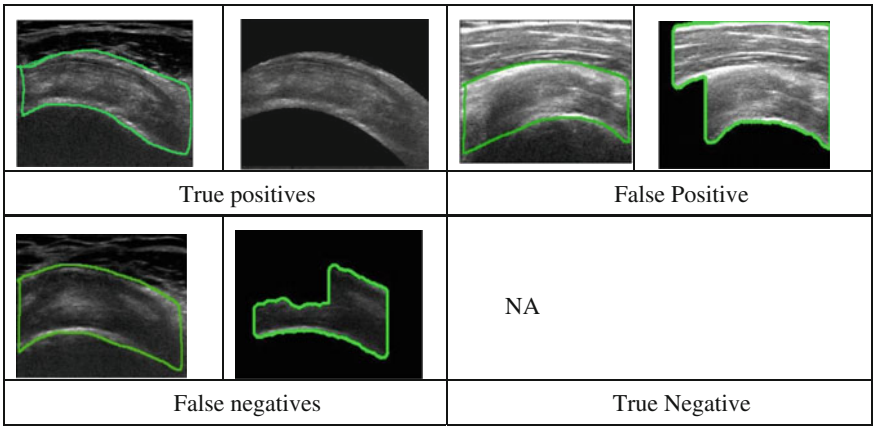

Fig. 10 Results from manual segmentation of radiologist and automatic segmentation using proposed algorithm

Table 12 Performance result of the algorithm

Performance metric	Evaluation result
True positive rate (TPR)	0.9137
False positive rate (FPR)	0.0862
Accuracy (ACC)	0.9482

Performance of Segmentation Algorithm: Qualitative Assessment

The quantitative assessment of results obtained using proposed algorithm was performed using true positive rate, false positive rate and accuracy of segmentation. Table 12 shows the measurement values of the algorithm for true positive rate, false positive rate and accuracy. The accuracy of the algorithm obtained for the provided data set was 94.82 % i.e. out of 116 images taken, the proposed algorithm was able to segment SSP tendon from 103 images successfully. And the true positive rate of 91.37 % which is number correct segmentation over total correct segments and false negatives and false positive rate of 8.62 % which is total number of false positive over conditional negatives.

The performance of the algorithm was also tested based on the improvement in the diagnostic capabilities due to focused SSP tendon image generated by algorithm. The assessment was performed with the help of radiologist and discussed in next section.

Performance on Diagnostics: Qualitative Assessment

The qualitative assessment was performed to estimate the improvement in diagnosis of pathologies such as partial thickness tears (PTTs) and full thickness tears (FTTs). The radiologist assessment was performed for the diagnosis of SSP tendon for PTTs and FTTs. The result of radiologist assessment is shown in Table 13.

In [53], 40 images were used to compute the sensitivity and specificity of the diagnosis of PTTs and FTTs in SSP tendon, whereas Singh [54] uses 36 images to quantify the diagnosis of PTTs and FTTs in SSP tendon and Rutten et al. [55] uses a database of 68 images to quantify the diagnosis of PTTs and FTTs in SSP tendon using ultrasound images. In this work, 116 ultrasound images were considered to

Table 13 Comparison of results for focused pathology (PTT—Partial thickness tear; FTT—Full thickness tear)

Author	Images	Partial thickness tear		Full thickness tear	
		Sens.	Spec.	Sens.	Spec.
E. ElGawad et al. [53]	40	92.3	92.6	92.6	94
Singh [54]	36	66.7	93.5	92.3	94.4
Rutten et al. [55]	68	92	33.5	94	94
Prop. method	116	94	93.6	95.6	95

qualitatively evaluate the performance of proposed method for assessment of PTTs and FTTs in ultrasound images. The sensitivity and specificity values for PTTs computed using [53–55] are 92.3 % and 92.6 %, 66.7 % and 93.5 %, 92 % and 33.5 % whereas using the proposed method the values are 94 and 93.6 %. Similarly, for FTTs sensitivity and specificity for [53–55] are 92.6 % and 94 %, 92.3 % and 94.4 %, 94 % and 94 % respectively whereas sensitivity and specificity for diagnosis of FTTs using segmented SSP tendon are 95.6 % and 95 % respectively.

6 Summary

Image quality assessment (IQA) is of utmost importance with the increasing amount of usage of digital media for communication. The data is being transferred at a very high pace and therefore the quality check is very important at the receiver end. Most of the IQA techniques developed attempt to imitate the human visual system which is by far considered as best visual system due to the randomness in the neurons and its response towards particular images at different time interval with different references.. Researchers are attempting to estimate the parameters of HVS and their behavior towards different kind of images. So far much has been done regarding development of IQA algorithms but still we are very far from accurately imitating the human visual system. The validation in medical images is subjective to operators experience and no benchmark database is available for assessment of ultrasound medical images. In presented work, the qualitative and quantitative assessment is performed to testify the results of algorithms. The qualitative and quantitative results are in accordance thereby suggesting the efficacy of the method.

References

1. Goldmark, P., Dyer, J.: Quality in television pictures. Proc. Inst. Radio Eng. **28**(8), 343–350 (1940)
2. Fellgett, P.B., Linfoot, E.H.: On the assessment of optical images. Philos. Trans. R. Soc. Lond. **247**(931), 369–407 (1955)
3. Budrikis, Z.L.: Visual fidelity criterion and modeling. Proc. IEEE **60**(7), 771–779 (1972). doi:10.1109/proc.1972.8776
4. Chandler, D.M.: Seven challenges in image quality assessment: past, present, and future research. ISRN Signal Process. **2013**, 53 (2013). doi:10.1155/2013/905685
5. Zhou, W.: Applications of objective image quality assessment methods [applications corner]. Sig. Process. Mag. IEEE **28**(6), 137–142 (2011). doi:10.1109/msp.2011.942295
6. Schade, O.: Image Quality: A Comparison of Photographic and Television Systems. RCA Laboratories (1975)
7. Gupta, P., Srivastava, P., Bhardwaj, S., Bhateja, V.: A novel full reference image quality index for color images. In: Satapathy, S., Avadhani, P.S., Abraham, A. (eds.) Proceedings of the International Conference on Information Systems Design and Intelligent Applications 2012

(INDIA 2012) held in Visakhapatnam, India, January 2012, vol. 132, pp. 245–253. Springer, Berlin (2012)
8. Bhateja, V., Kalsi, A., Srivastava, A., Lay-Ekuakille, A.: A reduced reference distortion measure for performance improvement of smart cameras. Sens. J. IEEE **15**(5), 2531–2540 (2015). doi:10.1109/jsen.2014.2361286
9. Bhateja, V., Srivastava, A., Kalsi, A.: Fast SSIM index for color images employing reduced-reference evaluation. In: Satapathy, S.C., Udgata, S.K., Biswal, B.N. (eds.) Proceedings of the International Conference on Frontiers of Intelligent Computing: Theory and Applications (FICTA) 2013, vol. 247, pp. 451–458. Springer International Publishing (2014)
10. Watson, A.B., Taylor, M., Borthwick, R.: Image quality and entropy masking. In: Human Vision, Visual Processing, and Digital Display VIII, Proceedings of SPIE, vol. 3016, pp. 2–12 (1997)
11. Ninassi, A., LeMeur, O., Le Callet, P., Barba, D.: Does where you gaze on an image affect your perception of quality? Applying visual attention to image quality metric. In: Proceedings of the 14th IEEE International Conference on Image Processing (ICIP '07), pp. II169–II172 (2007)
12. Rouse, D.M., Hemami, S.S., Pépion, R., Callet, P.L.: Estimating the usefulness of distorted natural images using an image contour degradation measure. J. Opt. Soc. Am. **28**(2), 157–188 (2011)
13. Vilankar, K., Vasu, L., Chandler, D.M.: On the visual perception of phase distortion. In: Rogowitz, B.E., Pappas, T.N. (eds.) HumanVision and Electronic Imaging, Proceedings of SPIE, San Francisco, Calif, USA (2011)
14. Gaubatz, M.D., Chandler, D.M., Hemami, S.S.: A patchbased structural masking model with an application to compression. Eurasip J. Image Video Process. **2009** (Article ID 649316) (2009)
15. Nadenau, M.J., Reichel, J.: Image compression related contrast masking measurements. In: Proceedings of the Human Vision and Electronic Imaging, vol. 3959, pp. 188–199 (2000)
16. DeValois, R.L., DeValois, K.K.: Spatial Vision. Oxford University Press (1990)
17. Barten, P.G.J.: Formula for the contrast sensitivity of the human eye. In: Imaging Quality and System Performance, Proceedings of SPIE, pp. 231–238 (2004)
18. Legge, G.E., Foley, J.M.: Contrastmasking in human vision. J. Opt. Soc. Am. **70**, 1458–1470 (1980)
19. Watson, A.B., Yang, G.Y., Solomon, J.A., Villasenor, J.: Visibility of wavelet quantization noise. IEEE Trans. Image Process. **6**(8), 1164–1175 (1997)
20. Daly, S.: Visible differences predictor: an algorithm for the assessment of image fidelity. Digital Images and Human Vision, pp. 179–206 (1993)
21. Zeng, W., Daly, S., Lei, S.: Point-wise extended visual masking for JPEG-2000 image compression. In: International Conference on Image Processing, pp. 657–660 (2000)
22. Zhang, Y., Pham, B., Eckstein, M.P.: Investigation of JPEG 2000 encoder options on model observer performance in signal known exactly but variable tasks (SKEV). In: Chakraborty, A. K.D.P. (ed.) Medical Imaging: Image Perception, Observer Performance, and Technology Assessment, Proceedings of SPIE, vol. 5034, pp. 371–382 (2003)
23. Campbell, F.W., Robson, J.G.: Application of fourier analysis to the visibility of gratings. J. Physiol. **197**(3), 551–566 (1968)
24. Schade, O.H.: Optical and photoelectric analog of the eye. J. Opt. Soc. Am. **46**(9), 721–739 (1956)
25. Graham, N.: Visual Pattern Analyzers. Oxford University Press, New York (1989)
26. Watson, A.B., Solomon, J.A.: A model of visual contrast gain control and pattern masking. J. Opt. Soc. Am. **14**, 2378–2390 (1997)
27. Teo, P., Heeger, D.: Perceptual image distortion. In: Proceedings of the IEEE International Conference Image Processing (ICIP'94), vol. 2(982–986) (1994)
28. Lambrecht, C.J.B.: Working spatio-temporal model of the human visual system for image restoration and quality assessment applications. In: Proceedings of the IEEE International

Conference on Acoustics, Speech, and Signal Processing (ICASSP '96), pp. 2291–2294 (1996)
29. Hassenpflug, P., Prager, R.W., Treece, G.M., Gee, A.H.: Speckle classification for sensorless freehand 3-D ultrasound. Ultrasound Med. Biol. **31**(11), 1499–1508 (2005). doi:10.1016/j.ultrasmedbio.2005.07.007
30. Ledesma-Carbayo, M.J., Kybic, J., Desco, M., Santos, A., Suhling, M., Hunziker, P., Unser, M.: Spatio-temporal nonrigid registration for ultrasound cardiac motion estimation. IEEE Trans. Med. Imaging **24**(9), 1113–1126 (2005). doi:10.1109/tmi.2005.852050
31. Nadenau, M.J., Reichel, J.: Image compression related contrast masking measurements. In: Proceedings of the Human Vision and Electronic Imaging V, vol. 3959, pp. 188–199 (2000)
32. Winkler, S., Süsstrunk, S.: Visibility of noise in natural images. Human Vision and Electronic Imaging IX, Proceedings of SPIE, pp. 121–129 (2004)
33. Araki, T., Ikeda, N., Dey, N., Chakraborty, S., Saba, L., Kumar, D., Suri, J.S.: A comparative approach of four different image registration techniques for quantitative assessment of coronary artery calcium lesions using intravascular ultrasound. Comput. Methods Programs Biomed. **118**(2), 158–172 (2015). doi:10.1016/j.cmpb.2014.11.006
34. Tay, P.C., Acton, S.T., Hossack, J.A.: Ultrasound despeckling using an adaptive window stochastic approach. In: 2006 IEEE International Conference on Paper Presented at the Image Processing, 8–11 Oct. 2006
35. Noble, J.A., Boukerroui, D.: Ultrasound image segmentation: a survey. IEEE Trans. Med. Imaging **25**(8), 987–1010 (2006). doi:10.1109/tmi.2006.877092
36. Ghose, S., Oliver, A., Marti, R., Llado, X., Vilanova, J.C., Freixenet, J., Meriaudeau, F.: A survey of prostate segmentation methodologies in ultrasound, magnetic resonance and computed tomography images. Comput. Methods Programs Biomed. **108**(1), 262–287 (2012). doi:10.1016/j.cmpb.2012.04.006
37. Massich, J., Meriaudeau, F., Pérez, E., Martí, R., Oliver, A., Martí, J.: Lesion segmentation in breast sonography. In: Martí, J., Oliver, A., Freixenet, J., Martí, R. (eds.) Digital Mammography, vol. 6136, pp. 39–45. Springer, Berlin (2010)
38. Noble, J.A.: Ultrasound image segmentation and tissue characterization. Proc. Inst. Mech. Eng. H **224**(2), 307–316 (2010)
39. Prevost, R., Mory, B., Cuingnet, R., Correas, J.-M., Cohen, L., Ardon, R.: Kidney Detection and Segmentation in Contrast-Enhanced Ultrasound 3D Images. In: El-Baz, A.S., Saba, L., Suri, J. (eds.) Abdomen and Thoracic Imaging, pp. 37–67. Springer, US (2014)
40. Rueda, S., Fathima, S., Knight, C.L., Yaqub, M., Papageorghiou, A.T., Rahmatullah, B., Noble, J.A.: Evaluation and comparison of current fetal ultrasound image segmentation methods for biometric measurements: a grand challenge. IEEE Trans. Med. Imaging **33**(4), 797–813 (2014). doi:10.1109/tmi.2013.2276943
41. Massich, J., Meriaudeau, F., Sentís, M., Ganau, S., Pérez, E., Martí, R., Martí, J.: Automatic seed placement for breast lesion segmentation on US images. In: Maidment, A.A., Bakic, P., Gavenonis, S. (eds.) Breast Imaging, vol. 7361, pp. 308–315. Springer, Berlin (2012)
42. Ahumada, A.J., Null, C. H.: Digital images and human vision. In: chapter Image Quality: A Multidimensional Problem. MIT Press, Cambridge (1993)
43. Lenza, M., Buchbinder, R., Takwoingi, Y., Johnston, R.V., Hanchard, N.C., Faloppa, F.: Magnetic resonance imaging, magnetic resonance arthrography and ultrasonography for assessing rotator cuff tears in people with shoulder pain for whom surgery is being considered. Cochrane Database Syst. Rev. **9**, CD009020 (2013). doi:10.1002/14651858.CD009020.pub2
44. Teefey, S.A., Rubin, D.A., Middleton, W.D., Hildebolt, C.F., Leibold, R.A., Yamaguchi, K.: Detection and quantification of rotator cuff tears. Comparison of ultrasonographic, magnetic resonance imaging, and arthroscopic findings in seventy-one consecutive cases. J. Bone Joint Surg. Am. **86-A**(4), 708–716 (2004)
45. Harold, L., Kundel, M.P.: Measurement of observer agreement. Radiology **228**, 303–308 (2003)
46. Naredo, E., Moller, I., Moragues, C., de Agustin, J.J., Scheel, A.K., Grassi, W., Werner, C.: Interobserver reliability in musculoskeletal ultrasonography: results from a "Teach the

Teachers" rheumatologist course. Ann. Rheum. Dis. **65**(1), 14–19 (2006). doi:10.1136/ard.2005.037382
47. Zhong, T., Tagare, H.D., Beaty, J.D.: Evaluation of four probability distribution models for speckle in clinical cardiac ultrasound images. IEEE Trans. Med. Imaging **25**(11), 1483–1491 (2006). doi:10.1109/tmi.2006.881376
48. Drakonaki, E.E., Allen, G.M., Wilson, D.J.: Real-time ultrasound elastography of the normal Achilles tendon: reproducibility and pattern description. Clin. Radiol. **64**(12), 1196–1202 (2009). doi:10.1016/j.crad.2009.08.006
49. Ottenheijm, R.P., van't Klooster, I.G., Starmans, L.M., Vanderdood, K., de Bie, R.A., Dinant, G.J., Cals, J.W.: Ultrasound-diagnosed disorders in shoulder patients in daily general practice: a retrospective observational study. BMC Fam. Pract. **15**, 115 (2014). doi:10.1186/1471-2296-15-115
50. Landis, J.R., Koch, G.G.: The measurement of observer agreement for categorical data. Biometrics **33**, 159–174 (1977)
51. Zhou, W., Bovik, A.C.: A universal image quality index. Signal Process. Lett. IEEE **9**(3), 81–84 (2002). doi:10.1109/97.995823
52. Madabhushi, A., Metaxas, D.N.: Combining low-, high-level and empirical domain knowledge for automated segmentation of ultrasonic breast lesions. IEEE Trans. Med. Imaging **22**(2), 155–169 (2003). doi:10.1109/tmi.2002.808364
53. Abd-ElGawad, E.A., Ibraheem, M.A., Fouly, E.H.: Evaluation of supraspinatus muscle tears by ultrasonography and magnetic resonance imaging in comparison with surgical findings. Egypt. J. Radiol. Nuclear Med. **44**(4), 829–834 (2013). doi:10.1016/j.ejrnm.2013.08.001
54. Singh, J.P.: Shoulder ultrasound: what you need to know. Indian J. Radiol. Imaging **22**(4), 284–292 (2012). doi:10.4103/0971-3026.111481
55. Rutten, M.J., Jager, G.J., Kiemeney, L.A.: Ultrasound detection of rotator cuff tears: observer agreement related to increasing experience. AJR Am. J. Roentgenol. **195**(6), W440–W446 (2010). doi:10.2214/ajr.10.4526

Development of EOG and EMG-Based Multimodal Assistive Systems

Biswajeet Champaty, D.N. Tibarewala, Biswajit Mohapatra and Kunal Pal

Abstract This study discusses a human-computer interface (HCI)- based novel approach for designing a computer-aided control and communication system using electrooculogram (EOG) and electromyogram (EMG) signals for people with severe hindrance to motor activities and communication. The EOG and EMG signals were attributed to eye movements and voluntary eye blinks, respectively. The acquired signals were processed and classified in a MATLAB-based graphical user interface (GUI) to detect different eye movements. A couple of Hall-effect sensors were conditioned to be used concurrently with multidirectional eye movements or voluntary eye blinks to generate multipurpose serial commands to control the movement of a robotic vehicle (representative assistive aid) and communications support systems. The user details were registered and the system operability was monitored in the same GUI. Due to multitasking and ease of use of the proposed device, the quality of life of the incapacitated individuals can be improved with greater independence.

Keywords Human-computer interface · Incapacitated patients · Electrooculogram · Electromyogram · Graphical user interface · Hall-effect sensor · MATLAB

B. Champaty · K. Pal (✉)
Department of Biotechnology & Medical Engineering,
National Institute of Technology, Rourkela 769008, Odisha, India
e-mail: kpal.nitrkl@gmail.com

D.N. Tibarewala
School of Bioscience & Engineering, Jadavpur University,
Kolkata 700032, West Bengal, India

B. Mohapatra
Vesaj Patel Hospital, Rourkela 769004, Odisha, India

N. Dey et al. (eds.), *Medical Imaging in Clinical Applications*,
Studies in Computational Intelligence 651, DOI 10.1007/978-3-319-33793-7_13

1 Introduction

1.1 Motivation

In recent years, there has been an enormous rise in the research on the development of assistive technologies for providing support to the individuals with severe disabilities. This has been made possible due to the advancements in the field of control and communication technologies, which has facilitated the improvement of the quality of the human-machine interface (HMI) or human-computer interface (HCI) devices [1]. This discipline of technology has a great potential to enable the severely disabled persons to operate computer and other assistive gadgets directly by biopotentials (e.g. electroencephalogram (EEG) [2–4], electrooculogram (EOG) [5, 6], electromyogram (EMG) [7, 8] etc.). These biopotentials are also used for wireless tele-monitoring [9, 10]. Individuals suffering from amyotrophic lateral sclerosis (ALS), brain or spinal cord injury, multiple sclerosis and muscular dystrophies have been reported to have severe inabilities to perform speech and/or motor activities [11, 12]. Therefore, they face difficulties in locomotion as well as conveying their intentions. This significantly reduces their ability to interact, which in turn, compromises the quality of life of such individuals. Due to this reason, these individuals are forced to rely on the peripheral aids like computer-aided assistive and augmentative communication systems for conveying their intentions to others and to perform other daily activities. In these individuals, it has been found that the functionality of the muscles responsible for ocular movement remains intact [13]. These muscles are responsible for the significant voluntary activity associated with the eye movement. The biopotential generated due to the movement of the eyes regarded as EOG. Hence, EOG has been used as the input signal for control and communication interactive assistive devices.

1.2 Literature Review

Several methods, based on EOG controlled man-machine interfaces (multimode controller communication assistive devices), have been reported [11–23]. EOG has been employed to control the prosthesis for footdrop correction [24]. Robotic prosthetic arms have also been guided by EOG signals [23, 25]. A lot of research has been carried out in the movement of wheelchairs, a major mobility aid for the motor disabled individuals [5, 15, 26–29]. Additionally, EOG has found tremendous applications in facilitating communications by controlling keyboards, mouse and joystick functions [6, 13, 18, 19, 30–32]. In the last decade, home automation using EOG has also found substantial attention [20, 31, 33–36]. Though different technologies are available for expressing the intentions of the severely disabled individuals using EOG based HCIs, many of them are quite expensive [37], unreliable, inaccurate [38] and are complex to operate [38]. Further, none of the

studies has reported the concurrent use of the assistive devices for both control and communication purposes.

1.3 Contribution and Benefit Over Existing System

Taking inspiration from the above, in this paper, we propose a novel real-time EOG based computer assistive technology to develop a robust hardware-software system that combines the control activities with communication activities. The device can be effectively used by the severely disabled individuals having volitional eye movement and minimum finger movements. In this study, EOG signal was acquired from a dual channel (horizontal and vertical) bioamplifier and was band-limited (0.16–33.88 Hz). The band-limited signal was acquired in a computer, processed and finally classified using a MATLAB program. The classification of the EOG signals helped in detecting various eye movements. As a representative mobility aid, an electromechanical robotic vehicle was designed. The first-stage activation and the end-stage deactivation of the robotic vehicle were achieved using voluntary eye blink. The functioning (movements) of the robotic vehicle was controlled by up, down, left and right movements of the eye. To avoid any accidental initiation of the tasks, a switching system was introduced using a couple of HE sensors, attached to the index and middle fingers. The signals obtained from the eye movements, voluntary blink and triggering of the HE sensors were used in different combinations to control either the functioning of the robotic vehicle or initiating communication (making calls and sending emails). A GPRS shield, piggybacked on Arduino Mega ADK, was used to facilitate the control of the communication unit for making voice calls through serial communication. The control signals were generated with the help of a customized graphical user interface (GUI) designed in MATLAB. Conscious efforts were made to make the device robust, partially intricate and user-friendly to render a disabled individual to lead an independent lifestyle for social integration. The implementation of the multimodal control systems, i.e., controlling the assistive device (robotic vehicle) and alerting the attendant or the health caregivers through mobile and internet communication system is the key advantage of the proposed study over existing similar studies.

1.4 Organization of the Paper

The paper has been organized into five different thematic sections. Following the first introductory sections, the second section briefly presents the generation of electrooculogram signal. Section three describes the materials and methods. Section four discusses the results of the study. Finally, section five provides a closing discussion and conclusion. All the referred research works are cited in the text and are listed under the reference section.

2 Electrooculogram: A Brief Introduction

Human eye can be depicted as a fixed dipole that allows the generation of electric field. The cornea behaves as the positive pole, whereas the retina behaves as the negative pole. The relative electric potential in the retina is due to the higher metabolic rate rather than its excitable nature. This corneo-retinal potential, which gives rise to a fixed dipole, is in the range 0.4–1.0 mV [39]. This difference in potential, due to the rotation of the eye, can be acquired by surface electrodes placed around the eye at specific locations. This signal is known as electrooculogram (EOG). The EOG can be generated both in darkness and closing the eyes. The EOG signal can be employed by the researchers for developing real-time assistive devices. The EOG signals can also be recorded and analyzed by the optometrists to diagnose different ophthalmic disorders.

3 Materials and Methods

3.1 Materials

AD-620 (Analog Devices, India) [5], NI USB-6008 (National Instruments, USA) [40], Arduino ADK Mega (Arduino, Italy) [41], Arduino UNO (Arduino, Italy) [5], Arduino wireless proto shield (Arduino, Italy) [42], Xbee-S1 wireless transceiver module (Digi International, USA) [42], GPRS Shield V1.0 (Seeed Technology Limited, China) [41], AH-34 Hall effect sensor (Triax Corporation, Japan) [41], Ag/AgCl disposable electrodes (BPL, India) with connecting clips [24], freeware EAGLE PCB Design Software (CadSoft Inc., USA) and licensed MATLAB® R2014a (MathWorks, USA) were used in this study. A laptop, with processor specification Intel (R) Core (TM) i7-2600 CPU @ 3.40 GHz, was used in this study.

3.2 Informed Consent

15 volunteers from National Institute of Technology Rourkela, India, of either sex, were selected for this study. All the volunteers were in the age group of 22–30 years. Prior to experimental involvement, all the volunteers were verbally made aware of the study and the experimental procedure. The volunteers had to sign an informed consent form to participate in the experiment. None of the volunteers was suffering from any health issues or had any adversity to the experimental conditions. A prior ethical clearance was obtained from the Institute ethical clearance committee vide order No. (NITR/IEC/FORM/2/25/4/11/002).

3.3 Development of EOG Acquisition System

The EOG biopotential amplifier reported in [5] was modified for the present study. The improvement in the circuit was achieved through modifications in the power supply section. The circuit was developed using the commercially available instrumentation amplifier IC AD-620. A resistor of 560Ω (gain resistor) was used to achieve a 1st stage gain of 90. Like EEG [43] and EMG [44], the EOG signal is also a random process. Hence, the presence of unpredictable noise is obvious. It has been reported that the frequency range of the EOG signal is 0.1–30 Hz [45]. Hence, the amplified signal was filtered using a 1st order passive band-pass filter with lower and upper cut-off frequencies of 0.16 and 33.88 Hz [46], respectively. Subsequently, the pre-amplified signal was smoothened using a 2nd order low-pass filter with cut-off frequency of 33.88 Hz. The smoothened band limited EOG signal was further amplified using AD-620 with a gain of 12. The signal was further processed through a 2nd order low-pass filter with a cut-off frequency of 33.88 Hz. This constituted the first EOG amplifier (EOG-I). Similar to the EOG-I amplifier, EOG-II amplifier was designed having similar specifications.

EOG-I amplifier was used for recording the vertical eye movements (up and down) by placing the electrodes in the orbital position. EOG-II amplifier was used to record the horizontal eye movements (left and right) by placing the electrodes in the canthi position. The output of both the amplifiers was acquired into a laptop (operating in battery mode) using a NI USB-6008 data acquisition system. The sampling rate of the USB-6008 was set at 10 KS/s. The output of the EOG-I amplifier was acquired from the AI0 input terminal, whereas, the output of the EOG-II amplifier was acquired from the AI1 input terminal. The biopotential amplifier circuit was powered by a ±12 V power supply. The power supply was developed using a DC-DC converter (IC MAU-108) [47]. The MAU-108 accepts an input voltage of +5 V and generates an output of ±12 V. The MAU-108 was powered from the USB-6008. The circuit diagram of the biopotential amplifiers (EOG-I and EOG-II) and the functioning circuit of MAU-108 to generate ±12 V have been shown in Fig. 1. The V-channel in the Fig. 1, signifies the conditioned output of the vertical (up-down) eye movements. Similarly, the H-channel denotes the conditioned output of the horizontal (left-right) eye movements.

3.4 Acquisition of the EOG Signals

A 5-marker panel was designed. It has been reported that the accommodation of the eye up to a distance of 2 m produces important cues that influences the space perception [48]. Hence, based on the space availability, the distance between the patient and the panel was fixed to 150 cm. The central marker was at the level of the

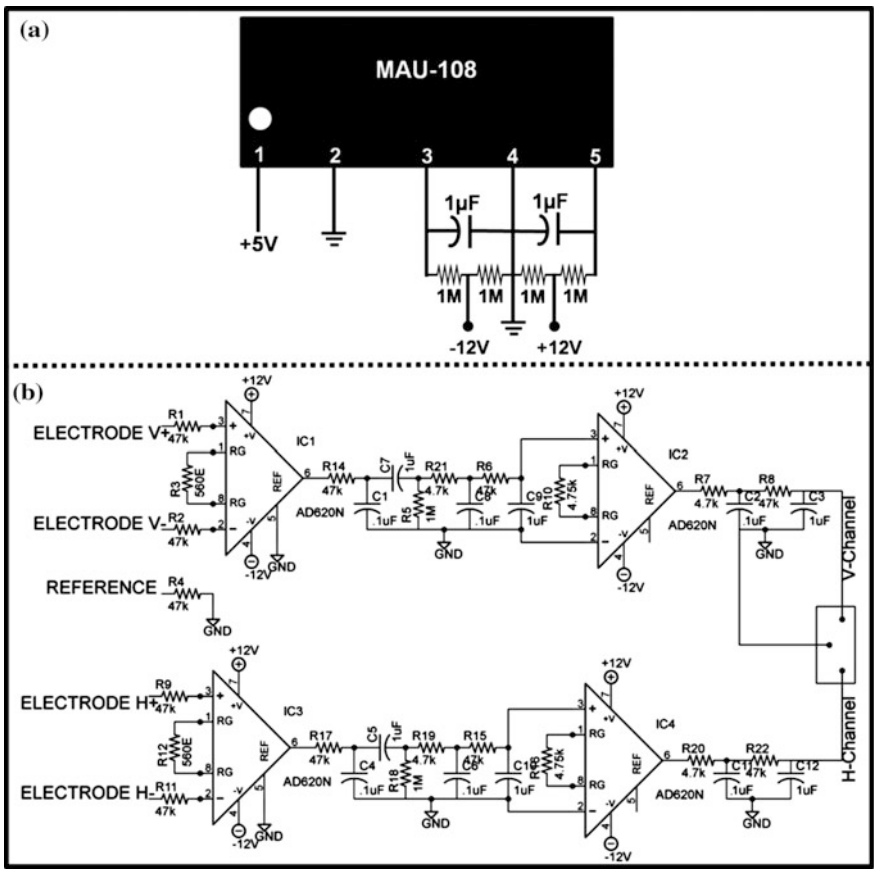

Fig. 1 Circuitry assemblage **a** power supply circuit, and **b** EOG biopotential *amplifier*

eyes of the volunteers. The horizontal markers were at a distance of 140 cm on either side of the central marker. The vertical markers were 75 cm apart on either side of the central marker. This arrangement (Fig. 2) created an angel of ±30° and ±50° [13] in the vertical and horizontal directions, respectively. The volunteers were verbally commanded to look at the specific markers and the corresponding EOG signals were recorded. By default, the volunteers were pre-advised to always look at the central marker always. If only the distance between the central marker and the subject will increase (fixing the distance of the peripheral markers), there will be a significant change in the height and width of the signal.

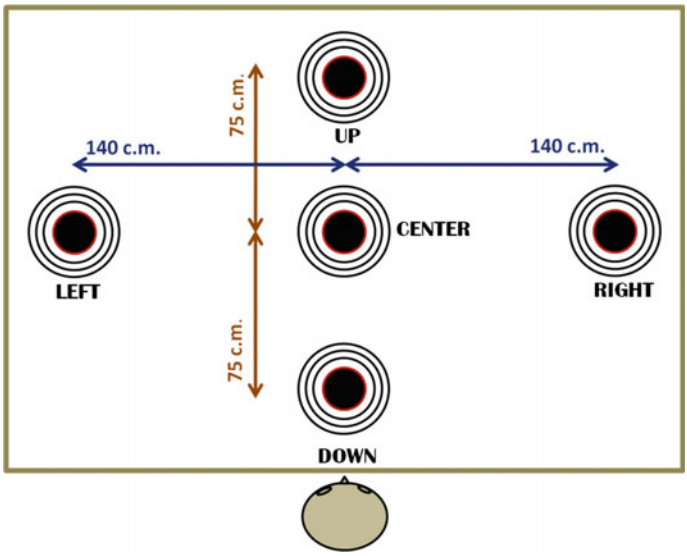

Fig. 2 Markers location for EOG recording

3.5 *Processing of EOG Signal for Generation of Control Signals*

500 samples of the EOG signals were used for processing. The acquired EOG signals were initially processed to remove the baseline drift by subtracting the mean of the acquired signal from the original signal. Thereafter, the signal was processed using a moving averager (triangular method). The width of the moving average was 10. Subsequently, the averaged signal was filtered using a moving-average filter which was implemented as a direct from II transposed structure. This filter was used to calculate the rolling average of the moving averaged EOG signal using a window size of 500. The filtered signal was used for further classification of the eye movements. Dual threshold comparison logic was employed to detect the movement of the eye. The signals from EOG-I was used for the detection of voluntary blink and up-down movements of the eye. The signal from EOG-II was used for detecting the left -right movement of the eye.

3.6 *Development of GUI*

The graphical user interface design environment (GUIDE) in MATLAB provided a way to design customized user interfaces using the in-built interactive tools. All the user interfaces, used in this study, were graphically designed in the GUIDE Layout

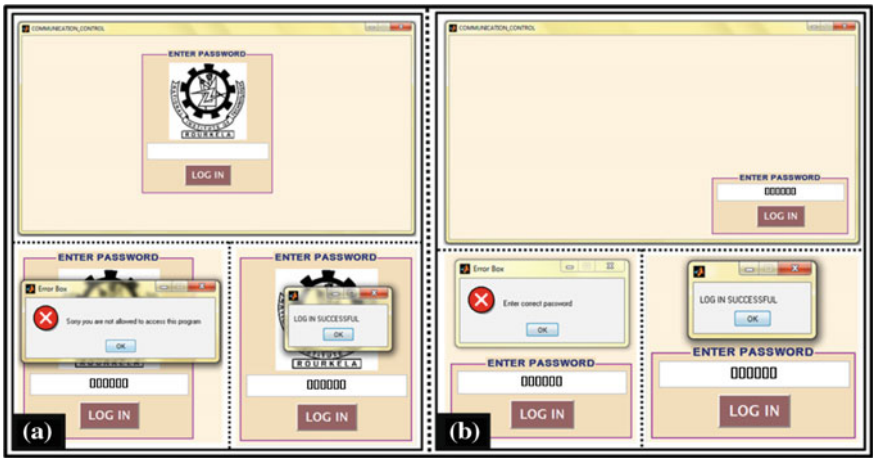

Fig. 3 Password protection for the GUIs **a** password protected primary GUI, and **b** password protected sub-GUI

Editor. As per the layout construction, MATLAB codes were generated automatically. The auto-generated MATLAB codes were edited and modified to behave as per the desired applications. A password protected GUI was designed to avoid any unauthorized access (Fig. 3a). Provisions were made to save the patient history in an Excel file and to save the contact details of the persons to whom the patient may make calls and send emails. The above functions were implemented through two sub-GUIs. The sub GUI for saving communication details was also password protected (Fig. 3b). The primary GUI contains two major sections, namely, control unit and communication unit (Fig. 4). The control unit showed the generation of the control signals used for controlling the functionality of the robotic vehicle. The

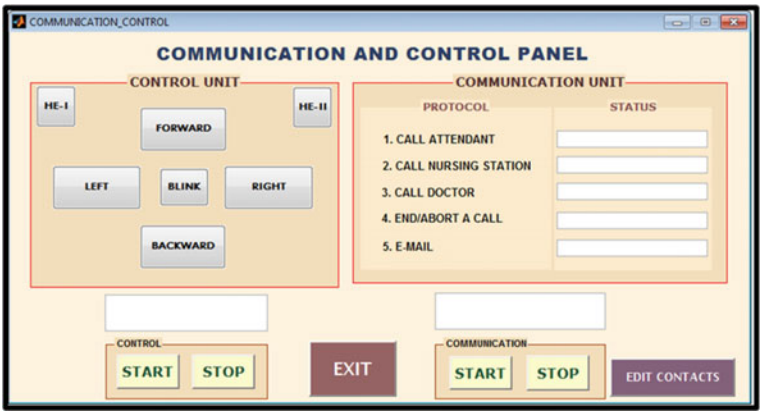

Fig. 4 Primary GUI showing the entire user interface controls

detailed explanation to the demonstration of Fig. 4 has been given in the result section via Figs. 12, 13, 14, 15, 16, 17 and 18. On the other hand, the control signals generated for the communication unit was used for sending emails and making voice calls to particular persons. Also, provisions were made to abort a call if anybody calls to the patient.

3.7 Development of Control System

The generated classified eye movement signals, in combination with the HE sensors, were used to control the functioning of the robotic vehicle and to initiate communication. The control unit for the robotic vehicle was activated by simultaneous voluntary blink and activation of the HE-I sensors at a time. During the process of activation, the inputs of the two H-bridges of the motor shield were enabled. Thereafter, the movement of the eye in the specific directions helped in generating the control signal for specific functions of the robotic vehicle. The control signals were generated only if the HE-I sensor was triggered within 10 s of activating the device. Otherwise, the control unit was deactivated, i.e., the inputs of the two H-bridges of the motor shield were disabled. The movement of the eye, in addition to an activated HE-I sensor, initiated the functioning of the robotic vehicle. The deactivation of the HE-I sensor for more than 10 s deactivated the control unit as well. Similar to the program made for the movement of the control unit, a program was made for controlling the communication unit under the primary GUI. The HE-I sensor was used as a supplementary switch for operating the control unit, whereas, HE-II sensor was used as the supplementary switching device for the functioning of the communication unit. The developed system needs a laptop to process the EOG signals and to generate the control commands.

4 Results

4.1 Development of EOG Acquisition System

The EOG acquisition system was developed as per the circuit given in Fig. 1. A PCB was designed on a copper clad board by carbon transfer and etching of the copper layer. The PCB layout was designed using the freeware Eagle software (version 7.3.0). The designed PCB layout has been shown in Fig. 5a. A PCB was designed from the layout, and the picture of the designed PCB has been shown in Fig. 5b. The designed circuit had a theoretical combined gain of 1080 ($A_{1st\ stage} = 90$ and $A_{2nd\ stage} = 12$). A differential sinusoidal signal of 1 $mV_{P\text{-}P}$ was used as the input and the output of the EOG amplifier was measured to be 1.01 $V_{P\text{-}P}$ with an error of 6.48 %. This confirmed the practical gain of the amplifier to be

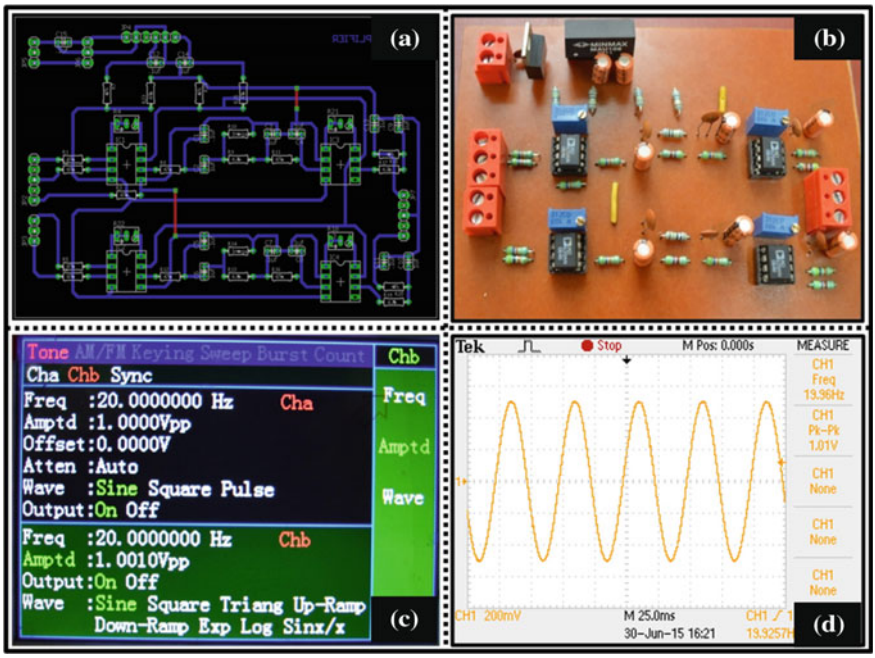

Fig. 5 EOG bioamplifier design and analysis **a** PCB layout diagram in Eagle **b** developed PCB **c** differential input to the circuit, and **d** amplified output

$\sim$1000. The picture of the input and the output signals, as observed on the oscilloscope, has been shown in Fig. 5c, d. From the results, it can be concluded that the circuit was functioning as desired.

4.2 Acquisition of the EOG Signals

The EOG signals were acquired using the developed EOG amplifier. The output of the signal was taken into a laptop using USB-6008 data acquisition system. The complete setup of the EOG signal acquisition system which was used for the acquisition of the signal into the system has been shown in Fig. 6a. The orbital electrodes were placed on the either side of the right orbit. The canthi electrodes were placed at the lateral side of each eye. The reference electrode was placed on the left-hand side of the forehead [15]. The placement of the electrodes has been shown in Fig. 6b. The placement of the HE sensors and their functional activation has been shown in Figs. 6c1–c4. The volunteers were asked to sit on a chair in a relaxed position and were instructed to look at the central marker in the 5-marker panel without any head movement. Subsequently, they were advised to move the eyes in different directions as per the verbal instructions. The corresponding EOG

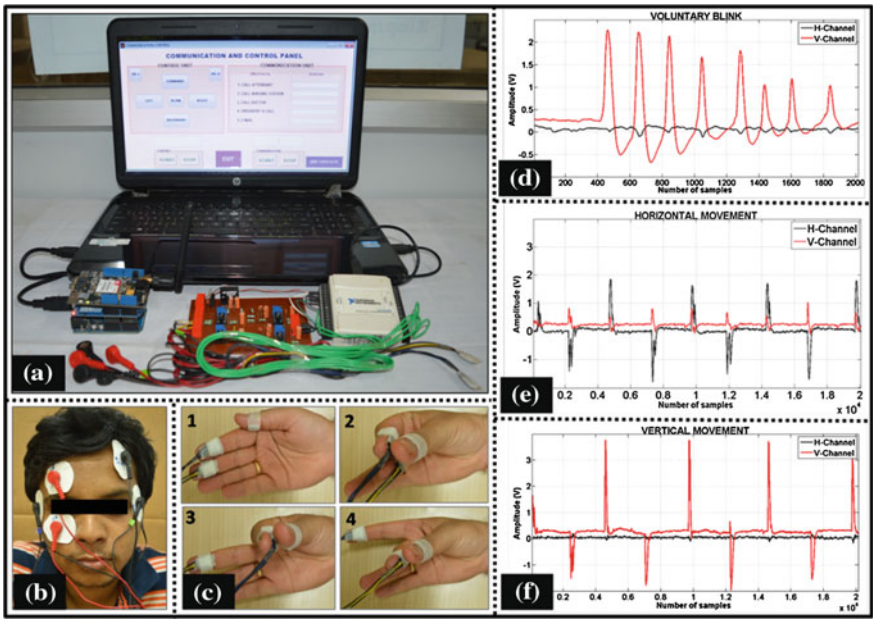

Fig. 6 Experimental compilation **a** setup of the EOG signal acquisition system, processing and control unit **b** electrode placement **c** HE sensor placement and functional activation **d** unprocessed voluntary blink signal **e** unprocessed horizontal signal, and **f** unprocessed vertical signal

signals were recorded. Figure 6d–f shows a representative output from EOG-I and EOG-II amplifiers when the volunteers were asked to move their eyes left, right, up, down and voluntary blink.

4.3 Processing of EOG Signals for Generation of Control Signals

The baseline of the EOG signal varies due to imperfect electrode-skin interface during electrode placement and movement of body parts [49, 50], which degrades the biosignals [51]. The acquired EOG signal was processed so as to remove the baseline drift, which appeared in the acquired EOG signal. Baseline drift was eliminated by the conventional baseline drift elimination method, i.e., subtracting the mean of the signal from the acquired signal. Thereafter, the signal was averaged using a moving average (triangular method). The triangular moving average (TMA) is a simple moving average (SMA) that has been averaged again, i.e., averaging the average. It produces an extra smooth moving average plot. The small ripples superimposed on the EOG signals were abolished after smoothening [52]. The equations of the averaging process are given below:

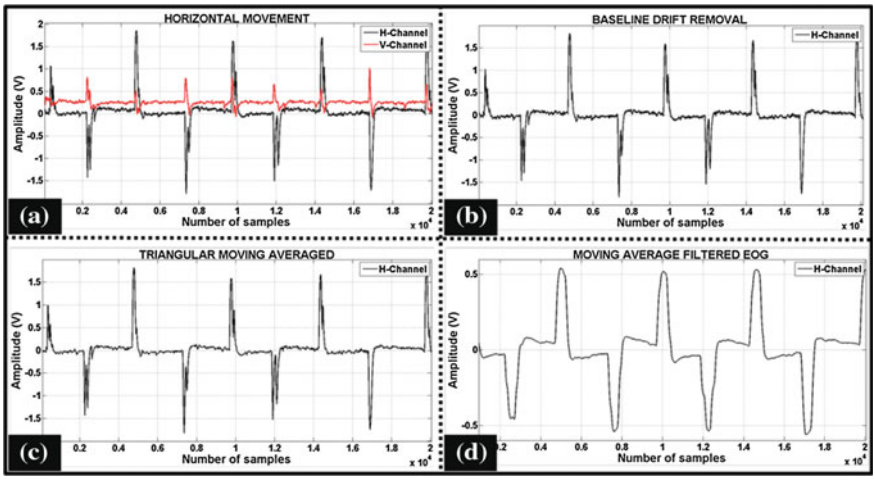

Fig. 7 EOG signal processing **a** unprocessed horizontal signal with vertical channel response **b** horizontal signal isolation and baseline drift removal **c** triangular moving averaged signal, and **d** moving average filtered signal

$$\mathrm{SMA} = (x_1 + x_2 + x_3 + \cdots x_N)/N \tag{1}$$

$$\mathrm{TMA} = (\mathrm{SMA}_1 + \mathrm{SMA}_2 + \mathrm{SMA}_3 + \cdots + \mathrm{SMA}_N)/N. \tag{2}$$

where

N	No. of periods
$x_1 \ldots\ldots x_N$	'N' number of data samples
$\mathrm{SMA}_1 \ldots\ldots \mathrm{SMA}_N$	Simple moving average of $x_1 \ldots\ldots x_N$ number of samples

Subsequently, the signal was filtered using a moving average filter having a window size of 500. Figure 7 shows the output of the processed signal at different stages of processing. The final processed EOG signals has been showed in Fig. 8 and the flowchart for classifying the up, down, left, right and voluntary blink using the threshold limits has been showed in Fig. 9. Each kind of eye movements and voluntary blink were associated with specific control commands (numerical values). These commands were used to activate a specific function in the control unit and were serially transmitted to the Arduino Mega ADK to achieve particular communication tasks through the GPRS shield. The multidirectional eye movements and HE sensor triggering in logical combination with voluntary eye blinks concurrently produced a set of commands responsible for accomplishing control and communication protocols. Tasks like making voice calls, aborting a call, and sending emails were programmed under communication protocol. The control unit guided the direction of the robotic vehicle in four different directions. The logical combination for activation of the control and the communication protocols has been given in Table 1.

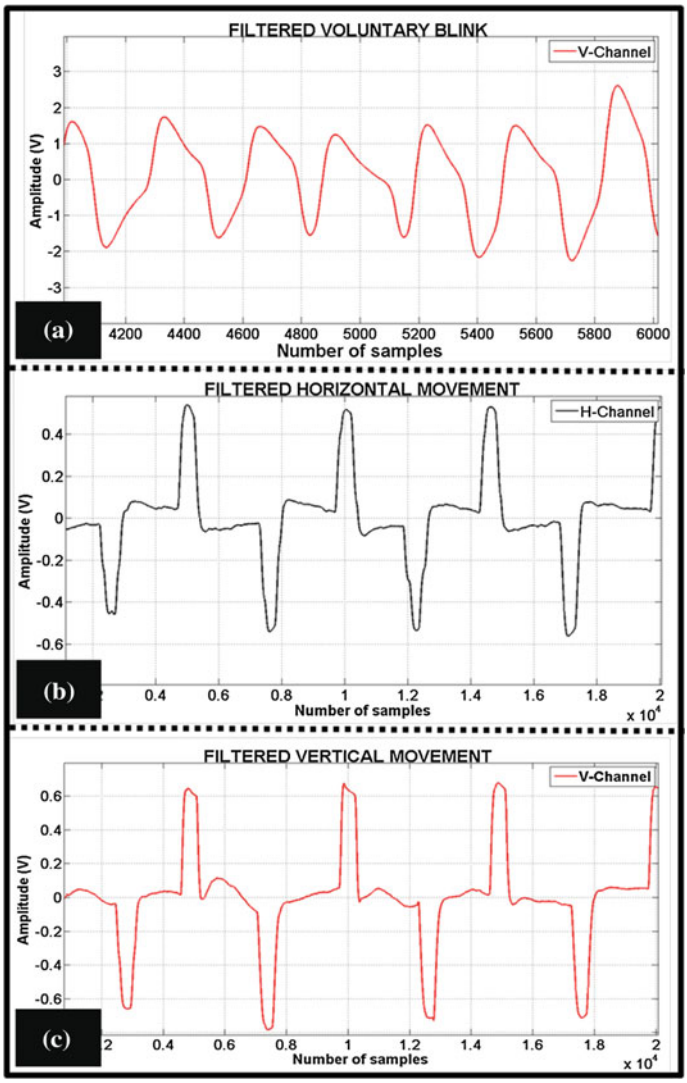

Fig. 8 Final processed EOG signals **a** voluntary blink **b** horizontal movement, and **c** vertical movement

4.4 Functionality of the Developed GUI

A MATLAB based password protected GUI was developed such that only the authorized personnel can access the GUI by entering a correct password. After the successful login, a patient history GUI will automatically pops-up. It allows to save the address, contact and official (ward name and bed no.) details are entered in the GUI. Clicking the *continue* button in the GUI allows the user to save the patient

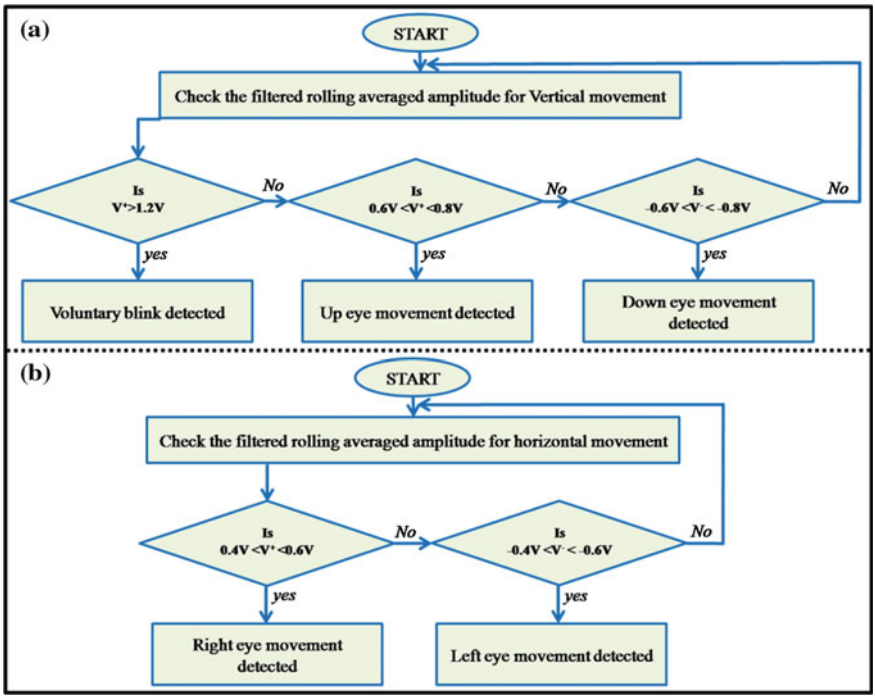

Fig. 9 Analogy for eye movement classification **a** flowchart for voluntary blink, up and down eye movement detection **b** flowchart for left and right eye movement detection

Table 1 Logical combination of eye movements and HE sensors in control and communication protocol activation

HE-I sensor	HE-II sensor	Types of eye movements	Proposed tasks	Figure demonstration
√	√	Voluntary blink	Activates the motor shield	12a
x	–	–	Deactivate the motor shield	12b
√	x	Left	Left movement	13a
√	x	Right	Right movement	13b
√	x	Up	Forward movement	13c
√	x	Down	Backward movement	13d
x	√	Up	Call to attendant	14
x	√	Right	Call to nursing station	15
x	√	Left	Call to doctor	16
x	√	Down	Email to doctor, nursing station and attendant	17
x	√	Voluntary blink	Abort a call	18b

√ = activated; x = deactivated; – = idle

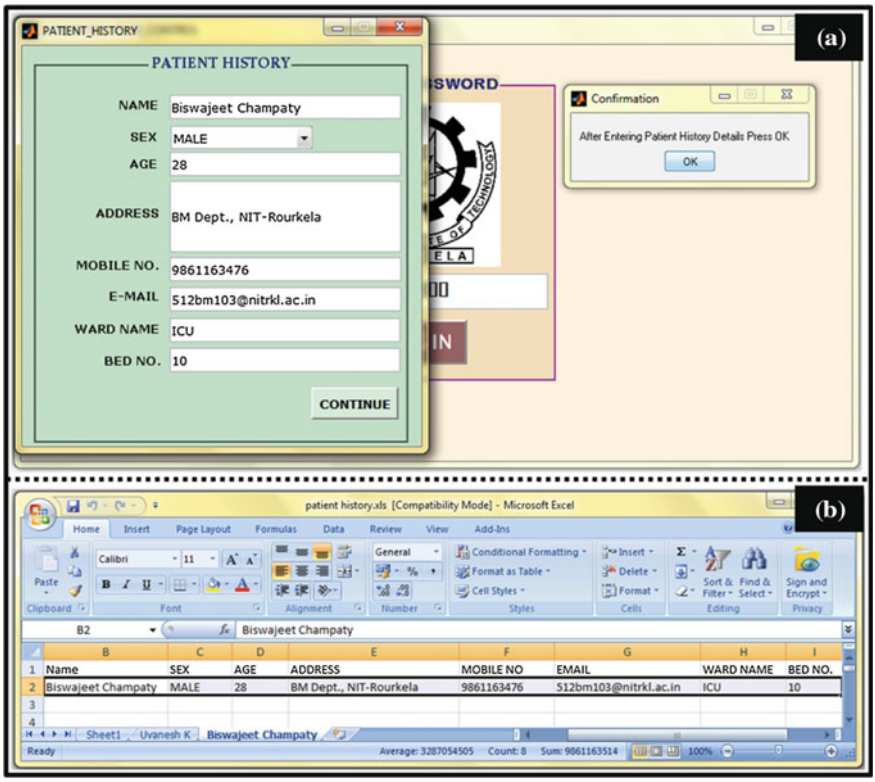

Fig. 10 Sub-GUI-I **a** patient history entered **b** history saved in a separate tab as per the patient name in an excel sheet "patient history"

history in a particular excel file (under a new tab). Subsequently, the GUI is opened. The sub-GUI for saving patient history has been shown in Fig. 10. The main GUI contains two segments, namely, control unit and communication unit. The communication segment includes an *edit contact* button. Clicking the edit contact button results in the opening of another sub-GUI, which allows the users to change and save the contact details of the person to whom the communication to be made (Fig. 11). This GUI is also password protected for authorized access only.

The control unit has seven virtual indicators (virtual LEDs) displaying left, right, forward, backward, stop, HE-I sensor and HE-II sensor. A couple of pushbuttons at the bottom of the GUI are intended for activating (ON) and deactivating (OFF) the unit. The unit is activated just by a by pressing th START button but does not initiate the tasks. The unit does not start functioning unless a simultaneous signal from HE-I and HE-II sensors and a voluntary blink is detected. The activation is confirmed by a display note ("ACTIVATED...!!!") in the same unit (Fig. 12). As per Table 1, the virtual indicators are activated (change in background color) during specific operations associated with different eye movements, voluntary blink and

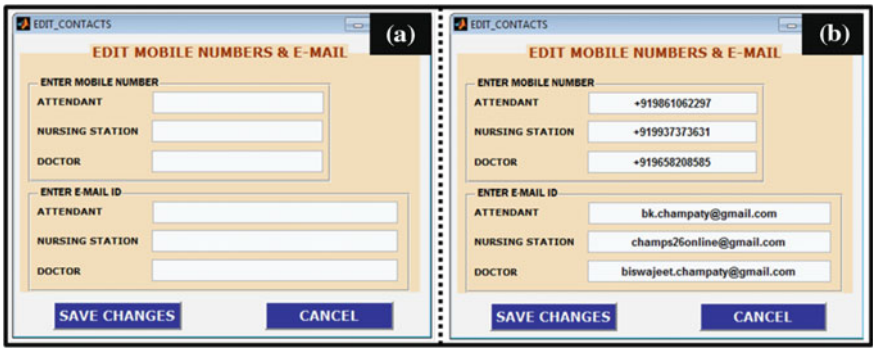

Fig. 11 Sub-GUI-II **a** contact options, and **b** enter contact details and save

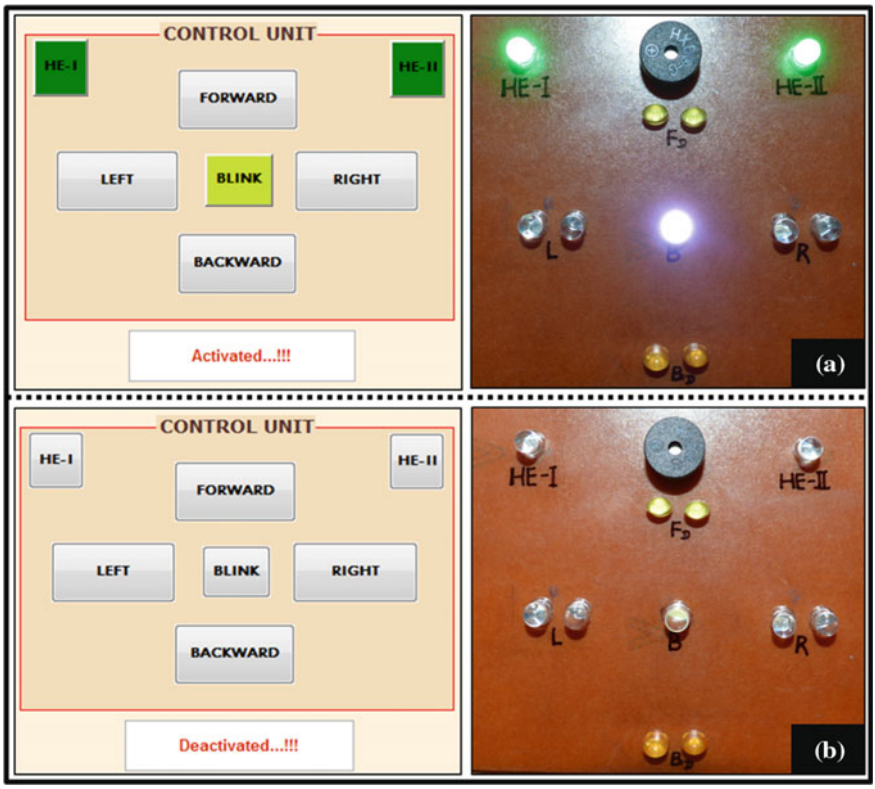

Fig. 12 **a** Activation of control unit, and **b** deactivation of control unit

triggering of HE sensors (Fig. 13). STOP button makes the unit dormant. Due to line-of-sight communication, the duration lapse between the initiations of the control signal to the actual response/action time for the robotic vehicle is 117 ms.

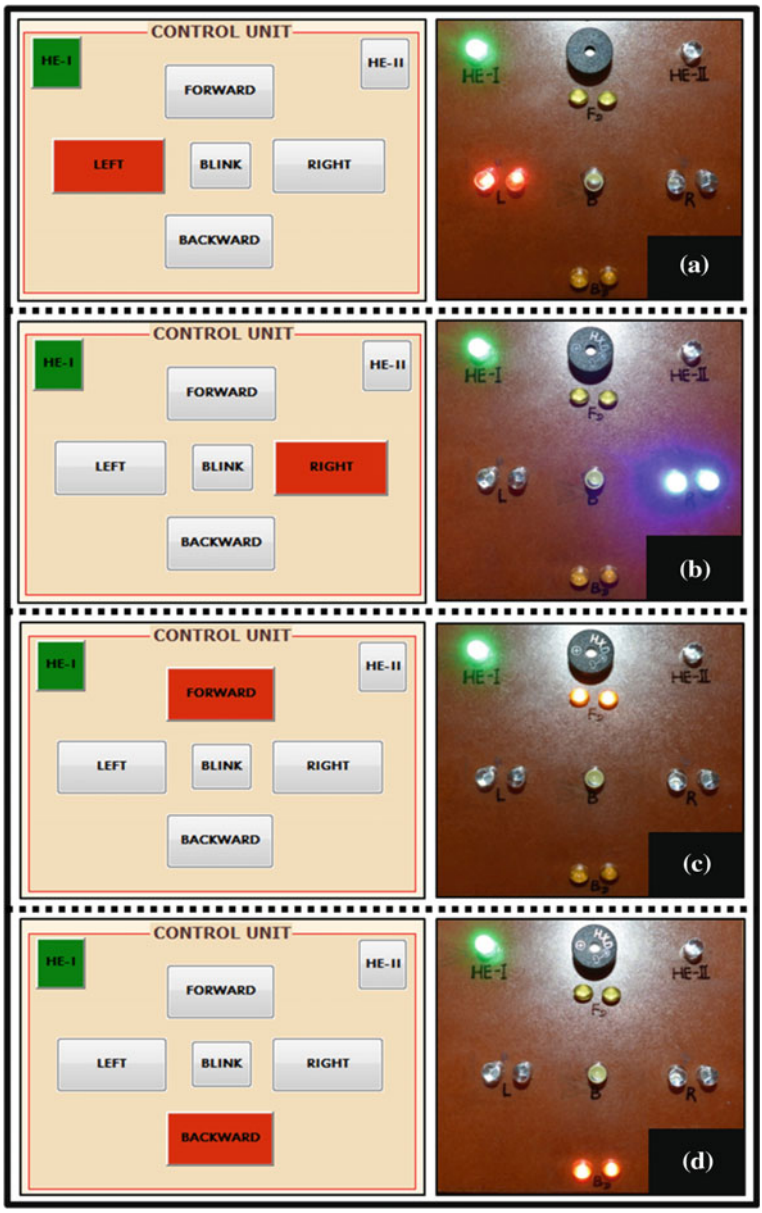

Fig. 13 Control task execution and hardware realization **a** left eye movement-left command **b** right eye movement-right command **c** up eye movement- forward command, and **d** down eye movement- backward command

Like control unit, the communication unit too has activation and deactivation processes. The communication operations are set off by software switches. A GPRS Shield V1.0 instilled into the Arduino Mega ADK provides a way to use the GSM cell phone network. It is controlled via AT commands (GSM 07.07, 07.05 and SIMCOM enhanced AT Commands). Each communication protocol in the GUI generates a specific serial data which gets transmitted to the microcontroller. The GSM shield starts doing particular functions like making voice calls, abort a call, etc. when a specific serial command reaches the Arduino Mega ADK. All the voice calls were directed to the saved contacts. The patient mobile number should be saved in the recipients' (attendant, nursing station and doctor) mobile as <Ward Name>, <Bed No. (BN)> during the process of patient registration. Due to the vast usage of smartphones, email facility was employed as one of the prime communication protocols in our study. All the emails are programmed to be sent through NIT-RKL Cyberoam server client that supports Post Office Protocol (POP). The content of subject in the mail is like—"Please attend the patient—<Patient Name>, <Ward Name> <Bed No. (BN)>". The content is sent in the subject line for quick viewing. The patient name, ward name and bed number were accessed from the patient history saved earlier. As per Table-1, all the communication tasks were carried out in the GUI. Figures 14, 15, 16 show the incoming call to the attendant, nursing station and doctor and their respective GUI demonstration, respectively.

Fig. 14 Calling attendant **a**, **b** GUI demonstration, and **b** an incoming call on the attendant's mobile

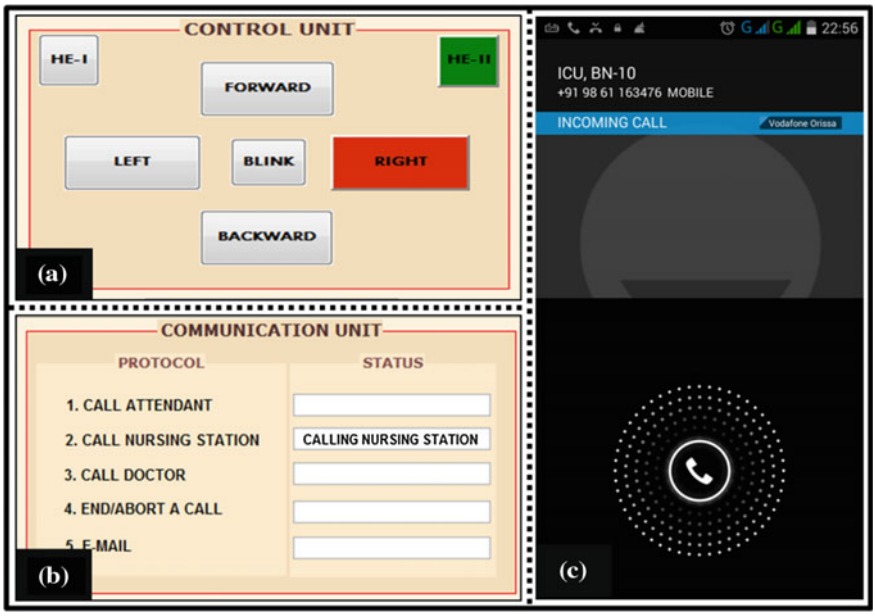

Fig. 15 Calling nursing station **a**, **b** GUI demonstration, and **b** an incoming call on the nursing station mobile

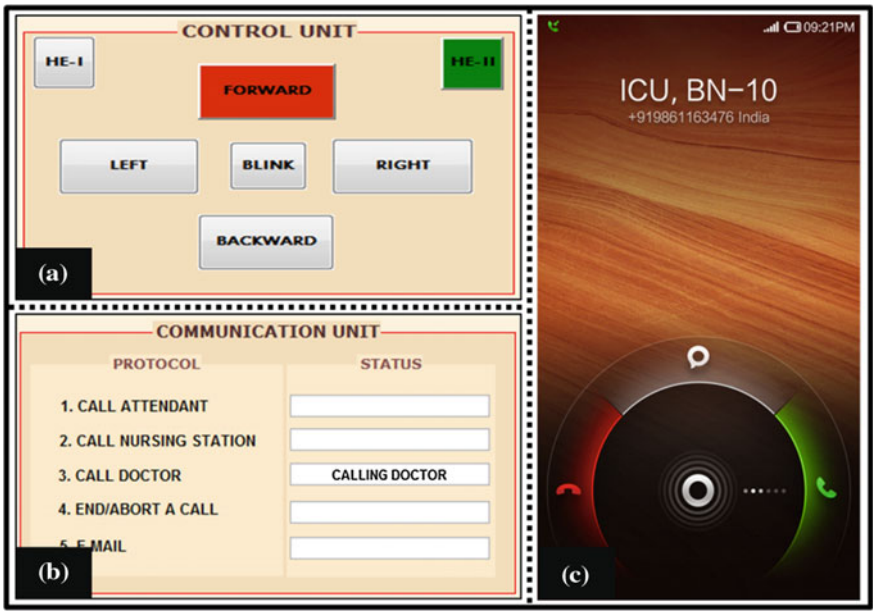

Fig. 16 Calling doctor **a**, **b** GUI demonstration, and **b** an incoming call on the doctor's mobile

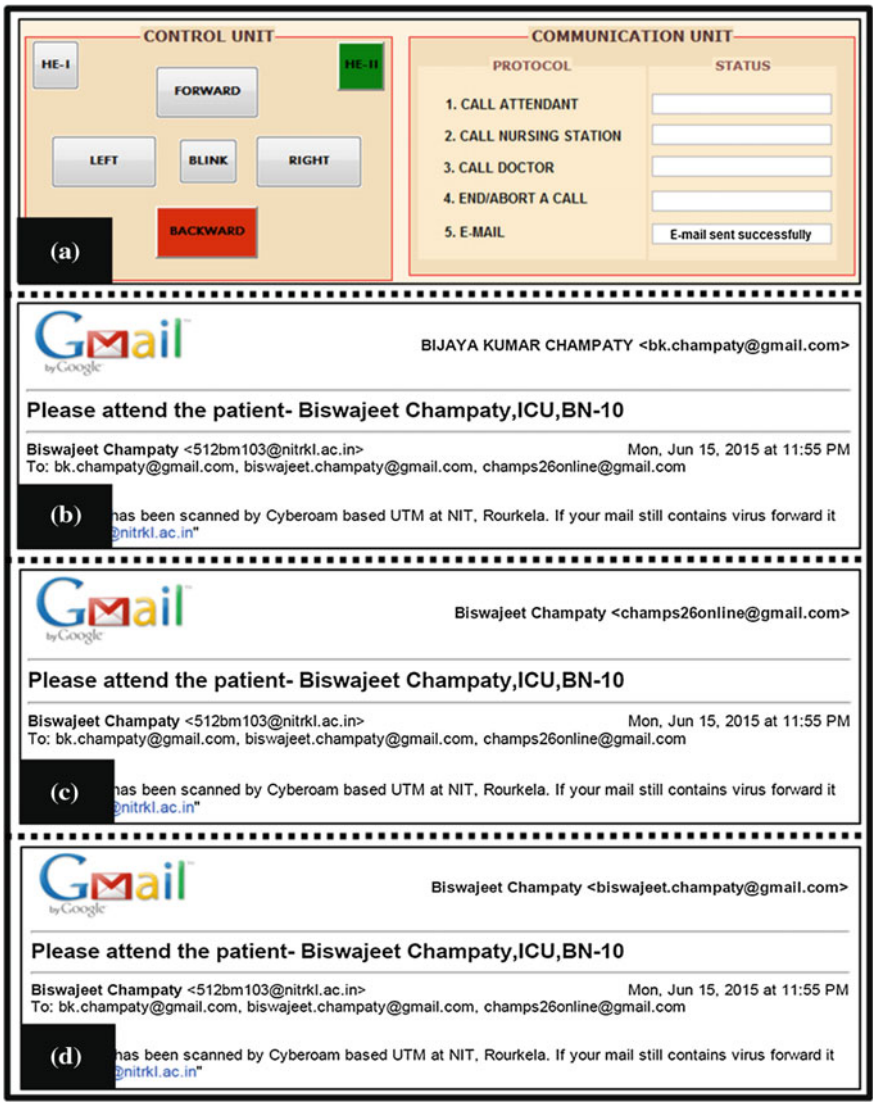

Fig. 17 E-mail delivery **a** delivered to attendant **b** delivered to nursing station, and **c** delivered to doctor

Figure 17 shows the email delivery to the attendant, nursing station and the doctor. An incoming call to the patient's mobile number and the aborting the call has been shown in Fig. 18.

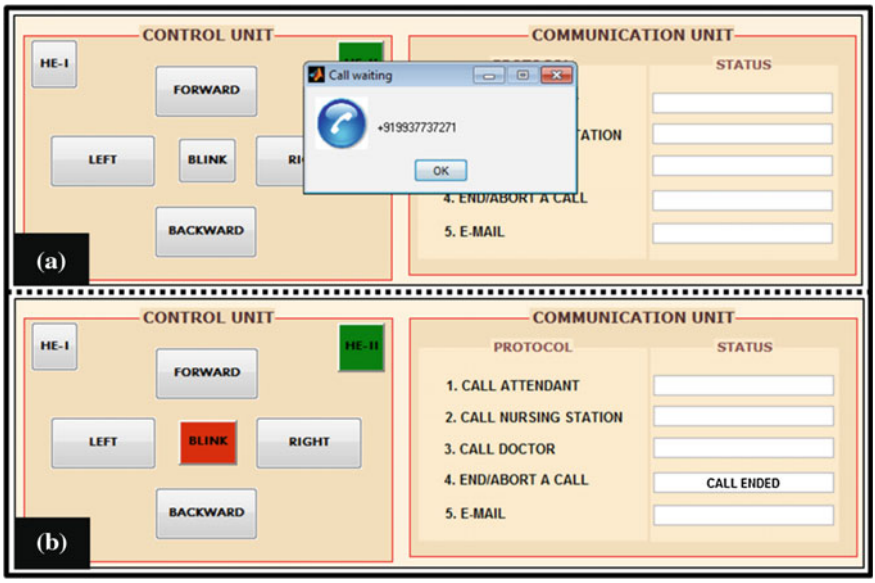

Fig. 18 **a** Incoming call to the patient's mobile number, and **b** aborting the call

4.5 Development of Control System

A control system was developed using the five control signals produced as a result of eye movements. Signals from the two HE sensors were acquired into the laptop and were integrated with the program for doing specific tasks (control and communication tasks). The HE-I sensor (accompanied by eye movements) was used to control the control unit, whereas, HE-II sensor (attached to the middle finger) was used to initiate tasks in control unit. In this study, a robotic vehicle was used as the representative assistive device. After switching on the HE-I sensor, a voluntary eye blink activated the control unit. The movement of the eye in different directions was detected by the EOG signal processing program, which in turn, generated control signals. The generated control signals were visualized in the control unit segment of the GUI. Virtual indicators like left, right, forward, backward, stop, HE-I sensor activation and HE-II sensor activation were activated (change in background color). This segment can be used by the patients for proper training from time to time. It has been reported that visual feedback of biosignals helped the disabled persons to strengthen their ocular activities. Also, the control signals were transmitted to a robotic vehicle via a pair of wireless XBee shields. The various control signals were used to control the movement of the robotic vehicle. As mentioned earlier, after the activation of the control unit (switching on the HE-I sensor and voluntary blink concurrently), the movement of the eye to the right, left, up and down directed the

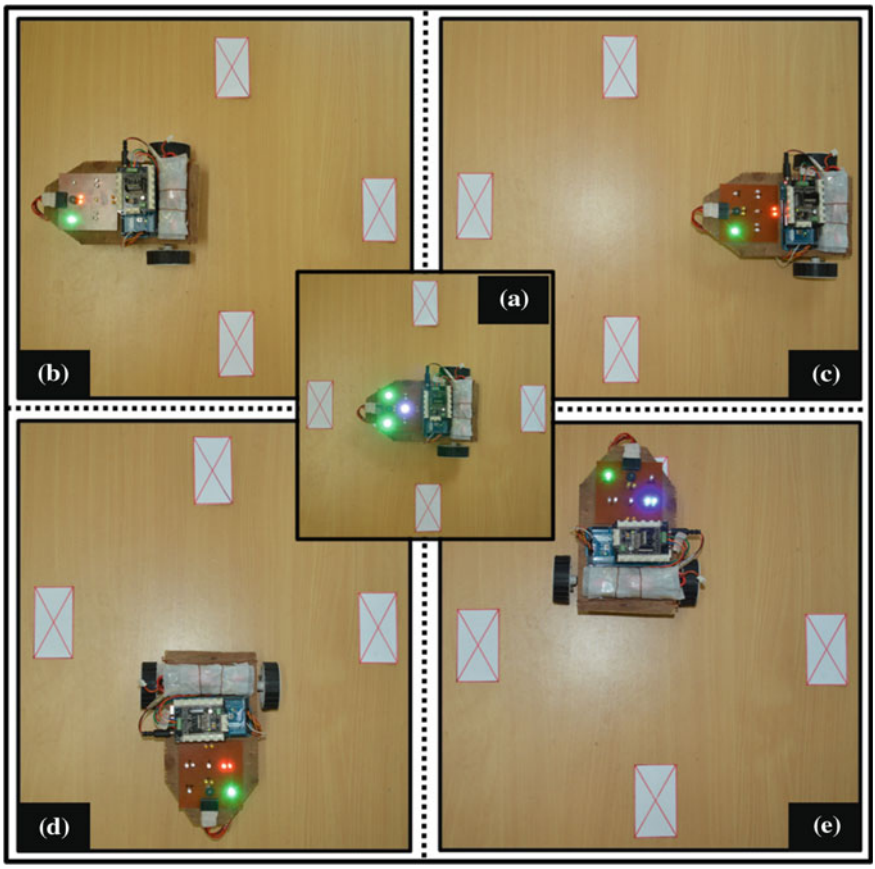

Fig. 19 Robotic vehicle movements **a** activated at the centre **b** forward **c** backward **d** left, and **e** right

robotic vehicle to move right, left, forward and backward, respectively. The switching-off of the HE-I sensor halts the movement of the robotic vehicle. If the HE-I sensor is in the switched off condition for more than 10 s, the control unit is deactivated. The functioning of the control unit for controlling the movement of the robotic vehicle was successfully tested. The activation and the movement of the robotic vehicle in different directions have been showed in Fig. 19. All the 15 volunteers were trained for 20 min to get familiar with the working of the device. Therefore, all of them were able to complete the tasks without any false positive result. No movement was observed in the robotic vehicle, if the eye motion wasn't one of the specified five cases reported in the control unit.

5 Conclusion

The purpose of the study was to develop a robust EOG based HCI device, which can be diversified both as a control system for the functioning of the assistive devices and for initiating communication with the healthcare and non-healthcare personnel in case of any emergency and need. The proposed hardware-software device can be used for the severely disabled persons who have limited motor activity. Excluding the cost of the laptop, the total cost of the system is nearly $267. This has been reported that the energy required for moving the eyes are much lower as compared to the other motor activities in the disabled person. Also, the individuals suffering from neuromuscular diseases are left with the activities of the ocular muscles even in the late stages of the disease. Due to these reasons, EOG based HCIs gained much importance in the development of assistive devices. In this study, as a representative assistive device, the robotic vehicle was directed to different directions using the EOG signal and helped in testing of the developed control system. The successful testing of the control of the robotic vehicle throughout the study concluded that the control system developed using the EOG signals may be used for controlling robotic arms, wheelchairs, home automation systems etc. in future. In addition to the existing control commands, more control commands can be generated by moving the eyes in diagonal directions like up-right, up-left, down-right and down-left. The developed EOG biopotential amplifier has the capability to record these additional eye movements. Additionally, by slightly modifying the hardware components, it was possible to initiate various communication protocols for the severely disabled persons.

In gist, in this study, EOG signals were used to manipulate a robotic vehicle and a communicationdevice suggesting that the proposed device can be used for multi-tasking.

References

1. Vaish, A., Kumari, P.: A comparative study on machine learning algorithms in emotion state recognition using ECG. In: Proceedings of the Second International Conference on Soft Computing for Problem Solving (SocProS 2012), Dec 28–30, 2012, pp. 1467–1476. Springer (2014)
2. Choi, K., Cichocki, A.: Control of a wheelchair by motor imagery in real time. Intelligent Data Engineering and Automated Learning–IDEAL 2008, pp. 330–337. Springer (2008)
3. Tanaka, K., Matsunaga, K., Wang, H.O.: Electroencephalogram-based control of an electric wheelchair. IEEE Trans. Robot. **21**, 762–766 (2005)
4. Sharma, P., Vaish, A.: Information-Theoretic Measures on Intrinsic Mode Function for the Individual Identification Using EEG Sensors
5. Champaty, B., Jose, J., Pal, K., Thirugnanam, A.: Development of EOG based human machine interface control system for motorized wheelchair. In: 2014 Annual International Conference on Emerging Research Areas: Magnetics, Machines and Drives (AICERA/iCMMD), pp. 1–7. IEEE (2014)

6. Yamagishi, K., Hori, J., Miyakawa, M.: Development of EOG-based communication system controlled by eight-directional eye movements. In: Engineering in Medicine and Biology Society, 2006. EMBS'06. 28th Annual International Conference of the IEEE, pp. 2574–2577. IEEE (2006)
7. Han, J.-S., Bien, Z.Z., Kim, D.-J., Lee, H.-E., Kim, J.-S.: Human-machine interface for wheelchair control with EMG and its evaluation. In: Engineering in Medicine and Biology Society, 2003. Proceedings of the 25th Annual International Conference of the IEEE, pp. 1602–1605. IEEE (2003)
8. Moon, I., Lee, M., Chu, J., Mun, M.: Wearable EMG-based HCI for electric-powered wheelchair users with motor disabilities. In: Proceedings of the 2005 IEEE International Conference on Robotics and Automation, 2005. ICRA 2005, pp. 2649–2654. IEEE (2005)
9. Dey, N., Dey, G., Chakraborty, S., Chaudhuri, S.S.: Feature analysis of blind watermarked electromyogram signal in wireless telemonitoring. Concepts and Trends in Healthcare Information Systems, pp. 205–229. Springer (2014)
10. Mukherjee, A., Dey, G., Dey, M., Dey, N.: Web-based intelligent EEG signal authentication and tamper detection system for secure telemonitoring. Brain-Computer Interfaces, pp. 295–312. Springer (2015)
11. Coco, G.L., Coco, D.L., Cicero, V., Oliveri, A., Verso, G.L., Piccoli, F., La Bella, V.: Individual and health-related quality of life assessment in amyotrophic lateral sclerosis patients and their caregivers. J. Neurol. Sci. **238**, 11–17 (2005)
12. Nathan, D.S., Vinod, A.P., Thomas, K.P.: An electrooculogram based assistive communication system with improved speed and accuracy using multi-directional eye movements. In: 2012 35th International Conference on Telecommunications and Signal Processing (TSP), pp. 554–558. IEEE (2012)
13. Dhillon, H.S., Singla, R., Rekhi, N.S., Jha, R.: EOG and EMG based virtual keyboard: a brain-computer interface. In: 2nd IEEE International Conference on Computer Science and Information Technology, 2009. ICCSIT 2009, pp. 259–262. IEEE (2009)
14. Akan, B., Argunsah, A.O.: A human-computer interface (HCI) based on electrooculogram (EOG) for handicapped. In: Signal Processing and Communications Applications, 2007. SIU 2007. IEEE 15th, pp. 1–3. IEEE (2007)
15. Barea, R., Boquete, L., Mazo, M., López, E.: System for assisted mobility using eye movements based on electrooculography. IEEE Trans. Neural Syst. Rehabil. Eng. **10**, 209–218 (2002)
16. Chen, Y., Newman, W.S.: A human-robot interface based on electrooculography. In: 2004 IEEE International Conference on Robotics and Automation, 2004. Proceedings. ICRA'04, pp. 243–248. IEEE (2004)
17. Hiley, J.B., Redekopp, A.H., Fazel-Rezai, R.: A low cost human computer interface based on eye tracking. In: Engineering in Medicine and Biology Society, 2006. EMBS'06. 28th Annual International Conference of the IEEE, pp. 3226–3229. IEEE (2006)
18. Junichi, H., Sakano, K., Saitoh, Y.: Development of a communication support device controlled by eye movements and voluntary eye blink. IEICE Trans. Inf. Syst. **89**, 1790–1797 (2006)
19. Kim, Y., Doh, N., Youm, Y., Chung, W.K.: Development of human-mobile communication system using electrooculogram signals. In: Proceedings. 2001 IEEE/RSJ International Conference on Intelligent Robots and Systems, 2001, pp. 2160–2165. IEEE (2001)
20. LaCourse, J.R., Hludik Jr., F.C.: An eye movement communication-control system for the disabled. IEEE Trans. Bio-med. Eng. **37**, 1215–1220 (1990)
21. Pander, T., Przybyla, T., Czabanski, R.: An application of detection function for the eye blinking detection. In: 2008 Conference on Human System Interactions, pp. 287–291. IEEE (2008)
22. Tecce, J.J., Gips, J., Olivieri, C.P., Pok, L.J., Consiglio, M.R.: Eye movement control of computer functions. Int. J. Psychophysiol. **29**, 319–325 (1998)
23. Ubeda, A., Ianez, E., Azorin, J.M.: Wireless and portable EOG-based interface for assisting disabled people. IEEE/ASME Trans. Mechatron. **16**, 870–873 (2011)

24. Champaty, B., Pal, K., Dash, A.: Functional electrical stimulation using voluntary eyeblink for foot drop correction. In: 2013 Annual International Conference on Emerging Research Areas and 2013 International Conference on Microelectronics, Communications and Renewable Energy (AICERA/ICMiCR), pp. 1–4. IEEE (2013)
25. Iáñez, E., Úbeda, A., Azorín, J.M., Perez-Vidal, C.: Assistive robot application based on an RFID control architecture and a wireless EOG interface. Robot. Auton. Syst. **60**, 1069–1077 (2012)
26. Barea, R., Boquete, L., Mazo, M., López, E.: Guidance of a wheelchair using electrooculography. In: Proceeding of the 3rd IMACS International Multiconference on Circuits, Systems, Communications and Computers (CSCC'99). Citeseer (1999)
27. Dev, A.: Eye controlled wheel chair using EOG. Program. Device Circuits Syst. **4**, 592–595 (2012)
28. Tsui, C.S.L., Jia, P., Gan, J.Q., Hu, H., Yuan, K.: EMG-based hands-free wheelchair control with EOG attention shift detection. In: IEEE International Conference on Robotics and Biomimetics, 2007. ROBIO 2007, pp. 1266–1271. IEEE (2007)
29. Wijesoma, W.S., Wee, K.S., Wee, O.C., Balasuriya, A.P., San, K.T., Soon, L.K.: EOG based control of mobile assistive platforms for the severely disabled. In: 2005 IEEE International Conference on Robotics and Biomimetics (ROBIO), pp. 490–494. IEEE (2005)
30. Chambayil, B., Singla, R., Jha, R.: Virtual keyboard BCI using Eye blinks in EEG. In: WiMob, pp. 466–470 (2010)
31. Ding, Q., Tong, K., Li, G.: Development of an EOG (electro-oculography) based human-computer interface. In: 27th Annual International Conference of the Engineering in Medicine and Biology Society, 2005. IEEE-EMBS 2005, pp. 6829–6831. IEEE (2006)
32. Tamura, H., Miyashita, M., Tanno, K., Fuse, Y.: Mouse cursor control system using electrooculogram signals. In: World Automation Congress (WAC), 2010, pp. 1–6. IEEE (2010)
33. Lv, Z., Wu, X., Li, M., Zhang, C.: Implementation of the EOG-based human computer interface system. In: The 2nd International Conference on Bioinformatics and Biomedical Engineering, 2008. ICBBE 2008, pp. 2188–2191. IEEE (2008)
34. Rajan, A., Shivakeshavan, R., Ramnath, J.: Electrooculogram based instrumentation and control system (IC system) and its applications for severely paralysed patients. In: International Conference on Biomedical and Pharmaceutical Engineering, 2006. ICBPE 2006, pp. 1–4. IEEE (2006)
35. Zheng, X., Li, X., Liu, J., Chen, W., Hao, Y.: A portable wireless eye movement-controlled human-computer interface for the disabled. In: ICME International Conference on Complex Medical Engineering, 2009. CME, pp. 1–5. IEEE (2009)
36. Li, L., Wu, X.: Design and implementation of multimedia control system based on bluetooth and electrooculogram (EOG). In: 2011 5th International Conference on Bioinformatics and Biomedical Engineering, (iCBBE), pp. 1–4. IEEE (2011)
37. Navallas, J., Ariz, M., Villanueva, A., San Agustín, J., Cabeza, R.: Optimizing interoperability between video-oculographic and electromyographic systems. J. Rehabil. Res. Dev. **48**, 253–266 (2011)
38. Hutchinson, T.E., White Jr, K.P., Martin, W.N., Reichert, K.C., Frey, L.A.: Human-computer interaction using eye-gaze input. IEEE Trans. Syst. Man Cybern. **19**, 1527–1534 (1989)
39. Heide, W., Koenig, E., Trillenberg, P., Kömpf, D., Zee, D.: Electrooculography: technical standards and applications. Electroencephalogr. Clin. Neurophysiol. **1999**, 223–240 (1999)
40. Kumar, U., Champaty, B., Shashikala, P., Pal, K.: Design of low-cost continuous temperature and water spillage monitoring system. In: 2013 International Conference on Information Communication and Embedded Systems (ICICES), pp. 1156–1159. IEEE (2013)
41. Dutta, D., Champaty, B., Banerjee, I., Pal, K., Tibarewala, D.: Development of a wireless attendant calling system for improved patient care. Advancements of Medical Electronics, pp. 185–191. Springer (2015)
42. Champaty, B., Dubey, P., Sahoo, S., Ray, S.S., Pal, K., Anis, A.: Development of wireless EMG control system for rehabilitation devices. In: 2014 Annual International Conference on

Emerging Research Areas: Magnetics, Machines and Drives (AICERA/iCMMD), pp. 1–4. IEEE (2014)
43. Lay-Ekuakille, A., Vergallo, P., Griffo, G., Conversano, F., Casciaro, S., Urooj, S., Bhateja, V., Trabacca, A.: Entropy index in quantitative EEG measurement for diagnosis accuracy. IEEE Trans. Instrum. Meas. **63**, 1440–1450 (2014)
44. Reaz, M., Hussain, M., Mohd-Yasin, F.: Techniques of EMG signal analysis: detection, processing, classification and applications. Biol. Proced. Online **8**, 11–35 (2006)
45. Malcolm, B., Michael, M., Vaegan, E., Mitchell, B., Michael, B.: ISCEV standard for clinical electro-oculography (EOG). Doc. Ophthalmol. **113**, 205–212 (2006)
46. Chang, N., Gupta, V.: PS/2 Mouse Control with EOG/EMG Signals. ECE (2004)
47. Banerjee, A., Datta, S., Konar, A., Tibarewala, D.: Development strategy of eye movement controlled rehabilitation aid using Electro-oculogram. Int. J. Sci. Eng. Res. **3**, 1–6 (2012)
48. Ellis, S.R., Menges, B.M.: Judgments of the distance to nearby virtual objects: interaction of viewing conditions and accommodative demand. Presence (Cambridge, Mass.), vol. 6, pp. 452–460 (1997)
49. Dobrev, D., Neycheva, T., Mudrov, N.: Simple high-Q comb filter for mains interference and baseline drift suppression. Ann. J. Electron. **3**, 50–52 (2009)
50. Pandey, V.K., Naidu, N.K.S., Pandey, P.C.: Tracking based baseline restoration for acquisition of impedance cardiogram and other biosignals. In: 27th Annual International Conference of the Engineering in Medicine and Biology Society, 2005. IEEE-EMBS 2005, pp. 3486–3489. IEEE (2006)
51. Bhateja, V., Verma, R., Mehrotra, R., Urooj, S.: A non-linear approach to ECG signal processing using morphological filters. Int. J. Measur. Technol. Instrum. Eng. (IJMTIE) **3**, 46–59 (2013)
52. Kawasaki, K., Tamura, T.: Automated measurement of the electro-oculogram for clinical use. Doc. Ophthalmol. **66**, 85–94 (1987)

Theory of Parallel MRI and Cartesian SENSE Reconstruction: Highlight

Joseph Suresh Paul, Raji Susan Mathew and M.S. Renjith

Abstract Magnetic resonance imaging (MRI) is a well-known medical imaging technique, that exclusively uses the response of the hydrogen nucleus which is abundant in the human body. In recent years, parallel MRI techniques have been developed to accelerate image acquisition. A notable development in parallel MRI was the introduction of SMASH by Sodicksen and Manning. Since then, great progress in the development and improvement of parallel imaging reconstruction methods has taken place. The Sensitivity Encoding (SENSE) proposed by Preussmann and Weiger is the most widely used image-domain parallel MR image reconstruction technique. SENSE uses an initial estimate of the coil sensitivity in combination with an SNR optimized noise inversion to obtain the final reconstructed image. This chapter starts with a brief history of the parallel imaging, discusses the estimation of sensitivity and SENSE reconstruction.

1 Introduction to Parallel Imaging

Magnetic resonance imaging (MRI) is a well-known medical imaging technique that exclusively uses the response of the hydrogen nucleus which is abundant in the human body [1]. Variation of hydrogen density and specifically its molecular binding in different tissues produces a much better soft tissue contrast than CT. MRI has some further advantages if compared with x-ray and CT: (i) MRI does not use ionizing radiation. (ii) Images can be generated with arbitrary slice orientation including coronal and sagittal views. (iii) Several different functional attributes can be imaged with MRI. (iv) Capability to provide risk-free diagnostic assessment. However, rapid switching of magnetic field gradients often causes severe discomfort to the subject being scanned. This forms a serious impediment requiring

J.S. Paul (✉) · R.S. Mathew · M.S. Renjith
Medical Image Computing and Signal Processing Laboratory,
Indian Institute of Information Technology and Management-Kerala,
Thiruvananthapuram, India
e-mail: j.paul@iiitmk.ac.in

N. Dey et al. (eds.), *Medical Imaging in Clinical Applications*,
Studies in Computational Intelligence 651, DOI 10.1007/978-3-319-33793-7_14

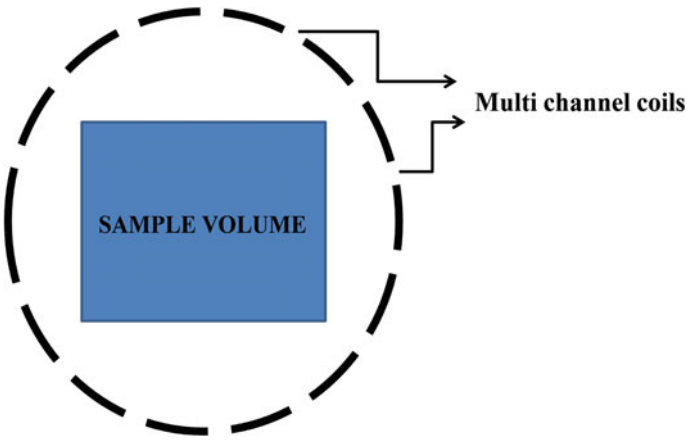

Fig. 1 Schematic representation of parallel imaging

scanning protocols to be implemented in a shorter period of time, simultaneously maintaining the image quality. Imaging speed is a crucial consideration for magnetic resonance imaging (MRI). The speed of conventional MRI is limited by hardware performance and physiological safety measures. In the recent years, parallel MRI techniques have been developed that utilize radiofrequency (RF) coil arrays to accelerate image acquisition beyond these previous limits [2–10].

"Parallel" MRI is a new technique that circumvents these limitations by utilizing arrays of radio frequency detector coils to acquire data in parallel, thereby enabling still higher imaging speeds. In parallel MRI, coil arrays are used to accomplish part of the spatial encoding that was traditionally performed by magnetic field gradients alone. A schematic representation of parallel MRI is given in Fig. 1. The term parallel imaging comes from the fact that signals are acquired simultaneously from multiple coils. The effective use of multiple coils in parallel has been shown to multiply imaging speed, without increasing gradient switching rate or RF power deposition. In parallel imaging, the acquisition is speeded up by under-sampling the data received from the multiple coils. Under-sampling is described by factor called acceleration factor. The resulting data loss and consequent aliasing is compensated by the use of additional spatial information obtained from several receiver coils.

Spatial localization in conventional MRI is accomplished using a set of magnetic field gradients. The spatially varying fields resulting from the application of each gradient pulse spatially encodes the received signal, and generates an image using Fourier approximation. In conventional MR acquisition, the Fourier space is scanned line-by-line [11, 12]. This considerably limits the speed of image acquisition. Protocols with delayed scan times are not desirable, particularly for imaging applications involving repeated acquisitions. This includes functional imaging, perfusion and diffusion imaging, and imaging of the beating heart. Even though methods are available for tracking motion [13, 14], or reduction of accompanying

motion induced artifacts [15], accelerated MRI provides better solution for above applications.

Parallel MRI (pMRI) uses spatially separated receiver coils to perform spatial encoding. Though the theoretical foundation of pMRI was established in 1980s [16], not much was done in terms of its implementation due to the inability to design parallel coils capable of providing high Signal-to-Noise Ratio (SNR) images in a large enough Field Of View (FOV). Due to this, several attempts were made to accelerate MR acquisition using alternate means such as minimization of TR (Repetition Time) by increasing the gradient strength, and single shot imaging [17]. However, the performance of above methods was limited by the allowable strength of gradient pulse amplitudes. The idea of using phased array coils for MRI dates back to the early eighties, wherein the design efforts were largely concentrated in building array coils with reduced coil-to-coil coupling [18, 19]. The phased array coils are beneficial due to their ability to generate high SNR signals with reduced motion artifacts. The first phased array MRI system implemented by Roemar et al. [20] in the form of two inductively coupled resonant rings, electrically isolated from each other with a decoupling element connected between the rings. In this, differential weighting of signals from the two coils were used for signal localization, thereby reducing the need for time consuming gradient-encoding steps. Enhancement of SNR was achieved by means of the decoupling circuitry. For n_c independent coils in the absence of mutual coupling, the SNR is increased by a factor of square root of n_c. A detailed description of phased-array MRI technology is provided in the review article [21]. Recent advances in the design of MRI equipment and imaging procedures is described in [22].

In conventional MR imaging, the phase-encoding steps are performed in sequential order by switching the magnetic field gradient step-by step, which in turn determines the speed of acquisition. Since the switching is expensive, acceleration is achieved by skipping alternate phase encoding lines. This was first implemented in 1989 by under sampling the k-space in PE (Phase Encode) direction [23]. Since SNR is dependent on the number of phase encoding steps used, accelerated image acquisition can be achieved only at the expense of reduction in SNR. However, the reduced SNR is compromised by elimination of phase related distortion. Irrespective of the MRI sequence used, parallel imaging maintains image contrast without need for higher gradient system performance.

We now come to the question of how parallel MRI makes imaging faster. Assume the number of voxels, the number of receiver channels, the number of frequency encoding steps and the number of phase encoding steps are n_v, n_c, N_{fe} and N_{pe}, respectively. Obviously, the number of measured samples is $n_c \times N_{fe} \times N_{pe} = n_c \times n_k = N_s$ (where n_k is the number of sampling positions in k-space). To make reconstructions feasible, it is necessary that

$$N_s \geq n_v \tag{1}$$

In conventional single channel MRI, $N_s = N_{fe} \times N_{pe} = n_v$. For example, to obtain a 256×256 image, the acquisition matrix is also 256×256. In parallel MRI, since

$n_c > 1$, it is possible that we reduce the number of frequency encoding or phase encoding steps while still having enough information for a feasible reconstruction. Usually, the k-space is evenly under-sampled in the phase encoding direction to reduce the scanning time. The rate at which under-sampling is performed is called acceleration factor or acceleration rate [3, 4]. An obvious implication of Eq. (1) is that the largest possible acceleration rate is equal to the number of channels.

In summary, if an array of RF coils is used to acquire MR signals simultaneously and the coil sensitivities are available, the spin density may be determined from a reduced set of phase encodings. This is the basic principle of parallel imaging.

2 Background

2.1 History of Parallel Imaging Methods

The performance of pMRI is largely determined by the coil geometry. For instance, large coils cover large areas of the subject, resulting in low SNR due to small fraction of the sensitive volume occupied by the sample. The coil sensitivity can be considered as a point spread function that serves to degenerate the received signal, in addition to the additive noise. However, the spatial sensitivity profiles of each receiver coil serve to provide an additional encoding in pMRI. Better image reconstruction becomes possible only with prior knowledge of the coil sensitivities.

The first step towards pMRI was proposed by Carlson [16] in 1987. His method consisted of a uniform sensitivity pattern in one coil while applying linear gradient in the other. In this fashion, a Fourier series expansion was used to reconstruct the unfolded image data in k-space. Kelton et al. [22] proposed a second method of reconstruction in the spatial domain, wherein a matrix inversion was employed to unalias the image. Subsequently, this method was further modified to include reduction factors greater than two, but less than the number of coils used [2]. Theoretically, imaging time reduces by number of array coils, but practically lesser due to sensitivity noise, and increased coupling between coils. The basic limitation for all the above studies was the need for a reliable method to determine the individual coil sensitivity function.

A notable development following this period was the introduction of Simultaneous Acquisition of Spatial Harmonics (SMASH) method by Sodickson and Manning [3]. SMASH is the first experimentally successful parallel imaging technique that uses linear combinations of coil sensitivity profiles to generate low-order spatial harmonics of the desired FOV. Sodickson and Griswold then presented a successful in vivo implementation of pMRI using the SMASH technique, thereby starting the rapidly growing field of parallel imaging [24]. Only one year later, Pruessmann and Weiger proposed the concept of sensitivity encoding (SENSE) [3] which is strongly related to the early proposals of Kelton [23], Ra and Rim [2]. The difference between the two is that SENSE uses an SNR optimized

matrix inversion in combination with an initial estimate of the coil sensitivity mapping. Since then, great progress in the development and improvement of parallel imaging reconstruction methods has taken place, thereby producing a multitude of different and somewhat related techniques and strategies [3–5, 9, 10, 24–26]. Currently, the best-known are SMASH [3], SENSE [4] and GRAPPA [9]. However, various other techniques, such as AUTOSMASH [25], VD-AUTO-SMASH [26], Generalized SMASH [10], mSENSE [27], PILS [6] and SPACERIP [5] have also been proposed.

2.2 Spatial Encoding and Image Reconstruction

The general equation of multi-channel MR acquisition can be expressed as

$$s_l(k_x, k_y) = \iint_{xy} C_l(x, y)\rho(x, y)\, e^{-i2\pi(k_x x + k_y y)} dxdy \tag{2}$$

where $C_l(x, y)$ denotes the coil sensitivity profile of the lth channel [28]. Here, the signal comprises an integration of the spin density $\rho(x, y)$ against the spatial encoding function consisting of coil sensitivity and gradient modulation. Unlike Fourier encoding where off-resonance frequencies are determined in accordance with spatial positions, the sensitivity encoding functions serve to differentially sample the image based on the spatial positions closer to the respective coils. These functions may be regarded as representing different "views" or "projections" of the image to be reconstructed, with each measured signal point representing the appearance of the image from the corresponding perspective, as illustrated in Fig. 2.

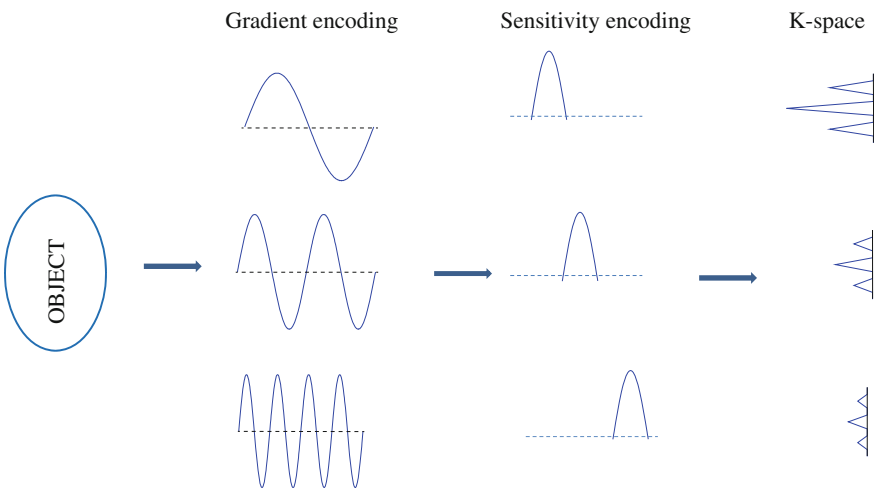

Fig. 2 Encoding scheme in pMRI

In multi-channel acquisition, the received signal in each coil is weighted by the coil sensitivity function $C_l(r)$, and the magnetic field $B(r)$. In terms of the weighting functions, the spatial encoding function of MR acquisition can be expressed as

$$E_\varsigma(r) = \frac{\gamma^2\hbar}{4k_BT}\, C_l(r)\, B(r)\, e^{-i\gamma[B(r)-B_0]t}\Big|_{t=t_\varsigma} \tag{3}$$

The discrete time measured signal can be generalized to be the inner product

$$s_\varsigma = \langle E_\varsigma(r),\ \rho(r)\rangle \tag{4}$$

For a k-space with N points, the basis vectors then produce a signal vector with N elements

$$s = \begin{bmatrix} s_1 \\ s_2 \\ \bullet \\ \bullet \\ \bullet \\ s_N \end{bmatrix} = \begin{bmatrix} \langle E_1(r)\ , \rho(r)\rangle \\ \langle E_2(r)\ , \rho(r)\rangle \\ \bullet \\ \bullet \\ \bullet \\ \langle E_N(r)\ , \rho(r)\rangle \end{bmatrix} \tag{5}$$

For each discretized location r, Eq. (5) can be represented in the matrix form

$$s = \boldsymbol{E}\rho \tag{6}$$

where s and ρ contain the measured samples and image pixels, respectively. $\boldsymbol{E}$ is referred to as the generalized encoding matrix (GEM) [8] with dimension $N_s \times n_p$. Equation (6) shows that the encoding of MRI is essentially a linear transform, and the reconstruction in general involves inverse problems, namely,

$$\hat{\rho} = E^{-1}s \tag{7}$$

The major difficulty is that the dimension of the GEM $\boldsymbol{E}$, is in general, rather large and direct inversion is prohibitively time-consuming and memory-intensive. The inversion operation is simplified using different pMRI reconstruction methods. In further discussions, the number of voxels, the number of receiver channels, the number of frequency encoding steps and the number of phase encoding steps are denoted by n_v, n_c, N_{fe} and N_{pe}, respectively. Obviously, the number of measured samples will be $n_c \times N_{fe} \times N_{pe} = n_c \times n_k = N_s$ (where n_k is the number of sampling position in k-space) and the encoding matrix E is of dimension $N_s \times n_v$. To make reconstructions feasible, it is necessary that $N_s \geq n_v$.

2.3 Sensitivity Calibration to Obtain the Encoding Matrix E

At a given sampling location, the encoding function and coil sensitivity are related in the form

$$E_{k,l}(r) = \frac{\gamma^2 \hbar^2}{4k_B T} C_l(r)\, e^{ik.r} \tag{8}$$

The coil sensitivities are calculated from the knowledge of coil array geometry. For flexible coil arrays, the coil sensitivity functions are to be recalibrated due to scan-to-scan changes in the coil locations. The coil modulated images are given by

$$\rho_l(r) = C_l(r)\rho(r) \tag{9}$$

The coil images have a non-unifrom intensity distribution due to the spatially varying sensitivity values. Meaningful information about the image can only be obtained once the individual coil images are combined so as to have a uniform spatial sensitivity C_0 at all spatial location. The uniform spatial profile is obtained in practice by using a bird-cage body coil. The ratio of channel image to the body coil image, therefore, yields

$$\frac{\rho_l(r)}{\rho_{body-coil}(r)} = \frac{C_l(r)}{C_0} \tag{10}$$

Alternatively, a sum-of-squares combination yields

$$\frac{\rho_l(r)}{\sqrt{\sum_l |\rho_l(r)|^2}} = \frac{C_l(r)}{\sqrt{\sum_l |C_l(r)|^2}} \tag{11}$$

Since the multiplication of $\frac{1}{\sqrt{\sum_l |C_l(r)|^2}}$ is common to all coils, it can be incorporated in the formulation of an effective encoding function which differs from the original encoding Eq. (8) as follows:

$$\tilde{E}_{k,l}(r) = \frac{E_{k,l}(r)}{\sqrt{\sum_l |C_l(r)|^2}} \tag{12}$$

All pMRI methods effectively reconstruct the image $\tilde{\rho}(r)$ given by

$$\hat{\rho}(r) = \sqrt{\sum_l |C_l(r)|^2}\, \rho(r) \tag{13}$$

Calibration data, used to reconstruct the coil images can be obtained from a separate scan before or after the image acquisition. Because of the requirement of external information, this approach is generally known as external calibration. Alternatively, the calibration scan can be incorporated as a part of the image acquisition, and the calibration data can be extracted from the image dataset. This approach is called auto-calibration or self-calibration. The crucial difference between the external- and self-calibration approaches lies in the timing of the acquisition of calibration data relative to the image acquisition.

SENSE reconstruction methods require a prior knowledge of the coil sensitivity profiles. The SENSE method is mathematically an exact reconstruction method proposed by Pruessmann et al. [4]. SENSE is the most popular image-space based pMRI technique, which is being offered by many companies particularly Philips (SENSE), Siemens (mSENSE), General Electric (ASSET), and Thoshiba (SPEEDER). SENSE is the most used pMRI method for clinical applications due to its broad availability and the enhanced image acquisition capabilities.

The SENSE method addresses the most general case of combined gradient and sensitivity encoding. The two reconstruction approaches in SENSE include strong reconstruction for optimal voxel shape and weak reconstruction for approximate voxel shape using Dirac function [4] accompanied by SNR reduction. The reconstruction algorithm for both the approaches are numerically demanding due to the hybrid encoding nature. Use of FFT (Fast Fourier Transform) is possible only in the case of weak reconstruction for Cartesian SENSE.

3 SENSE Methods

3.1 Representation of Aliased Images

For achieving scan time reduction in pMRI, phase encoding lines are under-sampled by an acceleration factor R. Therefore, the distance between phase encoding lines is increased by R. Even though number of phase encoding steps N_{pe} is reduced, the maximum gradient strength $N_{\mathrm{pe}} \times G_{\mathrm{y}}$ remains same. This results in aliased image reconstruction. The k-space s_l^r retrieved with an acceleration factor R is identical to complete k-space s_l excluding the unacquired lines. The FOV is reduced only in the phase encoding direction, because the 2D Fourier transformation is separable. The aliased image is obtained by an inverse Fourier transformation of s_l^r in y direction.

$$\begin{aligned}\rho_l^r(x,y) &= DFT_y^{-1}\left\{s_l^r(x,k_y)\right\} \\ &= \frac{R}{N_{pe}} \sum_{k_y=0,R,2R,\cdots}^{N_{pe}-R} s_l(x,k_y)\, e^{ik_y y} \\ &= \frac{R}{N_{pe}} \sum_{k_y=0,R,2R,\cdots}^{N_{pe}-R} e^{ik_y y} \sum_{y'=0}^{N_{pe}-1} \rho(x,y')\, e^{-ik_y y'} \\ &= \frac{R}{N_{pe}} \sum_{y'=0}^{N_{pe}-1} \rho(x,y') \sum_{k_y=0,R,2R,\cdots}^{N_{pe}-R} e^{ik_y y}\, e^{-ik_y y'} \\ &= \frac{R}{N_{pe}} \sum_{y'=0}^{N_{pe}-1} \rho(x,y') \sum_{k_y=0,1,2,\cdots}^{\frac{N_{pe}}{R}-1} e^{ik_y y}\, e^{-ik_y y'}\end{aligned} \tag{14}$$

Since $e^{ik_y y}$ *and* $e^{-ik_y y'}$ are orthogonal, the sum over k_y for $R = 1$ gives zero for all $y \neq y'$. $\frac{R}{N_{pe}}$ is assumed to be an integer for simplicity. For $R > 1$ the exponential functions can be represented as the sum of R Kronecker delta functions.

$$\begin{aligned}\rho_l^r(x,y) &= \sum_{y'=0}^{N_{pe}-1} \sum_{m=0}^{R-1} \delta(y', y \bmod \frac{N_{pe}}{R} + m \times \frac{N_{pe}}{R})\, \rho(x,y') \\ &= \sum_{m=0}^{R-1} \rho(x, y \bmod \frac{N_{pe}}{R} + m \times \frac{N_{pe}}{R})\end{aligned} \tag{15}$$

Each value in aliased image ρ_l^r is a superposition of R values from the original image.

3.2 SENSE Reconstruction Using Encoding Matrix Formulation

The ideal image ρ and k-space values $s_l(k_x, k_y)$ are related using the encoding matrix E.

$$s_l(k_x,k_y) = \sum_{k_x,k_y} \rho(x,y)\, E_{l,k_x,k_y}(x,y) \tag{16}$$

where the encoding matrix E is

$$\mathrm{E}_{\mathrm{l},\mathrm{k_x},\mathrm{k_y}}(\mathrm{x},\mathrm{y}) = \mathrm{e}^{-\mathrm{i}\pi(\mathrm{k_x x}+\mathrm{k_y y})}\mathrm{C_l}(\mathrm{x},\mathrm{y}) \tag{17}$$

The image reconstruction is performed using the linear reconstruction matrix F

$$\hat{\rho}(\mathrm{x},\mathrm{y}) = \sum_{\mathrm{l},\mathrm{k_x},\mathrm{k_y}} \mathrm{F}_{\mathrm{l},\mathrm{k_x},\mathrm{k_y}}(\mathrm{x},\mathrm{y})\, \mathrm{s}_{\mathrm{l}}(\mathrm{k_x},\mathrm{k_y}) \tag{18}$$

The reconstruction matrix F is estimated using weak voxel criterion, where the voxel functions are approximated using Dirac function. The $F_{[x,y;l,k_x,k_y]}$ and $E_{[l,k_x,k_y;x,y]}$ related by

$$\mathrm{FE} = \mathrm{Id}_{\mathrm{n_v}} \tag{19}$$

where $\mathrm{Id}_{\mathrm{n_v}}$ is an $n_v \times n_v$ identity matrix. Equation (19) is valid only under ideal conditions when the data is fully sampled and the receiver coils have no overlap. However, the latter condition is not fully valid for phased arrays for which the relation between reconstruction and encoding matrices are determined by a sample noise matrix. A detailed discussion of these effects are presented in the next section.

3.3 Phased Arrays

One of the basic requirement of parallel MRI is to acquire MR signals simultaneously using multiple coil elements from a receiver coil array. The coil arrays are conventionally called "phased array", had been invented and widely used in MRI even before the advent of parallel imaging. It was developed in 1990 by Roemer [29], improve SNR for large FOV applications.

The concept of phased array was first introduced in phased array radar and ultrasound. In an array data is acquired simultaneously and combined subsequently from a multitude of closely positioned receive coils so that SNR and resolution of small surface coils can be obtained over a large FOV normally associated with body imaging with no increase in imaging time. An important issue compared to the design of a single surface coil is that there may be interactions among nearby coil elements, commonly called "mutual coupling". To minimize the coupling effect various techniques, such as overlapping [29], low impedance preamplifier [29], interconnecting capacitors/inductors have been proposed.

Figure 3a shows a schematic of a 4-element phased array using Shepp-Logan phantom image. Each receiver acquires MR signals independently. The absolute magnitude single-coil images from the four channels are displayed in Fig. 3b. It is shown that for each channel, high SNR is observed in a certain region of the FOV; after combination, it is expected that we can obtain high SNR over the entire FOV. The data combination algorithms are discussed as follows.

For an N-element phased array, let Y denote the $N \times N$ receiver noise matrix, with the m-nth entry representing noise correlation between the mth and the nth channel, and the mth diagonal element representing the noise level of the mth

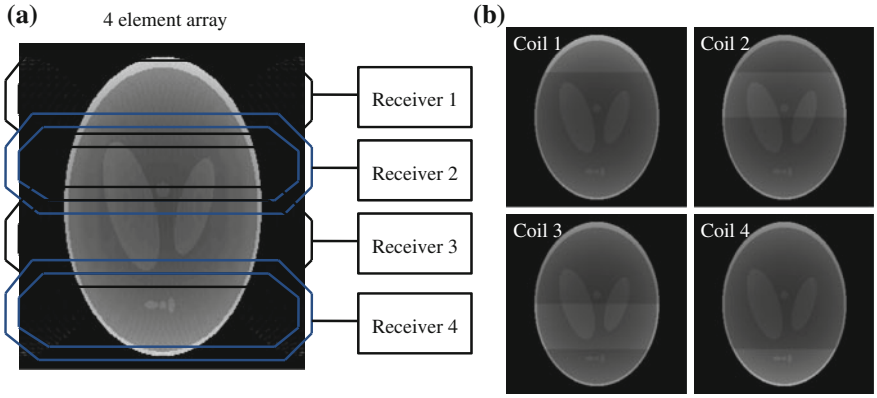

Fig. 3 **a** Schematic of a phased array coil using Shepp-Logan, **b** Absolute magnitude single-coil images from the four channels

channel. For a given point (x, y), let p_i denote the pixel value from the ith channel and $P = [p_1\ p_2\ p_3 \ldots p_N]^T$, let c_i denote the complex sensitivity of the ith coil at that point and $C = [c_1\ c_2\ c_3 \ldots c_N]$. The combined pixel value with optimized SNR, according to [19], is expressed as

$$p_{combine} = \lambda P^T \Psi^{-1} C \tag{20}$$

where λ is a constant scaling factor. The optimum data combination can be obtained as a linear combination of data from individual channels with appropriate weightings to each position. When the noise correlation is negligible, it is easily shown that the SNR-optimized composite image is a combination of single-coil images weighted by their respective sensitivities.

The accurate knowledge of sensitivity is required to combine the data as shown in Eq. (20). Since in some cases, measuring the sensitivity of each coil is excessive, it is desirable to have a technique which combines the data without detailed knowledge of the coil sensitivity while at the same time preserves high SNR. For this purpose, the coil sensitivities in Eq. (3) are approximated by the single-coil images themselves. This leads to the more commonly used "sum-of squares" combination [29], which takes a simpler form

$$p_{combine} = \sqrt{P^H P} \tag{21}$$

where the superscript H denotes conjugate transpose.

If the different coils have a significant overlap, the matrix inversion in Eq. (7) is challenging because the rows of the sensitivity matrix C_l becomes linearly dependent. This leads to noise amplification in the reconstructed image. The noise arises due to the reduced amount of acquired data. Due to the mutual coupling between coils, this noise is spatially varying. The spatial variation in noise is

quantified using a noise covariance matrix. With $\boldsymbol{\rho}_{\mathrm{p}}$ representing a vector consisting of signals $\rho_{\mathrm{l,p}}$ from the same location in each coil element, SNR of the Root Sum-of-Squares (RSoS) image is expressed as

$$\mathrm{SNR}_{\mathrm{RSoS}}(\mathrm{p}) = \sqrt{\boldsymbol{\rho}_p^H \boldsymbol{\psi}^{-1} \boldsymbol{\rho}_p} \tag{22}$$

where $\boldsymbol{\psi}$ denotes the noise covariance matrix, that is approximated by summing the scalar dot product of coil sensitivities over a number of points. The (i, j)th element of this matrix is obtained as

$$\boldsymbol{\psi}_{i,j} = \sum_{\mathrm{p}=1}^{\mathrm{n_v}} C_i(p) \cdot C_j(p), \quad for \quad i,j = 1, 2, \ldots, n_c. \tag{23}$$

The ψ is the $n_c \times n_c$ receiver noise matrix which denotes the variance in each coil as well as correlation between coils. The propagation of noise from k-space to image-space is described by the sample noise matrix $\tilde{\psi} = \psi \otimes Id_{n_k}$ and image noise matrix X in which the pth diagonal element represents the noise variance in the pth image value and off-diagonal elements provides noise correlation between image values. The relation between sample noise and image noise matrices are given by

$$X = F \tilde{\psi} F^H \tag{24}$$

This variance is minimized for each pixel using the Lagrangian multipliers, using the constraint in Eq. (19) yielding the SENSE solution

$$F = (E^H \tilde{\psi}^{-1} E)^{-1} E^H \tilde{\psi}^{-1} \tag{25}$$

3.4 Cartesian SENSE

In the standard cartesian sampling, k-space is undersampled with a reduction factor R in the Fourier domain and aliased reduced FOV image $\hat{\rho}_l^r$ is obtained in the spatial domain for each of the n_c array coils. Each pixel in the aliased image contains the local coil sensitivity weighted by signal contribution from the R pixels in the original full-FOV image ρ. From Fig. 4, it is clear that the contributing pixel positions form a cartesian grid corresponding to the size of the reduced FOV.

To reconstruct the full-FOV image $\hat{\rho}$, one must undo the signal superposition underlying the fold-over effect Fig. 3. The SENSE reconstruction process is sketched in Fig. 5.

The time and space complexity of Eq. (27) is reduced using cartesian SENSE. From Eq. (15), it is clear that value of each aliased pixel is a linear combination of

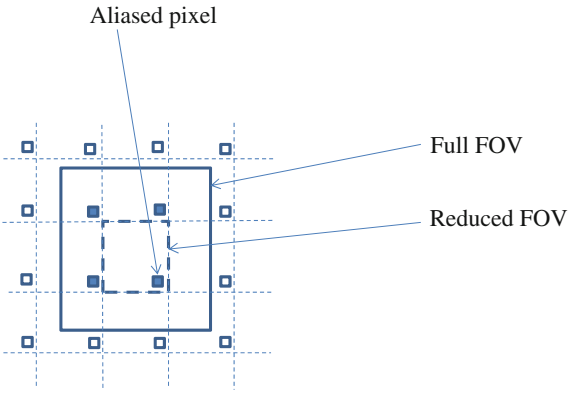

Fig. 4 Aliasing in 2D cartesian sampling

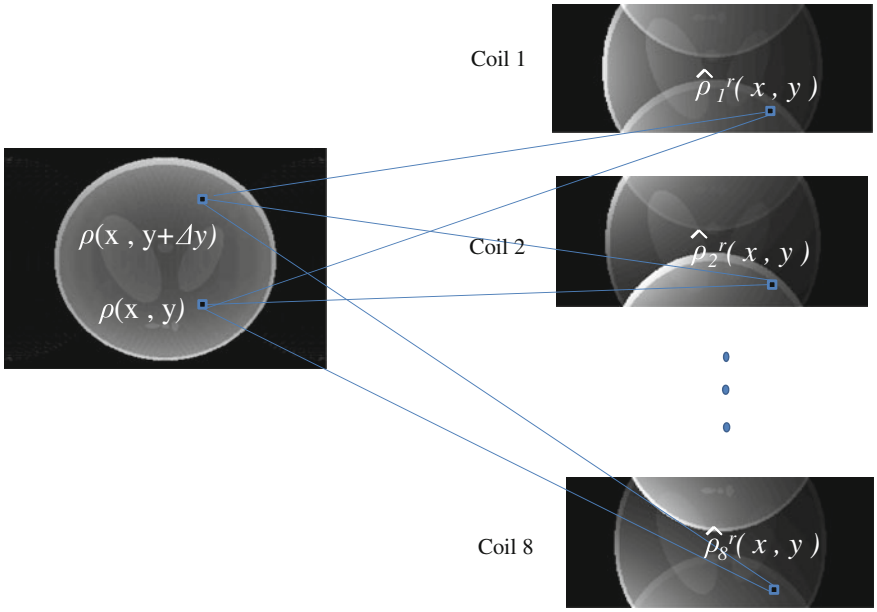

Fig. 5 Fold over in SENSE

R pixel values. Therefore, the encoding matrix E becomes block diagonal. Let $\rho_l^{r(i)}$,$C_l^{(i)}$, $\rho^{(i)}$ represent the ith column of ρ_l^r, C_l, and ρ respectively. Each column consists of R blocks. Each block represents a partitioning of signals into R aliasing components under cartesian sampling.

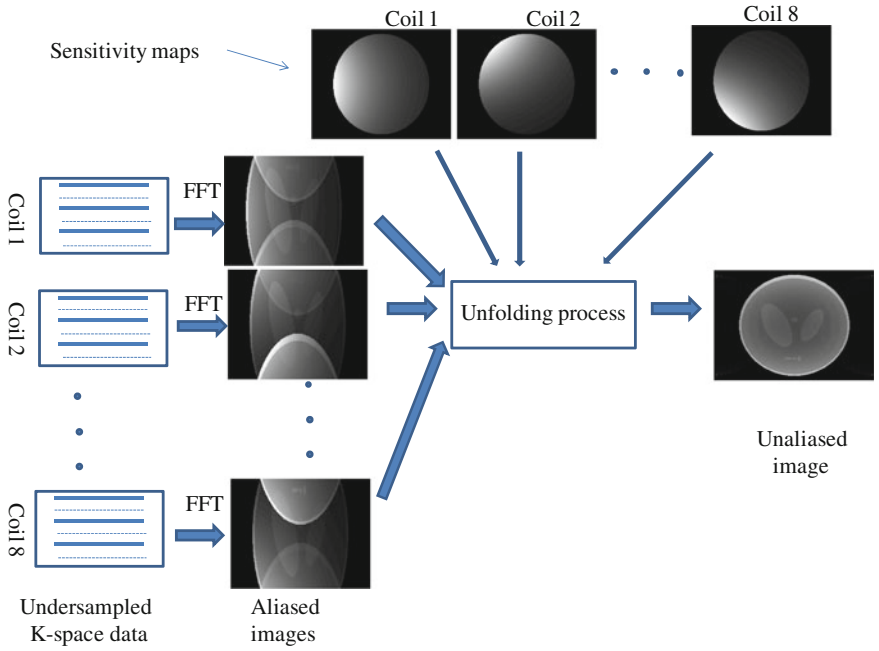

Fig. 6 The SENSE process

$$\rho^{(i)} = \begin{bmatrix} \rho_1^{(i)} \\ \rho_2^{(i)} \\ \vdots \\ \rho_R^{(i)} \end{bmatrix}, \; C_l^{(i)} = \begin{bmatrix} C_{l,1}^{(i)} \\ C_{l,2}^{(i)} \\ \vdots \\ C_{l,R}^{(i)} \end{bmatrix} \tag{26}$$

As illustrated in (Fig. 6), the jth element of rth block ($r = 1, \ldots, R$) of the ith column of image ρ is given by

$$\rho_r^{(i)}(j) = \rho^{(i)}\left(\frac{N_{pe}}{R} \times (r-1) + j\right), \quad where\ j = 1, \ldots, \frac{N_{pe}}{R} \tag{27}$$

The corresponding element of sensitivity vectors for each coil $l \in \{1, \ldots, n_c\}$ are given by

$$\mathrm{C}_{\mathrm{l,r}}^{(\mathrm{i})}(\mathrm{j}) = \mathrm{C}_{\mathrm{l}}^{(\mathrm{i})}\left(\frac{\mathrm{N_{pe}}}{\mathrm{R}} \times (\mathrm{r}-1) + \mathrm{j}\right), \quad \text{where } \mathrm{j} = 1, \ldots, \frac{\mathrm{N_{pe}}}{\mathrm{R}} \tag{28}$$

diag $(C_{l,r}^{(i)})$ represents a diagonal matrix of size $\frac{N_{pe}}{R} \times \frac{N_{pe}}{R}$. These diagonal matrices from one column are now cascaded to form a $\frac{N_{pe}}{R} \times N_{pe}$ matrix representation of the

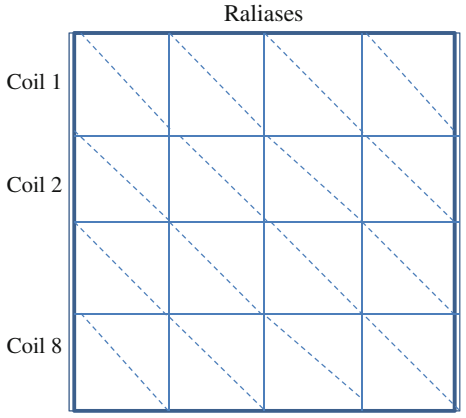

Fig. 7 R aliases in SENSE

*i*th column in the *l*th coil. The encoding matrix elements of the *l*th coil E_l is now constructed by cascading the above diagonal matrix blocks of size $\frac{N_{pe}}{R} \times N_{pe}$ corresponding to all the columns. The stack representing each coil is now cascaded row-wise to form the encoding matrix E,

$$\begin{aligned} \mathrm{E} = \left\{\mathrm{E}_{\mathrm{l}}^{\mathrm{r}}\right\} \quad \text{where } \mathrm{r} = 1, \ldots, \mathrm{R} \\ \mathrm{l} = 1, \ldots, \mathrm{n_c} \end{aligned} \tag{29}$$

This is depicted in Fig. 7.

The inversion of each block corresponding to each pixel can be done independently. The encoding process given by Eq. (17) is then simplified to

$$\rho_l^r(x,y) = \sum_{m=0}^{R-1} \rho(x, y \bmod \frac{N_{pe}}{R} + m \times \frac{N_{pe}}{R}) \times C_l(x, y \bmod \frac{N_{pe}}{R} + m \times \frac{N_{pe}}{R}) \tag{30}$$

In matrix form, this becomes

$$\begin{pmatrix} \hat{\rho}_1^r(x,y) \\ \hat{\rho}_2^r(x,y) \\ \vdots \\ \hat{\rho}_{n_c}^r(x,y) \end{pmatrix} = \begin{pmatrix} C_1(x,y),\ C_1(x,y+N_{pe}/R), \ldots, C_1(x,y+(R-1)N_{pe}/R) \\ C_2(x,y),\ C_2(x,y+N_{pe}/R), \ldots, C_2(x,y+(R-1)N_{pe}/R) \\ \vdots \\ C_{n_c}(x,y),\ C_{n_c}(x,y+N_{pe}/R), \ldots, C_{n_c}(x,y+(R-1)N_{pe}/R) \end{pmatrix} \begin{pmatrix} \rho(x,y) \\ \rho(x,y+N_{pe}/R) \\ \vdots \\ \rho(x,y+(R-1)N_{pe}/R) \end{pmatrix} \tag{31}$$

where $N_{pe}.N_{fe}$ is the FOV size in pixels, $x = 1, \ldots, N_{fe}$ *and* $y = 1, \ldots, \frac{N_{pe}}{R}$

When the $c = \begin{pmatrix} C_1(x,y),\ C_1(x,y+N_{pe}/R), \ldots, C_1(x,y+(R-1)N_{pe}/R) \\ C_2(x,y),\ C_2(x,y+N_{pe}/R), \ldots, C_2(x,y+(R-1)N_{pe}/R) \\ \vdots \\ C_{n_c}(x,y),\ C_{n_c}(x,y+N_{pe}/R), \ldots, C_{n_c}(x,y+(R-1)N_{pe}/R) \end{pmatrix}$ matrix is non-singular for all x and y, the reconstruction problem will not be ill posed.The unfolding matrix U is then given by

$$U = (c^H \psi^{-1} c)^{-1} c^H \psi^{-1} \tag{32}$$

Therefore, the R reconstructed pixels in vector form is given by

$$\begin{pmatrix} \hat{\rho}(x,y) \\ \hat{\rho}(x,y+N_{pe}/R) \\ \vdots \\ \hat{\rho}(x,y+\ (R-1)N_{pe}/R) \end{pmatrix} = U \begin{pmatrix} \hat{\rho}_1^r(x,y) \\ \hat{\rho}_2^r(x,y) \\ \vdots \\ \hat{\rho}_{n_c}^r(x,y) \end{pmatrix} \tag{33}$$

3.5 SENSE for Optimum SNR Imaging

Parallel acquisition techniques suffer from loss in SNR when compared with optimum array imaging. In general, the SNR in the parallel MR reconstructed image is decreased by the square root of the reduction factor R as well as by an additional coil geometry dependent factor-geometry factor (g-factor) [30–32]. In SENSE, the loss in SNR arises due to ill-conditioning of the matrix inverse in SENSE reconstruction, and depends on the acceleration rate, the number of coils, and coil geometry. This loss can he explained through additional constraints imposed on the choice of array weighting factors. In standard array coil imaging, weighting factors are chosen to maximize SNR at a given point P. SENSE reconstruction has the same requirement, but in addition to that, SNR has to be minimized at a number of points P. The ultimate sensitivity limit for SENSE reconstruction can he calculated from sensitivity maps for optimum SNR imaging.

4 Conclusion

This approach of parallel MRI, the under-sampled MR data acquired with a set of phased-array detection coils are combined using reconstruction techniques. In SENSE, the spatial sensitivity information of the coil array needs to be determined for spatial encoding. It is very important that the calculated sensitivities are

accurate, otherwise can result in aliasing artifacts. Apart from this, parallel acquisition techniques suffer from loss in SNR when compared with optimum array imaging. All these factors need to be well addressed for optimum reconstruction in parallel MRI.

References

1. Zhu, H.: Medical Image Processing Overview. University of Calgary
2. Ra, J.B., Rim, C.Y.: Fast imaging using subencoding data sets from multiple detectors. Magn. Reson. Med. **30**(1), 142–145 (1993)
3. Sodickson, D.K., Manning, W.J.: Simultaneous acquisition of spatial harmonics (SMASH): fast imaging with radiofrequency coil arrays. Magn. Reson. Med. **38**(4), 591–603 (1997)
4. Pruesmann, K., Weiger, M., Scheidegger, M., Boesiger, P.: SENSE: sensitivity encoding for fast MRI. Mag. Res. Med. **42**, 952–962 (1999)
5. Kyriakos, W.E., Panych, L.P., Kacher, D.F., Westin, C.F., Bao, S.M., Mulkern, R.V., Jolesz, F.A.: Sensitivity profiles from an array of coils for encoding and reconstruction in parallel (SPACE RIP). Magn. Reson. Med. **44**(2), 301–308 (2000)
6. Griswold, M.A., Jakob, P.M., Nittka, M., Goldfarb, J.W., Haase, A.: Partially parallel imaging with localized sensitivities (PILS). Magn. Reson. Med. **44**(4), 602–609 (2000)
7. McKenzie, C.A., Yeh, E.N., Sodickson, D.K.: Improved spatial harmonic selection for SMASH image reconstructions. Magn. Reson. Med. **46**(4), 831–836 (2001)
8. Sodickson, D.K., McKenzie, C.A.: A generalized approach to parallel magnetic resonance imaging. Med. Phys. **28**(8), 1629–1643 (2001)
9. Griswold, M.A., Jakob, P.M., Heidemann, R.M., Nittka, M., Jellus, V., Wang, J., Kiefer, B., Haase, A.: Generalized autocalibrating partially parallel acquisitions (GRAPPA). Magn. Reson. Med. **47**(6), 1202–1210 (2002)
10. Bydder, M., Larkman, D.J., Hajnal, J.V.: Generalized SMASH imaging. Magn. Reson. Med. **47**, 160–170 (2002)
11. Lauterbur, P.C.: Image formation by induced local interactions: examples employing nuclear magnetic resonance. Nature **242**, 190–191 (1973)
12. Mansfield, P., Grannell, P.K.: NMR 'diffraction' in solids. J. Phys. C: Solid State Phys. **6**(22) (1973)
13. Glover, G.H., Pelc, N.J.: A rapid-gated cine MRI technique. Magn. Reson, Annual (1988)
14. Ehman, R.L., Felmlee, J.P.: Adaptive technique for high-definition MR imaging of moving structures. Radiology **173**(1), 255–263 (1989)
15. Bloomgarden, D.C., Fayad, Z.A., Ferrari, V.A., Chin, B., Sutton, M.G., Axel, L.: Global cardiac function using fast breath-hold MRI: validation of new acquisition and analysis techniques. Magn. Reson. Med. **37**(5), 683–692 (1997)
16. Carlson, J.W.: An algorithm for NMR imaging reconstruction based on multiple RF receiver coils. J. Magn. Reson. **74**(2), 376–380 (1987)
17. Hutchinson, M., Raff, U.: Fast MRI data acquisition using multiple detectors. Magn. Reson. Med. **6**(1), 87–91 (1988)
18. Schenck, J.F., Hart, H.R., Foster, T.H., Edelstein, W.A., Bottomley, P.A., Hardy, C.J., Zimmerman, R.A., Bilaniuk, L.T.: Improved MR imaging of the orbit 1.5T with surface coils. Am. J. Neuroradiol. **6**, 193–196 (1985)
19. Hyde, J.S., Jesmanowicz, A., Gristand, T.M., Froncisz, W., Kneeland, J.B.: Quadrature detection surface coil. Magn. Reson. Med. **4**, 179–184 (1987)
20. Roemer, P.B., Edelstein, W.A., Hayes, C.E., Souza, S.P., Mueller, O.M.: The NMR pased array. Magn. Reson. Med. **16**(2), 192–225 (1990)

21. Wright, S.M., Wald, L.L.: Theory and application of array coils in MR sectroscopy. NMR Biomed. **10**(8), 394–410 (1997)
22. Steckner, M.C.: Advances in MRI equipment design, software, and imaging procedures. Hitachi Medical Systems America, Inc. AAPM (2006)
23. Kelton, J.R., Magin, R.L., Wright, S.M.: An algorithm for rapid image acquisition using multiple receiver coils. In: Proceedings of the SMRM 8th Annual Meeting, Amsterdam, pp. 1172 (1989)
24. Sodickson, D.K., Griswold, M.A., Edelman, R.R., Manning, W.J.: Accelerated spin echo and gradient echo imaging in the abdomen and thorax using simultaneous acquisition of spatial harmonics (SMASH). In: Proceedings of the ISMRM Annual Meeting, Vancouver, Canada, Abstract 1818 (1997)
25. Jakob, P.M., Griswold, M.A., Edelman, R.R., Sodickson, D.K.: AUTO-SMASH: a self-calibrating technique for SMASH imaging. Simultaneous acquisition of spatial harmonics. MAGMA **7**(1), 42–54 (1998)
26. Heidemann, R.M., Griswold, M.A., Haase, A., Jakob, P.M.: VD-AUTO-SMASH imaging. Magn. Reson. Med. **45**(6), 1066–1074 (2001)
27. Wang, J., Kluge, T., Nittka, M., Jellus, V., Kühn, B., Kiefer, B.: Parallel acquisition techniques with modified SENSE reconstruction mSENSE. In: First International Workshop on Parallel MRI, Wurzburg, Germany, p. 398 (2001)
28. Yanasak, N., Clarke, G., Stafford, R.J., Goerner, F., Steckner, M., Bercha, I., Och, J., Amurao, M.: Parallel Imaging in MRI: Technology, Applications, and Quality Control, American Association of Physicists in Medicine (2015)
29. Qu, P., Zhang, B., Luo, J., Wang, J., Shen, G.X.: Improved iterative non-cartesian SENSE reconstruction using inner-regularization. In: Proceedings of the ISMRM 14, Seattle (2006)
30. Ali, A.S., Hussien, A.S., Tolba, M.F., Youssef, A.H.: Visualization of large time-varying vector data. In: 3rd IEEE International Conference on Computer Science and Information Technology, Art no. 5565176, pp. 210–215 (2010)
31. Breuer, F.A., Kannengiesser, A.R.S., Blaimer, M., Seiberlich, N., Jakob, P.M., Griswold, M. A.: General formulation for quantitative G-factor calculation in GRAPPA Reconstructions. Magn. Reson. Med. **62**, 739–746 (2009)
32. Ohliger, M.A., Sodickson, D.K.: An introduction to coil array design for parallel MRI. NMR Biomed. **19**, 300–315 (2006)

Applications of Bio-molecular Databases in Bioinformatics

Archana Kumari, Swarna Kanchan, Rajeshwar P. Sinha and Minu Kesheri

Abstract Discovery of genome as well as protein sequencing aroused interest in bioinformatics and propelled the necessity to create databases of biological sequences. These data are processed in useful knowledge/information by data mining before storing into databases. This book chapter aims to present a detailed overview of different types of database called as primary, secondary and composite databases along with many specialized biological databases for RNA molecules, protein-protein interaction, genome information, metabolic pathways, phylogenetic information etc. Attempt has also been made to focus on drawbacks of present biological databases. Moreover, this book chapter provides an elaborate and illustrative discussion about various bioinformatics tools used for gene prediction, sequence analysis, phylogenetic analysis, protein structure as well as function prediction, molecular interactions prediction for several purposes including discovery of new gene as well as conserved regions in protein families, estimation of evolutionary relationships among organisms, 3D structure prediction of drug targets for exploring the mechanism as well as new drug discovery and protein-protein interactions for exploring the signaling pathways.

Keywords Bioinformatics · Data mining · Biological databases · Gene prediction · Sequence analysis · Phylogeny · Structure prediction · Molecular interaction

A. Kumari
Department of Bio-Engineering, Birla Institute of Technology Mesra, Ranchi, India

S. Kanchan
Department of Biological Sciences, Birla Institute of Technology and Science, Pilani 333031, Rajasthan, India

R.P. Sinha · M. Kesheri (✉)
Laboratory of Photobiology and Molecular Microbiology, Centre of Advanced Study in Botany, Banaras Hindu University, Varanasi 221005, India
e-mail: minubhu@gmail.com

N. Dey et al. (eds.), *Medical Imaging in Clinical Applications*,
Studies in Computational Intelligence 651, DOI 10.1007/978-3-319-33793-7_15

1 Introduction

Bioinformatics presents one of best example of interdisciplinary science. Actually, it is the mixture of various disciplines such as biology, mathematics, computer science and statistics. The term 'Bioinformatics' was given by a Dutch system-biologist Paulien Hogeweg, in the year of 1970 [1]. For the last few decades, it has become an important part of biological research to process the biological data quickly. Nowadays, bioinformatics tools are regularly used for identification of novel genes and their characterization. Bioinformatics is also used for calculating physiochemical properties, prediction of tertiary structure of proteins, evolutionary relationship and biomolecular interactions. Although these bioinformatics tools cannot generate as reliable information as those generated by experimentation. But the experimental techniques are difficult, costly and time consuming. Therefore the in silico approach facilitates in reaching an approximate informed decision for conducting the wet lab experiment. The role of bioinformatics is not only limited to generation of data but also extended to storage of large amount of biological data, retrieval, and sharing of data among researchers. The design of databases, development of tools to retrieve data from the databases and creation of user web interfaces are the major roles of bioinformatics scientists. Life sciences researchers are using these databases since 1960s [2]. In mid 1980s, bioinformatics came into existence and National Center for Biotechnology Information in 1988 was established by USA government.

There are many types of biological databases which are called primary, secondary and composite databases. Primary databases contain gene and protein sequence information as well as structure information only. Secondary databases contain derived information from primary databases and composite databases contain criteria for searching multiple resources. Along with theses databases Literature databases, Structural databases, Metabolic pathway databases, Genome databases for specific organisms, protein-protein interaction databases, phylogenetic information databases, RNA molecules databases and protein signalling databases are also discussed in detail.

Bioinformatics is also used to integrate the data mining techniques e.g. Genetic algorithms, Support vector machines, Artificial intelligence, Hidden Markov model etc. for developing software for sequence, structure and function based analysis.

Due to flooding of genome sequencing projects, vast amount of data have been accumulated at very high rate. However, pure data are not meaningful because knowledge/information in such data is hidden. Knowledge/information is much more valuable than data many times. Thus, a new technology field has emerged in mid 1990s to extract knowledge/information from raw data which is called *knowledge discovery in databases* (*KDD*) or simply *data mining* (*DM*) [3, 4]. First of all, Data which is the raw material and related to some specific problem are

collected, checked and finally selected. After careful selection of data, preprocessing of data is required i.e. erroneous data which is also called outliers are identified and removed. After preprocessing, algorithms or mathematical models are applied to extract the useful patterns, which are called data mining. These patterns are interpreted by experts and thereafter evaluated for by their novelty, correctness, comprehensibility and usefulness. Finally, information in graphics or presentable form is available to the end user in databases. The systematic diagram of KDD process in the form of flow chart is shown in Fig. 1.

A number of reviews and scientific articles related to databases have been published in the specialized area of Bioinformatics [5, 6]. However, none of these articles prove useful for a scientist who is not from bioinformatics/computational biology discipline. Therefore in the present chapter, we proceed to introduce various bioinformatics databases to a non-specialist reader to help extract useful information regarding his/her project. In this chapter every section contains a basic idea of each area supported by the literature and a tabulated summary of related databases, where necessary, towards the end of each section.

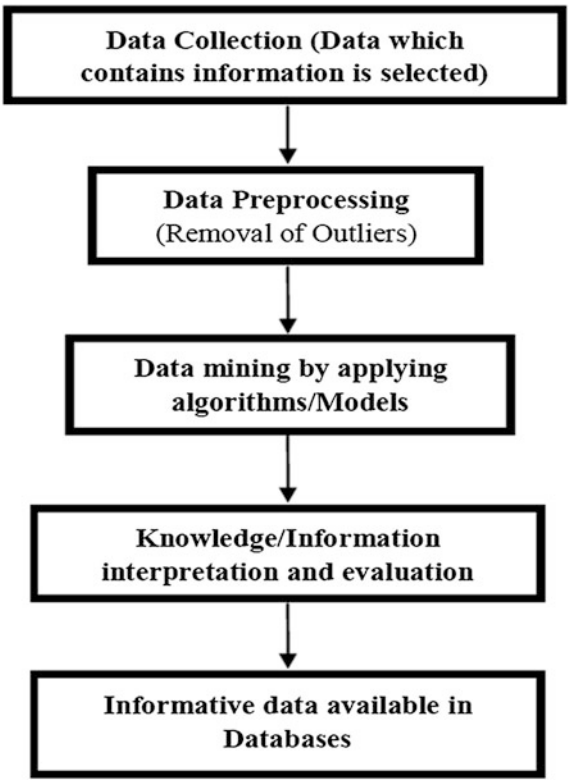

Fig. 1 Systematic diagram of KDD process

2 Biological Databases

Due to advancement in the high throughput sequencing techniques, sequencing of whole genome sequence of organisms are quite easy today and thereby leading to production of massive amount of data. Storage of large amount of biological data, retrieval and sharing of data among researchers are efficiently done by creation of databases which is a large, organized body of persistent data in a meaningful way. These databases were usually associated with computerized software designed to update, query, and retrieve the various components of the data stored in databases. There are different types of databases, which is based on the nature of the information being stored (e.g., sequences, structures, 2D gel or 3D structure images, and so on) as well as on the manner of data storage (e.g., whether in flat-files, tables in a relational database, or objects in an object-oriented databases. The sequence submission and storage of this information turn out to be freely accessible to the scientific world has directed to develop a number of databases worldwide. Respectively, every database becomes an autonomous illustration of a molecular unit of life.

Biological sequence database refers to a massive collection of data which have biological significance. Each biological molecule such as nucleic acids, proteins and polymers is identified by a unique key. The stored information can be used for future but also serves as an important input which for sequence and structure analyses. Biological Databases are mainly categorized into primary, secondary and composite databases and are discussed in detail in following sections.

2.1 Primary Databases

In primary database, the data related to sequence or structure are obtained through experiments such as yeast-two hybrid assay, affinity chromatography, XRD or NMR approaches. SWISS-PROT [7], UniProt [8–10], PIR [11], TrEMBL (translation of DNA sequences in EMBL) [7], GenBank [12], EMBL [13], DDBJ [14], Protein Databank PDB [15] and wwPDB (worldwide Protein DataBank) [16] are the well known examples of primary databases. A primary database is basically a collection of gene, protein sequence and structure information only. GenBank (USA), EMBL (Europe) and DDBJ (Japan) exchange data on a daily basis to ensure comprehensive coverage of these databases. SWISS-PROT is a protein sequence database which was established in 1986, collaboratively by University of Geneva and the EMBL [17]. SWISS-PROT includes annotations which has made it the database of choice for most of the researchers. The SWISS-PROT [17] contains information of its entries, which has been produced both by wet lab work as well dry lab. It is also interconnected to several other databases such as GenBank, EMBL, DDBJ, PDB and several other secondary protein databases. The protein data in SWISS-PROT mainly focuses only on model organisms and human only. On the other hand, the TrEMBL provides information on proteins from all

organisms [7]. Similarly, the PIR is one more inclusive collection of protein sequences which provides its user several attractive features like enabling to search for a protein molecule through text search. PIR also provides facility for web based analyses such as sequence alignment, identification of peptide molecules and peptide mass calculations [11, 17, 18]. The PIR Protein Sequence Database was developed by National Biomedical Research Foundation (NBRF) in 1960 s by Margaret Dayhoff. PIR is a database of protein sequences for investigating evolutionary relationships among proteins [11, 17, 18]. UniProt is another comprehensive collection of protein sequence which is available freely. The UniProt database is combination of SWISS-PROT, PIR and TrEMBL [8–10]. The worldwide Protein Data Bank (wwPDB) contains over 83,000 structures and they planned to provide each single 3D structure of protein molecules freely to the scientific community.

2.2 Secondary Databases

A secondary database is based on derived information from the primary database i.e. it contains information about the conserved sequence, active site residues of the protein families, patterns and motifs [19, 20]. Examples of secondary databases are SCOP [21], CATH [22], PROSITE [23], PRINTS [24] and eMOTIF [25]. The first secondary database to be developed was PROSITE, which is maintained by Swiss Institute of Bioinformatics. Within PROSITE, motifs are encoded as regular expressions which are also called patterns. PRINTS fingerprint database is another secondary database, which is maintained in University College London (UCL) and contains motifs as ungapped, unweighted local alignments [24]. The SCOP (Structural Classification of Proteins) database is maintained by MRC Laboratory and Centre for Protein Engineering which describes structural and evolutionary relationships among proteins for which structure are known [21]. In SCOP, proteins are classified in a hierarchical fashion to reflect their structural and evolutionary relationship. This hierarchy basically describes the family, superfamily and fold. The CATH (Class, Architecture, Topology, and Homology) is another secondary database which is a hierarchical classification of protein structures maintained at UCL [26]. CATH includes five levels within the hierarchy which are as follows:

- Class includes secondary structure content and packing. Four classes of domain are recognised: (i) mainly-α, (ii) mainly-β, (iii) α−β, which includes both alternating α/β and α + β structures, and (iv) Protein structures with low secondary structure content.
- Architecture includes arrangement of secondary structures, without connectivities; (e.g., barrel, roll, sandwich, etc.).
- Topology describes the overall shape and the connectivity of secondary structures.

- Homology includes domains that share 35 % sequence identity and are thought to share a common ancestor, i.e. are homologous.
- Sequence is the last level, where structures are clustered on the basis of sequence identity.

2.3 Composite Databases

Composite database is basically an amalgamation of variety of different primary database sources, which are meant to search multiple resources by putting different criteria in their search algorithm. Example of composite database is National Center for Biotechnology Information (NCBI) which is an extensive collection of nucleotide, protein sequence and many other databases providing free access to research community. NCBI provides interconnections between genetic sequence data, protein sequence data, structure data, phylogenetic tree based data, Genomes data and literature references. These links may also be between the same types of records in different databases, for example, literature articles in literature database Pubmed provide gene sequences, protein sequences, 3D structure, genome information and their links. Links between genetic sequences records are based on Blast sequence comparisons [27] while structure records are based on Vast structure comparisons [28]. NCBI includes one of the literature database called PubMed contains citations for biomedical literature from MEDLINE, journals and online books. NCBI also includes nucleotide sequence database called GenBank [12] which is collection of genome sequences of more than 2,50,000 species and these data can be retrieved by the NCBI's integrated retrieval system, i.e. Entrez, whereas the literature is easily accessible via PubMed [12, 29, 109]. It provides the information for related literature, organism, untranslated regions, exons/introns, repeat regions, coding regions, terminators, translations, promoters, bibliography etc. for each sequence. Sequence submission in GenBank can be done by individual laboratories along with large-scale genome sequencing projects. Protein sequence database in NCBI contains sequences from several sources which includes translations from annotated coding regions in GenBank, RefSeq. It also contains data records from SwissProt, PIR, PRF and PDB. The genome database in NCBI contains information on genomes which includes sequences, maps, chromosomes, assemblies as well as annotations. Protein structure databases at NCBI is called Molecular Modeling Database (MMDB) which contains data from experimentally resolved proteins structures, RNA and DNA molecules which are derived from the Protein Data Bank (PDB). MMDB also aid value-added features such as computationally identified 3D domains which can be used to identify similar 3D structures, as well as links to literature and information about chemicals/drug bound to the structures. Small chemical structure database integrated with NCBI is called Pubchem which includes small chemical structure and their biological activity (Fig. 2).

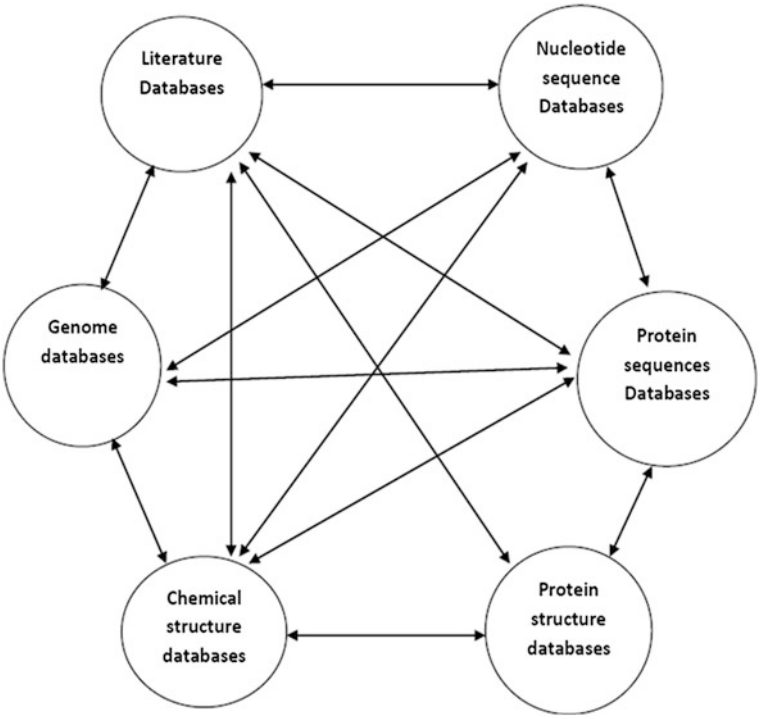

Fig. 2 *Circles* represent various databases; *straight* lines between *circles* represent links between different data types among different databases

NRDB (Non-Redundant DataBase) is another composite database which contains data from GenPept (derived from automatic GenBank CDS translations), SWISS-PROT, PIR, GenPeptupdate (the daily updates of GenPept), SPupdate (the weekly updates of SWISS-PROT) and PDB sequences. Similarly, INSD (International Nucleotide Sequence Database) is another composite database, which is collection of nucleic acid sequences from EMBL, GenBank and DDBJ. The UniProt (universal protein sequence database) which is also a composite database which contains sequences derived from various other databases such as PIRPSD, Swiss-Prot, and TrEMBL. In the same way, wwPDB (worldwide PDB) is a composite database of 3D structures which is maintained by RCSB (Research Collaboratory for Structural Bioinformatics), PDB, MSD and PDBj [30].

2.4 Specialized Databases

The Rfam database contains secondary structure of RNA molecules and their gene expression pattern. This database is introduced by the Wellcome Trust Sanger

Institute and it is similar to the Pfam database for annotating protein families [31]. There are numerous curated databases which are accessible worldwide such as IntAct contains data of various protein interactions. MINT (Molecular INTeraction database) is another curated database which is merged with IntAct database maintained by EMBL-EBI [32]. MINT is basically a database that stores information about protein-protein interactions derived from published articles [33]. For the metabolic pathway analysis in human, Reactome is one of the freely available databases which provide the diverse information regarding metabolic pathway and signal transduction pathways in human [34].

The Transporters Classification Database (TCDB) is a database of membrane transporters [35] which is based on Transport Classification (TC) system for the classification of protein similar to that of Enzyme Commission [36]. Similarly, the Carbohydrate-Active enzyme Database (CAZy) is a database of carbohydrate modifying enzymes and relevant information related to them. These enzymes are classified into different families which are based on the amino acid similarities or the presence of various catalytic domains [37].

Xenbase is a specialized database which contains genomic and biological informations about frogs [38], whereas the Saccharomyces Genome Database (SGD) provides complete information about yeast (*Saccharomyces cerevisiae*) which also offers web based bioinformatics tools to analyse the data available in SGD [39]. The SGD may be used to study functional interactions among gene sequence and gene products in other fungi including eukaryotes. Likewise, WormBase is a specialized database which is developed and maintained by an international consortium to make available precise, recent data related to the molecular biology of *C. elegans* and other associated nematodes. Wormbase also provides some web based tools for analysis of the stored information. Another up-to-date database is "FlyBase" devoted to provide information on the genes and genomes of *Drosophila melanogaster* along with various web based bioinformatics tools to search gene sequences, alleles, different phenotypes as well as images of the *Drosophila* species [40]. Similarly, wFleaBase provides information on genes and genomes for species of the genus *Daphnia* (water flea). *Daphnia* is considered as a model organism to study and understand the complex interplay between genome structures, gene expression and population level responses to chemicals and environmental changes. Although, wFleaBase contains data for all *Daphnia* species but the primary species are *D. pulex* and *D. magna*.

MetaCyc is a curated database of metabolic pathways which were taken from published literatures from all domains of life. It contains 2260 pathways from 2600 different organisms. MetaCyc contains pathways which are involved in both primary and secondary metabolism. It also includes their reactions, enzymes and associated genes [41]. PANTHER (Protein ANalysis THrough Evolutionary Relationships) is another metabolic pathway which consists of over 177 primarily signaling pathways. It contains different pathway components where component is basically a single protein/group of proteins in a given organism [42]. Pathway diagrams are interactive which also includes bioinformatics tools for visualizing gene expression data. KEGG (Kyoto Encyclopedia of Genes and Genomes) is a database of many

databases which was developed and maintained by Bioinformatics Center of Kyoto University and the Human Genome Center of the University of Tokyo [43]. KEGG covers metabolic pathways in yeast, mouse and human etc. KEGG has expanded these days by the addition of signaling pathways for cell cycles and apoptosis. Reactome is a collection of metabolic and signaling pathways and their reactions [34]. Theses pathways and reactions can be viewed but not edited through a web browser. Although humans are the main organism catalogued, but this database also contains data for 22 other species such as mouse and rat.

TreeBASE is a collection of phylogenetic trees and the data associated to construct them. TreeBASE accepts all types of phylogenetic data for species tree as well as gene tree from all domains of life [44]. PhylomeDB [45] is another public database of phylogenetic information based on genes which allows users to explore evolutionary history of genes. Moreover, phylomeDB provides automated pipeline used to reconstruct trees of different genomes based on phylogenetic trees. Table 1 illustrates a list of genomic, protein sequences and specialized databases.

Table 1 List of gene and protein based databases, their description along with their webpage's URL

Databases	Description	Web link
Nucleotide databases		
DDBJ [14]	It is the member of International Nucleotide Sequence Databases (INSD) and is one of the biggest resources for nucleotide sequences	http://www.ddbj.nig.ac.jp/
European Nucleotide Archive	It captures and presents information relating to experimental workflows that are based around nucleotide sequencing	http://www.ebi.ac.uk/ena
GenBank [29]	It is the member of International Nucleotide Sequence Databases (INSD) and is a nucleotide sequence resource	http://www.ncbi.nlm.nih.gov/genbank/
Rfam [31]	A collection of RNA families, represented by multiple sequence alignments	http://rfam.xfam.org/
Protein databases		
InterPro [46]	Describes the protein families, conserved domains and actives sites	http://www.ebi.ac.uk/interpro/
Pfam [19]	Collection of protein families	http://pfam.xfam.org/
Prosite [23]	Provides information on protein families, conserved domains and actives sites of the proteins	http://prosite.expasy.org/
Protein Data Bank 2000 [15]	This is the most popular database of experimentally-determined structures of nucleic acids, proteins, and other complex assemblies	http://www.rcsb.org/pdb/home/home.do
Proteomics Identifications Database [47]	A public source, contain supporting evidence for post-translation modification and functional characterization of proteins and peptides	http://www.ebi.ac.uk/pride/archive/

(continued)

Table 1 (continued)

Databases	Description	Web link
SWISS-PROT [7]	A section of the UniProt Knowledgebase containing the manually annotated protein sequences	www.ebi.ac.uk/swissprot/
Uniprot [8–10]	One of the largest collection of protein sequences which contains curated as well as automated generated entries about protein sequences	http://www.uniprot.org/
PIR [11]	An integrated public resource to support genomic and proteomic research	http://pir.georgetown.edu/
Specialized databases		
Ensembl [48]	It is a database containing annotated genomes of eukaryotes, including human, mouse and other vertebrates	http://www.ensembl.org/index.html
DictyBase [49]	DictyBase is an online bioinformatics database for *Dictyostelium discoideum*	http://www.dictybase.org/
Medherb [50]	An important resource database for medicinally important herbs	https://www.medherbs.de/site/
TAIR [51]	The Arabidopsis Information Resource (TAIR) maintains a database of genetic and molecular data for the model plant Arabidopsis thaliana. This database also provides information on gene structure, gene product, gene expression, genome maps, genetic and physical markers	http://www.arabidopsis.org/
TextPresso [52]	This database provides full text literature searches of model organism research which helps database curators to identify and extract biological entities which include new allele and gene names and human disease gene orthologs	http://www.textpresso.org/
Reactome [34]	A peer-reviewed resource of human biological processes i.e. metabolic pathways	http://www.reactome.org/
CMAP [53]	Complement Map Database is a novel and easily accessible research tool to assist the complement community and scientists. This database explores the complement network and discovers new connections	http://www.complement.us/labweb/cmap/
HMDB [54]	The Human Metabolome Database (HMDB) is the most comprehensive curated collection of human metabolite and human metabolism data in the world	http://www.hmdb.ca/
KEGG [43]	KEGG is a suite of databases and associated software for understanding and simulating higher-order functional behaviours of the cell or the organism from its genome information	http://www.genome.jp/kegg/

(continued)

Table 1 (continued)

Databases	Description	Web link
PID [55]	The Pathway Interaction Database (PID) is a collection of curated and peer-reviewed pathways. It is mainly composed of human molecular signaling and regulatory events and key cellular processes related to cancer	http://pid.nci.nih.gov/
SGMP [56]	The Signaling Gateway Molecule Pages (SGMP) database which provides highly structured data on proteins. It also identifies different functional states of the proteins which participate in signal transduction pathways	www.signaling-gateway.org/molecule

2.5 Drawbacks of Biological Databases

Many times life sciences researchers are interested not only in a few entries of a database but in huge amount of entries or large amount of data, which needs to be processed further, searching through web interfaces are not good options. To support large amount of data, the collection of relevant data and its processing must be automated. Therefore, each database should have programming options which make bioinformatics software developers to query and search databases from their own programs [57]. Modern database management systems such as ODBC (Open Database Connectivity) and JDBC (Java Database Connectivity) provide these web interfaces for bioinformatics programmers to query, search and analyze data. But the major limitation is that database providers allow public access only sometimes to these interfaces. These databases are DDBJ (DNA Data Bank of Japan) and KEGG (Kyoto Encyclopedia of Genes and Genomes). Apart from lacking in providing the programming interfaces, present biological databases also contain other limitations/drawbacks such as description of the database contents and authenticity of data produced and data sources. One of the drawbacks associated with these web interfaces is that these interfaces don't allow to be searched by using all fields in a database. These search modes such as 'and', 'or' and 'not' are not supported at all. Mostly theses modes are supported only in a limited way. Hence desired results for the query are not obtained. It is observed that in primary nucleotide and sequence databases, redundancy of many nucleotide and protein sequences are present, which should be removed. Biologists are usually not familiar with the principles of database design languages. Biologists are mostly ignorant about database query languages also and they should have knowledge of the database schema. In biological databases, in most of the cases flat files are used for data exchange which does not have standardized format. There are many formats for thousands of

biological databases which create problem in biological data preprocessing. Many types of information are often missing in biological databases which include functional annotations of genes and proteins. Many biological databases also provide missing information in terms of genotype phenotype relationships along with detailed pathway information and their reactions.

3 Gene Identification and Sequence Analyses

Due to lack of genome annotation and high-throughput experimental approaches computational gene prediction has become challenging and interesting area for bioinformatics/computational biology scientists. Gene prediction is very crucial especially for disease identification in human. Computational gene prediction can be categorized into two major classes which are ab initio methods and similarity/homology based methods [58]. These types of analyses are mainly useful for gene expression analysis. Gene expression is directly or indirectly related to the identification of promoter, terminator and untranslated regions. These regions are involved in the expression regulations, recognition of a transit peptide, introns/exons as well as an open reading frame (ORF). These regions are also involved in identification of variable regions which are used as signatures for various diagnostic purposes. Therefore, sequence analyses are one of the commonly used analyses for gene prediction in bioinformatics.

Gene prediction is relatively more difficult in eukaryotes as compared to prokaryotes due to presence of introns. Homology based gene predictions depend on complementary DNA (cDNA) and Expressed Sequence Tags (ESTs), though, the cDNA/ESTs information is often unusual and incomplete, and thus makes the task of finding novel genes extremely difficult. Homology based on sequence based information has been shown to be useful for better identification of prokaryotic and eukaryotic genes with higher accuracy. Local and global sequence alignments are performed by BLAST and NEEDLE respectively which is widely used in homology/similarity based gene prediction. These days protein homology has been introduced in many gene prediction programmes such as GENEWISE [59] and GENOMESCAN [60] GeneParser [61] and GRAIL [62]. Novel gene finding is often possible by ab initio gene identification. Examples of ab initio programs are GENSCAN [63], GENIE [64], HMMGene [65] and GENEID [66]. These methods were used in *Drosophila melanogaster* where it showed a very low rate of false-positive. These methods also predict 88 % of exons (already verified) and 90 % of the coding sequences [67]. Due to high accuracy, this methodology could be used for annotating large genomic sequences and prediction of new genes.

Recently, Lencz et al. identified an intergenic single nucleotide polymorphism (SNP; rs11098403) at chromosome 4q26 which was linked with schizophrenia and bipolar disorder. They performed a genome wide association study (GWAS) which was coupled with cDNA as well as RNA Seq on a set of 23,191 individuals [68]. Similarly, Peng and co-workers predicted 31,987 genes from *Phyllostachys heterocycle* draft genome by gene prediction approaches based on FgeneSH ++ [69]. Sequence analyses refer to the understanding of various features of biomolecules like nucleic acids and proteins, which are responsible for providing unique function(s). The first step is retrieval of sequences from public databases which are subjected to analysis by various tools which help in the prediction of specific features which might be associated to their function, structure, evolutionary relationship or identification of homologs with high accuracy. The database should be selected depending upon the nature of analysis. For example, Entrez of PubMed [70] allows one to search about different patterns in the given data. Also, pattern discovery can be performed by Expression Profiler [71], GeneQ [72] which allow scientists to search out different patterns in the given data. A different set of databases are dedicated to carry out sequence comparison like BLAST (Basic Local Alignment Search Tool) [27], ClustalW [73], for data visualization Jalview [74], GeneView [75], TreeView [76] and Genes-Graphs [77] allowing researchers to visualize data in graphic representation. Table 2 illustrates a list of databases used in primary sequence analyses.

4 Phylogenetic Analyses

Phylogenetic analysis help to determine the evolutionary relationship among a group of related organism or related genes and proteins [83, 84], to predict the specific feature of a molecule with unknown functions, to track the gene flow and also to determine genetic relatedness [85]. Phylogenetic analysis is mainly based similarity at sequence level i.e. higher is the similarity; the closer will be the organisms on a tree. Phylogenetic tree is constructed by various methods which are distance, parsimony and maximum likelihood methods. None of the methods is perfect; each one has its own strengths and weaknesses. For example, the distance based methods performs average whereas the maximum parsimony and maximum likelihood methods are accurate. The major disadvantage of maximum parsimony and maximum likelihood methods is these methods takes more time to run as compared to distance based methods [86]. Among the distance-matrix methods Neighbour Joining (NJ) or Unweighted Pair Group Method with Arithmetic mean (UPGMA) are the simplest. Table 2 illustrates a list of phylogenetic analyses programmes. (Table 3).

Table 2 List of gene identification and sequence analyses programmes and their description along with their webpage's URL

Software tools	Description	Web link
BLAST [27]	Used for database sequence searching for protein and DNA homologs	http://blast.ncbi.nlm.nih.gov/Blast.cgi
Clustal Omega [78]	Used for Multiple sequence alignments of DNA and protein sequences	http://www.ebi.ac.uk/Tools/msa/clustalo/
Genscan [63]	Used to predict the exon-intron sites in genomic sequences	http://genes.mit.edu/GENSCAN.html
HMMER [79]	A tool which is used for homologous protein sequence search	http://hmmer.janelia.org/
JIGSAW [80]	Used for identification of gene and their splice site prediction in the selected DNA sequences	http://cbcb.umd.edu/software/jigsaw
novoSNP [81]	Used to find the single nucleotide variation in the DNA sequence	http://www.molgen.ua.ac.be/bioinfo/novosnp/
ORF Finder	The putative genes may be subjected to this tool to find Open Reading Frame (ORF)	http://www.ncbi.nlm.nih.gov/projects/gorf/
PPP	Prokaryotic promoter prediction tool used to predict the promoter sequences present up-stream in the gene	http://bioinformatics.biol.rug.nl/websoftware/ppp/ppp_start.php
ProtParam [82]	Used to predict the physico-chemical properties of proteins	http://web.expasy.org/protparam/
Sequerome	The tool which is mainly used for sequence profiling	www.bioinformatics.org/sequerome/
Softberry Tools	Several tools are specialized in annotation of animal, plant, and bacterial genomes along with the structure and function prediction of RNA and proteins	http://www.softberry.com/
Virtual Foorprint	Whole prokaryotic genome (with one regular pattern) may be analyzed using this program along with promoter regions with several regulator patterns	http://www.prodoric.de/vfp/
WebGeSTer	The database which is composed of sequences of transcription terminator sequences and is used to predict the termination sites of the genes during transcription	http://pallab.serc.iisc.ernet.in/gester/dbsearch.php

In functional genomics where a function of a particular gene is not known phylogenetic analysis is used to find their relative genes which ultimately help to the identification their function and other features of that particular gene.

Table 3 List of phylogenetic analyses programmes and their description along with their webpage's URL

Software tools	Description	Web link
JStree	An open-source library for viewing and editing phylogenetic trees for presentation improvement	www.jstree.com/
MEGA [87]	A tool to construct phylogenetic trees to by parsimony, distance based and maximum likehood based tree construction and to study the evolutionary relationships	http://www.megasoftware.net/
MOLPHY	Phylogenetic analysis tool based on maximum likelihood method	http://www.ism.ac.jp/ismlib/softother.e.html
PAML	A phylogenetic analysis tool based on maximum likelihood	http://abacus.gene.ucl.ac.uk/software/paml.html
PHYLIP	A complete software package for phylogenetic tree generation for DNA and protein sequences	http://evolution.genetics.washington.edu/phylip.html
TreeView [76]	It is a tool for visualisation of the phylogenetic trees	http://taxonomy.zoology.gla.ac.uk/rod/treeview.html

5 Predicting Protein Structure and Function

Protein molecules initiate their life as amorphous amino acid strings, which finally fold up into a three-dimensional (3D) structure. The folding of the protein into a correct topology is needed for proteins to perform its biological functions. Usually, 3D structures are mostly determined by X-ray crystallography and NMR which are costly, difficult and time taking. X ray crystallography method fails if we do not get good crystals. Moreover NMR is limited to small proteins [88]. There are very few structures submitted monthly using NMR and XRD in NCBI. Correct prediction of secondary and tertiary structure of proteins is one of the challenging tasks for bioinformatics/computational biologist till date. Predicting the correct secondary structure is the key to predict not only a good/satisfactory tertiary structure of the protein but also helps in prediction of protein function [88]. Protein structure prediction is classified into three categories: (i) Ab initio modeling [89] (ii) Threading or Fold recognition [90] and (iii) Homology or Comparative modeling (Šali and Blundell 1993 [91]. Threading and comparative modeling build protein models by aligning query sequences with known structures which are determined by X-ray crystallography or NMR. When templates having identity ≥ 30 % are found, high resolution models could be built by the template-based methods. If templates are not available from the protein data bank (PDB), these models are built from scratch, i.e. ab initio modeling [92]. Homology modeling is the most accurate prediction method so far and it is used frequently. In one of our studies good quality homology models of superoxide dismutase (SOD) has been obtained by Modeller software package in antarctic cyanobacterium *Nostoc*

Table 4 List of protein structure and function predictions programmes their description along with their webpage's URL

Software tools	Description	Web link
RaptorX [94]	It facilitates the user to predict protein structure based on either a single- or multi-template threading	http://raptorx.uchicago.edu/
JPRED [95]	Used to predict secondary structures of proteins	http://www.compbio.dundee.ac.uk/www-jpred/
HMMSTR [96]	A hidden Markov model for the prediction of sequence-structure correlations in proteins	http://www.bioinfo.rpi.edu/bystrc/hmmstr/server.php
APSSP2 [97]	Predicts the secondary structure of proteins	http://omictools.com/apssp2-s7458.html
MODELLER [98]	Predicts 3D structure of protein based on comparative modelling	https://salilab.org/modeller/
Phyre and Phyre2 [99]	Web-based servers for protein structure prediction by threading algorithm	http://www.sbg.bio.ic.ac.uk/phyre2/html/page.cgi?id=index

commune which aids to cope with environmental stresses prevailing at its natural habitat [93]. Bioinformatics tools can also identify secondary structure elements such as helices, sheets and coils. Protein tertiary structures are stabilized by the presence of helices, sheets and coils which play an important role in establishing weaker electrostatic forces. Table 4 illustrates a list of tools to predict the secondary structure of protein molecules.

6 Predicting Molecular Interactions

Biomolecules interacting with each other affect various biological activities which has nowadays become one of the popular areas for research [100]. For example, protein-protein interaction, protein-DNA or protein-RNA interaction etc. Protein-protein interactions play an essential role in various cellular activities like signalling and transportation. Protein-protein interactions also play major role in homeostasis, cellular metabolism etc. [101]. In this regard, bioinformatics helps to predict the 3D structure of proteins and also helps in predicting the interaction pattern between different biomolecules. These predictions are based on various parameters such as interface size, amino acid position, types of chemical groups involved. These predictions are also based on vander wall forces, electrostatic interaction and hydrogen bonds. Table 5 illustrates a list of tools to study protein-protein interactions.

Table 5 List of molecular interactions database and programmes, their description along with their webpage's URL

Software tools	Description	Web link
SMART [102]	A Simple Modular Architecture Retrieval Tool; describes multiple information about the protein query	http://smart.embl-heidelberg.de/
AutoDock [103]	Predicts protein-ligand interaction and is considered as reliable tool	http://autodock.scripps.edu/
HADDOCK [104]	Describes the modelling and interaction of bio-molecular complexes such as protein-protein, protein-DNA	http://haddock.science.uu.nl/
STRING [105]	A database of both known and predicted protein interactions	http://string-db.org/
IntAct [32]	It is an open source database system which is used for molecular interaction data	http://www.ebi.ac.uk/intact/
Graemlin [106]	It is capable of scalable multiple network alignment with its functional evolution model that allows both the generalization of existing alignment scoring schemes. This tool also model the location of conserved network topologies other than protein complexes and metabolic pathways	http://graemlin.stanford.edu/
PathBLAST [107]	This tool is to search protein-protein interaction network of the any selected organism and extracts all interaction pathways that align with the query	http://www.pathblast.org/
CFinder [108]	This tool is capable of finding and visualizing the overlapping dense groups of nodes in networks, and quantitative description of the evolution of social groups	http://www.cfinder.org/

7 Discussion, Conclusion and Future Prospects

Bioinformatics has emerged as a challenging discipline which has developed very fast in the last few years due to generation of large amount of data generated by various genome sequencing projects. Such a large amount of data needs pre-processing to extract useful knowledge/information by data mining techniques. These processed data are not only stored but also retrieved in a meaningful manner from biological databases. These biological databases containing nucleotide and protein sequences are called primary databases. These primary databases have a drawback that these databases contain redundant sequences. Secondary database has solved this issue to a greater extent which contain derived information from primary databases and redundancy is also minimized at lowest in Swiss-Prot database. Composite databases e.g. NCBI provides better search criteria to search multiple primary resources at a time. NCBI also provides the linking with literature, structure, chemical molecules, genome information, gene and protein sequences databases. Apart from these databases, various specialized databases are also available these days which provide informations about protein-protein interactions,

protein families, experimentally known metabolic pathways, genome sequence, protein structure and phylogenetic tree for evolutionary relationship. These databases also have few drawbacks e.g. lack of description of data contained, redundancy of sequences etc. One of the major drawbacks of most of the databases is that they don't provide the programming interface so that researchers can write their programmes to download and process huge amount of stored data from the database. Bioinformatics is not only used in designing the biological databases but also used in developing software tools for sequence, structure and evolutionary analysis of genes/proteins etc. which save our time, energy and cost in biological research. A number of bioinformatics softwares were designed to predict the correct genes in genomic sequences which use various machine learning approaches like artificial intelligence, genetic algorithm, support vector machine, hidden markov model, dynamic programming etc. However, the best predictors are based on hybrid methods which use more than one machine learning approaches to predict the correct genes. Bioinformatics tools were also developed to construct parsimony, distance based and maximum likelihood based trees to explore the evolutionary relationship among species. Parsimony method is successful when sequence identity is high while maximum likelihood performs well when sequence variation is high. Bioinformatics have proved to be a boon in structure based drug design by predicting the structure of drug targets immaterial of whether template structure are available in PDB or not by different approaches. Homology modelling proved the best predictor among all the methods. Moreover, bioinformatics tools also predict protein-protein interactions which play an essential role in various cellular activities like signalling, transportation, homeostasis, cellular metabolism and also various biochemical processes. It can also be expected, based on the developments in the field of bioinformatics, that the bioinformatics tools and software packages would be able to give more specific, more accurate and more reliable in upcoming years. In future the field of bioinformatics will contribute in functional understanding of whole genome of organisms which will lead to enhanced discovery of gene expression, their interaction pattern, individualised gene therapy and new drug discovery. Thus, bioinformatics and other scientific disciplines should move together in order to flourish for the welfare of humanity.

References

1. Hogeweg, P.: The roots of bioinformatics in theoretical biology. PLoS Comput. Biol. **7**, e1002021 (2011)
2. Neufeld, L., Cornog, M.: Database history: from dinosaurs to compact discs. J Am. Soc. Inf. Sci. **37**, 183–190 (1999)
3. Chen, M.-S., Han, J., Yu, P.S.: Data mining: an overview from a database perspective. IEEE Trans. Knowl. Data Eng. **8**(6), 866–883 (1996)
4. Fayyad, U.M., Piatetsky-Shapiro, G., Smyth, P., et al. (eds.): Advance in Knowledge Discovery and Data Mining. AAAI/MIT Press, Menlo Park, Cambridge (1996)

5. Ouzounis, C.A., Valencia, A.: Early bioinformatics: the birth of a discipline-a personal view. Bioinformatics **19**, 2176–2190 (2003)
6. Hassanie, A.E.: Classification and feature selection of breast cancer data based on decision tree algorithm. Stud. Inform. Control **12**(1), 33–40
7. Boeckmann, B., Bairoch, A., Apweiler, R., et al.: The SWISS-PROT protein knowledge base and its supplement TrEMBL in 2003. Nucleic Acids Res. **31**, 365–370 (2003)
8. UniProt Consortium: The universal protein resource (UniProt). Nucleic Acids Res. **36**, D190–D195 (2008)
9. UniProt Consortium: The universal protein resource (UniProt) in 2010. Nucleic Acids Res. **38**, D142–D148 (2010)
10. UniProt Consortium: Activities at the universal protein resource (UniProt). Nucleic Acids Res. **42**, D191–D198 (2014)
11. Wu, C.H., Yeh, L.S., Huang, H., et al.: The protein information resource. Nucleic Acids Res. **31**(1), 345–347 (2003)
12. Benson, D.A., Karsch-Mizrachi, I., Lipman, D.J., et al.: GenBank. Nucleic Acids Res. **36**, D25–D30 (2008)
13. Kanz, C., Aldebert, P., Althorpe, N., et al.: The EMBL nucleotide sequence database. Nucleic Acids Res. **33**, D29–D33 (2005)
14. Miyazaki, S., Sugawara, H., Gojobori, T., et al.: DNA data bank of Japan (DDBJ) in xml. Nucleic Acids Res. **31**, 13–16 (2003)
15. Berman, H.M., Westbrook, J., Feng, Z., et al.: The protein data bank. Nucleic Acids Res. **28**, 235–242 (2000)
16. Berman, H., Henrick, K., Nakamura, H.: Announcing the worldwide protein data bank. Nat. Struct. Mol. Biol. **10**, 980 (2003)
17. Barker, W.C., Garavelli, J.S., Huang, H., et al.: The protein information resource (PIR). Nucleic Acids Res. **28**, 41–44 (2000)
18. Barker, W.C., Garavelli, J.S., Haft, D.H., et al.: The PIR-international protein sequence database. Nucleic Acids Res. **26**(1), 27–32 (1998)
19. Finn, R.D., Bateman, A., Clements, J., et al.: Pfam: the protein families database. Nucleic Acids Res. **42**, D222–D230 (2014)
20. Gonzalez, S., Binato, R., Guida, L., et al.: Conserved transcription factor binding sites suggest an activator basal promoter and a distal inhibitor in the galanin gene promoter in mouse ES cells. Gene **538**, 228–234 (2014)
21. Murzin, A.G., Brenner, S.E., Hubbard, T., et al.: Scop: a structural classification of proteins database for the investigation of sequences and structures. J. Mol. Biol. **247**, 536–540 (1995)
22. Pearl, F., Todd, A., Sillitoe, I., et al.: The CATH domain structure database and related resources Gene3D and DHS provide comprehensive domain family information for genome analysis. Nucleic Acids Res. **33**, D247–D251 (2005)
23. Sigrist, C.J., de Castro, E., Cerutti, L., et al.: New and continuing developments at PROSITE. Nucleic Acids Res. **41**, D344–D347 (2013)
24. Attwood, T.K., Beck, M.E., Flower, D.R., et al.: The PRINTS protein fingerprint database in its fifth year. Nucleic Acids Res. **26**(1), 304–308 (1998)
25. Huang, J.Y., Brutlag, D.L.: The EMOTIF database. Nucleic Acids Res. **29**, 202–204 (2001)
26. Orengo, C.A., Michie, A.D., Jones, S., et al.: CATH—a hierarchic classification of protein domain structures. Structure **5**(8), 1093–1108 (1997)
27. Altschul, S.F., Madden, T.L., Schäffer, A.A., et al.: Gapped BLAST and PSI-BLAST: a new generation of protein database search programs. Nucleic Acids Res. **25**, 3389–3402 (1997)
28. Gibrat, J.F., Madej, T., Bryant, S.H.: Surprising similarities in structure comparison. Curr. Opin. Struct. Biol. **6**, 377–385 (1996)
29. Benson, D.A., Karsch-Mizrachi, I., Clark, K., et al.: GenBank. Nucleic Acids Res. **40**, D48–D53 (2012)
30. Kinjo, A.R., Suzuki, H., Yamashita, R., et al.: Protein data bank Japan (PDBj): maintaining a structural data archive and resource description framework format. Nucleic Acids Res. **40**, D453–D460 (2012)

31. Burge, S.W., Daub, J., Eberhardt, R., et al.: Rfam 11.0: 10 years of RNA famlies. Nucleic Acids Res. **4**, D226–D232 (2013)
32. Orchard, S., Ammari, M., Aranda, B., et al.: The MIntAct project–IntAct as a common curation platform for 11 molecular interaction databases. Nucleic Acids Res. **42**, D358–D363 (2014)
33. Zanzoni, A., Montecchi-Palazzi, L., Quondam, M., et al.: MINT: a molecular INTeraction database. FEBS Lett. **513**, 135–140 (2002)
34. Joshi-Tope, G., Gillespie, M., Vastrik, I., et al.: Reactome: a knowledgebase of biological pathways. Nucleic Acids Res. **33**, D428–D432 (2005)
35. Saier Jr, M.H., Tran, C.V., Barabote, R.D.: TCDB: the transporter classification database for membrane transport protein analyses and information. Nucleic Acids Res. **34**, D181–D186 (2006)
36. Saier Jr, M.H., Reddy, V.S., Tamang, D.G., et al.: The transporter classification database. Nucleic Acids Res. **42**, D251–D258 (2014)
37. Lombard, V., Golaconda, H., Drula, R.E., et al.: The carbohydrate-active enzymes database (CAZy) in 2013. Nucleic Acids Res. **42**(D1), D490–D495 (2014)
38. Bowes, J.B., Snyder, K.A., Segerdell, E., et al.: Xenbase: gene expression and improved integration. Nucleic Acids Res. **38**, D607–D612 (2010)
39. Cherry, J.M., Hong, E.L., Amundsen, C., et al.: Saccharomyces genome database: the genomics resource of budding yeast. Nucleic Acids Res. **40**(D): D700–705 (2012)
40. St. Pierre, S.E., Ponting, L., Stefancsik, R., et al.: FlyBase 102–advanced approaches to interrogating FlyBase. Nucleic Acids Res. **42**: D780–788 (2014)
41. Caspi, R., Altman, T., Billington, R.: The MetaCyc database of metabolic pathways and enzymes and the BioCyc collection of pathway/genome databases. Nucleic Acids Res. **42**, D459–D471 (2014)
42. Thomas, P.D., Campbell, M.J., Kejariwal, A., et al.: PANTHER: a library of protein families and subfamilies indexed by function. Genome Res. **13**(9), 2129–2141 (2003)
43. Kanehisa, M.: The KEGG database. Silico Simul. Biological Process. **247**, 91–103 (2002)
44. Morell, V.: TreeBASE: the roots of phylogeny. Science **273**, 569 (1996)
45. Huerta-Cepas, J., Capella-Gutiérrez, S., Pryszcz, L.P., et al.: PhylomeDB v4: zooming into the plurality of evolutionary histories of a genome. Nucleic Acids Res. **42**, D897–D902 (2014)
46. Mitchell, A., Chang, H.-Y., Daugherty, L., et al.: InterPro protein families database: the classification resource after 15 years. Nucleic Acids Res. **43**, D213–D221 (2015)
47. Martens, L., Hermjakob, H., Jones, P., et al.: PRIDE: the proteomics identifications database. Proteomics **5**, 3537–3545 (2005)
48. Flicek, P., Amode, M.R., Barrell, D., et al.: Ensembl Nucleic Acids Res. **40**, D84–D90 (2012)
49. Gaudet, P., Fey, P., Basu, S., et al.: dictyBase update 2011: web 2.0 functionality and the initial steps towards a genome portal for the Amoebozoa. Nucleic Acids Res. **39**, D620–D624 (2011)
50. Rajoka, M.I., Idrees, S., Khalid, S., et al.: Medherb: an interactive bioinformatics database and analysis resource for medicinally important herbs. Curr. Bioinformatics **9**, 23–27 (2014)
51. Lamesch, P., Berardini, T.Z., Li, D., et al.: The arabidopsis information resource (TAIR): improved gene annotation and new tools. Nucleic Acids Res. **2011**, 1–9 (2011)
52. Muller, H.M., Kenny, E.E., Sternberg, P.W.: Textpresso: an ontology-based information retrieval and extraction system for biological literature. PLoS Biol. **2**(11), e309 (2004)
53. Yang, K., Dinasarapu, A.R., Reis, E.S., et al.: CMAP: complement map database. Bioinformatics **29**(14), 1832–1833 (2013)
54. Wishart, D.S., Tzur, D., Knox, C., et al.: HMDB: the human metabolome database. Nucleic Acids Res. **35**, D521–D526 (2007)
55. Schaefer, C.F., Anthony, K., Krupa, S., et al.: PID: the pathway interaction database. Nucleic Acids Res. **37**, D674–D679 (2009)

56. Dinasarapu, A.R., Saunders, B., Ozerlat, I., et al.: Signaling gateway molecule pages–a data model perspective. Bioinformatics **27**(12), 1736–1738 (2011)
57. Philippi, S., Köhler, J.: Addressing the problems with life-science databases for traditional uses and systems biology. Nat. Rev. Genet. **7**(6), 482–488 (2000)
58. Lewis, S., Ashburner, M., Reese, M.G.: Annotating eukaryote genomes. Curr. Opin. Struct. Biol. **10**, 349–354 (2000)
59. Birney, E., Durbin, R.: Using GeneWise in the Drosophila annotation experiment. Genome Res. **10**, 547–548 (2000)
60. Yeh, R.-F., Lim, L.P., Burge, C.B.: Computational inference of homologous gene structures in the human genome. Genome Res. **11**, 803–816 (2001)
61. Snyder, E.E., Stormo, G.D.: Identification of protein coding regions in genomic DNA. J. Mol. Biol. **248**, 1–18 (1995)
62. Uberbacher, E.C., Mural, R.J.: Locating protein-coding regions in human DNA sequences by a multiple sensor-neural network approach. Proc. Natl. Acad. Sci. USA **88**, 11261–11265 (1991)
63. Burge, C., Karlin, S.: Prediction of complete gene structures in human genomic DNA. J. Mol. Biol. **268**, 78–94 (1997)
64. Kulp, D., Haussler, D., Reese, M.G., et al.: A generalized hidden Markov model for the recognition of human genes in DNA. In: Proceedings of the International Conference on Intelligent Systems for Molecular Biology, vol. 4, pp. 134–142 (1996)
65. Krogh, A.: Two methods for improving performance of an HMM and their application for gene-finding. In: Proceedings of the International Conference on Intelligent Systems for Molecular Biology (ISMB‘97), vol. 5, pp. 179–186 (1997)
66. Parra, G., Blanco, E., Guig´o, R.: GeneID in Drosophila. Genome Res. **10**, 391–393 (2000)
67. Salamov, A.A., Solovyev, V.V.: Ab initio gene finding in Drosophila genomic DNA. Genome Res. **10**, 516–522 (2000)
68. Lencz, T., Guha, S., Liu, C., Rosenfeld, J., et al.: Genome-wide association study implicates NDST3 in schizophrenia and bipolar disorder. Nat. Commun. **4**, 2739 (2013)
69. Peng, Z., Lu, Y., Li, L., et al.: The draft genome of the fastgrowing non-timber forest species moso bamboo (Phyllostachys heterocycla). Nat. Genet. **45**, 456–461 (2013)
70. Geer, R.C., Sayers, E.W.: Entrez: making use of its power. Brief Bioinform. **4**, 179–184 (2003)
71. Parmigiani, G., Garrett, E.S., Irizarry, R.A., et al.: The analysis of gene expression data: an overview of methods and software. Springer, New York (2003)
72. Hoersch, S., Leroy, C., Brown, N.P., et al.: The GeneQuiz web server: protein functional analysis through the web. Trends Biochem. Sci. **25**, 33–35 (2000)
73. Thompson, J.D., Higgins, D.G., Gibson, T.J.: CLUSTAL W: improving the sensitivity of progressive multiple sequence alignment through sequence weighting, position-specific gap penalties and weight matrix choice. Nucleic Acids Res. **22**, 4673–4680 (1994)
74. Waterhouse, A.M., Procter, J.B., Martin, D.M.A., et al.: Jalview version 2-a multiple sequence alignment editor and analysis workbench. Bioinformatics **25**, 1189–1191 (2009)
75. Thomas, P., Starlinger, J., Vowinkel, A., Arzt, S., Leser, U.: GeneView: a comprehensive semantic search engine for PubMed. Nucleic Acids Res. **40**, W585–W591 (2012)
76. Page, R.D.M.: TREEVIEW: An application to display phylogenetic trees on personal computers. Comput. Appl. Biosci. **12**, 357–358 (1996)
77. Zhang, Y., Phillips, C.A., Rogers, G.L., et al.: On finding bicliques in bipartite graphs: a novel algorithm and its application to the integration of diverse biological data types. BMC Bioinformatics **15**, 110 (2014)
78. Sievers, F., Wilm, A., Dineen, D.G., et al.: Fast, scalable generation of high-quality protein multiple sequence alignments using Clustal Omega. Mol. Syst. Biol. **7**, 539 (2011)
79. Finn, R.D., Clements, J., Eddy, S.R.: HMMER web server: interactive sequence similarity searching. Nucleic Acids Res. **39**, W29–W37 (2011)
80. Allen, J.E., Salzberg, S.L.: JIGSAW: integration of multiple sources of evidence for gene prediction. Bioinformatics **21**(18), 3596–3603 (2005)

81. Weckx, S., Del-Favero, J., Rademakers, R.: novoSNP, a novel computational tool for sequence variation discovery. Genome Res. **15**(3), 436–442 (2005)
82. Gasteiger, E., Hoogland, C., Gattiker, A., et al.: Protein identification and analysis tools on the expasy server. In: Walker, J.M. (ed.) The Proteomics Protocols Handbook. Humana Press, p 571–607 (2005)
83. Kanchan, S., Mehrotra, R., Chowdhury, S.: Evolutionary pattern of four representative DNA repair proteins across six model organisms: an in silico analysis. Netw. Model Anal. Health Inf. Bioinform **3**, 70 (2014)
84. Kanchan, S., Mehrotra, R., Chowdhury, S.: In Silico analysis of the Endonuclease III protein family identifies key residues and processes during evolution. J. Mol. Evol. **81**(1–2), 54–67 (2015)
85. Khan, F.A., Phillips, C.D., Baker, R.J.: Timeframes of speciation, reticulation, and hybridization in the bulldog bat explained through phylogenetic analyses of all genetic transmission elements. Syst. Biol. **63**, 96–110 (2014)
86. Price, M.N., Dehal, P.S., Arkin, A.P.: FastTree 2–approximately maximum likelihood trees for large alignments. PLoS ONE **5**, e9490 (2010)
87. Kumar, S., Tamura, K., Nei, M.: MEGA: molecular evolutionary genetics analysis software for microcomputers. Comput. Appl. Biosci. **10**, 189–191 (1994)
88. Huang, T., He, Z.S., Cui, W.R., et al.: A sequence-based approach for predicting protein disordered regions. Protein Pept. Lett. **20**, 243–248 (2013)
89. Liwo, A., Lee, J., Ripoll, D.R., et al.: Protein structure predictionby global optimization of a potential energy function. Proc. Natl. Acad. Sci. USA **96**(10), 5482–5485 (1999)
90. Bowie, J., Luthy, R., Eisenberg, D.: A method to identify protein sequences that fold into a known three-dimensional structure. Science **253**(5016), 164–170 (1991)
91. Šali, A., Blundell, T.L.: Comparative protein modelling by satisfaction of spatial restraints. J. Mol. Biol. **234**(3), 779–815 (1993)
92. Kesheri, M., Kanchan, S., Chowdhury, S., et al.: Secondary and tertiary structure prediction of proteins: a bioinformatic approach. In: Zhu, Q., Azar, A.T. (eds.) Complex System Modelling and Control Through Intelligent Soft Computations, pp. 541–569. Springer International Publishing, Switzerland (2015)
93. Kesheri, M., Kanchan, S., Richa, et al.: Isolation and in silico analysis of Fe-superoxide dismutase in the cyanobacterium Nostoc commune. Gene. **553**(2): 117–125 (2014)
94. Källberg, M., Wang, H., Wang, S., et al.: Template-based protein structure modeling using the RaptorX web server. Nat. Protoc. **7**, 1511–1522 (2012)
95. Cuff, J.A., Clamp, M.E., Siddiqui, A.S., et al.: JPred: a consensus secondary structure prediction server. Bioinformatics **14**, 892–893 (1998)
96. Bystroff, C., Thorsson, V., Baker, D.: HMMSTR: a hidden Markov model for local sequence-structure correlations in proteins. J. Mol. Biol. **301**, 173–190 (2000)
97. Raghava, G.: APSSP2: a combination method for protein secondary structure prediction based on neural network and example based learning. CASP5 A-132 (2002)
98. Eswar, N., Eramian, D., Webb, B., et al.: Protein structure modeling with MODELLER. Methods Mol. Biol. **426**, 145–159 (2008)
99. Kelley, L.A., Sternberg, M.J.: Protein structure prediction on the web: a case study using the Phyre server. Nat. Protoc. **4**, 363–371 (2009)
100. Wang, L., Huang, C., Yang, M.Q., et al.: BindN + for accurate prediction of DNA and RNA-binding residues from protein sequence features. BMC Syst. Biol. **4**(1), S3 (2010)
101. Vinayagam, A., Zirin, J., Roesel, C., et al.: Integrating protein-protein interaction networks with phenotypes reveals signs of interactions. Nat. Methods **11**, 94–99 (2014)
102. Schultz, J., Copley, R.R., Doerks, T., et al.: SMART: A Web-based tool for the study of genetically mobile domains. Nucleic Acids Res. **28**, 231–234 (2000)
103. Morris, G.M., Huey, R., Lindstrom, W., et al.: AutoDock4 and AutoDockTools4: automated docking with selective receptor flexibility. J. Comput. Chem. **30**, 2785–2791 (2009)
104. De Vries, S.J., van Dijk, M., Bonvin, A.M.: The HADDOCK web server for data driven biomolecular docking. Nat. Protoc. **5**, 883–897 (2010)

105. Franceschini, A., Szklarczyk, D., Frankild, S., et al.: STRING v9.1: protein-protein interaction networks, with increased coverage and integration. Nucleic Acids Res. **41**, D808–D815 (2013)
106. Flannick, J., Novak, A., Srinivasan, B.S., et al.: Graemlin: general and robust alignment of multiple large interaction networks. Genome Res. **16**, 1169–1181 (2006)
107. Kelley, B.P., Yuan, B., Lewitter, F., et al.: PathBLAST: a tool for alignment of protein interaction networks. Nucleic Acids Res. **32**, W83–W88 (2004)
108. Adamcsek, B., Palla, G., Farkas, I.J., et al.: CFinder: locating cliques and overlapping modules in biological networks. Bioinformatics **22**, 1021–1023 (2006)
109. Fathy, M.E., Hussein, A.S., Tolba, M.F.: Fundamental matrix estimation: a study of error criteria. Pattern Recogn. Lett. **32**(2), 383–391 (2011)

Statistical Methods for Managing Missing Data: Application to Medical Diagnosis

Souad Guessoum, Hadjer Zaayout, Nabiha Azizi, Nadjet Dendani and Hayet Djellali

Abstract This paper presents a work consisting in realizing a decision support system based on the technique of case-base reasoning and dedicated to the diagnosis of a very dangerous pulmonary pathology: lung cancer. The system is realized for the oncology department of Ibn roch hospital of Annaba (Algeria) and will help young oncologist physicians in their activity by providing them with the experience of experts in the same domain. The principle issue in this work is the missing data in the system memory relating to the patient's state. Indeed, missing values prevent the achievement of the diagnosis process. The problem is treated by proposing two statistical approaches in addition to re-evaluate in this new domain some ones which have been already proposed and evaluated in a previously domain. The validation is made on a base of 40 real cases collected from the archive of oncology department. Cases are collected as paper documents.

Keywords Artificial intelligence · Case-based reasoning technique · Decision support system · Medical diagnosis · Respiratory diseases · Missing data problem · Lung cancer

S. Guessoum (✉) · H. Djellali
LRS Laboratory, Badji Mokhtar University, Annaba, Algeria
e-mail: souadguessoum@yahoo.fr

H. Djellali
e-mail: hayetdjellali@yahoo.fr

H. Zaayout
Informatics Department, Badji Mokhtar University, Annaba, Algeria
e-mail: zaayouthadjer@yahoo.fr

N. Azizi (✉) · N. Dendani (✉)
Labged Laboratory, Badji Mokhtar University, Annaba, Algeria
e-mail: nabiha111@yahoo.fr; azizi@labged.com

N. Dendani
e-mail: ndendani@yahoo.fr

N. Dey et al. (eds.), *Medical Imaging in Clinical Applications*,
Studies in Computational Intelligence 651, DOI 10.1007/978-3-319-33793-7_16

1 Introduction

The lung cancer is a very dangerous disease which represents the cause of 1.3 million deaths a year in the world. Its principal cause is the chronic exposure to tobacco smoke, including passive smoking. The incidence of lung cancer among no-smokers, represents 15 % of cases and is often attributed to a combination of genetic factors and pollution air. According to the World Health Organization, the lung cancer is the most frequent cause of cancer death among men, and after breast cancer among women. The lung cancer is characterized by a set of clinical symptoms. Its diagnosis needs in addition some radiological examinations to search data required for accurate diagnosis. So physicians may ask for different examinations like thoracic scanner, abdominal scanner, endoscopy, MRI (Magnetic Resonance Imaging), and thoracic radiograph. Provide assistance to physicians in the diagnosis of this disease is the aim of the system presented in this paper.

To solve problems of daily life, we naturally use our old experiences, by remembering similar situations already encountered, which are compare with the current situation for building a new solution which in turn, be added to our experience. This human reasoning is often used by physicians during their activity of diagnose and treat patients. Since Artificial Intelligence (AI) is interesting in reproducing human reasoning on machine, there was a technique named Case-Based Reasoning (CBR) which reproduces the human behavior in his recourse to his past experiences to solve his new problems. So, the global idea of CBR is to solve a new problem by finding similar case(s) in a knowledge base and to adapt it (them) to the new situation.

This work is a continuation of a former one presented in [1], which involved the development of a support system dedicated to the medical decision. It was applied to the diagnosis of a dangerous respiratory disease caused by tobacco: Chronic Obstructive Pulmonary Disease (COPD). The system is called RespiDiag and is based on CBR technique principles. As its name suggests, RespiDiag (for Respiratory diseases Diagnosis) is supposed go beyond the diagnosis of COPD for extending to other pathologies of the same field. In this vision, the work is expanded this time to the diagnosis of lung cancer. However, and currently, the implementation of the system is done separately of RespiDiag pending its integration in a future step.

In this work, we are cooperating with specialist physicians of the oncology department in Ibn Rochd hospital of Annaba (Algeria) for giving a decision support system that can help young clinicians in the diagnosis of lung cancer. The system will give help for future oncologist physicians because it gathers experiences of many experts in the domain who are not always available. Some statistical methods are integrated in this system for managing the problem of missing data in its case base.

Knowing that the aim of the work is twofold: first, the realization of the CBR decision support system with the implementation of all phases of CBR cycle, and

secondly, the managing of the problem of missing data that can appear in the case base and/or in the new problem, the paper is organized as follows: Sect. 2 provides an overview on some cbr medical systems that can be found in the literature, while Sect. 3 presents principles and cycle of the CBR technique. Section 4 presents the work methodology and the application field.

The contribution of the paper begins in Sect. 5 that describes all the details on the CBR process with all similarity metrics proposed and used in the system. The same section introduces the problem of missing data, and gives all details on the second contribution of the paper with the proposed approaches for managing the missing data. Experimentations results are presented, compared and evaluated in Sect. 6. The paper is concluded by the last section.

2 Related Works

In the literature, many works focalized on the medical CBR systems can be found. This is motivated mainly by the fact that the case-based reasoning is very similar to clinical reasoning. Indeed, given a patient to diagnose, physician uses his past experiences to look for any resemblance between former patient's symptoms and those of the new patient. Such resemblance (if it exists) can help immensely in the decision about the new patient, in term of making the most precise diagnosis or proposing the most efficient treatment. And it is in this way that the competence of a physician relies heavily on his own experiences. So, CBR systems which modelise very well the reasoning on experiences, can be so helpful to support physicians in their decision about diagnoses/therapies.

Many medical fields of diagnosis or therapy, have benefited of CBR decision support systems. Each of these ones have targeted a specific problem with the CBR process or the considered field.

Among many medical CBR systems we can mention some ones as CASEY [2] dedicated to the diagnosis of heart failure, FM-Ultranet [3] which diagnoses fetal deformations, KASIMIR [4] which provides a treatment for breast cancer, the system developed in [5] for the diagnosis of acute bacterial meningitis and RespiDiag [1] for the diagnosis of COPD.

In the last one, the retrieval phase has been developed in depth and saw the proposal of some similarity metrics for specific attributes to the field of COPD, for which conventional metrics were inappropriate. Another problem has been studied in the same phase, that of the missing data which prevented the completion of its process. The work has seen the proposal and the evaluation of several approaches to manage it. And the present work is a continuation for RespiDiag that would see an enlargement to other respiratory diseases (as its name suggests).

In [6], it can be found a work that compares bayesian inferences and CBR applied to the diagnosis of acute bacterial meningitis. The comparison of results shows that the CBR system diagnosis was more accurate than the bayesian system

one. Results of the CBR system before and after the reuse phase were compared too and conclude that the adaptation step gives more flexibility and more robustness to the system.

3 The Case-Based Reasoning

The main idea of CBR consists of reusing the solution of a former similar problem to solve a new one. All past experiences are gathered in the memory system called "case base", where the case is a couple of descriptors of the problem and its solution. In this technique, the new problem is called "target case" and the former cases which are already solved and saved in the case base are named "source cases". When we develop a CBR system, we don't need to know how the expert thinks for resolving the problem, because the knowledge in such system consists just of establishing a description of a problem and its solution.

CBR cycle is identified by Aamodt and Plaza in [7] as a process of four steps:

- The Retrieval phase: which is the most important phase of the cycle. It consists of calculating the similarity between the current problem and all previous problems gathered in the case base, in order to retrieve one or more most similar case(s). The number of retrieved cases depends on the decision of the constructor of the system. The process of this first phase is mainly based on similarity metrics,
- The Reuse phase: it is the most delicate step; it consists in adapting (if need be) the solution of the most similar source case to the target problem. Its difficulty is mainly due to the strong dependence of the heuristics and knowledge adaptation of the application fields. For this reason, the collaboration of experts is required during all throughout the conception process of these heuristics that are usually in rules form. For certain CBR systems dedicated particularly to the medical diagnosis, this phase is ignored, and the process consists just in finding the most similar diagnosis,
- The Revise phase: during which the adapted solution is presented to the user who will decide on his validity. In the affirmative case the last phase is begun. This step gives then, the possibility to the user of changing the details of proposed solution according his opinion. It will be a new experience for the system.
- The Retain phase: it consists of adding the new problem with its validated solution to the case base. And so the system learns of its new experiences!

Figure 1 gives the CBR cycle.

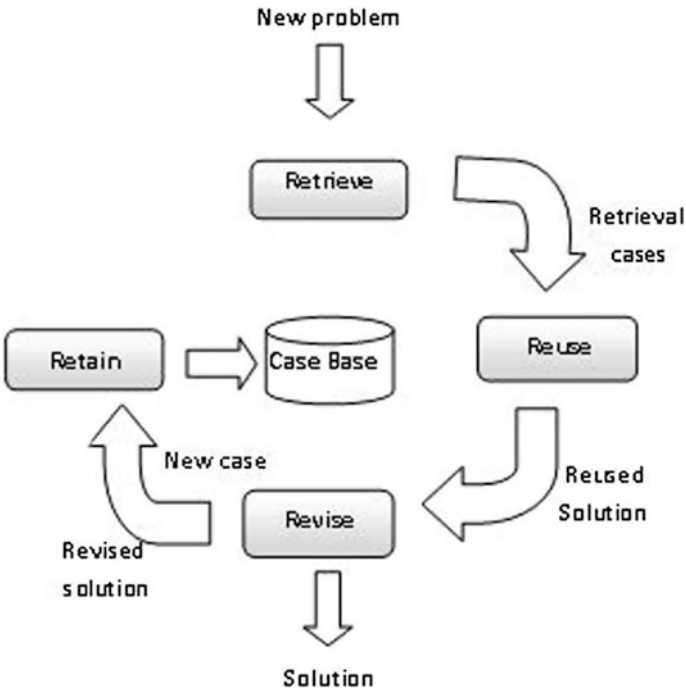

Fig. 1 CBR cycle

4 Methodology

The system presented in this work is based on CBR principles, and its process involves the four phases of CBR cycle that are detailed in Sect. 3. And so, the first step is consisting in estimating similarity between the new problem and former situations gathered in the knowledge base of the system, in order to select the most similar one. This step is realized in this work by proposing general and some specific metrics for the field in question. The second phase is the reuse which adapts the retrieved solution to the new problem. it is conceived in the system by modeling a set of rules established with the collaboration of experts. The last two phases are realized in a simple way and their details are not subject of this paper.

The principal issue in this work is that the completion of the retrieval phase is prevented by a very common problem in medical systems, which is the missing data relating to patient's informations. This issue was already addressed in RespiDiag where two types of strategies have been proposed. The first one is called *online approaches* and aims to find an outcome for the retrieval process of the system by assigning values to local similarities when missing data appears. It's about *pessimistic*, *optimistic* and *medium* approaches.

The second strategy type is called *offline approaches*, and aims for its part to fill the void in the case base with plausible values estimated according to the principle of the proposed approaches. It's about the *statistical*, and *CBR* approaches.

The current work re-evaluates former approaches in the new case base containing lung cancer cases with different missing data rates of those in the first application. The work proposes also two others statistical methods. They are variants of the first ones which see changes made in their principles to obtain the *online statistic* and the *offline statistic** approaches. A comparison is dressed at the end of the evaluation of all these strategies.

4.1 Considered Data and Symptoms

The following set of data and symptoms is considered in the work:

- *age*: lung cancer patients are generally aged over 40 years. For physicians, this data is also necessary to specify the treatment,
- *sex*: in Algeria, men are more exposed to attrap lung cancer than women, because the majority of smokers are men,
- *profession*: this data informs physicians on the possibility for the patient to attrap lung cancer due to its polluted workplace,
- *toxic exposure*: this data informs that the patient is or not alcoholic, because alcohol increases the risk of developing lung cancer,
- *smoking*: including passive smoking,
- *packet number per year*: it is the average of number of smoked packets per year. The danger starts when this number exceeds 120 packets.
- *former health disorders*: that can be asthma, pulmonary tuberculosis, diabetes… etc.
- *chronic tiredness*,
- *anorexia*: that means loss of appetite,
- *sudden weight loss*,
- *night sweat*,
- *fever*,
- *cough*: that does not disappear and that intensifies with time,
- *thoracic pain*: that is constant and that is intensifies when breathing deeply,
- *dyspnea*: that intensifies with effort,
- *pleural effusion*: that means accumulation of fluid around the lungs,
- *hemoptysis*: that is rejection of blood from the respiratory tract following coughing,
- *swollen lymph nodes*: in the neck or over the clavicle,
- *opacity*: that means the presence of opaque spots on the thoracic radiograph,
- *hyper intensity*: that means the presence of an hyper intensity on the scanner image. We distinguish here hyper intensity on the thoracic scanner, named in this work *hyperintensity* and the hyper intensity on the abdominal scanner,

named in this work *hyper intensity's* that indicates the presence of adrenal, biliary or liver cancer which has metastasized to the lungs,
- *tumor mass*: this data informs on the presence/absence of the tumor mass seen in a review of endoscopy,
- *mass length, mass width* and *mass height*: are the measures of the tumor mass,
- *hyper fixation*: this data informs on the fixation of slightly radioactive substance (injected in the body) seen on the review of the bone scintigraphy. It indicates that the cancer has bone origin and has metastasized to the lungs,
- *hyper signal*: that indicates the presence of brain cancer that has metastasized to the lungs. This information is located on the review MRI,
- *metastasis*: this data informs on if the lung cancer has or not metastasized, it can be brain, liver, liver, bone biliary or adrenal metastasis. There may also be multiple metastases at the same time.

4.2 Considered Diagnoses

Two types of lung cancer are essentially considered, they are of variable severity:

- *small-cell lung carcinoma* [8]
- *non-small-cell lung carcinoma* [9] which are essentially of three types:
  - *adenocarcinoma*
  - *squamous cell lung carcinoma*
  - *large cell lung carcinoma*

With the aim not to encumber the reader with medical information, details on these diagnoses are given in the Appendix.

5 The System Process

As already mentioned, the work aim to realize a decision support system for the diagnosis of lung cancer based on the principles of case-based reasoning. For the representation of cases, a set of 29 symptoms (descriptors) of the patient state is established with the collaboration of physicians. It is denoted in this work by `Attributes`. The new problem is denoted `tgt` where the former case is denoted `srce`.

A case is a couple of descriptions of the problem and its solution: case = (`pb`, `sol(pb)`) where `pb` is a problem describing the patient's conditions and `sol(pb)` is a diagnosis solution associated to `pb`:

- `pb` is described by the following set of attributes: `age`, `sex`, `fever`, `cough`, `dyspnea`, `profession`, `pollutedWorkplace`, `toxicExposure`,

chronicTiredness, formerHealthDisorders, nightSweat, anorexia, suddenWeightLoss, smoking, packetNumberPerYear, pleuralEffusion, thoracicPain, opacity, hemoptysis, swollenLymphNodes, hyperIntensity, hyperIntensitys, hyperFixation, hyperSignal, tumorMass, massLength, metastasis, massWidth and massHeight.

- sol(pb) is one of following diagnoses: *small cell lung carcinoma*, *pulmonary adenocarcinoma*, *bronchial adenocarcinoma*, *broncho-pulmonary adenocarcinoma*, *squamous cell lung carcinoma*, *large cell lung carcinoma* and *solitary fibrous tumor.*

The attribute pollutedWorkplace is added intentionally as a binary data for the need to estimate similarity between different values of the attribute profession. See Sect. 5.1.1 for more details. So in total we have a set of 29 Attributes.

5.1 The Retrieval Phase

By entering data of the tgt problem, the system will extract the most similar srce case existing in the CaseBase. This process is realized by comparing the attributes of tgt to attributes of srce and the comparison is done by assessing similarity expressed by:

$$\mathcal{S}(\texttt{srce}, \texttt{tgt}) = \frac{\sum_{a \in \texttt{Attributes}} w_a \times \mathcal{S}_a(\texttt{srce}.a, \texttt{tgt}.a)}{\sum_{a \in \texttt{Attributes}} w_a} \tag{1}$$

where $w_a > 0$ is the weight of the attribute a and $\mathcal{S}_a$ is a similarity measure defined on the range of a. The estimation of $\mathcal{S}_a$ depends on the type of a.

5.1.1 Similarity Metrics for Different Types of Attributes

When the type of a is boolean, it is defined by:

$$\mathcal{S}_a(x, y) = \begin{cases} 1 & \text{if } x = y \\ 0 & \text{else} \end{cases} \text{for} \quad x, y \in \{\texttt{false}, \texttt{true}\} \tag{2}$$

It's the case of following attributes: sex, pollutedWorkplace, smoking, dyspnea, fever, nightSweat, pleuralEffusion, cough, hemoptysis, toxicExposure, chronicTiredness, anorexia, suddenWeightLoss, thoracicPain, opacity, swollenLymphNodes,

hyperIntensity, hyperIntensitys, hyperFixation, hyperSignal, and tumorMass.

If the attribute a is of a numeric type, $\mathcal{S}_a$ is defined by

$$\mathcal{S}_a(x, y) = 1 - \frac{|y - x|}{B_a} \tag{3}$$

where B_a is the "breadth" of the range of a, i.e., it is the difference between the maximal value of this range and its minimal value.

This equation is valid for the following numerical attributes: age, packetNumberPerYear, massLength, massWidth and massHeight.

In this application we dispose of three symbolic attributes which are profession, metastasis and formerHealthDisorders. Each of these attributes has an enumerated list of possible values.

For the estimation of similarity between the values of the attribute profession, we propose the following formula based on the profession value in addition to the information given in the attribute pollutedWorkplace. So, for the attribute profession we use:

$$\mathcal{S}_a(\texttt{tgt}, \texttt{srce}) = \begin{cases} 1 & \text{if } \texttt{tgt}.\text{profession} = \texttt{srce}.\text{profession} \\ 0.8 & \text{if } \texttt{tgt}.\text{profession} \neq \texttt{srce}.\text{profession and} \\ & \texttt{tgt}.\text{pollutedWorkplace} = \texttt{srce}.\text{pollutedWorkplace} \\ 0 & \text{else} \end{cases} \tag{4}$$

The attribute metastasis contains the name of the organ where the lung cancer has metastasized. Knowing that the basic values of the attribute: liver, adrenal, bone, biliary, or absence of metastasis, we note that can contain multiple informations at the same time. Indeed, cancer metastasis may be in one or more organs at once.

The separation between these different values for the same patient, is done simply by commas. We have chosen that the similarity between two elementary values of this attribute is to be estimated by the formula 2.

In order to calculate the similarity between composed values of srce. metastasis and tgt. metastasis, we proposed using the following formula:

$$\mathcal{S}_a(\texttt{srce}, \texttt{tgt}) = \frac{\sum_{a \in \texttt{Attributes}} \mathcal{S}_a(\texttt{srce}.a, \texttt{tgt}.a)}{MaxCard} \tag{5}$$

where MaxCard is the maximum number of elementary values in srce. metastasis and tgt. metastasis.

For the attribute formerHealthDisorders, the same principle used for the metastasis attribute is kept. So, binary similarity is calculated between each two basic values in tgt and srce, after, the sum of all these is estimated and

divided by the maximum cardinality of the two sets of composite values in `srce` and `tgt`.

5.2 Attributes Weights

The `Attributes` weights have been estimated with the collaboration of experts according to the respective importances of each one for the diagnosis. Table 1 shows the importance of attributes estimated by physicians who have expressed importance by the following expressions:

Table 1 The weights estimated by physicians

Attribute	Type	Weight
age	Numeric	0.4
sex	Boolean	0.8
profession	Symbolic	0.1
pollutedWorkplace	Boolean	0.1
formerHealthDisorders	Symbolic	0.4
smoking	Boolean	0.8
packetNumberPerYear	Numeric	0.8
dyspnea	Boolean	0.4
fever	Boolean	0.2
nightSweat	Boolean	0.2
pleuralEffusion	Boolean	0.8
cough	Boolean	0.2
thoracicPain	Boolean	0.4
hemoptysis	Boolean	0.8
chronicTiredness	Boolean	0.2
toxicExposure	Boolean	0.2
suddenWeightLoss	Boolean	0.8
anorexia	Boolean	0.4
swollenLymphNodes	Boolean	0.8
opacity	Boolean	0.4
metastasis	Symbolic	0.8
hyperIntensity	Boolean	0.8
hyperIntensitys	Boolean	0.8
hyperFixation	Boolean	0.8
hyperSignal	Boolean	0.8
tumorMass	Boolean	0.8
massLength	Numeric	0.2
massWidth	Numeric	0.2
massHeight	Numeric	0.2

- Very High Importance (VHI) reflected into the system by the value 0.8
- Average Importance (AI) reflected in the system by the value 0.4
- Low Importance (LI) reflected into the system by the value 0.2

It is noteworthy that the importance of `profession` data is relative to the working environment which can be polluted, so it becomes a risk factor for catching a lung cancer. In the system object of this paper, this data was reinforced by another information `pollutedWorkplace` of the binary type (yes, no). Thus the weighting coefficient of the attribute `profession` which was estimated by physicians to 0.2 (low importance), was divided by two: between `profession` and `pollutedWorkplace` with the aim to maintain balance between the weights estimated by physicians.

5.3 The Problem of Missing Data

During cases collecting from the archive of oncology department of Annaba, it has been observed that patient's files contain missing data which can be about different informations. Indeed, sometimes physicians may avoid certain examinations for a given patient, depending on its state or on its examinations results already obtained. It is noteworthy here that patient's files on which this work has been done are even in paper format. Naturally, the missing data in patient's files are reflected in the case base of the system by missing values that can be appeared in different attributes.

The problem of missing data raises a difficulty to achieve the case retrieval process. Indeed, the similarity value $\mathcal{S}(\texttt{srce}, \texttt{tgt})$ cannot be computed if for at least one attribute a, $\texttt{srce}.a$ and/or $\texttt{tgt}.a$ is unknown. In the following, the notation "$\texttt{pb}.a = ?$" (resp., "$\texttt{pb}.a \neq ?$") means that the value of a for the problem pb is unknown (resp., is known).

The case base is structured in twenty nine attributes corresponding to the problem descriptors plus one attribute corresponding to the solution descriptor (the diagnosis). With the collaboration of physicians, 40 real cases were collected from the archive of the oncology department. This set of cases has been selected so as to have maximum diversity in symptoms for the same diagnosis, it is the set of the source cases. In the following, the case base is denoted by `CaseBase`. Table 2 shows some statistics on the `CaseBase`.

Another set of 20 real cases has been selected from the same archive. This set will serve as a test sample for the system. Cases of this set also contain gaps left by

Table 2 Statistics on the `CaseBase`

	Number	Percentage
Cases	40	
All data required	1160	100 %
Present data	872	75.17 %
Missing data	288	24.82 %

Table 3 Statistics on the sample test

	Number	Percentage
Cases	20	
All data required	580	100 %
Present data	447	77.06 %
Missing data	133	22.93 %

missing data, and constitute the targets cases that will allow us to compare and evaluate results of all proposed approaches.

Table 3 shows some statistics on the sample test.

5.4 *Previously Approaches Re-evaluated in This Application*

In this section, some approaches proposed and evaluated in the previously work [1] are summarized. They aim to manage the problem of missing data simultaneously in the case base and in the new problem. These selected approaches are included in this work for a second evaluation in the new application field which has another rates of missing data. This work propose in addition its own two new statistical approaches which are presented in Sect. 5.5.

In [1], can be found the *online approaches*, which are invoked during the system retrieval process, and each time where a missing value in the `tgt/srce` case appears. These *online approaches* are intended to assign a value to the local similarity without filling the gap left by the missing value. Three *online* strategies of them named each according to its principle, the *optimistic, pessimistic*, and *medium* approaches are reused in this work.

In the same reference, it has been proposed another type of strategies called *offline approaches* which aimed to fill the gaps in the case base. These approaches are executed outside of the system process, hence their name of *offline*, and are only concerned with the missing data in the case base (and not in the target problem). So, they consist in attributing a plausible value υ to $\texttt{srce}.a$, when $\texttt{srce}.a = ?$. This attribution is denoted by $\texttt{srce}.a := \upsilon$.

5.4.1 The Online Optimistic Approach

This approach proposes to give the most possible optimistic value to the similarity assumption that the missing value can be as close as possible to the present value, and the contribution of the local similarity $\mathcal{S}_a(\texttt{srce}.a, \texttt{tgt}.a)$ to the global similarity $\mathcal{S}(\texttt{srce}, \texttt{tgt})$ is maximal, so:

$$\mathcal{S}_a(\texttt{srce}.a, \texttt{tgt}.a) := 1 \tag{6}$$

5.4.2 The Online Pessimistic Approach

A pessimistic strategy would consist in assuming that $\mathcal{S}_a(\texttt{srce}.a, \texttt{tgt}.a)$ is minimal:

$$\begin{aligned}
&\text{if } \texttt{srce}.a = \,?\, \text{ and } \texttt{tgt}.a \neq \,?\, \mathcal{S}_a(\texttt{srce}.a, \texttt{tgt}.a) := \inf_{x \in \texttt{range}(a)} \mathcal{S}_a(x, \texttt{tgt}.a) \\
&\text{if } \texttt{srce}.a \neq \,?\, \text{ and } \texttt{tgt}.a = \,?\, \mathcal{S}_a(\texttt{srce}.a, \texttt{tgt}.a) := \inf_{y \in \texttt{range}(a)} \mathcal{S}_a(\texttt{srce}.a, y) \\
&\text{if } \texttt{srce}.a = \,?\, \text{ and } \texttt{tgt}.a = \,?\, \mathcal{S}_a(\texttt{srce}.a, \texttt{tgt}.a) := \inf_{x,y \in \texttt{range}(a)} \mathcal{S}_a(x, y)
\end{aligned} \tag{7}$$

5.4.3 The Online Medium Approach

This approach considers the balance between the last two approaches. So, it consists in estimating the average of the pessimistic value (denoted by υ_p in the following) and the optimistic one (i.e., 1):

$$\mathcal{S}_a(\texttt{srce}.a, \texttt{tgt}.a) := \frac{1 + \upsilon_p}{2} \tag{8}$$

5.4.4 The Offline Statistical Approach

This approach is based on statistics. Let $\texttt{SPWKV}_a$ be the set of the source problems with known values for attribute a:

$$\texttt{SPWKV}_a = \{\texttt{srce}' | (\texttt{srce}', \texttt{sol}(\texttt{srce}')) \in \texttt{CaseBase} \text{ and } \texttt{srce}'.a \neq \,?\,\}$$

When a is a numerical attribute, the value of the attribute a for srce consists simply in estimating the average of all values of a for the source problems for which these values are known:

$$\texttt{srce}.a := \frac{\sum_{\texttt{srce}' \in \texttt{SPWKV}_a} \texttt{srce}'.a}{\text{card}\, \texttt{SPWKV}_a} \tag{9}$$

where card X is the number of elements of the finite set X.

When a is non numerical (i.e., boolean or symbolic), the statistical approach consists in making a vote:

$$\texttt{srce}.a := \operatorname*{argmax}_{\upsilon \in \texttt{range}(a)} \text{card}\{\texttt{srce}' \in \texttt{SPWKV}_\texttt{a} | \, \texttt{srce}'.a = \upsilon\} \tag{10}$$

5.4.5 The Offline CBR Approach

In this approach, the CBR process itself is used to propose a value to $\texttt{srce}\,.\,a$. In this way, a source case is decomposed in a different way as before: a problem is defined by all the attributes of $\texttt{srce}$ except a and a solution is a value for a.

A new similarity measure $\mathcal{S}^a$ has been defined between these new source cases.

$$\mathcal{S}^a(\texttt{srce}_1, \texttt{srce}_2) = \frac{\sum_{b \in \texttt{Attributes} \setminus \{\texttt{a}\}} w_b^a \times \mathcal{S}_b(\texttt{srce}_1\,.\,b, \texttt{srce}_2\,.\,b)}{\sum_{b \in \texttt{Attributes} \setminus \{a\}} w_b^a} \tag{11}$$

The main difference between the *offline statistical approach* and the *offline cbr approach* one is that the values $\texttt{srce}'.\ a$ are weighted by $\mathcal{S}^a(\texttt{srce}', \texttt{srce})$.

That means that if a is a numerical attribute, then:

$$\texttt{srce}\,.\,a := \frac{\sum_{\texttt{srce}' \in \texttt{SPWKV}_\texttt{a}} \mathcal{S}^a(\texttt{srce}', \texttt{srce}) \times \texttt{srce}'\,.\,a}{\sum_{\texttt{srce}' \in \texttt{SPWKV}_a} \mathcal{S}^a(\texttt{srce}', \texttt{srce})} \tag{12}$$

And if a is a non numerical attribute, then a weighted vote approach is used:

$$\texttt{srce}\,.\,a := \underset{\upsilon \in \texttt{range}(a)}{\text{argmax}} \sum \{\mathcal{S}^a(\texttt{srce}', \texttt{srce}) | \texttt{srce}' \in \texttt{SPWKV}_\texttt{a} \text{ and } \texttt{srce}'.\,\texttt{a} = \upsilon\} \tag{13}$$

where $\sum X = \sum_{x \in X} x$ for any finite set of numbers X.

5.5 *New Proposed Approaches*

We were inspired by these last offline approaches, to propose and evaluate two new strategies in this work. The first one, is a variant of the offline statistic approach but is used during the online process of the system, while the second is a variant of the offline CBR approach and used outside the system process.

5.5.1 The Online Statistic Approach

This approach is inspired by the *offline statistical approach*, whose principle is detailed in Sect. 5.4.4. Indeed, in this strategy, the principle of the average of all informed values of a in source problems is kept. So, the same formula (9) mentioned in the precedent section for the numerical attributes is used here. The

principle of the vote concerning binary or symbolic attributes (formula 10) is also kept.

The first modification brought to the *offline statistical approach* is that it is executed during the *online* system process, specifically during the retrieval phase, hence its name *online statistical approach*. It treats simultaneously the missing value in `tgt` and `srce` cases, while the first one concerned only the missing data in the case base.

The second change is in the method principle itself. Indeed, when a missing value appears in the `tgt` and/or `srce` case, it will be replaced by a plausible value *virtually* and not physically as in the first approach. The virtual replacement of a missing value means that the plausible value is considered in the calculation of local similarity without being stored in the concerned attribute. So the gap is still existing, whereas the retrieval process can be completed and therefore the most similar case can be selected from the case base despite the missing data.

Note here that if we have the missing data to both in the same attribute of `tgt` and `srce` cases, gaps will be replaced virtually by the same value, hence the local similarity will necessarily be equal to 1, which joined here the principle of the *optimistic approach*.

The virtual replacement is motivated primarily by the fact that the case base is in permanent enrichment, which can give better estimates of the missing values for future needs and therefore more reliable and more accurate diagnoses. The disadvantage of this approach is the requirement to recalculate averages that may slow down the system response time.

5.5.2 The Offline CBR Approach*

This *offline approach* is executed outside the system process and is concerning only the missing data in the case base. It's inspired of the strategy summarized in the Sect. 5.4.5. A modification is brought on its principle consisting in reusing the value $\texttt{srce}'.a$ of the `srce` case closest to `srce`, according to $\mathcal{S}_a$, instead of taking into account *all* the source cases $\texttt{srce}' \in \texttt{SPWKV}_a$ like in our old cbr approach.

Indeed, in this new approach, the cbr principle is used: it consists in estimating similarity between `srce` cases and `tgt` case, for selecting the most similar cases to the `tgt` one. In this approach the number of retrieved cases depends of the type of missing data to bridge. It is equal to 2 when the missing value is of numerical type and so, their average is considered for filling the gaps. If this missing value is binary, three (3) most similar cases are retrieved from the case base, and the approach proceeds to the vote for selecting the value whose number of occurrences is maximal and which will replace the gap. When the missing value is symbolic, only one most similar case is selected, and its value fills the gap.

5.6 The Reuse Phase

This phase consists in adapting the solution of the most similar case retrieved from the case base to the `tgt` case. It is the most delicate phase of the cbr process because of its strong dependence on the application field. With the collaboration of the experts physicians, a set of rules is established for adapting the diagnosis of the retrieved case (`srce`, `sol(srce)`). These rules are based mainly on the attributes having the highest weights. An example of rules is given below.

$$\begin{aligned} \textit{if } \texttt{sol(srce)} = \textit{bronchial} - \textit{adenocarcinoma and} \\ \texttt{tgt}.\textit{tumorMass}, = \text{``}\textit{no}'' \textit{ and} \\ \texttt{tgt}.\textit{hyperIntensity}, = \text{``}\textit{Yes}'' \textit{ and} \\ \texttt{tgt}.\textit{opacity}, = \text{``}\textit{no}' \textit{ then} \\ \texttt{sol}.(\texttt{tgt}) = \text{``}\textit{broncho} - \textit{pulmonary} - \textit{adenocarcinoma}'' \end{aligned}$$

Some work remains to be done about the adaptation process. However, the adaptation rules acquired so far have improved the performance of the system, when compared to a null adaptation approach (see Sect. 6).

6 Evaluation, Comparison and Discussion

The evaluation of the system considers three case bases: Base A, Base B and Base C. Only the first one contains missing data, whereas the two others are completely filled.

- Base A is the original case base which contains missing data (cf. Table 2),
- Base B is obtained by applying the *offline statistical approach* on Base A (cf. Sect. 5.4.4),
- Base C is obtained by applying our new *offline cbr approach** on Base A (cf. Sect. 5.5.2).

The evaluation consists first in gathering the diagnoses given by the system. These diagnoses correspond to each $\texttt{CaseBase} \in \{\text{Base A, Base B, Base C}\}$ each of the four *online approaches* (Sects. 5.4.1–5.4.3 and 5.5.1) each of the 20 `tgt` problems taken from the sample test.

Thus $3 \times 4 \times 20 = 240$ diagnoses are generated by the system. Then, these diagnoses are compared to the real diagnoses of the sample test given in the following section.

The evaluation of the system is conducted in two steps:

- after the input of data relating to the target problem, the most similar diagnosis is given without the application of adaptation rules. It is saved with the aim to evaluate the online approaches.

- In the second time adaptation is launched on the same diagnosis to give the final result of the system.

6.1 Results of Approaches

Tables 4, 5 and 6 show the different diagnoses given by the online statistic approach when applied on bases A, B and C (respectively). Tables 7, 8 and 9 show the different results given by the online pessimistic approach when applied on the bases A, B and C (respectively), while Tables 10 and 11 show the different results given by the online medium approach when applied on the bases A and B (respectively).

6.2 Comparison and Discussion

The following (Tables 12, 13, 14, 15, 16, 17, 18 and 19) gives the different percentages of each response quality, of each approach applied on the three bases. Note here that to assess the results quality of the system before and after the adaptation process, diagnoses were grouped into class according to their likeness. A diagnosis result is considered "good" when it is exactly the same as the real diagnosis of the test case. It is considered "average" when it belongs to the real diagnosis class, and it is "low" when it is out this class.

By observing the first and the second Tables 12 and 13, we can see that the online statistical approach is combined, significantly better with the offline statistical approach that fulfilled the base B, where it gives its best rate of "Good response" that reaches 30 % before the adaptation and which passes to 45 % after adaptation. This can be interpreted by the rapprochement between the principles of the two statistical approaches offline and online which apparently complement well. We note that the second approach was inspired from the first one.

The results of this approach in this context is not absolute, a future evaluation of it can be done by considering some existing data as missed and compare this data with the virtual values estimated by the approach. An estimation of response time is also possible in a future work to assess the potential slowdown when the case base is growing in number of records.

For the pessimistic approach (Tables 14 and 15), note that adaptation was able to double the rate of correct responses on the bases B and C. Indeed it rises from 20 to 40 % and from 15 to 30 % (respectively), while for the base A that contains the missing data, rates made a big leap from 10 to 15 %. This brings into focus the efficacy of rules adaptation that are established in the system. We also can see that the pessimistic approach gives its better score of good response when it is applied on the base B.

Table 4 Results of the online statistic approach on the Base A

Attribute	Real diagnosis	Diagnosis before adaptation	Similarity	Diagnosis after adaptation
1	Broncho-pulmonary adenocarcinoma	Bronchial adenocarcinoma	0.71	Broncho-pulmonary adenocarcinoma
2	Broncho-pulmonary adenocarcinoma	Lung adenocarcinoma	0.90	Broncho-pulmonary adenocarcinoma
3	Lung adenocarcinoma	Bronchial adenocarcinoma	0.74	Bronchial adenocarcinoma
4	Lung adenocarcinoma	Lung adenocarcinoma	0.83	Broncho-pulmonary adenocarcinoma
5	Bronchial adenocarcinoma	Broncho-pulmonary adenocarcinoma	0.78	Broncho-pulmonary adenocarcinoma
6	Bronchial adenocarcinoma	Lung adenocarcinoma	0.80	Lung adenocarcinoma
7	Squamous cell carcinoma	Small cell carcinoma	0.77	Small cell carcinoma
8	Squamous cell carcinoma	Squamous cell carcinoma	0.93	Squamous cell carcinoma
9	Squamous cell carcinoma	Lung adenocarcinoma	0.85	Lung adenocarcinoma
10	Small cell carcinoma	Clear cell carcinoma	0.74	Clear cell carcinoma
11	Small cell carcinoma	Lung adenocarcinoma	0.80	Lung adenocarcinoma
12	Pulmonary small cell carcinoma	Small cell carcinoma	0.88	Small cell carcinoma
13	Bronchial carcinoma	Small cell carcinoma	0.88	Small cell carcinoma
14	Solitary fibrous tumor	Small cell carcinoma	0.90	Small cell carcinoma
15	Pulmonary small cell carcinoma	Squamous cell carcinoma	0.71	Squamous cell carcinoma
16	Squamous cell carcinoma	Squamous cell carcinoma	0.88	Squamous cell carcinoma
17	Small cell carcinoma	Lung adenocarcinoma	0.82	Lung adenocarcinoma
18	Broncho-pulmonary adenocarcinoma	Lung adenocarcinoma	0.93	Broncho-pulmonary adenocarcinoma
19	Lung adenocarcinoma	Lung adenocarcinoma	0.86	Lung adenocarcinoma
20	Bronchial adenocarcinoma	Lung adenocarcinoma	0.81	Lung adenocarcinoma

Finally, for the medium and optimistic approaches (Tables 16, 17, 18 and 19), it can observed that before adaptation, they give almost the same rate of good responses on the three bases, neighboring 15 %, whereas they give a rate of 45 % if we consider responses of average quality, which all become good ones after the adaptation process.

Table 5 Results of the online statistic approach on the Base B

Attribute	Real diagnosis	Diagnosis before adaptation	Similarity	Diagnosis after adaptation
1	Broncho-pulmonary adenocarcinoma	Bronchial adenocarcinoma	0.71	Broncho-pulmonary adenocarcinoma
2	Broncho-pulmonary adenocarcinoma	Lung adenocarcinoma	0.90	Broncho-pulmonary adenocarcinoma
3	Lung adenocarcinoma	Lung adenocarcinoma	0.74	Broncho-pulmonary adenocarcinoma
4	Lung adenocarcinoma	Lung adenocarcinoma	0.81	Broncho-pulmonary adenocarcinoma
5	Bronchial adenocarcinoma	Broncho-pulmonary adenocarcinoma	0.79	Broncho-pulmonary adenocarcinoma
6	Bronchial adenocarcinoma	Lung adenocarcinoma	0.80	Lung adenocarcinoma
7	Squamous cell carcinoma	Small cell carcinoma	0.78	Small cell carcinoma
8	Squamous cell carcinoma	Squamous cell carcinoma	0.87	Squamous cell carcinoma
9	Squamous cell carcinoma	Squamous cell carcinoma	0.83	Squamous cell carcinoma
10	Small cell carcinoma	Bronchial adenocarcinoma	0.71	Bronchial adenocarcinoma
11	Small cell carcinoma	Lung adenocarcinoma	0.75	Lung adenocarcinoma
12	Pulmonary small cell carcinoma	Small cell carcinoma	0.86	Small cell carcinoma
13	Bronchial carcinoma	Small cell carcinoma	0.85	Small cell carcinoma
14	Solitary fibrous tumor	Squamous cell carcinoma	0.89	Small cell carcinoma
15	Pulmonary small cell carcinoma	Squamous cell carcinoma	0.71	Squamous cell carcinoma
16	Squamous cell carcinoma	Squamous cell carcinoma	0.81	Squamous cell carcinoma
17	Small cell carcinoma	Lung adenocarcinoma	0.82	Lung adenocarcinoma
18	Broncho-pulmonary adenocarcinoma	Lung adenocarcinoma	0.87	Broncho-pulmonary adenocarcinoma
19	Lung adenocarcinoma	Lung adenocarcinoma	0.86	Lung adenocarcinoma
20	Bronchial adenocarcinoma	Lung adenocarcinoma	0.82	Lung adenocarcinoma

For the offline cbr approach*, we can observe that the rate of good responses is always between the rates corespondent to the bases A and B, which means that this approach that gave the base C completely filled, improved the quality of results regarding the original case base that contains the missing data.

Table 6 Results of the online statistic approach on the Base C

Attribute	Real diagnosis	Diagnosis before adaptation	Similarity	Diagnosis after adaptation
1	Broncho-pulmonary adenocarcinoma	Bronchial adenocarcinoma	0.71	Broncho-pulmonary adenocarcinoma
2	Broncho-pulmonary adenocarcinoma	Lung adenocarcinoma	0.90	Broncho-pulmonary adenocarcinoma
3	Lung adenocarcinoma	Bronchial adenocarcinoma	0.74	Bronchial adenocarcinoma
4	Lung adenocarcinoma	Bronchial adenocarcinoma	0.83	Broncho-pulmonary adenocarcinoma
5	Bronchial adenocarcinoma	Broncho-pulmonary adenocarcinoma	0.78	Broncho-pulmonary adenocarcinoma
6	Bronchial adenocarcinoma	Lung adenocarcinoma	0.80	Lung adenocarcinoma
7	Squamous cell carcinoma	Lung adenocarcinoma	0.77	Small cell carcinoma
8	Squamous cell carcinoma	Squamous cell carcinoma	0.93	Squamous cell carcinoma
9	Squamous cell carcinoma	Lung adenocarcinoma	0.85	Lung adenocarcinoma
10	Small cell carcinoma	Clear cell carcinoma	0.74	Clear cell carcinoma
11	Small cell carcinoma	Lung adenocarcinoma	0.80	Lung adenocarcinoma
12	Pulmonary small cell carcinoma	Small cell carcinoma	0.88	Small cell carcinoma
13	Bronchial Carcinoma	Squamous cell carcinoma	0.88	Small cell carcinoma
14	Solitary fibrous tumor	Squamous cell carcinoma	0.90	Small cell carcinoma
15	Pulmonary small cell carcinoma	Lung adenocarcinoma	0.71	Squamous cell carcinoma
16	Squamous cell carcinoma	Lung adenocarcinoma	0.84	Squamous cell carcinoma
17	Small cell carcinoma	Bronchial carcinoma	0.82	Lung adenocarcinoma
18	Broncho-pulmonary adenocarcinoma	Lung adenocarcinoma	0.93	Broncho-pulmonary adenocarcinoma
19	Lung adenocarcinoma	Bronchial adenocarcinoma	0.86	Lung adenocarcinoma
20	Bronchial adenocarcinoma	Small cell carcinoma	0.81	Lung adenocarcinoma

Table 7 Results of the pessimistic approach on the Base A

Attribute	Real diagnosis	Diagnosis before adaptation	Similarity	Diagnosis after adaptation
1	Broncho-pulmonary adenocarcinoma	Bronchial adenocarcinoma	0.53	Broncho-pulmonary adenocarcinoma
2	Broncho-pulmonary adenocarcinoma	Lung adenocarcinoma	0.80	Broncho-pulmonary adenocarcinoma
3	Lung adenocarcinoma	Bronchial adenocarcinoma	0.63	Bronchial adenocarcinoma
4	Lung adenocarcinoma	Bronchial adenocarcinoma	0.69	Bronchial adenocarcinoma
5	Bronchial adenocarcinoma	Bronchial adenocarcinoma	0.44	Bronchial adenocarcinoma
6	Bronchial adenocarcinoma	Lung adenocarcinoma	0.57	Lung adenocarcinoma
7	Squamous cell carcinoma	Lung adenocarcinoma	0.67	Lung adenocarcinoma
8	Squamous cell carcinoma	Squamous cell carcinoma	0.74	Squamous cell carcinoma
9	Squamous cell carcinoma	Lung adenocarcinoma	0.68	Lung adenocarcinoma
10	Small cell carcinoma	Clear cell carcinoma	0.59	Clear cell carcinoma
11	Small cell carcinoma	Lung adenocarcinoma	0.57	Lung adenocarcinoma
12	Pulmonary small cell carcinoma	Squamous cell carcinoma	0.68	Squamous cell carcinoma
13	Bronchial carcinoma	Squamous cell carcinoma	0.67	Squamous cell carcinoma
14	Solitary fibrous tumor	Squamous cell carcinoma	0.70	Squamous cell carcinoma
15	Pulmonary small cell carcinoma	Squamous cell carcinoma	0.57	Squamous cell carcinoma
16	Squamous cell carcinoma	Solitary fibrous tumor	0.66	Solitary fibrous tumor
17	Small cell carcinoma	Lung adenocarcinoma	0.55	Lung adenocarcinoma
18	Broncho-pulmonary adenocarcinoma	Lung adenocarcinoma	0.67	Broncho-pulmonary adenocarcinoma
19	Lung adenocarcinoma	Squamous cell carcinoma	0.64	Squamous cell carcinoma
20	Bronchial adenocarcinoma	Squamous cell carcinoma	0.52	Squamous cell carcinoma

Table 8 Results of the pessimistic approach on the Base B

Attribute	Real diagnosis	Diagnosis before adaptation	Similarity	Diagnosis after adaptation
1	Broncho-pulmonary adenocarcinoma	Bronchial adenocarcinoma	0.53	Broncho-pulmonary adenocarcinoma
2	Broncho-pulmonary adenocarcinoma	Lung adenocarcinoma	0.80	Broncho-pulmonary adenocarcinoma
3	Lung adenocarcinoma	Bronchial adenocarcinoma	0.63	Bronchial adenocarcinoma
4	Lung adenocarcinoma	Bronchial adenocarcinoma	0.69	Bronchial adenocarcinoma
5	Bronchial adenocarcinoma	Bronchial adenocarcinoma	0.44	Bronchial adenocarcinoma
6	Bronchial adenocarcinoma	Lung adenocarcinoma	0.57	Lung adenocarcinoma
7	Squamous cell carcinoma	Lung adenocarcinoma	0.67	Lung adenocarcinoma
8	Squamous cell carcinoma	Squamous cell carcinoma	0.74	Squamous cell carcinoma
9	Squamous cell carcinoma	Lung adenocarcinoma	0.68	Lung adenocarcinoma
10	Small cell carcinoma	Clear cell carcinoma	0.59	Clear cell carcinoma
11	Small cell carcinoma	Lung adenocarcinoma	0.57	Lung adenocarcinoma
12	Pulmonary small cell carcinoma	Squamous cell carcinoma	0.68	Squamous cell carcinoma
13	Bronchial carcinoma	Squamous cell carcinoma	0.67	Squamous cell carcinoma
14	Solitary fibrous tumor	Squamous cell carcinoma	0.70	Squamous cell carcinoma
15	Pulmonary small cell carcinoma	Squamous cell carcinoma	0.57	Squamous cell carcinoma
16	Squamous cell carcinoma	Solitary fibrous tumor	0.66	Solitary fibrous tumor
17	Small cell carcinoma	Lung adenocarcinoma	0.55	Lung adenocarcinoma
18	Broncho-pulmonary adenocarcinoma	Lung adenocarcinoma	0.67	Broncho-pulmonary adenocarcinoma
19	Lung adenocarcinoma	Squamous cell carcinoma	0.64	Squamous cell carcinoma
20	Bronchial adenocarcinoma	Squamous cell carcinoma	0.52	Squamous cell carcinoma

Table 9 Results of the pessimistic approach on the Base C

Attribute	Real diagnosis	Diagnosis before adaptation	Similarity	Diagnosis after adaptation
1	Broncho-pulmonary adenocarcinoma	Bronchial adenocarcinoma	0.53	Broncho-pulmonary adenocarcinoma
2	Broncho-pulmonary adenocarcinoma	Lung adenocarcinoma	0.80	Broncho-pulmonary adenocarcinoma
3	Lung adenocarcinoma	Bronchial adenocarcinoma	0.63	Bronchial adenocarcinoma
4	Lung adenocarcinoma	Bronchial adenocarcinoma	0.69	Bronchial adenocarcinoma
5	Bronchial adenocarcinoma	Bronchial adenocarcinoma	0.44	Bronchial adenocarcinoma
6	Bronchial adenocarcinoma	Lung adenocarcinoma	0.57	Lung adenocarcinoma
7	Squamous cell carcinoma	Lung adenocarcinoma	0.67	Lung adenocarcinoma
8	Squamous cell carcinoma	Squamous cell carcinoma	0.74	Squamous cell carcinoma
9	Squamous cell carcinoma	Lung adenocarcinoma	0.68	Lung adenocarcinoma
10	Small cell carcinoma	Clear cell carcinoma	0.59	Clear cell carcinoma
11	Small cell carcinoma	Lung adenocarcinoma	0.57	Lung adenocarcinoma
12	Pulmonary small cell carcinoma	Squamous cell carcinoma	0.68	Squamous cell carcinoma
13	Bronchial carcinoma	Squamous cell carcinoma	0.67	Squamous cell carcinoma
14	Solitary fibrous tumor	Squamous cell carcinoma	0.70	Squamous cell carcinoma
15	Pulmonary small cell carcinoma	squamous cell carcinoma	0.57	Squamous cell carcinoma
16	Squamous cell carcinoma	Solitary fibrous tumor	0.66	Solitary fibrous tumor
17	Small cell carcinoma	Lung adenocarcinoma	0.55	Lung adenocarcinoma
18	Broncho-pulmonary adenocarcinoma	Lung adenocarcinoma	0.67	Broncho-pulmonary adenocarcinoma
19	Lung adenocarcinoma	Squamous cell carcinoma	0.64	Squamous cell carcinoma
20	Bronchial adenocarcinoma	Squamous cell carcinoma	0.52	Squamous cell carcinoma

Table 10 Results of the medium approach on the Base A

Attribute	Real diagnosis	Diagnosis before adaptation	Similarity	Diagnosis after adaptation
1	Broncho-pulmonary adenocarcinoma	Bronchial adenocarcinoma	0.65	Broncho-pulmonary adenocarcinoma
2	Broncho-pulmonary adenocarcinoma	Lung adenocarcinoma	0.86	Broncho-pulmonary adenocarcinoma
3	Lung adenocarcinoma	Bronchial adenocarcinoma	0.73	Bronchial adenocarcinoma
4	Lung adenocarcinoma	Lung adenocarcinoma	0.78	Bronchial-pulmonary adenocarcinoma
5	Bronchial adenocarcinoma	Bronchial adenocarcinoma	0.65	Bronchial adenocarcinoma
6	Bronchial adenocarcinoma	Bronchial adenocarcinoma	0.73	Lung adenocarcinoma
7	Squamous cell carcinoma	Lung adenocarcinoma	0.79	Lung adenocarcinoma
8	Squamous cell carcinoma	Squamous cell carcinoma	0.83	Squamous cell carcinoma
9	Squamous cell carcinoma	Lung adenocarcinoma	0.82	Lung adenocarcinoma
10	Small cell carcinoma	Clear cell carcinoma	0.76	Clear cell carcinoma
11	Small cell carcinoma	Lung adenocarcinoma	0.72	Lung adenocarcinoma
12	Pulmonary small cell carcinoma	Lung adenocarcinoma	0.77	Squamous cell carcinoma
13	Bronchial carcinoma	Lung adenocarcinoma	0.78	Squamous cell carcinoma
14	Solitary fibrous tumor	Squamous cell carcinoma	0.80	Squamous cell carcinoma
15	Pulmonary small cell carcinoma	Squamous cell carcinoma	0.68	Squamous cell carcinoma
16	Squamous cell carcinoma	Squamous cell carcinoma	0.74	Squamous cell carcinoma
17	Small cell carcinoma	Lung adenocarcinoma	0.72	Lung adenocarcinoma
18	Broncho-pulmonary adenocarcinoma	Lung adenocarcinoma	0.77	Broncho-pulmonary adenocarcinoma
19	Lung adenocarcinoma	Squamous cell carcinoma	0.78	Squamous cell carcinoma
20	Bronchial adenocarcinoma	Squamous cell carcinoma	0.72	Squamous cell carcinoma

Table 11 Results of the medium approach on the Base B

Attribute	Real diagnosis	Diagnosis before adaptation	Similarity	Diagnosis after adaptation
1	Broncho-pulmonary adenocarcinoma	Bronchial adenocarcinoma	0.65	Broncho-pulmonary adenocarcinoma
2	Broncho-pulmonary adenocarcinoma	Lung adenocarcinoma	0.88	Broncho-pulmonary adenocarcinoma
3	Lung adenocarcinoma	bronchial adenocarcinoma	0.72	Bronchial adenocarcinoma
4	Lung adenocarcinoma	Bronchial adenocarcinoma	0.84	Bronchial adenocarcinoma
5	Bronchial adenocarcinoma	Bronchial adenocarcinoma	0.65	Bronchial adenocarcinoma
6	Bronchial adenocarcinoma	Lung adenocarcinoma	0.70	Lung adenocarcinoma
7	Squamous cell carcinoma	Lung adenocarcinoma	0.74	Lung adenocarcinoma
8	Squamous cell carcinoma	Squamous cell carcinoma	0.88	Squamous cell carcinoma
9	Squamous cell carcinoma	Lung adenocarcinoma	0.83	Lung adenocarcinoma
10	Small cell carcinoma	Clear cell carcinoma	0.73	Clear cell carcinoma
11	Small cell carcinoma	Lung adenocarcinoma	0.74	Lung adenocarcinoma
12	Pulmonary small cell carcinoma	Squamous cell carcinoma	0.84	Squamous cell carcinoma
13	Bronchial carcinoma	Squamous cell carcinoma	0.84	Squamous cell carcinoma
14	Solitary fibrous tumor	Squamous cell carcinoma	0.83	Squamous cell carcinoma
15	Pulmonary small cell carcinoma	Squamous cell carcinoma	0.66	Squamous cell carcinoma
16	Squamous cell carcinoma	Solitary fibrous tumor	0.80	Solitary fibrous tumor
17	Small cell carcinoma	Lung adenocarcinoma	0.72	Lung adenocarcinoma
18	Broncho-pulmonary adenocarcinoma	Lung adenocarcinoma	0.87	Broncho-pulmonary adenocarcinoma
19	Lung adenocarcinoma	Squamous cell carcinoma	0.78	Squamous cell carcinoma
20	Bronchial adenocarcinoma	Squamous cell carcinoma	0.70	Squamous cell carcinoma

Table 12 Results quality of the online statistic approach before adaptation

Base	Good response (%)	Average response (%)	Low response (%)
Base A	20	40	40
Base B	30	35	35
Base C	15	35	50

Table 13 Results quality of the online statistic approach after adaptation

Base	Good response (%)	Average response (%)	Low response (%)
Base A	40	20	40
Base B	45	20	35
Base C	30	20	50

Table 14 Results quality of the pessimistic approach before adaptation

Base	Good response (%)	Average response (%)	Low response (%)
Base A	10	30	60
Base B	20	45	35
Base C	15	30	55

Table 15 Results quality of the pessimistic approach after adaptation

Base	Good response (%)	Average response (%)	Low response (%)
Base A	25	15	60
Base B	40	25	35
Base C	30	15	55

Table 16 Results quality of the medium approach before adaptation

Base	Good response (%)	Average response (%)	Low response (%)
Base A	20	30	50
Base B	20	45	35
Base C	20	35	45

Table 17 Results quality of the medium approach after adaptation

Base	Good response (%)	Average response (%)	Low response (%)
Base A	40	10	50
Base B	40	25	35
Base C	35	20	45

Table 18 Results quality of the optimistic approach before adaptation

Base	Good response (%)	Average response (%)	Low response (%)
Base A	15	35	50
Base B	20	45	35
Base C	20	35	45

Table 19 Results quality of the optimistic approach after adaptation

Base	Good response (%)	Average response (%)	Low response (%)
Base A	40	10	50
Base B	40	25	35
Base C	35	20	45

7 Conclusion

This article presents a case-based decision support system dedicated to the diagnosis of lung cancer, which is a very lethal disease caused mainly by tobacco. The system describes a patient thanks to 29 numerical, boolean and symbolic attributes. The retrieval phase of the CBR process of the system is based on a similarity measure S defined as a weighted average of local similarity measures S_a associated with each attribute a, while the adaptation phase is based on a set of rules.

The main issue for this application is related to the missing data in the case base (about 25 %) and in the target problem (about 23 % in the sample test). In order to manage this problem, 2 approaches are defined in this paper, and are inspired by the previously strategies presented in [1], where some approaches are selected to be re-evaluate in the new domain of lung cancer diagnosis. All these approaches are distinguished into 2 categories: *online* and *offline* strategies. The first one aims at estimating, at runtime, the value of the local similarity of an attribute for which the values in the source case and/or in the target problem are unknown. The evaluation has shown that the new proposed approach online gives the best results on the sample test with a rate of 45 % of "Good responses" which coincide with the real diagnoses made by experts.

The second category is the offline strategies which aim at filling the gaps in the case base. The evaluation has shown that the new CBR offline approach* always gives the best results regarding the base case containing the missing data, but of lower quality relative to the base case filled with former statistical method of work.

All these results are related to a well-defined context data/absent and with well-defined rates. When these rates increase, the possibility of degradation of performance of one or the other approach is here. The same work can be redone, increasing the rate of missing data with the objective to evaluate the behavior of these approaches.

Appendix

Considered Diagnoses

There are essentially two types of lung cancer of variable severity:

- *small-cell lung carcinoma* [8] (SCLC): is a type of highly malignant cancer that arises most commonly within the lung, although it can occasionally arise in other body sites, such as the cervix, prostate, and gastrointestinal tract. Compared to non-small cell carcinoma, SCLC has a shorter doubling time, higher growth fraction, and earlier development of metastases. SCLCs represent about 20 % of lung cancers and are difficult to treat. They grow rapidly and, when diagnosed, it is common that cancer cells are already scattered throughout the rest of the body to form metastases (secondary tumors). In 95 % of cases, lung cancers are small cell linked to smoking.
- *non-small-cell lung carcinoma* [9] (NSCLC): is any type of epithelial lung cancer other than small cell lung carcinoma. As a class, NSCLCs are relatively insensitive to chemotherapy, compared to small cell carcinoma. When possible, they are primarily treated by surgical resection with curative intent, although chemotherapy is increasingly being used both pre-operatively and post-operatively. NSCLCs represent about 80 % of lung cancers and heal more easily because they grow more slowly. Lung cancer NON-small cell are essentially of three types:
  - *adenocarcinoma* (ADC), which account for 40 % of non-small cell cancers, sometimes affecting the alveoli and are slightly more common among non-smokers and women.
  - *squamous cell lung carcinoma*, which are more common in men than in women. They also represent 40 % of non-small cell cancers, they reach the bronchi and are associated directly to smoking,
  - *large cell lung carcinoma*, which represent 20 % of non-small cell cancers, with a faster growth than the other two types, that are caused by 90 % of tobacco consumption.

Each of these lung cancer may be bronchial, pulmonary or bronco-pulmonary. We note that there is another type of lung cancer benign, which is named solitary fibrous tumor.

References

1. Guessoum, S., Laskri, M.T., Lieber, J.: RespiDiag: a case-based reasoning system for the diagnosis of chronic obstructive pulmonary disease. Exp. Syst. Appl. **41**(2), 267–273 (2014)
2. Koton, P.: Reasoning about evidence in causal explanations. In: Kolodner, J. (ed.) Proceedings of the Case-Based Reasoning Workshop, Clearwater Beach, Florida (1988)

3. El Balaa, Z., Strauss, A., Uziel, P., Maximini, K., Traphner, R.: FM-Ultranet: a decision support system using case-based reasoning applied to ultrasonography. In: McGinty, L. (ed.) Workshop Proceedings of the International Conference on Case-Based Reasoning, p. 3744 (2003)
4. Lieber, J., Bresson, B.: Case-based reasoning for breast cancer treatment decision helping. In: Blanzieri, E., Portinale, L. (eds.) Advances in case-based reasoning. In: Proceedings of the European Workshop on Case-Based Reasoning, EWCBR. Lecture Notes in Artificial Intelligence, vol. 1898, pp. 173–185 (2000)
5. Maurente, C., Edye, E.O., Delgado, S.H., GarcÃ-a, D.R.: Evaluation of case based reasoning for clinical decision support systems applied to acute meningitis diagnose. Innov. Adv. Comput. Sci. Eng. 259–264 (2010)
6. Ocampo, E., Maceiras, M., Herrera, S., Maurente, C., Rodriguez, R., Sicilia, M.: Comparing Bayesian inference and case-based reasoning as support techniques in the diagnosis of acute bacterial meningitis. Exp. Syst. Appl. **38**, 10343–10354 (2011)
7. Aamodt, A., Plaza, E.: Case-based reasoning: foundational issues, methodological variations, and system approaches. AI Commun. **7**(1), 39–59 (1994). IOS Press
8. https://en.wikipedia.org/wiki/Smallcell_carcinoma
9. https://en.wikipedia.org/wiki/Non-small-cell_lung_carcinoma
10. Lin, J.H., Haug, P.J.: Exploiting missing clinical data in Bayesian network modeling for predicting medical problems. J. Biomed. Inform. **41**, 1–14 (2008)

Advances in Soft Computing Approaches for Gene Prediction: A Bioinformatics Approach

Minu Kesheri, Rajeshwar P. Sinha and Swarna Kanchan

Abstract The flooding of gene sequencing projects lead to the deposition of large amount of genomic data in public databases. These public databases contribute in genome annotation which helps in discovering the new genes and finding their function. Due to lack of genome annotation and high-throughput experimental approaches, computational gene prediction has always been one of the challenging areas for bioinformatics/computational biology scientists. Gene finding is more difficult in eukaryotes as compared to prokaryotes due to presence of introns. Gene prediction in very crucial especially for disease identification in human, which will help a lot in bio-medical research. Ab intio gene prediction is a difficult method which uses signal and content sensors to make predictions while homology based method makes use of homology with known genes. This chapter describes various gene structure prediction programmes which are based on individual/hybrid soft computing approaches. Soft computing approaches include Genetic algorithm, Hidden Markov Model, Fast Fourier Transformation, Support vector Machine, Dynamic programming and Artificial Neural Network. Hybrid soft computing approaches combine the results of several soft computing programs to deliver better accuracy than individual single soft computing approaches. Moreover, various parameters for measuring the accuracy of gene prediction programs will also be discussed.

M. Kesheri · R.P. Sinha
Laboratory of Photobiology and Molecular Microbiology,
Centre of Advanced Study in Botany, Banaras Hindu University,
Varanasi 221005, India

S. Kanchan (✉)
Department of Biological Sciences, Birla Institute of Technology and Science,
Pilani 333031, Rajasthan, India
e-mail: swarnabioinfo@gmail.com

N. Dey et al. (eds.), *Medical Imaging in Clinical Applications*,
Studies in Computational Intelligence 651, DOI 10.1007/978-3-319-33793-7_17

1 Introduction

The announcement of the human genome sequence in 2001 was followed by flooding of projects targeting sequencing of several other model organisms which lead to the generation and finally deposition of large amount of genomic data in public databases [1]. The increase in the amount of genomic sequence data has increased the numbers of unknown gene [2]. After 12 years of sequencing of human genome, nearly 23,000 coding genes are documented yet, a number of genes still remain undiscovered in human. Genome annotation is one of the major processes in discovering the new genes and finding their function.

Gene structure refers to the sequential arrangement of exons and introns spanning a genomic DNA fragment [3]. Gene finding typically refers to an area of computational biology/bioinformatics which is concerned with identifying the stretches of sequences, usually genomic DNA that are biologically significant and are called genes. Genes are transcribed in mRNA which are finally translated into protein. Noncoding genes e.g. functional RNA molecules often involved in the regulation of gene expression and protein synthesis are also present in organisms. Since, these genes are not translated into proteins and they lack sequence features of coding sequences, their detection by traditional gene finding programs becomes difficult.

Gene discovery in prokaryotes is less difficult, owing to higher gene density due to absence of introns in protein coding regions [4]. Prokaryote gene annotation can be complicated by overlapping regions which makes identification of translation start sites difficult [5]. For finding gene sequences that encode protein, it is required to search the open reading frames which can be defined as contiguous set of codons. There are six possible set of open reading frames (ORFs) in each DNA sequence. Three ORFs are in the given sequence from 5′ to 3′ and other three in 5′–3′ direction in complementary sequence [6]. However it is true that all the ORFs cannot be the probable gene candidates [7]. In prokaryotes and in some simple eukaryotes (such as *Saccharomyces cerevisiae*), genes normally have longest single continuous ORF and adjacent genes are separated by short intergenic regions. However in prokaryotes, genes may often overlap each other and thus causing difficulty in correct prediction of gene. An improved gene prediction tool called GeneScan which is used frequently for bacterial and organellar genomes has a sensitivity of 100 % for *Plasmodium falciparum* and 98 % for the *Mycoplasma genitaliumand* and *Haemophilus influenza* [8]. Another new gene prediction algorithm called PRODYGAL (PROkaryotic DYnamic programming Gene-finding ALgorithm) with improved gene structure and translation initiation site predictions. PRODYGAL also reduced false positives in gene prediction which is specially designed for microbial genomes [9].

The genes in eukaryotes are not contiguous but are often split into alternating coding and noncoding segments. The main characteristic feature of an eukaryotic

gene is the organization of its structure into exons and introns. When the gene is transcribed, the thousands of bases are converted into RNA molecule. The introns are then cut out in a process called splicing and only exon sequences are attached together again for being translated into protein. Furthermore, eukaryote coding segments are subject to alternative splicing in which exons are joined in different ways during RNA splicing [10]. To determine the gene structure, many attempts are made to detect either the introns or the exons. In vertebrates, the internal exons are small in length ($\sim$140 nucleotides on average), whereas introns are much larger (some are even more than 100 kb) in length. Coding segments (CDS's) of genes are characterized by four types of signals: start codons (ATG in eukaryotes), stop codons (usually TAG, TGA, or TAA), donor sites (usually GT), and acceptor sites (AG). Regions of the gene outside the CDS are called UTR's (untranslated regions), and are mostly ignored by gene finders, although they are important for regulatory functions [11–15]. Recently scientists have developed various methods to predict as well as validate gene models by using PacBio single-molecule and real-time (SMRT) cDNA reads [16]. Not only DNA and CDNA sequences, but extensive RNA sequence data also improved the accuracy as well number of actual genes in eukaryotes [17, 18]. Gene predictions in eukaryotes have also improved which is based on only the annotations from another similar species. By aligning the exon sequences from annotated species to the unannotated genome by (Genome Annotation based on Species Similarity (GASS) facilitates the detection of the optimal transcript annotation in unannotated species [19]. Gene prediction tool called Bagheera is also developed for eukaryotes which use different codons to code the same amino acid. For example, most Saccharomycetes, including *Saccharomyces cerevisiae*, use the standard genetic code which code CUG codon as leucine in many but not in all. However, one of the Saccharomycetes known as *Candida*, translate the same codon as serine [20].

Computational gene finding has evolved steadily over the past 30 years. One of the first computational gene finding method for identifying protein coding regions in genomic DNA elucidated that open reading frames (ORFs), start codons, codon preference, ribosome binding sites, and splice sites were considered as useful sensors for coding sequence [21]. Computational gene prediction can be categorized into two major classes of techniques for the prediction of genes: ab initio methods and similarity/homology based methods [22]. A systematic diagramme for the gene prediction process in the form of flow chart is shown in Fig. 1.

In a nutshell this chapter is broadly divided into seven sections. Section 1 briefly introduces the chapter. Section 2 throws light on ab intio gene finding methods which is further divided into sub-sections dealing with consent and signal sensors. Section 3 describes homology based gene prediction methods. Section 4 is divided into seven sub-sections which describe various soft computing approaches. Section 5 elucidates hybrid soft computing methods which are capable of delivering better results with higher accuracy than individual soft computing approaches. Section 6 deals with various parameters for measuring the accuracy of the gene prediction programs. Section 7 throws light on future prospects of soft computing approaches for gene prediction.

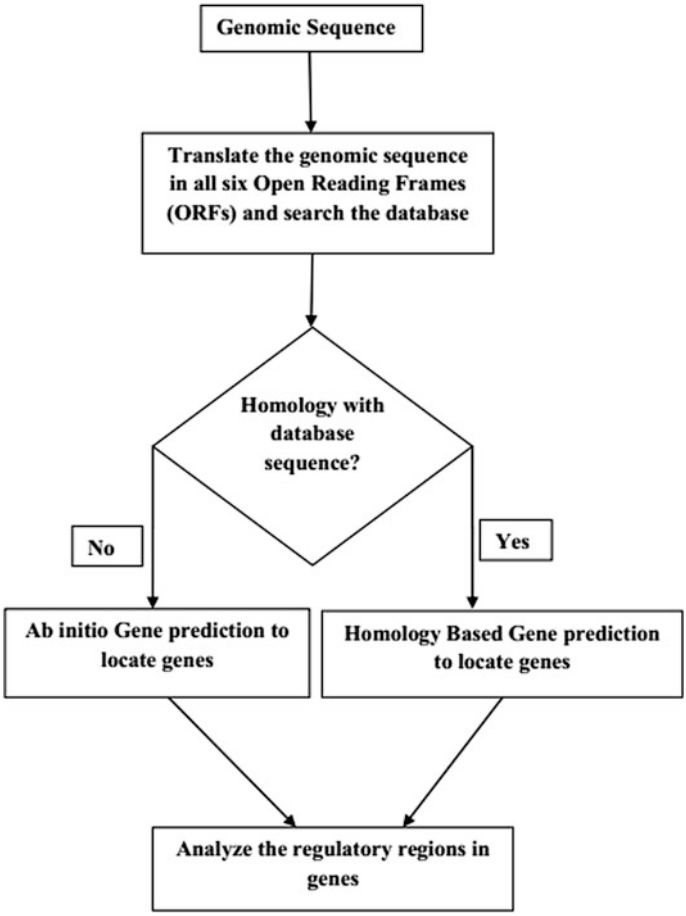

Fig. 1 Flow chart illustrating gene prediction procedure in a stepwise manner

2 Ab initio Gene Prediction Methods

Ab initio gene prediction methods are categorized mainly as 'content' and 'signal' sensors [23]. Examples of ab initio programs are GENSCAN [24], GENIE [25], HMMGene [26] and GENEID [27]. Chemgenome is also *ab intio* gene prediction software, which finds genes in prokaryotic genomes in all six reading frames which follows a physico-chemical approach validated on 372 prokaryotic genomes [28]. The following sub-sections discuss about 'content' and 'signal' sensors as ab initio gene-finding methods.

2.1 Content Sensors

Content sensors help in predicting the gene structure by considering the content of a candidate gene region, such as the base composition or length distribution of a candidate exon or intron. Content sensor refers to the coding and non coding region of the genome. Content sensors can be further categorized into extrinsic and intrinsic [23]. Extrinsic content based gene prediction programmes are mainly based on similarity search by optimal Smith-Waterman algorithm or by heuristic Blast or FastA programmes from the publically available sequence databases [29]. It is estimated that almost 50 % of the genes can be identified by database search. Intrinsic Content gene finding locates all the gene elements that occur in a genomic sequence, including possible partial gene structures at the border of the sequence [30]. The structure of a genome and the density of its genes vary significantly with the GC-content which can be defined as two light groups (L) and three heavy groups (H). These light groups are L1 (<38 % GC-content) L2 (38–42 % GC-content) while heavy groups are H1 (42–47 % GC-content), H2 (47–52 % GC-content) and H3 (>52 % GC-content) in human. Codon usage is another most important content sensor used in many computational gene prediction algorithms [31]. Determination of the exact borders of exon and intron or gene regions is still a challenging task for computational biologist. Splice site predictions has proved useful in gene prediction because sequences at boundaries exhibit characteristics that are different from that of other sequences. Theses sequences provide strong indicators of boundaries between exons and introns in multi-exon genes by splice site prediction and finally used as important ingredient in many gene prediction algorithms.

Expressed Sequence Tags (ESTs) and mRNA (or cDNAs) provides information to identify (partial) exons. However, ESTs give only local and limited information on the gene structure as they represent only partial mRNA. An interesting study on the human genome concluded that EST databases could be an effective probe for gene detection in the human genome [32].

2.2 Signal Sensors

Signal sensors model the gene prediction by the transition between states which helps to detect the boundaries between exons and introns in the sequence. Signal refers to the presence of functional sites in the genome, for example, slice sites, polyadenylation sites, start and stop codons, branch points, promoters and terminators of transcription and splice junctions etc. Identifying the 5′ end of a gene is one of the most difficult tasks in gene finding. This is mainly due to the hurdles in identifying the promoter and the Transcriptional Start Site (TSS) sequences. There are many promoter-prediction and TSS-prediction programs; however, their performance with respect to the control of false-positive predictions is still

unsatisfactory. To bridge this shortcoming, a new program, Eponine, performs well to Promoter Inspector and is able to predict the location of the TSS in a better way by exploiting significant discriminating features such as the TATA box and CpG islands [30, 33].

3 Homology/Similarity Based Methods

Several gene-finding methods include the results of sequence similarity searches to improve the overall prediction accuracy. Homology based informations are useful for better identification of prokaryotic and eukaryotic genes which increases accuracy as well. Sequence homology search is a commonly used approach that is based on finding similarity in gene sequences by direct matching of the genomic DNA sequence and a reference protein. In other way, matching of ESTs (expressed sequence tags) to the input genome/DNA segment is done in sequence similarity searching. Similarity based programs use external information about the input sequence. EST-based sequence similarity usually has its own limitation because ESTs only correspond to small portions of the gene sequence i.e. partial mRNA. Local alignment and global alignment are two methods widely used in similarity based gene prediction. BLAST and NEEDLE are the most widely used algorithms for local and global alignment based similarity searches. The method of integrating protein homology has been applied in many gene prediction programmes such as GENEWISE [34], GENOMESCAN [35] GeneParser [36], GRAIL [37, 38], Genie [25] and HMMgene [26]. Similarity-based programs use various nucleic acid and protein sequence databases. The prediction accuracy of gene prediction methods increased a lot when ab initio and similarity information both are used together. However, older methods were purely based on ab initio approaches or homology based methods [39].

The first generation of programs such as GRAIL was dedicated to identify the approximate locations of coding regions in genomic DNA [37]. The second generation programmes, such as Xpound [40] combined splice signal and coding region identification while third generation of programs GeneID [27], GeneParser [41] and FGENEH [42] attempted the prediction of complete gene structure in entire genomic DNA. Low performance of the above programs inspired the development of fourth generation programmes GENSCAN [43] and AUGUSTUS [44] which further improved the accuracy and applicability.

Several algorithms are applied for gene structure predictions, such as Dynamic Programming, Hidden Markov Model, Support vector machine, Fourier Transformation, Decision Tree and Artificial Neural Network. Among these algorithms, programmes based on Hidden Markov Model are the most accurate and widely used.

4 Soft Computing Approaches for Gene Prediction

This section describes various soft computing approaches in its seven sub-sections which deal with genetic algorithms, fast fourier transform technique, artificial neural network, and hidden markov model.

4.1 Genetic Algorithm

The Genetic algorithm is machine learning approach which was first proposed by J. H. Holland which applies the principles of evolution found in nature. It has no direct relation with biology since it was invented by computer scientists. Genetic algorithms are suitable for solving problems that need optimization to produce near to close and approximate solutions. In genetic algorithms, each potential solution to a problem is represented in the form of a string, which contains parameters of the solution. A string is either chromosome or an individual, while a parameter refers to an attribute [45]. A group of strings constitute the population. The degree of goodness of a string is measured by defining a fitness function. Fitness function calculation is based on in-frame hexamer frequency and positional weight matrix using site and content statistics. Furthermore the formation of a new population of strings for the next generation is further created by applying genetic operators (crossover and mutation) on the few strings, chosen from the population. The process of selection, crossover and mutation are repeated in each of the subsequent generations until a termination condition is reached [45]. In other words, genetic algorithms are mainly based on the principle of 'survival of the fittest'.

The basic genetic algorithm is represented by flow chart in Fig. 2 and can be summarized in a few simple steps as follows:

(i) Start with n number of random population of chromosomes.
(ii) Validate the fitness of each chromosome.
(iii) Create the new population by selection based on fitness, making crossover of each chromosome for a better offspring and mutate the offspring at each chromosome position. Finally evaluate the fitness of the new population.
(iv) If the end condition is met, return the highest scoring member as the solution, if not then repeat the entire process.

In 2001, first attempt was made to use genetic algorithm as a main tool for gene prediction [46]. Genetic algorithm (GA) is also used in ANN software programme to decide about the network architecture, and fitness of the hidden layers of artificial neural network. GA is also used for recognizing promoter regions of eukaryotic genes in *Drosophila melanogaster* [47] as well as it used for generating the multiple sequence alignment [43] and splice site prediction [48]. GA is also used in one algorithmic framework called EFFECT for automated detection of functional

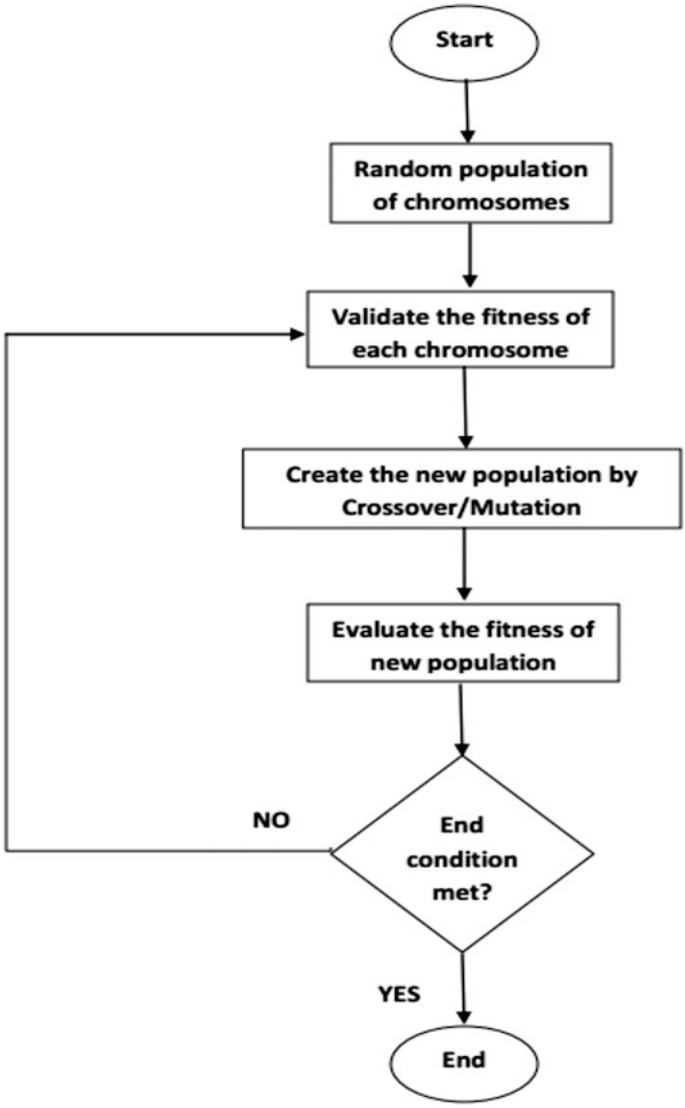

Fig. 2 Systematic diagram of genetic algorithm in stepwise manner

signals in biological sequence which could be useful for gene prediction from DNA sequences [49]. An advantage of genetic algorithms over other methods is that movement from one generation to another generation is very fast and abrupt. The major disadvantage of genetic algorithm is that it is biased towards fit individuals which reproduce more quickly than less fit which finally results in the population of similar individuals.

4.2 Fast Fourier Transform

Fast Fourier transform (FFT) is a technique which is based on a distinctive characteristic feature of protein-coding regions of DNA sequences which is known as the three-base periodicity in the nucleotide arrangement. This feature is illustrated as a sharp peak at a particular frequency in fourier spectrum. The significance of Fourier analysis for identification of protein-coding genes in DNA sequence has been well recognized [50]. The basic FFT can be summarized in a few simple steps which are shown in flow chart below (Fig. 3).

From extensive spectral analysis of DNA sequences for various organisms, the relative height of the peak in the Fourier spectrum is indicator of coding region. These features could be utilized for detecting probable coding regions in DNA sequences. GENESCAN has emerged as one of the popular gene prediction programmes utilizing three-base periodicity based Fourier transformation [51]. FFT is more efficient in detecting the periodicity in a longer sequence in comparison to shorter sequences. In order to overcome this limitation of FFT, an algorithm called LENGTHENS– SHUFFLE has been discovered [52]. FTG is a web server for analyzing nucleotide sequences to predict the genes using Fourier transform techniques which uses Genescan and LENGTHEN–SHUFFLE algorithms to improve the accuracy of gene prediction [53]. FFT has the advantage over other methods

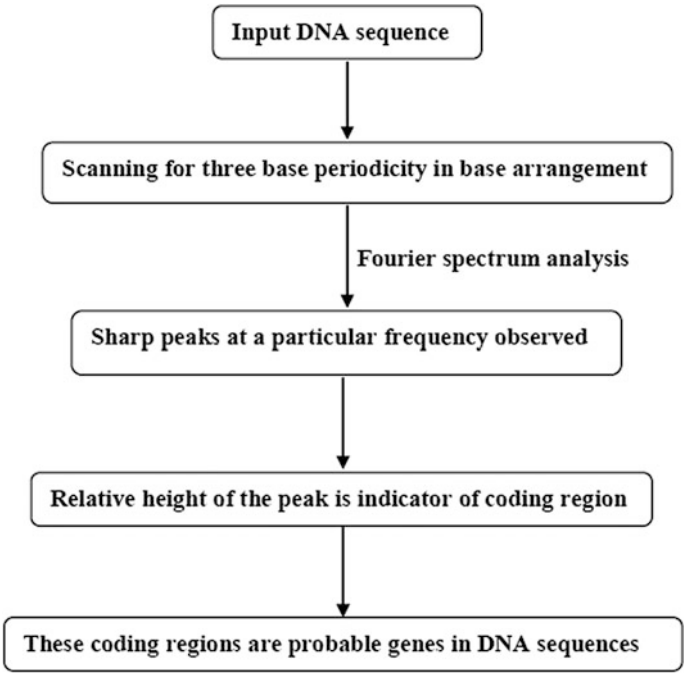

Fig. 3 Systematic diagram of Fast Fourier transform in gene prediction in stepwise manner

like Markov models, neural networks and homology-based methods. FFT does not require a learning set as compared to other gene prediction tools, thus facilitates the identification of a protein-coding gene with no known homolog.

4.3 *Artificial Neural Network*

Artificial neural network (ANN) is a soft computing tool which process information that is used to represent complex input–output relationships. ANN algorithm is basically a tool which has an ability to learn. The key element of the ANN model is the novel structure of the information processing system. Gene prediction programs applied to various organisms, based on Artificial Neural Network (ANN) method along with their webpage's URL are listed in Table 1. Being an interconnected group of artificial neurons ANN is known to be composed of many highly interconnected processing elements which are tied together with weighted connections that are analogous to synapses [54]. ANN is successfully applied to solve a variety of problems of biological importance such as gene identification as well as protein structure prediction [55]. Neural network is basically represented as multiple layers of neurons in parallel which score an exon candidate present in the gene which are based on local information. Apart from neural network scores, the final exon prediction requires more global information, such as whether exon candidates are spliceable or not. The architecture of a neural network is usually either feed-forward or recurrent. A feed-forward network doesn't have loops and are acyclic, where the information moves in only one direction, from the input nodes to hidden layers, and finally to output nodes. On the other hand, its counterpart, recurrent networks, contain cycles. One node is connected from other node or layers with some weights based on the training data. Suppose the input values x1, … ,xN in input layer are fed into the node through edges and associated weights are suppose w1, … ,wN then integration score (a) will be as follows:

$$a = \sum_{i=1}^{N} wix_i \tag{1}$$

Table 1 List of gene prediction programs applied to genomes of various organisms, based on Artificial Neural Network (ANN) method along with their webpage's URL

Software programme and their webpage URL	Organisms
GRAILExp [41, 56] http://compbio.ornl.gov/grailexp/	Bacteria and Eukaryotes
NetStart [57] http://www.cbs.dtu.dk/services/NetStart/	Eukaryotes
Grail-II [38] http://compbio.ornl.gov/	Eukaryotes
NetAspGene [58] http://www.cbs.dtu.dk/services/NetAspGene/	*Aspergillus* sp. (Eukaryote)

Equation (1) integration score (a) where are xi represent input values and wi represent the associated weights.

The basic architecture of ANN can be presented as in the following block diagram as shown in Fig. 4.

This gives a total score of input layer to hidden layer. Similarly weights are calculated for hidden layers and their edges. The final score associated with output layer is sum of all theses scores. Most of the applications in computational biology/bioinformatics e.g., gene prediction, protein secondary structure prediction etc. use layered feed-forward network models. The use of Neural network for gene prediction started with the introduction of GRAIL (gene recognition and analysis internet link) in 1991. GRAIL scores potential exons by combining the scores of a number of content and signal sensors. The GRAIL neural network consists of 13 input nodes, two hidden layers with seven and three nodes, respectively, and one output node. GRAIL is available in two versions: GRAIL-I [37] and GRAIL-II [38]. GRAIL-II finds the protein coding regions, poly (A) sites, promoters, constructs gene models, predicts gene and provides database searching capability. Input for GRAIL-II includes several indicators of sequence patterns. These important indicators are scores of 6mer in the flanking region, in-frame-6mer score, flanking region GC composition, markov model score and candidate region GC composition. In GRAIL-II, DNA sequence is evaluated by calculating the pattern frequencies in terms of values 0 and 1 in neural network. If the value is close to 1, then the region is predicted as exon and if the value is close to 0 then the region is termed as intron. Homology information has been incorporated into GrailExp (latest

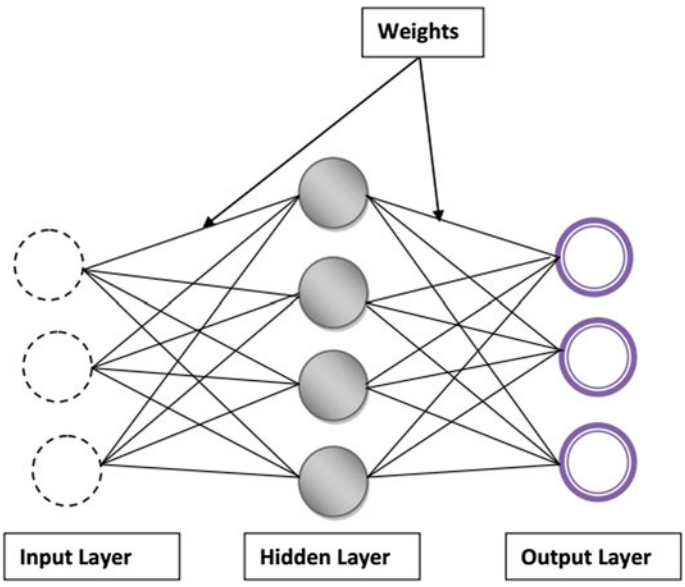

Fig. 4 Schematic diagram of feed forward neural network

version of GRAIL) which resulted in improved performance [41, 56]. GrailEXP provides gene models as well as alternatively spliced constructs for each gene by making use of sequence similarity with Expressed Sequence Tags (ESTs) and known genes [56]. GrailEXP is a software package that predicts exons, genes, promoters, polyas, CpG islands, EST similarities, and repetitive elements within DNA sequence. NetStart [57] is another gene prediction programme based on artificial neural networks to predict the start codon in an mRNA sequence. NetAspGene also uses multiple artificial neural networks to predict both exon/intron gene structure and splice sites by a combined algorithm [58].

4.4 Hidden Markov Model

Markov models, due to their flexibility emerged as popular model where most processes can be approximated by a Markov chain. Markov chain is a random process where the next jump only depends on the current state, and not on the previous state.

A sequence of random variables X_1, X_2, X_3… which pick values in a countable set Q, is called a Markov chain of order $k \geq 1$ if for all $i > k$ and all x_1, x_2, x_3 …, $xi \in Q$.

$P(X_i = x_i | X_1 = x_1, \ldots, X_{i-1} = x_{i-1}) = P(X_i = x_i | X_{i-k} = x_{i-k}, \ldots, X_{i-1} = x_{i-1})$. If $P(X_i = x_{k+1} \mid X_{i-k} = x_1, \ldots, X_{i-1} = x_k)$ does not depend on i ($x_1, \ldots, x_{k+1} \in Q$), sequence is called a homogenous markov chain.

Markov model is a well studied soft computing tool which is extended further to Hidden markov model (HMM). A standard Markov model basically consists of various states. HMM comprises of two interrelated random processes, a hidden process and an observed process. HMM is a probabilistic model which was first developed for speech recognition. A major problem with standard HMM is the intrinsic modeling of duration of states which is sometimes exponential. Thus it is unsuitable for many applications and is rectified by a Generalized HMM (GHMM) where length distribution is defined by us [24]. Another extension of markov model is called as Interpolated Markov Model (IMM) in which the order of the model is not fixed.

Nowadays, HMMs have become an integral part of bioinformatics having applications in protein and DNA sequence pattern recognition, multiple sequence alignment and sequence evolution. In gene finding, it consists of states corresponding to a biological significance (e.g. intron, exon, splice site) which allows transitions between these states. The model defines a probability distribution of strings like DNA sequences and gene structure as well as the transition probabilities between them using a training set of annotated sequences for respective species [44]. Markov models are ‘hidden’ when one or more states cannot be observed directly.

One of the examples of a HMM model is a machine that generates a DNA sequence. In this example, the four states A, T G and C in a set S = {A, C, G, T}

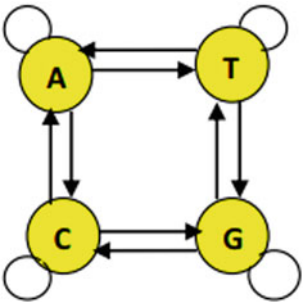

Fig. 5 Four states are shown by A, C, G, and T in the DNA alphabet. *Arrows* indicate the transition from one state to another where each *arrow* is also associated with transition probability

are represented as circles and the arrows between them represent the transitions between theses states which is shown in Fig. 5. The machine starts with any state then moves to new state according to transition probabilities. Model parameters are known by counting the number of times a particular state is followed by another state. Number of times of a particular state corresponds to frequency of single and dinucleotide states which further help in prediction of the next nucleotide in the DNA sequence.

Various gene finding tool which are accurate for prokaryotic gene finding are based on hiden markov model algorithms. Gene prediction programs applied to various organisms based on Hidden Markov Model (HMM) method along with their webpage's URL has been listed in Table 2.

Table 2 List of gene prediction programs applied to genomes of various organisms, based on Hidden Markov model (HMM) method along with their webpage's URL

Software programs and their webpage URL	Organisms
GeneMark [90] http://opal.biology.gatech.edu/GeneMark/	Bacteria, Archaea, Eukaryotes and Viruses
Glimmer [91] https://ccb.jhu.edu/software/glimmer/	Bacteria, Archaea and Viruses
AMIGene [61] http://www.genoscope.cns.fr/agc/tools/amiga/Form/form.php	Bacteria
FGENESH [92] http://www.softberry.com/berry.phtml?topic=fgenesh&group=help&subgroup=gfind	Eukaryotes
GenScan [24] http://genes.mit.edu/GENSCAN.html	Eukaryotes
FragGeneScan reads [59] http://omics.informatics.indiana.edu/FragGeneScan/	Prokaryotes
HmmGene [26] http://www.cbs.dtu.dk/services/HMMgene	*Homo Sapiens, C. elegans*
Genemark.hmm [93] http://intron.biology.gatech.edu/GeneMark	Bacteria
EasyGene [62] http://www.cbs.dtu.dk/services/EasyGene	Prokaryotes
WebAUGUSTUS [50, 95] http://bioinf.uni-greifswald.de/webaugustus	Eukaryotes

The Genie program was the first gene prediction tool which introduced HMM for gene prediction. AUGUSTUS is another gene prediction programme based on HMM which performed significantly better for long DNA sequences compared to programmes based on ab initio methods [44]. The GeneMark.hmm is another HMM based algorithm designed for the advancement of gene prediction quality in terms of finding exact gene boundaries as compared to older version called GeneMark [40]. GeneMark.hmm and GeneMark have complementary properties i.e. genes missed by GeneMark.hmm may be identified by GeneMark. Partial gene predictions which are made by GeneMark might also be corrected by GeneMark.hmm as well. GLIMMER (Gene Locator and Interpolated Markov ModelER) is another gene prediction program which uses interpolated Markov models to identify coding regions in microbial DNA. GLIMMER basically consists of two submodules. One of the submodules builds the IMM from training data while another submodule uses the resulting model to score new sequences [41]. HMMgene is also based on a hidden Markov model which predicts whole genes correctly [26]. Gene prediction tools which are developed for whole genomes (e.g. Glimmer) and metagenomic sequences showed a significant decline in performance due to increase in sequencing error rates. FragGeneScan which is comparable to Glimmer and MetaGene for complete genomes is also based on HMM. FragGeneScan combines sequencing error models as well as codon usages to improve the prediction of protein coding region in short reads [59]. GeneWise [34] combines a gene-prediction HMM with the protein-profile HMM (Pfam) in order to achieve simultaneous gene prediction and alignment. However it predicts accurately one gene per genomic sequence. Multiple genes prediction on both strands was initially implemented in Genscan. Later on it was also adopted by other HMM-based algorithms, such as GeneMark and Fgenes. It is better to consider both strands simultaneously in order to avoid the prediction of genes that overlap on the two strands as two separate genes in mammalian genomes [60]. Annotation of MIcrobial Genes (AMIGene) is another prediction tool which automatically identifies the coding sequences (CDs) in completely sequenced bacterial genome sequence. Construction of Markov models that fit the input genomic data (i.e. the gene model) is followed by the combination of known gene finding programmes and a heuristic approach for the selection of the most likely CDs [61]. EasyGene is another example of gene prediction tool which is based on HMM which automatically estimates the new genome by checking similarities in Swiss-Prot, where a high quality training set of genes is automatically extracted from the genome [62]. SnowyOwl is a new gene prediction tool which was developed for rapid and accurate prediction of the genes which uses RNA-Seq data to train as well as to provide clues for the generation of Hidden Markov Model (HMM)-based gene predictions [63]. These HMM based programs not only predicts gene or exon regions but can also predict model promoters, poly(A) signals and the 5′ UTRs or 3′ UTRs (including possible introns). Many programs such as Fgenesh, GeneMark, Genie, Genscan, HMMgene, Morgan and MZEF were the programmes which were tested on 195 newly sequenced genomes. Accuracy level of gene prediction about $\sim$70–90 % at the nucleotide level and $\sim$40–70 % at the exon level were showed by these two gene prediction tools [64].

5 Hybrid Soft Computing Approaches for Gene Prediction

These methods combine two or more machine learning tools or algorithms to solve a problem. Use of hybrid methods is very popular nowadays due to many reasons. Hybrid methods improve the performance of any single method used for gene prediction. Another important reason for using hybrid method is that it improves the quality of the solutions obtained by any single methods such as genetic algorithm, dynamic programming or artificial neural network. The last reason for using hybrid methods is that these hybrid methods can be used for larger systems.

The program GeneParser is a hybrid gene prediction method which scores the sequence of interest for splice sites and for introns and exon specific content sensors such as codon usage, local compositional complexity, 6-tuple frequency, length distribution and periodic asymmetry. GeneParser based on dynamic programming [65] is used to predict the position of introns and exons adjacent and non overlapping to each other in entire sequence length. Dynamic programming (DP) basically aligns sequences to obtain a most likely alignment for a given scoring system with scores for matches, mismatches and gaps. GAZE [66] and GeneBuilder [67] are popular gene prediction programmes which are based on dynamic programming. GeneParser uses dynamic programming along with feed forward artificial neural network which are used to generate likelihood score for each sequence position either in exon or in intron and also predicts the most likely combination of exons and introns in the entire sequnce. In GeneParser, weights are calculated by feed forward artificial neural network which increases the number of correct predictions by the gene prediction programme [41].

mGene is a hybrid method which combines the flexibility of generalized hidden Markov models (gHMMs) with Support Vector Machines (SVMs). The combination of these two algorithms showed the excellent performace for the genome of the nematode *Caenorhabditis elegans* [68]. Support vector machines (SVMs) [69] are supervised machine learning algorithm with a strong theoretical foundation typically used in regression and binary classification problems [70]. The idea of SVMs is to identify the boundary that best separates the two classes. SVM has been used to improve classification accuracy in biological research such as the detection of protein family members [71], RNA and DNA binding proteins [72], functional classification of gene expression data [73] and gene prediction. MetaGun is one of the popular gene prediction programme based on support vector machines [74]. SVMs also accurately discriminated cytoplasmic ribosomal protein encoding genes from all other genes of a known function in *Saccharomyces cerevisiae, Escherichia coli* and *Mycobacterium tuberculosis*. SVM separates two different types of genes based on codon composition comprising of a fusion of codon usage bias and amino acid composition [75].

Another hybrid method is GISMO (Gene Identification using a Support Vector Machine for ORF classification), which also combines the feature of HMM for searching the protein domains. GISMO combines support vector machine along

with HMM which is used for composition based identification of protein-encoding genes [76]. HMM is also used in finding the genes with new order of protein domains in different proteins. GISMO was evaluated with 165 prokaryotic chromosomes and 223 plasmid sequences. The results obtained by GISMO showed 94.3 % of the genes (98.9 % for genes with annotated function) corresponding to annotated genes [76].

MORGAN (Multi-frame Optimal Rule-based Gene ANalyzer) is another hybrid gene finding tool that combines decision trees with dynamic programming and signal sensor algorithms. Decision trees are simple but powerful soft computing technique which identifies various ways of splitting a data set into branch like segments. An advantage of decision tree algorithm is that it converts complex data sets into simple and comprehensible data structures. However, decision tree technique doesn't guarantee to find the optimal solution. Depending on features considered, there are many ways to build a decision tree from the same training data set. Decision tree is also used alone to predict genes in many programmes e.g. C4.5 [77] and Jigsaw [78]. Decision trees were also used to predict *S. cerevisiae* gene which could be up or down regulated under different conditions of transcription regulator expression [79]. MORGAN also uses dynamic programming algorithm to search the entire sequence. In MORGAN, scoring is done by decision tree algorithm as well as by signal sensors which score the exons of potential candidate gene [80].

Gene prediction based on hybrid approach is named as Radial Basis Function Network (RBFN)-combining method. It uses genetic algorithm along with artificial neural network for the prediction of exon regions in the DNA sequence [81]. This hybrid method combined three different gene finding tools having different sequence based features to increase the accuracy. At the first stage high prediction tools like GenScan, HMMgene and Glimmer were used. After that genetic algorithm (GA) was used to calculate the equitable weighted parameters. Finally, these results obtained by different tools were used to train RBFN [81].

ZUPLS is another effective linear hybrid method which uses Z-curve and other sequence-based features. The main aim of ZUPLS was to improve the accuracy and speed for identification of prokaryotic genes [82]. ZUPUS includes gene size, frequencies of amino acids as well as codon adaptation index features in order to predict the potential candidate gene. These features can be calculated immediately from the DNA/amino acid sequences which are used as input. In predicting the essential genes of newly sequenced species, ZUPLS was found better as compared to the other existing approaches [82].

Another hybrid method called Anti-notch/Goertzel algorithm for gene prediction were found faster in predicting the potential candidate gene as compared to other conventional methods. This hybrid method identified the coding protein regions more accurately by Goertzel algorithm. This hybrid algorithm was evaluated for several genes which also include genes available in databases BG570 and HMR195. These results are compared to Discrete Fourier Transform (DFT) and Multi-Stage Filter (MS) methods which showed better performance measured by specificity and approximate correlation (AC) values and lower computational time [83].

Table 3 List of gene prediction programs applied to genomes of various organisms, based on hybrid soft computing methods along with their webpage's URL

Software programme and their webpage URL	Algorithms	Organisms
mGene.web [94] http://www.mgene.org/web	HMM + SVM	Eukaryotes
GeneParser [41] http://stormo.wustl.edu/gslab/?page_id=376	DP + ANN	Eukaryotes
GISMO [76] http://www.CeBiTec.Uni-Bielefeld.DE/groups/brf/software/gismo.	HMM + SVM	Prokaryotes
MORGAN [78] http://www.cbcb.umd.edu/∼salzberg/morgan.html	DP + Decision Tree	Eukaryotes

Along with the hybrid method, nowadays next generation sequencing technologies have become one of the important tools for disease-gene identification especially in human [84–87]. A number of gene prediction programs applied to genomes of various organisms based on hybrid soft computing methods are listed in Table 3.

6 Gene Predictions Accuracy

Coding nucleotide sequence, gene structure and protein as product are three different levels which are used frequently for determining the accuracy of gene prediction programmes. Very few programmes predict complete gene structure accurately for genes which have many exons in their structure. Sensitivity and specificity are the two popular parameters which are used to evaluate the performance of many gene prediction programs [54]. This section focuses on measuring the accuracy of the programs based on exon and nucleotide level. The evaluation of gene prediction program is mainly based on a number of true positives (where the gene length and end sequence positions are correctly predicted), false positives (where the positive predictions are over-predicted), true negative (TN) and false negatives (where the predictions are either under predicted or missed one). Sensitivity and specificity [24, 64, 88] at nucleotide level are defined as follows:

$$\text{Sensitivity} = \frac{TP}{TP + FN} \tag{2}$$

Equation (2) Sensitivity where, TP is the true positive and FN is the false negatives.

$$\text{Specificity} = \frac{TP}{TP + FP} \tag{3}$$

Equation (3) Specificity where TP is the true positives and FP is the false positives.

Another method for evaluation of gene prediction programs at nucleotide level is called Correlation Coefficient (CC). By this coefficient, all correct predictions would score 1, and worst prediction will score 0 [64, 88]. Correlation Coefficient can be calculated by following equation.

$$\mathrm{CC} = [(TP)(TN) - (FP)(FN)/[(AN)(PP)(AP)(PN)] \tag{4}$$

Equation (4) Correlation Coefficient (CC), where, AN (Actual Negatives) = FP + TN, PP (Predicted Positives) = TP + FP, AP (Actual Positives) = TP + FN, PN (Predicted Negatives) = TN + FN.

Another measure called Approximate Correlation (AC) [64, 88], can be represented by following equation

$$\mathrm{AC} = (ACP - 0.5) * 2 \tag{5}$$

Equation (5) Approximate Correlation (AC) where

$$\mathrm{ACP} = \frac{1}{4}\left(\frac{TP}{TP+FN} + \frac{TP}{TP+FP} + \frac{TN}{TN+FP} + \frac{TN}{TN+FN}\right) \tag{6}$$

Equation (6) ACP where, AN (Actual Negatives) = FP + TN, PP (Predicted Positives) = TP + FP, AP (Actual Positives) = TP + FN, PN (Predicted Negatives) = TN + FN.

This coefficient is similar to CC and this could also be used as evaluation of gene prediction programme. All correct predictions would score 1, and worst prediction will score −1 [64, 88].

Nucleotide level accuracy mainly measures the content element of the program while exon level prediction accuracy measures signal element of the programme. Exon level prediction is also estimated by similar methods which are sensitivity and specificity [64].

$$\mathrm{Sensitivity} = \frac{TE}{AE} \tag{7}$$

Equation (7) Sensitivity, where TE = True exons which is the number of exactly predicted exons, AE = Annotated exons.

$$\mathrm{Specificity} = \frac{TE}{PE} \tag{8}$$

Equation (8) Specificity where TE = True exons which is the number of exactly predicted exons, PE = Predcited exons.

Rogic et al. analyzed seven recently developed programs FGENES, GeneMark.hmm, Genie, Genscan, HMMgene, Morgan and MZEF which use only coding and signal information for computational gene prediction [89]. They used a dataset named HMR195 containing 195 sequences with single-exon or multi-exons genes

from *Homo sapiens*, *Mus musculus* and *Rattus norvegicus*. HMR195 dataset is available at http://www.cs.ubc.ca/~rogic/evaluation/dataset.html. It was observed that new generations of programs possess significantly higher accuracy than the programs analyzed by Burset and Guigo [88]. Based on the HMR195 datasets, results showed that approximate correlation value has improved from 0.78 (FGENEH) to 0.91 (Genscan and HMMgene) i.e. 13 %. Exon sensitivity and specificity has improved from 0.64 (FGENEH) to 0.76 (HMMgene) i.e. 12 % based on the results from HMR195 dataset.

7 Conclusion

Gene-prediction soft computing approaches have been steadily improving by various machine learning soft computing techniques but by the introduction of hybrid soft computing approaches computational gene prediction methods accuracy has improved dramatically. High-throughput experimental approaches to identify genes are still lacking which in turn inspire the bioinformatics/computational biologist to predict the genes computationally. Bioinformatics is driven mainly by integration of information technology with the large scale genomic data but still automated accurate gene prediction pipelines for whole genomes are lacking. Identifying short exons and prediction of very long exons as well as non-translated exons are still a challenging task for bioinformatician/computational biologist. Still, multiple genes are not accurately predicted by many soft computing approaches due to lack our understanding of various factors which should be taken care of during algorithm development. Computational prediction of alternatively spliced gene products is also a major concern that still needs to be extensively explored by computational biologist or bioinformatics researchers for accurate prediction owing to its importance as a significant regulatory mechanism in higher eukaryotes.

References

1. Venter, J.C., et al.: The sequence of the human genome. Science **291**(5507), 1304–1351 (2001)
2. Loha, S.K., Lowa, S.T., Mohamada, M.S., et al.: A review of software for predicting gene function. Int. J. Bio-Sc. Bio-Tech. **7**(2), 57–70 (2015)
3. Lewin, B.: Genes. Pearson Prentice Hall, New Jersey (2004)
4. Wang, Z., Chen, Y., Li, Y.: A brief review of computational gene prediction methods. Genomics, Proteomics Bioinform. **2**, 216–221 (2004)
5. Palleja, A., Harrington, E.D., Bork, P.: Large gene overlaps in prokaryotic genomes: result of functional constraints or mispredictions? BMC Genom. **9**, 335 (2008)
6. Xiong, J.: Essential Bioinformatics. Cambridge University Press, New York (2006)
7. Fickett, J.W.: ORFs and genes: how strong a connection? J. Comput. Biol. **2**, 117–123 (1995)
8. Ramakrishna, R., Srinivasan, R.: Gene identification in bacterial and organellar genomes using GeneScan. Comp. Chem. **23**, 165–174 (1999)

9. Hyatt, D., Chen, G.L., Locascio, P.F.: Prodigal: prokaryotic gene recognition and translation initiation site identification. BMC Bioinform. **11**, 119 (2010)
10. Schellenberg, M.J., Ritchie, D.B., MacMillan, A.M.: PremRNA splicing: a complex picture in higher definition. Trends Biochem. Sci. **33**(6), 243–246 (2008)
11. Frishman, D., Mironov, A., Gelfand, M.: Starts of bacterial genes: estimating the reliability of computer predictions. Gene **234**, 257–265 (1999)
12. Allen, J.E., Pertea, M., Salzberg, S.L.: Computational gene prediction using multiple sources of evidence. Genome Res. **14**, 142–148 (2004)
13. Fickett, J.W., Hatzigeorgiou, A.G.: Eukaryotic promoter prediction. Genome Res. **7**, 861–878 (1997)
14. Prestridge, D.S.: Predicting pol II promoter sequences using transcription factor binding sites. J. Mol. Bio. **249**, 923–932 (1995)
15. Sharp, P.A., Burge, C.B.: Classification of introns: U2-type or 1.112-type. Cell **91**, 875–879 (1997)
16. Minoche, A.E., Dohm, J.C., Schneider, J., et al.: Exploiting single-molecule transcript sequencing for eukaryotic gene prediction. Genome Biol. **16**, 184 (2015)
17. Rawat, V., Abdelsamad, A., Pietzenuk, B., et al.: Improving the Annotation of *Arabidopsis lyrata* Using RNA-Seq Data. PLoS ONE **10**(9), e0137391 (2015)
18. Testa, A.C., Hane, J.K., Ellwood, S.R., et al.: CodingQuarry: highly accurate hidden Markov model gene prediction in fungal genomes using RNA-seq transcripts. BMC Genom. **16**, 170 (2015)
19. Wang, Y., Chen, L., Song, N., et al.: GASS: genome structural annotation for Eukaryotes based on species similarity. BMC Genom. **16**, 150 (2015)
20. Mühlhausen, S., Kollmar, M.: Predicting the fungal CUG codon translation with Bagheera. BMC Genom. **15**, 411 (2014)
21. Staden, R., McLachlan, A.D.: Codon preference and its use in identifying protein coding regions in long DNA sequences. Nucleic Acids Res. **10**(1), 141–156 (1982)
22. Lewis, S., Ashburner, M., Reese, M.G.: Annotating eukaryote genomes. Curr. Opin. Struc. Biol. **10**, 349–354 (2000)
23. Mathe, C., Sagot, M.-F., Schiex, T., et al.: Current methods for gene prediction, their strengths and weakness. Nucleic Acid Res. **30**(19), 4103–4117 (2002)
24. Burge, C., Karlin, S.: Prediction of complete gene structures in human genomic DNA. J. Mol. Biol. **268**, 78–94 (1997)
25. Kulp, D., Haussler, D., Reese, M.G., et al.: A generalized hidden Markov model for the recognition of human genes in DNA. In: Proceedings of the International Conference on intelligent Systems for Molecular Biology, vol. 4, pp. 134–142 (1996)
26. Krogh, A.: Two methods for improving performance of an HMM and their application for gene-finding. In: Proceedings of the International Conference on intelligent Systems for Molecular Biology (ISMB '97), vol. 5, pp. 179–186 (1997)
27. Parra, G., Blanco, E., Guigó, R.: GeneID in Drosophila. Genome Res. **10**, 391–393 (2000)
28. Khandelwal, G., Jayaram, B.: Phenomenological model for predicting melting temperatures of DNA sequences. PLoS ONE **5**(8), e12433 (2010)
29. Borodovsky, M., Rudd, K.E., Koonin, E.V.: Intrinsic and extrinsic approaches for detecting genes in a bacterial genome. Nucleic Acids Res. **22**(22), 4756–4767 (1994)
30. Down, T.A., Hubbard, T.J.P.: Computational detection and location of transcription start sites in mammalian genomic DNA. Genome Res. **12**, 458–461 (2002)
31. Mathé, C., Peresetsky, A., Déhais, P., Van Montagu, M., et al.: Classification of *Arabidopsis thaliana* gene sequences: clustering of coding sequences into two groups according to codon usage improves gene prediction. J. Mol. Biol. **285**, 1977–1991 (1999)
32. Bailey, L.C., Searls, D.B., Overton, G.C.: Analysis of EST driven gene annotation in human genomic sequence. Genome Res. **8**, 362–376 (1998)
33. Bucher, P.: Weight matrix descriptions of four eukaryotic RNA polymerase II promoter elements derived from 5' unrelated promoter sequences. J. Mol. Biol. **212**, 563–578 (1990)

34. Birney, E., Durbin, R.: Using GeneWise in the Drosophila annotation experiment. Genome Res. **10**, 547–548 (2000)
35. Yeh, R.-F., Lim, L.P., Burge, C.B.: Computational inference of homologous gene structures in the human genome. Genome Res. **11**, 803–816 (2001)
36. Snyder, E.E., Stormo, G.D.: Identification of protein coding regions in genomic DNA. J. Mol. Biol. **248**, 1–18 (1995)
37. Uberbacher, E.C., Mural, R.J.: Locating protein-coding regions in human DNA sequences by a multiple sensor-neural network approach. Proc. Natl. Acad. Sci. U.S.A. **88**, 11261–11265 (1991)
38. Xu, Y., Einstein, J.R., Shah, M., et al: An improved system for exon recognition and gene modeling in human DNA sequences. In: Proceedings of the International Conference on intelligent Systems for Molecular Biology, pp. 376–383. AAAI/MIT Press (1994)
39. Yandell, M., Ence, D.: A beginner's guide to eukaryotic genome annotation. Nat. Rev. Genet. **13**, 329–342 (2012)
40. Thomas, A., Skolnick, M.H.: A probabilistic model for detecting coding regions in DNA sequences. IMA J. Math. Appl. Med. Biol. **11**, 149–160 (1994)
41. Snyder, E.E., Stormo, G.D.: Identification of protein coding regions in genomic DNA. J. Mol. Biol. **248**, 1–18 (1995)
42. Solovyev, V.V., Salamov, A.A., Lawrence, C.B.: Predicting internal exons by oligonucleotide composition and discriminant analysis of spliceable open reading frames. Nucleic Acids Res. **22**(24), 5156–5163 (1994)
43. Notredame, C., Higgins, D.G.: SAGA: sequence alignment by genetic algorithm. Nucleic Acids Res. **24**, 1515–1524 (1996)
44. Stanke, M., Waack, S.: Gene prediction with a hidden Markov model and a new intron submodel. Bioinformatics **19**(2), ii215–ii225 (2003)
45. Ooi, C.H., Tan, P.: Genetic algorithms applied to multi-class prediction for the analysis of gene expression data. Bioinformatics **19**(1), 37–44 (2003)
46. Perez-Rodriguez, J., Garcia-Pedrajas, N.: An evolutionary algorithm for gene structure prediction. In: Industrial Engineering and Other Applications of Applied Intelligent Systems II, vol. 6704, pp. 386–395. Springer, Heidelberg (2011)
47. Levitsky, V.G., Katokhin, A.V.: Recognition of eukaryotic promoters using a genetic algorithm based on iterative discriminant analysis. In Silico Biol. **3**(1–2), 81–87 (2003)
48. Kamath, U., Compton, J., Islamaj-Doğan, R., et al.: An evolutionary algorithm approach for feature generation from sequence data and its application to DNA splice site prediction. IEEE/ACM Trans. Comput. Biol. Bioinform. **9**(5), 1387–1398 (2012)
49. Kamath, U., Jong, K.E., Snehu, A.: Effective automated feature construction and selection for classification of biological sequences. PLoS ONE **9**(7), e99982 (2014)
50. Fickett, J.W., Tung, C.-S.: Assessment of protein coding measures. Nucleic Acids Res. **20**(24), 6441–6450 (1992)
51. Tiwari, S., Ramachandran, S., Bhattacharya, A., et al.: Prediction of probable genes by fourier analysis of genomic sequences. Bioinformatics **13**(3), 263–270 (1997)
52. Yan, M., Lin, Z.-S., Zhang, C.-T., et al.: A new fourier transform approach for protein coding measure based on the format of the Z curve. Bioinformatics **14**(8), 685–690 (1998)
53. Issac, B., Singh, H., Kaur, H., et al.: Locating probable genes using Fourier transform approach. Bioinformatics **18**(1), 196–197 (2002)
54. Goel, N., Singh, S., Aseri, T.C.: A review of soft computing techniques for gene prediction. ISRN Genom **2013**, 191206 (2013)
55. Wu, C.H.: Artificial neural networks for molecular sequence analysis. Comput. Chem. **21**(4), 237–256 (1997)
56. Uberbacher, E.C., Hyatt, D., Shah, M.: GrailEXP and genome analysis pipeline for genome annotation. Current Protocols in Bioinformatics. Chapter 4, unit 4.9, pp. 4.9.1–4.9.15 (2004)
57. Pedersen, A.G., Nielsen, H.: Neural network prediction of translation initiation sites in eukaryotes: perspectives for EST and genome analysis. In: Proceedings of the International Conference on intelligent Systems for Molecular Biology, vol. *5*, pp. 226–233 (1997)

58. Wang, K., Ussery, D.W., Brunak, S.: Analysis and prediction of gene splice sites in four Aspergillus genomes. Fungal Genet. Biol. **46**(1), S14–S18 (2009)
59. Rho, M., Tang, H., Ye, Y.: FragGeneScan: predicting genes in short and error-prone reads. Nucleic Acids Res. **38**(20), e191 (2010)
60. Zhang, M.Q.: Computational prediction of eukaryotic protein-coding genes. Nat. Rev. Genet. **3**, 698–709 (2002)
61. Bocs, S., Cruveiller, S., Vallenet, D., et al.: AMIGENE: annotation of microbial genes. Nucleic Acids Res. **31**(13), 3723–3726 (2003)
62. Larsen, T.S., Krogh, A.: EasyGene a prokaryotic gene finder that ranks ORFs by statistical significance. BMC Bioinform. **4**, 21 (2003)
63. Reid, I., O'Toole, N., Zabaneh, O., et al.: SnowyOwl: accurate prediction of fungal genes by using RNA-Seq and homology information to select among ab initio models. BMC Bioinform. **15**, 229 (2014)
64. Rogic, S., Mackworth, A.K., Ouellette, F.B.F., et al.: Evaluation of gene-finding programs on mammalian sequences. Genome Res. **11**, 817–832 (2001)
65. Guigó, R.: Assembling genes from predicted exons in linear time with dynamic programming. J. Comput. Biol. **5**(4), 681–702 (1998)
66. Howe, K.L., Chothia, T., Durbin, R.: GAZE: a generic framework for the integration of gene-prediction data by dynamic programming. Genome Res. **12**, 1418–1427 (2002)
67. Milanesi, L., D'Angelo, D., Rogozin, I.B.: GeneBuilder: interactive in silico prediction of gene structure. Bioinformatics **15**(7–8), 612–621 (1999)
68. Schweikert, G., Zien, A., Zeller, G., et al.: mGene: accurate SVM-based gene finding with an application to nematode genomes. Genome Res. **19**(11), 2133–2243 (2009)
69. Cortes, C., Vapnik, V.: Support-vector networks. Mach. Learn. **20**(3), 273–297 (1995)
70. Boser, B., Guyon, I., Vapnik, V.N. et al: Proceedings of the 5th Annual ACM Workshop on Computational Learning Theory, pp. 144–152. ACM Press (1992)
71. Hou, Y., Hsu, W., Lee, M.L., et al.: Efficient remote homology detection using local structure. Bioinformatics **19**(17), 2294–2301 (2003)
72. Cai, Y.D., Lin, S.L.: Support vector machines for predicting rRNA-, RNA-, and DNA-binding proteins from amino acid sequence. Biochim. Biophys. Acta **1648**, 127–133 (2003)
73. Brown, M.P.S., Grundy, W.N., Lin, D., et al.: Knowledge-based analysis of microarray gene expression data by using support vector machines. Proc. Natl. Acad. Sci. U.S.A. **97**(1), 262–267 (2000)
74. Liu, Y., Guo, J., Hu, G., Zhu, H., et al.: Gene prediction in metagenomic fragments based on the SVM algorithm. BMC Bioinform. **14**(5), S12 (2013)
75. Lin, K., Kuang, Y., Joseph, J.S., et al.: Conserved codon composition of ribosomal protein coding genes in Escherichia coli, Mycobacterium tuberculosis and Saccharomyces cerevisiae: lessons from supervised machine learning in functional genomics. Nucleic Acids Res. **30**(11), 2599–2607 (2002)
76. Krause, L., McHardy, A.C., Nattkemper, T.W., et al.: GISMO—gene identification using a support vector machine for ORF classification. Nucleic Acids Res. **35**(2), 540–549 (2007)
77. Quinlan J.R C4.5: Programs for Machine Learning. Morgan Kaufmann, San Mateo (1993)
78. Allen, J.E., Majoros, W.H., Pertea, M., et al.: JIGSAW, GeneZilla, and GlimmerHMM: puzzling out the features of human genes in the ENCODE regions. Genome Biol. **7**(1), S9 (2006)
79. Middendorf, M., Kundaje, A., Wiggins, C., et al.: Predicting genetic regulatory response using classification. Bioinformatics **20**(1), i232–i240 (2004)
80. Salzberg, S., Delcher, A.L., Fasman, K.H., et al.: Decision tree system for finding genes in DNA. J. Comput. Biol. **5**, 667–680 (1998)
81. Zhou, Y., Liang, Y., Hu, C., et al.: An artificial neural network method for combining gene prediction based on equitable weights. Neurocomputing **71**(4–6), 538–543 (2008)
82. Song, K., Tong, T., Wu, F., et al.: Predicting essential genes in prokaryotic genomes using a linear method: ZUPLS. Integr. Biol. **6**, 460–469 (2014)

83. Saberkari, H., shamsi, M., Sedaaghi, M.H.: A Hybrid Anti-notch/Goertzel model for gene prediction in DNA sequences. Appl. Med. Inf. **34**(2), 13–22 (2014)
84. Piro, R.M., Di, C.F.: Computational approaches to disease-gene prediction: rationale, classification and successes. FEBS J. **279**(5), 678–696 (2012)
85. Piro, R.M., Ala, U., Molineris, I., et al.: An atlas of tissue-specific conserved coexpression for functional annotation and disease gene prediction. Eur. J. Hum. Genet. **19**, 1173–1180 (2011)
86. Lee, I., Blom, U.M., Wang, P.I., et al.: Prioritizing candidate disease genes by networkbased boosting of genome-wide association data. Genome Res. **21**, 1109–1121 (2011)
87. Yandell, M., Huff, C., Hu, H., et al.: A probabilistic disease-gene finder for personal genomes. Genome Res. **21**, 1529–1542 (2011)
88. Burset, M., Guigo, R.: Evaluation of gene structure prediction programs. Genomics **34**, 353–367 (1996)
89. Rogic, S., Mackworth, A.K., Ouellette, F.B.: Evaluation of gene-finding programs on mammalian sequences. Genome Res. **11**(5), 817–832 (2001)
90. Borodovsky, M., McIninch, J.: GeneMark: parallel gene recognition for both DNA strands. Comput. Chem. **17**(2), 123–133 (1993)
91. Delcher, A.L., Harmon, D., Kasif, S., et al.: Improved microbial gene identification with GLIMMER. Nucleic Acids Res. **27**(23), 4636–4641 (1999)
92. Salamov, A.A., Solovyev, V.V.: Ab initio gene finding in Drosophila genomic DNA. Genome Res. **10**, 516–522 (2000)
93. Lukashin, A.V., Borodovsky, M.: GeneMark.hmm: new solutions for gene finding. Nucleic Acids Res. **26**(4), 1107–1115 (1998)
94. Schweikert, G., Behr, J., Zien, A., et al.: mGene.web: a web service for accurate computational gene finding. Nucleic Acids Res. **37**(2), W312–W316 (2009)
95. Hoff, K.J., Stanke, M.: WebAUGUSTUS—a web service for training AUGUSTUS and predicting genes in eukaryotes. Nucleic Acids Res. **41**(W1), W123–W128 (2013)

Part IV
Bio-inspiring Based Computer Aided Diagnosis Techniques

Artificial Bee Colony Based Segmentation for CT Liver Images

Abdalla Mostafa, Ahmed Fouad, Mohamed Abd Elfattah, Aboul Ella Hassanien and Hesham Hefny

Abstract The objective of this paper is to evaluate an approach for CT liver image segmentation, to separate the liver, and segment it into a set of regions of interest (ROIs). The automated segmentation of liver is an essential phase in all liver diagnosis systems for different types of medical images. In this paper, the artificial bee colony optimization algorithm (ABC) aides to segment the whole liver. It is implemented as a clustering technique to achieve this mission. ABC calculates the centroid values of image clusters in CT images. Using the least distance between every pixel value and different centroids will result in a binary image for each cluster. Applying some morphological operations on every binary clustered image can help to remove small and thin objects. These objects represent parts of flesh tissues adjacent to the liver, sharp edges of other organs and tiny lesions spots inside the liver. This is followed by filling the large regions in each cluster binary image. Summation of the clusters' binary images results in a reasonable image of segmented liver. Then, the segmented image of liver is enhanced using simple region growing technique (RG). Finally, one of ABC algorithm or watershed is applied once to extract the lesioned regions in the liver, which can be used by any classifier to determine the type of lesion. A set of 38 images, taken in pre-contrast phase, was used to segment the liver and test the proposed approach. Testing the results is handled using similarity index to validate the success of the approach. The

A. Mostafa (✉) · H. Hefny
Institute of Statistical Studies and Researches, Cairo University, Giza, Egypt
e-mail: abdalla_mosta75@yahoo.com

A. Fouad
Faculty of Computers and Information, Suez Canal University, Ismailia, Egypt

M.A. Elfattah
Faculty of Computers and Information, Mansoura University, Mansoura, Egypt

A.E. Hassanien
Faculty of Computers and Information, Cairo University, Giza, Egypt

A. Mostafa · A. Fouad · M.A. Elfattah · A.E. Hassanien
Scientific Research Group in Egypt (SRGE), Giza, Egypt

N. Dey et al. (eds.), *Medical Imaging in Clinical Applications*,
Studies in Computational Intelligence 651, DOI 10.1007/978-3-319-33793-7_18

experimental results showed that the overall accuracy offered by the proposed approach, results in 93.73 % accuracy.

Keywords Artificial bee colony optimization · Region growing · Filtering · Segmentation

1 Introduction

Nowadays, many researches have been doing a lot of efforts to support radiologists decision making in liver diagnosis systems. These efforts try to offer a reliable and efficient CAD system. Every CAD system is comprised of some main phases, including image acquisition, preprocessing, segmentation and classification. The phase of preprocessing is interested in the initial preparation of image for next segmentation phase. It includes the process of cleaning the image by removing machine's bed and the annotation of the patient's information. It also includes ribs connection which is a drawn white line to separate the liver from the adjacent flesh and muscles in the left side of the abdominal image. Enhancing liver segmentation is a crucial and difficult task in computer-aided diagnosis systems (CAD). Its difficulty is caused by the similarity between its intensity values and other adjacent organs as kidney, stomach and spleen. The main key of segmentation is the intensity value of the grey image. Hounsfield unit (HU) is a quantitative scale that describes the intensity values used in DICOM images. Its range resides between −1500 and 1500. JPG is the standardized format of the image from the Joint Photographic Experts Group. JPG also has its intensity values that range between 0 and 512. Both of these formats could be implemented here [1]. Artificial bee colony optimization technique (ABC) is used to calculate the centroids of the clusters of different intensities of the image. Each cluster's image is manipulated by morphological operations to remove the small objects. These objects represent parts of dark boundaries between organs, flesh and muscles. The removal of these objects cuts the connection between liver tissues and other organs. All clusters' binary images, except the clusters with highest two centroids, are summed in one image. The summed clusters image is multiplied by the original image. Then, region growing is applied on the resulting image to enhance the result of the segmented liver. ABC is applied once more on the segmented liver to extract the lesioned regions. Also, watershed can be used for extracting ROIs. The evaluation of the accuracy of the proposed system is implemented using similarity index measure.

Liver is the largest organ in the body of an adult. It is a reddish-brown colour organ and weights 1200–1500 grams and anatomically has two lobes with blood vessels (portal vein, inferior vena cava and hepatic artery) and biliary ducts. It is situated under the diaphragm in the upper abdominal cavity. It is held in place by the falciform ligament [2]. It is important to say that, falciform ligament separates liver's lobes as a boundary, which could be a kind of difficulty in segmenting the liver from other regions. Also, some abnormality of liver anatomy may affect the

liver shape as having an accessory lobe, atrophy of the left lobe and cough furrows which is caused by the chronic cough and affects the convexity of the right lobe [3]. In brief, falciform ligament, blood supply and anatomical abnormality of liver affect the segmentation process.

A CT (computed tomography) image is taken by a special scanning machine. It is a kind of X-ray machine. X-ray machine sends a single X-ray through the body. But, CT machine simultaneously, sends several beams, from different angles against the human body. The X-rays from the beams are detected, and their strength is measured. Beams passing through less dense tissue, such as the lungs will be stronger, whereas beams passing through denser tissue, such as bone will be weaker. This way, it is possible for a computer to create an image of different tissues according to its relative density. Each set of measurements made by the scanner is considered a cross-section through the body. It is displayed as a two-dimensional image [4]. CT images have been chosen, because of its reliable details compared with X-ray and its affordability compared with magnetic reasoning image (MRI).

In most CAD systems, preprocessing phase depends on filtering techniques to increase the reliability and accuracy. The inverse contrast and mean filters proved efficiency and reliability to aid the preprocessing process. Inverse contrast is used to aid stressing the ribs, while smoothing mean hides the small details like veins and ligaments [5].

ABC [6] is an intelligent optimization tool used for solving a computational problem in different areas. Honey bees are one of the most well studied social pests. In the early years, many reviews based on the different bee behaviours have been developed to solve compound combinatorial and numerical optimization problems [7].

The artificial bee colony (ABC) is the one which has been most widely studied and applied to solve the real world problems. Gradually the number of researchers being interested in ABC algorithm increases quickly [8]. Karaboga used ABC algorithm (ABC) for solving multi-dimensional and multi-modal optimization problems. He replicates this algorithm for three continuous functions; Sphere function, Rosenbrock function and Rastrigin function. The results reached, had proved a successful optimization for this kind of problems [9].

In [10], ABC is used to search for multiple thresholds. These thresholds are very close to the optimal ones examined by the exhaustive search method. Compared the ABC with other famous algorithms; the hybrid cooperative-comprehensive learning based PSO algorithm (HCOCLPSO), the Fast Otsus method, the honey bee mating optimization (HBMO) and the particle swarm optimization (PSO), ABC achieved the best result.

In [11], a CT liver image diagnostic classification system is presented. It automatically extracts the CT liver boundary and classify liver diseases. This system consists of two phases. First phase finds the liver boundary and second phase uses a modified probabilistic neural network (PNN) [MPNN] in conjunction with feature descriptors, generated by fractal feature information and the grey-level co-occurrence

matrix. This classifies two types of liver tumours, hepatoma and hemangioma. This system provides efficient result based on 30 liver cases.

In [12], a liver segmentation approach is presented, using fuzzy c-mean clustering and level set. In the first phase, the contrast of original image is enhanced; in the second phase, a spatial fuzzy c-mean clustering combined with anatomical prior knowledge is employed to extract liver region automatically. In third phase, a distance regularized level set is used for refinement. Finally, morphological operations are used as post-processing. The experiment result showed that this method can achieve high accuracy.

In [13], liver region in abdominal CT images is segmented based on Snakes Model and GrowCut algorithm. In [14], an automatic system for liver CT image segmentation is based on Markov Random Fields to obtain an initial contour of the liver. It improves the initial estimate and segment the liver using gradient vector fields (GVF) and active contours. Sharma and Kaur [15] used region approach for segmenting liver and liver tumour from CT scan images, then compared between Seeker Optimization algorithm (SOA) and Particle Swarm Optimization (PSO) for tumour classification using CT scan images.

In [16], a novel segmentation method based on a nested particle swarm optimization (PSO) method is used, to find the optimal number of clusters for segmenting a grayscale image. This method has two functions (i) find the most adequate number of clusters using the silhouette index as a measure of similarity; and (ii) segment the image using the Fuzzy C-Means (FCM) approach using the number of clusters previously retrieved.

In [17], an automatic Computer Aided Diagnostic system (CAD) is proposed to detect some liver diseases like hepatoma and hemangioma from abdominal Computed Tomography (CT) images using an approach for feature selection. This paper used adaptive thresholding for liver segmentation, and the Binary Particle Swarm Optimization (BPSO) is applied to get the best reduced feature set.

The remainder of this paper is ordered as follows. Section 2 gives an overview about ABC algorithm. Details of the proposed approach is shown in Sect. 3. Section 4 shows the experimental results and analysis. Finally, conclusions and future work are discussed in Sect. 5.

2 Artificial Bee Colony Algorithm

In this section, the main concepts and structure of the artificial bee colony algorithm are highlighted as follows.

2.1 Main Concepts

While searching the food, the bees in swarm can communicate, share, store and memorize the information according to changes in the environment. Each bee in the swarm can update its position according to these information. The behaviour of the bees can be summarized as follows.

Food sources A flower represents the food source for a bee. A bee collects all information from the food source such as the amount of nectar in the flower, the distance and direction to the nest. A bee stores and shares these information with other bees in the swarm.

Employed bees There are two types of bees, employed bees and unemployed bees. The employed bees are responsible for exploiting the food source and keep the profitability of associated food source.

Unemployed bees The unemployed bees represent the other type in the bee colony. They are sharing the information with the employed bees with a certain probability in order to select a food source. The unemployed bees are divided into two categories as onlooker bees and scout bees. The onlooker bees are collecting the information from the employed bees in order to select a food source for themselves. The scout bees are responsible for searching about the new food sources when the existing food sources exhaust. Usually, the employed bee represent 50 % of the bee swarm, while the unemployed bees represent the rest of the swarm. On average the scout bees represent 10 % of the total bees.

Foraging behaviour In foraging process, a bee starts searching the food and extracting the nectar from the food source. The amount of the extracted nectar depends on the distance of food source from hive and the richness. The bee uses the enzymes in its stomach in order to make honey. The bee shares its information with the other bees in the swarm by dancing in various forms.

Dance The bee shares the food source information by dancing in various ways. The bee uses one of the following three dance forms.

- **Round dance**. The bee does this type of dance when the food source is near to hive.
- **Waggle dance**. The employed bees select this type of dance when the food source is far from the hive. The speed of dance is proportional to the distance between the food source and the hive.
- **Tremble dance**. This type of dance means, the bee takes long time to unload the nectar and it does not know about the current profitability of its food source.

2.2 ABC Algorithm

The artificial bee colony (ABC) algorithm is a population based meta-heuristics algorithm based on the foraging behavior of honey bee colonies. It was proposed by

Dervis Karaboga in 2005 [9, 6]. There are four phases in the ABC algorithms as follows.

The initial population phase In the ABC algorithm, the initial population is generated randomly. The population contains *NS* solutions, where each solution x_i is a *D* dimensional vector, x_i represents the *i*th food source. Each solution in the population is generated as follows. The main structure of the ABC algorithm is presented in Algorithm 1. The steps of the ABC algorithm can be summarized as follows.

$$x_{ij} = x_{Lj} + r(x_{jU} - x_{jL}), \quad j = 1, 2, \ldots, D. \tag{1}$$

where L, U are bounds of x_i in *j*th direction and r is a random number, $r \in [0, 1]$.

The employed bees phase The employed bees modify the current solution according to the information of fitness values of each solution (nectar amount). The bee updates its position if the fitness value of the new food source is better than the old food source. The bee position is updated as follows.

$$v_{ij} = x_{ij} + \phi_{ij}(x_{ij} - x_{kj}). \tag{2}$$

where $\phi_{ij}(x_{ij} - x_{kj})$ is the step size, k, j are randomly selected indices, $k \in 1, 2, \ldots, NS, j \in 1, 2, \ldots, D$ and ϕ_{ij} is a random number, $\phi_{ij}(x_{ij} - x_{kj}) \in [-1, 1]$.

Onlooker bees phase The employed bees share the fitness values of the food source and their position information with the onlooker bees. The onlooker bees select a solution with a probability p_i based on the solution fitness value. The probability can be calculated as follows.

$$p_i = \frac{f_i}{\sum_{j=1}^{\mathrm{NS}} f_j} \tag{3}$$

where f_i is the fitness value of the *i*th solution.

Scout bees phase The food source is abandoned when the position of the food source is not updated for a predetermined number of cycles. The associated bee with the abandoned food source (solution) becomes scout bee and it starts to generate a new food source within the environment (search space). The new solution is generated randomly as follows.

$$x_{ij} = x_{Lj} + r(x_{jU} - x_{jL}), \quad j = 1, 2, \ldots, D. \tag{4}$$

where L, U are bounds of x_i in *j*th direction and r is a random number, $r \in [0, 1]$. The steps of ABC algorithm is described as follows.

- **Step 1**. The ABC generates a randomly distributed initial population of *NS* solutions (food source positions), where *NS* denotes the size of population. Each solution $x_i (i = 1, 2, \ldots, NS)$ is a D-dimensional vector.

- **Step 2**. Each solution in the population is evaluated by calculating its fitness function, and the best solution in the population is memorized.
- **Step 3**. The cycle counter is initialized, and the following steps are repeated until termination criteria is satisfied.
- **Step 4**. A new solution is generated from each old solution as shown in Eq. 1.
- **Step 5**. Each solution in the population is evaluated by calculating its fitness function, and the best solution in the population is assigned and memorized as follows.

$$f(x_i) = \begin{cases} \frac{1}{1+f(x_i)} & \text{if } f(x_i) \geq 0 \\ 1 + abs(f(x_i)) & \text{if } f(x_i) < 0 \end{cases}$$

- **Step 6**. The probability of each solution is calculated in order to generate a new trail solution v_i by an onlooker bees. The associated probability of each food source p_i is defined as shown in Eq. 3.
- **Step 7**. The trail solution is generated and evaluated, and if it is better than or equal to the old solution, then the old solution is replaced with the new solution, otherwise the old solution is retained. The best solution is memorized. If the food source cannot be improved for a limited number of cycles, which is called "limit", the food source is considered to be abandoned, and replaced with a new food source by scout.
- **Step 8**. The operation is repeated until termination criteria is satisfied, i.e. the algorithm reaches maximum cycle number (*MCN*).

Algorithm 1 describes how ABC is implemented.

Algorithm 1 ABC algorithm

1: Generate the initial population x_i randomly, $i = \{1, \ldots, NS\}$ {**Initialization**}
2: Evaluate the fitness function $f(x_i)$ of all solutions in the population
3: Keep the best solution x_{best} in the population {**Memorize the best solution** }
4: Set cycle=1
5: **repeat**
6: Generate a new solution v_i from the old solution x_i, where $v_{ij} = x_{ij} + \phi_{ij}(x_{ij} - x_{kj})$, $\phi_{ij} \in [-1, 1]$, $k \in \{1, 2, \ldots, NS\}$, $j \in \{1, 2, \ldots, D\}$ and $i \neq k$ {**Employed bees**}
7: Evaluate the fitness function $f(v_{ij})$ for all solutions in the population
8: Keep the best solution between current and candidate solutions {**Greedy selection**}
9: Calculate the probability p_i, for the solutions x_i, where $p_i = \frac{f_i}{\sum_{j=1}^{NS} f_j}$
10: Generate the new solutions v_i from the selected solutions depending on its p_i {**Onlooker bees**}
11: Evaluate the fitness function f_i for all solutions in the population
12: Keep the best solution between current and candidate solutions {**Greedy selection**}
13: Determine the abandoned solution. If exists, replace it with a new random solution x_i {**Scout bee**}
14: Keep the best solution x_{best} found so far in the population
15: $cycle = cycle + 1$
16: **until** cycle $\leq MCN$

3 Proposed CT Liver Segmentation Approach

The proposed segmentation approach consists of some main phases:

- **Pre-processing phase**
  Using the ABC-based proposed approach makes the preprocessing phase simpler. It depends only on image cleaning for the patient's information and connecting ribs. All printed description of patient and image information are removed. Then the ribs are connected using contrast stretching filter to stress the white ribs and trace its pixels. Every two close ribs are connected by drawing a white line between them.
- **Artificial bee colony phase**
  Artificial bee colony phase is the most important phase in the proposed approach. It does most of the work by dividing the image into a number of clusters according to the intensity values. ABC is applied in the proposed approach using Algorithm 1, which divides the image into a number of clusters. Each cluster has a centroid intensity value. Each cluster separated in a binary image, will have either parts of liver and other organs or parts of edges between the organs. The manipulation of the clustered binary image using the morphological operations will help to remove the edges and turn it into black pixels. This operation will stress the boundaries when gathering all clustered images (except the two highest clusters) in one image.
- **Region growing phase**
  The resulting image of ABC is enhanced using simple region growing technique. In this technique, some seed points are provided by the user and used to grow the area. This enhancement results in a whole liver segmented image. The segmented image is validated using similarity index measure, which compares the segmented image with a manual annotated image to calculate the accuracy.
- **ROI segmentation phase**
  In this phase, the required regions of interest are extracted using two different ways. The first is using ABC algorithm once more to separate the low intensity valued clusters, representing lesions, or using watershed to separate the whole liver into a number of homogeneous ROIs, which could be normal tissue or lesioned tissue. Later on, it is possible to calculate texture features for every ROI to be passed to any classifier.

These phases are described in detail in the following section, including all involved steps and the characteristics of each phase.

Algorithm 2 shows the steps of the proposed approach.

Algorithm 2 Proposed liver segmentation approach

1: Clean the image from the patient information and machine bed.
2: Connect ribs to isolate liver tissues from the flesh and muscles.
3: Apply ABC algorithm to cluster the intensity values of the image and sort the centroids values of the clusters ascending.
4: Separate each cluster in a binary image.
5: For each cluster, change the value of a part of the right down quarter into zero, implement close and fill the holes operations, and multiply the resulting image by the original image.
6: Add all clusters' resulting images, except the last two highest clusters, in one image.
7: Enhance the segmented ABC image using region growing to get the whole liver.
8: Use similarity index (SI) to calculate the accuracy of segmentation process.
9: Get the regions of interest using one of the following:

1. Apply ABC algorithm on the segmented liver to get the regions of interest (ROI). Then extract the least valued three clusters, which represent the darked values of lesions.
2. Apply watershed segmentation methods to the segmented liver to segment it into different number of ROIs.

3.1 Preprocessing Phase

In this paper, the need for filters is very limited for image preprocessing. Only mean filter is used in cleaning the image annotation and contrast stretching filter is used for connecting ribs. The first step of preprocessing is to clean the image from its annotations. It removes the patient's information and machine's bed to make it easier for the next operation of connecting ribs [18]. In brief, the usage of opening, closing and erosion, cleans the image in different aspects. It removes the annotation of the image, erodes the skin and a part of flesh and muscles from the abdomen, and also removes the machine's bed. Ribs boundary algorithm can handle the problem of flesh and muscles. These tissues are close to the liver and have a similar intensity value. When segmenting the liver, it acts as a bridge or a thin path between the liver in the left side of the image and other organs as spleen in the right side of the image. The algorithm uses contrast stretching filter to highlight the bones of the ribs. Then it uses a threshold close to white colour of ribs to isolate them. The ribs white pixels are traced and connected by drawing a white line in the original image between the edges of the ribs. This white line connects the ribs and acts like a wall between the flesh and muscles and the liver tissues. The bones are replaced by black colour. See connecting ribs algorithm in details in [18].

3.2 Artificial Bee Colony Phase

The artificial bee colony is inspired by bee behaviour in nature. It mainly creates a colony of artificial bees to solve difficult optimization problems. In our proposed approach, ABC is not used as an optimization technique, it is used as a clustering technique to segment the liver in CT images. The main sensitive key that should be handled carefully is the parameter settings of ABC algorithm. First of all, the number of clusters has an obvious effect on the resulting segmented image. There are two extreme intensity values in the image, represented by the black background and white bones. In addition to these values, we have liver boundaries, lesion and other organs. Seven clusters proved the best efficiency in segmentation as we will explain later. Also, we need to investigate the number of employed and onlooker bees in the colony. The last parameter is the number of iterations, used to get the segmented liver. A fitness function is used to determine the vector of the new solution in every iteration. The centroids of the required clusters will be the resulting best solution (global parameters). Algorithm 3 shows the steps of using ABC as a clustering technique to segment the liver.

Algorithm 3 Artificial bee colony phase

1: Set the value of different parameters of clusters, colony members and the iterations.
2: Apply ABC on the image.
3: Get the vector of global parameters, which represent the values of clusters' centroids.
4: Sort the resulting clusters centroids ascending.
5: Extract the binary clustered images.
6: Change the intensity of a part of right down quarter of the image into black. This change cuts the closed area of spleen. This way, the stomach and spleen are not filled in the next step.
7: Remove the small objects in every clustered image and fill the holes.
8: Excluding highest two clusters, sum clustered images together.
9: Get a binary image of the summed clusters where image value greater than zero.
10: Multiply the binary image by the original image to get the segmented image.

The advantage of using ABC this way, is that it is not affected by noise at all. Since noise is always small pixels, they are filled by morphological operations step.

3.3 Region Growing Phase

Region-based segmentation techniques apply the similarity difference to extract regions. Level set and fast marching can be used to extract one object using an initial contour. Watershed uses the idea of water drops to create the boundaries of all objects in an image [19]. Also region growing can do the same as level set and

fast marching. The advantages of region growing are its simplicity, speed and low cost of computational calculations. In this paper, region growing has been chosen to accomplish the mission of ABC segmentation. The ABC segmented image is enhanced using region growing.

3.4 ROI Segmentation Phase

The segmentation of regions of interest can be applied using two different methods. The first method can be done by applying ABC algorithm once again on the whole liver segmented image using the same idea of ignoring the highest two clusters. To understand how it works, we must notice that lesion tissue is darker than the normal liver tissues, and the first cluster represents background and highest clusters represent the normal tissues. So, excluding the two highest clusters will remove most of the normal liver tissues. The remaining regions will represent the lesions or the thin dark boundary of the liver. The second way is to apply watershed technique on the whole liver segmented image. Watershed divides all the image into homogeneous regions. For both methods, every region is extracted to calculate the texture features to be passed to any classifier.

4 Experimental Results and Discussion

A set of 38 CT images is used to apply the experiments of the proposed approach. The images were taken in the first phase of CT scan before patient injection with contrast materials. Figure 1 shows the preprocessing phase including the results of image cleaning and rib connection.

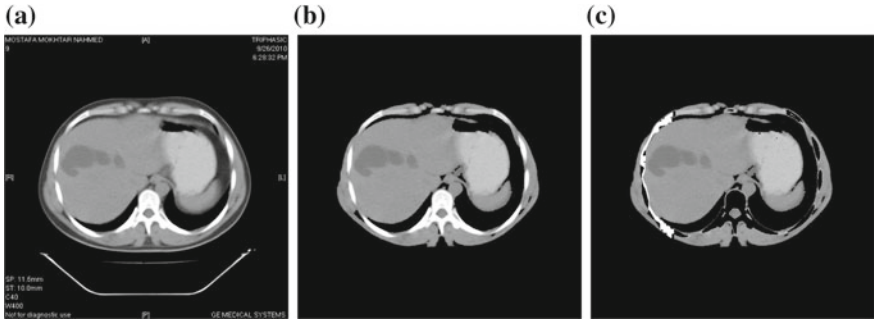

Fig. 1 Preprocessing phase: **a** Original image, **b** Cleaned image, **c** Connected ribs

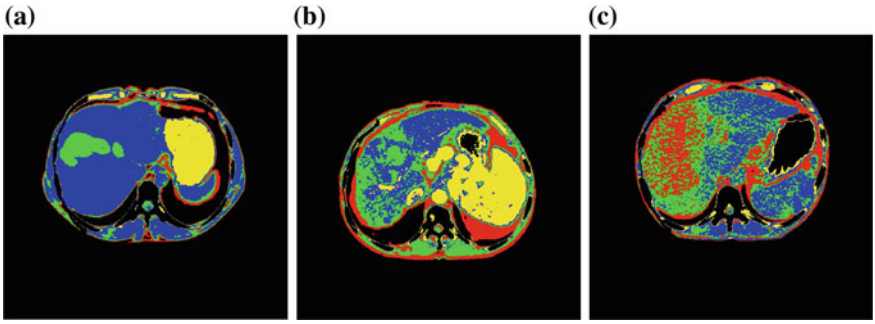

Fig. 2 Clustered results of different images using ABC

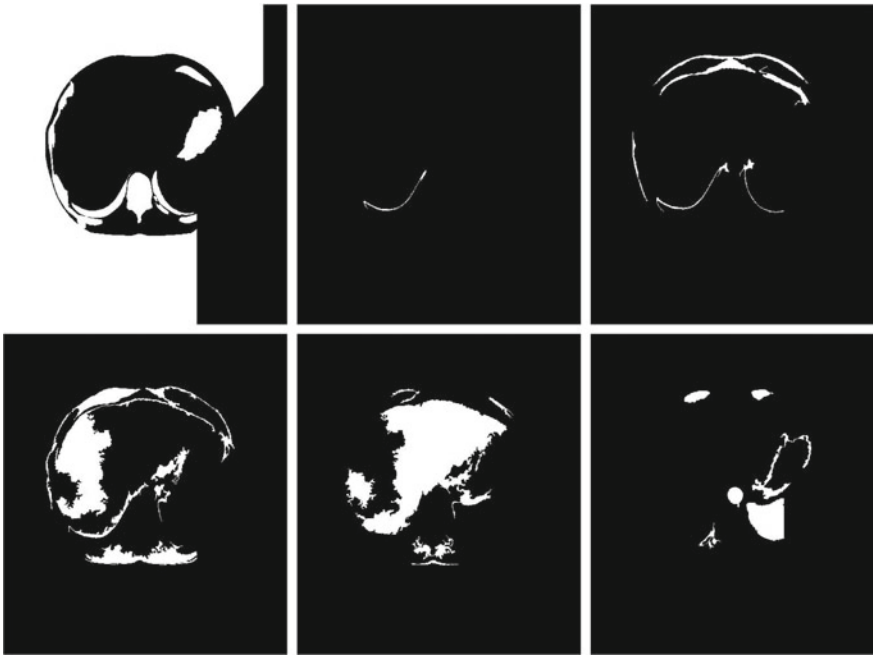

Fig. 3 Clusters' binary images resulting from ABC

Figure 2 shows a number of different clustered images using ABC algorithm. Each cluster has a different colour. It shows that ABC resulting clusters can be very sensitive for the different values in the liver tissues.

Figure 3 shows the extracted binary images of the different clusters resulting after applying ABC. It shows that some binary images have the boundary fragments separated from organs. Applying the morphological operations can remove these small fragments to deepen the edges. Some small fragments might be inside the liver. When the liver is extracted, these holes can be filled easily.

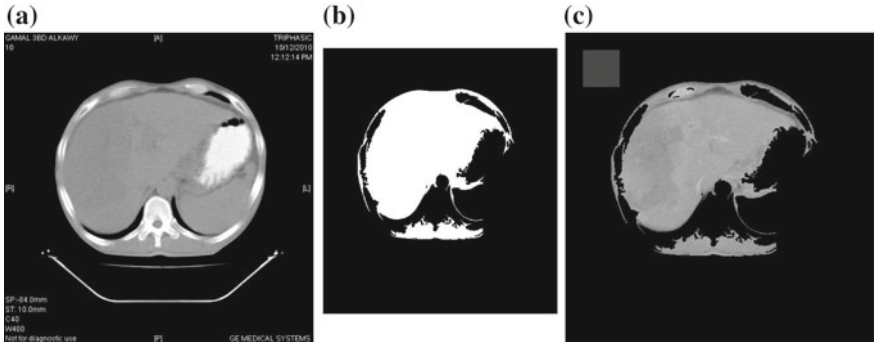

Fig. 4 ABC liver segmentation, **a** Original image, **b** ABC binary image, **c** ABC segmented image

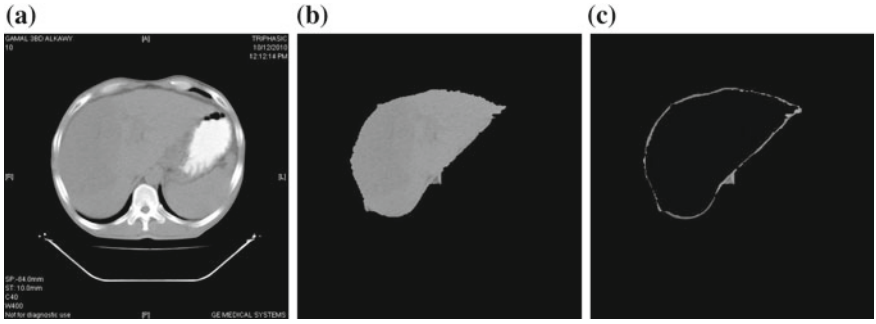

Fig. 5 Final liver segmented image compared to the annotated image: **a** Original image, **b** Segmented image, **c** Difference image

Figure 4 shows the binary image of ABC and the liver segmented image. The figure shows that the result of the segmented image is considerably satisfying. It has the liver and some boundaries, which can be ignored when using any region-base segmentation method.

Finally, the segmented image using ABC is enhanced using simple region growing technique. Figure 5 shows the difference between the segmented image and annotated one. It shows a very thin boundary of the liver as a difference.

Parameters in ABC algorithm is the key in a successful implementation. ABC uses three main parameters that affect the accuracy and speed of execution. The algorithm is tested initially using five random CT images. The main parameters are as follows.

1. Population size:
   It represents the total number of bees, used in searching the main clusters centroids. Table 1 shows the results of testing ABC algorithm using different values for population size. The first column represents the different tested sizes, ranging between 10 to 100. The next five columns represent the image number.

Table 1 Parameter setting for population size

Size	1	2	3	4	5	Result
10	0.970	0.916	0.909	0.954	0.959	0.9416
20	0.968	0.916	0.899	0.952	0.953	0.9376
30	0.968	0.917	0.897	0.938	0.956	0.9352
40	0.967	0.916	0.899	0.953	0.958	0.9386
50	0.968	0.916	0.918	0.953	0.953	0.9416
60	0.967	0.916	0.897	0.971	0.957	0.9416
70	0.967	0.916	0.897	0.968	0.957	0.9410
80	0.968	0.916	0.901	0.952	0.957	0.9388
90	0.968	0.916	0.901	0.971	0.957	0.9426
100	0.968	0.916	0.897	0.952	0.957	0.9380

Finally, the last column represents the average accuracy result for each trial. The table shows that the best result is 94.26 % for size of 90, and 94.16 % for the sizes 10, 50 and 60. Size 10 is preferred to be used, because it decreases 89 % of computational cost and time, compared with the best result. Figure 6 shows the evaluation of different values of the population size.

2. Number of iterations:
   It represents the number of loops used in the algorithm. Table 2 shows the results of testing ABC algorithm using different numbers of iterations for testing 5 random CT images. The table shows that the best result is 93.80 % for 20 iterations. Figure 7 shows the evaluation of the effect of number of iterations on the average accuracy.

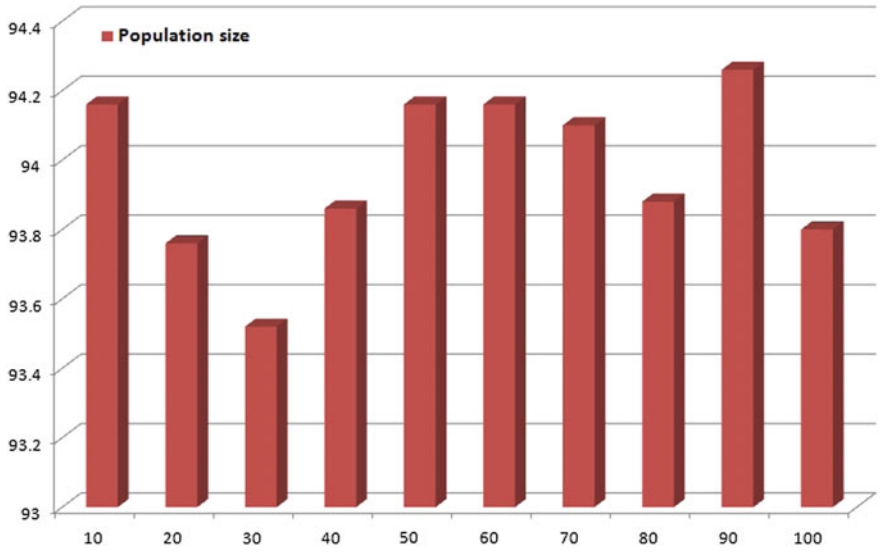

Fig. 6 Evaluating the change of population size

Table 2 Parameter setting for number of iterations

Iter.	1	2	3	4	5	Result
1	0	0	0	0	0	0
2	0.968	0.917	0.314	0	0	0.4397
3	0.968	0.409	0.899	0.952	0	0.6456
4	0.968	0.911	0.000	0.952	0	0.5662
5	0.977	0.913	0.899	0.727	0.956	0.8944
10	0.968	0.409	0.612	0.953	0.959	0.7802
15	0.976	0.911	0.676	0.968	0.948	0.8958
20	0.984	0.915	0.895	0.938	0.958	0.9380
25	0.968	0.910	0.893	0.952	0.956	0.9358
30	0.982	0.771	0.895	0.968	0.950	0.9132

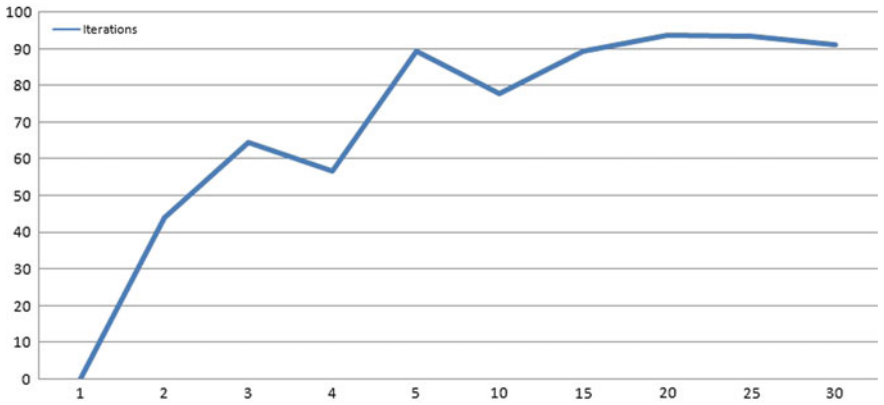

Fig. 7 Evaluation the change the number of iterations

3. Number of clusters:
   It represents the number of centroids of the clusters, used to segment the liver. The clusters centroids range from 0 to 255. The value of class one which is zero, represents the black value of the background. The highest class represent bones and the spots that have the injected radial therapy. The more the clusters, the more the separation of the intensity values. Table 3 shows the results of testing ABC algorithm using different cluster's values. The algorithm is tested for 10 values. The table shows that the best result is 94.2 % for using 7 clusters. Figure 8 shows the evaluation of different values of the clusters.

Evaluation is performed using similarity index (SI) defined using the following equation:

$$SI(I_{auto}, I_{man}) = \frac{I_{auto} \bigcap I_{man}}{I_{auto} \bigcup I_{man}} \quad (5)$$

Table 3 Parameter setting for number of clusters

Cluster	1	2	3	4	5	Result
1	0	0	0	0	0	0
2	0	0	0	0	0	0
3	0	0	0	0	0	0
4	0.968	0.852	0.751	0.679	0.959	0.8418
5	0.968	0.806	0.675	0.953	0.944	0.8692
6	0.968	0.91	0.893	0.952	0.956	0.9358
7	0.967	0.915	0.906	0.971	0.951	0.942
8	0.966	0.914	0.906	0.969	0.948	0.9406
9	0.968	0.915	0.905	0.959	0.928	0.935
10	0.968	0.915	0.905	0.967	0.938	0.9386

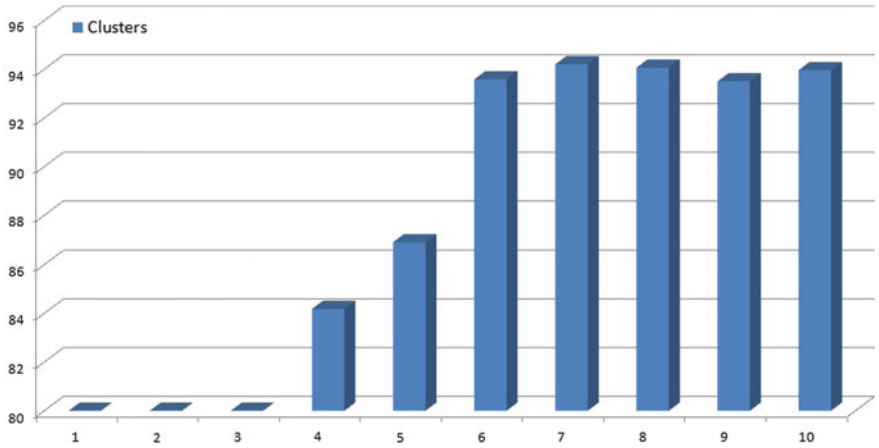

Fig. 8 Evaluating the change of the number of clusters

where SI is the similarity index, I_{auto} is the binary automated segmented image, resulting from the phase of final segmentation of the whole liver in the used approach and I_{man} is the binary manual segmented image by a radiology specialist. The experiments of liver segmentation using ABC proved its efficiency in clustering the image. The highest clusters represent all regions that have intensity values greater than liver intensity. Applying the morphological operations on every clustered image will remove the small parts which represent boundaries between objects. That deepens the edges of organs. Also, we noticed that the lesions intensity values reside in the least clusters less than liver intensity values. Finally using region growing in the segmented image will enhance the segmented whole liver. Table 4 shows the results of the proposed approach compared to region

Table 4 Results of proposed approach compared to region growing

Image no.	Region growing	Proposed	Image no.	Region growing	Proposed
1	0.881	0.981	20	0.880	0.925
2	0.927	0.911	21	0.708	0.924
3	0.831	0.947	22	0.616	0.945
4	0.740	0.910	23	0.696	0.945
5	0.868	0.969	24	0.820	0.913
6	0.849	0.951	25	0.913	0.902
7	0.956	0.949	26	0.930	0.940
8	0.934	0.891	27	0.921	0.951
9	0.923	0.951	28	0.908	0.948
10	0.939	0.945	29	0.920	0.948
11	0.890	0.953	30	0.947	0.945
12	0.893	0.935	31	0.941	0.921
13	0.757	0.940	32	0.942	0.921
14	0.917	0.959	33	0.888	0.905
15	0.902	0.935	34	0.856	0.938
16	0.938	0.948	35	0.855	0.961
17	0.910	0.940	36	0.913	0.942
18	0.898	0.905	37	0.671	0.959
19	0.536	0.917	38	0.661	0.946
Result	84.82	93.73			

growing method. It shows that the average performance of liver images segmentation is improved using the proposed approach. Segmentation using region growing has average result of SI = 84.82 %. This result is improved using the proposed approach with SI = 93.73 %.

Figure 9 shows *SI* for thirty eight CT liver images, where each point in the figure represents the similarity of one segmented image, compared to its annotated image. Table 4 shows the results of the implementation of the proposed approach compared with region growing method. It shows the enhancement of the result using ABC in the proposed approach. We can mention that using ABC for segmenting the whole liver is not affected by noise and there is no need for using any filter in the segmentation process.

Table 5 compares the results of proposed approach to other approaches. The compared approaches are region growing, level set which is an enhanced region-based approach, which depends on evolving an initial contour towards the boundary of the object, and k-means clustering technique. It shows that the proposed approach achieved the best result.

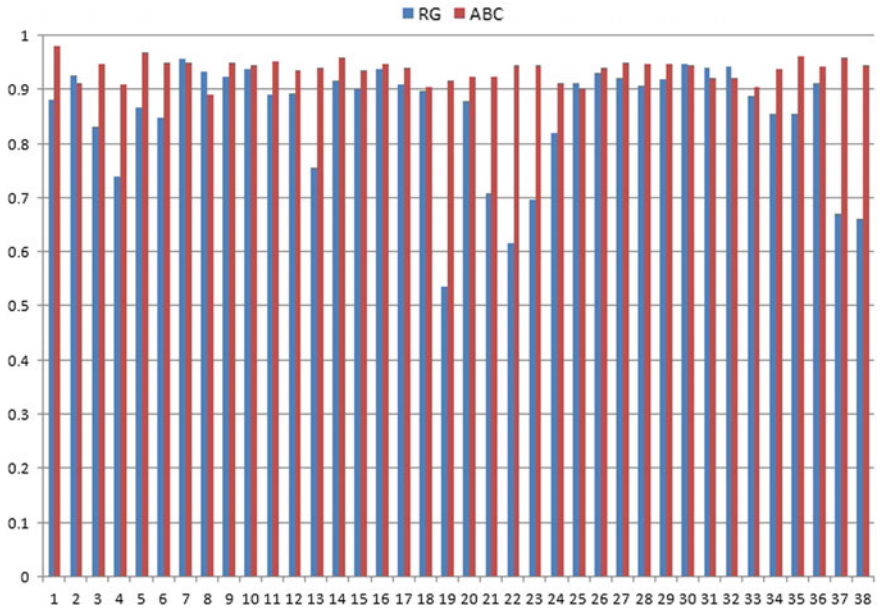

Fig. 9 Similarity index results for 38 segmented images

Table 5 Comparison of proposed approach with other approaches

Ser.	Approach	Result
1	Region growing	84.82
2	Level set	92.10
3	K-means with RG	92.38
4	Proposed approach with RG	93.73

Finally, ABC is applied once more on the whole liver segmented image. The lesion regions is always darker than the normal liver tissues colour. So, removing the tow highest clusters values results in the lesion's ROI. Then the image of ROI can be passed to a classifier later on. Figure 10 shows the results of applying ABC on the segmented liver.

Also, watershed is applied on the whole liver segmented image. The image is segmented into a number of segmented closed regions. Then every region is extracted to calculate texture features to be passed to a classifier later on. Figure 11 shows the results of applying ABC on the segmented liver.

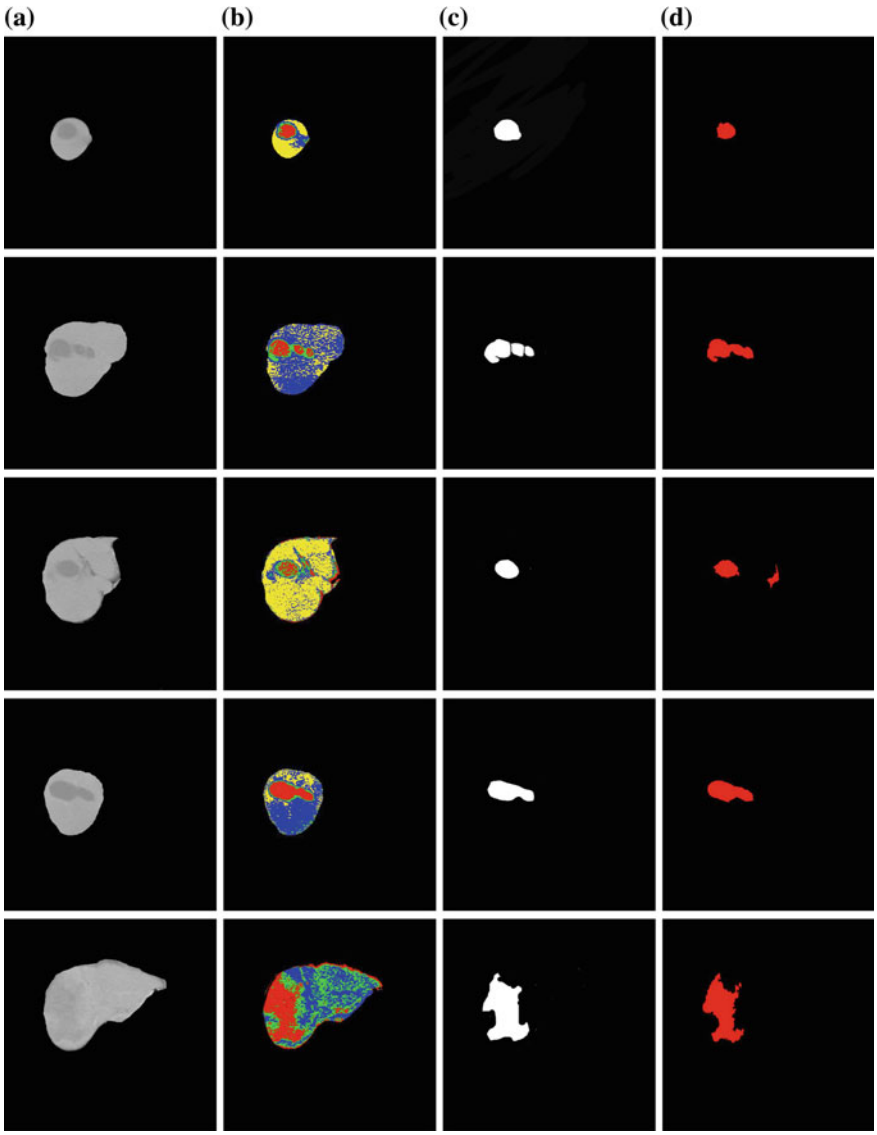

Fig. 10 Lesion segmentation, **a** ABC segmented image, **b** ABC clusters image, **c** Annotated image, **d** ABC segmented lesion

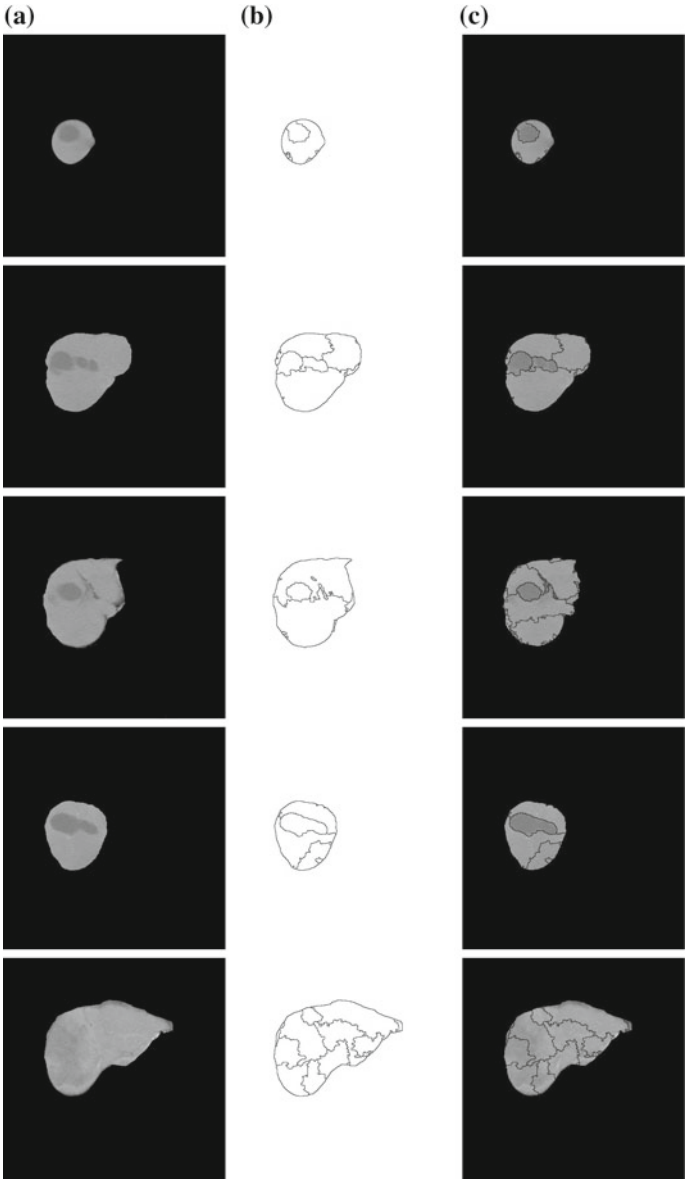

Fig. 11 Watershed segmentation, **a** ABC segmented image, **b** Watershed binary image, **c** Annotated image, **d** Watershed segmented image

5 Conclusion and Future Work

Any CAD system must include the phase of segmentation. Liver segmentation is divided into the phases of preprocessing and segmentation. In this paper preprocessing is involved in cleaning image annotations and connecting ribs. Segmentation phase relies on the ABC algorithm as a clustering technique, dividing the image into a number of clusters that fills the whole levels of the intensity values that ranges from 0 to 255. Morphological operations play a significant role, when applied to each clustered binary image. It removes small unconnected boundaries and objects. Then, all binary clustered images are summed in one binary image except the highest clusters. This results in a binary segmented liver, which is multiplied by the original image. Then region growing is used to enhance the segmented liver image. The segmented liver can be manipulated by ABC or watershed to segment ROIs to calculate texture features for each region and pass it to a classifier. The whole liver segmentation using ABC and region growing has a considerable average accuracy rate 93.73 % using *SI*. So, ABC optimization technique is very promising for being used in classification. It can be used in future work as a classifier for liver anomalies.

References

1. Motley, G., Dalrymple, N., Keesling, C., Fischer, J., Harmon, W.: Hounsfield unit density in the determination of urinary stone composition. Urology **58**(2), 170–173 (2001). IEEE Trans. Syst. Man Cybern. **SMC-9**(1) (1979)
2. Sherlock, S., Summerfield, J.: A Colour Atlas of Liver Disease. Wolfe, London (1979)
3. Sherlock, S.: Diseases of the Liver and Biliary System, 5th edn. Blackwell, London (1973)
4. Chen, M.Y.M., Pope, T.L., Ott, D.J.: Basic Radiology, 2nd edn. McGrow Hill, US (2011)
5. Mostafa, A., Hefny, H., Ghali, N.I., Hassanien, A., Schaefer, G.: Evaluating the effects of image filters in CT Liver CAD system. In: IEEE-EMBS International Conference on Biomedical and Health Informatics (BHI2012). The Chinese University of Hong Kong, Hong Kong SAR, on Jan 5–7 (2012)
6. Karaboga, D.: An Idea Based On Honey Bee Swarm For Numerical Optimization, Technical Report-TR06, Erciyes University, Engineering Faculty, Computer Engineering Department (2005)
7. Bitam, S., Batouche, M., Talbi, E.: A survey on bee colony algorithms. In: 2010 IEEE International Symposium on Parallel and Distributed Processing, Workshops and Phd Forum (IPDPSW), pp. 1–8 (2010)
8. Karaboga, D., Gorkemli, B., Ozturk, C., Karaboga, N.: A comprehensive survey: artificial bee colony (ABC) algorithm and applications. Artif. Intell. Rev. **42**(1), 21–57 (2014)
9. Basturk, B., Karaboga, D.: An artificial bee colony (ABC) algorithm for numeric function optimization. In: IEEE Swarm Intelligence Symposium 2006, May 12– 14, Indianapolis, Indiana, USA (2006)
10. Horng, M.: Multilevel thresholding selection based on the artificial bee colony algorithm for image segmentation. Expert Syst. Appl. **38**(11), 13785–13791 (2011)
11. Chen, E., Chung, P., Chen, C., Tsai, H., Chang, C.: An automatic diagnostic system for CT liver image classification. IEEE Trans. Biomed. Eng. **45**(6), 783–794 (1998)

12. Xuechen, L., Luo, S., Jaming, L.: Liver segmentation from CT image using fuzzy clustering and level set. J.Signal Inf. Process. **4**(3), 36–42 (2013)
13. Jiang, H., Ma, B., Zong, M., Zhou, X.: Liver segmentation based on snakes model and improved GrowCut algorithm in abdominal CT image. Computational and Mathematical Methods in Medicine (2013)
14. Alomari, R., Kompalli, S., Chaudhary, V.: Segmentation of the liver from abdominal CT using Markov random field model and GVF snakes. In: Complex, International Conference on Intelligent and Software Intensive Systems, CISIS, pp. 293–298 (2008)
15. Sharma, A., Kaur, P.: Optimized liver tumor detection and segmentation using neural network. Int. J. Recent Technol. Eng. (IJRTE) **2**(5), 7–10 (2013)
16. Ali, A., Couceiro, M., Hassenian, A.: Towards an optimal number of clusters using a nested particle swarm approach for liver CT image segmentation. Adv. Mach. Learn. Technol. Appl. **488**, 331–343 (2014)
17. Selvaraj, G., Janakiraman, S.: Improved feature selection based on particle swarm optimization for liver disease diagnosis. In: Swarm, Evolutionary, and Memetic Computing, vol. 8298, pp. 214–225. Springer International Publishing (2013)
18. Zidan, A., Ghali, N.I., Hassanien, A., Hefny, H.: Level set-based CT liver computer aided diagnosis system. Int. J. Imaging Robot. **9** (2013)
19. Vanhamel, I., Pratikakis, I., Sahli, H.: Multiscale gradient watersheds of color images. IEEE Trans. Image Process. **12**(6), 617–626 (2003)
20. Kowalczyk, M., Koza, P., Kupidura, P., Marciniak, J.: Application of mathematical morphology operations for simplification and improvement of correlation of image in close-range photomography. In: The International Archives of the Photogrammetry, Remote Sensing and Spatial Information Sciences, vol. XXXVII. Part B5. Beijing (2008)

Nature Inspired Optimization Algorithms for CT Liver Segmentation

Ahmed Fouad Ali, Abdalla Mostafa, Gehad Ismail Sayed, Mohamed Abd Elfattah and Aboul Ella Hassanien

Abstract Nature inspired optimization algorithms have gained popularity in the last two decades due to their efficiency and flexibility when they applied to solve global optimization problems. These algorithms are inspired from the biological behavior by swarms of birds, fish and bees. In this chapter, we give an overview of some of nature inspired optimization algorithms such as Artificial Bee Colony (ABC), Cuckoo Search (CS), Social Spider Optimization (SSO) and Grey Wolf Optimization (GWO). Also, we present the usage of ABC and GWO algorithms for CT liver segmentation. The experimental results of the two selected algorithms show that the two algorithms are powerful and can obtain good results when applied to segment medical images.

Keywords Artificial bee colony · Cuckoo search · Social spider · Grey wolf · Segmentation

A.F. Ali (✉)
Faculty of Computers and Information, Department of Computer Science, Suez Canal University, Ismailia, Egypt
e-mail: ahmed_fouad@ci.suez.edu.eg

A. Mostafa (✉)
Institute of Statistical Studies and Research, Cairo University, Cairo, Egypt
e-mail: abdalla_mosta75@yahoo.com

G.I. Sayed
Faculty of Computers and Information, Department of Information Technology, Cairo University, Cairo, Egypt

M.A. Elfattah
Faculty of Computers and Information, Mansoura University, Cairo, Egypt

A.E. Hassanien
Faculty of Computers and Information, Cairo University, Cairo, Egypt

A.F. Ali · A. Mostafa · G.I. Sayed · M.A. Elfattah · A.E. Hassanien
Chair of Scientific Research Group in Egypt, Cairo, Egypt

N. Dey et al. (eds.), *Medical Imaging in Clinical Applications*,
Studies in Computational Intelligence 651, DOI 10.1007/978-3-319-33793-7_19

1 Introduction

The complexity of segmentation problem in medical imaging is the motivation for the researchers to find new efficient methods. Observing nature and swarms have inspired and paved the way to create different metaheuristic algorithms. The individual behaviour of the swarms is simple, but with the astonishing co-ordination and organization, they present a remarkable structured social organization. Swarm intelligence is a biologically inspired algorithms, focusing on the amazing collective behaviour of swarms. It tries to mimic the successful capabilities of swarms to solve a problem, depending on their distributed members behaviour which is coordinated and collective. Researchers are trying to trace the steps of swarms to develop sophisticated methods to solve complex optimization problems.

Medical imaging uses different modalities to aid diagnosis of abnormality. The imaging categories depend on the usage of radiography of x-ray, radio frequencies pulses, sound waves, and gamma rays. Its application has a wide range in different branches of medical diagnosis including hepatology, oncology and cardiology… etc. The most common modality of imaging is CT scan. It depends on the radiography of x-rays. It sends different surrounding beams of x-rays against the patient. The reflection of the beams determines the intensity values of the picked image. CT images are suitable for the diagnosis and detection of hepatic diseases which is applied in this paper. Magnetic resonance imaging (MRI) is another modality that uses the radio frequencies for imaging. MRI is very efficient in cardiovascular diseases. Ultrasound (US) imaging uses sound waves higher than the limit of human hearing. it is efficient in the detection of pregnancy and blood clotting. Sometimes, it can help in diagnosis of apparent tumors of organs in the abdominal cavity as liver. Nuclear medicine can handle both of treatment and imaging. The gamma rays are the base for the positron emission tomography (PET) and single-photon emission computed tomography (SPECT).

Liver is the biggest gland in human body. It has some difficult characteristics that makes the process of segmentation difficult. Liver segmentation difficulties include having different shapes im different slides of images. Besides, there is a similarity between the intensity of liver and other organs as spleen, stomach, flesh and muscles. Another difficulty is the falciform ligament that divided the area of liver into two regions. Liver segmentation in CT images is the backbone of the discussed implementation of segmentation methods of bio-inspired optimization techniques.

Sathya et al. used Particle swarm optimization (PSO) for multi-level thresholding in image segmentation. PSO is used to maximize the objective functions of Kapur and Otsu [1]. Also, E. Cuevas et al. implemented Artificial Bee Colony (ABC) optimization to compute image threshold for image segmentation [2]. A. Mostafa et al. used ABC algorithm as a clustering technique combined with simple region growing for the whole liver segmentation [3]. Y. Linag et al. combined the Ant Colony Optimization (ACO) algorithm and Otsu with expectation and maximization algorithm for selecting multilevel threshold for segmenting the objects with complex structure. They combined the non-parametric ACO with the

parametric EM [4]. Sivaramakrishnan et al., designed a system to diagnose breast tumors in mamograp images using Fish Swarm Algorithm, combined with ABC algorithm [5]. W. Alomoush et al. built a system depends of hybrid firefly and Fuzzy C-means to detect brain tumors in MRI images [6]. R. Jagadeesan enhanced Fuzzy C-means with firefly algorithm in order to segment brain tumor in MRI images. The Firefly algorithm is optimizes the Fuzzy C-means membership function to guarantee an efficient segmentation [7]. L. Sankari overcomes the problem of the maxima in Expectation-Maximization (EM) algorithm by combining Glowworm swarm optimization (GSO) algorithm with EM algorithm. GSO finds the initial seed points by clustering the image and pass it to EM algorithm segmentation [8]. S. Jindal presented Bacterial foraging optimization algorithm (BFOA), which is inspired by a type of bacteria called Escherichia coli. It has an advantage of needing no thresholding in image segmentation. BFOA reduces the computational complexity and time [9]. This paper concentrates on four bio-inspired optimization techniques, Artificial Bee Colony, Cuckoo Search, Social Spider and Grey Wolf.

The remainder of this paper is ordered as follows. Section 2 gives an overview about the nature inspired optimization techniques, including Artificial Bee Colony algorithm (ABC) in Sect. 2.1, Cuckoo Search (CSO) in Sect. 2.2, Social Spider optimization algorithm (SSO)in Sect. 2.3, and Gray Wolf Algorithm (GW) in Sect. 2.4. Section 3 presents the implementation of the first application of ABC, its algorithm and experimental results. Also, Sect. 4 presents the implementation of the second application of GW, its algorithm and experimental results. Finally, conclusions and future work are discussed in Sect. 5.

2 Nature Inspired Optimization Algorithms

Nature inspired algorithms are based on the social behavior of animals and birds which can be observed in nature, such as ant colonies, flocks of birds, fish schools and bee hives. In the following subsections, we present four nature inspired algorithms as follow.

2.1 Artificial Bee Colony Algorithm

In this section, we highlight the main concepts and structure of the artificial bee colony algorithm as follows.

Main concepts While searching the food, the bees in swarm can communicate, share, store and memorize the information according to changes in the environment. Each bee in the swarm can update its position according to these information. The behavior of the bees can be summarized as follows.

Food sources A flower represents the food source for a bee. A bee collects all information from the food source such as the amount of nectar in the flower, the distance and direction to the nest. A bee stores and shares these information with other bees in the swarm.

Employed bees There are two types of bees, employed bees and unemployed bees as shown in Fig. 1. The employed bees are responsible for exploiting the food source and keep the profitability of associated food source.

Unemployed bees The unemployed bees represent the other type in the bee colony. They are sharing the information with the employed bees with a certain probability in order to select a food source. The unemployed bees are divided into two categories as onlooker bees and scout bees. The onlooker bees are collecting the information from the employed bees in order to select a food source for themselves. The scout bees are responsible for searching about the new food sources when the existing food sources exhaust. Usually, the employed bee represent 50 % of the bee swarm, while the unemployed bees represent the rest of the swarm. On average the scout bees represent 10 % of the total bees.

Foraging behavior In foraging process, a bee starts searching the food and extracting the nectar from the food source. The amount of the extracted nectar depends on the distance of food source from hive and the richness. The bee uses the enzymes in its stomach in order to make honey. The bee shares its information with the other bees in the swarm by dancing in various forms.

Dance The bee shares the food source information by dancing in various ways. The bee uses one of the following three dance forms.

- **Round dance**. The bee does this type of dance when the food source is near to hive.
- **Waggle dance**. The employed bees select this type of dance when the food source is far from the hive. The speed of dance is proportional to the distance between the food source and the hive.
- **Tremble dance**. This type of dance means, the bee takes long time to unload the nectar and she does not know about the current profitability of its food source.

ABC algorithm The artificial bee colony (ABC) algorithm is a population based meta-heuristics algorithm based on the foraging behavior of honey bee colonies. It was proposed by Karaboga [10, 11]. There are four phases in the ABC algorithms as follows.

The initial population phase In the ABC algorithm, the initial population is generated randomly. The population contains *NS* solutions, where each solution x_i is a *D* dimensional vector, x_i represents the *i*th food source. Each solution in the

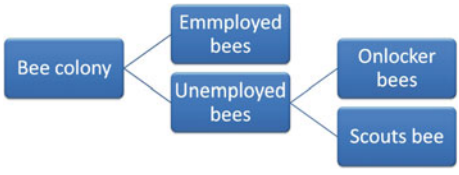

Fig. 1 Bee colony types

population is generated as follows. The main structure of the ABC algorithm is presented in Algorithm 1. The steps of the ABC algorithm can be summarized as follows.

$$x_{ij} = x_{Lj} + r(x_{jU} - x_{jL}),\ j = 1, 2, \ldots, D. \tag{1}$$

where L, U are bounds of x_i in jth direction and r is a random number, $r \in [0, 1]$.

The employed bees phase The employed bees modify the current solution according to the information of fitness values of each solution (nectar amount). The bee updates its position if the fitness value of the new food source is better than the old food source. The bee position is updated as follows.

$$\upsilon_{ij} = x_{ij} + \phi_{ij}(x_{ij} - x_{kj}). \tag{2}$$

where $\phi_{ij}(x_{ij} - x_{kj})$ is the step size, k, j are randomly selected indices, $k \in 1, 2, \ldots, NS, j \in 1, 2, \ldots, D$ and ϕ_{ij} is a random number, $\phi_{ij}(x_{ij} - x_{kj}) \in [-1, 1]$.

Onlooker bees phase The employed bees share the fitness values of the food source and their position information with the onlooker bees. The onlooker bees select a solution with a probability p_i based on the solution fitness value. The probability can be calculated as follows.

$$p_i = \frac{f_i}{\sum_{j=1}^{NS} f_j} \tag{3}$$

where f_i is the fitness value of the ith solution.

Scout bees phase The food source is abandoned when the position of the food source is not updated for a predetermined number of cycles. The associated bee with the abandoned food source (solution) becomes scout bee and it starts to generate a new food source within the environment (search space). The new solution is generated randomly as follows.

$$x_{ij} = x_{Lj} + r(x_{jU} - x_{jL}), \quad j = 1, 2, \ldots, D. \tag{4}$$

where L, U are bounds of x_i in jth direction and r is a random number, $r \in [0, 1]$. The steps of ABC algorithm is described as follows.

- **Step 1**. The ABC generates a randomly distributed initial population of NS solutions (food source positions), where NS denotes the size of population. Each solution $x_i (i = 1, 2, \ldots, NS)$ is a D-dimensional vector.
- **Step 2**. Each solution in the population is evaluated by calculating its fitness function, and the best solution in the population is memorized.
- **Step 3**. The cycle counter is initialized, and the following steps are repeated until termination criteria is satisfied.
- **Step 4**. A new solution is generated from each old solution as shown in Eq. 1.

- **Step 5**. Each solution in the population is evaluated by calculating its fitness function, and the best solution in the population is assigned and memorized as follows.

$$f(x_i) = \begin{cases} \frac{1}{1+f(x_i)} & \text{if} \quad f(x_i) \geq 0 \\ 1 + abs(f(x_i)) & \text{if} \quad f(x_i) < 0 \end{cases}$$

- **Step 6**. The probability of each solution is calculated in order to generate a new trail solution v_i by an onlooker bees. The associated probability of each food source p_i is defined as shown in Eq. 3.
- **Step 7**. The trail solution is generated and evaluated, and if it is better than or equal to the old solution, then the old solution is replaced with the new solution, otherwise the old solution is retained. The best solution is memorized. If the food source cannot be improved for a limited number of cycles, which is called "limit", the food source is considered to be abandoned, and replaced with a new food source by scout.
- **Step 8**. The operation is repeated until termination criteria is satisfied, i.e. the algorithm reaches maximum cycle number (*MCN*).

Algorithm (1) describes how ABC is implemented.

Algorithm 1 ABC algorithm

1: Generate the initial population x_i randomly, $i = \{1, \ldots, NS\}$ {**Initialization**}
2: Evaluate the fitness function $f(x_i)$ of all solutions in the population
3: Keep the best solution x_{best} in the population {**Memorize the best solution** }
4: Set cycle=1
5: **repeat**
6: Generate a new solution v_i from the old solution x_i, where $v_{ij} = x_{ij} + \phi_{ij}(x_{ij} - x_{kj})$, $\phi_{ij} \in [-1, 1]$, $k \in \{1, 2, \ldots, NS\}$, $j \in \{1, 2, \ldots, D\}$ and $i \neq k$ {**Employed bees**}
7: Evaluate the fitness function $f(v_{ij})$ for all solutions in the population
8: Keep the best solution between current and candidate solutions {**Greedy selection**}
9: Calculate the probability p_i, for the solutions x_i, where $p_i = \frac{f_i}{\sum_{j=1}^{NS} f_j}$
10: Generate the new solutions v_i from the selected solutions depending on its p_i {**Onlooker bees**}
11: Evaluate the fitness function f_i for all solutions in the population
12: Keep the best solution between current and candidate solutions {**Greedy selection**}
13: Determine the abandoned solution. If exists, replace it with a new random solution x_i {**Scout bee**}
14: Keep the best solution x_{best} found so far in the population
15: $cycle = cycle + 1$
16: **until** cycle $\leq MCN$

2.2 Cuckoo Search

Cuckoo search (CS) is a population based metaheuristics algorithm developed by Yang and Deb [12]. The concepts of the CS algorithm are presented as follow.

Main concepts Cuckoo search algorithm is a population based metaheuristic algorithm inspired from the reproduction strategy of the cuckoo birds. The cuckoo birds lay their eggs in a communal nests and they may remove other's eggs to increase the probability of hatching their own eggs [13]. This method of laying the eggs in other's nests is called obligate brood parasitism. Some host bird can discover the eggs are not its own and throw these eggs away or abandons its nest and build a new nest in a new place. Some kind cuckoo birds can mimic the color and the pattern of the eggs of a few host bird in order to reduce the probability of discovering the intruding eggs. The cuckoos laid their eggs in a nest where the host bird just laid its own eggs, since the cuckoo eggs are hatching earlier than the host bird eggs. Once the eggs are hatching, the cuckoo chick's starts to propel the host eggs out the of the nest in order to increase its share of food provided by its host bird.

Lévy flights Recent studies show that the behavior of many animals when searching for foods have the typical characteristics of Lévy Flights [14–16]. Lévy flight [14] is a random walk in which the step-lengths are distributed according to a heavy-tailed probability distribution. After a large number of steps, the distance from the origin of the random walk tends to a stable distribution.

Cuckoo search characteristic The cuckoo search algorithm is based on the following three rules.

- At a time, cuckoo chose a nest randomly to lay an egg.
- The best nest is the nest with high quality eggs and the nest will carry over to the next generation.
- The number of available host nests is fixed. The probability of discovering an intruding egg by the host bird is $p_a \in [0, 1]$. If the host bird discovers the intruding egg it throw it away the nest or abandon the nest and starts to build a new nest elsewhere.

Cuckoo search algorithm In this section, we present in details the main steps of the CS algorithm as shown in Algorithm 2.

Algorithm 2 Cuckoo search algorithm

1: Set the initial value of the host nest size n, probability $p_a \in [0, 1]$ and maximum number of iterations Max_{itr}.
2: Set $t := 0$. {Counter initialization}.
3: **for** $(i = 1 : i \leq n)$ **do**
4: Generate initial population of n host $x_i^{(t)}$. {n is the population size}.
5: Evaluate the fitness function $f(x_i^{(t)})$.
6: **end for**
7: **repeat**
8: Generate a new solution (Cuckoo) $x_i^{(t+1)}$ randomly by Lévy flight.
9: Evaluate the fitness function of a solution $x_i^{(t+1)}$ $f(x_i^{(t+1)})$
10: Choose a nest x_j among n solutions randomly.
11: **if** $(f(x_i^{(t+1)}) > f(x_j^{(t)}))$ **then**
12: Replace the solution x_j with the solution $x_i^{(t+1)}$
13: **end if**
14: Abandon a fraction p_a of worse nests.
15: Build new nests at new locations using Lévy flight a fraction p_a of worse nests
16: Keep the best solutions (nests with quality solutions)
17: Rank the solutions and find the current best solution
18: Set $t = t + 1$. {Iteration counter increasing}.
19: **until** $(t < Max_{itr})$. {Termination criteria satisfied}.
20: Produce the best solution.

- **Step 1**. The standard cuckoo search algorithm starts with the initial values of population size n, probability $p_a \in [0, 1]$, maximum number of iterations Max_{itr} and the initial iteration counter t is setting. **Lines 1–2**
- **Step 2**. The initial population n is generated randomly and each solution x_i in the population is evaluated by calculating its fitness function $f(x_i)$. **Lines 3–6**
- **Step 3**. The following steps are repeated until the termination criterion satisfied
  - **Step 3.1**. A new solution is generated randomly using a Lévy flight as follow.

$$x_i^{t+1} = x_i^t + \alpha \oplus L\text{é}vy(\lambda), \tag{5}$$

    where $\oplus$ denotes entry-wise multiplication, α is the step size, and Lévy (λ) is the Lévy distribution. **Lines 8–9**
  - **Step 3.2**. The new solution is replaced with a random selected solution if its objective function is better than the objective function of the selected random solution. **Lines 10–13**
  - **Step 3.3**. A fraction $(1 - p_a)$ of the solutions selected randomly and abandoned and replaced by new solutions generated by using local random walks as follow.

$$x_i^{t+1} = x_i^t + \gamma(x_j^t - x_k^t), \tag{6}$$

where x_j^t and x_k^t are two different solutions selected randomly and γ is a random number. **Lines 14–15**

– **Step 3.4**. The solutions are ranked according to their objective values and the best solution is assigned and the iteration counter increases. **Lines 16–18**

- **Step 4**. The operation is repeated until the termination criteria are satisfied. **Line 19**
- **Step 6**. Produce the best found solution so far. **Line 20**

2.3 Social Spider Optimization

The social spider optimization (SSO) algorithm is a population based nature inspired algorithm proposed by Cuevas [17]. In the following subsections, we highlight the SSO algorithm and its concepts.

Main concepts and inspiration There are two fundamental components of a social spider colony, social members and communal web. The social members is divided into males and females. The number of female spiders reaches 70 %, while the number of male reaches 30 % of the total colony members [18, 19]. Each member in the colony cooperate in different activities such as building and maintaining the communal web, prey capturing, mating [20]. Female spiders show a major tendency to socialize present an attraction or dislike is developed over other spiders according to their vibrations based on the weight and distance of the members [21]. Male spiders are divided into two classes, dominate and non-dominate male spiders [22]. Dominant male spiders, have better fitness characteristics in comparison to non-dominant. Mating operation allows the information exchange among members and it is performed by dominant males and female. A dominant male mates with one or all females within a specific range to produce offspring. In the social spider optimization algorithm (SSO), the communal web represents the search space, each solution within the search space represents a spider position. The weight of each spider represents the fitness value of the solution.

Initializing the population The algorithm starts by initializing the population S of N spider positions (solution). The population contains of females f_i and males m_i. The number of females is randomly selected within the range of 65–90 % and calculated by the following equation:

$$N_f = floor[(0.9 - rand(0,1).0.25).N] \tag{7}$$

where rand is a random number between (0, 1), floor(.) maps a real number to an integer number. The number of male spiders N_m is calculated as follows.

$$N_m = N - N_f \tag{8}$$

The female spider position f_i is generated randomly between the lower initial parameter bound p_j^{low} and the upper initial parameter bound p_j^{high} as follow.

$$f_{i,j}^0 = p_j^{low} + rand(0,1).(p_j^{high} - p_j^{low}) \tag{9}$$

$$i = 1, 2, \ldots, N_f; \;\; j = 1, 2, \ldots, n$$

While the male spider position m_i is generated randomly as follow.

$$m_{i,j}^0 = p_j^{low} + rand(0,1).(p_j^{high} - p_j^{low}) \tag{10}$$

$$i = 1, 2, \ldots, N_m; j = 1, 2, \ldots, n$$

where j, i and k are the parameter and individual indexes respectively. The function rand(0, 1) generates a random number between 0 and 1.

Fitness evaluation in the SSO algorithm, the weight of each spider represents the solution quality. The function value of each solution i is calculated as follow.

$$w_i = \frac{J(s_i) - worst_s}{best_s - worst_s} \tag{11}$$

where $J(s_i)$ is the fitness value obtained of the spider position s_i, the values $worst_s$ and $best_s$ are the maximum and the minimum values of the solution in the population respectively (minimization problem).

Modeling of the vibrations through the communal web The information among the colony members is transmitted through the communal web. The information is encoded as a small vibrations that are critical for the collective coordination of all individual in the population. The vibrations depend on the weight and distance of the spider which has generated them. The information transmitted (vibrations) perceived by the individual i from member j are modeled as follow.

$$Vib_{i,j} = w_j.e^{-d_{i,j}^2} \tag{12}$$

where the $d_{i,j}$ is the Euclidian distance between the spiders i and j.

There are three special relationships of the vibrations between any pair of individuals as follows.

- **Vibrations** $Vibc_i$. The transmitted information (vibrations) between the individual i and the member c (s_c) which is the nearest member to i with a higher weight can be defined as follow.

$$Vibc_i = w_c.e^{-d_{i,c}^2} \tag{13}$$

- **Vibrations** $Vibb_i$. The transmitted information (vibrations) between the individual i and the member b (s_b) which is the best member in the population S can be defined as follow.

$$Vibb_i = w_b.e^{-d_{i,b}^2} \tag{14}$$

- **Vibrations** $Vibf_i$. The transmitted information (vibrations) between the individual i and the nearest female individual $f(s_f)$ can be defined as follow.

$$Vibf_i = w_f.e^{-d_{i,f}^2} \tag{15}$$

The vibrations $Vibc_i$, vibrations $Vibb_i$ and vibrations $Vibf_i$ are presented in Fig. 2a–c respectively.

Female cooperative operator The female spiders present an attraction or dislike over other irrespective of gender. The movement of attraction or repulsion depends on several random phenomena. A uniform random number r_m is generated within the range [0, 1]. If r_m is smaller than a threshold PF, an attraction movement is generated; otherwise, a repulsion movement is produced as follows.

$$f_i^{t+1} = \begin{cases} f_i^t + \alpha.Vibc_i.(s_c - f_i^t) + \beta.Vibb_i.(s_b - f_i^t) + \delta.(rand - 0.5) & \text{with probability } PF \\ f_i^t - \alpha.Vibc_i.(s_c - f_i^t) - \beta.Vibb_i.(s_b - f_i^t) + \delta.(rand - 0.5) & \text{with probability } 1 - PF \end{cases}$$

where α, β, δ and rand are random number between [0, 1], t is the iteration number.

Male cooperative operator The male spider with a weight value above the median value of the male population is called a dominant D, on the other hand the other males with weights under the median are called non-dominant ND. The median weight is indexed by $N_f + m$. The position of the male spider can be modeled as follows.

$$m_i^{t+1} = \begin{cases} m_i^t + \alpha.Vibf_i.(s_f - m_i^t) + \delta.(rand - 0.5) & \text{if} \quad w_{N_f+i} > w_{N_f+m} \\ m_i^t + \alpha.\left(\frac{\sum_{h=1}^{N_m} m_h^t.w_{N_f+h}}{\sum_{h=1}^{N_m} w_{N_f+h}} - m_i^t\right) \end{cases}$$

where the individual s_f represents the nearest female individual to the male member i.

Mating operator The mating in a social spider colony is performed by the dominant males and the female members. When a dominant male m_g spider locates a set E^g of female members within a specific range r (range of mating), which is calculated as follow.

$$r = \frac{\sum_{j=1}^{n} (p_j^{high} - p_j^{low})}{2.n} \tag{16}$$

The spider holding a heavier weight are more likely to influence the new product. The influence probability Ps_i of each member is assigned by the roulette wheal method as follows:

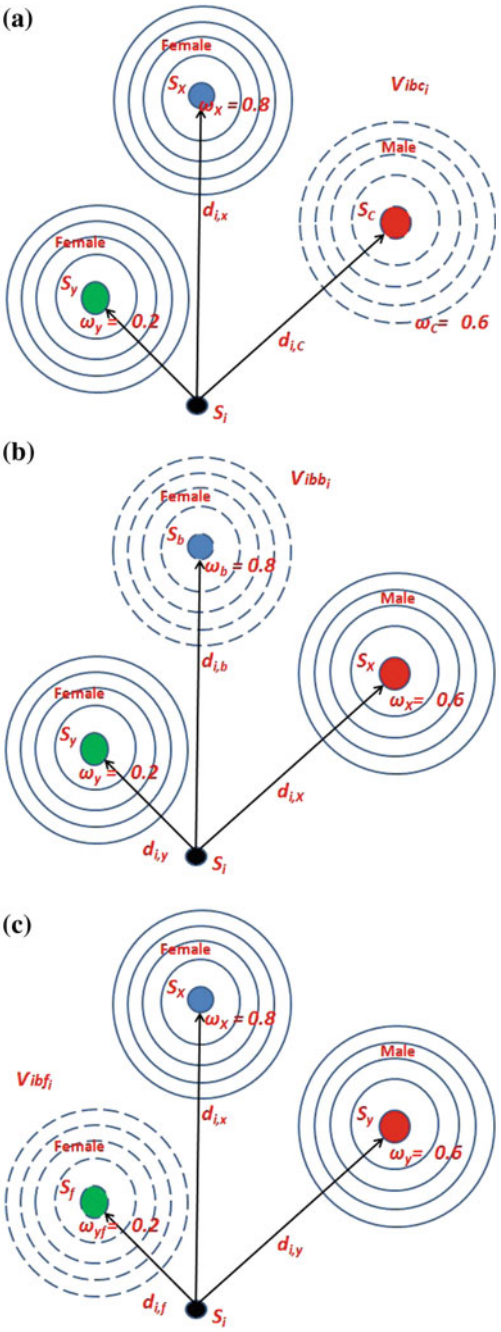

Fig. 2 Configuration of each special relation: **a** $Vibc_i$, **b** $Vibb_i$ and **c** $Vibf_i$

$$Ps_i = \frac{w_i}{\sum_{j \in T^t} w_j} \tag{17}$$

Social spider optimization algorithm In this subsection, we present in details the main steps of the proposed SSO algorithm as shown in Algorithm 3.

Algorithm 3 Social spider optimization algorithm

Set the initial value of total number of solutions N in the population size S, threshold PF, and maximum number of iterations Max_{itr}.
Set the number of female spiders N_f and number of males spiders N_m as shown in Equations 7, 8.
Set $t := 0$. {**Counter initialization**}.
for $(i = 1; i < N_f + 1; i++)$ **do**
  for $(j = 1; j < n + 1; j++)$ **do**
    $f_{i,j}^t = p_j^{low} + rand(0,1).(P_j^{high} - p_j^{low})$
  end for
end for{**Initialize randomly the female spider**}.
for $(k = 1; k < N_m + 1; k++)$ **do**
  for $(j = 1; j < n + 1; j++)$ **do**
    $m_{k,j}^t = p_j^{low} + rand(0,1).(P_j^{high} - p_j^{low})$
  end for
end for{**Initialize randomly the male spider**}.
repeat
  for $(i = 1; i < N + 1; i++)$ **do**
    $w_i = \frac{J(s_i) - worst_s}{best_s - worst_s}$
  end for{**Evaluate the weight (fitness function) of each spider**}.
  for $(i = 1; i < N_f + 1; i++)$ **do**
    Calculate the vibrations of the best local and best global solutions $Vibc_i$ and $Vibb_i$ as shown in Equations 13, 14.
    if $(r_m < PF)$ **then**
      $f_i^{t+1} = f_i^t + \alpha.Vibc_i.(s_c - f_i^t) + \beta.Vibb_i.(s_b - f_i^t) + \delta.(rand - 0.5)$
    else
      $f_i^{t+1} = f_i^t - \alpha.Vibc_i.(s_c - f_i^t) - \beta.Vibb_i.(s_b - f_i^t) + \delta.(rand - 0.5)$
    end if
  end for
  Find the median male individual (w_{N_f+m}) from M.
  for $(i = 1; i < N_m + 1; i++)$ **do**
    Calculate $Vibf_i$ as shown in Equation 15
    if $(w_{N_f i} > w_{N_f+m})$ **then**
      $m_i^{t+1} = m_i^t + \alpha.Vibf_i.(s_f - m_i^t) + \delta.(rand - 0.5)$
    else
      $m_i^{t+1} = m_i^t + \alpha.\left(\frac{\sum_{h=1}^{N_m} m_h^t.w_{N_f+h}}{\sum_{h=1}^{N_m} .w_{N_f+h}} - m_i^t\right)$
    end if
  end for
  Calculate the radius of mating r, where $r = \frac{\sum_{j=1}^{n}(p_i^{high} - p_j^{low})}{2.n}$ {**Perform the mating operation**}
  for $(i = 1; i < N_m + 1; i++)$ **do**
    if $(m_i \in D)$ **then**
      Find E^i
      if E^i is not empty **then**
        Form s_{new} using the roulette method
        if $w_{new} > w_{wo}$ **then**
          Set $s_{wo} = s_{new}$.
        end if
      end if
    end if
  end for
  $t = t + 1$ {**Iteration counter increasing**}.
until $(t < Max_{itr})$. {**Termination criteria satisfied**}.
Produce the best solution.

- **Step 1**. The algorithms starts by setting the initial values of the number of solutions N in the population size S, threshold PF and maximum number of iterations max_{itr}. Line (1)
- **Step 2**. The number of females and males are setting as shown in Eqs. 7 and 8. Line (2)
- **Step 3**. The initial iteration counter is initialized. Line (3).
- **Step 4**. The initial population is generated randomly for the females and the males solutions. Lines (4–13).
- **Step 5**. The following process are repeated until termination criteria satisfied
  - **Step 5.1**. Each solution in the population is evaluated by calculating its weight (fitness function as shown in Eq. 11. Lines (15–17).
  - **Step 5.2**. Move female spiders according to the female cooperative operator after calculating the vibrations of the local and global best spiders as shown in Eqs. 13 and 14. Lines (18–25).
  - **Step 5.3**. Move the male spiders according to the male cooperative operator after calculating the median male individual w_{N_f+m} from all male spiders. Lines (27–34).
  - **Step 5.4**. Perform the mating operation after calculating the radius of matting as shown in Eq. 16. Lines (35–46).
- **Step 6**. The number of iterations are increased. Line (47).
- **Step 7**. The best obtained solution is produced. Line (49).

2.4 Grey Wolf Optimization

Grey wolf optimizer (GWO) is a population based meta-heuristics algorithm simulates the leadership hierarchy and hunting mechanism of gray wolves in nature proposed by Mirjalili et al. [23]. In the following subsection, we will give an overview of the main concepts and structure of the grey wolf optimizer algorithm as follow.

Main concepts and inspiration Grey wolves are considered as apex predators, which they are at the top of the food chain. Grey wolves prefer to live in a group (pack), each group contains 5–12 members on average. All the members in the group have a very strict social dominant hierarchy as shown in Fig. 3. The social hierarchy consists of four levels as follow.

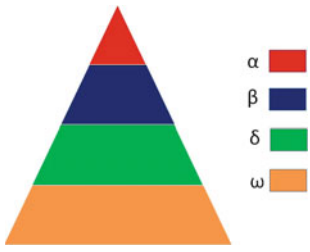

Fig. 3 Social hierarchy of grey wolf

- **The first level is called Alpha** (α) The alpha wolves are the leaders of the pack and they are a male and a female. They are responsible for making decisions about hunting, time to walk, sleeping place and so on. The pack members have to dictate the alpha decisions and they acknowledge the alpha by holding their tails down. The alpha wolf is considered the dominant wolf in the pack and all his/her orders should be followed by the pack members.
- **The second level is called Beta** (β) The betas are subordinate wolves, which help the alpha in decision making. The beta wolf can e either male or female and it consider the best candidate to be the alpha when the alpha passes away or becomes very old. The beta reinforce the alpha's commands throughout the pack and gives the feedback to alpha.
- **The third level is called Delta** (δ) The delta wolves are not alpha or beta wolves and they are called subordinates. Delta wolves have to submit to the alpha and beta but they dominate the omega (the lowest level in wolves social hierarchy). There are different categories of delta as follows
  - **Scouts**. The scout wolves are responsible for watching the boundaries of the territory and warning the pack in case of any danger.
  - **Sentinels** The sentinel wolves are responsible for protecting the pack.
  - **Elders** The elder wolves are the experienced wolves who used to be alpha or beta.
  - **Hunters** The hunters wolves are responsible for helping the alpha and beta wolves in hunting and providing food for the pack.
  - **Caretakers** The caretakers are responsible for caring for the ill, weak and wounded wolves in the pack.
- **The fourth (lowest) level is called Omega** (ω) The omega wolves are considered the scapegoat in the pack, they have to submit to all the other dominant wolves. They may seem are not important individuals in the pack and they are the last allowed wolves to eat. The whole pack are fighting in case of losing the omega.

In the following subsection, we present the mathematical models of the social hierarchy, tracking, encircling and attacking prey as follows.

Social hierarchy In the grey wolf optimizer (GWO), we consider the fittest solution as the alpha α, while the second and the third fittest solutions are named beta β and delta δ, respectively. The rest of the solutions are considered omega ω. In GWO algorithm, the hunting is guided by α, β and δ. The ω solutions follow these three wolves.

Encircling prey During the hunting, the grey wolves encircle prey. The mathematical model of the encircling behavior is presented in the following equations.

$$\boldsymbol{D} = |\boldsymbol{C} \cdot \boldsymbol{X_p}(t) - \boldsymbol{A} \cdot \boldsymbol{X}(t)| \tag{18}$$

$$\boldsymbol{X}(t+1) = \boldsymbol{X_p}(t) - \boldsymbol{A} \cdot \boldsymbol{D} \tag{19}$$

where t is the current iteration, $\boldsymbol{A}$ and $\boldsymbol{C}$ are coefficient vectors, $\boldsymbol{X_p}$ is the position vector of the prey, and $\boldsymbol{X}$ indicates the position vector of a grey wolf.

The vectors $\boldsymbol{A}$ and $\boldsymbol{C}$ are calculated as follows:

$$\boldsymbol{A} = 2\boldsymbol{a} \cdot \boldsymbol{r}_1 - \boldsymbol{a} \tag{20}$$

$$\boldsymbol{C} = 2 \cdot \boldsymbol{r}_2 \tag{21}$$

where components of $\boldsymbol{a}$ are linearly decreased from 2 to 0 over the course of iterations and $\boldsymbol{r}_1$, $\boldsymbol{r}_2$ are random vectors in $[0, 1]$.

Hunting The hunting operation is usually guided by the alpha α. The beta β and delta δ might participate in hunting occasionally. In the mathematical model of hunting behavior of grey wolves, we assumed the alpha α, beta β and delta δ have better knowledge about the potential location of prey. The first three best solutions are saved and the other agent are oblige to update their positions according to the position of the best search agents as shown in the following equations.

$$\begin{aligned} \boldsymbol{D}_\alpha &= |\boldsymbol{C}_1.\boldsymbol{X}_\alpha - \boldsymbol{X}|, \\ \boldsymbol{D}_\beta &= |\boldsymbol{C}_2.\boldsymbol{X}_\beta - \boldsymbol{X}|, \\ \boldsymbol{D}_\delta &= |\boldsymbol{C}_3.\boldsymbol{X}_\delta - \boldsymbol{X}|. \end{aligned} \tag{22}$$

$$\begin{aligned} \boldsymbol{X}_1 &= \boldsymbol{X}_\alpha - \boldsymbol{A}_1 \cdot (\boldsymbol{D}_\alpha), \\ \boldsymbol{X}_2 &= \boldsymbol{X}_\beta - \boldsymbol{A}_2 \cdot (\boldsymbol{D}_\beta), \\ \boldsymbol{X}_3 &= \boldsymbol{X}_\delta - \boldsymbol{A}_3 \cdot (\boldsymbol{D}_\delta). \end{aligned} \tag{23}$$

$$\boldsymbol{X}(t+1) = \frac{\boldsymbol{X}_1 + \boldsymbol{X}_2 + \boldsymbol{X}_3}{3}. \tag{24}$$

The search agent position updating process is shown in Fig. 4.

Attacking prey (exploitation) The grey wolf finish the hunt by attacking the prey when it stop moving. The vector $\boldsymbol{A}$ is a random value in interval $[-2a, 2a]$, where a is decreased from 2 to 0 over the course of iterations. When $|A| < 1$, the wolves attack towards the prey, which represents an exploitation process.

Search for prey (exploration) The exploration process in GWO is applied according to the position α, β and δ, that diverge from each other to search for prey and converge to attack prey. The exploration process is modeled mathematically by utilizing $\boldsymbol{A}$ with random values greater than 1 or less than –1 to oblige the search agent to diverge from the prey. When $|A| > 1$, the wolves are forced to diverge from the prey to fined a fitter prey. In the following subsection, we present the GWO algorithm as follows.

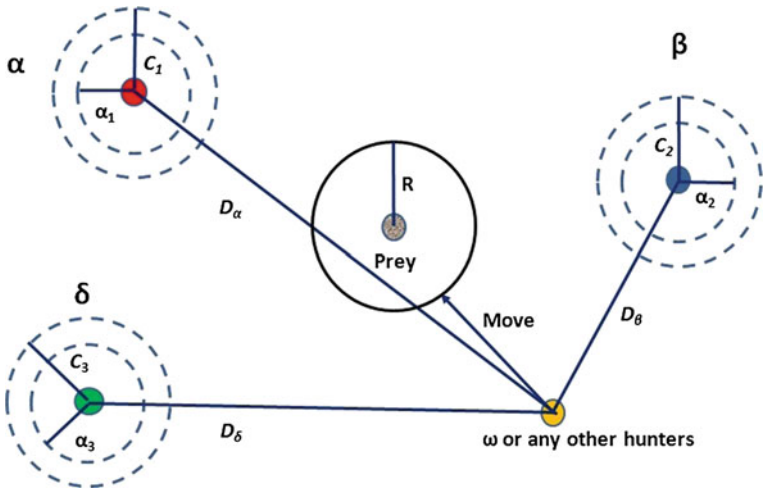

Fig. 4 Position updating in GWO

GWO algorithm

Algorithm 4 Grey wolf optimizer algorithm

1: Set the initial values of the population size n, parameter a, coefficient vectors $\boldsymbol{A}$, $\boldsymbol{C}$ and the maximum number of iterations Max_{itr}.
2: Set $t := 0$. {Counter initialization}.
3: **for** $(i = 1 : i \leq n)$ **do**
4: Generate an initial population $\boldsymbol{X_i(t)}$ randomly.
5: Evaluate the fitness function of each search agent (solution) $f(\boldsymbol{X_i})$.
6: **end for**
7: Assign the values of the first, second and the third best solution $\boldsymbol{X_\alpha}$, $\boldsymbol{X_\beta}$ and $\boldsymbol{X_\delta}$, respectively.
8: **repeat**
9: **for** $(i = 1 : i \leq n)$ **do**
10: Update each search agent in the population as shown in Equation 24.
11: Decrease the parameter a from 2 to 0.
12: Update the coefficients $\boldsymbol{A}$ and $\boldsymbol{C}$ as shown in Equations 20, 21, respectively.
13: Evaluate the fitness function of each search agent (vector) $f(\boldsymbol{X_i})$.
14: **end for**
15: Update the vectors $\boldsymbol{X_\alpha}$, $\boldsymbol{X_\beta}$ and $\boldsymbol{X_\delta}$.
16: Set $t = t + 1$. {Iteration counter increasing}.
17: **until** $(t < Max_{itr})$. {Termination criteria satisfied}.
18: Produce the best solution $\boldsymbol{X_\alpha}$.

- **Step 1**. The standard grey wolf optimizer algorithm starts by setting the initial values of the population size n, the parameter a, coefficients $\boldsymbol{A}$ and $\boldsymbol{C}$ and the maximum number of iterations max_{itr}. **Line 1**.

- **Step 2**. Initialize the iteration counter t. **Lines 2**.
- **Step 2**. The initial population n is generated randomly and each search agent $\boldsymbol{X}_i$ in the population is evaluated by calculating its fitness function $f(\boldsymbol{X}_i)$. **Lines 3–6**
- **Step 3**. Assign the values of the first, second and the third best solution $\boldsymbol{X}_\alpha$, $\boldsymbol{X}_\beta$ and $\boldsymbol{\delta}$, respectively. **Line 7**
- **Step 4**. The following steps are repeated until the termination criterion satisfied. **Lines 9–14**
  - **Step 4.1**. Each search agent (solution) in the population is updated as shown in Eq. 24. **Line 10**
  - **Step 4.2**. Decrease the parameter a from 2 to 0. **Line 11**
  - **Step 4.3**. The coefficients $\boldsymbol{A}$ and $\boldsymbol{C}$ are updated as shown in Eqs. 20 and 21, respectively. **Line 12**
  - **Step 4.4**. Each search agent in the population is evaluated by calculating its fitness function $f(\boldsymbol{X}_i)$. **Line 13**
- **Step 5**. The first, second and the third best solutions are updated $\boldsymbol{X}_\alpha$, $\boldsymbol{X}_\beta$ and $\boldsymbol{X}_\delta$, respectively. **Line 15**
- **Step 6**. The iteration counter is increasing $t = t + 1$. **Line 16**
- **Step 7**. The overall process is repeated until termination criteria satisfied. **Line 17**
- **Step 6**. Produce the best found search agent (solution) so far $\boldsymbol{X}_\alpha$. **Line 18**

3 Application 1: ABC Approach for CT Liver Segmentation

The Artificial Bee Colony (ABC) segmentation approach consists of three main phases: The usage of ABC makes the preprocessing phase easier and simpler, depending only on image cleaning for the patient's information and connecting ribs. In this phase there is no implementation of any other filters or morphological operations for preprocessing.

In the second Artificial bee colony phase, the image is clustered into a number of clusters that represents the centroids of the intensity values in the image. Each cluster is separated in a binary image. Then, some morphological operations are implemented on each cluster in a binary image. Finally the images of the clusters are gathered in one binary image.

In the third phase, the resulting binary image is multiplied by the original image, and enhanced by using simple region growing technique. The segmented image is validated using similarity index measure to calculate the accuracy. These phases are described in detail in the following section, along with the involved steps and the characteristics of each phase.

3.1 Preprocessing Phase: Ribs Boundary Connection

The usage of ABC eliminate the need for filtering in image preprocessing. Median filter is used in cleaning the image annotation and contrast stretching is used for connecting ribs.

A step of image cleaning starts the preprocessing phase, removing image annotation and machine's bed. It facilitates the next step of connecting ribs. Figure 5 shows the result of this step.

There is a problem of tissues of flesh and muscles which are adjacent and connected to liver in the left side of CT image. Connecting ribs aids to overcome this problem, using contrast stretching and a threshold close to white colour of ribs to isolate the ribs. In the original image, a line is drawn between the edges of the ribs to connect them. This separates the muscles from the liver tissues. See cleaning image and connecting ribs algorithms in details in [3, 24]. Figure 6 shows the result of connecting ribs process.

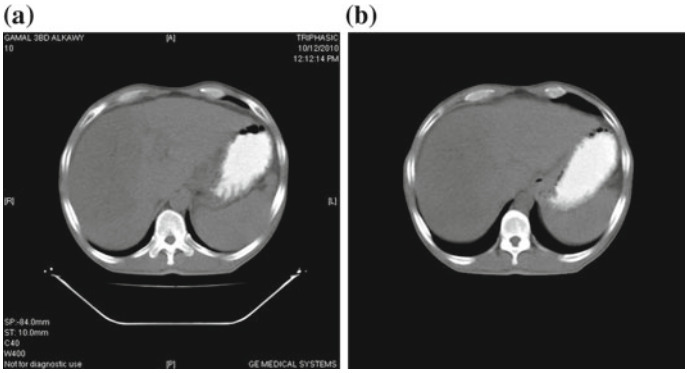

Fig. 5 Cleaning image. **a** Original image, **b** cleaned image

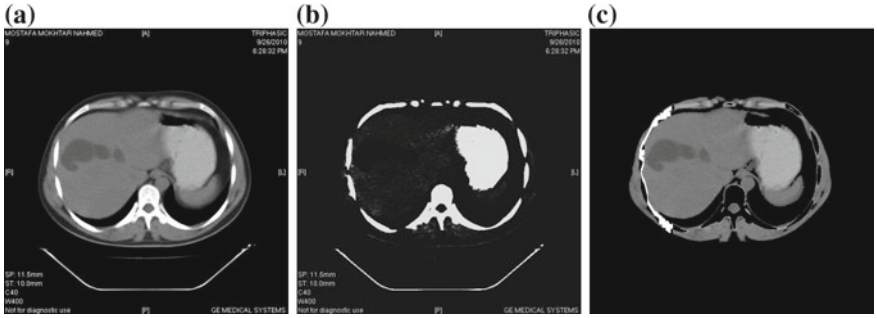

Fig. 6 Connecting ribs in the image: **a** Original image, **b** contrast stretching filter, **c** connected ribs

3.2 *Artificial Bee Colony Phase*

The ABC can be used as a clustering technique in the purpose of liver segmentation. Handling parameters settings of ABC algorithm leads to a better performance. The number of clusters is very important in this process. Liver CT image has two extreme intensity values which are the black background and white bones. Besides, there are intensity values of liver boundaries, lesion and other organs. Also we need to adjust the number of employed and onlooker bees in the colony, and we need to reduce the maximum iterations to reduce implementation cost. A fitness function helps to determine the new solution in every iteration. The resulting solutions of clusters (global parameters or best solution) will be the centroids of the required clusters.

The algorithm sets the parameters values and apply the ABC algorithm on the preprocessed image. ABC results in a number of clusters centroids, which is applied on all intensity values to determine the cluster that each point in the image belongs to. The clusters are sorted and extracted in binary images. Morphological operations are applied on each binary image to remove boundaries and small objects. Then we exclude the lowest and highest clusters and add other clustered images together. Finally, the resulting binary images multiplied by the original image to get the segmented one. Figure 7 shows a number of different clustered images using ABC algorithm.

Table 1 describes the successful parameter settings when applying the proposed algorithm.

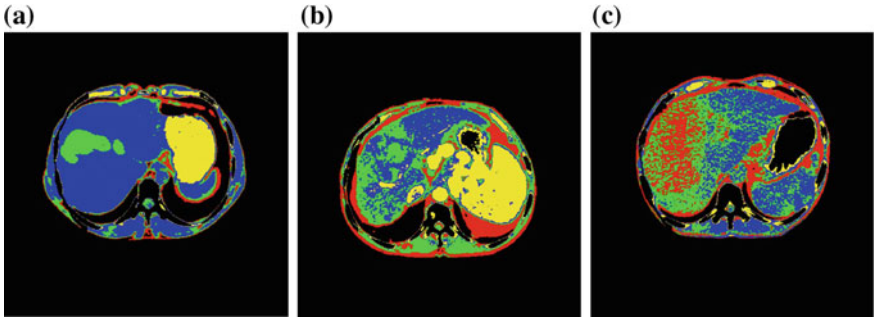

Fig. 7 Clustered results of different images using ABC

Table 1 Parameters of proposed approach

Ser.	Parameter	Setting
1	Population size	50
2	Food	25
3	Number of solutions	50
4	Maximum iterations	30
5	Number of clusters	6

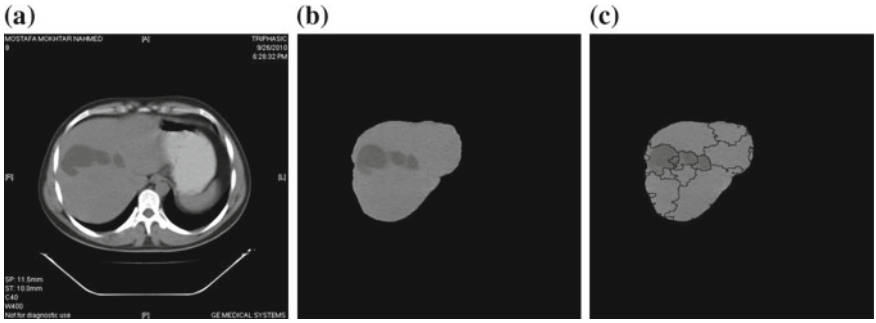

Fig. 8 Liver segmentation using region growing and watershed techniques: **a** Original image, **b** region growing image, **c** watershed image

There is an advantage of using ABC regarding the noise. It is not affected by noise at all. Because noise is small pixels, filled by morphological operations step.

3.3 Region Growing Phase

Similarity difference concept is used in region-based techniques to extract regions from the image. Some techniques as level set and fast marching use an initial contour to extract one region. Watershed technique is used to draw a closed boundary around all available objects [25]. Also region growing can do the same as level set and fast marching. Region growing has some advantages against other techniques. The advantages reside in its simplicity, speed and low cost of computational calculations. In this phase, region growing has been chosen to enhance the result of ABC segmentation. Figure 8 shows the implementation of region growing and watershed techniques.

3.4 Experimental Results and Discussion

A set of 38 CT images were used to experiment the proposed approach. The used images were taken in the first phase of CT scan before the patient is injected with contrast materials. Figure 9 shows the binary image of ABC and the liver segmented images.

Finally, the ABC segmented image is enhanced using simple region growing technique. Figure 10 shows the difference between the segmented image and annotated one.

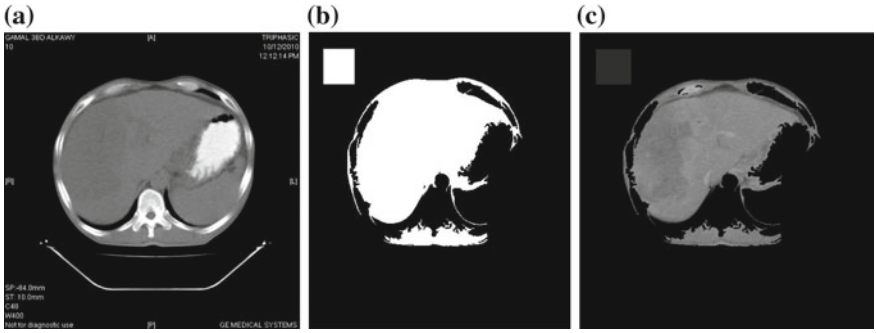

Fig. 9 ABC liver segmentation, **a** original image, **b** ABC binary image, **c** ABC segmented image

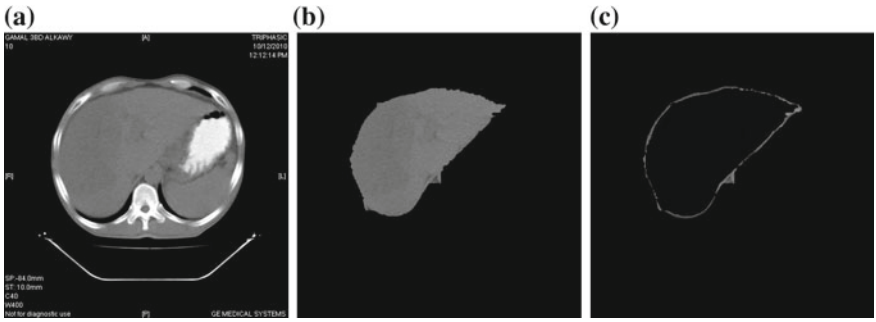

Fig. 10 Final liver segmented image compared to the annotated image: **a** Original image, **b** segmented image, **c** difference image

Evaluation is performed using similarity index (SI) defined using the following equations:

$$SI(I_{auto}, I_{man}) = \frac{I_{auto} \cap I_{man}}{I_{auto} \cup I_{man}} \tag{25}$$

where SI is the similarity index, I_{auto} is the binary automated segmented image, resulting from the phase of final segmentation of the whole liver in the used approach and I_{man} is the binary manual segmented image by a radiology specialist.

It shows that the average performance of liver images segmentation is improved using the proposed approach. Segmentation using region growing has average result of SI = 84.82 %. This result is improved using the proposed approach with SI = 93.73.

Table 2 compares the results of proposed approach to other methods.

Table 2 Comparison of Proposed approach with other methods

Ser.	Method	Result
1	Region growing	84.82
2	Level set	92.10
3	K-means with RG	92.38
4	Proposed approach with RG	93.73

4 Application 2: Grey Wolf Optimization for Abdominal CT Liver Parenchyma Segmentation

4.1 The Proposed Segmentation Approach

The proposed abdominal CT Liver parenchyma segmentation approach is comprised of three phases. The three phases are described in detail in the following section along with the steps involved and the characteristics feature for each phase and the overall architecture of the introduced approach is described in Fig. 11.

4.2 Preprocessing Phase

Preprocessing is the initial step for CT liver image clustering. It divided to two steps. They are: CT image resizing and Noise removal.

- **CT image resizing**. The goal of image resizing the image is to reduce computational time. In this work, CT image is resized to 256 * 256.
- **Noise removal**. Noise removal of image is most commonly used step in preprocessing phase. When image transforms from one form to another like scanning some degradation may occur in this case. Enhancement methods are needed in order to enhance the degraded image. A kind of these degradations is image noise. It can be defined as the random variation of color or brightness

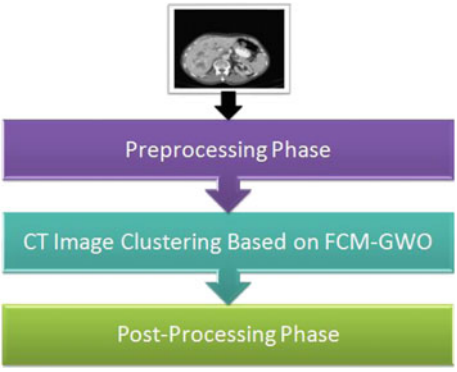

Fig. 11 Proposed Automatic CT liver Segmentation Architecture

information in images [26]. These noises are always undesirable. Removing these noises with preserving edges of the image plays a vital role in image processing. Median filter is one of the simplest and most popular approaches for removing noise like salt and pepper. In this work, median filter with window size 3 * 3 is applied to remove noise from CT image.

4.3 CT Image Clustering Based on FCM-GWO Phase

FCM is one of most commonly used clustering algorithm. The basic concept of FCM is to find optimal cluster centroids that minimize dissimilarity function, however, the main drawback of FCM is the local minimum. In order to solve this problem, a hybrid approach based on using FCM and GWO is proposed. The main goal of using GWO in this work is to enhance clustering results produced by using FCM and find optimal thresholds values. The great significant characteristic of any particle swarm versions is that it needs less parameter to adjust unlike Genetic Algorithm (GA). This characteristic obviously can highly influence the precision and efficiency of the algorithm [27]. Algorithm 5 describes the proposed clustering algorithm. Moreover, the initial values used for both Fuzzy Logic and GWO parameters are described in Table 3. These parameters values are found to best initial values from experimental results.

Algorithm 5 FCM-GWO Pseudo Algorithm.

Read enhanced CT image produced from previous phase $\bar{I}$
Get cluster centroids $C_j where j = 1, 2, ...NumofClusters$ of $\bar{I}$ from FCM
Initialize grey wolf positions P_i where i = 1,2, ... n with C_j
Initialize α, β and δ
Initialize wolves positions P_α, P_β and P_δ
while stopping criteria (convergence) do
  for each search agent **do**
    Update the position of current search agent
  end for
  Calculate fitness function for all search agents
  Update P_α, P_β and P_δ
end while

Table 3 Parameters setting of FCM-GWO algorithm

Parameter	Value (s)
Number of fuzzy clusters	3
Number of search agents	10
Number of iterations	5
Range (boundary of search space)	[0 255]
dimension	2

4.4 Post-pocessing Phase

This phase is divided to two steps. They are: Selection of best cluster image and Segmented region enhancement.

- **Selection of best cluster image**. In this step, the best cluster image obtained from the proposed FCM-GWO approach will be selected based on maximum mean value, where it found best representative feature of liver region in cluster image.
- **Segmented region enhancement**. Morphological operation is considered an important step for enhancement the image. Open, close are the used morphological operation to enhance the liver cluster image and to focus on liver parenchyma. Closing morphological operation defined at Eq. 26 and opening morphological operation at Eq. 27. Then the largest region will be taken as the final segmented liver region, as liver is the largest area in the middle cross sections of the abdominal liver CT image [28].

$$I \ominus H = \bigcap_{h \in H} I_{-h} \tag{26}$$

$$I \circ H = (I \ominus H) \oplus H \tag{27}$$

where H structure element and I image.

4.5 Results and Discussion

A set of 62 middle slice abdominal liver CT images taken from different patients are used to test system performance. The proposed CT image segmentation approach was programmed in MATLABR 2007 on a computer having Intel Core I3 and 2 GB of memory. Table 4 compares the result of FCM-GWO and PSO and in terms of Dice Coefficient, Correlation, Precision, Accuracy, Jacard Index, F-measure and Sensitivity for the used dataset. Table 5 compares the results of proposed system

Table 4 Comparison between segmentation results obtained from PSO and GWO

	FCM-GWO (%)	PSO (%)
F-measure	92.66	89.08
Precision	93.99	94.70
Sensitivity	91.94	84.02
Correlation	91.43	87.00
Accuracy	95.51	94.02
Dice	92.66	88.24
Jacard	86.52	81.22

Table 5 Comparison with existing work on liver segmentation

Method	Accuracy (%)
Level set [29]	70
Intensity-based partation and region-based texture [30]	86
Region Growing [31]	84
Enhanced Level set [32]	92
Adaptive threshold, morphological operators and connected component [33]	93
K-Means clustering, k-medoids clustering and hierarchical clustering [34]	87
FCM-GWO	96

with other traditional previous approach on CT liver segmentation from abdominal CT. As it can be seen, the proposed approach gives better results. Morever It's fully automatic system and it can extract for only one liver's slice in less than 8 s. Figure 12 shows the result from proposed approach. Figure 12a represent the middle slice original image, Fig. 12b shows the produced image after applying median filter, Fig. 12c shows labeled clustered image produced from FCM-GWO on CT image, Fig. 12d shows produced image after converted to binary image, Fig. 12e shows the produced image after applying open morphology operators, 12f shows produced image after selecting the largest objects, Fig. 12g shows produced image after applying close morphology operators, Fig. 12h shows produced image after filling holes, Fig. 12i shows final extracted liver region and Fig. 12j shows the obtained result from proposed approach and ground truth one where the result from proposed approach colored with purple and ground truth colored with pink. Table 6 shows the system affectiveness for different number of clusters of fuzzy in terms of Dice Coefficient, Correlation, Precision, Accuracy, Jacard Index, F-measure and Sensitivity. Figures 13 and 14 show system performance of different number of

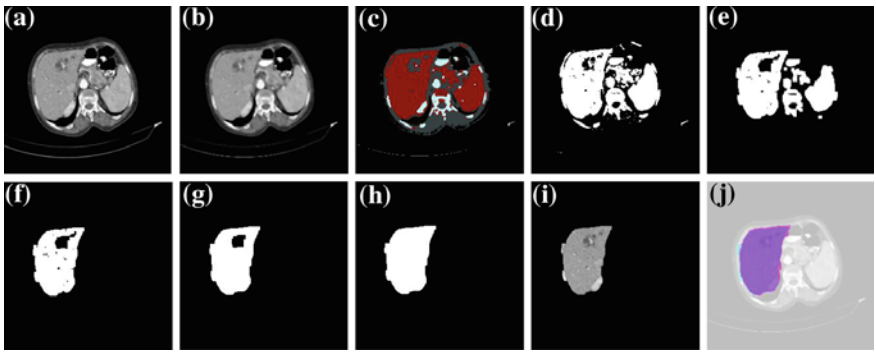

Fig. 12 Results of the proposed approach. **a** Original image, **b** image after applying median filter, **c** clustering results of FCM-GWO, **d** binarized clustered image, **e** image after applying open morphology, **f** image after filling holes, **g** image after applying close morphology, **h** image after filling holes, **i** automated extracted liver region and **j** the result from proposed approach and ground truth one

Table 6 The system affectiveness for different number of clusters of fuzzy

	C = 2 (%)	C = 3 (%)	C = 4 (%)	C = 5 (%)
F-measure	93.11	92.66	90.99	90.01
Precision	93.81	93.99	94.39	93.76
Sensitivity	92.74	91.94	89.14	91.52
Correlation	91.96	91.43	89.95	91.22
Accuracy	95.99	95.51	95.19	95.43
Dice	93.11	92.66	90.99	92.01
Jacard	87.17	86.52	84.21	84.51

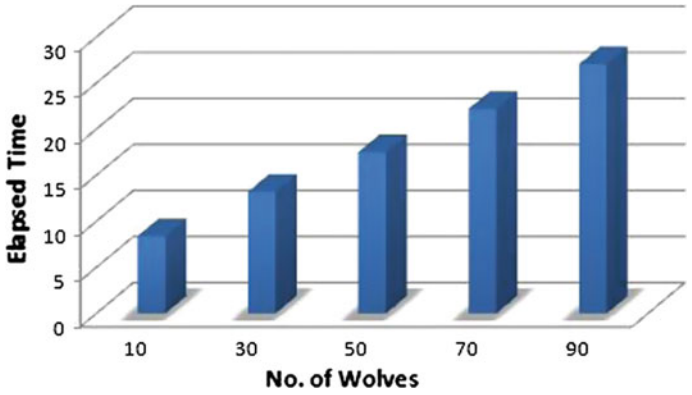

Fig. 13 The system performance based on different no. of wolves

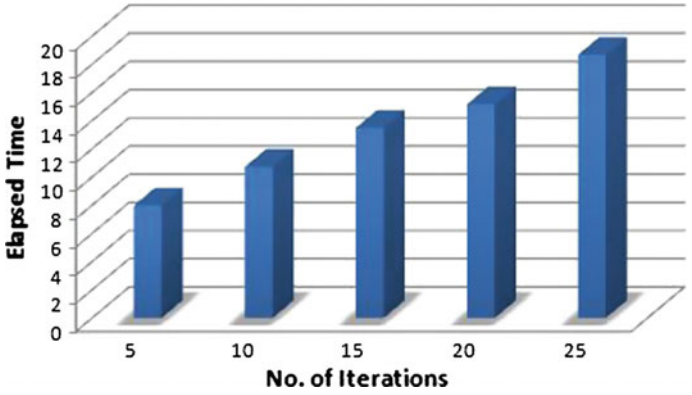

Fig. 14 The system performance based on different no. of iterations

iterations and different number of wolves (search agents) in terms of CPU process time in seconds. As we can see, elapsed time increased almost exponentially as we increase the number of iterations and number of wolves.

5 Conclusion and Future Work

In this chapter, we presented the main concepts of some of nature inspired algorithms such as Artificial Bee Colony, Cuckoo Search, Social Spider Optimization and Grey Wolf optimization. We highlighted the CT liver segmentation problem and how the nature inspired algorithms can be applied to solve this problem. Also, we described the use of ABC and Grey wolf optimization algorithms to solve the CT liver segmentation problems with different techniques. The experimental results showed the efficiency of the two algorithms. In the future work, we will apply more nature inspired algorithms with different medical imaging applications.

References

1. Duraisamy, S.P., Kayalvizhi, Ramanujam: A new multilevel thresholding method using swarm intelligence algorithm for image segmentation. J. Intell. Learn. Syst. Appl. **2**, 126–138 (2010)
2. Cuevas, E., Sencin, F., Zaldivar, D., Perez-Cisneros, M., Sossa, H.: Applied Intelligence (2012). doi:10.1007/s10489-011-0330-z
3. Mostafaa,A., Fouad, A., Abd Elfattah, M., Hassanien, A.E., Hefny, H., Zhu, S.Y., Schaefer, G.: CT liver segmentation using artificial bee colony optimisation. In: 19th International Conference on Knowledge Based and Intelligent Information and Engineering Systems, Procedia Computer Science, vol. 60, pp. 1622–1630 (2015)
4. Liang,Y., Yin, Y.: A New Multilevel Thresholding approach based on the ant colony system and the EM algorithm. Int. J. Innovative Comput. Inform. Control **9**(1) (2013)
5. Sivaramakrishnan, A., Karnan, M.: Medical image segmentation using firefly algorithm and enhanced bee colony optimization. In: International Conference on Information and Image Processing (ICIIP-2014), 316–321
6. Alomoush,W., Sheikh Abdullah, S.N., Sahran, S., Hussain, R.Q.: MRI brain segmentation via hybrid firefly search algorithm. J. Theor. Appl. Inform. Technol. **61** (2014)
7. Jagadeesan, R.: An Artificial Fish Swarm Optimized Fuzzy MRI Image Segmentation Approach for Improving Identification of Brain Tumour. In: Int. J. Comput. Sci. Eng. **5**(07) (2013)
8. Sankari, L.: Image segmentation using glowworm swarm optimization for finding initial seed. Int. J. Sci. Res. **3**(8) (2014)
9. Jindal, S.: A Systematic way for Image Segmentation based on Bacteria Foraging Optimization Technique (Its implementation and analysis for image segmentation). Int. J. Comput. Sci. Inform. Technol. **5**(1), 130–133 (2014)
10. Basturk,B., Karaboga, D. (2006) An artificial bee colony (ABC) algorithm for numeric function optimization. In: IEEE Swarm Intelligence Symposium 2006, Indianapolis, Indiana, USA, 12–14 May 2006

11. Karaboga, D.: An Idea Based On Honey Bee Swarm For Numerical Optimization, Technical Report-TR06, Erciyes University, Engineering Faculty, Computer Engineering Department, 2005
12. Yang, B., Chen, Y., Zhao, Z.: A hybrid evolutionary algorithm by combination of PSO and GA for unconstrained and constrained optimization problems. In: Proceedings of the IEEE International Conference on Control and Automation, pp. 166–170 (2007)
13. Payne, R.B., Sorenson, M.D., Klitz, K.: The Cuckoos. Oxford University Press (2005)
14. Brown, C., Liebovitch, L.S., Glendon, R.: Lévy flights in Dobe Ju/hoansi foraging patterns. Human Ecol. **35**, 129–138 (2007)
15. Pavlyukevich, I.: Lévy flights, non-local search and simulated annealing. J. Comput. Phys. **226**, 1830–1844 (2007)
16. Reynolds, A.M., Frye, M.A.: Free-flight odor tracking in Drosophila is consistent with an optimal intermittent scale-free search. PLoS ONE **2**, e354 (2007)
17. Cuevas, E., Cienfuegos, M., Zaldevar, D., Perez-Cisneros, M.: A swarm optimization algorithm inspired in the behavior of the social-spider. Expert Syst. Appl. **40**(16), 6374–6384 (2013)
18. Aviles, L.: Sex-ratio bias and possible group selection in the social spider Anelosimus eximius. Am. Nat. **128**(1), 1–12 (1986)
19. Aviles, L.: Causes and consequences of cooperation and permanent-sociality in spiders. In: Choe, B.C. (ed.) The Evolution of Social Behavior in Insects and Arachnids, pp. 476–498. Cambridge University Press, Cambridge (1997)
20. Eric, C., Yip, K.S.: Cooperative capture of large prey solves scaling challenge faced by spider societies. Proc. Natl. Acad. Sci. USA **105**(33), 11818–11822 (2008)
21. Maxence, S.: Social organization of the colonial spider Leucauge sp. in the Neotropics: vertical stratification within colonies. J. Arachnol. **38**, 446–451 (2010)
22. Pasquet, A.: Cooperation and prey capture efficiency in a social spider, Anelosimus eximius (Araneae, Theridiidae). Ethology **90**, 121–133 (1991)
23. Mirjalili, S., Mirjalili, S.M., Lewis, A.: Grey Wolf Optimizer. Adv. Eng. Softw. **69**, 46–61 (2014)
24. Zidan, A., Ghali, N.I., Hassanien, A., Hefny, H.: Level Set-based CT Liver Computer Aided Diagnosis System. Int. J. Imaging Robot. **9** (2013)
25. Vanhamel, I., Pratikakis, I., Sahli, H.: Multiscale gradient watersheds of color images. IEEE Trans. Image Process. **12**(6), 617–626 (2003)
26. Sakthive, N., Prabhu, L.: Mean—Median Filtering For Impulsive Noise Removal. Int. J. Basics Appl. Sci. **2**(4), 47–57 (2014)
27. Suzuki, K., Kohlbrenner, R., Epstein, M.L., Obajuluwa, A.M., Xu, J., Hori, M.: Computer-aided measurement of liver volumes in CT by means of geodesic active contour segmentation coupled with level-set algorithms. Med. Phys. **37**(5), 2159–2166 (2010)
28. Zayane, O., Jouini, B., Mahjoub, M.A.: Automatic liver segmentation method in CT images. ICanadian J. Image Process. Comput. Vis. **2**(8), 92–95 (2011)
29. Jeongjin, L., Namkug, K., Ho, L., Joon, B., Hyung, J., Yong, M., Yeong, S., Soo Hong, K.: Efficient liver segmentation using a level-set method with optimal detection of the initial liver boundary from level-set speed images. Elsevier, Comput. Methods Programs Biomed. **88**, 26–38 (2007)
30. Ruchaneewan, S., Daniela, S., Jacob,F.: A hybrid approach for liver segmentation. Intelligent Multimedia Processing Laboratory, 3D Segmentation in The Clinic: A Grand Challenge, pp. 151–160 (2007)
31. Abdalla, M., Hesham, H., Neven, I.G., Aboul Ella, H., Gerald, S.: Evaluating the Effects of Image Filters in CT Liver CAD System, In: Proceeding of: IEEE-EMBS International Conference on Biomedical and Health Informatics, The Chinese University of Hong Kong, Hong Kong (2012)
32. Abdalla, Z., Neveen, I.G., Aboul Ella, H., Hesham, A.H.: Level set-based CT liver image segmentation with watershed and artificial neural networks, IEEE, pp. 96–102 (2012)

33. Anter, A., Azar, A., Hassanien, A., El-Bendary, N., ElSoud, M.: Automatic computer aided segmentation for liver and hepatic lesions using hybrid segmentations techniques In: IEEE Proceedings of Federated Conference on Computer Science and Information Systems, pp. 193–198 (2013)
34. Aldeek, N., Alomari, R., Al-Zoubi, M., Hiary, H.: Liver Segmentation from Abdomen Ct Images with Bayesian Model. J. Theor. Appl. Inform. Technol. **60**(3), 483–490 (2014)

Optimized Multi Threshold Brain Tumor Image Segmentation Using Two Dimensional Minimum Cross Entropy Based on Co-occurrence Matrix

Taranjit Kaur, Barjinder Singh Saini and Savita Gupta

Abstract The present chapter proposes an automatic segmentation method that performs multilevel image thresholding by using the spatial information encoded in the gray level co-occurrence matrix (GLCM). The 2D local cross entropy approach that has been designed by extending the one dimensional (1-D) cross entropy thresholding method to a two dimensional (2D) one using the GLCM, serves as a fitness function. The use of conventional exhaustive search based implementations for multilevel thresholding are computationally expensive. Under such conditions evolutionary algorithm like particle swarm optimization (PSO) has been used. The effectiveness of this method was tested on brain tumor MR images and comparison was done with seven other level set based segmentation algorithms, using three different measures (1) Jaccard, (2) Dice and (3) Root mean square error (RMSE). The results demonstrate that average metric values were equal to 0.881902, 0.936394 and 0.070123 for proposed approach, which were significantly better than existing techniques.

Keywords Automatic segmentation · Multilevel thresholding · Cross entropy · Gray level co-occurrence matrix · Particle swarm optimization

T. Kaur (✉) · B.S. Saini (✉)
Department of Electronics and Communication Engineering,
Dr. B. R. Ambedkar National Institute of Technology, Jalandhar
Punjab, India
e-mail: taran.rehal@yahoo.com

B.S. Saini
e-mail: sainibss@gmail.com

S. Gupta (✉)
Department of Computer Science and Engineering,
University Institute of Engineering and Technology (UIET),
Panjab University, Chandigarh, India
e-mail: savita2k8@yahoo.com

N. Dey et al. (eds.), *Medical Imaging in Clinical Applications*,
Studies in Computational Intelligence 651, DOI 10.1007/978-3-319-33793-7_20

1 Introduction

The process of image segmentation refers to the mechanism of extracting different objects from an image. Segmentation in case of medical images has a variety of applications ranging from the lesion quantification to surgical planning. Computed tomography (CT) and MRI are two imaging modalities that help researchers and medical practitioners to study the brain by looking at it non-invasively [1–3]. MR imaging is generally a modality of choice for the visualization of various metabolic brain diseases due to its excellent soft tissue contrast and availability of multispectral images [4, 5]. The radiologists normally combine the information from these multiple images in order to give their final decision about the true extent of lesion and the appropriate therapy treatment. Abnormal regions of interest in images can be either manually marked by radiologists [6–8] or by the use of computer assisted techniques which can be automatic or semi-automatic. Since the conventional imaging modalities like CT and MRI are 3D in nature the manual segmentation is not only tedious and time consuming but also suffers from the inter observer variability [9–11]. Also in case of the tumorous MR images the segmentation is even more challenging because of the unclear and irregular boundaries of the various high grade tumors [12–14]. A large number of methods exist in the literature for the purpose of segmentation and the prominent among them are pixel classification [15, 16], modelbased [17, 18] and thresholding based [19] approaches.

2 Related Work

Caselles et al. [17] introduced a contour based method in which the gradient of the image was used to compute the force function. The designed method does not require any regularization term. The proposed method, referred to as the Geodesic Active Contour combines the classical "snakes" and the geometric active contour method for the object segmentation. The experiments on the real images including objects with holes and medical data (MR images with tumor and ultrasound images) demonstrate its capability for efficient image segmentation. Also, the algorithm possesses the ability in detecting the interior and exterior boundaries of the object.

Joe et al. [20] proposed a semi-automated threshold based method for computing the enhancing brain tumor volume in the case of patients with high grade glioma using T1 images. The efficiency of the proposed method was justified in terms of lesser computational time in comparison to manual trace methods by an average of 4.6 min per patient. Fletcher-Heath et al. [21] employed Fuzzy C-means clustering along with knowledge based techniques for the delineation of non-enhancing brain tumor region from the normal brain tissues using T1, T2 and Proton Density (PD) images. The efficacy of the proposed method was quantitatively evaluated by the measures of correspondence ratio and the % age match which were in range from 0.368–0.871 and 0.530–0.909 per volume. Chan and Vese [22] formulated a new

model for active contour that performs the object detection in a given image based on the techniques of curve evolution. The stopping term does-not depend on the gradient of the image but is related to the segmentation of the current image. Numerical results on the various synthetic and real images illustrate the segmentation efficiency of the method qualitatively. The method also eliminates the need to smooth the initial image before processing it, in case it was noisy.

Liu et al. [23] devised a fuzzy connectedness algorithm for the segmentation of Glioblastoma multiforme brain tumor (GBM) using T1, T1-CE and FLAIR images. The computed coefficient of variation in the computation of volume due to the specification of the seed points was less than 1 %. Vijaykumar et al. [24] used self organizing maps for the segmentation of tumor, edema, necrosis, white matter (wm), gray matter (gm) and cerebral spinal fluid (csf) from the dataset containing both high and low grade tumors. The images employed were T2, FLAIR and apparent diffusion coefficient maps and the observed sensitivity and specificity were 0.86 and 0.93 respectively. Corso et al. [9] devised a model based method along with graph cuts for the delineation of GBM brain tumor and its various constituents using T1 precontrast, T1-CE, FLAIR and T2 images. The efficacy of the proposed method was compared with conventional affinity, saliency based extraction, cross validation and single voxel methods using volume overlap (VO) measure which was 69 % for tumor training and testing dataset.

Shi et al. [18] proposed a two cycle algorithm to approximate level set based curve evolution without the need of solving the partial differential equation (PDE). The authors separated the evolution process into two different cycles, one cycle for the data dependent term and the second cycle for the smoothness regularization. Comparison with the PDE-based narrow band algorithm in insight toolkit ITK [25] on the set of images and video processing applications indicate the designed algorithm was computationally much faster (nearly 25 times faster than ITK per iteration).

Li et al. [26] developed a region-based active contour model that draws upon the intensity information in local regions at a controllable scale to counteract with the intensity inhomogeneity problem. The experimental results were obtained using the synthetic and real images from various modalities like CT and MRI. The results were compared with the PS model and mean shift algorithm on the measures of computation time and accuracy. The devised algorithm was 15–60 times faster than the PS model.

Lankton et al. [27] employed a region-based method using the local image statistics for the evolution of the contour. The algorithm allows for the reformulation of the region based segmentation energy and thereby proves to be efficient in segmenting images with the heterogeneous feature profiles. The improvements obtained by the localization was illustrated by its comparison with the global counterparts using the convergence and timing properties. Although the proposed algorithm was sensitive to initialization, the experimentation on various natural and biomedical images like those of heart and brain indicated its proficiency in terms of the computational time which was 4–5 s.

Wang et al. [28] devised Fluid vector flow method for the segmentation of synthetic, pediatric head and brain tumor T1 MRI images taken from Internet Brain Segmentation Repository (IBSR). The effectiveness of the method was justified by its ability to extract concave shapes and capture large ranges. The computed measures i.e. mean, median and standard deviation (SD) were 0.61, 0.60 and 0.05 respectively.

Bernard et al. [29] designed a region based level set approach in which the implicit function was modeled as a continuous parametric function expressed on a B-spline basis. Simulated and biomedical images were used for the evaluation of the designed technique using the dice measure at different levels of the additive gaussian noise. For a particular leaf image corrupted with the Gaussian noise of SNR equal to 30 dB, the total running time (seconds), number of iterations, time required for the estimation of the various parameters (seconds) and dice coefficient were equal to 15.48, 33, 4.19 and 0.985 respectively using the designed approach. Comparison with the existing fast two-cycle algorithm (FTC) clearly justifies the potential of the designed method in terms of the computation time.

Khotanlou et al. [30] employed Fuzzy possibilistic C-Means algorithm (FPCM) and symmetry analysis method for the segmentation of various cerebral tumors using T1 and T1-CE images. The final tumor boundary was refined using deformable models constrained by spatial relations. The efficiency was evaluated by measures of ratio of correct detection (T_p), ratio of false detection (F_p), similarity index (s), Hausdorff distance (D_H) and average distance (D_m) which were: −s = 92/90, T_p = 93/90, F_p = 7.92/9.08 %, D_H = 4.57/4.92 mm and D_m = 0.69/0.71 mm respectively for symmetry analysis and FPCM approach. Iftekharuddin et al. [31] used self-organizing maps for the segmentation of tumors in the pediatric patients by employing T1-CE, T2 and FLAIR images. The segmentation efficiency using single modality images ranged from 57–95 % and using multimodality images it was 100 %.

Ahmed et al. [32] used expectation maximization and graph cuts for the segmentation of tumors in the posterior Fossa region using T1, T2 and FLAIR images. The radar plots for the similarity metrics i.e. Jaccard, Dice, Sokal and Sneath (SS) and Russel and Rao (RR) ratios were constructed. From the plots the overall Jacard score and RR measures were about 60 %, Dice overlap measure was >80 % and SS measure was >60 %.

Dang et al. [33] employed level set method for the meningioma tumor volume computation using T1-CE images. The results were compared with those obtained by the modified Mcdonalds (MM) and manual trace method through the measures of computational time which were 1.20 (mm:s) for level set method, 1.35 for MM method and 9.35 for the manual trace approach.

Islam et al. [34] proposed a modified adaboost classifier for the separation of tumor from the non-tumor regions using T1, T2 and FLAIR images of pediatric patients. The efficiency was computed through the measures of Jaccard coefficient, Dice similarity index, SS ratio, Roger and Tanimoto index, True positive fraction and false positive fraction which were 0.71, 0.83, 0.55, 0.73, 0.79 and 0.11

respectively and its applicability to the publically available low grade glioma BRATS2012 dataset.

Arakeri and Reddy [35] employed modified FCM (MFCM) for the segmentation of benign and malignant brain tumors from the T1-CE and T2 images. The MFCM performs the clustering on the basis of grey level histogram instead of pixels in the image and it resulted in overall mean value of VO, D_H and Symmetric mean absolute surface distance (SMD) equal to 89.35 %, 3.62 and 0.54 mm respectively.

Hemanth et al. [10] also proposed a modified distance metric based Fuzzy C Means clustering algorithm for the segmentation of meningiomas, astrocytoma, gliomas and metastatic brain tumors. The modified FCM reduced the computation time by a factor of 8 in comparison to the FCM algorithm without compromising much for the segmentation efficiency which was 97.5 and 98 % using the algorithms.

Thapaliya et al. [36] devised a new level set approach combining the advantages of the Chan Vese and Geodesic Active Contour (GAC) method. The authors introduced a new signed pressure function that effectually stops the contour at weak or blurred edges. The various parameters involved in the algorithm were computed automatically. The thresholding parameter was adaptively adjusted for different MR images. The validation dataset consists of eight tumor MR images acquired from internet repository. The Jaccard, Dice, Root mean square error (RMSE) and computational time were used to access the performance of the proposed approach. The results of the lesion segmentation for the designed method were compared with the Chumming, region growing and Singh and Dubey method. Performance estimation in context to the manually segmented ground truth verifies that the object is extracted efficiently regardless of the evolution of the contour.

Among all the approaches discussed above, the simplest technique of the thresholding has been limited explored for tumor segmentation application. The next discussion pertains to the description about the various existing thresholding approaches. Threshold based approaches are broadly divided into parametric and nonparametric methods [37]. The parametric methods works by computing parameters of the probability density function that will best fit the given histogram data. This is a nonlinear optimization problem for which the output solution is computationally expensive and time consuming [38]. The nonparametric techniques on the other hand determine the optimal thresholds by optimizing certain objective function [39]. In the category of nonparametric methods the most efficient are the entropy based approaches such as Kapurs Entropy, Tsallis Entropy, Cross Entropy, Renyi Entropy, Fuzzy Entropy and the entropies computed from the gray level co-occurrence matrices [40, 41]. Among these thresholding methods, minimum cross entropy based approach has been widely adopted for its simplicity and the measurement accuracy [42].

The minimum cross entropy criteria works well for the bilevel thresholding problem but suffers from the exponential increase in the computational complexity when it involves the calculation of the multiple thresholds. For fastening the threshold selection process and eliminating the exhaustive search mechanism meta-heuristic algorithms have been incorporated with this entropy measure. Yin [43] employed a recursive programming technique along with the particle swarm

optimization (PSO) algorithm to compute the optimal set of thresholds using this criteria. The estimation of the algorithm effectuality was done using the measure of computation time.

The experimentations were done on the standard images and the thresholds nearly equal to those computed by exhaustive search method were obtained at the minimum computation cost of 0.01 s. Horng [38] proposed a minimum cross entropy (MCE) algorithm based on Honey bee mating optimization algorithm (HBMO). The segmentation analysis were done on the set of the five standard images and the results were compared with the PSO and the quantum PSO (QPSO) method. The author concluded that the maximum peak signal to noise ratio (PSNR) was achieved using the HBMO technique and the obtained thresholds were similar to that obtained using the exhaustive search approach. For a particular Goldhill image the obtained value of the computational time was 0.504 s at a PSNR value of 20.75 in comparison to the PSO and QPSO based approaches in which they were 0.486 s, 20.73 and 0.417 s and 20.61 respectively. The analysis shows a comparable computational time but the PSNR and the fitness value were significantly better for the proposed approach.

Later on the same author did the investigation using a new technique called as firefly (FF) algorithm [44] and concluded that FF based minimum cross entropy thresholding (MCET) approach was efficient in terms of PSNR value and the computation time, with respect to PSO, QPSO, HBMO and exhaustive search methods. The analysis was done on the same set of images, and the results were compared with the exhaustive search, PSO, QPSO and HBMO techniques. Least computational time was obtained using the FF based MCET algorithm. For e.g. for a particular Goldhill image of dimensions 256×256 the computational time was 0.134 s at a PSNR value of 20.75. For other approaches, it was 444.569 s, 259.65 ms, 292.84 ms and 258.54 ms respectively.

Tang et al. [42] employed a recursive programming technique along with the real coded Genetic algorithm (GA) to compute the optimal set of thresholds using the MCET technique. The efficacy of the approach was justified by its faster computation time and better uniformity values in comparison to the exhaustive search technique. For a particular Lena image of dimensions 512×512 and a four level thresholding problem, the CPU time using recursive GA approach was found to be 0.0269 s with a uniformity value of 0.993859. The results were better than exhaustive search approach for which it was 850.2065 s for a uniformity value equal to 0.993971.

Sarkar et al. [45] explored the effectiveness of the MCET technique for the color image segmentation using the Differential Evolution (DE). The superiority of the approach was justified in terms of lesser number of function evaluations in comparison to GA, PSO and Artificial Bee Colony (ABC) algorithm. The analysis were done on Berkley Segmentation Dataset and the effectuality of the algorithm was verified both quantitatively and qualitatively with seven existing techniques in literature. The achieved values of the boundary displacement error (BDE), Probabilistic Rand Index (PRI), Global consistency error (GCE) and Variation of information (VOI) were 9.3468, 0.7552, 0.2485 and 2.1675 respectively for a 10

level segmentation. All the methods which are discussed above employs the information extracted from the one dimensional (1-D) histogram of the image in one way or the other. These methods suffer from the drawback that they do not take into account the image spatial correlation. As a result of which, images having the same type of histogram resulted in the same value of thresholds. Such a drawback was mitigated by the evolution of 2D approaches which takes into account the inter-pixel spatial correlation in different ways. In this category techniques based on the construction of 2D histogram from the 1D histogram and the local average pixel values and those based on GLCM are most common. Better performance of the GLCM based approaches had been verified for the image segmentation in works by [46–48].

Mokji and Abu Bakar [46] devised an adaptive thresholding technique based on the co-occurrence matrix (GLCM). The proposed method was tested on starfruit defect images. Since the images had fuzzy boundaries, they were better segmented using the designed method as it had more flexibility in edge definition. Comparison of the designed scheme with three other existing techniques namely Otsu, entropy based and Li et al. [49] method indicated the superiority of the approach when estimated visually.

El-Feghi et al. [48] devised an improved co-occurrence matrix information measure for thresholding the natural images. The improved matrix utilized more local neighborhood information than the traditional co-occurrence matrix. The proposed bi-level thresholding method had a high robustness to noise in contrast to the conventional approach.

Extension of the 1D cross entropy based thresholding into 2D using GLCM to incorporate the above stated advantages have been verified in the works by [50]. Eight images were used in the experiment, and the bilevel thresholding results were compared with the eight existing methods. The effectiveness of the proposed method was demonstrated both visually and quantitatively using the measures of the uniformity and shape. For a particular Tank image, the uniformity value equal to 0.9908 and shape measure equal to 0.9964 was obtained using the designed approach. On a thorough analysis, on the computational complexity it was concluded that the time consumption of the proposed method was the most nearly greater than 1 s for most of the images. Such an approach would lead to an exponential increase in the computational complexity when applied to a multilevel thresholding problem. Until now most of such approaches which involve the GLCM information into a cross entropy framework, were bilevel, no multilevel 2D entropy based scheme can be found in literature. The endeavor of this chapter is focused, on developing a multilevel thresholding algorithm which incorporates the advantages of cross entropy and GLCM to obtain efficient tumor image segmentation when computationally aided with PSO algorithm.

The chapter is organized as follows, Sect. 3 outlines the problem formulation, Sect. 4 gives the brief review about the PSO algorithm and its incorporation with the constructed objective function, Sect. 5 presents the database and the performance measures, Sect. 6 provides the results and discussions and finally Sect. 7 concludes the chapter.

3 Problem Formulation Using the Cross Entropy and GLCM

3.1 Cross Entropy

The concept of the cross entropy was first proposed by Kullback [51] in the year 1968. This entropy was devised as an information theoretic distance between two probability distributions on the same set [42]. The cross entropy criteria as given by Li and Lee [52] can be defined as follows:

$$D(t) = \sum_{i=0}^{t} ih_i \log(i/\mu_1(t)) + \sum_{i=t+1}^{L-1} ih_i \log(i/\mu_2(t)) \tag{1}$$

where

$$\mu_1(t) = \frac{\sum_{i=0}^{t}(ih_i)}{\sum_{i=0}^{t}(h_i)} \quad \mu_2(t) = \frac{\sum_{i=t+1}^{L-1}(ih_i)}{\sum_{i=t+1}^{L-1}(h_i)} \tag{2}$$

Here t denotes the threshold value, h_i denotes the frequency of the gray level and L denotes the total number of the gray levels. The optimal threshold for the bi level thresholding is chosen as the one which minimizes the Eq. (1). Mathematically it is given as:

$$t* = \arg\ \min[D(t)] \tag{3}$$

The formula given by Eq. (1) utilizes only the information extracted from the image histogram but does not take into account the spatial relationship of the pixels in the image. As a result when thresholds are computed, using the cross entropy measure for the different images having the same histogram distribution, it would result in same threshold value which is inappropriate. So in order to account for the spatial distribution, 2D local cross entropy is defined over the GLCM sub-blocks which is then minimized for the computation of the optimal thresholds. The next sub sections outlines the concept of GLCM and construction of 2D local cross entropy function with its multilevel extension.

3.2 GLCM

The co-occurrence matrix encodes the information about the transition of intensities between the adjacent pixels. For an image $I = [f(x, y)]_{MXN}$ with size $M \times N$ with

L gray levels the GLCM matrix is a $L \times L$ square matrix denoted by $V = [R_{ij}]_{L\times L}$ where R_{ij} denotes the $(i,\ j)th$ element of the co-occurrence matrix. Mathematically it is defined as [46]

$$R_{ij} = \sum_{m=1}^{M} \sum_{n=1}^{N} \delta_{mn} \tag{4}$$

$$\delta_{mn} = \begin{pmatrix} 1, & if \begin{Bmatrix} f(m,n) = i \quad and \quad f(m+1,n) = j \\ and/or \\ f(m,n) = i \quad and \quad f(m,n+1) = j \end{Bmatrix} \\ 0, & otherwise \end{pmatrix} \tag{5}$$

The transition probability from a gray level i to j is obtained by:

$$p_{ij} = \frac{R_{ij}}{\sum_{k=0}^{L-1} \sum_{l=0}^{L-1} R_{kl}} \tag{6}$$

3.3 2D Multi-level Local Cross-Entropy Thresholding Scheme

The brain tumor MRI image primarily comprises of the white matter, gray matter, cerebral spinal fluid region (CSF), the abnormality (complete tumor area) and the background region. The goal of the segmentation algorithm would be the efficient delineation of these constituents. For partitioning the brain tumor image into five regions, four thresholds would be required.

The reason for using four thresholds was to separate out the four tissue constituents and the background region from the given tumorous MR image, as four thresholds would partition the image into five regions. As the number of the thresholds increases the segmented images become more uniform, smoother and resembles the original image. Also, finer details would more be prominent, and tumor constituents like necrosis, solid region and edema can also be delineated. Since the present data set contains only the enhancing tumor region, so a total of four thresholds are sufficient for tracking the diseased region.

So in the presented work:

Required number of thresholds = Total number of Image constituents −1.

Those set of optimal thresholds are chosen that efficiently partition the GLCM into twenty five sub-blocks, A to Y as shown in Fig. 1. The sub-blocks A, G, M, S and Y represents the local transitions within the background and foreground. The left over sub-blocks are associated with the transitions across the boundaries between the background and the foreground. So, among the 25 possible sub blocks,

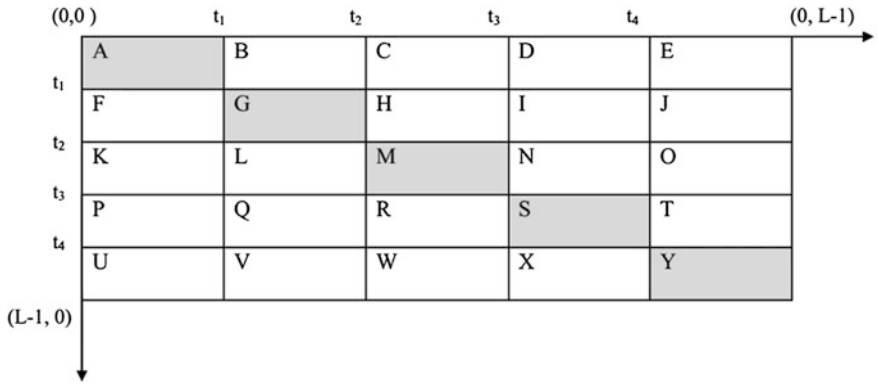

Fig. 1 Sub-blocks of the GLCM for a 5 level segmentation

only the diagonal sub blocks are chosen for the better separation between the object and the background. Rest all can be neglected as they mostly contain the edges and the noise, which has also been verified in the works by [50, 53]. So, the transition probabilities associated with each of the diagonal sub-block are defined as follows:

$$P_A^t = \sum_{i=0}^{t_1} \sum_{j=0}^{t_1} p_{ij} \tag{7}$$

$$P_G^t = \sum_{i=t_1+1}^{t_2} \sum_{j=t_1+1}^{t_2} p_{ij} \tag{8}$$

$$P_M^t = \sum_{i=t_2+1}^{t_3} \sum_{j=t_2+1}^{t_3} p_{ij} \tag{9}$$

$$P_S^t = \sum_{i=t_3+1}^{t_4} \sum_{j=t_3+1}^{t_4} p_{ij} \tag{10}$$

$$P_Y^t = \sum_{i=t_4+1}^{L-1} \sum_{j=t_4+1}^{L-1} p_{ij} \tag{11}$$

Let μ_A^t, μ_G^t, μ_M^t, μ_S^t, μ_Y^t denotes the pixel average value for the segmented sub blocks which are obtained using the thresholds t_1, t_2, t_3 and t_4 and are given by the expressions below:

$$\mu_A^t = \frac{1}{P_A^t} \sum_{i=0}^{t_1} \sum_{j=0}^{t_1} (ijp_{ij}) \tag{12}$$

$$\mu_G^t = \frac{1}{P_G^t} \sum_{i=t_1+1}^{t_2} \sum_{j=t_1+1}^{t_2} (ijp_{ij}) \tag{13}$$

$$\mu_M^t = \frac{1}{P_M^t} \sum_{i=t_2+1}^{t_3} \sum_{j=t_2+1}^{t_3} (ijp_{ij}) \tag{14}$$

$$\mu_S^t = \frac{1}{P_S^t} \sum_{i=t_3+1}^{t_4} \sum_{j=t_3+1}^{t_4} (ijp_{ij}) \tag{15}$$

$$\mu_Y^t = \frac{1}{P_Y^t} \sum_{i=t_4+1}^{L-1} \sum_{j=t_4+1}^{L-1} (ijp_{ij}) \tag{16}$$

The 2D local cross entropy, which is computed between the original and the thresholded image about the sub-blocks A, G, M, S and Y can be defined as follows:

$$J(A|t) = \sum_{i=0}^{t_1} \sum_{j=0}^{t_1} ijp_{ij} \log(ij/\mu_A^t) + \sum_{i=0}^{t_1} \sum_{j=0}^{t_1} \mu_A^t p_{ij} \log(\mu_A^t/ij) \tag{17}$$

$$J(G|t) = \sum_{i=t_1+1}^{t_2} \sum_{j=t_1+1}^{t_2} ijp_{ij} \log(ij/\mu_G^t) + \sum_{i=t_1+1}^{t_2} \sum_{j=t_1+1}^{t_2} \mu_G^t p_{ij} \log(\mu_G^t/ij) \tag{18}$$

$$J(M|t) = \sum_{i=t_2+1}^{t_3} \sum_{j=t_2+1}^{t_3} ijp_{ij} \log(ij/\mu_M^t) + \sum_{i=t_2+1}^{t_3} \sum_{j=t_2+1}^{t_3} \mu_M^t p_{ij} \log(\mu_M^t/ij) \tag{19}$$

$$J(S|t) = \sum_{i=t_3+1}^{t_4} \sum_{j=t_3+1}^{t_4} ijp_{ij} \log(ij/\mu_S^t) + \sum_{i=t_3+1}^{t_4} \sum_{j=t_3+1}^{t_4} \mu_S^t p_{ij} \log(\mu_S^t/ij) \tag{20}$$

$$J(Y|t) = \sum_{i=t_4+1}^{L-1} \sum_{j=t_4+1}^{L-1} ijp_{ij} \log(ij/\mu_Y^t) + \sum_{i=t_4+1}^{L-1} \sum_{j=t_4+1}^{L-1} \mu_Y^t p_{ij} \log(\mu_Y^t/ij) \tag{21}$$

The criteria for the image thresholding is given as:

$$J_{LCE}(t) = J(A|t) + J(G|t) + J(M|t) + J(S|t) + J(Y|t) \tag{22}$$

Those set of the four thresholds are chosen which minimizes the above equation and mathematically it is given as:

$$(t_1, t_2, t_3, t_4) = \arg\min(J_{LCE}(t)) \tag{23}$$

The computational complexity of GLCM based method is of the order $O(L^2)$ for a bi-level thresholding. It increases exponentially with the increase in the number of thresholds i.e. for a four level thresholding problem ($m = 4$), as the present case, the complexity would be of the order $O(L^2)^m$. Here L denotes the total number of gray levels used in the image. For the designed approach as seen from the Eqs. (17)–(22) the computation involves the process of division, logarithmic and multiplication for each element in the quadrants A, G, M, S and Y of the GLCM. Also, the computational time depends upon the number of such operations. In our present work, the PSO algorithm minimized the designed objective function i.e. $J_{LCE}(t)$, resulting in the reduction of the computational complexity and thereby the computational time. The run-time complexity of the algorithm will then be of the order of $O(ss \times iterations)$ where ss is the size of the population and *iterations* is the number of iterations.

4 Optimized 2D Multilevel Local Cross-Entropy Thresholding Approach Using Particle Swarm Optimization Algorithm (PSO)

4.1 PSO

The present work employs PSO algorithm for the minimization of the constructed fitness function. Least computational complexity of the PSO algorithm had been verified in the work by Bhandari et al. [41] on satellite image segmentation using Kapur's, Otsu and Tsallis functions.

The aim of the study was not to compare different optimization algorithms but to compare the efficiency of different segmentation methods for the application of brain tumor segmentation. Since earlier version of the objective function was only designed for a bi-level thresholding problem with the disadvantage of the algorithm complexity. The designed approach mitigated this drawback, also highlighting the capability of the thresholding approach in segmenting the complex tumor images which has never been examined before.

The PSO algorithm is based upon the collective behavior exhibited by the birds and termites and was proposed by Kennedy and Eberhart [54] in the year 1995. It consist of a d dimensional search space in which the set of particles evolve. The particles explore the search space by adjusting their flying, according to their own flying experience and that of the neighboring particles. Each particle keeps track of the coordinates of the solution search space which are associated with best position each particle has achieved so far, referred to as *pbest* value and the best position achieved by any particle in the neighborhood which is represented as *gbest* value.

The position (x), velocity (v), *pbest* value (P_i) and *gbest* value (P_g) are represented as d dimensional vector and given as $x_i = (x_{i1}, x_{i2}, \ldots, x_{id})$, $V_i = (v_{i1}, v_{i2}, \ldots, v_{id})$, $P_i = (p_{i1}, p_{i2}, \ldots, p_{id})$ and $P_g = (p_{g1}, p_{g2}, \ldots, p_{gd})$ respectively. According to the specified user defined objective function, at every iteration the position and velocities are updated using the following equations [54]

$$v_{ij}(t+1) = wv_{ij}(t) + c_1 r_1 (p_{ij}(t) - x_{ij}(t)) + c_2 r_2 (p_{gj}(t) - x_{ij}(t)) \tag{24}$$

$$x_{ij}(t+1) = x_{ij}(t) + v_{ij}(t+1) \tag{25}$$

Here, j varies from (1, 2, ..., n), where n represents dimension and i ranges from (1, 2, …, N) where N defines the number of particles, t denotes the iteration counter; r_1 and r_2 denotes the random numbers uniformly distributed within the range of [0, 1], c_1, c_2 are called the cognitive and social learning parameters respectively.

The basic PSO has the disadvantage of premature convergence as a result of which the swarm diversity was reduced. To increase the exploration capabilities a constant called inertia weight was added to the previous velocity term which was proposed by Shi and Eberhart [55].

The inertia weight w varied linearly from 0.9 to 0.4 and it resulted in faster convergence to the global optimum solution. The larger value of w in beginning favors exploration in the early phase of the search and a local search in the later half, thereby favoring convergence to global best value. In context to values of c_1 and c_2, for a larger global search higher value of c_1 and c_2 are favored and for a more refined local search around the best position, smaller values of c_1 and c_2 are chosen [56]. The step by step procedure for the computation of the optimal thresholds using the PSO algorithm and employing $J_{LCE}(t)$ as a fitness function is given in the next sub-section and the same is summarized in the flowchart shown in Fig. 2.

Proposed Methodology

1. Set the control parameters of the PSO Algorithm. *SS* = swarm size; w = inertia weight; c_1 = cognitive component; c_2 = social component; *iterations* = maximum number of iterations; *thr* = number of optimal thresholds.
2. The w, c_1 and c_2 were linearly varied from 0.9 to 0.4, 0.5 to 2.5 and 2.5 to 0.5 respectively. The swarm size was fixed at 10, maximum number of iterations were fixed at 25 and the dimension of the problem (referring to number of optimal thresholds) was kept as four.
3. Depending upon the gray levels L present in the image construct a square GLCM matrix of the order $L \times L$ using Eqs. (4) and (5).
4. Compute the transition probability matrix by dividing the every entry of the GLCM matrix by the total number of transitions in the co-occurrence matrix using Eq. (6).

5. The position of every particle was randomly initialized in the range from [0, *L*-1] on each dimension with the constraint that the positions in the succeeding dimensions follow an increasing order (Referring it to t_1, t_2, t_3 and t_4 where t corresponds to the threshold). The velocity was also randomly assigned for each particle in each dimension.
6. For each particle position value, i.e. for each value of threshold parameters
   i. Divide the GLCM matrix into the 25 sub blocks using the thresholds t_1, t_2, t_3 and t_4 as shown in Fig. 1.
   ii. Compute the transition probabilities associated with each diagonal sub-block as given in Eqs. (7)–(11).
   iii. Compute the pixels average gray value for the diagonal sub blocks as defined in Eqs. (12)–(16).
   iv. Calculate the 2D local cross entropy measure about the divided sub-blocks *A*, *G*, *M*, *S* and *Y* using the Eqs. (17)–(21).
   v. The total fitness measure was then determined by adding all the cross entropy values computed for the different set of sub blocks as defined in Eq. (22) and is represented as $J_{LCE}(t)$. Choose the global best particle as the one for which $J_{LCE}(t)$ is minimum.
7. For the first iteration, set the current particle position as the local best position.
8. For each particle and every iteration perform the following operations:
   i. Update the velocity and the position of the particle, using the Eqs. (24) and (25).
   where

$$w(t) = w_{up} - (w_{up} - w_{low})t/T_{\max} \tag{26}$$

   Here t stands for the current iteration, w_{low} and w_{up} are the lower and upper bounds of w and T_{max} is the total allowed number of iterations.
   ii. Compute the fitness $J_{LCE}(t)$ for the new position vectors using step (6).
   iii. If the fitness function using the updated position vector value is better than the fitness for the local best position, then set the updated position of the particle as the local best position.
   iv. Choose the global best particle from the local best particles for which the fitness value is minimum and that particle position value corresponds to the optimal set of thresholds.

Repeat the step (9) till the termination criteria, i.e. the maximum number of iterations is not reached (Fig. 2).

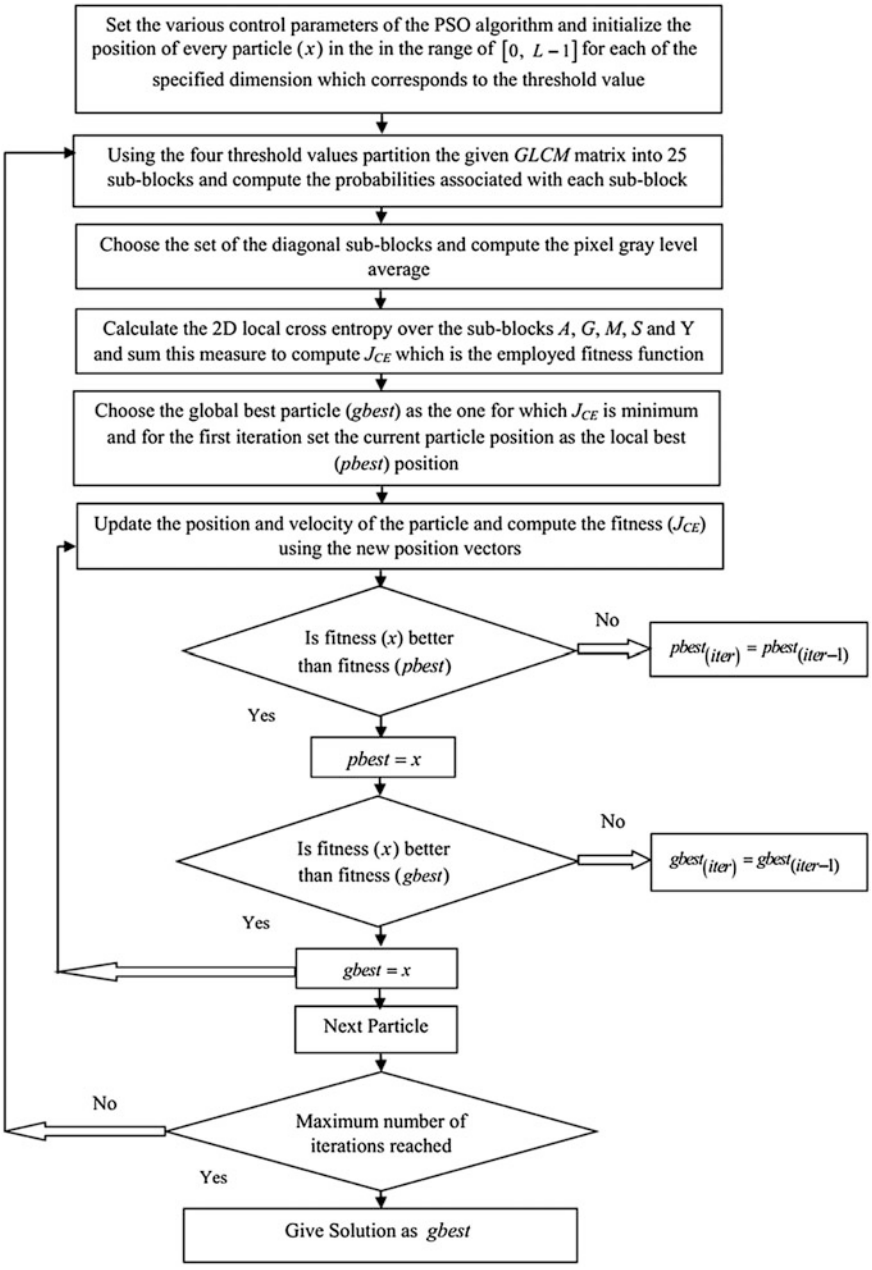

Fig. 2 Flowchart

5 Database and Performance Measures

5.1 Database

The performance of the proposed algorithm was examined over the brain tumor images acquired from the internet repository [3, 57, 58, 59, 60, 61]. Six tumor images were used in the study. The sizes of various images are as follows 240×240, 240×240, 200×200, 200×200, 400×400 and 200×200.

The attained results were compared with those obtained using the existing level set algorithms. For the comparison, the methods given by Bernard et al. [29], Caselles et al. [17], Chan and Vese [22], Lankton et al. [27], Li et al. [26], Shi et al. [18] and Thapaliya et al. [36] have been used. The source codes for all the methods except for that by Thapaliya et al. [36] were obtained using the creaseg software [62].

5.2 Performance Measures

All the obtained results were compared quantitatively with the manual segmentations provided by the expert radiologist using the following metrics.

Jaccard

The *Jaccard* measure computes the spatial overlap for the pair of segmentations, and is computed using the formula [36]:

$$Jaccard = \frac{a}{a+b} \tag{27}$$

where a represents the number of the pixels which belong to both the manual and the automatic segmented region and b represents the number of pixels where the decision mismatches.

Dice

The *Dice* coefficient also computes the mean overlap between the ground truth and the automatic segmented results [63]. It is defined as:

$$Dice = \frac{2a}{2a+b} \tag{28}$$

where a and b are explained above. The value of *Jaccard* and *Dice* coefficient, is 1 if there is exact overlap of the estimated segment to the ground truth, whereas a 0 value signifies a complete disagreement in the matching of the both the masks.

Root Mean Square Error (RMSE)

This measure computes the average magnitude of the error between the pair of the segmentations. If R_M and R_A denotes the set of tumor voxels segmented

manually and using different automatic or semiautomatic methods then *RMSE* value is calculated as follows [36]

$$RMSE = \sqrt{\frac{\sum_{i=1}^{n} (R_M - R_A)^2}{n}} \tag{29}$$

where n denotes the total number of pixels in the image. Smaller is value of *RMSE* better is the correspondence between the segmented output and the ground truth.

6 Experimental Results and Discussions

To evaluate the efficiency of the proposed segmentation technique, which is referred to as the optimized 2D multilevel local cross entropy approach, the experimentations were done on six tumor images, the details of which, were given in the previous section. The segmentation stage is preceded by the skull stripping mechanism, as the skull region possesses the intensities similar to the normal brain tissues. The skull region was removed by first converting the MR image to binary image using Ostu's method. Thereafter a search was made for the largest connected component. Finally only the pixels present in that largest component were retained which corresponded to the brain region. The Table 1 shows the value of the *Jaccard* measure for the proposed method and the existing level set methods. The number of iterations for all the level set methods were kept equal to 200, as further increase in the number of iterations did not have any significant increase on the performance metrics. It is significant to mention here that the proposed approach required only 25 iterations with a particle size equal to 10 to achieve the desired result of maximum spatial overlap, which clearly highlights its less computational complexity in terms of the function evaluations as compared to other methods.

Table 1 Comparison of *Jaccard* measure for tumor dataset using different methods

Images	M1	M2	M3	M4	M5	M6	M7	Proposed
Image 1	0.612900	0.652800	0.111000	0.408400	0.156000	0.169500	0.682500	0.838506
Image 2	0.550300	0.666600	0.136300	0.190400	0.075200	0.652800	0.865600	0.866502
Image 3	0.754300	0.941700	0.162700	0.428500	0.156000	0.941700	0.912400	0.951220
Image 4	0.503700	0.834800	0.176400	0.333300	0.212100	0.197600	0.937600	0.942917
Image 5	0.369800	0.851800	0.052600	0.250000	0.058200	0.851800	0.834800	0.890820
Image 6	0.092800	0.694900	0.025600	0.098900	0.036200	0.639300	0.747180	0.801552
Average	0.480600	0.773800	0.110800	0.284900	0.115600	0.575500	0.830000	0.881919

M1—Bernard et al. [29], M2—Caselles et al. [17], M3—Chan and Vese [22], M4—Lankton et al. [27], M5—Li et al. [26], M6—Shi et al. [18] and M7—Thapaliya et al. [36]

After analyzing these values it was verified that the devised technique achieved the highest *Jaccard* value for the entire set of images as indicated in bold. The effectuality was also highlighted in terms of the average measure which was maximum equal to 0.8819 for the developed approach in contrast to the value of 0.4806, 0.7738, 0.1108, 0.2849, 0.1156, 0.5755 and 0.8300 obtained for M1, M2, M3, M4, M5, M6 and M7. Similar findings were also graphically ascertained for all the images, as shown clearly in Fig. 3.

The Table 2 shows the value of the *Dice* measure for the developed technique and the existing level set methods.

From the tabular findings it can be concluded that the proposed approach obtained the maximum *Dice* value for all the images as indicated by bold notation. Superiority was also justified in terms of the average *Dice* value which was maximum equal to 0.9364 for the proposed approach in comparison to methods M1, M2, M3, M4, M5, M6 and M7 for which it was 0.6183, 0.8633, 0.1950, 0.4300, 0.2017, 0.6800 and 0.9045 respectively.

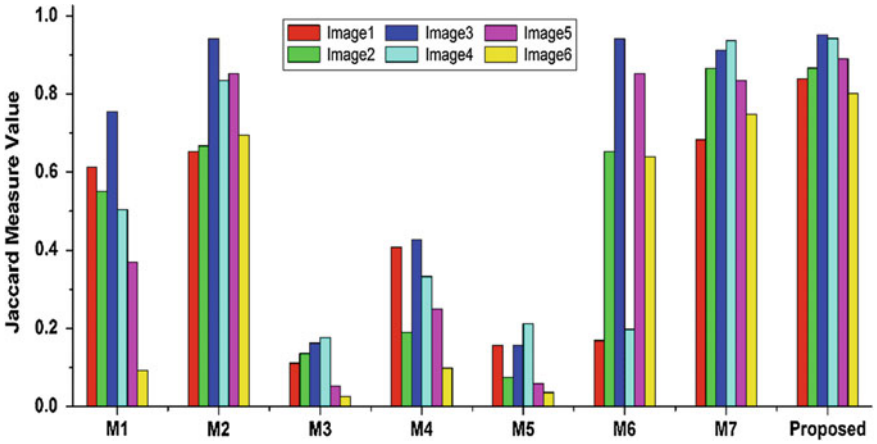

Fig. 3 Jaccard measure for the proposed and other level set methods

Table 2 Comparison of *Dice* measure for tumor dataset using different methods

Images	M1	M2	M3	M4	M5	M6	M7	Proposed
Image 1	0.760000	0.790000	0.200000	0.580000	0.270000	0.290000	0.811300	0.912160
Image 2	0.710000	0.800000	0.240000	0.320000	0.140000	0.790000	0.928000	0.928477
Image 3	0.860000	0.970000	0.280000	0.600000	0.270000	0.970000	0.954200	0.975000
Image 4	0.670000	0.910000	0.300000	0.500000	0.350000	0.330000	0.967800	0.970620
Image 5	0.540000	0.920000	0.100000	0.400000	0.110000	0.920000	0.910000	0.942258
Image 6	0.170000	0.820000	0.050000	0.180000	0.070000	0.780000	0.855300	0.889846
Average	0.618300	0.868330	0.195000	0.430000	0.201700	0.680000	0.904400	0.936394

M1—Bernard et al. [29], M2—Caselles et al. [17], M3—Chan and Vese [22], M4—Lankton et al. [27], M5—Li et al. [26], M6—Shi et al. [18] and M7—Thapaliya et al. [36]

Graphically the per image analysis can be shown in Fig. 4, which clearly indicates that the proposed method outperformed all other existing techniques.

The values of the segmentation error which was quantified in terms of the *RMSE* value is given in Table 3. From the scrutinization of results it was seen that least value of *RMSE* was obtained using the proposed technique which was 0.0701 on an average in contrast to other methods for which it was 2.2246, 1.6868, 9.4956, 2.6927, 9.5329, 3.7913 and 0.0861 respectively.

The per image trend for the obtained *RMSE* value for different methods can be analyzed in Figs. 5 and 6. Graphically it was also ascertained that the least value was obtained using the developed approach. Since the dynamic range for the RMSE value is different for the different methods a clear distinction between the M7 and the proposed method could not be made from Fig. 5. Figure 6 gives a more clear illustration for the proposed and M7 method error values thereby highlighting the superiority of the designed approach.

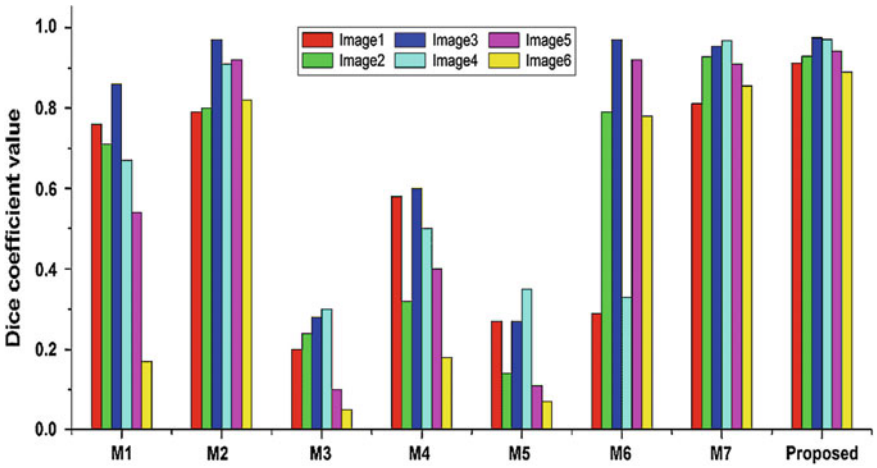

Fig. 4 Dice coefficient measure for the proposed and the other level set methods

Table 3 Comparison of *RMSE* measure for tumor dataset using different methods

Images	M1	M2	M3	M4	M5	M6	M7	Proposed
Image 1	2.100246	2.436521	9.167905	2.595793	7.812141	7.486349	0.130000	**0.08599**
Image 2	2.403090	2.504783	8.516675	3.197202	12.45289	2.616797	**0.076000**	0.08700
Image 3	1.701387	0.867567	7.705541	2.551544	7.812736	0.860604	0.075000	**0.04949**
Image 4	3.264150	1.998803	9.789716	3.756385	8.979871	9.295443	0.074800	**0.071951**
Image 5	2.134372	1.104765	10.145420	2.318836	10.908630	1.126601	0.078000	**0.059412**
Image 6	1.744898	1.208565	11.648500	1.736881	9.231454	1.362292	0.083000	**0.066895**
Average	2.224691	1.686834	9.495626	2.692774	9.532954	3.791348	0.086133	**0.070123**

M1—Bernard et al. [29], M2—Caselles et al. [17], M3—Chan and Vese [22], M4—Lankton et al. [27], M5—Li et al. [26], M6—Shi et al. [18] and M7—Thapaliya et al. [36]

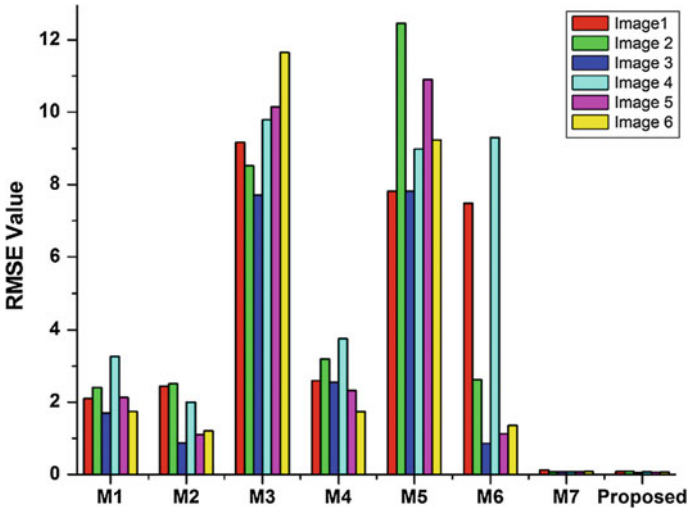

Fig. 5 RMSE value for the proposed and other level set methods

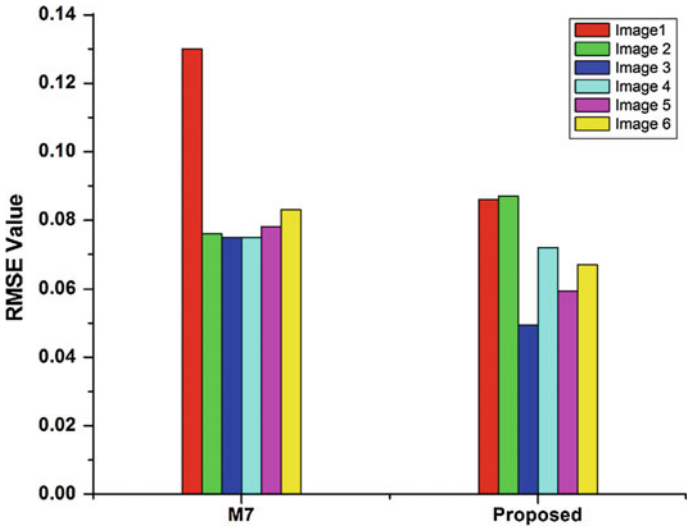

Fig. 6 RMSE value for M7 and the proposed method

The subjective quality analysis for the proposed method was also performed. The Fig. 7 shows the output images obtained using the proposed method. In comparison to the existing methods the proposed algorithm had better output results when compared visually. The sequence of steps which were followed for the generation of the final segmented output image involve skull stripping, computation

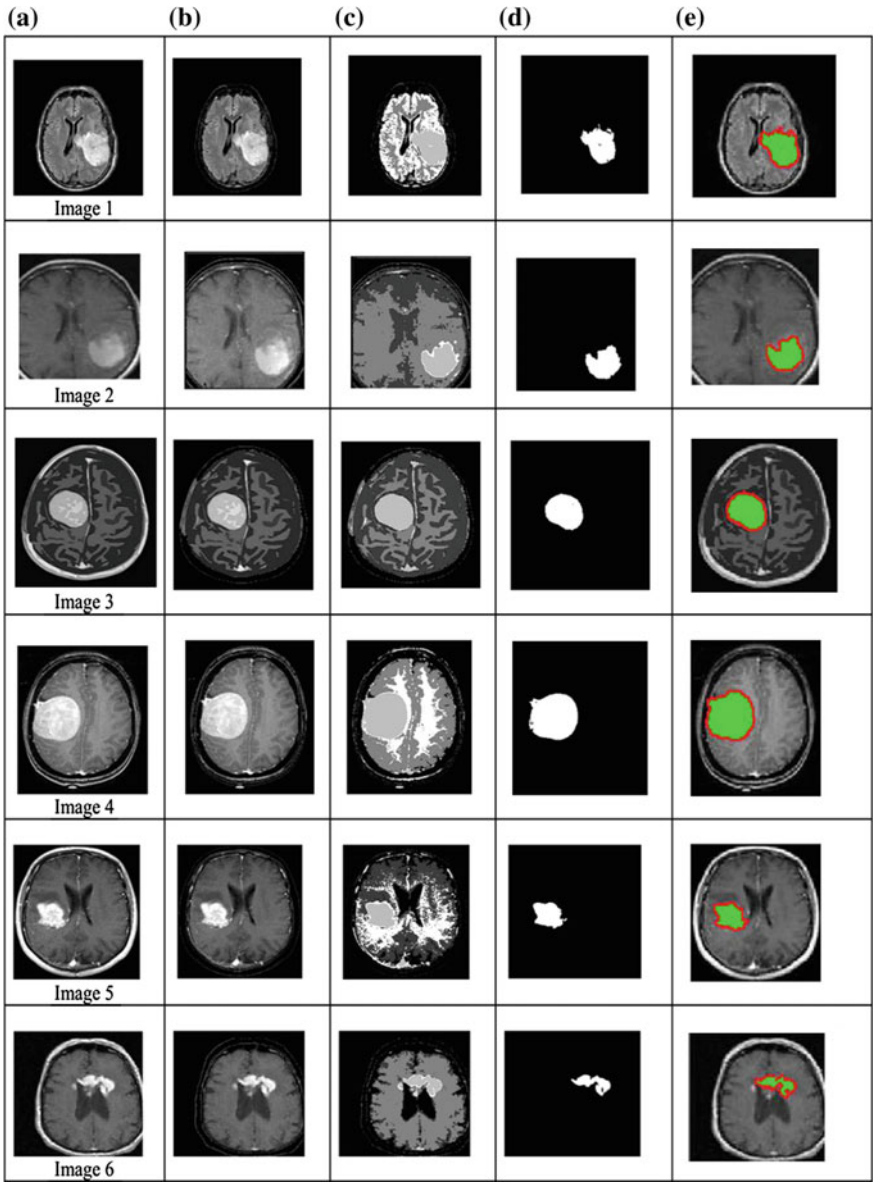

Fig. 7 Procedure for the extraction of the tumor region using the proposed method. **a** Original image. **b** Skull stripped image. **c** Output clustered image. **d** Extracted segmented region. **e** Output results overlaid on the original image

Table 4 Comparison of the computational time required for each of the algorithm in seconds

Images	M1	M2	M3	M4	M5	M6	M7	Proposed
Image 1	1.520	1.620	13.840	1.620	38.440	9.310	16.198	2.277
Image 2	1.910	1.750	16.320	1.560	66.370	1.250	13.169	2.715
Image 3	1.260	0.450	10.960	0.870	81.480	0.290	10.814	2.378
Image 4	1.710	1.870	15.630	1.470	44.170	10.030	10.678	2.333
Image 5	4.920	5.200	44.000	2.840	466.420	3.770	8.4100	3.067
Image 6	0.150	0.980	11.420	0.120	25.990	0.390	10.254	2.020
Average	1.912	1.978	18.695	1.413	120.478	4.173	11.587	2.465

M1—Bernard et al. [29], M2—Caselles et al. [17], M3—Chan and Vese [22], M4—Lankton et al. [27], M5—Li et al. [26], M6—Shi et al. [18] and M7—Thapaliya et al. [36]

of thresholds using the developed approach, generation of the clustered image, extraction of region having maximum *Dice* with respect to ground truth and finally the overlaying of the results on the original image.

Apart from the quantitative and the qualitative analysis of the results, the algorithm complexity was also analyzed in terms of the computational time to validate its applicability for the real time applications. The calculation of the time complexity was performed in Matlab platform with a 2.40 GHz intel core i7 processor. The Table 4 summarizes the time taken by each algorithm to generate the final segmented output.

From the tabular values it can be concluded that the algorithm takes a comparable computational time equal to 2.465 s on an average in comparison to the other methods. The advantage of the proposed algorithm is its ability in providing the best quality solution without the need of the initial contour generation and that also with a marginal increase in computational cost.

7 Conclusion

In this paper an evolutionary algorithm called PSO has been used for solving the multilevel thresholding problem in 2D with the endeavor to minimize the 2D local cross entropy function. Firstly the multilevel extension of the 2D local cross entropy has been developed and then it was optimized. The applicability of the proposed algorithm has been demonstrated by considering several tumorous MR images and the obtained results were compared with that obtained using the seven existing level set approaches. The experimental results showed its superiority and effectiveness over other methods in terms of *Jaccard*, *Dice*, *RMSE* and computational time measures which were 0.881902, 0.936394, 0.070123 and 2.465000 s on an average. The spatial overlap accuracy and the computational simplicity of the algorithm makes it suitable as an additional tool for the clinician to consistently evaluate the tumor progression.

Acknowledgments The authors gratefully acknowledge the efforts by Dr. Sandeep Singh Pawar (Advance Diagnostic Centre, Ludhiana, Punjab) for providing the clinical interpretations.

References

1. Gondal, A.H., Khan, M.N.A.: A review of fully automated techniques for brain tumor detection from MR images. Int. J. Mod. Educ. Comput. Sci. **5**, 55–61 (2013)
2. Hassanien, A.E.: Classification and feature selection of breast cancer data based on decision tree algorithm. Int. J. Stud. Inform. Control J SI **12**(1), 33–39 (2003)
3. http://www.oncolink.org/resources/images/md2b/Image11.gif/. Accessed 12 May 2015
4. Krishn, A., Bhateja, V., Patel, H., Sahu, A.: Medical image fusion in wavelet and ridgelet domains: a comparative evaluation. Int. J. Rough Sets Data Anal. **2**, 78–91 (2015)
5. Bhateja, V., Patel, H., Krishn, A., Sahu, A., Lay-Ekuakille, A.: Multimodal medical image sensor fusion framework using cascade of wavelet and contourlet transform domains. IEEE Sens. J. **15**, 6783–6790 (2015)
6. Georgiadis, P., Cavouras, D., Kalatzis, I., Daskalakis, A., Kagadis, G.C., Sifaki, K., Malamas, M., Nikiforidis, G., Solomou, E.: Improving brain tumor characterization on MRI by probabilistic neural networks and non-linear transformation of textural features. Comput. Methods Programs Biomed. **89**, 24–32 (2008)
7. Georgiadis, P., Cavouras, D., Kalatzis, I., Daskalakis, A.: Non-linear least squares features transformation for improving the performance of probabilistic neural networks in classifying human brain tumors on MRI. In: Computational Science and Its Applications—ICCSA 2007, pp. 239–247. Springer, Berlin, Heidelberg (2007)
8. Zacharaki, E.I., Wang, S., Chawla, S., Soo, D.: Classification of brain tumor type and grade using MRI texture and shape in a machine learning scheme. Magn. Reson. Med. **62**, 1609–1618 (2009)
9. Corso, J.J., Sharon, E., Dube, S., El-Saden, S., Sinha, U., Yuille, A.: Efficient multilevel brain tumor segmentation with integrated bayesian model classification. IEEE Trans. Med. Imaging **27**, 629–640 (2008)
10. Hemanth, D.J., Vijila, C.K.S., Selvakumar, A.I., Anitha, J.: Distance metric-based time efficient fuzzy algorithm for abnormal magnetic resonance brain image segmentation. Neural Comput. Appl. **22**, 1013–1022 (2013)
11. Dou, W., Ruan, S., Chen, Y., Bloyet, D., Constans, J.: A framework of fuzzy information fusion for the segmentation of brain tumor tissues on MR images. Image Vis. Comput. **25**, 164–171 (2007)
12. Shrivastava, A., Raj, A., Bhateja, V.: Combination of wavelet transform and morphological filtering for enhancement of magnetic resonance images. In: International Conference on Digital Information Processing and Communications, pp. 460–474. Springer, Berlin, Heidelberg (2011)
13. Bhateja, V., Tiwari, H., Srivastava, A.: A non-local means filtering algorithm for restoration of Rician distributed MRI. In: Emerging ICT for Bridging the Future -Proceedings of the 49th Annual Convention of the Computer Society of India CSI, vol. 2. pp. 1–8. Springer International Publishing (2014)
14. Alankrita Raj, A., Srivastava, A., Bhateja, V.: Computer aided detection of brain tumorin magnetic resonance images. Int. J. Eng. Technol. 3, 523–532 (2011)
15. Dey, N., Roy, A.B., Pal, M., Das, A., Bengal, W., Bengal, W., Bengal, W., Bengal, W.: FCM based blood vessel segmentation method for retinal images. Int. J. Comput. Sci. Networks **1**, 1–5 (2012)
16. Hassanien A.E., Moftah, H.M., Azar, A.T., Shoman, M.: MRI breast cancer diagnosis hybrid approach using adaptive ant-based segmentation and multilayer perception neural networks classifier. Appl. Soft Comput. **14**, 62–71 (2014)

17. Caselles, V., Kimmel, R., Sapiro, G.: Geodesic active contours. Int. J. Comput. Vis. **22**, 61–79 (1997)
18. Shi, Y., Karl, W.C., Member, S.: A real-time algorithm for the approximation of level-set based curve evolution. IEEE Trans. Image Process. **17**, 645–656 (2008)
19. Samanta, S., Dey, N., Das, P., Acharjee, S.: multilevel threshold based gray scale image segmentation using cuckoo search. In: International Conference on Emerging Trends in Electrical, Communication and Information Technologies, pp. 27–34. Anatapur, India (2012)
20. Joe, B.N., Fukui, M.B., Meltzer, C.C., Huang, Q., Day, R.S., Greer, P.J., Bozik, M.E.: Brain tumor volume measurement: comparison of manual and semi automated methods. Radiology **212**, 811–816 (1999)
21. Fletcher-Heath, L.M., Hall, L.O., Goldgof, D.B., Murtagh, F.R.: Automatic segmentation of non-enhancing brain tumors in magnetic resonance images. Artif. Intell. Med. **21**, 43–63 (2001)
22. Chan, T., Vese, L.: Active contours without edges. IEEE Trans. Image Process. **10**, 266–277 (2001)
23. Liu, J., Udupa, J.K., Odhner, D., Hackney, D., Moonis, G.: A System for brain tumor volume estimation via mr imaging and fuzzy connectedness. Comput. Med. Imaging Graph. **29**, 21–34 (2005)
24. Vijayakumar, C., Damayanti, G., Pant, R., Sreedhar, C.M.: Segmentation and grading of brain tumors on apparent diffusion coefficient images using self-organizing maps. Comput. Med. Imaging Graph. **31**, 473–484 (2007)
25. The Insight Toolkit. http://www.itk.org
26. Li, C., Kao, C., Gore, J.C., Ding, Z.: Minimization of region-scalable fitting energy for image segmentation. IEEE Trans. Image Process. **17**, 1940–1949 (2008)
27. Lankton, S., Member, S., Tannenbaum, A.: Localizing region-based active contours. IEEE Trans. Image Process. **17**, 2029–2039 (2008)
28. Wang, T., Cheng, I., Basu, A.: Fluid vector flow and applications in brain tumor segmentation. IEEE Trans. Biomed. Eng. **56**, 781–789 (2009)
29. Bernard, O., Friboulet, D., Thevenaz, P., Unser, M.: Variational B-spline level-set: a linear filtering approach for fast deformable model evolution. IEEE Trans. Image Process. **18**, 1179–1191 (2009)
30. Khotanlou, H., Colliot, O., Atif, J., Bloch, I.: 3D brain tumor segmentation in MRI using fuzzy classification, symmetry analysis and spatially constrained deformable models. Fuzzy Sets Syst. **160**, 1457–1473 (2009)
31. Iftekharuddin, K.M., Zheng, J., Islam, M.A., Ogg, R.J.: Fractal-based brain tumor detection in multimodal MRI. Appl. Math. Comput. **207**, 23–41 (2009)
32. Ahmed, S., Iftekharuddin, K.M., Vossough, A.: Efficacy of texture, shape, and intensity feature fusion for posterior-fossa tumor segmentation in MRI. IEEE Trans. Inf Technol. Biomed. **15**, 206–213 (2011)
33. Dang, M., Modi, J., Roberts, M., Chan, C., Mitchell, J.R.: Validation study of a fast, accurate, and precise brain tumor volume measurement. Comput. Methods Programs Biomed. **111**, 480–487 (2013)
34. Islam, A., Reza, S.M.S., Iftekharuddin, K.M.: Multifractal texture estimation for detection and segmentation of brain tumors. IEEE Trans. Biomed. Eng. **60**, 3204–3215 (2013)
35. Arakeri, M.P., Reddy, G.R.M.: Computer-aided diagnosis system for tissue characterization of brain tumor on magnetic resonance images. Signal, Image Video Process. **7**, 1–17 (2013)
36. Thapaliya, K., Pyun, J., Park, C., Kwon, G.: Level set method with automatic selective local statistics for brain tumor segmentation in mr images. Comput. Med. Imaging Graph. **37**, 522–537 (2013)
37. Kapur, J.N., Sahoo, P.K., Wong, A.K.C.: A new method for gray-level picture thresholding using the entropy of the histogram. Comput. Vision, Graph. Image Process **29**, 273–285 (1985)

38. Horng, M.H.: Multilevel minimum cross entropy threshold selection based on the honey bee mating optimization. Expert Syst. Appl. **37**, 4580–4592 (2010)
39. Dey, N., Sayan, C., Samanta, S.: Optimization of Watermarking in Biomedical Signal. LAP Lambert Academic Publishing (2014)
40. Yin, S., Zhao, X., Wang, W., Gong, M.: Efficient multilevel image segmentation through fuzzy entropy maximization and graph cut optimization. Pattern Recognit. **47**, 2894–2907 (2014)
41. Bhandari, A.K., Kumar, A., Singh, G.K.: Modified artificial bee colony based computationally efficient multilevel thresholding for satellite image segmentation using kapur's, Otsu and Tsallis functions. Expert Syst. Appl. **42**, 1573–1601 (2015)
42. Tang, K., Yuan, X., Sun, T., Yang, J., Gao, S.: An improved scheme for minimum cross entropy threshold selection based on genetic algorithm. Knowledge-Based Syst. **24**, 1131–1138 (2011)
43. Yin, P.-Y.: Multilevel minimum cross entropy threshold selection based on particle swarm optimization. Appl. Math. Comput. **184**, 503–513 (2007)
44. Horng, M.-H., Liou, R.-J.: Multilevel minimum cross entropy threshold selection based on the firefly algorithm. Expert Syst. Appl. **38**, 14805–14811 (2011)
45. Sarkar, S., Das, S., Sinha, S.: A multilevel color image thresholding scheme based on minimum cross entropy and differential evolution. Pattern Recognit. Lett. **54**, 27–35 (2015)
46. Mokji, M.M., Abu Bakar, S.A.R.: Adaptive thresholding based on co-occurrence matrix edge information. J. Comput. **2**, 44–52 (2007)
47. Corneloup, G., Moysan, J., Magnin, I.E.: BSCAN Image Segmentation by Thresholding using Cooccurrence Matrix Analysis. Pattern Recognit. **29**, 281–296 (1996)
48. El-Feghi, I., Adem, N., Sid-Ahmed, M.A., Ahmadi, M.: Improved co-occurrence matrix as a feature space for relative entropy-based image thresholding. In: Fourth International Conference on Computer graphics, Imaging and Visualization, pp. 314–320. IEEE, Bangkok (2007)
49. Li, Y.L.Y., Cheriet, M.C.M., Suen, C.Y.: A threshold selection method based on multiscale and graylevel co-occurrence matrix analysis. In: Eighth International Conference on Document Analysis and Recognition (ICDAR'05), pp. 575–578. IEEE (2005)
50. Nie, F., Gao, C., Guo, Y., Gan, M.: Two-dimensional minimum local cross-entropy thresholding based on co-occurrence matrix. Comput. Electr. Eng. **37**, 757–767 (2011)
51. Kullback, S.: Information Theory and Statistics. Dover, New York (1968)
52. Li, C.H., Lee, C.K.: Minimum cross entropy thresholding. Pattern Recognit. **26**, 617–625 (1993)
53. Sarkar, S., Das, S.: Multilevel image thresholding based on 2d histogram and maximum tsallis entropy—a differential evolution approach. IEEE Trans. Image Process. **22**, 4788–4797 (2013)
54. Kennedy, J., Eberhart, R.: Particle swarm optimization. In: International Conference on Neural Networks (ICNN'95), pp. 1942–1948. IEEE, Perth, WA (1995)
55. Shi, Y., Eberhart, R.C.: Emperical study of particle swarm optimization. In: IEEE Congress on Evolutionary Computation, pp. 101–106. IEEE, Washington, DC (1999)
56. Ratnaweera, A., Halgamuge, S.K., Watson, H.C.: Self-organizing hierarchical particle swarm optimizer with time-varying acceleration coefficients. IEEE Trans. Evol. Comput. **8**, 240–255 (2004)
57. Kharrat, A., Benamrane, N., Messaoud, M.B., Abid, M.: Detection of brain tumor in medical images. In: 2009 3rd International Conference on Signals, Circuits and Systems (SCS), pp. 1–6. IEEE, Medenine (2009)
58. http://imageshack.us/photo/my-images/196/img6oe.jpg/. Accessed 12 May 2015
59. http://simplicitywebdesigns.com/images/marks_brain.gif/. Accessed 12 May 2015
60. https://www.mc.vanderbilt.edu/documents/neurosurgery/images/headfilm.JPG/. Accessed 12 May 2015

61. http://41.media.tumblr.com/cc88f088c55886d50f109f8e5b6ec484/tumblr_nm7vt1nC5s1tqnywjo1_1280.jpg/. Accessed 12 May 2015
62. Dietenbeck, T., Alessandrini, M., Friboulet, D., Bernard, D.: CREASEG: a free software for the evaluation of image segmentation algorithms based on level set. In: 17th International Conference on Image Processing, pp. 665–668. IEEE, Hong Kong (2010)
63. Bauer, S., May, C., Dionysiou, D., Stamatakos, G., Buchler, P., Reyes, M.: Multiscale modeling for image analysis of brain tumor studies. IEEE Trans. Biomed. Eng. **59**, 25–29 (2012)

Bio-inspired Swarm Techniques for Thermogram Breast Cancer Detection

Gehad Ismail Sayed, Mona Soliman and Aboul Ella Hassanien

Abstract Bio-inspired swarm techniques are a well-established paradigm with current systems having many of the characteristics of biological computers and capable of performing a variety of tasks that are difficult to do using conventional techniques. These techniques involving the study of collective behavior in decentralized systems. Such systems are made up by a population of simple agents interacting locally with one other and with their environment. The system is initialized with a population of individuals (i.e., potential solutions). These individuals are then manipulated over many iteration steps by mimicking the social behavior of insects or animals, in an effort to find the optima in the problem space. A potential solution simplifies through the search space by modifying itself according to its past experience and its relationship with other individuals in the population and the environment. Problems like finding and storing foods, selecting and picking up materials for future usage require a detailed planning, and are solved by insect colonies without any kind of supervisor or controller. Since 1990, several collective behavior (like social insects, bird flocking) inspired algorithms have been proposed. The objective of this article is to present to the swarms and biomedical engineering research communities some of the state-of-the-art in swarms applications to biomedical engineering and motivate research in new trend-setting directions. In this article, we present four swarms algorithms including Particle swarm optimization (PSO), Grey Wolf Optimizer (GWO), Moth Flame Optimization (MFO), and Firefly Algorithm Optimization (FA) and how these techniques could be successfully employed to tackle segmentation biomedical imaging problem. An

G.I. Sayed (✉) · M. Soliman · A.E. Hassanien
Faculty of Computers and Information, Cairo University, Cairo, Egypt
e-mail: gehad.ismail@egyptscience.net
URL: http://www.egyptscience.net

A.E. Hassanien
Faculty of Computers and Information, BeniSuef University, Beni Suef, Egypt

G.I. Sayed · M. Soliman · A.E. Hassanien
Scientific Research Group in Egypt (SRGE), Cairo, Egypt

N. Dey et al. (eds.), *Medical Imaging in Clinical Applications*,
Studies in Computational Intelligence 651, DOI 10.1007/978-3-319-33793-7_21

application of thermography breast cancer imaging has been chosen and the scheme have been applied to see their ability and accuracy to classify the breast cancer images into two outcomes: normal or non-normal.

1 Introduction

The breast cancer is considered the most common type of cancer among the women, and is the second leading cause of cancer-related death for the women. So the early detection of a breast tumor, before they metastasize and escalate to the neighboring cells, could minimize mortality rate. However, the breast cancer is a heterogeneous disease which makes the early detection of the disease as a major clinical challenge. There are lots of imaging techniques available in the field of early breast cancer detection. Among them, the most commonly used method, the gold standard, presently called as X-ray mammography [1, 2].

Mammography considered as the best screening tool that uses low dose X-rays to create an image of the breast to find breast cancer. Mammography has been proved to be effective in screening asymptomatic women to reduce mortality by as much as 30 % [3]. Although mammography proven its effectiveness, it has many limitations and drawbacks. The cancerous structures have many features in common with normal breast tissue which make the detection process of breast cancer in mammograms is a challenging task. This means that a high number of false positives or false negatives are possible [4]. Dense breast tissue can look white or light gray on a mammogram. This can make mammograms harder to interpret in younger women, who tend to have denser breasts. Many breast conditions mimic the symptoms of cancer and need tests and sometimes a biopsy for diagnosis [3]. Moreover, the major problems with X-ray mammography based breast screening are that it is an invasive technique, and the electromagnetic radiation itself helps the growth of breast tumor by 2 % during each periodic inspection [5].

There are other breast-testing options that are more effective and safe. Thermography, also known as thermal imaging or infrared imaging is a non-invasive, non-contact system of recording body temperature by measuring infrared radiation emitted by the body surface [6]. Digital infrared imaging has been used in medical diagnostics since the 1960s and in 1982 it was approved by the US Food and Drug Administration (FDA) as an adjunctive tool for the diagnosis of breast cancer [7], since this time a more effort is given to increasing the sensitivity of infrared imaging technology. Now thermography, or thermal imaging is considered a better tool for breast cancer diagnosis [8]. The idea behind using thermal imaging depend on the fact that the IRT camera visualizes any changes in the bodys heat caused by abnormalities in the blood flow existed in the surface of diseased areas. Knowing that cancerous tumors have an increased blood supply and cell growth, make it possible for using thermal imaging in breast cancer detection. In thermal imaging there is no compression of the breast so women may find it more comfortable, thermal imaging does not expose the woman to any radiation, as

occurs with mammography, fast, low cost and sensitive method [5]. The results of thermography could be able to apprise women of breast cancer up to 8–10 years before mammography can detect.

Any Computer-Aided Detection (CAD) system for breast cancer detection can be divided into mainly three stages: a region of interest segmentation (ROI), feature extraction, classification and performance analysis. ROI segmentation aims to separate breast region from the rest of thermal images, after such segmentation some features are extracted. In order to classify the breast to be normal or abnormal some kinds of artificial classifications algorithms are applied [9]. Classification results of breast thermal images depend mainly on segmentation result. Accurate segmentation of region of interest from medical thermal images still remains as an open problem. Absence of clear edges, low contrast nature and low signal to noise ratio are inherent limitations of thermal image. Complex pre segmentation steps remain a problem due to the more intricate intensity field of breast thermograms. Many attempts had been done to provide a CAD system for breast cancer detection but we will limit our focus on research work have done using the DMR-IR database [10]. These efforts can be classified into: automatic segmentation of breast regions [11, 12] and classification based on the asymmetry analysis to normal and abnormal cases [13, 14].

In order to distinguish the normal and abnormal tissues in breast thermal images [13] proposed the use of Gabor wavelet transform. The proposed work is done to differentiate the normal and various abnormal conditions such as carcinoma, nodule and fibro adenoma. Total 20 images are considered among which nine are carcinomas, six are nodules and five are fibro adenomas. The primary step is the manual removal of non-breast and extra regions such as shoulder and hand from underlying images. Followed by segmentation of breast tissues in thermal images is performed using ground truth masks and raw images. Normal and abnormal regions are grouped according to the healthy and pathology conditions. Both the groups are subjected to Gabor wavelet transform. Features such as energy and amplitude for different scales and orientations are extracted. Anisotropy index is calculated using extracted energy information. The results showed that derived features are highly correlated to the image contrast. Particularly, anisotropy measure of carcinoma tissues showed the largest energy and high anisotropic nature. It appears that the Gabor wavelet based features could be one of the structure descriptor in thermal images for automated and early diagnosis of breast cancer. Another attempt of asymmetry analysis in breast thermograms is proposed in [14]. In this work Prabha proposed the use of non-linear total variation diffusion filter and reaction diffusion based level set method in order to segment the breast tissues using TV edge map as stopping boundary function. Asymmetry analysis is performed on the segmented breast tissues using wavelet based structural texture features. Twenty images that have pathologies either in left or right region are considered. The segmented area of TV based level set is linear and high correlation 0.99 indicating the better performance of this segmentation method. The values of structural texture features namely, contrast and directionality are found to be distinct for normal and abnormal

tissues. Structural texture features extracted from the wavelet coefficients are found to be significant in demarcating normal and abnormal tissues.

Suganthi [11] propose a beast segmentation from breast thermograms using active contour based level set method. In order to improve signal to noise ratio and contrast of thermal images before using level set, a statistical based noise removal technique and contrast limited adaptive histogram equalization were used. Verification and validation of the segmented results were carried out against the ground truths. Few overlap measures such as accuracy, sensitivity, specificity, positive predictive value (PDP) and negative predictive value (PDN) were computed to determine the percentage of similarity between the segmented results and ground truths. A modification of breast cancer ROI segmentation using level set is enhanced in [12]. In the proposed work of [12] the distance regularized level set method is modified by adopting an improved diffusion rate model. The level set function is evolved based on phase information of the image. To perform this study, 72 gray scale images of size 320×240 pixels are considered. The selected images are subjected to proposed PBMDRLS method. The segmented region of interests are verified and validated against the ground truth images. Region based statistics and overlap analysis are performed. The overlap measures showed 97 % of average similarity between four sets ground truths and segmented region of interests. A recently research work on automatic ROI segmentation is proposed in [5, 9]. In [5] an automatic segmentation and classification is introduced by utilizing both Neutrosophic sets (NS) and optimized Fast Fuzzy c-mean (F-FCM) algorithm In this work, post-segmentation process was suggested to segment breast parenchyma (i.e. ROI) from thermogram images. SVM is used in classification step to classify breast parenchyma into normal or abnormal cases. The proposed system in [5] was evaluated through recall, accuracy, precision, and error rate measurements proving its success compared to other automatic ROI segmentation methods [15]. A new idea of using data acquisition protocol parameter in automatic ROI segmentation is proposed in [9]. This method is based on the data acquisition protocol parameter (the distance from the patient to the camera) and the image statistics of DMR-IR database. Having ROI segmented some statistical and texture features were extracted. These features are used with SVM classifier to detect the normal and abnormal breasts.

The breast cancer research is still in its early stage, and there are no such robust segmentation methods, and optimum feature extraction techniques are available. Hence, in this chapter, we have proposed an automatic CAD system that depends on using automatic ROI segmentation. The segmentation process utilize the benefits of Bio-Inspired techniques such as Particle Swarm Optimization (PSO), Grey Wolf Optimizer (GWO), Moth Flame Optimization (MFO), and Firefly Algorithm (FA) in providing more accurate results. As soon as ROI had been segmented, different features can be extracted from this region. In this work we successfully extract different types of features. These features include: statistical, texture and gabor features. The system will use these extracted features in last stage of the proposed CAD system. These features will be used to classify breast parenchyma into normal or abnormal cases. Support Vector Machine (SVM) with different kernel functions (i.e. polynomial, RBF, Linear and quadratic) will be used as a classifier.

Bio-Inspired optimization algorithms also known as nature inspired optimization algorithms is a well-established paradigm with current systems having many of the characteristics of biological computers and capable of performing a variety of tasks that are difficult to do using conventional techniques. Bio-Inspired algorithms is considered as one of the most important increasing fields, which attract a large number of researchers and scientists working in areas such as neuro-computing, global optimization, swarms and evolutionary computing [16]. Bio-Inspired computing algorithms has been applied to different kinds of optimization problems in computer networks, control systems, bioinformatics, economics and finance, forecasting problems, game theory, mu- sic, biometrics, power systems, image processing, industry and engineering, parallel and distributed computing, data mining, robotics, applications involving the security of information systems etc. [17]. Optimization can be defined as an art of selecting the best alternative among a given set of options. The success of most of the metaheuristics optimization algorithms depends to a large extent on the careful balance of two conflicting goals, exploration (diversification) and exploitation (intensification) [18]. While exploration is important to ensure that every part of the solution domain is searched enough to provide a reliable estimate of the global optimum; exploitation, on the other hand, is important to concentrate the search effort around the best solutions found so far by searching their neighborhoods to reach better solutions [19]. Biologically inspired computing still has much room to grow since this research community is quite young.

The main contribution of this work is our success in providing automatic ROI segmentation method using recent bio-inspired algorithms. The experimental studies showed that it is very promising to use these set of bio-inspiring algorithms in ROI segmentation and how it improves the CAD system performance in terms of specificity, sensitivity, precision and accuracy. In this work we use a benchmark database [10] containing 149 patients of total 63 cases, 29 healthy and 34 malignant. We use leave-one-out cross validation method in order to provide more accurate results of the proposed CAD system. The reminder of this chapter is organized as follow. Section 2 will illustrate in more details the basics of nature inspired optimization algorithms. These algorithms include Particle Swarm Optimization, Grey Wolf Optimizer (GWO), Moth Flame Optimization (MFO), and Firefly Algorithm Optimization (FA). In Sect. 3 a full description of our proposed CAD system for breast cancer detection is given. Experimental results and system evaluation will be discussed in Sect. 4. Finally, the conclusion and future work are discussed in Sect. 5.

2 Bio-inspired Swarm Optimization Algorithms

Nature inspired algorithms are algorithms inspired from social behavior of animals and birds. In the following sections, four nature inspired algorithms including Particle swarm optimization, Grey Wolf Optimizer (GWO), Moth Flame Optimization (MFO), and Firefly Algorithm Optimization (FA) will discusses briefly.

2.1 Particle Swarm Optimization

PSO algorithm originally developed by Eberhart and Kennedy [20], which is taking advantage of the swarm intelligence concept, for example bird flocks and fish schools.

Main concepts PSO applies the social interaction concept to problem solving. The usual aim of the particle swarm optimization (PSO) algorithm is to solve continuous and discrete optimization problems. It is a population-based method, that is iteratively changed until a termination criterion is satisfied. It uses a number of agents (particles) which represents a swarm moving around in the search space in order to look for the best solution. Each particle is treated as point in N-dimensional space. In addition, each particle keeps track of its coordinates in the solution that are associated with best particle solution (fitness). This value called **pbest** the personal best. Another best value called **gbest** which is the best value obtained so far by any particle in the neighborhood of that particle. The main concept of PSO depends on accelerating each particle toward **pbest and gbest** particle locations, with a random weighted acceleration at each time step.

Each particle update his location based on the current position, current velocity, distance between the current position and *pbest* and finally the distance between the current position and *gbest*.

Mathematical Model The population of feasible solutions $p = p_1, p_1, \ldots, p_n$ in PSO are often called a swarm. Each P is called particle. These particles travel through the search space to find the optimal solution. PSO segmentation based approach has been one of the most recently used. It has been compared with GA [21]. The results show that it gives better results in less time also it needs only few parameters to adjust. As PSO has no parameter of "mutation", "recombination", and no notion of the "survival of the fittest".

At the beginning of the PSO approach, particle position velocities are set to zero and their positions are randomly set within the boundaries of the search space. Global, Local and neighborhood are initialized with small values. Population size and stopping criteria are very important parameters that need to optimize in order to get an overall good solution with acceptable time limit. In each step of PSO algorithm fitness function is evaluated and each particle's position and velocity are updated according to Eqs. (1) and (2). The fitness function is used to indicate how close a particle to the optimal solution.

$$v_{i+1}^n = wv_i^n + \phi_1 r_1 (g_i^n - x_i^n) + \phi_2 r_2 (p_i^n - x_i^n) + \phi_3 r_3 (n_i^n - x_i^n) \tag{1}$$

$$x_{i+1}^n = x_i^n + v_{i+1}^n \tag{2}$$

where w, ϕ_1, ϕ_2 *and* ϕ_3 coefficients are assigned weights. w is inertial weight which represents memory of previous velocity and ϕ_1, ϕ_2 *and* ϕ_3 are acceleration coefficients which represent cognitive (personal), social (neighborhood) component usually set between 0 and 4. the symbols r_1, r_2 *and* r_3 represent random variables with uniform distribution between 0 and 1. g_i^n is global best information while n_i^n is neighborhood best and p_i^n is local best.

A large inertia weight (w), represents a global search while a small inertia weight, represents a local search. The linearly decreasing the inertia weight from a large value to a small value relatively through PSO process, it gives the best PSO performance compared with fixed inertia weight parameter settings.

2.2 Gray Wolf Optimizer (GWO)

Grey wolf optimizer (GWO) is a population based meta-heuristics approach simulates the leadership hierarchy and hunting mechanism of gray wolves in nature proposed by Mirjalili and Lewis [22]. In the following section, we will give an overview of the main concepts and structure of the grey wolf optimizer approach as follow.

Main concepts and inspiration Grey wolves are considered as apex predators, which they are at the top of the food chain. Grey wolves prefer to live in a group (pack), each group contains 5–12 members on average. All the members in the group have a very strict social dominant hierarchy. The social hierarchy consists of four levels as follow. (1) **The first level is called Alpha** (α) The alpha wolves are the leaders of the pack and they are a male and a female. They are responsible for making decisions about hunting, time to walk, sleeping place and so on. The pack members have to dictate the alpha decisions and they acknowledge the alpha by holding their tails down. The alpha wolf is considered the dominant wolf in the pack and all his/her orders should be followed by the pack members, (2) **The second level is called Beta** (β) The betas are subordinate wolves, which help the alpha in decision making. The beta wolf can e either male or female and it consider the best candidate to be the alpha when the alpha passes away or becomes very old. The beta reinforce the alpha's commands throughout the pack and gives the feedback to alpha, and (3) **The third level is called Delta** (δ) The delta wolves are not alpha or beta wolves and they are called subordinates. Delta wolves have to submit to the alpha and beta but they dominate the omega (the lowest level in wolves social hierarchy). There are different categories of delta as follows: (a) **Scouts**. The scout wolves are responsible for watching the boundaries of the territory and warning the pack in case of any danger, (b) **Sentinels** The sentinel wolves are responsible for protecting the pack, (c) **Elders** The elder wolves are the experienced wolves who used to be alpha or beta, (d) **Hunters** The hunters wolves are responsible for helping the alpha and beta wolves in hunting and providing food for the pack, and (e) **Caretakers** The caretakers are responsible for caring for the ill, weak and wounded wolves in the pack. (4) **The fourth (lowest) level is called**

Omega (ω) The omega wolves are considered the scapegoat in the pack, they have to submit to all the other dominant wolves. They may seem are not important individuals in the pack and they are the last allowed wolves to eat. The whole pack are fighting in case of losing the omega.

The mathematical models of the social hierarchy, tracking, encircling and attacking prey are discussed as follows:

Social hierarchy In the grey wolf optimizer (GWO), the fittest solution is considered as the alpha α, while the second and the third fittest solutions are named beta β and delta δ, respectively. The rest of the solutions are considered omega ω. In GWO approach, the hunting is guided by α, β and δ. The ω solutions follow these three wolves.

Encircling prey During the hunting, the grey wolves encircle prey. The mathematical model of the encircling behavior is presented in the following equations.

$$\boldsymbol{D} = \left|\boldsymbol{C} \cdot \boldsymbol{X_p}(t) - \boldsymbol{A} \cdot \boldsymbol{X}(t)\right| \tag{3}$$

$$\boldsymbol{X}(t+1) = \boldsymbol{X_p}(t) - \boldsymbol{A} \cdot \boldsymbol{D} \tag{4}$$

where t is the current iteration, $\boldsymbol{A}$ and $\boldsymbol{C}$ are coefficient vectors, $\boldsymbol{X_p}$ is the position vector of the prey, and $\boldsymbol{X}$ indicates the position vector of a grey wolf.

The vectors $\boldsymbol{A}$ and $\boldsymbol{C}$ are calculated as follows:

$$\boldsymbol{A} = 2\boldsymbol{a} \cdot \boldsymbol{r}_1 - \boldsymbol{a} \tag{5}$$

$$\boldsymbol{C} = 2 \cdot \boldsymbol{r_2} \tag{6}$$

where components of $\boldsymbol{a}$ are linearly decreased from 2 to 0 over the course of iterations and $\boldsymbol{r_1}, \boldsymbol{r_2}$ are random vectors in [0, 1].

Hunting The hunting operation is usually guided by the alpha α. The beta β and delta δ might participate in hunting occasionally. In the mathematical model of hunting behavior of grey wolves, the alpha α, beta β and delta δ have better knowledge about the potential location of prey. The first three best solutions are saved and the other agent are oblige to update their positions according to the position of the best search agents as shown in the following equations.

$$\begin{aligned} \boldsymbol{D_\alpha} &= |\boldsymbol{C}_1.\boldsymbol{X_\alpha} - \boldsymbol{X}|, \\ \boldsymbol{D_\beta} &= \left|\boldsymbol{C}_2.\boldsymbol{X_\beta} - \boldsymbol{X}\right|, \\ \boldsymbol{D_\delta} &= |\boldsymbol{C}_3.\boldsymbol{X_\delta} - \boldsymbol{X}| \end{aligned} \tag{7}$$

$$\begin{aligned} \boldsymbol{X}_1 &= \boldsymbol{X}_{\boldsymbol{\alpha}} - \boldsymbol{A}_1 \cdot (\boldsymbol{D}_{\boldsymbol{\alpha}}), \\ \boldsymbol{X}_2 &= \boldsymbol{X}_{\boldsymbol{\beta}} - \boldsymbol{A}_2 \cdot (\boldsymbol{D}_{\boldsymbol{\beta}}), \\ \boldsymbol{X}_3 &= \boldsymbol{X}_{\boldsymbol{\delta}} - \boldsymbol{A}_3 \cdot (\boldsymbol{D}_{\boldsymbol{\delta}}). \end{aligned} \tag{8}$$

$$\boldsymbol{X}(t+1) = \frac{\boldsymbol{X}_1 + \boldsymbol{X}_2 + \boldsymbol{X}_3}{3}, \tag{9}$$

Attacking prey (exploitation) The grey wolf finish the hunt by attacking the prey when it stop moving. The vector $\boldsymbol{A}$ is a random value in interval $[-2a, 2a]$, where a is decreased from 2 to 0 over the course of iterations. When $|A| < 1$, the wolves attack towards the prey, which represents an exploitation process.

Search for prey (exploration) The exploration process in GWO is applied according to the position α, β and δ, that diverge from each other to search for prey and converge to attack prey. The exploration process is modeled mathematically by utilizing $\boldsymbol{A}$ with random values greater than 1 or less than -1 to oblige the search agent to diverge from the prey. When $|A| > 1$, the wolves are forced to diverge from the prey to fined a fitter prey.

2.3 Moth Flame Optimization (MFO)

Moth Flame Optimization (MFO) is a population based meta-heuristics approach simulates the navigation method of moths in nature. It proposed by Mirjalili [23]. In the following section, we will give an overview of the main concepts and structure of the moth flame optimization approach as follow.

Inspiration The main inspiration of moth is their special navigation methods in night. They used to fly in night using the moon light which called transverse orientation. A moth flies to the moon by using a fixed angle regarding to the moon. The same kind of navigation method can be done by humans. Moths are tricked by artificial lights and show such behaviour. When the light source is very far, moths are moving in straight line using a similar angle.

MFO Algorithm Let M with size $n * d$ candidate solutions are the moths n and the problem variables are the position of moths in the space. The moths can fly in different or hyper dimensional d space by changing their position vectors. OM is an array for storing fitness function value. Moreover, F is same as M with same size but for flames and their corresponding array for sorting their fitness function OF. Each moth position is updated with respect to the flame using the following formula:

$$M_i = S(M_i, f_j) \tag{10}$$

where M_i indicates the ith moth, F_j is jth flame, and S is the spiral function.

2.4 Firefly Algorithm (FA)

Firefly Algorithm (FA) is population based a meta-heuristics approach was first developed by Xin-She Yang in 2009 at Cambridge University [24]. It simulates the flashing patterns and behaviour of fireflies. In the following section, we will give an overview of the main inspiration and structure of the firefly algorithm as follow:

Concept The main concept of FA is based upon idealizing the fireflies flashing characteristic. It uses three idealized rules which are: (1) Fireflies are irrespective and unisex so that one firefly will be attracted to other fireflies with respect to their sex, (2) The firefly attractiveness is proportional to the brightness. That means for any two flashing fireflies, the movement of firefly is from the less brighter one towards the brighter one. If there is no brighter one than a particular firefly, then the movement will move randomly, and (3) The brightness of a firefly is directly affected by the landscape of the objective function.

As the light intensity is proportional to a firefly's attractiveness. The variation of attractiveness β with the distance r is defined at the following equation.

$$\beta = \beta_0 e^{-\gamma r^2} \tag{11}$$

where β is the attractiveness at $r = 0$.

Moreover, the movement of a firefly i is attracted to another attractive (brighter) firefly j is defined by the following equation:

$$x_i^{t+1} = x_i^t + \beta_0 e^{-\gamma r_{i,j}^2}(x_j^t - x_i^t) + \alpha_t \varepsilon_i^t \tag{12}$$

where α_t is random parameter and ε_i^t is a vector of random numbers taken from a Gaussian or uniform distribution at time t.

3 Bio-inspired Swarm Techniques for Thermogram Breast Cancer Detection System

In this section, four swarm optimization approaches will be used in thermal imaging clustering. These swarms are: PSO, GWO, MFO and FA. Moreover, the clustering results from each swarm version will be compared with each other. The overall architecture of the proposed swarm-based segmentation is summarized in Fig. 1.

3.1 Preprocessing Phase

Noises are always undesirable. So removing noise with preserving edges of the image plays a vital role in image processing. Median filter is one of the simplest and

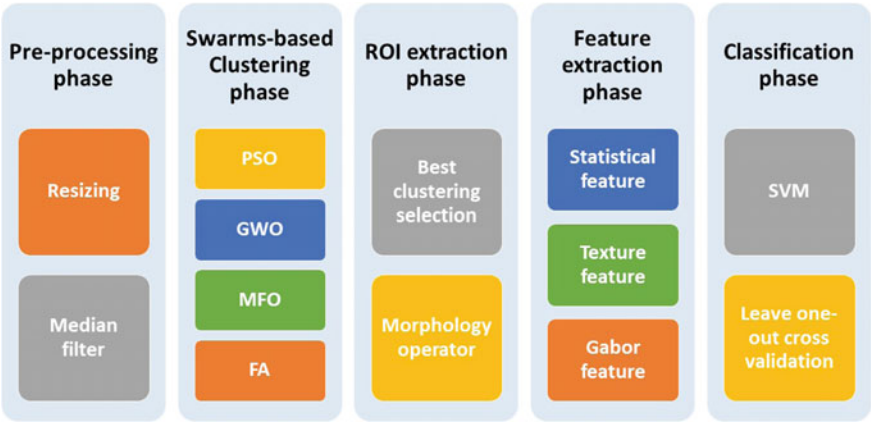

Fig. 1 The overall architecture of the proposed swarm-based segmentation

most popular approaches for removing noise like salt and pepper [25]. In this work, the original gray-scale thermal image will be resized in order to reduce computation time. Then, median filter with window size 3 * 3 is applied to enhance thermal image.

3.2 Thermal Image Clustering Phase

In this phase four versions of swarm will be adopted and the produced results from each of them will be compared with each other. For each version of swarm the adopted fitness function will be the maximum distance between each cluster. The parameters setting used for each version of swarm is summarized in Tables 1, 2, 3 and 4.

Table 1 Parameters setting of PSO

Population size	150
Number of iterations	10
ϕ_1	0.6
ϕ_2	0.6
x_{max}	255
x_{min}	0
v_{max}	2
v_{max}	−2
w	0.4
Number of levels	3

Table 2 Parameters setting of GWO

Parameter	Value (s)
Number of search agents	10
Number of iterations	5
Range (boundary of search space)	[0 255]
Dimension	2

Table 3 Parameters setting of FA

Parameter	Value (s)
Number of fireflies	10
Number of iterations	2
Range (boundary of search space)	[0 255]
Light absorption coefficient	1
Attraction coefficient base value	2
Dimension	2
Mutation coefficient	0.2
Mutation coefficient damping ratio	0.98

Table 4 Parameters setting of MFO

Parameter	Value (s)
Number of search agents	10
Number of iterations	5
Range (boundary of search space)	[0 255]
Dimension	2

3.3 ROI Extraction Phase

In this phase, the best cluster image which is representative of breast region of interest (ROI) will be selected from each swarm. In PSO, the best cluster image is selected based on maximum standard deviation calculated from each cluster image. In GWO, green channel of the produced cluster image is selected as the best cluster image. In MFO, red channel of the produced clustered image is selected as the best cluster image. In FA, green channel of the produced clustered image is selected as the best cluster image. After the best cluster image is selected, morphology operation like open and close are adopted in order to crop the breast region of interest. The pseudo steps of ROI extraction is same as in [5].

3.4 Features Extraction Phase

In this phase, several features are extracted from breast ROI. These features are: statistical, texture and gabor features. Texture feature is the property which represents the structure of an image. In this work, 22 texture features are calculated from

Haralick GLCM with the distance parameter $d = 1$ [26]. These features are: (1) Energy, (2) Entropy, (3) Dissimilarity, (4) Contrast, (5) Inverse difference, (6) Correlation, (7) Homogeneity, (8) Autocorrelation, (9) Cluster Shade, (10) Cluster Prominence, (11) Maximum probability, (12) Sum of Square, (13) Sum Average, (14) Sum Variance, (15) Sum Entropy, (16) Difference variance, (17) Difference entropy, (18) Information measures of correlation 1, (19) Information measures of correlation 2, (20) Maximal correlation coefficient, (21) Inverse difference normalized (IDN) and (22) Inverse difference moment normalized (IDMN). First statistical features (FOS) is the property which represents the statistical features of the image [27]. In this work, 5 statistical features are adopted. These features are: mean, standard deviation, median, mode, skewness and kurtosis. Gabor filters is defined as convolution kernel which is the product of a cosine function and a Gaussian. It characterized by specified orientation and specified spatial frequency [28]. In this work, 40 absolute Gabor coefficient features were extracted from the Gabor wavelet.

3.5 Classification Phase

In this section, SVM is adopted to classify the breast ROI to abnormal or normal. SVM is a supervised learning method that transforms input data to high-dimensional feature space using several kernel functions (i.e. polynomial, RBF, Linear and quadratic) where the transformed input data becomes more separable. It can solve linear and non-linear classification problem through finding optimal hyperplane with maximal margin [29]. Moreover, in order to evaluate the performance of each swarm version, one of cross validation algorithm is adopted. This algorithm is leave-one-out. Leave-one-out cross validation is one of the most commons of cross validation methods. It the degenerate case of K-Fold Cross Validation, where K is selected the total number of partitions. For a dataset with N points, perform N partitions, for each partition use N-1 for training and the left point for testing. The classification model is used to evaluate the error rate for only single point held out. A generalization error estimates is obtained by repeating the same procedure for each of training points partitions and then averaging the obtained results [30].

4 Experimental Results and Discussion

4.1 Dataset Description

A benchmark database [10] was used to evaluate the proposed CAD system. It contains 149 patients with images size of 640 * 480 pixels. Only frontal images are used to test the proposed CAD system. It contains 63 cases, 29 healthy and 34 malignant.

4.2 Results and Discussion

The proposed CAD system programmed in MATLAB-R 007 with Intel Core I3 and 2 GB of memory. Figures 2, 3, 4 and 5 show the clustering results and final extracted breast ROI using different version of swarm with same fitness function, (a) shows the original grayscale image after resizing it and applying median filter with size 3 * 3, (b) show the produced cluster results from using PSO, GWO, MFO and FA, (c) shows the selected cluster image, (d) shows the selected image after converting it to binary image using ostu' thresholding, (e) shows the binary image after applying open morphology and removing the connected regions to the boundary which are shoulders and stomach, (f) shows the results obtained after selecting the maximum region and get the maximum y-direction, (g) shows the ROI rectangle on the produced cluster image and (h) shows the final extracted ROI after enhancement through removing the background.

Figures 6, 7, 8 and 9 show the obtained classification results produced from each version of swarm using different kernel functions of svm and leave-one-out cross validation method in terms of specificity, sensitivity, precision and accuracy. As it can bee seen in Fig. 6, linear kernel function is best one which gives highest accuracy rate. It obtains overall Accuracy 85.71 %, Sensitivity 83.33 %, Specificity

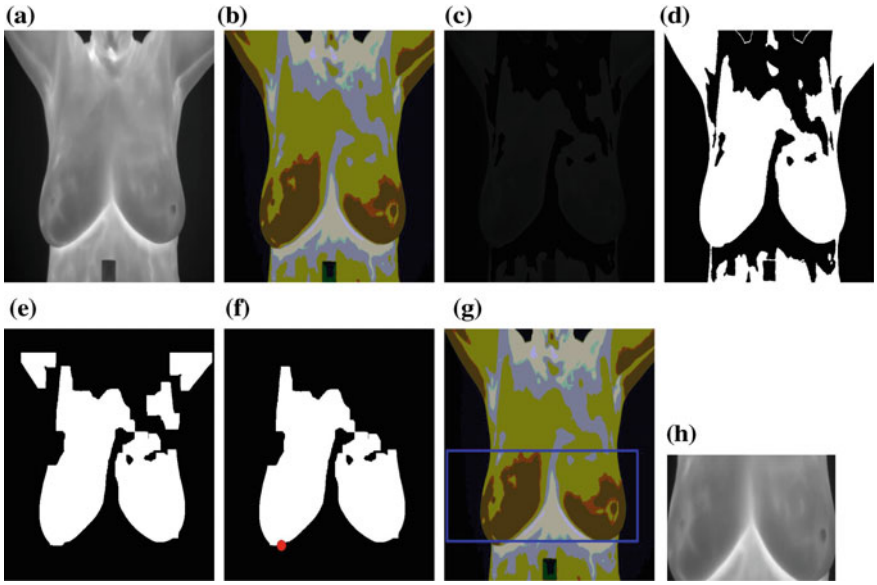

Fig. 2 Results of thermal image clustering and ROI extraction phase (PSO results). **a** Original thermal image after resizing and applying median filter, **b** PSO clustering results, **c** selected cluster image, **d** selected cluster image after converting it to binary, **e** image after remove regions connected to the boundary, **f** image after selecting maximum regions, **g** selected ROI and **h** final extracted ROI after enhancement

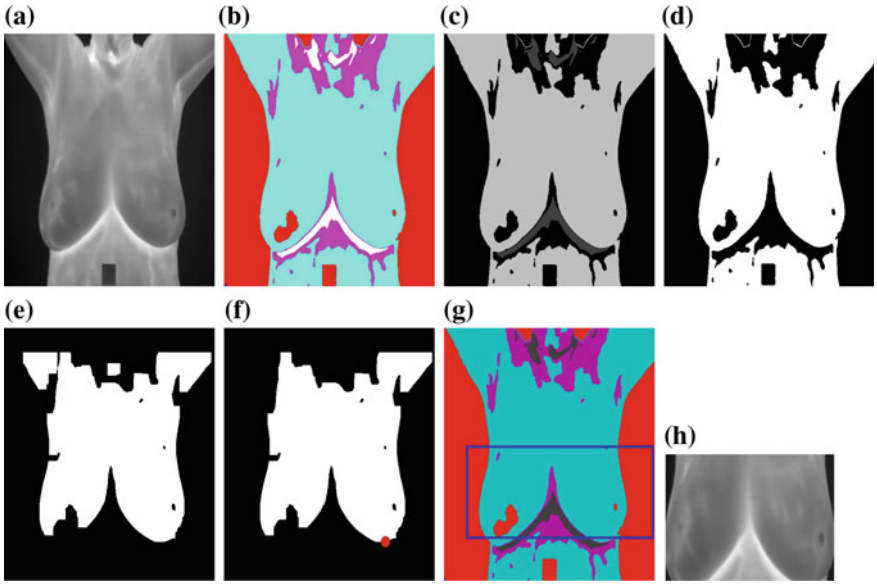

Fig. 3 Results of thermal image clustering and ROI extraction phase (GWO results). **a** Original thermal image after resizing and applying median filter, **b** GWO clustering results, **c** selected cluster image, **d** selected cluster image after converting it to binary, **e** image after remove regions connected to the boundary, **f** image after selecting maximum regions, **g** selected ROI and **h** final extracted ROI after enhancement

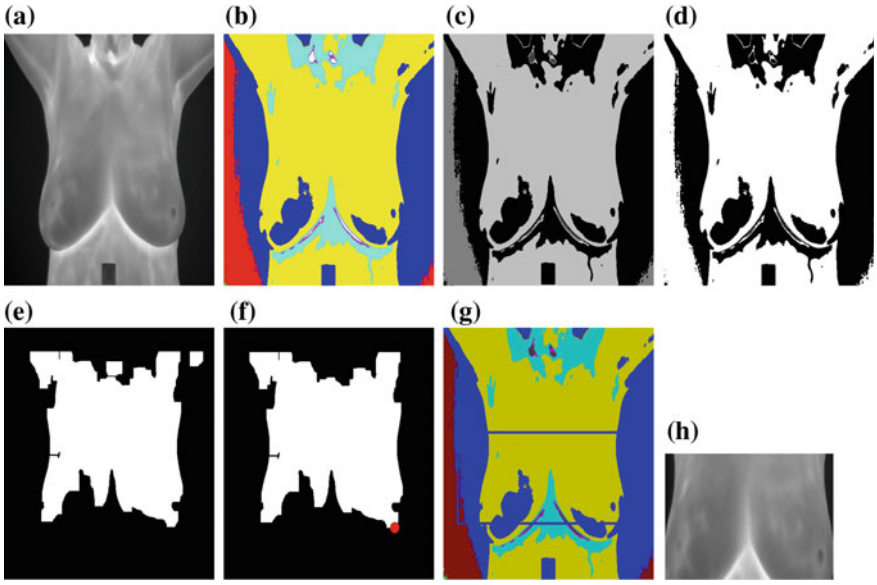

Fig. 4 Results of thermal image clustering and ROI extraction phase (MFO results). **a** Original thermal image after resizing and applying median filter, **b** MFO Clustering results, **c** selected cluster image, **d** selected cluster image after converting it to binary, **e** image after remove regions connected to the boundary, **f** image after selecting maximum regions, **g** selected ROI and **h** final extracted ROI after enhancement

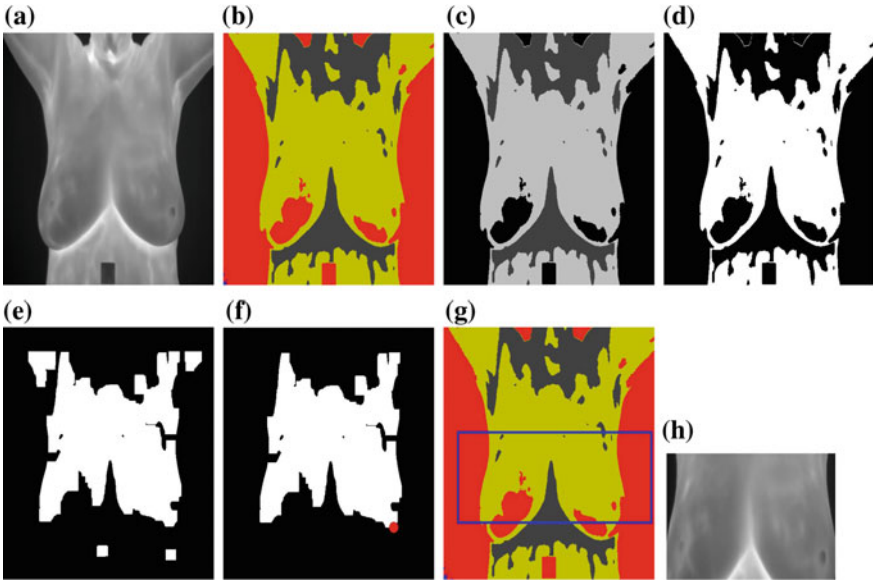

Fig. 5 Results of thermal image clustering and ROI extraction phase (FA results). **a** Original thermal image after resizing and applying median filter, **b** FA clustering results, **c** selected cluster image, **d** Selected cluster image after converting it to binary, **e** image after remove regions connected to the boundary, **f** image after selecting maximum regions, **g** selected ROI and **h** final extracted ROI after enhancement

88.89 % and Precision 90.91 %. Also Fig. 7 shows linear is best kernel function. It obtains overall Accuracy 84.12 %, Sensitivity 91.17 %, Specificity 75.56 % and Precision 81.58 %. For Fig. 8 polynomial is the best kernel function. It obtains

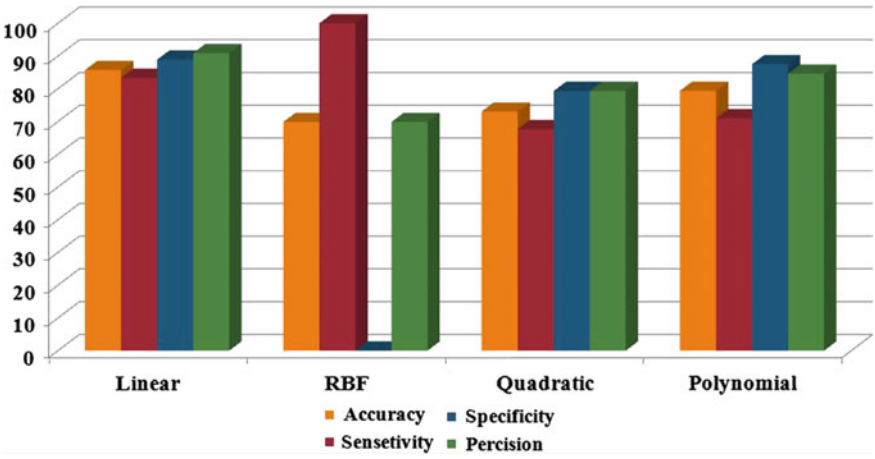

Fig. 6 Leave-one-out cross validation results of using PSO in CAD system

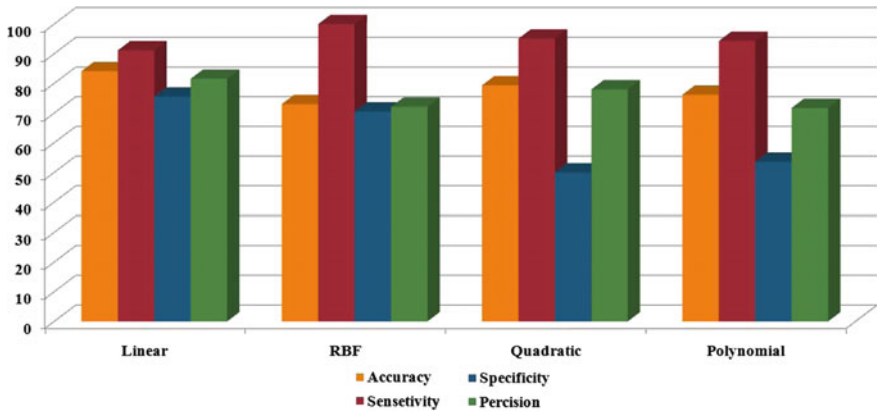

Fig. 7 Leave-one-out cross validation results of using GWO in CAD system

overall Accuracy 85.71 %, Sensitivity 97.14 %, Specificity 71.43 % and Precision 80.95 %. However, Fig. 9 shows linear is the best kernel function too. It obtains overall Accuracy 96.83 %, Selectivity 94.87 %, Specificity 100 % and Precision 100 %. Figure 10 compares the obtained the highest results obtained from using different swarm versions which mean the obtained results using linear kernel function for PSO, GWO and FA and the obtained results from polynomial kernel function for MFO. As it can be seen, FA is the best swarm version as it obtains highest accuracy, sensitivity, precision and specificity.

Figure 11 compares the elapsed time taken from each swarm in order to produce the clustering results. As it can be seen, MFO takes less time compared with the others and FA is in the second place.

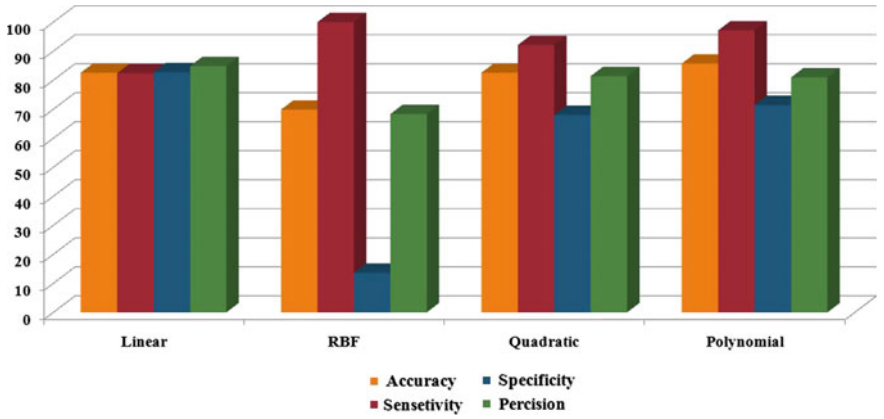

Fig. 8 Leave-one-out cross validation results of using MFO in CAD system

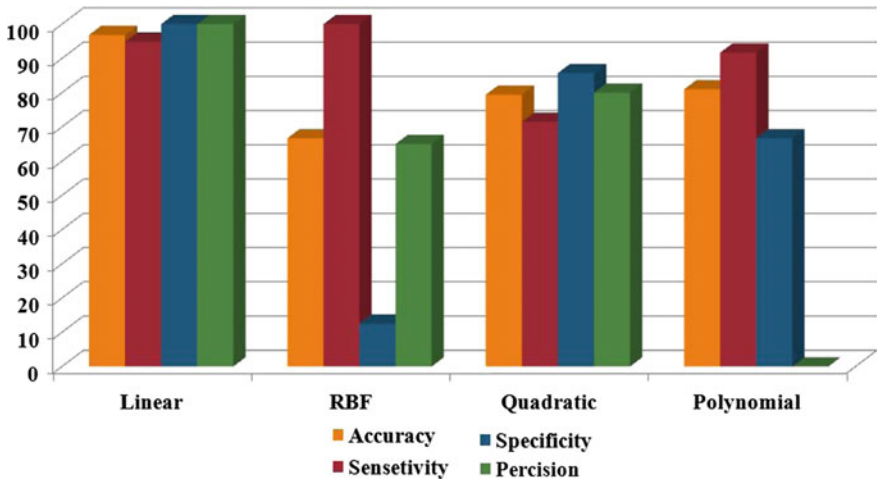

Fig. 9 Leave-one-out cross validation results of using FA in CAD system

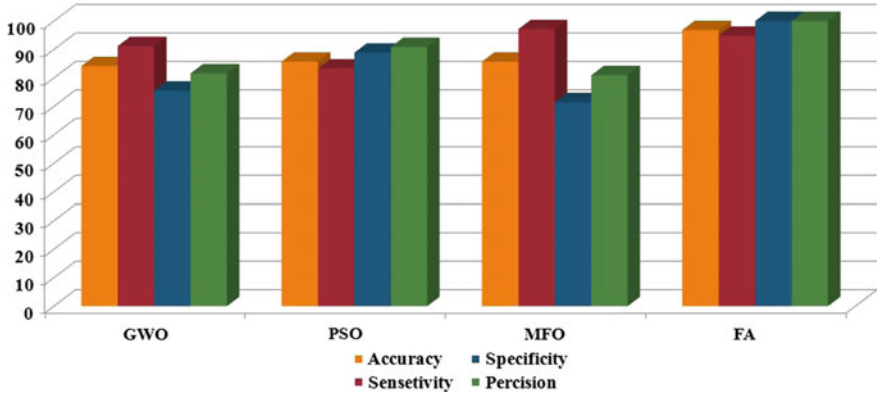

Fig. 10 Leave-one-out cross validation results of using different swarm versions in CAD System

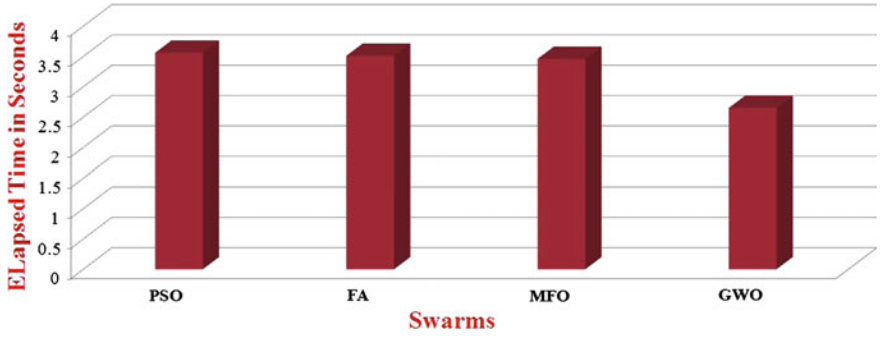

Fig. 11 Comparison between swarm versions in terms of processing time

5 Conclusions and Future Work

In this chapter, an automatic computer aided diagnosis scheme that uses four swarms techniques has been presented. An application of thermography breast cancer imaging has been chosen and the scheme have been applied to see their ability and accuracy to classify the breast cancer images into two outcomes: normal or non-normal. Support Vector Machine with its kernel functions was used to detect the normal and abnormal cases. Based the experimental results, it was found that the SVM-linear kernel function is best one which gives highest accuracy rate in all proposed swarms algorithms. Comparing different swarm versions with obtained results using linear kernel functions for PSO, GWO and FA and MFO is performed. It can be seen that, FA is the best swarm version as it obtains highest accuracy, sensitivity, precision and specificity. In the future, there is a research direction of increasing the dataset used in order to test the reliability of the proposed CAD system. Also, more enhancements could be provided to the system by using modified versions of different swarms algorithms. The modifications aim to reduce number of swarm parameters in order to limit user interaction with the automatic system.

References

1. Gogoi, U., Majumdar, G., Bhowmik, M., Ghosh, A., Bhattacharjee, D.: Breast abnormality detection through statistical feature analysis using infrared thermograms. In: International Symposium on Advanced Computing and Communication (ISACC), pp. 258–265 (2015)
2. Pramanik, S., Bhattacharjee, D., Nasipuri, M.: Wavelet based thermogram analysis for breast cancer detection. In: International Symposium on Advanced Computing and Communication (ISACC), pp. 205–212 (2015)
3. Dheeba, J., Singhemail, N., Selviemail, S.: Computer-aided detection of breast cancer on mammograms: a swarm intelligence optimized wavelet neural network approach. J. Biomed. Inform. **49**, 45–52 (2014)
4. Tahmoush, D.: Image similarity to improve the classification of breast cancer images. J. Algorithms 1503–1525 (2009)
5. Gaber, T., Sayed, G., Anter, A., Soliman, M., Ali, M., Semary, N., Hassanien, A., Snasel, V.: Thermogram breast cancer detection approach based on neutrosophic sets and fuzzy C-means algorithm. In: 37th Annual International Conference of the IEEE Engineering in Medicine and Biology Society (EMBC), IEEE, Milano, Italy, pp. 4254–4257 (2015)
6. Milosevic, M.: Dragan Jankovic and Aleksandar Peulic Comparative analysis of breast cancer detection in mammograms and thermograms. J. Biomed. Eng. **60**(1), 49–56 (2015)
7. Arora, N., Martins, D., Ruggerio, D., Tousimis, E., Swistel, A.J., Osborne, M.P., Simmons, R. M.: Effectiveness of a noninvasive digital infrared thermal imaging system in the detection of breast cancer. Am. J. Surg. 523–526 (2008)
8. Gonzlez, F.J.: Non-invasive estimation of the metabolic heat production of breast tumors using digital infrared imaging. Quant. InfraRed Thermography J. **8**, 139–148 (2011)
9. Ali, M., Sayed, G., Gaber, T.: Detection of breast abnormalities of thermograms based on a new segmentation method. In: Proceedings of the Federated Conference on Computer Science and Information System, vol. 5, pp. 255–261. doi:10.15439/2015F318 (2015)

10. Silva, L., Saade, D., Sequeiros, G., Silva, A., Paiva, A., Bravo, R., Conci, A.: A new database for breast research with infrared image, J. Med. Imaging Health Inform. **4**(1), 92–100 (2014)
11. Suganthi, S.S., Ramakrishnan, S.: Semi Automatic Segmentation of Breast Thermograms Using Variational Level Set Method. In: The 15th International Conference on Biomedical Engineering, IFMBE Proceedings, vol. 43, pp. 231–234 (2014)
12. Suganthi, S.S., Ramakrishnan, S.: Analysis of breast thermograms using gabor wavelet anisotropy index. J. Med. Syst. **38**(101), 1–7 (2014)
13. Suganthi, S., Ramakrishnan, S.: Analysis of breast thermogramsbusing gabor wavelet anisotropy index. J. Med. Syst. **38**(9), 1–7 (2014)
14. Prabha, S., Anandh, K., Sujatha, C., Ramakrishnan, S.: Total variation based edge enhancement for level set segmentation and asymmetry analysis in breast thermograms. In: 36th Annual International Conference of the IEEE in Engineering in Medicine and Biology Society (EMBC), pp. 6438–6441 (2014)
15. Fathy, M.E., Hussein, A.S., Tolba, M.F.: Fundamental matrix estimation: a study of error criteria. Pattern Recogn. Lett. **32**(2), 383–391 (2011)
16. Abraham, A., Hassanien, A.: Foundations of Computational Intelligence, vol. 4: Bio-Inspired data mining, Germany, studies in computational intelligence, Springer, Verlag (2009)
17. Neumann, F., Witt, C.: Bioinspired computation in combinatorial optimization: algorithms and their computational complexity. Natural Computing Series, Springer, ISBN 978–3-642-16543-6 (2010)
18. Thangaraj, R., Pant, M., Abraham, A., Bouvry, P. (2011) Particle swarm optimization: Hybridization perspectives and experimental illustrations. Appl. Math. Comput. **217**(12), 5208–5226 (2011)
19. Torn, A., Zilinskas, A. (eds.): Global Optimization. Lecture Notes in Computer Science, vol. 350. Springer (1989)
20. Kennedy, J., Eberhart, R.: Particle swarm optimization. In: Proceedings of IEEE International Conference on Neural Networks, vol. 4, pp. 1942–1948, Perth, WA (1995)
21. Hammouche, K, Diaf, M., Siarry, P.: A comparative study of various metaheuristic techniques applied to the multilevel thresholding problem. Engineering Applications of Artificial Intelligence, Elsevier, vol. 23, no. 5, pp. 676–688 (2010)
22. Mirjalili, S.M., Lewis, A.: Grey Wolf Optimizer. Elsevier **69**, 44–61 (2014)
23. Mirjalili, S.: Moth-flame optimization algorithm: a novel nature-inspired heuristic paradigm. Knowl.-Based Syst. Elsevier **89**, 228–249 (2015)
24. Yang, X.: Firefly algorithms for multimodal optimisation. Proceeding 5th Symposium on Stochastic Algorithms, Foundations and Applications, Lecture Notes in Computer Science, vol. 5792, pp. 169–178 (2009)
25. Sakthivel, N., Prabhu, L.: Mean-median filtering for impulsive noise removal. Int. J. Basics Appl. Sci. **2**(4), 47–57 (2014)
26. Haralick, R.M., Shanmugam, K., Dinstein, I.H.: Textural features for image classification. IEEE Trans. Syst. Man Cybern. **3**(6), 612–621 (1973)
27. Aggarwal, N., Agrawal, R.: First and second order statistics features for classification of magnetic resonance brain images. J. Signal Inform. Process. vol. 3, pp. 146–153 (2012)
28. Grigorescu, S., Petkov, N., Kruizinga, P.: Comparison of texture features based on Gabor filters. IEEE Trans. Image Process. **11**(10), 1160–1168 (2002)
29. Xu, H., Caramanis, C., Mannor, S.: Robustness and regularization of support vector machines. J. Mach. Learn. Res. **10**, 1485–1510 (2009)
30. Gawely, C.: Leave-One-Out Cross Validation Based Model Selection Criteria for Weighted LS-SVMS. In: International Joint Conference on Neural Networks (IJCNN), IEEE, Madrid, pp. 1661–1668 (2006)